PH

Volu

THE PHYSICAL REVIEW

A journal [illegible] and theoretical physics established by E. L. Nichols in 1893

Published by the American [illegible]
for the
AMERICAN PHYSICAL [illegible]

Officers

President

C. C. LAURITSEN
California Institute of [illegible]
Pasadena, California

Vice-President

J. H. VAN VLECK
Harvard University
Cambridge, Massachusetts

Secretary

K. K. DARROW
Bell Telephone Laboratories
Office:
Columbia University
New York 27, New York

Treasurer

G. B. PEGRAM
Columbia University
New York 27, New York

Local Secretary
for the Pacific Coast

J. KAPLAN
University of California
Angeles
Los Angeles, California

Managing Editor

S. A. GOUDSMIT
Brookhaven National Laboratory
Upton, Long Island
New York

BOARD OF EDITORS

Editor

S. A. Goudsmit

Assistant Editor

S. Borowitz

Associate Editors

J. Barnothy	Harvey Brooks	M. Goldhaber
F. Bloch	R. F. Christy	E. Hutchisson
E. U. Condon	C. L. Critchfield	A. W. Lawson
W. R. Leaf, Jr.	M. Deutsch	J. Peebles
A. J. F. Siegert	T. H. Johnson	R. Serber
W. E. Stephens	Bruno Rossi	C. H. Townes

Manuscripts for publication should be submitted to S. A. Goudsmit, Brookhaven National Laboratory, Upton, Long Island, New York. Authors' institutions are requested to pay a publication charge of $10 per page which, if honored, entitles them to 100 free reprints. Instructions will be sent with galley proofs.

Proof and all correspondence concerning papers in the process of publication should be addressed to the Publication Manager, American Institute of Physics, 57 East 55 Street, New York 22, New York.

Subscription Price

United States and Canada $12.00
Elsewhere $13.00

Back Numbers[1]

Yearly back number rate when complete year is available:
Prior to 1949: $20.00
Thereafter: $27.00

Single copies: $2.00 each, prior to July, 1929;
$1.00 each, July, 1929–December, 1941;
$2.00 each, January, 1942–December, 1946;
$1.00 each, January, 1947–December, 1948;
$1.25 each, thereafter.

General index, 1893–1920: $4.00.

Subscriptions, renewals, and orders for back numbers should be addressed to the American Institute of Physics, 57 East 55 Street, New York 22, New York.

Changes of address in the case of members of the American Physical Society should be addressed to the Treasurer; in the case of other subscribers to the American Institute of Physics.

[1] Per Series I [illegible] of Physics Department, Cornell University, Ithaca, New York.

The Physical Review is published [illegible] and monthly at Prince and Lemon Streets, Lancaster, Pennsylvania.

Entered as second-class matter [illegible], 1949, at the Post Office at Lancaster, Pennsylvania, under the Act of March 3, 1879.

Acceptance for mailing at special rate of postage provided for in paragraph (d-2), section 34.40, P. L. & R. of 1948, authorized January 23, 1925.

THE
PHYSICAL REVIEW

A journal of experimental and theoretical physics established by E. L. Nichols in 1893

SECOND SERIES, VOL. 84, NO. 4 NOVEMBER 15, 1951

The Drift Velocities of Molecular and Atomic Ions in Helium, Neon, and Argon

JOHN A. HORNBECK
Bell Telephone Laboratories, Murray Hill, New Jersey
(Received August 6, 1951)

Drift velocity measurements as a function of E/p_0, the ratio of field strength to normalized gas pressure, are presented for atomic and molecular ions of He, Ne, and A in their respective parent gases. Identification of the molecular ions is based upon the time resolution of the apparatus and the dependence of ion concentration on pressure, applied voltage, and gas purity. Extrapolation of the low field measurements to zero field yields mobility values for atomic ions, $\mu_0(He^+)=10.8$ cm²/volt sec, $\mu_0(Ne^+)=4.4$, and $\mu_0(A^+)=1.63$ in good agreement with theory: Massey and Mohr compute $\mu_0(He^+)=11$, and Holstein gives $\mu_0(Ne^+)=4.1$ and $\mu_0(A^+)=1.64$. Drift velocity data at low field for the molecular ions agree within experimental error with data of Tyndall and Powell (He), and Munson and Tyndall (Ne and A), which they assigned to atomic ions. A qualitative description in terms of ion-atom interaction forces is given for the observed field variation of the atomic ion drift velocities up to high E/p_0.

THE drift velocity of positive ions and its variation with the electric field are fundamental in any discussion of a gaseous discharge in which positive ions are an important carrier of current. From the viewpoint of more fundamental theory, drift velocity measurements provide information on the interaction forces between an ion and an atom as well as on the kinetic theory of ion motion in a gas at high fields, where the velocity distribution of the ions is not Maxwellian.

In this paper measurements are presented on the drift velocity of both molecular and atomic ions of helium, neon, and argon in their respective parent gases. Arguments for the identification of the ions are given, and it is shown that, as a result of this identification, good agreement results between theory and experiment for the drift velocities of both species of ions in all three gases. It is concluded that in some cases earlier workers incorrectly identified molecular ions as atomic ions. A mechanism of formation of the molecular ions that is consistent with the experiment is discussed briefly, as is the drift velocity variation of the atomic ions at high fields.

IDENTIFICATION OF MOLECULAR AND ATOMIC IONS

A method has been described[1] for measuring the drift velocity of positive ions in the parent gas by direct observation of the ion transit time between parallel plate electrodes in a uniform field. The experiment consists of measuring the time at which a sharp break occurs in the transient current following the release of a short (0.1 μsec) pulse of photoelectrons from the cathode of a Townsend discharge tube. An experimental transient current pattern, reproduced from a photograph of a cathode-ray-tube trace, is shown in Fig. 1. This pattern is typical of all three noble gases for $E/p>50$ volts/cm-mm Hg, where E is the electric field strength and p is the gas pressure.

If two species of ions are formed during the photoelectric pulse, two current breaks should occur. These will be resolved if the transit times for the two ions differ by more than about ten percent. Figure 2 is a transient current pattern in argon at lower E/p showing the presence of two different ions. Similar patterns are obtained in helium and neon. In each case, the ion that is found only at low E/p has the shorter transit time, i.e., it gives the first break in Fig. 2.

We identify the slow ion as the ordinary atomic ion of the parent gas (He^+, Ne^+, A^+) because it is easily formed by electron impact over a wide range of E/p. Formation of He^{++}, Ne^{++}, and A^{++} can be ruled out since both breaks are observed when the total voltage across the tube is less than the appearance potentials for these ions.

This leaves two reasonable hypotheses as to the

[1] J. A. Hornbeck, Phys. Rev. 83, 374 (1951).

FIG. 1. Oscillogram of transient current in argon. The sharp drop in current occurs at the time for one ion transit between the parallel plate electrodes. This and similar patterns in helium and neon are found for $E/p > 50$ volts/cm-mm Hg.

identity of the fast ions: (1) impurity ions, and (2) molecular ions (He_2^+, Ne_2^+, and A_2^+). Low E/p should favor ionization of an impurity atom relative to the main gas constituent, in general, because of the lower ionization potential of most non-rare-gas atoms. Both low E/p and high pressure favor the production of molecular ions in the formation process discussed below. The choice between these hypotheses must be made on the basis of experimental evidence.

The evidence at hand is the following: (1) The double break effect is observed to be reproducible in magnitude with different gas samples and different vacuum procedures. (2) Samples of the gases used, which were purchased as spectroscopically pure, have been sealed off from the experimental tube and subjected to mass spectrometer analysis. No impurities have been detected by this instrument, which had a sensitivity limit of 0.005 percent. (3) Flashing additional Ba-Mg getters in a tube filled with gas that had been sampled and analyzed in no way affected the observed pattern. (4) The residual gas pressure after exhaust of the tube and prior to the introduction of the gas was probably less than the ionization gauge reading of 2×10^{-8} mm Hg. This evidence suggested strongly that impurities in the gas could not account logically for the presence of the fast ion. We conclude that molecular ions, which are known to exist,[2] are formed quite easily at low E/p and moderate pressure.

The sharpness of the current break associated with the molecular ions restricts severely the number of mechanisms one might advance to account for their formation. As shown in Fig. 2, the time width of the two breaks is about the same, and this has been ascribed[1] to diffusion. From the width of the current break we conclude that the molecular ions are formed within about one microsecond, or less, after the initial photopulse. This rules out a process such as a three-body collision[3] between an atomic ion and two neutral atoms forming a molecular ion and, in general, a higher speed neutral atom; this process would smear out both current breaks, and also a longer time would be required before a three-body collision is very likely. Because of the time restrictions, the only reasonable process appears to be a collision between a neutral atom and an atom He* raised to a high-lying excited state (by electron impact during the photopulse) before the excited atom decays; for example,

$$He^* + He \rightarrow He_2^+ + e.$$

Here e stands for the liberated electron. The excited state involved cannot be a metastable state, as proposed by Arnot and M'Ewen[4] in the case of helium, because of the known long lifetimes of metastable atoms in the rare gases. The lifetimes of the states in question, therefore, are about 10^{-7} sec or less. Thus on the time scale of this experiment, the molecular ions observed are probably formed as fast as the atomic ions. Mass spectrometer studies that support the formation process discussed above are presented in the following article in this issue.

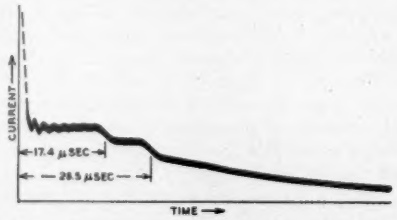

FIG. 2. Oscillogram of transient current in argon at low E/p ($p_0 = 5.13$ mm Hg, $E/p_0 = 36.6$ volts/cm-mm Hg). The current breaks at 17.4 μsec and 26.5 μsec indicate the presence of two ions of different transit times. The broken line at the start of the trace indicates the current due to the short photopulse that initiated the transient current. Similar oscillograms with two current breaks are found in helium and neon at low E/p.

GENERAL DRIFT VELOCITY MEASUREMENTS

Experimental data on the drift velocity of atomic ions are given in Fig. 3. Here on a log-log scale we plot the drift velocity v as a function of E/p_0. The normalized pressure is defined as $p_0 = 273p/T$, where p is the measured gas pressure and T is gas temperature, in our case $\simeq 300°K$. Three regions are readily identified in Fig. 3. At high E/p_0, v approaches tangency to a straight line of slope $\frac{1}{2}$ indicating $v \propto (E/p_0)^{\frac{1}{2}}$. At low E/p_0, v approaches tangency to a line of slope 1, indicating $v \propto E/p_0$. A transition region at intermediate E/p_0 connects the high and low field regions.

A qualitative explanation of these regions can be given in terms of the ion-atom interaction forces and the velocity distribution of the ions, factors that we shall now consider in a short digression. The major interaction forces[5] are: (a) gas kinetic repulsion, (b) polarization attraction, and (c) symmetry forces. We shall assume that gas kinetic repulsion can be accounted for by a model in which the ions and atoms are hard elastic spheres whose closest distance of approach is fixed by the sum of the radii of the colliding particles.

[2] O. Tüxen, Z. Physik **103**, 463 (1936).

[3] Molecular ions can probably be produced in this way at higher gas pressure.

[4] F. L. Arnot and M. B. M'Ewen, Proc. Roy. Soc. (London) **A171**, 106 (1939).

[5] Van der Waals attraction can probably be ignored here.

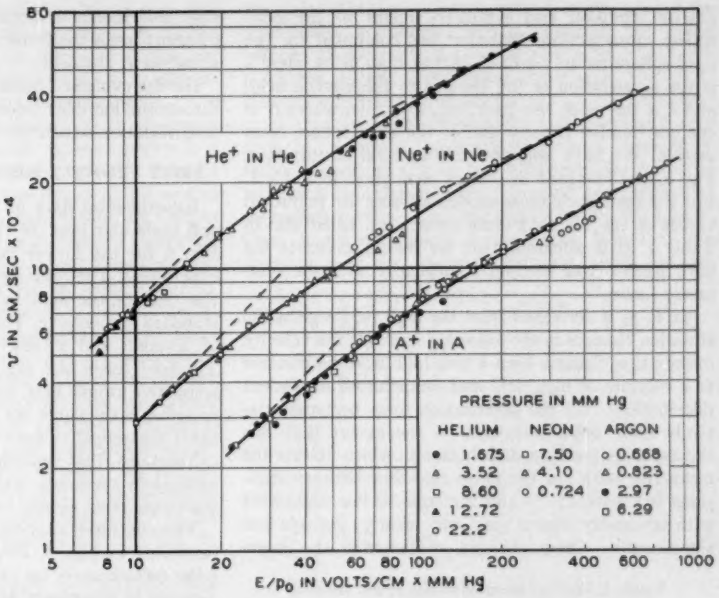

FIG. 3. The drift velocity of atomic ions in helium, neon, and argon as a function of E/p_0. The broken lines at the left of each experimental curve have slope = 1, whereas the broken lines at the right have slope = $\frac{1}{2}$.

Polarization attraction arises because an ion induces a dipole moment on a neighboring atom and thus attracts it. The magnitude of this force is directly proportional to the polarizability of the gas and inversely proportional to the fifth power of the separation of the particles. Massey and Mohr[6] have pointed out that symmetry effects, which arise on account of the identity of the cores of the atomic ion and gas atom, include what we may call resonance attraction and resonance repulsion together with charge exchange, i.e., the shuttling of an electron back and forth between the ion and atom during a collision. For helium they show that the symmetry forces vary rapidly in a short range and therefore are somewhat similar to gas kinetic repulsion although of longer range.

The elastic sphere model gives a collision cross section that is independent of the velocity of approach of the colliding particles and also a constant mean free path between collisions. The cross section for polarization attraction[7] is inversely proportional to the velocity of approach, which gives a constant mean free time between ion-atom collisions. As a whole, symmetry forces give a cross section that varies slowly with the relative velocity of approach of the ion and atom. No calculation of this variation in cross section is available in the literature. To the extent that this variation is small, a hard sphere model with its accompanying constant mean free path may be assumed. The evidence from this experiment supports making this assumption, as we shall point out.

The velocity distribution function of the ions is Maxwellian at very low fields because of sufficient energy interchange with gas atoms. At very high field strengths, where thermal energy is negligible compared with the energy derived from the field, the distribution function is known, through the work of Wannier,[8] only in the case of constant mean free time. Without knowing the distribution function explicitly, velocity averages have, however, also been computed by Wannier for the high field case in which the mean free path is constant. He finds in this case $v \propto (E/p_0)^{\frac{1}{2}}$, and he finds $v \propto E/p_0$ for the constant mean free time case. This last result is independent of the velocity distribution, i.e., applies regardless of the magnitude of E/p_0. We also know[9] that at very low fields the elastic sphere model by itself gives $v \propto E/p_0$. We are now ready to interpret the three regions in Fig. 3.

In the limit of high field and thus high velocity of approach, the cross section associated with polarization attraction becomes very small. The drift velocity should vary, therefore, as $(E/p_0)^{\frac{1}{2}}$ to the extent that symmetry effects and gas kinetic repulsion approximate the elastic sphere model. Experimentally we find no reason to dispute the hard sphere model although we recognize the limited range of the experiment. Theory aids us in estimating the relative contributions of gas

[6] H. S. W. Massey and C. B. O. Mohr, Proc. Roy. Soc. (London) A144, 188 (1934).

[7] The definition of this cross section requires especial care. It can be defined to a good approximation according to G. H. Wannier, private communication.

[8] G. H. Wannier, Phys. Rev. 83, 281 (1951).

[9] See H. R. Hassé, Phil. Mag. 1, 139 (1926).

kinetic repulsion and symmetry forces to the hard sphere cross section. Wannier[8] has computed for the hard sphere model $v=1.147(a\lambda)^{\frac{1}{2}}$ at high fields. Here a is the acceleration of the ion due to the electric field, and λ is the mean free path, i.e., $\lambda=1/N\sigma_i$ where N is the gas number density and σ_i the hard sphere cross section. We have applied[10] this formula to the data, Fig. 3, and obtained the values of σ_i given in Table I. For the gas kinetic cross section we may use published values of the viscosity cross section, σ_a, listed also in Table I. It is apparent that we should associate the hard sphere cross sections σ_i primarily with the symmetry forces.[11]

As E/p_0 is decreased from the high field region, the situation changes in the following way: (1) the velocity distribution changes from a true high field distribution to a mixture of high field and temperature dependent distributions; (2) the polarization force becomes relatively more important, and, to the extent that this occurs, there results a distribution in which neither the mean free path nor the mean free time between collisions is constant; (3) and the cross section associated with symmetry effects may vary slowly, perhaps not significantly. These changes characterize the intermediate region of Fig. 3. Of the three effects, the velocity distribution change appears to be the most important because even in the low field case, as we shall see, the hard sphere cross section seems to be the major factor in determining the drift velocity.

TABLE I. Hard sphere cross section σ_i and viscosity cross section σ_a.

	$\sigma_i \times 10^{15}$ cm^2	$\sigma_a \times 10^{15}$ cm^2
Helium	54.3	14.9
Neon	65.2	21.0
Argon	134	41.7

As E/p_0 is decreased still further, the above mentioned changes continue, and we approach the low field region. Here the energy contributed from the field is small (and this need not be very small) compared with thermal energy, the velocity distribution becomes Maxwellian, and v must become proportional to E/p_0 because the field is so small. It was mentioned above that if scattering in this region were caused primarily by the polarization force, the mobility would be constant (or nearly so) for this reason alone, regardless of the field strength. The evidence in the following section on low field mobility suggests that this effect is not very important at room temperature. Again, to the extent that polarization is important there will be a mixed constant mean free time and constant mean free path situation at low field.

Having explained qualitatively the E/p_0 variation of the atomic ion drift velocity, we now consider the low field variation separately.

DRIFT VELOCITY MEASUREMENTS AT LOW E/p_0

Experimental data on the drift velocity of atomic and molecular ions (in the parent gases) are given in Fig. 4 for the lowest range of E/p_0 reached in this experiment. The ordinate μ is the mobility, defined as the ratio of the drift velocity to the electric field at standard gas density. The experimental measurements of Tyndall and Powell[12] (helium) and Munson and Tyndall[13] (neon and argon), assigned by them to the respective atomic ions, are shown for comparison. Also included in the figure are the low field (essentially zero-field) theoretical values[6,14] for μ, which are based upon calculations that include charge exchange and the anomalous resonance interactions characteristic of the scattering of an atomic ion in the parent gas.

Two conclusions appear to be warranted from the data presented in Fig. 4. First, the measurements by the pulse technique on the atomic ions at low E/p_0 in each case are in agreement with the theoretically predicted "zero-field" mobility, μ_0: extrapolation of the experimental curves to $E/p_0=0$ yields, $\mu_0(He^+)=10.8$ cm^2/volt-sec, $\mu_0(Ne^+)=4.4$, and $\mu_0(A^+)=1.63$, whereas theory predicts $\mu_0^6(He^+)=11$, $\mu_0^{14}(Ne^+)=4.1$, and $\mu_0^{14}(A^+)=1.64$. Second, the measurements by the pulse technique on the molecular ions agree within experimental error with the measurements of Tyndall *et al.*, which they ascribed (quite understandably) to the atomic ions of the parent gases. Thus the long-standing discrepancy between theory and experiment as to the zero-field mobility of He^+ in helium apparently is resolved in accord with the suggestion of Meyerott[15] that Tyndall and Powell incorrectly identified the ion measured in their apparatus. It is significant that reproducible results on the mobilities of ions in the parent rare gases are now being obtained; for not only the molecular ion measurements just mentioned, but also other measurements[16] on $\mu_0(He^+)$ agree within experimental error with the data in Fig. 3.

In addition to the experimental error in measuring μ, another error arises in the predicted values of μ_0 from the present measurements because the correct procedure for extrapolating the data to zero field is not known. Some confidence in the simple method used

[10] J. A. Hornbeck and G. H. Wannier, Phys. Rev. **82**, 458 (1951).

[11] This treatment of the high field case is somewhat similar to that of L. Sena, J. Phys. (U.S.S.R.) **10**, 179 (1946) because the mean free path is assumed to be (approximately) constant. Attributing the constant mean free path to charge exchange alone, as Sena did, is incorrect in principle. It leads to obvious mistakes in the conclusion one reaches regarding the velocity distribution of the ions, and it leads to a predicted collision cross section that is too small, although of the right order of magnitude.

[12] A. M. Tyndall and C. F. Powell, Proc. Roy. Soc. (London) **A134**, 125 (1931).

[13] R. J. Munson and A. M. Tyndall, Proc. Roy. Soc. (London) **A177**, 187 (1940).

[14] T. Holstein, private communication.

[15] R. Meyerott, Phys. Rev. **70**, 671 (1946).

[16] M. A. Biondi and S. C. Brown, Phys. Rev. **75**, 1700 (1949). The identity of the ions in this experiment has not been established completely, however.

here can be obtained from reasoning based upon the Langevin mobility formula and a knowledge of the interaction forces between an ion and an atom. Because the Langevin formula will be of general use in our discussion, the assumptions behind it will be stated.

In the Langevin theory of ionic mobility it is assumed (1) that the ions are hard, elastic spheres moving in a polarizable gas comprised of elastic spheres; and (2) that the velocity distribution function of both ions and gas atoms is Maxwellian and characterized by the gas temperature. In this model the interaction forces are polarization attraction and gas kinetic repulsion. For a given gas density and at low applied field (because of the assumption regarding the velocity distribution of the ions), the mobility of an ion in a gas depends, then, only upon the polarizability of the gas, the hard sphere collision cross section, and the gas temperature. We are not restricted, however, to interpreting the hard sphere cross section as originating from gas kinetic repulsion; it cannot be smaller than the hard sphere cross section associated with symmetry effects, which we derived from the high field data. It is this latter cross section we shall interpret as the repulsion cross section in the Langevin theory and see what information can be obtained.

According to Langevin's theory, one limiting value of the mobility, dependent only on the repulsion cross section, derives from the case in which polarization attraction is negligible compared with the repulsion cross section. As polarization becomes more important relatively, the mobility increases from this limiting value and passes through a maximum somewhat before the other limit is reached of a repulsion cross section negligible compared with the polarization effect. Substitution of the hard sphere cross sections, Table I, and published values of the polarizability of the gases in the Langevin formula yields, in Hassé's[9] notation,[17] $A\lambda$ values of about 0.7 for the three gases. This indicates that the atomic ion mobilities do not depend greatly upon the polarization force because the limiting values of $A\lambda$ are 0.75 for the case of negligible polarization effect and 0 for the case of negligible hard sphere scattering. The theory, in fact, predicts fairly satisfactorily the low field mobilities of the atomic ions. It gives $\mu_0(He^+)=13.4$, $\mu_0(Ne^+)=4.85$, and $\mu_0(A^+)=1.67$. We conclude, therefore, that our interpretation of the symmetry forces as a hard sphere cross section is at least semiquantitative.

The results of the previous paragraph give us some confidence that the extrapolation of our data to zero field is not made through a maximum in the μ *vs* E/p_0 curve, which is found experimentally on occasion.[18] On the basis of the Langevin theory such a maximum could exist at room temperature if, in decreasing E/p_0 at low field towards the region where μ is independent of E/p_0, the major effect was to increase the predominance of the polarization scattering through lowering the mean velocity of approach of the particles, without altering much the velocity distribution of the ions. The result $A\lambda=0.7$ which we obtained for the atomic ions indicates that at room temperature and essentially zero field the ions are in the region where hard sphere scattering is predominant, in fact sufficiently far from the maximum mentioned in the preceding paragraph that we need not worry about the extrapolation. We expect, then, as we extrapolate towards zero field that the mobility rises and becomes constant when thermal

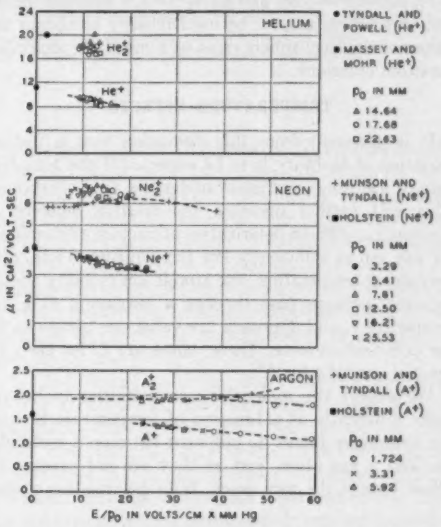

FIG. 4. The mobility at standard gas density, μ, of atomic and molecular ions in helium, neon, and argon as a function of E/p_0. The data shown were taken from only those oscillograms like Fig. 2 in which two current breaks were observed. This restricts the range of μ for the atomic ions in this figure to that in which molecular ion data could be obtained. Note that the drift velocity data, Fig. 3, could be converted to mobilities and used to continue the above atomic ion data to higher E/p_0. Theoretical calculations and experimental data of other investigators are included for comparison.

energy predominates sufficiently over the energy acquired from the field.

It is pertinent that energy arguments alone suggest that at the lowest E/p_0 obtained experimentally we are very close to a true measurement of μ_0 because the energy of field origin is small. The recent theory of Wannier[8] gives for the total mean energy of an ion in a gas whose temperature is T:

$$\text{Total energy}=mv^2+\tfrac{3}{2}kT.$$

Here m is the mass of the ion and v its drift velocity. In helium, at $E/p_0=8$ volts/cm-mm Hg the "field" energy is already smaller than thermal energy since the field contributes about 3×10^{-14} erg while at room

[17] The parameter λ has no connection with any mean free path.

[18] See L. B. Loeb, *Fundamental Processes of Electrical Discharge in Gases* (John Wiley & Sons, Inc., New York, 1939), page 76.

temperature $\frac{3}{2}kT \simeq 6\times10^{-14}$ erg. All of the above considerations imply that the error introduced by the extrapolation may well be less than ten percent.

In contrast to the atomic ions, the molecular ion mobility results indicate that at room temperature polarization attraction dominates strongly over the hard sphere cross section, which we now interpret as arising from gas kinetic repulsion because of the absence of symmetry effects in this case. The Langevin formula in the polarization limit predicts $\mu_0(He_2^+)=20$, $\mu_0(Ne_2^+)=6.0$, and $\mu_0(A_2^+)=2.1$. These values are so close to the experimental results, Fig. 4, *viz.*, $\mu_0(He_2^+)=19$, $\mu_0(Ne_2^+)=5.85$, and $\mu_0(A_2^+)=1.9$, that the theory and experiment cannot be used reliably to obtain the values of the hard sphere cross sections of the molecular ion-atom collisions.

TEMPERATURE EFFECTS

It is apparent from this discussion that a further variation of mobility is to be expected if the temperature of the gas is decreased under low field conditions. This will further decrease the relative velocity of approach and make polarization attraction predominate for any ion at sufficiently low temperature. Thus, with decreasing temperature, the atomic ion mobility should increase, perhaps pass through a maximum at a low temperature, and approach the value one computes for the polarization force. These values are 22 for He^+, 7.0 for Ne^+, and 2.4 for A^+.

We expect the molecular ion mobilities to behave quite differently as a function of temperature because the symmetry forces do not exist between a molecular ion and a gas atom, just as they are not present for alkali ions in the rare gases. With polarization attraction already predominant at room temperature, decreasing the temperature accentuates the predominance but there is not so far to go to reach the limit in which polarization alone is significant. Thus as the temperature is lowered, the atomic ion mobility should rise and eventually become larger[19] than the molecular ion mobility, the difference in limiting values resulting only from the mass difference of the two ions. In each gas the mass factor amounts to $(3/2)^{\frac{1}{2}}$, in accord with the limiting values quoted above.

Additional measurements of ionic mobilities at lower temperature are needed to settle the accuracy of these conjectures. Temperature measurements[20] with alkali ions in the noble gases indicate that the physical interpretation may not be so simple as that given here. On the other hand, measurements at Bristol[21] on the temperature dependence for the helium ion we believe to be He_2^+, but identified as He^+ by Tyndall, show just the type of behavior one predicts for molecular ions by the arguments above.

ACKNOWLEDGMENT

The advice and support of my colleagues has proved invaluable in this investigation, particularly P. W. Anderson, W. C. Herring, J. B. Johnson, J. P. Molnar, and A. H. White. The explanation presented here of the variation of drift velocity with electric field has evolved primarily from numerous discussions with G. H. Wannier.

[19] G. H. Wannier has pointed this out in a private communication.

[20] K. Hoselitz, Proc. Roy. Soc. (London), **A177**, 200 (1940).

[21] A. M. Tyndall, *The Mobility of Positive Ions in Gases* (Cambridge University Press, London, 1938), page 60.

Mass Spectrometric Studies of Molecular Ions in the Noble Gases

JOHN A. HORNBECK AND J. P. MOLNAR
Bell Telephone Laboratories, Murray Hill, New Jersey

(Received August 6, 1951)

Molecular ions of the rare gases (He_2^+, Ne_2^+, A_2^+, Kr_2^+, and Xe_2^+) produced by electron impact at gas pressures from 10^{-4} to 10^{-2} mm Hg have been studied with a small mass spectrometer. The ion intensity increased linearly with electron current and with the square of the gas pressure. The form of the ionization *versus* electron energy curves resembles closely curves of excitation probability by electron collision. The appearance potentials of the molecular ions were less than those of the atomic ions by $1.4^{+0.7}_{-0.2}$ volts in He, $0.7^{+0.7}_{-0.3}$ volt in Ne, $0.7^{+0.7}_{-0.2}$ volt in A, $0.7^{+0.7}_{-0.3}$ volt in Kr. These results can be interpreted, we believe, only by assuming that the process of formation of the molecular ions observed in this experiment is, using helium as an example, an excitation by electron impact, $He+e+K.E.\rightarrow He^*+e$, followed by the collision process, $He^*+He\rightarrow He_2^++e$, where He^* stands for a helium atom raised to a high-lying excited state. Our results differ from those of Arnot and M'Ewen on helium particularly in that they reported the appearance potential low enough to permit metastable atoms to form molecular ions.

INTRODUCTION

MOLECULAR ions of helium, neon, and argon were first identified by Tüxen[1] using a mass spectrometer. Later Arnot and M'Ewen[2] examined the appearance of He_2^+ using an electron space charge detector, but they were unsuccessful in their attempts to find Ne_2^+ and A_2^+ in the same apparatus. Subsequently these authors[3] reported mass spectrometric studies of He_2^+. They concluded that the process of formation of He_2^+ involved two stages, (1) the excitation of a neutral helium atom by electron impact

$$He+e+KE\rightarrow He^*+e,$$

and then, (2) collision between the excited atom, He^*, and another neutral atom

$$He^*+He\rightarrow He_2^++e.$$

Arnot and M'Ewen interpreted their appearance potential measurements to mean that He^* could be, among others, the metastable excited state at 19.8 electron volts. Because the lifetime of this state is, in general, many orders of magnitude longer than that of radiating states, they naturally supposed the important process of formation to be the one involving a metastable atom.

Independent evidence conflicts with this conclusion. Meyerott[4] deduced from theory and from experiments on enhanced spectra in helium that 22.5 volts were required to form He_2^+ in its ground state. In experiments[5] at these Laboratories the molecular ions He_2^+, Ne_2^+, and A_2^+ which were observed were formed in less than 10^{-6} sec after excitation of the respective gases by a short (10^{-7} sec) pulse of electrons passing through them. Although these experiments would not detect molecular ions formed from metastable atoms, by establishing that molecular ions could be formed in relatively large numbers from high-lying, short-lived excited states they indicated that formation from long-lived metastable states was quite unlikely. We, therefore, undertook to re-examine helium in a mass spectrometer and also to study the other rare gases in an attempt to establish more accurately the formation energies of the molecular ions and to clarify the understanding of at least one process[6] by which they are formed.

We have found molecular ions in krypton and xenon as well as in helium, neon, and argon; radon was not examined. The pressure and electron energy data, which were obtained only in the three lightest gases, indicate that in each gas molecular ions are produced by the same two-stage mechanism described above. In all the noble gases except xenon, which was not studied in detail, the appearance potential of the molecular ions seems to be about one to two volts less than the ionization potential of the corresponding atomic ions. Thus we conclude that the excited state involved cannot be a metastable state, but rather is a high-lying radiating state, in agreement with the formation process which was deduced to account for the molecular ions observed in the Townsend discharge.[5]

EXPERIMENTAL METHOD

The apparatus used in this investigation was assembled by one of us for other purposes and was used here because it was available. It is shown schematically in Fig. 1. The mass spectrometer, known as the Diatron[7] 20, is a small 180° spectrometer with an ion path of radius one centimeter. Electrons emitted by a tungsten filament are accelerated by an applied potential V_e before entering the ionization chamber where the

[1] O. Tüxen, Z. Physik **103**, 463 (1936).
[2] F. L. Arnot and M. B. M'Ewen, Proc. Roy. Soc. (London) **A166**, 543 (1938).
[3] F. L. Arnot and M. B. M'Ewen, Proc. Roy. Soc. (London) **A171**, 106 (1939).
[4] R. Meyerott, Phys. Rev. **70**, 671 (1946).
[5] J. A. Hornbeck, Phys. Rev. **84**, 615 (1951).
[6] It is likely that there exists more than one process of formation of the molecular ions, e.g., a three-body collision among two neutral atoms and an atomic ion.
[7] Manufactured by the Consolidated Engineering Corporation, Pasadena, California.

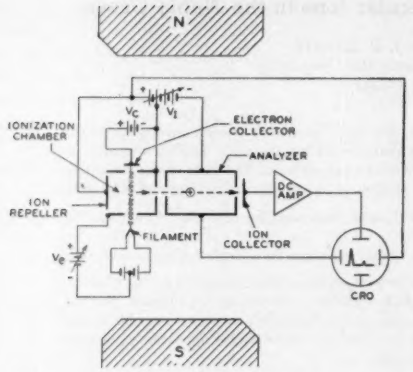

FIG. 1. Schematic diagram of mass spectrometer and associated electrical circuits. The resolving power of the apparatus was sufficient to separate the neon isotopes of masses 20, 21, and 22. Since the spectrometer was operated with a single vacuum pump, i.e., the pressure in the analyzer was the same as in the ionization chamber, the resolution was degraded somewhat at the higher gas pressures necessary to observe molecular ions. Noise in the dc amplifier restricted the detection of ion currents to values greater than 10^{-14} amp.

ions are formed. Collimation of the electron beam is achieved by the same magnetic field that bends the ions around the semicircular path of the analyzer, which is "unfolded" in Fig. 1. The electron beam on leaving the chamber is accelerated by the voltage V_e and collected. The ions formed by electron impact are repelled from the chamber by a small potential into a region where the ion accelerating voltage, V_I, draws them into the analyzer chamber. The values of V_I and the externally applied magnetic field determine the mass to charge ratio of the ions that go through the small exit slit of the analyzer and strike the ion collector. This ion current is amplified by a direct coupled amplifier, developing a voltage that is fed to the vertical plates of a No. 304-H Dumont dc oscilloscope. The voltage V_I is varied as a function of time at a pre-set repetition rate, usually about one cycle every two seconds, and connected to the horizontal plates of the cathode-ray tube. This gives a horizontal scale that depends (nonlinearly) on the mass/charge ratio. The oscilloscope trace, therefore, plots ion intensity *versus* the mass-to-charge ratio of the ions formed by the electron beam.

When measuring the intensities of two ion peaks, such as He^+ and He_2^+, as a function of the energy of the ionizing electrons, the magnetic field of several thousand gauss was adjusted so that the same value of V_I applied in each case. This assured the maintenance of the same electric fields within the spectrometer, an important feature when one is concerned about tenths of an electron volt in appearance potential measurements.

All the metal parts of the Diatron 20 except the collector are mounted on one press and fit into a small glass envelope, which was baked out at a temperature of 400°C before the gas was introduced. The gas pressure was measured by an ionization gauge.

Normally we admitted a single rare gas into the spectrometer and established the horizontal mass scale by marking the positions of the prevalent atomic ions, once, twice, or three times ionized. We also admitted on one occasion a small admixture of neon in helium

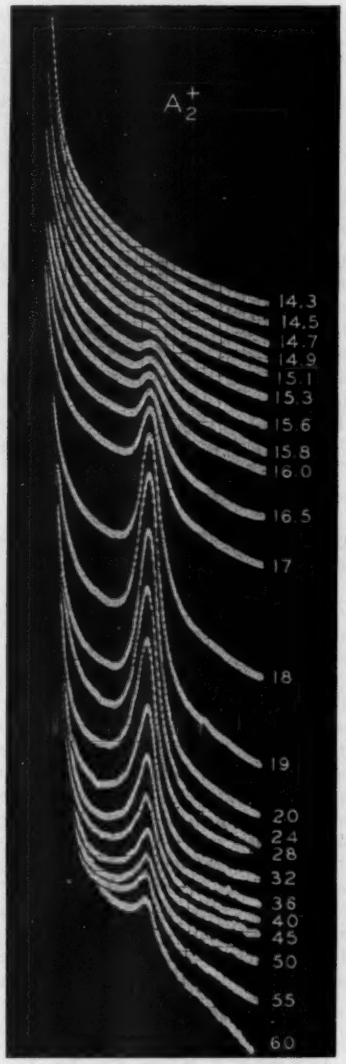

FIG. 2. Composite photograph of oscilloscope traces showing A_2^+ peaks for various electron accelerating voltages. The voltage corresponding to each trace is given.

permitting observation of He^+, Ne^+, and He_2^+ simultaneously. This mixture was useful in providing a cross check of the (relative) energy scale of the electrons; for with it we measured the difference in the appearance potentials of He^+ and Ne^+ to be 3.2 volts, whereas the more precise spectroscopic difference is 3.021 volts. With this internal consistency the accuracy in determining the appearance potentials of the molecular ions was limited mainly by the small number which were formed.

In the pressure and filament emission measurements the height of the ion peaks was read directly from the cathode-ray tube screen. The remainder of the data were obtained by photographing the *CRT* traces and subsequently measuring the peak heights on the photographic negatives.

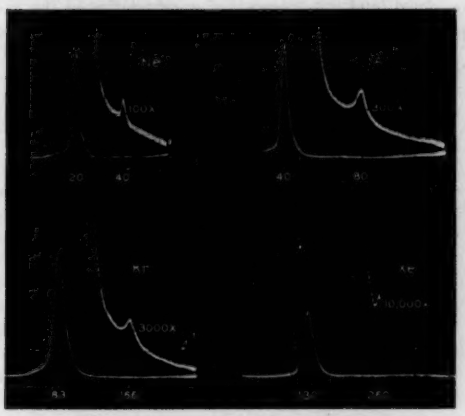

FIG. 3. Composite photograph showing atomic and molecular ion peaks. The mass value is given below each peak. The increased amplification of the molecular ion peak relative to the adjacent atomic ion peak is indicated.

Photographs of *CRT* traces showing the variation in A_2^+ peak height with the electron accelerating voltage are shown in composite form in Fig. 2. The peak is seen to fall on top of a background ion current that is decreasing in the direction of larger mass. The background effect is typical of all the molecular ions we observed and can be explained in the following way. At pressures low enough to avoid excessive scattering, the number of molecular ions formed is quite small compared with the number of atomic ions. As shown in Fig. 3, for example, the ratio of peak heights of atomic to molecular ions was about 500 to 1 in neon, 1200 to 1 in argon, 20,000 to 1 in krypton, and 40,000 to 1 in xenon. The same ratio in helium is 85 to 1. Hence the gain of the amplifier must be increased in order to observe the molecular ions at all. The increased amplification "blows up" the wings of the atomic ion peaks, which are broadened by scattering, so as to overlap the adjacent molecular ion peaks. This increases the difficulty of making reliable peak height measurements on the molecular ions; in fact, krypton, and xenon were extremely troublesome.

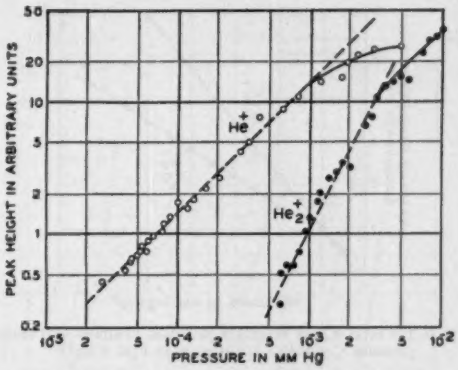

FIG. 4. Variation of ion peak height in helium with pressure. The electron current was constant at 150 μamp; the electron accelerating voltage was 25 volts for He_2^+ and 30 volts for He^+. The broken lines have slopes of one and two.

VARIATION WITH FILAMENT EMISSION AND PRESSURE

Both the molecular and atomic ion peaks were found to vary linearly with the electron beam current, in agreement with Arnot and M'Ewen. This indicates that only one excited atom (or ion) is involved in the formation mechanism.

With a fixed electron energy somewhat above the ionization potential of the atomic ion, the peak heights of the atomic and molecular ions were measured as a function of gas pressure, p. The results for helium and argon are shown in Fig. 4 and Fig. 5 on a log-log plot.

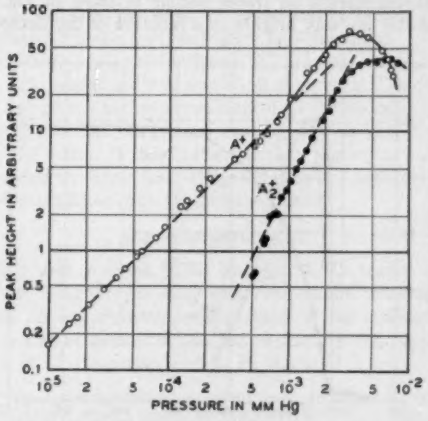

FIG. 5. Variation of ion peak height in argon with pressure. The electron current was constant at 200 μamp; the electron accelerating voltage was 19 volts for both ions. The broken lines have slopes of one and two.

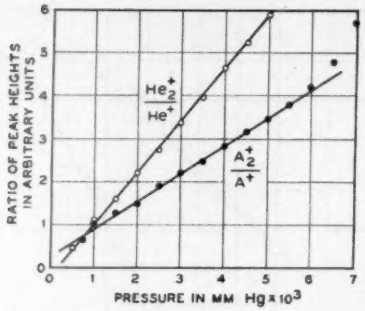

FIG. 6. The ratio of peak heights of molecular to atomic ions *versus* pressure. Conditions are as given in Figs. 4 and 5.

Within the experimental error these data indicate that the production of the molecular ions varies with p^2 whereas the atomic ion production is a linear function of p, as expected. The divergence of the experimental points at the highest pressures from the straight lines of slopes one and two in the figures is undoubtedly of instrumental origin. Above 10^{-3} mm Hg, measurement of the pressure with an ion gauge is obviously unsatisfactory, and also scattering in the analyzer of the spectrometer is a limitation. However, the ratios of the molecular to atomic ion peak heights *versus* p, plotted in Fig. 6, show a linear variation with pressure over a pressure range of a factor of ten.

We consider the above data sufficient evidence to conclude that the molecular ions are formed in a two-stage process involving first excitation (or ionization) and then collision of the excited atom (or ion) with a neutral one.

VARIATION WITH ELECTRON ENERGY

Measurements on traces similar to those in Fig. 2 give the ion peak heights as a function of the electron accelerating voltage, as plotted in Figs. 7, 8, and 9 for helium, neon, and argon. In each case we find, within experimental error, a typical ionization probability curve for the atomic ion production. For the molecular ions we find in each case a curve very similar to published curves of atomic excitation efficiency as a function of electron energy. In helium the results[8] are not dissimilar to calculations of excitation cross-sections by Massey and Mohr[9] for the optically allowed transitions $1s^2\ {}^1S\text{-}1s3p\ {}^1P^o$ and $1s^2\ {}^1S\text{-}1s3d\ {}^1D$. The curve is not so similar to the calculations for transitions to the $1s3p\ {}^3P^o$ and $1s3d\ {}^3D$ states, which cannot decay directly to the ground state, and to states of the configuration $1s2p$. The inference is strong that the formation mechanism involves the excitation rather than the direct ionization of a neutral helium atom by electron impact. Since a mixture of several atomic states is probably involved, and also because of uncertainties in the experimental data, it does not seem profitable to speculate from these data as to the particular states involved other than to notice the similarities pointed out above.

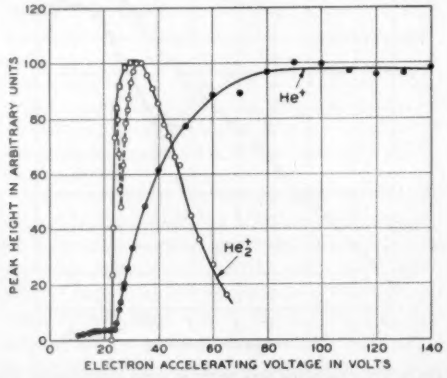

FIG. 7. Ionization in helium *versus* the electron accelerating voltage (uncorrected for contact potential difference). The broken line indicates a "ghost," as explained in reference 8.

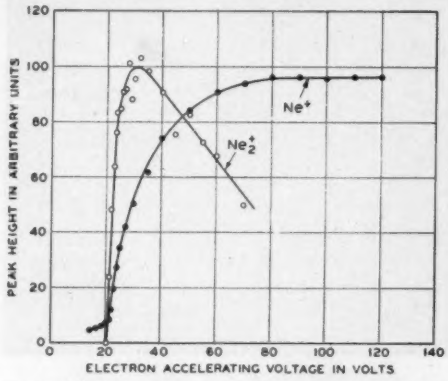

FIG. 8. Ionization in neon *versus* the electron accelerating voltage (uncorrected for contact potential difference).

APPEARANCE POTENTIAL MEASUREMENTS

Careful studies of the toes of the atomic ion curves, Figs. 7–9, and of the appearance of molecular ion peaks above the noise level of the apparatus yield information on the minimum energy of formation of the molecular ions. Characteristic data in this region are plotted in Fig. 10 for helium, neon, and argon. In these illustrations the zero of ordinates of the atomic ion curves has been adjusted so that the significant regions of the data can be shown in the same plot. The horizontal scale is electron accelerating voltage as indicated by a volt-

[8] The dip shown in Fig. 7 is a "ghost" which we do not explain. It was found only in helium, and its position on the voltage scale varied with gas pressure, repeller voltage, and other instrument settings. By making several "runs" under different conditions the entire excitation curve (solid line, Fig. 7) could be plotted.

[9] H. S. W. Massey and C. B. O. Mohr, Proc. Roy. Soc. (London) **A132**, 605 (1931).

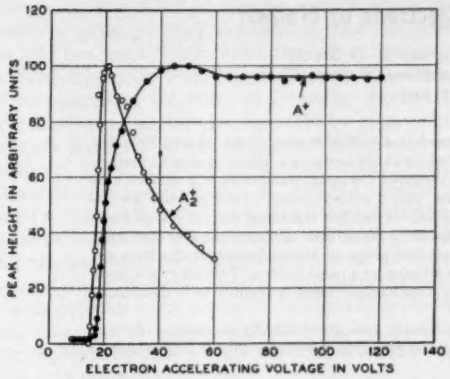

FIG. 9. Ionization in argon *versus* the electron accelerating voltage (uncorrected for contact potential difference).

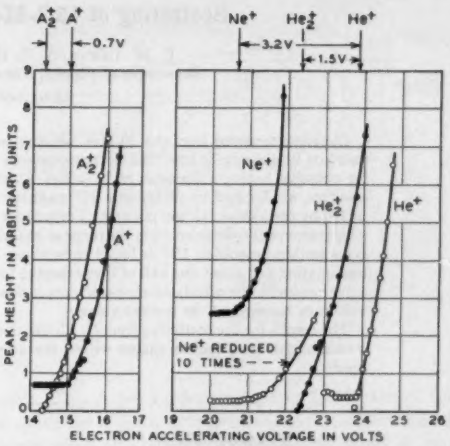

FIG. 10. Ionization *versus* the electron accelerating voltage (uncorrected) in argon and also in helium with a small admixture of neon. The zero of ordinates of the atomic ion data has been adjusted so that these curves can be plotted conveniently in the same figure. The arrows at the top give the relative appearance potentials of the ions.

meter, i.e., uncorrected for contact potential difference, for we are concerned only with the voltage difference between the appearance potentials of the molecular and atomic ions.

In the conventional way we interpret the onset of atomic ionization as the voltage at which the atomic peak increases abruptly with increased electron accelerating voltage. The ionization observed below this break in the curves is accounted for by recognizing that a small amount of ionization can occur whenever there is a voltage in the apparatus greater than the ionization potential. The electron collecting voltage, for example, meets this requirement.

The simplest interpretation of the data in Fig. 10 would be that the appearance potential of He_2^+ is 1.5 volts less than that of He^+, and that of A_2^+ is 0.7 volt less than A^+; and we would conclude that Ne^+ appears at 3.2 volts less than He^+. Because the number of molecular ions produced is so small, however, there is considerable difficulty in picking the voltage where the molecular ions are first detectable. Increasing the detection sensitivity of the instrument would probably increase the difference between the appearance potentials of the atomic and molecular ions. This problem is illustrated in Fig. 10 in which the Ne^+ curve is plotted on a scale reduced ten times. It is clear that if the uncertainty in the peak height measurement were to be increased also by a factor of ten, the observed appearance potential of Ne^+ would be about 0.5 volt higher.

In order to estimate the error in the above determinations, relative appearance potentials of the two ions were also measured when the amplifier gain was readjusted so that the maximum signal voltage (i.e., maximum peak height) of the two peaks was about the same at the optimum accelerating voltage in each case. This test indicated a probable error of slightly less than an electron volt in determining the appearance potentials from the data of Fig. 10. Since atomic excitation efficiency curves rise more sharply as a function of electron energy than the corresponding ionization efficiency curves, this estimate of the probable error seems reasonable. Our data, which include at least two "runs" in each gas, indicate that by taking the atomic ionization potentials of He^+, Ne^+, A^+, and Kr^+ to be 24.58, 21.56, 15.76, and 13.93 volts,[10] respectively, the appearance potentials of He_2^+, Ne_2^+, A_2^+, and Kr_2^+, respectively, are $23.18^{+0.2}_{-0.7}$, $20.86^{+0.3}_{-0.7}$, $15.06^{+0.2}_{-0.7}$, and $13.23^{+0.3}_{-0.7}$ volts. These values are higher than the energies of the metastable atoms by amounts believed to be outside the limit of experimental error. The metastable levels are listed[10] here for comparison: 19.81 and 20.61 in helium, 16.61 and 16.71 in neon, 11.55 and 11.72 in argon, and 9.77 and 10.52 in krypton. The data on helium are entirely consistent with the deduction of Meyerott[4] that the ground state of He_2^+ is very close to 22.5 volts. It may be noted that the lower value reported by Arnot and M'Ewen[3] does not seem to be well established even by their own data.

ACKNOWLEDGMENT

We wish to thank R. G. Brandes, A. Tartaglia, and H. W. Weinhart for their very considerable assistance with the experimental work. Others of our colleagues have also been most helpful, particularly P. W. Anderson, H. D. Hagstrum, and A. H. White.

[10] The values quoted here for helium, neon, and argon are taken from *Atomic Energy Levels*, by Charlotte E. Moore, National Bureau of Standards circular No. 467 (1949). Krypton is not included in this reference so the "old value" is given here. Likewise the energies of the metastable states are "new values" except for krypton.

Scattering of 15.7-Mev Electrons by Nuclei*

E. M. LYMAN, A. O. HANSON, AND M. B. SCOTT†
Department of Physics, University of Illinois, Urbana, Illinois
(Received July 3, 1951)

Electrons removed from the 20-Mev betatron are focused to a 0.08-inch spot about 10 feet from the betatron by a magnetic lens. The electrons impinge on thin foils at the center of a highly evacuated scattering chamber having a diameter of 20 inches. Elastically scattered electrons, selected by a $\frac{3}{8}$ inch×2 inch aperture, are focused by means of a 75° magnetic analyzer with 3 percent energy resolution and are detected by coincidence Geiger counters. Corrections are applied for multiple scattering and for energy losses which remove the electrons from the range of energies accepted by the detector arrangement. The scattering cross section for gold at 150° is found to be about 2.6 times that given by Mott's formula in the Born approximation and about one-half of that expected for the scattering by a point nucleus. This result is in good agreement with the calculations for electrons of this energy if the nuclear charge is assumed to be distributed uniformly throughout the nuclear volume.

The results for the scattering from C, Al, Cu, and Ag are also in agreement with the assumption of a uniformly distributed nuclear charge within the uncertainties involved in the theory and the experimental results.

INTRODUCTION

THE scattering of fast electrons by nuclei has been the subject of a large number of researches. The previous work in the energy range above 10 Mev has been done primarily with cloud chambers. The results are quite divergent but could be considered to be in qualitative agreement with theoretical calculations.[1]

At lower energies some accurate measurements have been made using electrons accelerated by an electrostatic generator to energies up to 2.25 Mev. These results, reported by Van de Graaff, Buechner, and Feshbach, for several elements and for a number of angles up to 50° are in good agreement with calculations.[2] The more recent work of Champion and Roy and that of Sigrist[3] indicate that the scattering at larger angles is also in agreement with calculations, although others report divergent results.[4]

It appears that the remaining discrepancies at these energies are due to experimental difficulties, and it will be assumed in this work that the scattering of electrons having energies up to 3 Mev are described by complete calculations[5,6] based on Mott's formulas for the scattering by a point charge.

At sufficiently high energies, Rose, and more recently Elton, have shown that the scattering of electrons by nuclei would be considerably modified by the fact that the size of the nuclear charge distribution is no longer small compared to the electron wavelength.[7]

An experimental investigation of the scattering of high energy electrons was made feasible by the successful extraction of the electron beam from the 20-Mev betatron. Preliminary results have been reported briefly[8] and have been compared with the accurate calculations by Elton.[9]

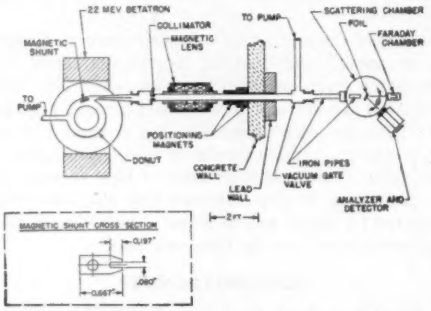

FIG. 1. Schematic showing betatron and scattering chamber.

I. APPARATUS AND EXPERIMENTAL METHOD

Production, Extraction, and Focusing of the Electron Beam

The experimental arrangement is shown schematically in Fig. 1. When electrons accelerated in the betatron donut reach 15.7 Mev, as determined by a flux

* Supported by the joint program of ONR and AEC.
† Now at Massachusetts Institute of Technology, Cambridge 39, Massachusetts.
[1] Randels, Chao, and Crane, Phys. Rev. **68**, 64 (1945). See also reference 18, p. 83.
[2] Van de Graaff, Buechner, and Feshbach, Phys. Rev. **69**, 452 (1946); Buechner, Van de Graaff, Sperduto, Burrill, and Feshbach, Phys. Rev. **72**, 678 (1947).
[3] F. C. Champion and R. R. Roy, Proc. Phys. Soc. (London) **61**, 532 (1948); W. Sigrist, Helv. Phys. Acta **16**, 471 (1943).
[4] Alichanian, Alichanow, and Weissenberg, J. Phys. (USSR) **9**, 280 (1945); W. Bothe, Z. Naturforsch. **4a**, 88 (1949).
Note added in proof:—Paul and Reich have recently reported general agreement with theory at 2.2 Mev except for somewhat low values for gold at 90° and 120°. (Private communication. Work to appear in *Zeitschrift für Physik*.)
[5] J. H. Bartlett and R. E. Watson, Proc. Am. Acad. Arts Sci. **74**, 53 (1940).
[6] W. A. McKinley and H. Feshbach, Phys. Rev. **74**, 1759 (1948).
[7] M. E. Rose, Phys. Rev. **73**, 279 (1948).
[8] Lyman, Hanson, and Scott, Phys. Rev. **79**, 228 (1950); Phys. Rev. **81**, 309 (1951).
[9] L. R. B. Elton, Phys. Rev. **79**, 412 (1950); Proc. Phys. Soc. (London) **A63**, 1115 (1950).

integrating circuit,[10,11] an expansion pulse causes their orbit to spiral outward and enter a magnetic shunt, or field free region,[12] from which they are able to escape the betatron guide field. The shape of the iron laminations comprising the shunt is shown by the inset in Fig. 1. The laminations are separated by mica spacers and the stack, 3.5 in. long, is located tangentially, at a radius of 8.6 in. from the center of the donut. The injector is at a radius of 8.75 in. and the equilibrium orbit at 7.6 in. The radial position of the magnetic shunt is rather critical; if it is located at too large a radius, the electron beam fails to enter the slot in the shunt; while if it is at too small a radius, the orbit expands into the shunt prematurely before the electrons have reached full energy. The proper orientation of the shunt is accomplished by selsyn remote control while the betatron is in operation.

The spray of electrons emerging from the magnetic shunt is about 1° high and 6° wide. The most intense portion of this beam is selected by a collimator subtending 1°, and passed down the axis of a magnetic lens which focuses it into a spot 0.08 in. in diameter at a point about 10 feet from the betatron. Positioning electromagnets provide a means of fine adjustment of the vertical and horizontal position of the focal spot.

Scattering Chamber, Energy Analyzer, and Detectors

The electron beam enters the scattering chamber shown in Fig. 2 through one of the port holes spaced at intervals of 30° in the cylindrical wall and comes to a focus on the target foil at the center. A thick aluminum faraday chamber diametrically opposite the beam entrance port is connected to a vibrating reed electrometer and serves to measure the charge incident upon the foil. The scattered beam of electrons is selected by a rectangular aperture $\frac{3}{8}$ in. wide and 2 in. high, located in the chamber wall 10 inches from the scattering foil. After passing through the aperture they enter the magnetic analyzer which focuses them upon a group of Geiger counters in coincidence.

The chamber, defining aperture, magnetic analyzer, counters and their shielding are all mounted on a rotating platform with its axis of rotation at the center of the target foil. The angle of scattering is changed by detaching the entrance tube and faraday chamber, rotating the table to the new position, then reconnecting the tube and faraday chamber. During this process, the chamber is isolated from the betatron and diffusion pumps by a system of vacuum gates. While operating, there are no foils or windows anywhere in the path of the incident beam.

Target selection is accomplished remotely by a selsyn system which drives the target holder through 0-ring seals. The target holder has spaces for 10 target foils, a space for a piece of fluorescent x-ray screen used for observation of the beam position and focus, a blank space for transmitting the incident beam directly to the faraday chamber without intervening scattering material, and a 20-mil vertical tungsten wire used for alignment purposes. The scattering angle is read from a vernier scale attached to the stationary part of the framework supporting the rotating platform.

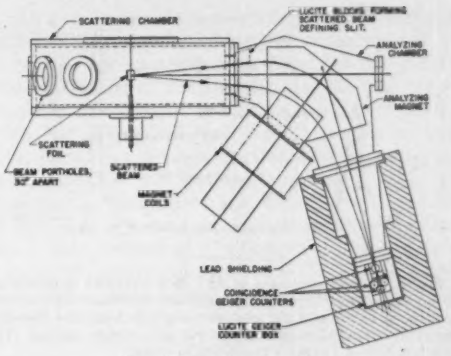

FIG. 2. Scattering chamber.

The magnetic analyzer focuses the elastically scattered electrons from the 0.08-inch beam incident on the scattering foils to a line about $\frac{1}{4}$ in. wide and 2 in. long. This beam is more than covered by the Geiger counter which has a diameter of $\frac{3}{4}$ in. and an active length of about 3 inches. The $\frac{3}{4}$-inch width of the Geiger counter corresponds to an energy range of 3 percent. Hence the maximum count obtained by varying the magnetic field will include all electrons which have lost less than 3 percent of the initial energy.

The field of the analyzer magnet is controlled to 0.1 percent by a servo system which derives its error signal by comparing the voltages developed in two rotating flip coils, one in the magnetic field and the other in a permanent magnet reference field. The position and nature of the focus of the analyzer magnet and its $H\rho$ calibration were determined by the well-known "hot-wire" method using No. 44 copper wire carrying about 1 ampere.

To eliminate serious interaction between the field of the analyzer magnet and the incident beam at large scattering angles, it was found to be necessary to shield the incident beam with iron pipe duct, both outside and inside the chamber.

Experimental Procedure

During the initial stages of extraction of the electron beam and alignment of the apparatus, a telescope, mirrors, and a piece of fluorescent x-ray screen were used to observe the beam position and intensity at various points in its path. First, the orientation of the magnetic shunt was adjusted to produce a small in-

[10] McElhinney, Hanson, Becker, Duffield, and Diven, Phys. Rev. **75**, 542 (1949).
[11] Katz, McNamara, Forsyth, Halsam, and Johns, Can. J. Research **A28**, 113 (1950).
[12] Skaggs, Almy, Kerst, and Lanzl, Radiology **50**, 167 (1948).

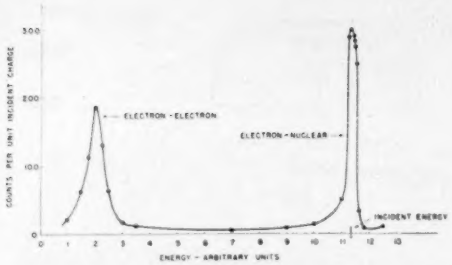

FIG. 3. Energy spectrum of 15.7-Mev electrons scattered at 30° by polystyrene (carbon). The ordinate represents the observed count as a function of the analyzer magnetic field, and does not represent the number of electrons per unit energy interval. The counters have a 3 percent resolution in energy.

tense spot at the exit port of the donut. Next, the duct leading to the scattering chamber was attached, evacuated, and oriented until maximum intensity was obtained at the chamber end. Further fine adjustment was continued with the magnetic lens current turned on, until a small, focused spot was formed centrally at the end of the duct and remained stationary upon reversal of the magnetic lens current, indicating coincidence of source, focal spot and axis of the lens. Under these conditions, the position of the beam was stable for slight variations in energy and magnetic lens current.

The final step in alignment consisted of locating the framework supporting the rotating platform and chamber so that the beam came to focus precisely at the center of the chamber. After careful visual alignment, exact centering was accomplished by placing the 20-mil vertical tungsten wire at the center of the chamber and measuring the beam scattered from it by an auxiliary ionization chamber at 30°. The position of the incident electron beam was then adjusted by the horizontal positioning electromagnet until the scattering was a maximum. It was necessary to repeat the centering adjustment at each scattering angle because of the slight interaction between analyzer field and incident beam.

The vernier dial reading corresponding to zero angle of scattering was determined by adjusting the chamber position until the beam passed centrally through the defining aperture into the detectors. Other scattering angles were read to 0.03° with reference to this position.

The shape and magnitude of the peak due to nuclear scattering and the background were determined for each foil at each angle of scattering. A typical complete spectrum is shown in Fig. 3.

Each point of the spectrum is the number of counts recorded (adjusted for counting-rate losses) while a given charge was being collected by the faraday chamber directly behind the foil. The faraday chamber was connected to a vibrating reed electrometer whose instrumental capacitance was increased by a calibrated polystyrene condenser connected between the input and inverse feedback terminals. With this connection, the charge was simply the product of voltage change and the capacitance, the effect of all other capacitances being degenerated to insignificance by the feedback.[13] The charge incident upon the foil was obtained from the charge measured by the faraday chamber and the foil transmission factor. The latter was determined by a series of measurements of the time required to collect a given charge, with the foil present and then absent, at constant beam intensity.

Shielding of the counter system from the x-ray background produced by the betatron was not difficult for scattering at 30°, but at 150° a foot-thick concrete wall and 6 inches of lead surrounding the counters were required.

II. TREATMENT OF DATA

The number of counts corresponding to the maximum of the approximately flat-topped elastic scattering peak for a given incident charge is a measure of the cross section for scattering at any particular angle. The fact that electrons were incident upon the foil in microsecond bursts 180 times per second, made it necessary to correct for the number of counts which correspond to more than one electron passing through the Geiger counters. This correction is given with sufficient accuracy by [14]

$$C=C_{\text{obs}}(1+C_{\text{obs}}/360t), \tag{1}$$

where C_{obs} is the number of counts recorded in t seconds. This correction was applied individually to every observation. In taking the data the counting rate was kept sufficiently low so that this correction did not exceed 10 percent.

A cross section can be obtained from the usual relation

$$\sigma_{\text{obs}}=C/nN\Omega, \tag{2}$$

where C is the count corrected for the above losses minus the count with the scattering foil absent; n is the number of electrons incident on the foil as determined by the charge collected in the faraday chamber and the transmission ratio; N is the number of atoms/cm² in the path of the beam as determined by the weight of the foils and the angle between the normal to the foils and the direction of the incident beam; and Ω is the solid angle determined by the aperture defining the scattered beam.

In comparing experimental cross sections with theory, it was found to be convenient to adjust the observed cross section to take account of (1) the small range of scattering angle of the electrons admitted to the detectors because of the finite size of the defining aperture and the size and angle of convergence of the incident beam, (2) effects due to the finite thickness of the scat-

[13] Palevsky, Swank, and Grenchick, Rev. Sci. Instr. **18**, 298 (1947).
[14] C. H. Westcott, Proc. Roy. Soc. (London) **A194**, 508 (1948).

tering foils, and (3) the effect of radiation associated with the single scattering process itself.

In calculating the geometrical corrections, it is sufficient to assume that the angular dependence of the scattering cross section is given by the Mott formula (Born approximation),

$$\sigma_M(\theta)=(Ze^2/2mv^2)^2(\csc^4\tfrac{1}{2}\theta-\beta^2\csc^2\tfrac{1}{2}\theta). \quad (3)$$

It can be shown from spherical trigonometry that an electron which enters the defining aperture making an angle θ_x, θ_y with respect to the line connecting the center of the foil with the center of the aperture has been scattered through an angle

$$\theta=\theta_0+\theta_x+\tfrac{1}{2}\theta_y^2\cot\theta_0, \quad (4)$$

where θ_0 is the scattering angle to the center of the aperture. The average intensity (I_{Av}) over the aperture is then given by

$$I_{Av}=I_0\left(1+\frac{\sigma'}{\sigma}\frac{h^2}{24}\cot\theta_0+\frac{\sigma''}{\sigma}\frac{W^2}{24}\right), \quad (5)$$

where I_0 is the intensity at θ_0. W and h represent the angular width and height of the aperture and σ' and σ'' represent derivatives of Eq. (3) with respect to θ. The correction to the observed cross section calculated from this equation resulted in an increase of 1.8 percent at 30° and a decrease of 1.3 percent at 150°, for example. The corrections for the width and angular divergence of the incident beam are negligible when superimposed on the aperture correction.

Multiple scattering of electrons in the foil results in a correction very similar to the aperture correction. Chase and Cox[16] have shown that the combination of single scattering superimposed upon the multiple scattering results in an additional averaging over the multiple scattering distribution such that the average intensity at θ_0 is

$$I=I_0[1+\tfrac{1}{4}\epsilon^2(\sigma'\cot\theta_0+\sigma'')/\sigma], \quad (6)$$

where ϵ represents the rms value of the multiple scattering distribution (the $1/e$ width, if the distribution is gaussian). In the angular range where the cross section varies as $1/\theta^4$ the above correction agrees with the first order term of the expression given by Butler.[16]

At scattering angles exceeding 90°, the scattered electrons must emerge from the same side of the foil as they enter. The probability of a double large angle scattering becomes important because of the increased path length for electrons scattered into the plane of the foil.[17] For example, for scattering at 150° from a foil with its plane perpendicular to the incident beam, the ratio of intensity I to the intensity I_0 due to single scattering alone may be estimated as

$$I/I_0\approx 1+[\sigma(90°)\sigma(60°)N\pi/\sigma(150°)]. \quad (7)$$

[15] C. T. Chase and R. T. Cox, Phys. Rev. **58**, 246 (1940).
[16] S. T. Butler, Proc. Phys. Soc. (London) **A63**, 599 (1950).
[17] G. Goertzel and R. T. Cox, Phys. Rev. **63**, 37 (1943).

Since the correction is proportional to the thickness of the foil, it may be determined experimentally by comparing the scattering from thick and thin foils of the same element. For the thin Au foil, the experimentally determined correction was 1.8±1.0 percent while that determined from Eq. (7) was 0.3 percent. The discrepancy between the experimental and calculated correction is in qualitative agreement with that observed by Shull, Chase, and Myers.[18]

The correction for loss of electrons from the peak due to energy degradation in electron-electron collisions is found by determining the fraction that lose more than 3 percent of their energy in traversing the foil. The effective cross section for loss of energy between E and $E+dE$ in a single small angle electron-electron collision is[19]

$$pdE\simeq(2\pi e^4/mv^2)(dE/E^2). \quad (8)$$

The cross section for the loss of more than 3 percent of the energy of a 15.7-Mev electron obtained by integrating Eq. (8) is found to be 0.542 barn per electron in the foil.

In addition to the correction for energy losses due to single electron-electron collisions, a small correction is included to account for the effect of double collisions in which the energy loss per collision is less than 3 percent.

The correction for loss of electrons from the peak due to energy degradation by radiation in small-angle nuclear collisions is found by calculating the number of photons produced whose energies exceed $0.03E_0$. For 15.7-Mev electrons, the number of such photons produced per Mev radiation loss by an electron is found from the bremsstrahlung spectrum to be 0.291 photon, where the total radiation loss is given by Heitler.[20] The fraction of electrons which lose 3 percent or more of their energy, and will therefore escape detection is approximately equal to 0.291 times the total radiation loss in the foil.

Superimposed on the energy losses of electrons in penetrating a foil, which are in all cases proportional to the thickness of the foil, is another radiative loss associated with the single large angle scattering being observed. This energy loss has a distribution qualitatively similar to the average bremsstrahlung spectrum radiated by electrons. There will therefore be no electrons which are scattered strictly elastically. Most will be scattered with small radiative losses and a certain number will fall out of the energy range ΔE accepted by the counters. This correction can be obtained from a calculation by Schwinger[21] which includes the reduction in cross section associated with the energy

[18] Shull, Chase, and Myers, Phys. Rev. **63**, 29 (1943).
[19] Mott and Massey, *Theory of Atomic Collisions* (Oxford University Press, London, 1949), second edition, p. 369.
[20] Heitler, *Quantum Theory of Radiation* (Oxford University Press, London, 1945), second edition, p. 191.
[21] J. Schwinger, Phys. Rev. **76**, 790 (1949); see also reference 19, p. 379.

TABLE I. Typical corrections. Percent corrections added to observed cross sections for thin and thick gold foils.

	30°		60°		90°		120°		150°	
	Thin	Thick	Thin	Thick	Thin	Thick	Thin	Thick	Thin	Thick
Multiple scattering	−1.0	−5.9	−0.3	−1.8	−0.2	−1.3	−0.2	−1.0	−0.3	−1.8
Radiation straggling	0.4	1.7	0.4	1.9	0.5	2.3	0.4	1.9	0.4	1.7
Electron-electron straggling	0.1	0.3	0.1	0.4	0.1	0.5	0.1	0.4	0.1	0.3
Double scattering	0	0	0	0	0	0	−0.5	−2.9	−1.7	−10.1
Schwinger formula (9)	5.4	5.4	7.0	7.0	7.9	7.9	8.5	8.5	9.1	9.1
Aperture size	1.8	1.8	0.3	0.3	−0.1	−0.1	−0.3	−0.3	−1.3	−1.3

loss ΔE as well as the effect of the more complete treatment of the interaction of the electron with the radiation field. This reduction in the cross section is given by the equation

$$\delta=\frac{4}{137\pi}\left[\left(\ln\frac{E}{\Delta E}-\frac{13}{12}\right)\left(\ln\left[\frac{2p_0\sin\frac{1}{2}\theta}{K}\right]-\tfrac{1}{2}\right)+\frac{17}{72}+\tfrac{1}{2}\sin^2\tfrac{1}{2}\theta F(\theta)\right], \quad (9)$$

where, for this work, $F(\theta)$ may be taken as unity, $\Delta E/E=0.03$, and $p_0/K=31.7$. The large part of this correction can be seen to be associated with the radiative losses. In order to put the observed results in a form which is independent of the energy band ΔE, accepted by the detectors the observed cross sections have been increased by the factor $1/(1-\delta)$. Values of δ for various angles are given in Table I. These values are taken as the same for all materials, although the calculation is not expected to be accurate for high Z materials.

The magnitudes of the corrections applied to the observed scattering cross sections for a typical element at various angles are summarized in Table I. This table is also representative of the other foils, since they were chosen to have approximately the same NZ^2. It can be seen that the effect of multiple scattering and energy straggling is small, especially for the thin foil. The corrections for the radiation loss associated with large angle scattering (δ) and the aperture correction are independent of the scattering material. The effect of double scattering is appreciable only at 120° and 150°. As mentioned previously, the magnitude of this correction was estimated from the variation of the observed scattering from two foils of the same material having different thicknesses, and is rather uncertain. Since these corrections are considerably larger than those calculated for this effect the increased scattering attributed here to double scattering may in part have some other interpretation.

It should be pointed out that the data from the thicker foils were not considered as reliable as those from the thinner foils and were used primarily to check or to determine the corrections which were applied to the thin target data.

III. EXPERIMENTAL RESULTS

The scattering cross sections measured for C, Al, Cu, Ag, and Au at scattering angles ranging from 30° to 150° are given in Table II. The numbers of atoms/cm² of the scattering foils are listed in column 2. In column 3, row a, are the observed, unadjusted scattering cross sections at 30° in barns per unit solid angle while in column 3, row b, are the same cross sections corrected for the effects listed in Table I, except for the correction calculated from the Schwinger formula. (This correction is not a function of foil thickness.) In column 4, the estimated standard error is given for the cases of the thin foils. Similar data for the other angles are given in columns 5 to 12.

The results listed in Table II were obtained from the last of a series of 5 runs, taken over a period of a year, during which a great effort was made to decrease random errors and eliminate all sources of systematic error.

The estimated standard errors shown in Table II are based solely upon the sources of random error in the experiment. For the majority of the points, the error due to counting statistics is about 1.2 percent, but at 150° due to low count and large background, it is about 3 percent on the average. In the case of polystyrene, which gave the lowest ratio of counts to background, the error is 10 percent. The estimated error in reading the meter which measured the charge incident upon the foil is 1 percent, in determining the foil transmission factor, 1 percent, and in measurement of the scattering angle (because of the uncertainty in locating the exact position of the incident beam), 1 percent. The total random errors for most of the points are then estimated to be of the order of 2 percent.

The number of atoms/cm² in the foils was determined by weighing an accurately cut area of the foil. Most foils were uniform to within 1 percent. The thinnest gold foil (10^{-4} inch) exhibited a thickness variation of 2 percent over the region struck by the incident beam.

The solid angle of the scattered beam admitted to the detector was the same for all angles and any error in it would affect all data equally. Two types of material for defining the aperture were tried; Lucite, 3 inches thick with sides curved to match the electron trajectories and gold, $\frac{1}{16}$ inch thick, backed by lead. The scattering cross sections observed with the two types of apertures were identical to within 1 percent.

TABLE II. Observed and adjusted scattering cross sections.

		30°		60°		90°		120°		150°	
Element	$N/cm^2\times10^{20}$	σ	%	$\sigma\times10^{+1}$	%	$\sigma\times10^{+2}$	%	$\sigma\times10^{+2}$	%	$\sigma\times10^{+1}$	%
C	11.18 [a]	0.1501		0.08305		0.1230		0.2881		0.4500	
Polystyrene	[b]	0.1502	2.4	0.08340	2.0	0.1238	2.4	0.2887	3.4	0.4476	10
Al	3.050 [a]	0.7078		0.3940		0.6447		...		...	
	15.21 [a]	0.7126		0.3881		0.6571		1.455		2.652	
	3.050 [b]	0.7065	2.2	0.3951	2.0	0.6477	1.8	...		...	
	15.21 [b]	0.7017		0.3932		0.6713		1.455	2.1	2.510	4.5
Cu	2.339 [a]	3.663		2.271		3.860		8.680		14.00	
	6.895 [a]	3.785		2.311		3.737		8.685		15.68	
	2.339 [b]	3.615	2.2	2.283	1.9	3.899	1.8	8.651	2	13.48	3.9
	6.895 [b]	3.596		2.339		3.835		8.529		13.57	
Ag	0.3889[a]	10.82		7.045		12.31		28.28		...	
	1.143 [a]	10.93		7.105		12.67		28.60		51.30	
	0.3889[b]	10.78	2.3	7.057	2	12.36	1.8	28.27	2.2	...	
	1.143 [b]	10.74		7.165		12.79		28.43		48.83	3.2
Au	0.1726[a]	33.67		25.30		49.65		134.2		323.5	
	0.7814[a]	35.63		28.71		51.11		124.3		247.9	
	0.1726[b]	33.49	2.2	25.36	2.0	49.87	2.1	133.9	2	228.8	3.8
	0.7814[b]	34.25		28.84		51.87		122.2		223.5	

[a] Observed.
[b] Corrected for geometry, multiple scattering, $e-e$ collisions, double scattering at large angles, and radiation in small-angle collisions.

Other tests indicated that the counting rates were proportional to the area of the aperture.

The ability of the thick-walled aluminum faraday chamber to retain all of the electron charge collected by it was tested by placing a lead disk at the bottom of the chamber to increase the scattering and the number of x-rays produced by the incident beam. It was found that the total charge retained by the chamber was 3 percent less with the lead bottom than with the usual all-aluminum chamber. From this it was estimated that the loss of charge by the standard aluminum chamber was about 1 percent.

IV. THEORY

In order to discuss the observed results it is convenient to display the ratio of the observed scattering cross sections to that calculated from the simple Mott formula. This formula has already been given as Eq. (3) and accounts for the very large variations in the cross sections. It is expected to represent the observed scattering at small angles for all values of Z and the scattering at all angles for very low Z.

McKinley and Feshbach[6] have given another formula which is essentially a first-order correction to the simple Mott formula. By their relation the ratio of the coulomb scattering to that given by Eq. (3) is

$$\frac{\sigma}{\sigma_M}=1+\frac{\pi Z\beta\sin\theta/2[1-\sin(\theta/2)]}{137[1-\beta^2\sin^2(\theta/2)]}. \qquad (10)$$

McKinley and Feshbach also obtained an expression involving terms to the fourth power of α, where $\alpha=Z/137$. These results, which will be referred to as the α^4 approximation, should be reliable for higher values of Z but are not good for the heavy elements where α is not small compared to unity.

The accurate evaluation of Mott's theory for the scattering of electrons by a heavy element is a difficult task and has been carried out in detail for ($Z=80$) by Bartlett and Watson using numerical methods,[5] and only recently for $Z=47$.[22]

The calculated values of σ_M and σ_e/σ_M for 15.7-Mev electrons are given in Table III. The values of σ_e/σ_M for carbon were calculated from Eq. (10). The values for copper are based on the α^4 approximation for $\beta=1$ as calculated by Acheson.[23] The values for silver are those given by Feshbach[22] and those for gold are obtained by a small extrapolation of the results of Bartlett and Watson to $Z=79$ and to $\beta=1$.[24]

A rough experimental check on the reliability of the calculations was made by reducing the energy of the electrons to 4.6 Mev during one of the runs at 150 degrees. Although the multiple and double scattering corrections were large the relative values were still fairly good for those foils where the corrections were about the same. The ratio of the scattering from gold and silver to that from aluminum was found to be in good agreement with the calculated ratio. The accuracy of these relative measurements was not high but the results lend support to the conclusion that the scatter-

[22] Private communication from H. Feshbach giving F and G values for high energy electrons on silver.
[23] L. K. Acheson Jr., Phys. Rev. 82, 488 (1951). We are indebted to Professor Feshbach for informing us of these calculations before publication.
[24] We are indebted to Professor Bartlett for assistance in extrapolating the calculations so as to be applicable to gold at these energies.

TABLE III. Calculated values for scattering from a point charge. (σ_M in barns per steradian).

	$\beta^2=0.999$				$E=31.72$ mc^2		Kinetic energy $=15.7$ Mev			
Z	30°		60°		90°		120°		150°	
	σ_M	σ_c/σ_M	$\sigma_M\times10^3$	σ_c/σ_M	$\sigma_M\times10^3$	σ_c/σ_M	$\sigma_M\times10^4$	σ_c/σ_M	$\sigma_M\times10^4$	σ_c/σ_M
6	0.1481	1.029	0.855	1.045	0.1425	1.057	3.17	1.063	0.566	1.067
13	0.6950	1.069	4.01	1.112	0.6692	1.143	14.9	1.154	2.608	1.154
29	3.459	1.165	19.97	1.300	3.330	1.387	74.1	1.444	12.98	1.437
47	9.085	1.300	52.44	1.630	8.747	1.852	194.6	2.126	34.09	2.211
79	25.67	1.456	148.2	2.482	24.71	3.795	550	4.828	96.3	5.54

ing theory, when completely evaluated, is sufficient to describe the observed results at lower energies.

Since the wavelength for 15.7-Mev electrons is comparable with nuclear dimensions, the observed scattering is reduced somewhat from that expected for the scattering by a point charge.

For light nuclei where the Born approximation expresses the scattering with reasonable accuracy, the ratio of scattering from a uniform charge distribution of radius R to that from a point charge can be expressed by the relation,[7,9]

$$\sigma/\sigma_c=[(3/K^3R^3)(\sin KR-KR\cos KR)]^2 \quad (11)$$

where K is the change in wave number associated with the angle of scattering as expressed by the relation $K=(2p/\hbar)\sin\frac{1}{2}\theta=(1.64\times10^{12}\sin\frac{1}{2}\theta\ \text{cm}^{-1})$. Although this relation is not accurate for any but the lightest nuclei, it is useful in estimating the magnitude of the effect and the manner in which the cross section depends on the nuclear radius.

Elton and Acheson have treated the size effect in more detail and have derived expressions for the reduction in the cross sections which should be quite reliable. In particular, Acheson[25] has shown that the effect of the finite distribution of the nuclear charge can be expressed in terms of the change in a single phase shift δ_1 in what corresponds to the S wave. According to Acheson the ratio can be written

$$\frac{\sigma}{\sigma_c}=1+\frac{4\cos^2\frac{1}{2}\theta}{|G|^2}\text{Re}\left[Ge^{-2i\chi_1}\left(\frac{e^{2i\delta_1}-1}{2i}\right)^*\right]+\frac{4\cos^4\frac{1}{2}\theta}{|G|^2}\sin^2\delta_1, \quad (12)$$

where G is the complex function determining the coulomb scattering in the approximation that $\beta=1$, χ_1 is the first-order phase shift for the scattering by a coulomb field, and $\delta_1=\eta_1-\chi_1$ is the change in the phase shift for the given charge distribution.

It may be pointed out that the ratio σ/σ_c is not independent of σ_c since $\sigma_c=\lambda^2|G|^2\sec^2\frac{1}{2}\theta$. Therefore, a calculation which gives too small a value for σ_c will at the same time predict too large a decrease in the ratio σ/σ_c for any given charge distribution. The experimental values for σ/σ_c for a given element as a function of angle are sufficient to determine only one constant, namely, δ_1. It is, therefore, not possible to use these results to determine the nuclear radius as well as the charge distribution.

Since there are several methods of measuring nuclear radii the values of the phase shifts determined from the present experiments may be used to distinguish between various possible nuclear charge distributions. For a given nuclear radius the phase shift for the case where the nuclear charge is distributed over the surface of the nuclear volume will be about 50 percent larger than that for the charge distributed uniformly throughout the nuclear volume. The deviations from coulomb scattering [Eq. (12)] will also be different by about 50 percent for these two cases. The difference for the heaviest elements is large enough to be experimentally distinguishable at this energy.

Recent determinations of nuclear radii as obtained from the scattering of fast neutrons indicate that on the average the radii are given by the relation $R=1.37A^{\frac{1}{3}}\times10^{-13}$.[25] This radius does not include the range of nuclear forces and should represent the effective radius

TABLE IV. Theoretical and experimental ratios of the scattering to that from a point charge. (σ/σ_c).

		30°		60°			90°			120°			150°		
		U		S	U		S	U		S	U		S	U		S
C	Theory	0.996		0.993	0.984		0.976	0.972		0.952	0.956		0.928	0.927		0.910
	exp't		1.003			1.004			0.878			0.935			0.833	
Al	Theory	0.992		0.986	0.971		0.948	0.942		0.897	0.915		0.864	0.890		0.823
	exp't		1.006			0.952			0.920			0.925			0.917	
Cu	Theory	0.981		0.969	0.928		0.880	0.872		0.760	0.794		0.654	0.744		0.574
	exp't		0.948			0.945			0.916			0.884			0.795	
Ag	Theory	0.962		0.945	0.863		0.806	0.754		0.656	0.685		0.567	0.636		0.512
	exp't		0.966			0.887			0.828			0.747			0.712	
Au	Theory	0.991		0.973	0.77		0.672	0.57		0.425	0.45		0.292	0.39		0.262
	exp't		0.978			0.741			0.577			0.551			0.472	

[25] Cook, McMillan, Petersen, and Sewell, Phys. Rev. **75**, 7 (1949); J. DeJuren and N. Knable, Phys. Rev. **77**, 606 (1950); H. Lu, Phys. Rev. **77**, 416 (1950).

containing all nuclear particles. It does not necessarily follow that the nuclear protons are distributed over this entire volume but this is the simplest assumption.

The values for σ/σ_s as based on the work of Acheson are given in Table IV for cases of uniform and surface distributions.

V. DISCUSSION OF RESULTS

Before comparing the experimental results with the calculations of the previous section it is necessary to make the adjustment discussed previously for the effect of radiative losses associated with the observed scattering. The experimental arrangement used was not designed to check this effect accurately and hence there is only indirect experimental evidence that the correction as calculated by Schwinger and shown in Table I is correct. The agreement of the results with theory, however, is better when the radiative correction is applied. This is particularly true in the case of polystyrene and aluminum scatterers. A systematic error, such as an error in the energy of the incident beam or an error in measuring the charge incident on the foil, which could change all the observed cross sections uniformly might be wrongly interpreted in terms of a larger or smaller radiative correction. The tabulated values of δ are not expected to be accurate for high values of Z, but are used here since there are no better calculations available.

The experimental cross sections, therefore, have been adjusted for the radiative losses, δ, and are presented as ratios to the point charge scattering in Table IV. The adjusted data are shown in Fig. 4 as ratios to the simple Mott formula. This plot shows very clearly the way the scattering deviates from the simple formula. The adjusted data are presented as ratios to coulomb scattering in Fig. 5. The solid lines in this figure represent the theoretical values for a uniform nuclear charge distribution over a radius given by $1.45A^{\frac{1}{3}}\cdot 10^{-13}$ cm as used by Acheson.

Upon comparing the experimental results with the calculated values the following conclusions might be drawn. In the case of gold where the decrease in the scattering is the greatest, the results agree fairly well with the assumption that the charge is distributed uniformly over the usually accepted nuclear volume. It is apparent that the agreement would be somewhat better if a radius about 20 percent smaller than that shown in the figure is used. This indicates that the proton distribution might be more densely packed toward the center of the nucleus as suggested by Born and Yang.[26]

If it is assumed that the charge density is distributed uniformly over the surface of the nuclear volume, it is found that the observed phase shift would give a nuclear radius for gold almost a factor of two smaller than that usually accepted. Although there are reasons to expect a charge distribution which has the greatest density toward the outside of the nucleus, the present measurements seem to exclude this distribution. The decrease in the cross section for silver can also be explained in terms of a uniform distribution of charge over a 20 percent smaller radius.

[26] M. Born and L. M. Yang, Nature 166, 399 (1950).

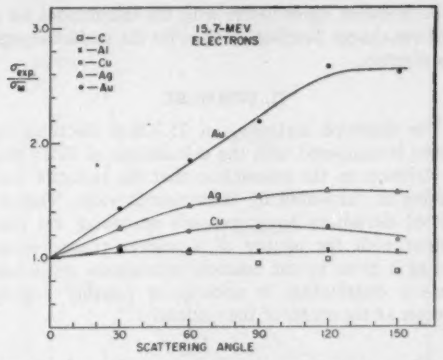

FIG. 4. Experimental results after correcting for counting losses due to radiation. The results are shown here as ratios to the simple Mott formula, Eq. (3). The solid lines sketched in are used merely to connect the experimental data and have no theoretical significance.

It is difficult to say much about nuclear size in the cases of C, Al, and Cu since the reduction from coulomb scattering is small and of the same order of magnitude as the uncertainties in the measurements. The over-all

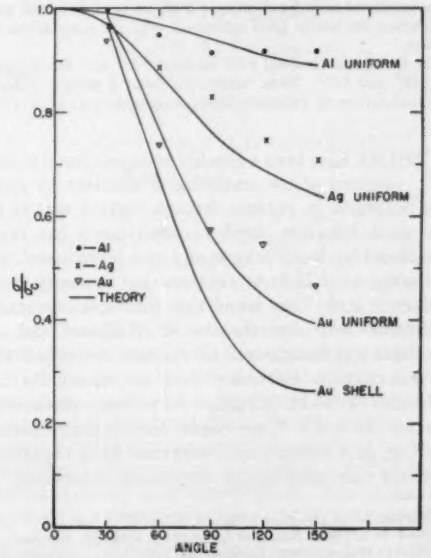

FIG. 5. Experimental results, as in Fig. 4, shown as ratios to coulomb scattering. The solid lines represent the calculated reduction in scattering for nuclear radii given by $R=1.45A^{\frac{1}{3}}\times 10^{-13}$. Calculated curves are shown only for a uniform distribution of charge except for gold where the curve for a surface charge distribution is also shown.

data, however, agree better with the calculations for a uniform charge distribution than for the surface charge distribution.

VI. SUMMARY

The observed scattering of 15.7-Mev electrons by nuclei is compared with the calculations of Elton and of Acheson on the assumption that the radiation correction as calculated by Schwinger is valid. The observed deviations from coulomb scattering are consistent with the picture of a nuclear charge whose radius is given by the neutron experiments and whose density distribution is uniform or possibly slightly greater at the center of the nucleus.

We wish to express our appreciation to S. M. Dancoff and S. Drell for preliminary discussions, to M. E. Rose and L. R. B. Elton for communications regarding the earlier results, and to J. H. Bartlett and J. M. Blatt for discussions regarding the calculations and the interpretation of the results. We are particularly indebted to H. Feshbach for his kind cooperation in sending us the results of pertinent calculations in advance of publication.

The valuable assistance of D. E. Riesen, J. R. Leiss, A. J. Petersen, A. R. Olson, F. Schroeder, K. Hiroshige, and B. A. Smith in building some of the equipment and carrying out the measurements is gratefully acknowledged.

PHYSICAL REVIEW VOLUME 84, NUMBER 4 NOVEMBER 15, 1951

Measurement of Multiple Scattering of 15.7-Mev Electrons*

A. O. HANSON, L. H. LANZL,† E. M. LYMAN, AND M. B. SCOTT‡
Department of Physics, University of Illinois, Urbana, Illinois
(Received July 3, 1951)

The angular distribution of electrons scattered by thin Be and Au foils has been measured for angles where the multiple scattering is important. The $1/e$ widths of the distributions obtained with Au foils of 18.66 and 37.28 mg/cm² are 2.58° and 3.76°, respectively. These widths are about 10 percent narrower than those calculated from the theories of Williams or of Goudsmit and Saunderson but are in good agreement with the calculations of Molière.

The $1/e$ widths obtained with Be foils of 257 and 495 mg/cm² are 3.06° and 4.25°. These widths are about 5 percent smaller than those given by Molière's theory increased by $(1+1/Z)^{\frac{1}{2}}$ for the contribution of electron-electron collisions. The discrepancy may be qualitatively explained by the fact that the Thomas-Fermi screening used in the calculation is different from the effective screening in the Be metal.

The scattering from the two Au foils was measured for larger angles where the scattering can be considered as single scattering modified by the effect of multiple scattering. The ratio of the scattering from the thick to the thin foil can be represented by the relation $2+95/\theta^2$ from 9° to 30°, and is in fair agreement with theoretical expressions for this ratio.

THERE have been a number of experimental investigations of the scattering of electrons by multiple collisions in passing through various materials. The most complete series of experiments has been carried out by Kulchitsky *et al.*,[1] who investigated the scattering of 2.25-Mev electrons by elements from lithium to lead. They found that their results were in agreement with the theories of Williams[2] and of Goudsmit and Saunderson[3] for the light elements if the electron-electron scattering were accounted for by increasing the width calculated for nuclear collisions by a factor $(1+1/Z)^{\frac{1}{2}}$. Their results for the heavy nuclei, however, gave widths which were from 10 to 15 percent narrower than predicted by the theories mentioned.

The present work[4] with higher energy electrons confirms the above results. It will be shown that the experimental results to be presented here, as well as those of Kulchitsky *et al.*, are in better agreement with the theory of Molière,[5] who has investigated the basic single scattering law at small angles, which enters into the theory, in more detail than other authors.

A brief resumè of the various theories is given by Groetzinger, Berger, and Ribe,[6] in connection with the discussion of some cloud chamber observations.

EXPERIMENTAL METHOD

The experimental arrangement used was the same as that described in the work on electron-electron scattering[7] except for the insertion of a smaller aperture defining the scattered beam, and the use of a different detector.

* Supported by the joint program of the ONR and AEC.
† Now at Argonne National Laboratory, Chicago, Illinois.
‡ Now at Massachusetts Institute of Technology, Cambridge 39, Massachusetts.
[1] L. A. Kulchitsky and G. D. Latyshev, Phys. Rev. **61**, 254 (1942); Andrievsky, Kulchitsky, and Latyshev, J. Phys. USSR **6**, 279 (1943).
[2] E. J. Williams, Phys. Rev. **58**, 306 (1940).
[3] S. Goudsmit and J. L. Saunderson, Phys. Rev. **58**, 36 (1940).
[4] Preliminary results were reported at the Chicago meeting of the Physical Society, Phys. Rev. **81**, 309 (1951).
[5] G. Molière, Z. Naturforsch **3a**, 78 (1948); **2a**, 133 (1947).
[6] Groetzinger, Berger, and Ribe, Phys. Rev. **77**, 584 (1950). See also Mott and Massey, *The Theory of Atomic Collisions* (Oxford University Press, London, 1949), second edition, p. 193.
[7] Scott, Hanson, and Lyman, Phys. Rev. **84**, 638 (1951).

The arrangement can be described briefly as follows: A monoenergetic 15.7-Mev electron beam was focused upon a scattering foil at the center of a scattering chamber 20 inches in diameter. The converging cone of electrons had a full angular width of about 1°, and was focused to a spot about 0.08 inch in diameter. The scattered electrons were selected by means of a $\frac{1}{32}$-inch hole in a $\frac{1}{4}$-inch thick lead plate, placed about 10 inches from the scattering foil. After passing through this aperture, the electrons were deflected by an analyzer magnet into a large ionization chamber. The exit port on the analyzer was enlarged so that all electrons whose energy was within 6 percent of the maximum energy entered the ionization chamber.

The incident current was measured by means of a faraday cage connected to a vacuum tube electrometer. This current was maintained at a constant value throughout the experiment. The scattered current was measured by a vibrating reed electrometer connected to the ionization chamber.

At small angles, it was necessary to remove the faraday cage from the forward direction, since it would have intercepted the scattered beam. This was done by remote control, so that a measure of the incident current could be obtained immediately before and after each measurement of the scattered current.

Measurements of the angular distribution were made on both sides of the incident beam for two gold and two beryllium foils from 0° to 6°, using the $\frac{1}{32}$-inch aperture. Measurements of the scattering from the gold foils were extended from 6° to 30° with the larger aperture used in the electron-electron scattering work (0.269×1.00-inch). The scattering by the beryllium foils at the larger angles was not measured, since the analyzer would have excluded the electrons scattered by atomic electrons, giving results which would not be directly comparable to measurements at small angles.

No corrections have been made for the angular width of the incident beam, as this width was small enough to have a negligible effect on the observed distributions.

RESULTS AND COMPARISON WITH THEORY

The observed distributions of electrons scattered by two gold foils are shown in Fig. 1. The measurements were made using the small aperture. The data were normalized so as to present the fractional scattering per unit solid angle in square degrees. The solid lines in the figure represent the distribution calculated from the theory of Molière. It can be seen that the agreement in the angular range given in the figure is very good. The broken lines indicate how the first term of Molière's formulation, the gaussian function $\exp(-\theta^2/B\chi_c^2)$, deviates from the more complete theory.

The distributions represented by the solid line can, however, be approximated quite accurately by a renormalized, slightly narrower gaussian which fits the experimental results very well up to angles (w) where the intensity is $1/e$ of the maximum. This $1/e$ width can be

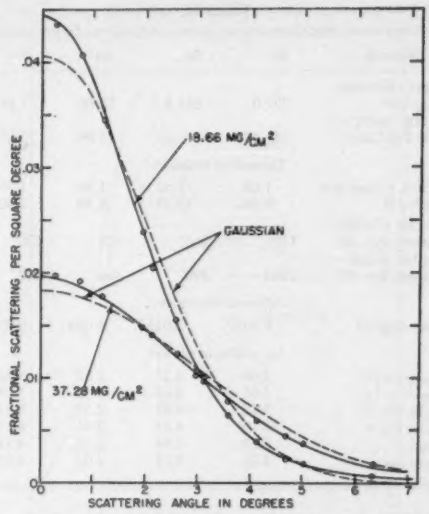

FIG. 1. Distribution of 15.7-Mev electrons passing through two thin gold foils in the region from 0° to 6°. The solid lines represent the theory of Molière. The dotted lines represent the first term of Molière, which is a gaussian having a width in agreement with the older theories.

obtained from the theory and is given to a good approximation by

$$w=\chi_c(B-1.2)^{\frac{1}{2}} \text{ (spatial)}, \quad (1)$$

$$w=\chi_c(B-0.7)^{\frac{1}{2}} \text{ (projected)}, \quad (2)$$

where

$$\chi_c^2=4\pi N(Z^2+Z)e^4/p^2v^2, \quad (3)$$

$$\chi_a^2=(\hbar Z^{\frac{1}{3}}/0.885pa_0)^2[1.13+3.76(Z/137\beta)^2], \quad (4)$$

$$\Omega_b=7e^B/6B=\chi_c^2/\chi_a^2, \quad (5)$$

where N is the number of atoms/cm², p and v the momentum and velocity of the incident electrons, and $a_0=\hbar^2/me^2$ is the Bohr radius of hydrogen. The effect of electron-electron collisions is taken into account by using Z^2+Z instead of Z^2 in Eq. (3). Ω_b can be seen to be proportional to the thickness and corresponds to the number of collisions in passing through the foil.

It might be pointed out that the projected distribution given by Molière is essentially the same as that calculated by Snyder and Scott[8] if the number of collisions is defined in the same way. Snyder and Scott's expression for the number of collisions is defined by the same equation if χ_a is determined in terms of the Born approximation solution to the scattering for exponential screening, namely

$$\chi_a=\hbar Z^{\frac{1}{3}}/pa_0. \quad (6)$$

For low Z, the Born approximation is valid and the difference between the two theories is slight. For high Z,

[8] H. Snyder and W. T. Scott, Phys. Rev. 76, 220 (1949).

TABLE I.

Material	Be	Be	Au	Au
Target thickness mg/cm²	257.0	491.3	18.66	37.28
Average energy in the foil (Mev)	15.47	15.24	15.69	15.67
	Theoretical constants			
Molière χ_c(degrees)	1.08	1.52	1.10	1.55
Molière B	9.56	10.29	6.49	7.30
Number of collisions Eq. (4)	1397	2667	118	236
Number of collisions Eq. (6)	2043	3907	366	732
	Central intensities			
I_0 per degree²	0.0317	0.0153	0.0441	0.0200
	$1/e$ widths in degrees			
w_{expt} (direct)	3.06	4.25	2.58	3.76
$w_{expt}(1/\sqrt{I_0})$	3.01	4.33	2.55	3.78
$(w_{th})_M$ Eq. 4	3.13	4.57	2.52	3.83
$(w_{th})_M$ Eq. 6	3.16	4.63	2.81	4.21
$(B^{\frac{1}{2}}\chi_c)$	3.34	4.94	2.81	4.18
$(w_{th})_{G \text{ and } S}$	3.23	4.65	2.92	4.23

Molière gives a number of collisions which is 2 to 3 times smaller than that of Snyder and Scott and corresponds to a width which is about 10 percent narrower.

The experimental $1/e$ widths (w) and the corresponding calculated widths are given in Table I. Two values for the experimental widths are given. One is the observed angle at which the intensity is reduced to I_0/e; the other is based on the magnitude of the central intensities, which should be inversely proportional to the square of the $1/e$ widths. The latter widths are normalized to the two gold foils and yield values for Be which agree with the direct measurement to about 2 percent. The theoretical values of the $1/e$ width included are those from the tables of Goudsmit and Saunderson, the basic gaussian used by Molière, and the $1/e$ value according to Molière. Theoretical widths using the values for χ_a from Eq. (6) are also given. It can be seen that the agreement between the experiment and Molière's theory is good for gold, but that the experimental $1/e$ widths for beryllium are 3 to 7 percent narrower.

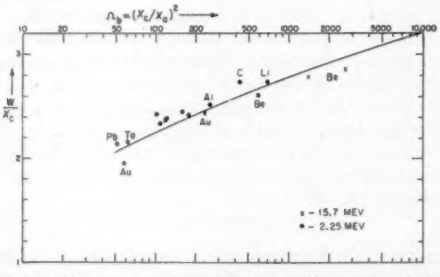

FIG. 2. Experimental values of the $1/e$ widths in units of w/χ_c, as a function of the number of collisions Ω_b. The line is that given by Molière's theory [Eq. (1)].

The results of Kulchitsky *et al.*, at 2.25 Mev, and the present results are shown as a function of the number of collisions, Ω_b, in Fig. 2. The solid line represents the theory of Molière, modified for the effect of electron-electron collisions by using the factor Z^2+Z as in Eq. (3). In such a plot, the light elements which yield a given width correspond to points at large Ω_b. It can be seen that the individual points scatter considerably, but that the over-all agreement is fairly good.

The discrepancy between the observed and calculated widths for Be can probably be explained by the fact that the effective screening of the nuclear charge in Be metal is considerably different than that given by the Thomas-Fermi screening used by Molière. Shinohara[9] has presented a treatment of multiple scattering based on the scattering from microcrystalline units in a solid. This appears to offer an optional way of calculating the scattering from solid materials and may ultimately describe the scattering somewhat better.

SINGLE SCATTERING REGION

The scattering for Au was observed for larger angles, by the use of the larger aperture. A correction (which was small except for the smallest angles) was made for the effect of the aperture size. The data extend from 6°, where they agree fairly well with the small angle data, to 30°, where they are normalized to agree with the observed results of the nuclear single scattering experiment. This single scattering at 30° was about 36 percent larger than that given by the relativistic Mott formula (Born approximation).[10] It was, for the purposes of this work, represented by the relation

$$f(\theta)=2\chi_c^2(1+0.012\theta)/\theta^4.$$

The observed points are shown on a logarithmic scale in Fig. 3, which also gives the complete Molière theory (solid line) over the entire angular range investigated.

The dotted line at smaller angles represents the tail of the gaussian in Fig. 1. The dotted line at larger angles represents the single scattering modified for the above-mentioned departure from the Born approximation.

The ratio of the theoretical scattering to single scattering as given by Molière at large angles is

$$\frac{I}{I_s}=1+\frac{4\chi_c^2}{\theta^2}\left[\ln\left(\frac{\Omega_b\theta^2}{\chi_c^2}\right)-2\right]. \quad (7)$$

The experimental points follow the theory reasonably well at very small and very large angles but are somewhat higher than theory in the region from 6 to 20 degrees.

At large angles, the effect of multiple scattering on the observed scattering may be presented in a manner

[9] Shinohara, Inoue, and Hirohata, J. Phys. Soc. (Japan) **4**, 227 (1949).

[10] Lyman, Hanson, and Scott, Phys. Rev. **84**, 626 (1951).

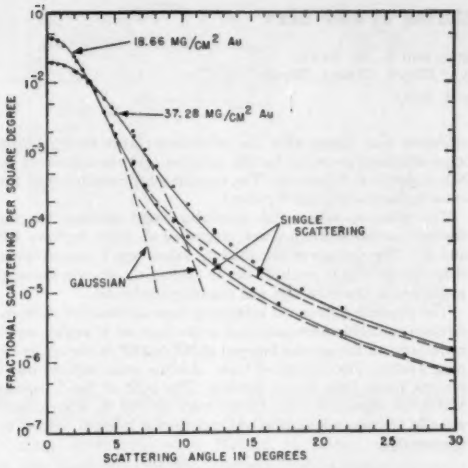

FIG. 3. Angular distribution of electrons from thick and thin gold foils from 0° to 30°. The solid line represents the theory of Molière extrapolated through the region where his small and large angle approximations give different values. The dotted lines at small angles represent the continuation of the gaussians of Fig. 1. At larger angles, the dotted line represents the single scattering contribution.

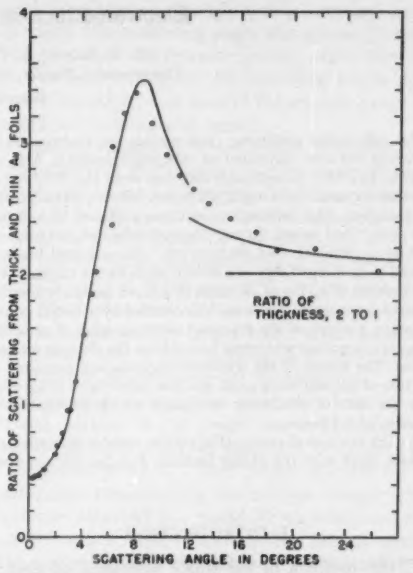

FIG. 4. Ratio of the scattering from thin and thick gold foils. The solid lines represent the values predicted by Molière's small and large angle approximations.

which is less dependent on the single scattering law. This is done by taking the ratio of the observed scattering intensities for the two gold foils. These ratios are shown in Fig. 4. It is found that these are represented fairly well by the expression $2+95/\theta^2$ in the region from 9° to 30°. The solid lines in the figure are values obtained from Molière's theory. The representations at small and large angles do not quite agree in the region in which they overlap. (This disagreement was ignored in the condensed scale used in Fig. 3.)

The ratio of scattering by two foils can also be obtained from the theory of Butler.[11] Good agreement is obtained with experiment if the gaussian used in Butler's theory is reduced by 9 percent. The deviation from the single scattering law at even larger angles has been discussed more generally by Chase and Cox.[12] At angles up to 30°, where the single scattering law can be represented by $1/\theta^4$, both Chase and Cox and Butler find that the increase in scattering can be represented to a first approximation by the factor $1+(4w^2/\theta^2)$. This factor is considerably smaller than Molière's at large angles. Butler's expression, including the higher order terms, represents the experimental results in this angular range somewhat better.

[11] S. T. Butler, Proc. Phys. Soc. (London) **63A**, 599 (1950).
[12] C. T. Chase and R. T. Cox, Phys. Rev. **58**, 246 (1940).

SUMMARY

The observed multiple scattering distributions of fast electrons after passing through thin gold foils is in good agreement with Molière's theory within the experimental accuracy of 2 to 3 percent. The widths are about 10 percent narrower than those given by the theories of Williams or Goudsmit and Saunderson.

The widths of the multiple scattering distributions for beryllium are slightly narrower than those given by Molière's theory. This result may be explained by the fact that the screening used in the theory is different than the effective screening in Be metal.

In the single scattering region, the departure from single scattering toward smaller angles is more rapid than that given by Molière's approximate formula.

We are indebted to D. E. Riesen, who was in charge of the betatron during these experiments, and to A. J. Peterson, J. R. Leiss, and G. E. Mader for assistance with the special equipment.

Electron-Electron Scattering at 15.7 Mev*

M. B. Scott,† A. O. Hanson, and E. M. Lyman
Department of Physics, University of Illinois, Urbana, Illinois
(Received July 3, 1951)

The differential scattering cross section for electron-electron scattering has been measured at relativistic energies. A focused beam of 15.7-Mev monokinetic electrons from the 22-Mev betatron was scattered by 1- and 2-mil Nylon foils in a 20-inch scattering chamber. The incident current was collected by a faraday cage after it had passed through the scattering foil and was measured by a vibrating reed electrometer. The scattered beam was defined by gold-lined slits at a known angle to the incident beam. The number of scattered electrons in a given momentum interval chosen by a magnetic analyzer was counted by a Geiger counter.

Energy analysis of the scattered electrons made it possible to separate the nuclear scattering events from the electron scattering events. The energy of the scattered electrons was measured as a function of the scattering angle and was found to be in agreement with the laws of relativistic mechanics within an experimental accuracy of 0.4 percent.

For the electron-electron collisions the relative scattering cross sections agree with the Møller formula. For the electron-nuclear collisions they agree with the relativistic Mott theory (Born approximation) corrected for the radiative losses as calculated by Schwinger (3 to 8 percent). The experimental consistency of the cross sections was about 4 percent.

The absolute differential scattering cross sections for the electron-nuclear scattering were measured at angles between 10° and 43°. The average of the absolute values was 2 percent lower than theory. This is probably due to systematic errors in the solid angle, and in the collection and counting efficiencies.

The absolute differential scattering cross sections for electron-electron scattering were measured at the same set of angles, which correspond to the angular interval of 70° to 150° in the center-of-mass system. The average of these absolute cross sections was 7 percent lower than theory predicts. The bulk of the 5 percent additional departure from theory may be due to a systematic error in the measurement of the momentum interval defined by the counter.

I. INTRODUCTION

THE problem of the single scattering of electrons by electrons has been treated from a theoretical point of view by several investigators.[1-3] The theory now generally accepted is due to Møller,[2] who gives the differential scattering cross section for the scattering of free electrons in the center-of-mass system as:

$$\sigma(\theta^*)d\Omega^*=\frac{\gamma+1}{2\gamma^2}\left(\frac{e^2}{mv^2}\right)^2\left\{\csc^4\frac{\theta^*}{2}+\sec^4\frac{\theta^*}{2}-\csc^2\frac{\theta^*}{2}\sec^2\frac{\theta^*}{2}+\left(\frac{\gamma-1}{\gamma}\right)^2\left[1+\csc^2\frac{\theta^*}{2}\sec^2\frac{\theta^*}{2}\right]\right\}, \quad (1)$$

where θ^* is the angle of scattering in the center-of-mass system, Ω^* is the solid angle in the center-of-mass system, γ is the total energy of the incident electron in units of mc^2 in the laboratory system, v is the velocity of the electron in the laboratory system, m is the rest mass of an electron, and e is the charge of an electron.

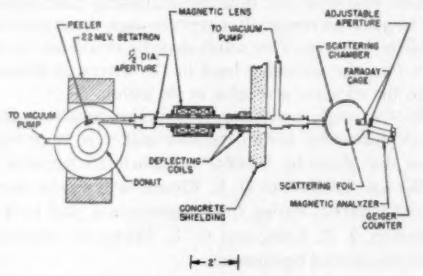

FIG. 1. Experimental arrangement showing the betatron, magnetic lens, and scattering chamber.

The first two angular terms in Eq. (1) represent the coulomb scattering and the corresponding recoil electrons and define a "classical" theory of scattering in which quantum-mechanical interference is not taken into account. The third angular term is the interference between the first two terms arising from the exclusion principle and the identity of the particles. The sum of the first three terms represents the angular dependence of the Mott[1] theory based on the nonrelativistic Schroedinger wave equation. The fourth term is a relativistic correction introduced by Møller arising from the use of the Dirac wave equation. In the nonrelativistic limit ($\gamma \to 1$) the Møller expression (1) reduces to the Mott formula. In the relativistic limit the Møller formula becomes approximately classical due to the near cancellation of the interference term by the relativistic correction.

Experimental study of the scattering problem has been carried out by several investigators. Williams[4] found good agreement with the nonrelativistic Mott theory for electrons of 20 kev, by counting forked tracks in a cloud chamber. After the theory of Møller indicated that deviations from the Mott formula might be expected for relativistic collisions, efforts were made to measure the scattering of fast beta-particles. Champion[5] found good agreement with the Møller theory for 250 collisions of radium E beta-particles in nitrogen found in cloud chamber pictures. More recently, Groetzinger

* Supported by the joint program of the ONR and AEC.
† Now at Massachusetts Institute of Technology, Cambridge 39, Massachusetts.
[1] N. F. Mott, Proc. Roy. Soc. (London) **A126**, 259 (1930).
[2] C. Møller, Ann. Physik **14**, 531 (1932).
[3] K. C. Kar and C. Basu, Indian J. Phys. **18**, 223 (1944).
[4] E. J. Williams, Proc. Roy. Soc. (London) **A128**, 459 (1930).
[5] F. C. Champion, Proc. Roy. Soc. (London) **A137**, 688 (1932).

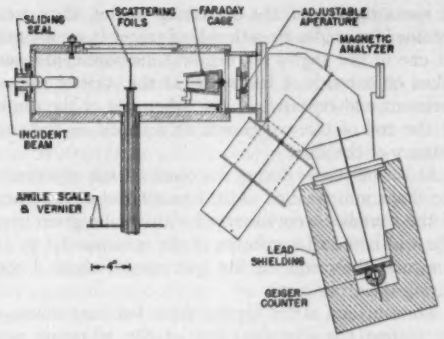

FIG. 2. Scattering chamber.

et al.,[6] have analyzed 98 electron-electron collisions using P^{32} beta-rays in a gas-filled cloud chamber obtaining agreement with Møller. However, the energy of the electrons was too low and the statistics too poor to distinguish unambiguously between the Møller theory, the relativistic Mott theory, or the theory of Kar and Basu.[3] Page and Woodward[7] have also reported good agreement with Møller for the scattering cross section. Champion[8] was the first to confirm the kinematic relations for relativistic collisions of electrons.

The present work was carried out to measure the differential scattering cross section and energy of relativistic electrons scattered by atomic electrons. The principal improvements in this experiment are the use of monokinetic electrons of high energy (15.7 Mev), which permitted the testing of the Møller relativistic correction, and the use of a counter as a detector of the scattered electrons to improve the statistics of the data.

II. EXPERIMENTAL ARRANGEMENT

The source of electrons for this experiment was the 22-Mev betatron with a special donut equipped with a magnetic shunt to extract the electron beam[9] (Fig. 1). The divergent beam from the betatron was collimated and focused by means of a magnetic lens to a spot about 2 mm in diameter on the scattering foil at the center of the scattering chamber ten feet from the betatron. The convergent cone of rays had a spread of about $\frac{1}{2}°$.

Electrons were admitted to the brass scattering chamber (Fig. 2) 6 inches high and 20 inches in diameter through a series of slots in the cylindrical wall. The slots were covered by a polished brass cylindrical cover plate. A sliding vacuum seal between the wall and plate was maintained by a single *O*-ring imbedded in the chamber wall and enclosing all of the slots. The beam entered the chamber through a tube attached to the cover plate. The scattering angle was altered by rotating the chamber and detector system, while the cover plate was held stationary. All scattering angles up to 53° were accessible, and most of the angular range was accessible on both sides of center.

A remotely controlled target holder in the center of the chamber had the following targets mounted on it: a fluorescent screen for locating the beam visually, a vertical 20-mil tungsten wire for measuring the shape and position of the beam by the scattering from the wire, a one-mil nylon scattering foil (2.287 mg/cm²), a two-mil Nylon foil (4.468 mg/cm²), and several blank spaces. The Nylon was $C_{12}H_{22}O_2N_2$, furnished by the DuPont Company. The target holder could be moved so as to bring any of the positions on it into the path of the beam without turning off the betatron.

After passing through the scattering foil, the unscattered portion of the beam was collected by an aluminum faraday chamber having a body depth of 1.6″ and subtending 12°. The charge collected by the chamber was measured by the voltage change across a condenser attached to a model 30 vibrating reed electrometer[10] which could be switched by remote control.

The scattered beam was defined by adjustable gold-edged slits (Fig. 3) located in the cylindrical wall of the scattering chamber. The slits were formed of two interlocking brass pieces $\frac{3}{4}$ inch thick, which could slide relative to each other, thereby changing the width of the slit up to a maximum of $\frac{3}{4}$ inch. The slit opening was one inch high and completely edged with a gold strip $\frac{1}{16}$ inch wide and $\frac{1}{8}$ inch deep inset into the brass. The brass behind the gold was relieved by 3° so that the electrons passing through the slit could be scattered only by the gold edges.

Electrons admitted by the defining slit passed through a 75° magnetic analyzer and into a thin-walled glass Geiger counter detector surrounded by lucite and lead shielding. With a 0.375-inch slit above the Geiger counter detector, the energy spectrum admitted to the counter was 1 percent wide at the peak. Except for the wall of the Geiger counter, the only scattering material in the path of the beam was the the scattering foil itself.

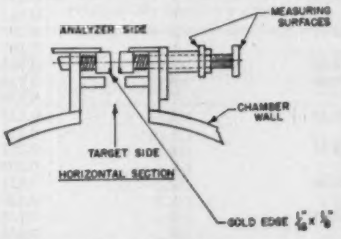

FIG. 3. Detail of defining aperture.

[6] Groetzinger, Leder, Ribe, and Berger, Phys. Rev. **79**, 454 (1950).
[7] L. A. Page and W. M. Woodward, Phys. Rev. **79**, 228 (1950).
[8] F. C. Champion, Proc. Roy. Soc. (London) **A136**, 630 (1932).
[9] Lyman, Hanson, and Scott, Phys. Rev. **84**, 626 (1951).
[10] Applied Physics Corporation, Pasadena, California.

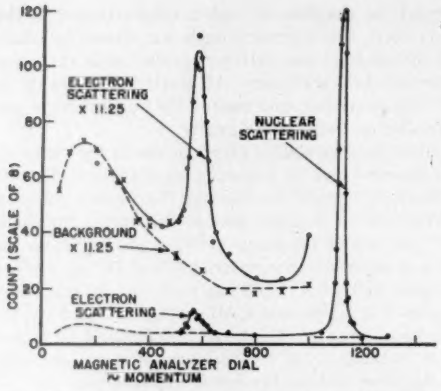

FIG. 4. Momentum spectrum of electrons scattered through 14 degrees. Laboratory angle = 14°. Center-of-mass angle = 90°.

III. EXPERIMENTAL PROCEDURE

The procedure for lining up the electron beam was to determine the path of the beam through the vacuum system as the system was built up piece by piece, either by observing the beam with x-ray film or by using a fluorescent screen and mirror-telescope arrangement. The final alignment was checked by passing the tungsten wire across the center of the chamber and observing the scattering from the wire to determine the size and position of the focused spot relative to the center of the chamber.

The data consisted of the observed number of scattered electrons per unit incident charge as a function of the analyzer magnetic field (i.e., the momentum of the scattered electrons). Counts were taken at intervals of 30 to 70 kev across the peak due to electron-electron scattering, at several points off this peak and across the elastic scattering peak for each foil, with foils absent, and at each of 9 angles. To eliminate systematic errors in measurement of the scattering angles, data were obtained for angles on each side of center in some cases. At one of the angles (14 degrees) measurements were taken on one side of the center at the start of the experiment and repeated on the other side of the center at the end of the experiment as a check on the consistency of the data.

At various times during the course of the experiment the shape and position of the focused spot at the center of the chamber were observed with the tungsten wire. The width at half-maximum of the spot was 1.5 to 2.0 mm, and the center of the spot moved about 1 mm during the experiment.

Transmission ratios for the thick foil were obtained by finding the charging time of the vibrating reed electrometer condenser for constant incident current, with and without the scattering foil in position. The transmission ratio of the thick foil was found to be 0.992 and the ratio for the thin foil was estimated to be 0.996.

In the case of one angle (14°) data were obtained for five different slit widths. The results indicated that the observed count was linear with the slit width up to at least 0.37 inch. At all the other angles the data were obtained with a slit width of 0.269 inch.

IV. TREATMENT OF DATA

In order to obtain the true number of counts corresponding to an observed number, it was necessary first to reduce the observed number by subtracting the natural background of the counter and second, to adjust for the fractional loss of counts due to the high peak intensities used. The fractional loss was taken to be the counting rate observed divided by twice the repetition frequency of the betatron (180 cps). This latter correction never exceeded 10 percent.

In order to obtain the true number of counts due only to electrons scattered by the target foil and to eliminate those due to electrons and x-rays scattered

TABLE I. Electron-electron scattering results.

Laboratory scattering angle (degrees)	Target thickness (mils)	Differential scattering cross section (lab system) (barns/sterad) experiment	Exp't / Møller	Experimental cross section in center-of-mass system (barns/sterad)	Scattering angle in center-of-mass system (degrees)
9.98	2	0.435	0.95	0.0144	70.9
	1	0.442	0.96	0.0146	
13.77	2	0.201	0.99	0.0111	89.5
	1	0.195	0.96	0.0107	
14.37	2	0.183	0.97	0.0109	92.0
16.98	2	0.124	0.83	0.0106	102.0
	1	0.136	0.91	0.0116	
19.33	2	0.125	0.94	0.0146	109.4
	1	0.118	0.88	0.0138	
23.57	2	0.113	0.91	0.0225	120.9
	1	0.109	0.87	0.0217	
27.84	2	0.124	0.95	0.0406	129.8
	1	0.120	0.92	0.0393	
33.83	2	0.133	0.88	0.081	139.5
	1	0.133	0.88	0.081	
42.65	2	0.212	0.99	0.286	150.0
	1	0.213	1.00	0.288	

about the room, the background count with no foil present was obtained and subtracted for each point of the energy spectrum.

Figure 4 is an example of the data obtained in this experiment. There are two peaks, one due to nuclear scattering at the incident energy, and one due to electron scattering at a lower energy. The energy lost in the latter case is carried away by the other electron participating in the collision. The upper curve is an expansion of the low energy end of the lower curve to show the relative size of the peak and background. The example shown is for the angle of symmetry in the center-of-mass system, for which the cross section is small and hence the background is large relative to the scattering. The electron peak has a considerable energy width due to the angular spread associated with the finite aperture of the detector and the multiple scattering in the foil.

The total number of electrons associated with the electron-electron scattering peak was determined from the area under this peak and the fractional resolution of the analyzer. The fractional momentum resolution of the analyzer (r) was obtained from the width at half-maximum, of the nuclear scattering peak which is nearly monoenergetic.

If we let $C_{\text{obs}}(p)$ be the observed count at an analyzer setting which admits to the detector electrons with an average momentum p in the small momentum interval rp, then the total number of electrons associated with the electron-electron peak is given by

$$C_t=\int_{\text{peak}} C_{\text{obs}}(p)/rp\,dp\cong(1/r\bar{p})\int_{\text{peak}} C_{\text{obs}}(p)dp,$$

where $\bar{p}$ is the momentum at the peak and the integral is the area under the experimental curves of the net count plotted as a function of the momentum.

V. EXPERIMENTAL RESULTS

The experimental results are given in Tables I, II, and III. Table I gives the differential scattering cross section for electron-electron scattering. The scattering angle of column 1 has been averaged over the defining slit in the laboratory system. The corresponding angle in the center-of-mass system is given in column 7. The target thicknesses in column 2 are approximate and are used only to identify the foil. The experimental scattering cross section in barns per unit solid angle per electron is given in column 3. The ratio of the experimental cross section to the theoretical cross section is given in column 4. The cross section in the center-of-mass system corresponding to the experimental cross section in the laboratory system (column 3) is given in column 5. Figure 5 shows the experimental cross sections from Table I, compared with the Møller, relativistic Mott, Kar, and classical theories. We can see that the experimental points follow the Møller theory and depart as much as 100 percent from the Mott theory for the 90°

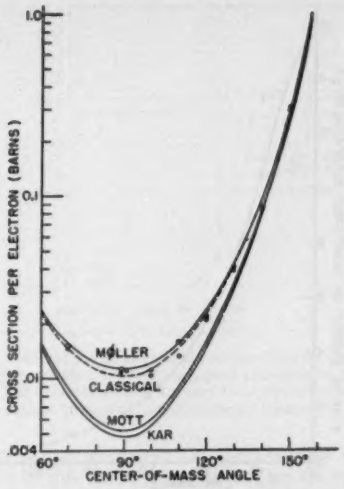

FIG. 5. Differential scattering cross section for electron-electron scattering as a function of the angle in the center-of-mass system. The curves represent the theoretical values according to the Møller, Kar, and Mott formulations. The curve indicated as classical represents the first two terms of the Møller formula.

scattering. The points average about 7 percent low, which may be due to a systematic error in the measurement of the momentum interval defined by the counter.

Table II gives the data on the kinetic energy of the scattered electrons as a function of the scattering angle. The calculated kinetic energy is based on the formulas:

$$T=T_0\cos^2\tfrac{1}{2}\theta^*;\quad(\tfrac{1}{2}T_0+1)^{\frac{1}{2}}\tan\theta=\tan\tfrac{1}{2}\theta^*,$$

where θ^* is the angle in the center-of-mass system, θ is the angle in the laboratory system, T is the kinetic energy in units of mc^2, and T_0 is the incident kinetic energy (15.7 Mev) in units of mc^2. These formulas are based on the assumption that during the collision energy and momentum are conserved and that the velocities combine according to the relativistic law of addition of velocities.

An experimental check on the absolute energy of the

TABLE II. Energy of scattered electrons vs laboratory scattering angle.

Average laboratory angle degrees	Observed kinetic energy Mev	Calculated kinetic energy Mev
0	15.672	15.700
9.98	10.413	10.420
13.77	7.924	7.918
14.37	7.567	7.570
16.98	6.211	6.216
19.33	5.212	5.210
23.57	3.829	3.816
27.84	2.808	2.822
33.83	1.893	1.880
42.65	1.037	1.055

FIG. 6. Energy of scattered electrons at the maximum of the electron-electron peak as a function of the angle. The solid line represents the theoretical variation of energy with the angle. The incident energy is 15.7 Mev.

incident electrons was obtained by comparing the observed variation of momentum of the scattered electrons as a function of the angle with that expected from the above kinematic relations. The absolute values listed in column 2 of Table II are based on a value of the incident energy determined in this way. The relative values in the column are determined from the observed magnetic field corresponding to the peak of the electron-electron distribution at the indicated angle. The calculated energies given in column 3 of the table are based on an incident energy of 15.7 Mev which is determined by using the value of 10.9±0.2 Mev for the threshold of the $Cu^{63}(\gamma, n)$ reaction. It can be observed that the energy scale obtained from the observed variation of the energy with angle in an electron-electron collision is in agreement with the energy scale usually used to better than 0.5 percent. The data of Table II are shown in Fig. 6, where the line is the theoretical calculation and the points are the experimental data.

Table III gives the nuclear scattering results. The scattering angle in column 1 is the angle to the center of the defining slit. In column 3 are the experimental differential cross sections in barns/sterad corrected for the finite size of the defining slit and reduced to $Z=1$. The corresponding theoretical cross section is given by Mott as:

$$\sigma(\theta)=\left(\frac{e^2}{2mc^2}\right)^2\frac{1-\beta^2}{\beta^4}\frac{1-\beta^2\sin^2\frac{1}{2}\theta}{\sin^4\frac{1}{2}\theta}. \qquad (2)$$

Column 5 is the ratio of the experimental to the theoretical cross section corrected for the loss of counts from a detector of 1 percent energy resolution due to radiation straggling and emission and reabsorption of virtual quanta as given by Schwinger.[11] This effect varies from 3 to 8 percent. The experimental data and the Schwinger correction are given in Fig. 7 as a function of the scat-

TABLE III. Experimental results—electron-nuclear scattering.

Scattering angle at center of defining slit degrees	Foil thickness mils	Experimental differential scattering cross section corrected to center of slit barns/sterad ($Z=1$)	Theoretical cross section (Mott)	Exp't/theory corrected for radiation (Schwinger)
9.88	2	0.353	0.357	1.023
	1	0.362		1.049
13.70	2	0.0869	0.0963	0.948
14.30	2	0.0742	0.0811	0.963
	1	0.0748		0.970
16.92	2	0.0358	0.0413	0.918
	1	0.0386		0.990
19.28	2	0.0224	0.0244	0.971
	1	0.0226		0.984
23.53	2	0.0106	0.0110	1.027
	1	0.0104		1.018
27.80	2	0.00492	0.00559	0.945
	1	0.00473		0.911
33.80	2	0.00226	0.00253	0.968
	1	0.00232		0.996
42.63	2	0.000918	0.000980	1.023
	1	0.000893		0.996

[11] J. Schwinger, Phys. Rev. **76**, 790 (1949).

tering angle, normalized to Mott scattering (2). The observed points follow somewhat better the line of the Mott theory with the Schwinger correction. The points average about 2 percent low, which is probably due to systematic errors in the solid angle and in the collection and counting efficiencies.

SUMMARY

The observed relative cross section for electron-electron scattering agrees with that given by the Møller formula. The relative cross section for nuclear scattering by light nuclei agrees fairly well with that given by the Mott formula [Eq. (2)] after correcting for the loss of counts due to the radiative losses by the Schwinger formula.

The individual values of the observed cross sections seem to be consistent to about 4 percent. The absolute cross sections are 7 percent low in the case of electron-electron scattering and 2 percent low for nuclear scattering. The departure of the absolute values from theory is not significant and may be due to systematic errors common to each group of measurements. The energy of the electrons scattered by electrons was investigated as a function of the scattering angle and was found to be in agreement with relativistic kinematics.

We wish to express our appreciation to many of the members of the laboratory for their interest and cooperation in this work. In particular, we are indebted to D. E. Riesen for the maintenance and operation of the betatron throughout this work, and to A. J. Petersen, J. E. Leiss, and G. E. Mader for valuable assistance in developing the equipment and in obtaining the data.

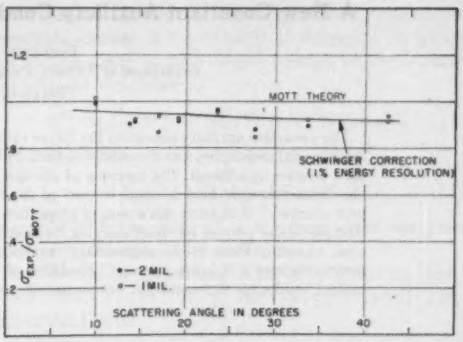

FIG. 7. Ratio of the experimental cross sections for the nuclear scattering from Nylon to those calculated according to the Mott formula. The curve takes into account the expected reduction in the cross section because of radiative energy losses.

A New Covariant Auxiliary Condition for Quantum Electrodynamics

FREDERIK J. BELINFANTE
Department of Physics, Purdue University, Lafayette, Indiana
(Received June 25, 1951)

The covariant auxiliary condition Eq. (3) or (15) is assumed to be valid for all states occurring in nature. Such special assumptions as the condition for a "photon vacuum" of the type of the noncovariant Eq. (18) then become superfluous. The meaning of the new auxiliary condition (15) is that the expectation value of the electromagnetic field is equal to that of the retarded field from charged matter: "All light has once been emitted." If in some discussion of properties of a particular photon one wants to ignore the source of that particular photon (without denying its existence), one can ignore Eqs. (3) and (15) in such a special case, replacing them by an appropriate "practical" boundary condition. In self-energy calculations one sometimes uses a "photon vacuum" condition of the type of Eq. (20). Such approximation to (15) gives correct results up to second but not to fourth powers of e.

I. AUXILIARY CONDITION FOR TRANSVERSE PHOTONS IN HEISENBERG REPRESENTATION

IN Fermi's quantum electrodynamics, the Lorentz condition ensures equality of the values of div $\mathbf{E}_{\text{II}}$ and $4\pi\rho$, and thus guarantees that all charges are surrounded by their longitudinal electric fields. In "gauge-independent" (G-I) quantum electrodynamics[1,2] the same is guaranteed by the definition of the longitudinal field.

It is however a common experience that there exists a second tie between matter and the Maxwell field, which may be expressed by saying that also each transverse wave that is observed was once emitted by a source. Although the most general solution of Maxwell's equations may be described by

$$A^\mu(\mathbf{x}, t)=A_{\text{ret}}{}^\mu(\mathbf{x}, t)+A_\circ{}^\mu(\mathbf{x}, t), \tag{1}$$

where $A_\circ{}^\mu$ is a solution of the homogeneous equations, we use to assume that in reality $A_\circ{}^\mu$ or at least its physically significant transverse part $\mathfrak{A}_\circ{}^\mu$ (with spatial part $\mathfrak{A}_\circ$) vanishes. Thus, light spots in the sky at night are interpreted as stars rather than as solutions of the homogeneous equations.

One may object that the vanishing of $A_\circ{}^\mu$ or[3] of $\mathfrak{A}_\circ{}^\mu$ is contrary to "the fact that" nature is symmetric in time. Yet, even if this symmetry of nature with respect to the sign of t would exist, there is the other fact that physics (which is our knowledge of nature) is not symmetric in time. In knowledge there is, for instance, a distinct difference between memory and prediction. If we say that $\mathfrak{A}_\circ{}^\mu$ vanishes, this is perhaps not a property of objective nature, but rather a property of supposed knowledge. Let us express this in the form of an equation.

The q-number $\mathfrak{A}_\circ{}^\mu$ is a part of the description of nature; there are arguments why it probably cannot vanish.[4] Our supposed knowledge of nature is described by the state vector, say Φ in Heisenberg representation. Our statement is then in the first place that the mean expectation value of $\mathfrak{A}_\circ$ vanishes:

$$(\Phi^*, {}^{\text{H}}\mathfrak{A}_\circ(\mathbf{x}, t)\,\Phi) = 0. \tag{2}$$

Here, $^{\text{H}}$ denotes Heisenberg representation. Equation (2) together with the equality of the mean expectation values of the longitudinal field $\mathbf{E}_{\text{II}}$ and the coulomb field $-\nabla\int d^3\mathbf{x}'\rho(\mathbf{x}')/r$, tells us how to interpret the dualism between the field concept and the action-at-a-distance concept in quantum electrodynamics.

It is impossible to postulate ${}^{\text{H}}\mathfrak{A}_\circ(\mathbf{x}, t)\Phi=0$, since the commutator Eq. (II.3) of the appendix does not vanish. But we want to state only that in the $\mathfrak{A}_\circ$-field "no photons are present." This we formulate by assuming[3,5,6]

$${}^{\text{H}}\mathfrak{A}_\circ{}^{(+)\mu}(\mathbf{x}, t)\,\Phi = 0, \tag{3}$$

where $\mathfrak{A}_\circ{}^{(+)}$ is Schwinger's "positive frequency" part of the $\mathfrak{A}_\circ$-field, which describes annihilation of photons only. In fact, Eq. (2) will now follow directly from Eq. (3) and its hermitian conjugate

$$\Phi^*\,{}^{\text{H}}\mathfrak{A}_\circ{}^{(-)\mu}(\mathbf{x}, t) = 0. \tag{4}$$

Note that (4) follows from (3); it is impossible to replace (4) by a similar formula with $(\mathfrak{A}-\mathfrak{A}_{\text{adv}})^{(-)}$ replacing $\mathfrak{A}_\circ{}^{(-)}\equiv(\mathfrak{A}-\mathfrak{A}_{\text{ret}})^{(-)}$, if we want to stick to (3).

It should be well understood that it was our assumption that in principle, for all states of nature considered in physics, condition (3) should hold rigorously. For many practical problems, however, Eq. (3) may be of little interest. Suppose we know what photons are present at a time represented by a space-like surface I in space-time, and that we want to make predictions on what will happen at later times. We can express $A_{\text{ret}}{}^\mu(\mathbf{x}, t)$ as an integral over space-time[6,7] as in Eq. (I.2) of the appendix, and we might divide the integral into two parts $A_{\text{ret}<I}{}^\mu(\mathbf{x}, t)$ and $A_{\text{ret}>I}{}^\mu(\mathbf{x}, t)$ corresponding to the parts of space-time before and after

[1] W. Pauli, Kapitel 2, B.8, p. 269 sqq. of Geiger and Scheel's *Handbuch der Physik*, second edition, Vol. 24/1 (1933).
[2] F. J. Belinfante and J. S. Lomont, Phys. Rev. 84, 541 (1951). We shall refer to equations from this paper by (G-I:).
[3] J. Schwinger, Phys. Rev. 74, 1439 (1948).
[4] F. J. Belinfante and J. S. Lomont, Phys. Rev. 78, 346(A) (1950).
[5] F. J. Belinfante, Phys. Rev. 75, 337(A) (1949).
[6] J. Schwinger, Phys. Rev. 75, 651 (1949).
[7] F. J. Belinfante, Phys. Rev. 76, 66 (1949).

the surface I,

$$ {}^{\mathrm{H}}A_{\mathrm{ret}>\mathrm{I}}{}^{\mu}(\mathbf{x}, t) = -4\pi \int_{I}^{t} d^4x\, D(x-x')\, {}^{\mathrm{H}}j^{\mu}(\mathbf{x}', t'), \quad (5) $$

where t on the integral denotes the surface $t=$ constant, $d^4x = d^3\mathbf{x}\, dx^0$ with $x^0 = -x_0 = ct$, and $D(x)$ is Schwinger's D-function.[3,6] ${}^{\mathrm{H}}A_{\mathrm{ret}<\mathrm{I}}{}^{\mu}$ is a similar expression with integral from $-\infty$ to I. Then, by (1),

$$ A^{\mu}(\mathbf{x}, t) = A_{\mathrm{I}}{}^{\mu}(\mathbf{x}, t) + A_{\mathrm{ret}>\mathrm{I}}{}^{\mu}(\mathbf{x}, t), \quad (6) $$

where

$$ A_{\mathrm{I}}{}^{\mu}(\mathbf{x}, t) = A_{\mathrm{o}}{}^{\mu}(\mathbf{x}, t) + A_{\mathrm{ret}<\mathrm{I}}{}^{\mu}(\mathbf{x}, t). \quad (7) $$

Now, in the problem considered, we may not be interested in this division (7) of $A_{\mathrm{I}}{}^{\mu}$ or of its transverse part $\mathfrak{A}_{\mathrm{I}}$ into two parts. We would simply postulate as initial condition the numbers of photons (and of other particles) present at I. For instance, in some very special problem, we may start out with a photon vacuum at I, so that we want to put

$$ {}^{\mathrm{H}}\mathfrak{A}_{\mathrm{I}}{}^{(+)}(\mathbf{x}, t)\, \Phi = 0, \quad \text{(photon vacuum at } I\text{)}. \quad (8) $$

Although we would believe that in principle Eq. (3) is still correct, we would make no attempt to use it or even to reconcile it with the condition (8), which is of more practical importance for such particular problem. The practical importance of Eq. (3), then,—beside its mere philosophical value as a general principle of physics,—lies in the fact that in many instances we idealize practical problems with initial photon vacuum at I, by taking the limit $I \to -\infty$. In such cases, the rigorous condition (3) can replace the ad hoc condition (8). But in a problem like the Compton effect, the ad hoc condition of presence of a photon at I would lead in the limit $I \to -\infty$ to a practical initial condition contrary to the fundamental but in this case not very interesting equation (3). In such case, we would therefore simply ignore Eq. (3) for the solution of such problem.

II. USE OF INTERACTION REPRESENTATION

The main task of this paper will further be to reformulate formula (3) in a different mathematical form, and to prove its covariance. For this purpose we shall relate our Heisenberg representation of q-numbers to an interaction representation ($^{\mathrm{I}}$) coinciding with the Heisenberg representation ($^{\mathrm{H}}$) on the initial surface I:

$$ {}^{\mathrm{H}}q(\mathbf{x}, t) = U_{\mathrm{I}}(t)^{-1} \cdot {}^{\mathrm{I}}q(\mathbf{x}, t) \cdot U_{\mathrm{I}}(t), \quad (9) $$

$$ U_{\mathrm{I}}(I) = 1. \quad (10) $$

We shall also consider the interaction representation ($^{\circ}$), which coincides with Heisenberg representation at $t = -\infty$:

$$ {}^{\mathrm{H}}q(\mathbf{x}, t) = U_{\mathrm{o}}(t)^{-1} \cdot {}^{\circ}q(\mathbf{x}, t) \cdot U_{\mathrm{o}}(t), \quad (9a) $$

$$ U_{\mathrm{o}}(-\infty) = 1. \quad (10a) $$

This is simply a special case of (9)–(10) for $I \to -\infty$. In both cases, U satisfies the usual generalized Schrödinger equation (similar to Eq. (G-I:9) of reference 2), which for infinitesimal parallel displacements of the surface $t=$ constant simplifies to

$$ i\hbar[dU_{\mathrm{I}}(t)/dt] = U_{\mathrm{I}}(t)\, {}^{\mathrm{H}}\mathfrak{W}(t) = {}^{\mathrm{I}}\mathfrak{W}(t) U_{\mathrm{I}}(t), \quad (11) $$

and its hermitian conjugate

$$ -i\hbar[dU_{\mathrm{I}}{}^{-1}/dt] = U_{\mathrm{I}}(t)^{-1}\, {}^{\mathrm{I}}\mathfrak{W}(t), \quad (12) $$

where $\mathfrak{W}(t)$ is the integral of the interaction operator $W(x)$ over the space-like surface t.

In Manifestly Covariant ("M.C.") Quantum Electrodynamics ("q.e.") it can then be shown easily (see Appendix I) that

$$ {}^{\mathrm{H}}A_{\mathrm{I}}{}^{\mu}(x)[\equiv {}^{\mathrm{H}}A^{\mu}(x) - {}^{\mathrm{H}}A_{\mathrm{ret}>\mathrm{I}}{}^{\mu}(x)] = {}^{\mathrm{I}}A^{\mu}(x). \quad (13) $$

In Gauge-Independent ("G.I.") q.e., no four-vector A^{μ} is defined, but one does define a solenoidal vector $\mathfrak{A}(x)$, which is equivalent to Schwinger's $\mathfrak{A}^{\mu}$ when $\mathfrak{A}^0$ vanishes. It is easily shown (see Appendix II) that in G.I.q.e.

$$ {}^{\mathrm{H}}\mathfrak{A}_{\mathrm{I}}(x)[\equiv {}^{\mathrm{H}}\mathfrak{A}(x) - {}^{\mathrm{H}}\mathfrak{A}_{\mathrm{ret}>\mathrm{I}}(x)] = {}^{\mathrm{I}}\mathfrak{A}(x), \quad (14) $$

where $\mathfrak{A}_{\mathrm{ret}}(x)$ is the transverse retarded vector potential, and where $>$I refers to sources "after" the surface I.

Taking in Eqs. (13)–(14) the limit $I \to \infty$, so that $\mathfrak{A}_{\mathrm{I}} \to \mathfrak{A}_{\mathrm{o}}$ and ${}^{\mathrm{I}}\mathfrak{A} \to {}^{\circ}\mathfrak{A}$, we can rewrite our fundamental auxiliary condition (3) as

$$ {}^{\circ}\mathfrak{A}^{(+)\mu}(\mathbf{x}, t)\, \Phi = 0. \quad (15) $$

In this fundamental formula, a "q-number in interaction representation" seems to operate on the state vector in Heisenberg representation. In fact, our result for $I \to -\infty$

$$ {}^{\circ}\mathfrak{A}^{\mu} = {}^{\mathrm{H}}\mathfrak{A}_{\mathrm{o}}{}^{\mu} \equiv {}^{\mathrm{H}}\mathfrak{A}^{\mu} - {}^{\mathrm{H}}\mathfrak{A}_{\mathrm{ret}}{}^{\mu} \quad (14a) $$

shows that Eq. (9a) can be regarded as a canonical transformation by which—in Heisenberg representation—new variables ${}^{\circ}q$ are introduced, in which the retarded fields have been rigorously separated from the electromagnetic field. The limitations to the usefulness of such canonical transformation (which according to Eq. (G-I:54) of reference 2 eliminates the electromagnetic interactions altogether), and a more useful transformation leaving the interaction with external fields, were discussed for instance by Dyson.[8]

Note that, even in M.C.q.e., one cannot "generalize" Eq. (15) by replacing $\mathfrak{A}$ in it by A. There is not only no physical reason for such a "generalization," but the $\mu=0$ component of such "generalized" Eq. (15) would even be an absurdity, as "there is no state, in which no scalar photons could be created."[9]

III. PROOF OF COVARIANCE

The Lorentz-invariance of (15) is not yet obvious. (By Lorentz-invariance we mean independence from the choice of the time-like four-vector n^{μ} used by

[8] F. J. Dyson, Phys. Rev. **75**, 486 (1949).
[9] F. J. Belinfante, Phys. Rev. **76**, 226 (1949).

Schwinger in his definition of $\mathfrak{A}$. We prefer to choose this n^μ always along the time-axis, so that out n^μ and $\mathfrak{A}^\mu$ do not transform as four-vectors.)

In M.C.q.e., the covariance of the condition (15) under Lorentz transformation of the time direction given by n can be proved as follows: By

$$^\circ A^\mu = {}^\mathrm{H}A_\circ{}^\mu \equiv {}^\mathrm{H}A^\mu - {}^\mathrm{H}A_{\mathrm{ret}}{}^\mu \tag{13a}$$

we find in Heisenberg representation

$$\partial_\mu {}^\circ A^\mu(x)\,\Phi = 0 \tag{16}$$

by subtracting the identity $\partial_\mu {}^\mathrm{H}A_{\mathrm{ret}}{}^\mu(x)=0$ from the Lorentz condition $\partial_\mu {}^\mathrm{H}A^\mu(x)\Phi=0$. But (16) with[8]

$$\Box\, {}^\circ A^\mu(x) = 0 \tag{17}$$

and the four-vector character of $^\circ A^\mu$ together guarantee the rigorous invariance of (15) by the same argument[8] as used to prove the invariance in zeroth-order approximation of the "photon vacuum" condition

$$^\mathrm{H}\{\mathfrak{A}^{(+)}(x)\}\,\Phi \approx 0$$

or

$$^\mathrm{I}\mathfrak{A}^{(+)}(\mathbf{x}, t)\,\Psi_\mathrm{I}(t) \approx 0, \tag{18}$$

which has been used in various older publications.[6,9]

In G.I.q.e., the covariance of the condition (15) follows from the invariance of the tensor formula

$$^\circ\mathfrak{F}_{\lambda\mu}{}^{(+)}(x)\,\Phi = 0, \tag{19}$$

where $^\circ\mathfrak{F}_{\lambda\mu}$ is the electromagnetic field $^\circ\mathfrak{E}$, $^\circ\mathfrak{B}$ in interaction representation. Equation (19) follows from (15) by $^\circ\mathfrak{F}_{\lambda\mu}{}^{(+)} = \partial_\lambda {}^\circ\mathfrak{A}_\mu{}^{(+)} - \partial_\mu {}^\circ\mathfrak{A}_\lambda{}^{(+)}$, while Eq. (15) (with $^\circ\mathfrak{A}^0=0$) again follows from the space-like components of (19) ($^\circ\mathfrak{B}^{(+)}\Phi=0$) by the definition Eq. (G-I:3) of reference 2, of $\mathfrak{A}$ in terms of $\mathfrak{B}$.

IV. COMPARISON OF AUXILIARY CONDITION WITH PHOTON VACUUM CONDITIONS

In earlier publications, Eq. (18) was meant as either only a zeroth-order approximation for the state-vector, or as a boundary condition on a specific initial surface I, where it is by $\Psi_\mathrm{I}(t)=U_\mathrm{I}(t)\Phi$ with (10) and (14) equivalent to the special "practical" assumption (8). Equation (18) was not rigorously covariant, but only in zeroth order.[9] This is due to the fact that from (18) we cannot conclude the vanishing of $^\mathrm{I}\mathfrak{E}^{(+)}(\mathbf{x}, t)\,\Psi_\mathrm{I}(t)$, since differentiation of (18) with respect to t introduces $d\Psi_\mathrm{I}/dt$. Thus, (19) is no longer valid, and in a different Lorentz frame $^\mathrm{I}\mathfrak{B}^{(+)}\Psi_\mathrm{I}$, and therefore $^\mathrm{I}\mathfrak{A}^{(+)}\Psi_\mathrm{I}$ will no longer vanish. On the other hand, the general law given by Eq. (15) (together with (16) in the M.F. theory) is rigorously covariant.

Let us remark here that in many calculations one uses neither (15) nor (18), but something in between:

$$^\circ\mathfrak{A}^{(+)}\,\Psi_\mathrm{I}[\sigma] = 0, \tag{20}$$

where Ψ_I is obtained from $\Psi_\circ = U_\circ\Phi$ by a transformation not quite equal to $U_\circ{}^{-1}$, but an approximation of it. With the first-order approximation sometimes used in the calculation of the self-energy of a free electron, use of (20) instead of (15) can be shown to lead to errors in the free-electron self-energy proportional to the fourth and higher powers of e only, so that, contrary to earlier belief,[10] this cannot account for the appearance of "kinetic self-energy" terms. (The latter are due to certain ambiguities in the evaluation of the divergent integrals of products of Schwinger's Δ and $\mathfrak{D}$ functions and their derivatives in the expression for the electron self-energy.)

APPENDIX

I. Manifestly Covariant Theory

In M.C.q.e. the interaction operator is

$$\mathfrak{W}(t) = -\int d^3\mathbf{x}\; j_\lambda(\mathbf{x}, t)\, A^\lambda(\mathbf{x}, t). \tag{I.1}$$

In Heisenberg representation, the retarded field from a source $^\mathrm{H}j_\mu(\mathbf{x}, t)$ (compare Eq. (9)) is given by[6,7]

$$^\mathrm{H}A_{\mathrm{ret}}{}^\mu(\mathbf{x}, t) = -4\pi \int_{-\infty}^{t} dt' \int d^3\mathbf{x}' U_\mathrm{I}(t')^{-1} \times D(x-x')\, {}^\mathrm{I}j^\mu(\mathbf{x}', t') U_\mathrm{I}(t'). \tag{I.2}$$

By[3]

$$4\pi i\hbar c\, g^{\mu\lambda} D(x-x') = [{}^\mathrm{I}A^\mu(x)\,;\, {}^\mathrm{I}A^\lambda(x')] \tag{I.3}$$

and by (I.1) we find from (I.2), for the part of the integral between the surfaces I and t as in Eq. (5),

$$\begin{aligned} &{}^\mathrm{H}A_{\mathrm{ret}>\mathrm{I}}{}^\mu(\mathbf{x}, t) \\ &= \int_I^t (dt'/i\hbar) U_\mathrm{I}(t')^{-1} [{}^\mathrm{I}A^\mu(\mathbf{x}, t)\,;\, {}^\mathrm{I}\mathfrak{W}(t')] U_\mathrm{I}(t') \\ &= \int_I^t dt'\, (d/dt')\{U_\mathrm{I}(t')^{-1}\, {}^\mathrm{I}A^\mu(\mathbf{x}, t)\, U_\mathrm{I}(t')\} \\ &= U_\mathrm{I}(t)^{-1}\, {}^\mathrm{I}A^\mu(\mathbf{x}, t)\, U_\mathrm{I}(t) - U_\mathrm{I}(I)^{-1}\, {}^\mathrm{I}A^\mu(\mathbf{x}, t)\, U_\mathrm{I}(I) \\ &= {}^\mathrm{H}A^\mu(\mathbf{x}, t) - {}^\mathrm{I}A^\mu(\mathbf{x}, t), \end{aligned} \tag{I.4}$$

where we used (11)–(12), (9), and (10). From (I.4) with the definition (6) follows Eq. (13).

II. Gauge-Independent Theory

In G.I.q.e. the interaction operator is given by Eq. (G-I:10) of reference 2, or

$$\mathfrak{W} = \int d^3\mathbf{x}\{(\mathbf{E}_\mathrm{II}{}^2/8\pi) - \mathfrak{A}\cdot\mathbf{j}\}. \tag{II.1}$$

Since in Heisenberg representation $^\mathrm{H}\mathfrak{A}$ satisfies the Maxwell equations (G-I:59–66), it must be equal, but for a solution $^\mathrm{H}\mathfrak{A}_\circ$ of the homogeneous equations, to

[10] Compare the wrong remark in F. J. Belinfante, Phys. Rev. **81**, 307(A) (1951), that the "kinetic self-energy" of an electron would be due to incorrect use of (20) instead of (15).

the retarded field, for which we find in Appendix III:

$$^{H}\mathfrak{A}_l^{ret}(\mathbf{x},t) = -4\pi\int_{-\infty}^{t} cdt' \int d^3\mathbf{x}'\, U_1(t')^{-1} \sum_{m=1}^{3} D_{lm}^{tr}(x-x') \times {}^{I}j_m(\mathbf{x}',t')\, U_1(t'). \quad \text{(II.2)}$$

Now, according to Eq. (3.14) of reference 3 and Eqs. (III.5–6) of Appendix III, we have[11]

$$[{}^{I}\mathfrak{A}_l(x);\, {}^{I}\mathfrak{A}_m(x')] = 4\pi ihc\{\delta_{lm}\Delta - \nabla_l\nabla_m\}\mathfrak{D}(x-x') = 4\pi ihc\, D_{lm}^{tr}(x-x'). \quad \text{(II.3)}$$

Further, the coulomb field ${}^{I}\mathbf{E}_{tl}(x')$ defined by Eqs. (G-I:6–7) of reference (2) commutes with ${}^{I}\mathfrak{A}(x)$ even for time-like $x-x'$. Therefore, we find for the part of the integral (II.2) between I and t as in Eq. (5), by Eqs. (II.1), (II.3), (11)–(12), (9), and (10):

$$^{H}\mathfrak{A}_l^{ret>I}(\mathbf{x},t) = \int_I^t (dt'/ih)U_1(t')^{-1}[{}^{I}\mathfrak{A}_l(\mathbf{x},t);\, {}^{I}\mathfrak{W}(t')]U_1(t') = \int_I^t dt'(d/dt')\{U_1(t')^{-1}\, {}^{I}\mathfrak{A}_l(\mathbf{x},t)\, U_1(t')\} = {}^{H}\mathfrak{A}_l(\mathbf{x},t) - {}^{I}\mathfrak{A}_l(\mathbf{x},t). \quad \text{(II.4)}$$

Subtracting this from ${}^{H}\mathfrak{A}_l(\mathbf{x},t)$ we get Eq. (14).

III. The Transverse *D*-Function

A solution of[12]

$$\Box\, {}^{H}\mathfrak{A}_l(x) = -4\pi({}^{H}j_\lambda)_l \equiv -(1/4\pi^3)\int d^4k \int d^4x'\{\delta_{lm} - (k_lk_m/\mathbf{k}^2)\}\, {}^{H}j^m(x') \times \exp\{ik_\mu(x-x')^\mu\} \quad \text{(III.1)}$$

(with summation over m from 1 to 3) is apparently given by

$$^{H}\mathfrak{A}_l^{mix}(x) = +(1/4\pi^3)\int d^4k \int d^4x'\,[k_\nu k^\nu]^{-1} \times\{\delta_{lm} - (k_lk_m/\mathbf{k}^2)\}\, {}^{H}j^m(x')\exp\{ik_\mu(x-x')^\mu\}. \quad \text{(III.2)}$$

As the integrand has singularities for $k^0 = \pm|\mathbf{k}|$, we take the principal value in these points. We complete the path of integration for $k^0(=-k_0)$ to a contour, closed along $\pm i\infty$ as $(t-t')\lesseqgtr 0$. Thence, with $\epsilon(t-t') = (t-t')/|t-t'|$, with $\Delta \equiv \nabla^2$, and with Schwinger's D- and $\mathfrak{D}$-function,[3,6,11]

$$\begin{aligned} ^{H}\mathfrak{A}_l^{mix}(\mathbf{x},t) &= (1/4\pi^2)\int d^4x'\,\epsilon(t-t')\int d^3\mathbf{k}\,|\mathbf{k}|^{-1} \times\textstyle\sum_m\{\delta_{lm} - (k_lk_m/\mathbf{k}^2)\}\, {}^{H}j^m(x') \\ &\quad \times\exp\{i\mathbf{k}\cdot(\mathbf{x}-\mathbf{x}')\}\,\sin\{kc(t-t')\} \\ &= -2\pi\int d^4x'\,\epsilon(t-t')\textstyle\sum_m {}^{H}j^m(x') \\ &\quad \times\{\delta_{lm} - (\nabla_l\nabla_m/\Delta)\}D(x-x') \\ &= -2\pi\int d^4x'\,\epsilon(t-t')\textstyle\sum_m {}^{H}j^m(x') \\ &\quad \times\{\delta_{lm}\Delta - \nabla_l\nabla_m\}\mathfrak{D}(x-x'). \end{aligned} \quad \text{(III.3)}$$

If the factor $\epsilon(t-t')$ is omitted, we apparently get a solution of the homogeneous equation, since $\Box\mathfrak{D}=0$. Adding this solution to ${}^{H}\mathfrak{A}_l^{mix}$, we find an integral over $t'<t$ only, therefore the retarded solution:

$$^{H}\mathfrak{A}_l^{ret}(\mathbf{x},t) = -4\pi\int_{-\infty}^{t} cdt' \int d^3\mathbf{x}' \sum_{m=1}^{3} \times D_{lm}^{tr}(x-x')\, {}^{H}j_m(\mathbf{x}',t'). \quad \text{(III.4)}$$

Here, we introduced the "transverse D-function," defined in analogy to the transverse delta-function[12] for $l, m = 1, 2, 3$ by

$$D_{lm}^{tr}(x) = \delta_{lm}D(x) - D_{lm}^{long}(x), \quad \text{(III.5)}$$

$$D_{lm}^{long}(x) = \nabla_l\nabla_m\mathfrak{D}(x); \quad D(x) = \textstyle\sum_l D_{ll}^{long}(x). \quad \text{(III.6)}$$

Some of its properties are

$$\Box\, D_{lm}^{tr}(x) = 0, \quad D_{lm}^{tr}(x) = D_{ml}^{tr}(x) = -D_{lm}^{tr}(-x), \quad \text{(III.7)}$$

and, by Eqs. (14a)–(14b) of reference 7 and Eqs. (12)–(13) and (17) of reference 12,

$$D_{lm}^{tr}(t=0) = 0, \quad \{\partial_0 D_{lm}^{tr}(x)\}_{t=0} = -\delta_{lm}{}^{tr}(\mathbf{x}). \quad \text{(III.8)}$$

Similar equations hold for $D_{lm}^{long}(x)$.

---

[11] The $\mathfrak{D}$-function has been defined by Schwinger (see references 3 and 6). It equals $\mathfrak{D}(\mathbf{r},t) = \{|r+ct| - |r-ct|\}/(8\pi r)$. (Similarly, Schwinger's $\mathfrak{D}^{(1)}$-function equals $[ct/4\pi^2 r]\ln\{|r+ct|/|r-ct|\} + [1/4\pi^2]\ln|r^2-c^2t^2| + \text{constant}$.)

[12] Compare Sec. 2 of F. J. Belinfante, Physica **12**, 1 (1946).

The Energy Density Tensor in Gauge-Independent Quantum Electrodynamics

FREDERIK J. BELINFANTE
Department of Physics, Purdue University, Lafayette, Indiana

(Received July 3, 1951)

In Heisenberg representation two different definitions of an energy density tensor are given for gauge-independent quantum electrodynamics, by Eqs. (1)–(4) and Eqs. (20)–(21), respectively. Both tensors lead to the same total energy and momentum, if we assume the interaction to vanish at $t=-\infty$. They both satisfy conservation laws. The tensor character of the first one is proved, and the tensor character of the second one is manifest. The first tensor is obtained by analogy with the result of a derivation of the energy density tensor as source of the gravitational field from general-relativistic considerations in manifestly covariant quantum electrodynamics, with subsequent omission of the "phantom terms" containing the redundant variables of this theory. The second tensor has the advantage of admitting a simple covariant subtraction of its vacuum value, and of simplifying even further by use of the new covariant auxiliary condition proposed recently by the author. Its disadvantage, though, is the impossibility of direct physical interpretation, as in Heisenberg representation it is not expressed in terms of field variables in Heisenberg representation. The inconclusiveness of an argument for possible equality of the two tensors is discussed. Both tensors contain the usual self-interaction effects, and the problem is posed of how to eliminate these effects.

I. DEFINITION OF AN ENERGY DENSITY TENSOR

IN a recent paper[1] the author has developed the formalism of a gauge-independent quantum electrodynamics, in interaction representation as well as in Heisenberg representation. It is plausible to identify in such theory the energy density with the sum of the ordinary free-particle energy density and the interaction operator used in the generalized Schrödinger equation.[2]

In manifestly covariant quantum electrodynamics, on the other hand, a scalar first-order[3,4] lagrangian is known,[5] so that the total[6] energy density tensor $T^{\lambda\mu}$ can simply be derived for it by the principles of general relativity theory as the source of the gravitational field.[3] The result is Eq. (46) of reference 5. In order to make the best use of the Lorentz auxiliary condition,[5] it is then convenient to separate the redundant longitudinal and scalar photon variables by a transformation introducing new field variables,[7] and by expressing $T^{\lambda\mu}$ in terms of them. If from the q-number expression for the energy density T^{00} thus obtained[8] one completely omits all so-called "phantom" terms[5] (which have vanishing value due to the Lorentz condition), one simply finds the expression just suggested for the energy density in the gauge-independent theory.[2]

This makes it seems appropriate to try a definition of the other components of $T^{\lambda\mu}$ in a similar way. This leads to the following expressions[8,9] for the energy density T^{00}, for $c\times$the momentum density $=(1/c)\times$the energy current density $=T^{k0}=T^{0k}$, and for the stress tensor $T^{kl}=T^{lk}$:

$$T^{\lambda\mu}=T_p{}^{\lambda\mu}+T_m{}^{\lambda\mu};\quad T_m{}^{\lambda\mu}=T_e{}^{\lambda\mu}+T_I{}^{\lambda\mu}, \tag{1}$$

with

$$\left.\begin{aligned} &T_p{}^{00}=\{\mathfrak{B}^2+\mathbf{E}^2\}/8\pi,\\ &T_p{}^{0k}=\textstyle\sum_l\{E_l\mathfrak{B}_{kl}+\mathfrak{B}_{kl}E_l\}/8\pi,\\ &T_p{}^{kl}=\delta_{kl}\{\mathfrak{B}^2+\mathbf{E}^2\}/8\pi-\{\mathfrak{B}_k\mathfrak{B}_l+E_kE_l\}/4\pi; \end{aligned}\right\} \tag{2}$$

$$\left.\begin{aligned} &T_I{}^{00}=-\mathbf{j}\cdot\mathfrak{A},\quad T_I{}^{0k}=-\rho\mathfrak{A}_k,\\ &T_I{}^{kl}=-\tfrac{1}{2}\{j_k\mathfrak{A}_l+j_l\mathfrak{A}_k\}; \end{aligned}\right\} \tag{3}$$

$$\left.\begin{aligned} &T_e{}^{00}=\mathfrak{R}\{\psi^\dagger H_0\psi\},\\ &T_e{}^{kl}=-\tfrac{1}{2}\mathfrak{R}\{\psi^\dagger ihc(\alpha_k\nabla_l+\alpha_l\nabla_k)\psi\},\\ &T_e{}^{0k}=-\mathfrak{R}\{\psi^\dagger ihc\nabla_k\psi\}+\tfrac{1}{4}hc\textstyle\sum_l\nabla_l\mathfrak{R}\{\psi^\dagger\sigma_{kl}\psi\}. \end{aligned}\right\} \tag{4}$$

Here

$$H_0=mc^2\beta-ihc\boldsymbol{\alpha}\cdot\boldsymbol{\nabla};\quad \sigma_{kl}=-\tfrac{1}{2}i(\alpha_k\alpha_l-\alpha_l\alpha_k); \tag{5}$$

$$\mathfrak{R}\{\psi^\dagger\Omega\varphi\}=\tfrac{1}{4}\{\psi^\dagger\Omega\varphi+\varphi^\dagger\Omega^\dagger\psi-\varphi^{\mathrm{T}}\Omega^{\mathrm{T}}\psi^*-\psi^{\mathrm{T}}\Omega^*\varphi^*\}, \tag{6}$$

where $^{\mathrm{T}}$ means transposition in the space of coordinates[10] and undor indices[11] (the latter meaning: interchanging rows and columns of Dirac matrices and Dirac wave functions), while * means hermitian conjugation in Hilbert space (including complex conjugation of c-numbers), and $^\dagger={}^{*\mathrm{T}}$. Further, ρ (in esu) and $\mathbf{j}$ (in emu) in Eq. (3) form a four-vector, which according to reference 5 is defined by

$$j^\mu=\mathfrak{R}\{e\psi^\dagger\alpha^\mu\psi\}=\mathfrak{R}\{ie\bar{\psi}\gamma^\mu\psi\}, \tag{7}$$

[1] F. J. Belinfante and J. S. Lomont, Phys. Rev. 84, 541 (1951). In the following we refer to its formulas by (G-I:).

[2] The real part of the integrand of Eq. (G-I:31), plus the expression (G-I:10); thence, the integrand in (G-I:56).

[3] F. J. Belinfante, Physica 7, 449 (1940).

[4] F. J. Belinfante, Phys. Rev. 74, 779 (1948).

[5] F. J. Belinfante, Physica 12, 17 (1946).

[6] F. J. Belinfante, Physica 6, 887 (1939).

[7] F. J. Belinfante, Physica 12, 1 (1946); in particular Sec. 4.

[8] Reference 5, Eqs. (48), (49), (50).

[9] For the notation used in reference 8, compare reference 5, Eq. (47), and Sec. 1 of reference 7. Italic indices run from 1 to 3, Greek from 0 to 3, with $x^0=-x_0=ct$, and $\nabla_0=-\nabla^0=\partial/c\partial t$. The symmetrization $E\mathfrak{B}+\mathfrak{B}E$ in Eq. (2) is due to a symmetrization in the lagrangian proposed in F. J. Belinfante, Physica 7, 765 (1940), and simplifies the derivation of the first of the Eqs. (18) below, but is further superfluous due to Eq. (G-I:2) with Eq. (A.7) of Appendix A. As in Eq. (G-I:56), we use here the abbreviation $\mathbf{E}=\mathbf{E}_{\mathrm{II}}+\mathfrak{C}$ (G-I:44), with $\mathbf{E}_{\mathrm{II}}$ given by Eqs. (G-I:6–7) of reference 1.

[10] Thus, $f\nabla_x{}^{\mathrm{T}}g$ means $(\partial f/\partial x)g$. Further, $\boldsymbol{\nabla}^*=\boldsymbol{\nabla}$ and $\boldsymbol{\nabla}^\dagger=\boldsymbol{\nabla}^{\mathrm{T}}$.

[11] F. J. Belinfante, Physica 6, 849 (1939).

with $\alpha^0=1$, $\gamma^\mu=-i\beta\alpha^\mu$, $\bar\psi=\psi^\dagger\beta$. One easily proves the formal equality[12] of this expression (7) first proposed by Dirac,[13] and the expression (G-I:8) of reference 1 first proposed by Furry and Oppenheimer.[14]

For T_m^{00}, another convenient expression is found by use of the field equation for ψ in Heisenberg representation (G-I:57), and of Eqs. (6) and (7):

$$\left.\begin{aligned} T_m^{00}&=T_{e'}^{00}+T_{I'}^{00};\quad T_{e'}^{00}=\mathfrak{R}\{\psi^\dagger i\hbar\partial_H\psi/\partial t\},\\ T_{I'}^{00}&=-\tfrac{1}{2}\rho V-\tfrac{1}{2}e\mathfrak{R}\{\psi^\dagger V\psi\}.\end{aligned}\right\}\quad(8)$$

Here, $\partial_H/\partial t$ means time differentiation in Heisenberg representation.

II. THE CONSERVATION LAWS

Using Eqs. (2), (G-I:64), and (G-I:66), we find

$$\nabla_\mu\,{}^HT_F^{0\mu}=-\tfrac{1}{2}(\mathbf{E}\cdot\mathbf{j}+\mathbf{j}\cdot\mathbf{E}).\quad(9)$$

In this and the following equations, all field variables, etc., are tacitly understood to be expressed in Heisenberg representation.

In Appendix A, we prove that

$$\nabla_\mu\,{}^HT_m^{0\mu}=+\tfrac{1}{2}(\mathbf{E}\cdot\mathbf{j}+\mathbf{j}\cdot\mathbf{E}),\quad(10)$$

so that, by Eq. (1), we find the law of conservation of energy

$$\nabla_\mu\,{}^HT^{0\mu}=0.\quad(11)$$

Similarly, Eqs. (2), (G-I:64), (G-I:65), (G-I:66), and (G-I:60), yield

$$\begin{aligned}\nabla_\mu\,{}^HT_F^{k\mu}&=-\{\tfrac{1}{2}(\mathbf{E}\rho+\rho\mathbf{E})+[\mathbf{j}\times\mathfrak{B}]\}_k\\&=-\tfrac{1}{2}(E_k\rho+\rho E_k)+\mathbf{j}\cdot(\nabla\,\mathfrak{A}_k-\nabla_k\mathfrak{A}).\end{aligned}\quad(12)$$

Equations (3), (G-I:58), and (G-I:59), yield

$$\nabla_\mu\,{}^HT_I^{k\mu}=\tfrac{1}{2}(\mathrm{div}\,\mathbf{j})\mathfrak{A}_k+\rho\mathfrak{E}_k-\tfrac{1}{2}\nabla\cdot(j_k\mathfrak{A})-\tfrac{1}{2}(\mathbf{j}\cdot\nabla)\mathfrak{A}_k.\quad(13)$$

By Eqs. (4), (G-I:57) and conjugate, (5), (6), (7), (G-I:6), and various reasonings analogous to (A.2)–(A.12) of Appendix A, also using Eq. (A.8) and conjugate, we find after somewhat lengthy calculation

$$\begin{aligned}\nabla_\mu\,{}^HT_e^{k\mu}=\mathbf{j}\cdot\nabla\,&\mathfrak{A}_k+\tfrac{1}{2}\nabla\cdot(j_k\mathfrak{A}-\mathbf{j}\mathfrak{A}_k)\\&+\tfrac{1}{2}(E_{11k}\rho+\rho E_{11k}),\end{aligned}\quad(14)$$

where we finally used the (not very convincing) Eq. (A.6) of Appendix A. [Otherwise, the expression (A.6) would have appeared added to the right-hand side of (14).] Adding (12), (13), and (14), we find the law of conservation of momentum

$$\nabla_\mu\,{}^HT^{k\mu}=0.\quad(15)$$

Equations (11) and (15) together can be written as

$$\nabla_\mu\,{}^HT^{\lambda\mu}=0,\quad(16)$$

which equation remains valid after subtraction of the (infinite) vacuum values of $T^{\lambda\mu}$, which are c-numbers not depending on $xyzt$. From the q-number relation (16), a similar equation follows for the expectation values of $T^{\lambda\mu}$, as the state vector in Heisenberg representation is a constant.

III. LORENTZ TRANSFORMATION OF THE ENERGY DENSITY TENSOR

For showing that the expectation values of $T^{\lambda\mu}$ form a tensor, it suffices to prove the tensor character of the q-numbers ${}^HT^{\lambda\mu}$ in Heisenberg representation (with its scalar state vector). We shall use the infinitesimal Lorentz transformation formulas for the field variables in Heisenberg representation derived in Chapter 6 of reference 1. Thus we find that, under the infinitesimal Lorentz transformation

$$\delta x^0=-\textstyle\sum_l b_l x^l,\quad \delta x^k=-b_k x^0,\quad (\mathbf{b}=\mathbf{v}/c),\quad(17)$$

${}^HT_F^{\lambda\mu}$ of Eq. (2) by itself transforms on account of (G-I:45) as a symmetric tensor, according to

$$\begin{aligned}\delta\,{}^HT^{00}&=-2\textstyle\sum_l b_l\,{}^HT^{0l},\quad \delta\,{}^HT^{kl}=-b_k\,{}^HT^{0l}-b_l\,{}^HT^{k0},\\ \delta\,{}^HT^{0k}&=-b_k\,{}^HT^{00}-\textstyle\sum_l b_l\,{}^HT^{lk}.\end{aligned}\quad(18)$$

We used here the fact that $E_k\mathfrak{B}_{lm}=\mathfrak{B}_{lm}E_k$ because of (G-I:2) with (A.7).

In Appendix B, we prove (Eqs. (B.10a-b-c)) that also ${}^HT_m^{\lambda\mu}$ is transformed according to (18) as a tensor, so that, by (1), also ${}^HT^{\lambda\mu}$ itself is a tensor.

If the "vacuum" can be defined in a covariant way, as a property invariant under Lorentz transformations, then also the c-number vacuum expectation value of $T^{\lambda\mu}$ should form a tensor, and therefore should then be expected to take the form

$$\langle T^{\lambda\mu}\rangle_{vac}=g^{\lambda\mu}T,\quad(19)$$

where T is some (infinite) c-number scalar. In that case, also $T^{\lambda\mu}-\langle T^{\lambda\mu}\rangle_{vac}$ is a tensor, satisfying conservation laws by (16) and following remarks.

IV. AN ALTERNATIVE ENERGY DENSITY TENSOR

Equations (1)–(4) for the energy density tensor of gauge-independent quantum electrodynamics were not

[12] Expand ψ in terms of eigenfunctions ϕ_n of H_0. Let w_n be the sign of the corresponding eigenvalues of H_0. In Heisenberg as well as in interaction representation, $\psi^{(+)}$ and $\psi^{(-)}$ are defined as the sum of the terms with $w_n=+1$ in this expansion. Then apparently $(1/e)\times$the difference between Eq. (G-I:8) and Eq. (7) is given by $:\psi^\dagger\alpha^\mu\psi:-\mathfrak{R}\{\psi^\dagger\alpha^\mu\psi\}=\frac{1}{2}\sum_n w_n(\phi_n^\dagger\alpha^\mu\phi_n)$. However, this infinite sum over n formally vanishes, as the c-number functions ϕ_n come in charge-conjugate pairs (see reference 11) for which $(\phi_n^\dagger\alpha^\mu\phi_n)$ has the same value, but w_n has opposite values.

[13] P. A. M. Dirac, "Théorie du Positron," *Structure et Propriétés des Noyaux Atomiques*, Rapports et Discussions du 7me Conseil de Physique tenu à Bruxelles du 22 au 29 octobre 1933. Institut International de Physique Solvay. (Gauthier Villars, Paris 1934), pp. 203–212 (Library of Congress QC1-I6-1933). See also P. A. M. Dirac, Proc. Cambridge Phil. Soc. **30**, 150 (1934).

[14] W. H. Furry and J. R. Oppenheimer, Phys. Rev. **45**, 245 (1934).

derived, but were based on an analogy. We could have made a different guess at an energy density tensor by writing

$$ {}^{\mathrm{H}}\mathfrak{T}_{\mathfrak{F}}{}^{\lambda\mu}={}^{\mathrm{H}}\mathfrak{T}_{F}{}^{\lambda\mu}+\tfrac{1}{2}\hbar c\{{}^{\circ}\bar{\psi}(\gamma^{\lambda}\nabla^{\mu}+\gamma^{\mu}\nabla^{\lambda})\,{}^{\circ}\psi\} \qquad (20) $$

with

$$ {}^{\mathrm{H}}\mathfrak{T}_{F}{}^{\lambda\mu}=(4\pi)^{-1}\{{}^{\circ}\mathfrak{F}^{\nu\mu}\,{}^{\circ}\mathfrak{F}_{\nu}{}^{\lambda}-\tfrac{1}{4}\delta^{\lambda\mu}\,{}^{\circ}\mathfrak{F}_{\nu\sigma}\,{}^{\circ}\mathfrak{F}^{\nu\sigma}\}. \qquad (21) $$

We have expressed $\mathfrak{T}^{\lambda\mu}$ here as a q-number in Heisenberg representation with the help of the variables $\mathfrak{F}^{\lambda\mu}$ (transverse electromagnetic field, with $\mathfrak{F}_{10}=\mathfrak{F}^{01}=\mathfrak{E}_x$, $\mathfrak{F}_{23}=\mathfrak{B}_x$, etc.) and ψ (matter field) in interaction representation. Since the transformation (G-I:37) with (G-I:34–35) between both representations, or

$$ {}^{\mathrm{H}}Q(t)={}^{\circ}Q(t)+(i\hbar)^{-1}\int_{-\infty}^{t}dt_1[{}^{\circ}Q(t);\,{}^{\circ}\mathfrak{W}(t_1)] $$

$$ +(i\hbar)^{-2}\int_{-\infty}^{t}dt_1\int_{-\infty}^{t_1}dt_2[[{}^{\circ}Q(t);\,{}^{\circ}\mathfrak{W}(t_1)];\,{}^{\circ}\mathfrak{W}(t_2)]+\cdots, \qquad (22) $$

is expressed by (G-I:10) with (G-I:3, 6, 7) in terms of gauge-independent variables, Eqs. (20)–(21) define a gauge-independent quantity, which has the following properties:

1. This gauge-independent quantity ${}^{\mathrm{H}}\mathfrak{T}^{\lambda\mu}$ is a manifestly covariant symmetric tensor.

2. Due to the field equations (G-I:29) in interaction representation,

$$ \left.\begin{aligned} &\nabla_{\mu}\,{}^{\circ}\mathfrak{F}^{\nu\mu}=0,\quad \nabla_{\mu}\,{}^{\circ}\mathfrak{F}_{\nu\lambda}+\nabla_{\nu}\,{}^{\circ}\mathfrak{F}_{\lambda\mu}+\nabla_{\lambda}\,{}^{\circ}\mathfrak{F}_{\mu\nu}=0,\\ &\gamma^{\mu}\nabla_{\mu}\,{}^{\circ}\psi=-\kappa\,{}^{\circ}\psi,\quad \nabla_{\mu}\,{}^{\circ}\bar{\psi}\gamma^{\mu}=+\kappa\,{}^{\circ}\bar{\psi},\\ &\qquad\qquad \Box\,{}^{\circ}\psi=\kappa^{2}\,{}^{\circ}\psi, \end{aligned}\right\} \qquad (23) $$

with

$$ \mathfrak{F}^{\mu\lambda}=-\mathfrak{F}^{\mu\lambda};\quad \Re\{\bar{\psi}\gamma^{\lambda}\psi\}=0=\Re\{(\nabla_{\mu}\bar{\psi})\gamma^{\lambda}(\nabla^{\mu}\psi)\}, \qquad (24) $$

the tensor $\mathfrak{T}^{\lambda\mu}$ satisfies conservation laws

$$ \nabla_{\mu}\,{}^{\mathrm{H}}\mathfrak{T}^{\lambda\mu}=0,\quad \text{thence}\quad \nabla_{\mu}(\mathfrak{T}^{\lambda\mu})_{\mathrm{av}}=0. \qquad (25) $$

3. Because of (25), the integrals of the density components $\mathfrak{T}^{\lambda 0}$ over space give constants of motion:

$$ c\,{}^{\mathrm{H}}\mathfrak{G}^{\lambda}=\int {}^{\mathrm{H}}\mathfrak{T}^{\lambda 0}d^{3}\mathbf{x},\quad \text{with}\quad \partial\,{}^{\mathrm{H}}\mathfrak{G}^{\lambda}/\partial t=0. \qquad (26) $$

4. The energy $c\,{}^{\mathrm{H}}\mathfrak{G}^{0}$ in Heisenberg representation thus defined is, by (20)–(21), (G-I:29), and (G-I:31), equal to ${}^{\circ}\mathfrak{H}_0$, and therefore, by (G-I:54) with (G-I:56) and (1)–(4), equal to the energy as calculated from ${}^{\mathrm{H}}T^{00}$. Remember that (G-I:54) was derived under the tacit assumption of vanishing of the interaction at $t=-\infty$ (compare footnote 13 of reference 1). In fact, by (G-I:52) and (G-I:37) with (G-I:33), and by the fact that ${}^{\circ}\mathfrak{H}_0$ and ${}^{\mathrm{H}}\mathfrak{H}$ both are integrals of motion, we have

$$ {}^{\mathrm{H}}\mathfrak{H}(t)={}^{\mathrm{H}}\mathfrak{H}(-\infty)={}^{\circ}\mathfrak{H}(-\infty)={}^{\circ}\mathfrak{H}_0(-\infty)+{}^{\circ}\mathfrak{W}(-\infty) $$

$$ \text{«=»}\ {}^{\circ}\mathfrak{H}_0(-\infty)={}^{\circ}\mathfrak{H}_0(t). \qquad (27) $$

5. By a similar argument, all components of ${}^{\mathrm{H}}T^{\lambda\mu}(x)$ and of ${}^{\mathrm{H}}\mathfrak{T}^{\lambda\mu}(x)$ $[\equiv {}^{\circ}T_{\mathrm{free}}{}^{\lambda\mu}(x)]$ are completely identical *at* $t=-\infty$, if we assume that the interaction constant e vanishes at $t=-\infty$. ("Interaction switched on adiabatically since the infinite past.") Here, "free" refers to omission of all interaction terms, including the difference between $\mathbf{E}$ and $\mathfrak{E}$.

6. Thence, also the momentum vectors ${}^{\mathrm{H}}\mathfrak{G}^{k}$ calculated according to (26) from ${}^{\mathrm{H}}T^{k0}$ and from ${}^{\mathrm{H}}\mathfrak{T}^{k0}$ will then be equal at $t=-\infty$, and therefore always, as they both are constants of motion:

$$ c\,{}^{\mathrm{H}}\mathfrak{G}^{\lambda}=\int {}^{\mathrm{H}}\mathfrak{T}^{\lambda 0}d^{3}\mathbf{x}=\int {}^{\mathrm{H}}T^{\lambda 0}d^{3}\mathbf{x}. \qquad (28) $$

Because of the above properties, ${}^{\mathrm{H}}\mathfrak{T}^{\lambda\mu}$ serves most purposes of a total energy density tensor, better than for instance the "canonical" energy density tensor.[6] However, it does not prove equality of $\mathfrak{T}^{\lambda\mu}$ and $T^{\lambda\mu}$.

The physical interpretation of $\mathfrak{T}^{\lambda\mu}$ is complicated by the fact that in Heisenberg representation it was expressed in terms of field variables (and therefore of creation and annihilation matrices) in interaction representation.[15] While we leave unanswered the question whether $\mathfrak{T}^{\lambda\mu}$ or $T^{\lambda\mu}$ is to be regarded as source of the gravitational field[3] (although the correctness of $\mathfrak{T}^{\lambda\mu}$ in this regard seems somewhat dubious), it must be admitted that the definition (20)–(21) of $\mathfrak{T}^{\lambda\mu}$ has the advantage of permitting an extremely simple subtraction of its covariantly defined vacuum value, by a simple rearrangement of factors as suggested by Furry and Oppenheimer[14] after splitting all field variables in interaction representation into positive and negative frequency parts according to Schwinger. After this has been done, the photon part ${}^{\mathrm{H}}\mathfrak{T}_{F}{}^{\lambda\mu}$ (21) will contain only products ${}^{\circ}\mathfrak{F}^{(+)}\,{}^{\circ}\mathfrak{F}^{(+)}$, ${}^{\circ}\mathfrak{F}^{(-)}\,{}^{\circ}\mathfrak{F}^{(+)}$, and ${}^{\circ}\mathfrak{F}^{(-)}\,{}^{\circ}\mathfrak{F}^{(-)}$. Then, the expectation value of $\mathfrak{T}_{F}{}^{\lambda\mu}$ after this subtraction is supposed to vanish completely by the new covariant auxiliary condition in Heisenberg representation ${}^{\circ}\mathfrak{F}_{\lambda\mu}{}^{(+)}\Phi=0=\Phi^{*}\,{}^{\circ}\mathfrak{F}_{\lambda\mu}{}^{(-)}$ proposed recently by the author,[16] and all energy and momentum is then due to the "matter" terms in (20). It should be kept in mind, though, that these "matter" terms would still depend on photon variables when expressed, by Eq. (22) or

---

[15] Re-interpretation of the q-number occupation numbers derived from field variables in interaction representation, as representing the numbers of particles in Heisenberg representation, was shown by F. J. Dyson, Phys. Rev. **75**, 486 (1949), to oversimplify the theory such as to completely eliminate all interactions. (Compare p. 489, same article.)

[16] F. J. Belinfante, Phys. Rev. **84**, 644 (1951).

by its inverse

$$^{\circ}q(t)={}^{H}q(t)+\sum_{n=1}^{\infty}\left(\frac{i}{\hbar}\right)^{n}\int_{-\infty}^{t}dt_1\int_{-\infty}^{t_1}dt_2\cdots\int_{-\infty}^{t_{n-1}}dt_n$$

$$\times[[\cdots[{}^{H}q(t);\,{}^{H}\mathcal{W}(t_1)];\,{}^{H}\mathcal{W}(t_2)];\cdots{}^{H}\mathcal{W}(t_n)],\quad(29)$$

in terms of variables in the Heisenberg representation used for describing the physical state by Φ. Moreover, as discussed earlier,[16] it is often convenient for practical reasons to ignore the new auxiliary condition notwithstanding its fundamental significance, and to do as if the photon terms (21) describe the energy density tensor of incident free photons.

Perhaps one may want to argue that the tensors $T^{\lambda\mu}$ and $\mathfrak{T}^{\lambda\mu}$ should be expected to be identical. If we call their difference $\mathfrak{X}^{\lambda\mu}$, then ${}^{H}\mathfrak{X}^{\lambda\mu}(-\infty)\equiv 0$ by the property (5) above in case of vanishing of interaction at $t=-\infty$. On the other hand, its time derivative

$$\partial\,{}^{H}\mathfrak{X}^{\lambda\mu}(x)/\partial t=(i\hbar)^{-1}[{}^{H}\mathfrak{X}^{\lambda\mu}(x)\,{}^{H}\mathfrak{H}\mathcal{C}-{}^{H}\mathfrak{H}\mathcal{C}\,{}^{H}\mathfrak{X}^{\lambda\mu}(x)]\quad(30)$$

vanishes wherever ${}^{H}\mathfrak{X}^{\lambda\mu}(x)$ itself vanishes. From this, one might be inclined to conclude the equality of $T^{\lambda\mu}$ and $\mathfrak{T}^{\lambda\mu}$ throughout space-time.[17]

It would have been more convincing, however, if equality of $T^{\lambda\mu}$ and $\mathfrak{T}^{\lambda\mu}$ could have been shown by explicit calculation, using Eq. (22) or (29), since the vanishing of $\mathfrak{X}^{\lambda\mu}$ at $t=-\infty$ was based on the vanishing of e there, and if yet e can differ from zero at later time, then also $\mathfrak{X}^{\lambda\mu}$ can, with some discontinuity in some (higher order) derivative of $\mathfrak{X}^{\lambda\mu}$. Moreover, one may well prefer, in defining the interaction representation by (G-I:33), to postulate the vanishing of the interaction terms in the energy density in the limit $t\to-\infty$ only, without $\mathfrak{X}^{\lambda\mu}$ being zero for any finite time, so that the above argument is not conclusive.

V. DISCUSSION

While the validity of conservation laws and of covariance for $T^{\lambda\mu}$ and $\mathfrak{T}^{\lambda\mu}$ seems to be satisfactory, they both have the disadvantage of taking infinite values (even after subtraction of their vacuum value) in states, in which a finite number of occupation numbers have nonvanishing values. For $T^{\lambda\mu}$ this is easily seen by calculating the expectation value of the term $\mathbf{E}_{\rm II}^{2}/8\pi$ in Eq. (2) (with (G-I:44)) in state with one free electron present. If $\Psi(\mathbf{x})$ is the c-number one-electron wave function of such electron, Fock's rules of second quantization[18] give, for one-electron theory and *without* the symmetrization (7) of the charge density,

$$\langle\rho(\mathbf{x}')\rho(\mathbf{x}'')\rangle_{h}=e^{2}\Psi^{\dagger}(\mathbf{x}')\delta(\mathbf{x}'-\mathbf{x}'')\Psi(\mathbf{x}''),\quad(31)$$

so that

$$\left\langle\frac{\mathbf{E}_{\rm II}(\mathbf{x})^{2}}{8\pi}\right\rangle_{h}=\frac{1}{8\pi}\int'\int''\left[\nabla\frac{1}{|\mathbf{x}-\mathbf{x}'|}\right]\cdot\left[\nabla\frac{1}{|\mathbf{x}-\mathbf{x}''|}\right]\langle\rho(\mathbf{x}')\rho(\mathbf{x}'')\rangle_{h}\quad(32)$$

$$=(e^{2}/8\pi)\int'|\Psi(\mathbf{x}')|^{2}r^{-4}d^{3}\mathbf{x}'.$$

In a point where $|\Psi(\mathbf{x})|^{2}\neq 0$, this integral diverges as $\frac{1}{2}e^{2}|\Psi(\mathbf{x})|^{2}\int_{0}r^{-3}dr$.

This one-electron theory is of course meaningless, but a similar slightly more involved treatment in position theory *with* use of Eq. (7) leads to the logarithmically divergent electrostatic self-energy calculated by Weisskopf.[19]

For $\mathfrak{T}^{\lambda\mu}$, the divergence of $\langle\mathfrak{T}^{\lambda\mu}\rangle_{h}$ is due to the commutators of ${}^{H}T_{tree}{}^{\lambda\mu}(t)$ with ${}^{H}\mathcal{W}(t_1)$, when Eq. (29) is used for expressing ${}^{H}\mathfrak{T}^{\lambda\mu}(={}^{\circ}T_{tree}{}^{\lambda\mu})$ in terms of field variables in Heisenberg representation.

To avoid the electrostatic self-energy difficulties, one would be tempted to rearrange ${}^{\circ}\psi^{(+)}$ and ${}^{\circ}\psi^{(-)}$ factors in the expression $({}^{\circ}\mathbf{E}_{\rm II}^{2}/8\pi)$ occurring in the interaction operator ${}^{\circ}W$ (G-I:10). However, this alone would disturb all our proofs of the integrability of the generalized Schrödinger equation[1] and of the covariance of the energy density tensor ${}^{H}T^{\lambda\mu}$. In a following paper, we shall discuss some possibilities of eliminating self-interaction effects without sacrificing covariance or integrability.[20]

APPENDIX A

Using Eqs. (3), (G-I:59), and (G-I:60), we find

$$\nabla_{\mu}\,{}^{H}T_{I}{}^{0\mu}=\mathbf{j}\cdot\mathfrak{E}-(\nabla_{0}\mathbf{j}+\nabla\rho)\cdot\mathfrak{A}.\quad(A.1)$$

(All quantities in Heisenberg representation.)

The anticommutation relations for ψ and $\psi^{\dagger}$ yield, for any Dirac matrix ω, and $t=t'$,

$$\psi^{\dagger}(\mathbf{x})\omega\psi(\mathbf{x}')+\psi^{\mathrm{T}}(\mathbf{x}')\omega^{\mathrm{T}}\psi^{*}(\mathbf{x})=(\mathrm{spur}\,\omega)\delta(\mathbf{x}-\mathbf{x}'),\quad(A.2)$$

which we shall assume to vanish even for $\mathbf{x}=\mathbf{x}'$, if spur $\omega=0$. For instance,

$$\psi^{\dagger}\alpha\psi+\psi^{\mathrm{T}}\alpha^{\mathrm{T}}\psi^{*}=0.\quad(A.3)$$

Similarly, we assume the vanishing of expressions like

$$(\nabla\psi)^{\dagger}\cdot\alpha\psi+\psi^{\mathrm{T}}\alpha^{\mathrm{T}}\cdot\nabla\psi^{*}=\{\nabla\delta(\mathbf{x}-\mathbf{x}')\cdot\mathrm{spur}\,\alpha\}_{\mathbf{x}'=\mathbf{x}}=0.\quad(A.4)$$

By a similar argument

$$\tfrac{1}{2}e\Re\{\psi^{\dagger}\mathbf{E}_{\rm II}\cdot\alpha\psi\}=\tfrac{1}{4}(\mathbf{E}_{\rm II}\cdot\mathbf{j}+\mathbf{j}\cdot\mathbf{E}_{\rm II}),\quad(A.5)$$

[17] A somewhat similar argument is used by G. Wentzel in his book *Einführung in die Quantentheorie der Wellenfelder* (F. Deuticke, Vienna, 1943) in Sec. 18, on page 137, for proving the vanishing of $(\Omega\Phi)$ for all times t_n. See also the translation *Quantum Theory of Fields* (Interscience Publishers, New York, New York, 1949), p. 143.

[18] V. Fock, Z. Physik **75**, 622 (1932); in particular Eq. (11a) of its second part, on page 639.

[19] V. F. Weisskopf, Phys. Rev. **56**, 72 (1939), and A. Pais, Proc. Roy. Acad. Amsterdam (Verhandelingen, 1e sectie) **19**, 5 (1947), in particular page 25, footnote.

[20] See also F. J. Belinfante, Phys. Rev. **82**, 767(A) (1951); Prog. Theor. Phys. **6**, 202 (1951); and F. J. Belinfante and J. S. Lomont, Phys. Rev. **83**, 225(A) (1951).

where we have taken $\mathbf{E}_{\parallel}$ first at a different point $\mathbf{x}'$, then used Eqs. (6), (G-I:48) for $[\mathbf{E}_{\parallel}'; \psi]$ and its conjugate for $[\psi^*; \mathbf{E}_{\parallel}']$, and finally Eq. (7) and Eq. (A.3) above, before equating $\mathbf{x}'$ to $\mathbf{x}$. Similarly one shows

$$\tfrac{1}{2}e\Re\{\psi^\dagger \mathbf{E}_{\parallel}\psi\}-\tfrac{1}{4}\{\mathbf{E}_{\parallel}\rho+\rho\mathbf{E}_{\parallel}\} =\tfrac{1}{4}e^2(\psi^\dagger\psi+\psi^{\mathrm{T}}\psi^*)[\boldsymbol{\nabla}'(1/r)]_{\mathbf{x}'=\mathbf{x}}=0 \quad \text{(A.6)}$$

"because of symmetry." Other symmetry arguments yield

$$[d\delta(x)/dx]_{x=0}=0, \quad \text{(A.7)}$$

so that

$$\psi^\dagger\boldsymbol{\nabla}\psi+(\boldsymbol{\nabla}\psi)^{\mathrm{T}}\psi^*=0. \quad \text{(A.8)}$$

Equation (6) with $\varphi=V\psi+\psi V$ and (A.3) also yields

$$\Re\{\psi^\dagger(i\boldsymbol{\alpha})(V\psi+\psi V)\} =\tfrac{1}{4}i[(\psi^\dagger\boldsymbol{\alpha}\psi+\psi^{\mathrm{T}}\boldsymbol{\alpha}^{\mathrm{T}}\psi^*); V]=0, \quad \text{(A.9)}$$

while

$$\Re\{i\psi^\dagger(\boldsymbol{\alpha}\cdot\mathfrak{A})(\mathfrak{A}\cdot\boldsymbol{\alpha}\psi)\}=0 \quad \text{(A.10)}$$

follows from (6) alone.

Equation (G-I:57) and conjugate, with Eqs. (A.9), (A.10), (6), and $2e\boldsymbol{\nabla}=-(e/ihc)(\boldsymbol{\alpha}H_0+H_0\boldsymbol{\alpha})$, yield, in Heisenberg representation,

$$\nabla_0\mathbf{j}+\boldsymbol{\nabla}\rho=\Re\{\psi^\dagger(2e/ihc)\boldsymbol{\alpha}H_0\psi\}+\Re\{2e\psi^\dagger\boldsymbol{\nabla}\psi\} =\Re\{\psi^\dagger(e/ihc)[\boldsymbol{\alpha}; H_0]\psi\}. \quad \text{(A.11)}$$

Finally, from Eqs. (5)–(6) follows

$$\Re\{(H_0\psi)^\dagger(-H_0/ihc)\psi\}=0=\Re\{(\boldsymbol{\nabla}\psi)^\dagger\cdot ihc\boldsymbol{\nabla}\psi\} \quad \text{(A.12)}$$

and, with $\triangle\equiv\boldsymbol{\nabla}^2$,

$$\Re\{\psi^\dagger(H_0/ihc)(H_0\psi)\}=\Re\{\psi^\dagger(H_0^2/ihc)\psi\} =\Re\{\psi^\dagger ihc\triangle\psi\}. \quad \text{(A.13)}$$

By Eqs. (4), (G-I:57) and conjugate, (A.12) and (A.13), and (6),

$$\begin{aligned}\nabla_\mu\,{}^{\mathrm{H}}T_{\mathrm{e}}{}^{0\mu}&=\nabla_0\Re\{\psi^\dagger H_0\psi\}+\textstyle\sum_k\nabla_k\Re\{-\psi^\dagger ihc\nabla_k\psi\}\\ &=\Re\{\psi^\dagger(e/ihc)[\mathfrak{A}\cdot\boldsymbol{\alpha}; H_0]\psi\}\\ &\quad+\Re\{\psi^\dagger(e/2ihc)[H_0; V]\psi\}\\ &\quad+(e/8ihc)[\{\psi^\dagger(H_0+H_0^\dagger)\psi\\ &\qquad+\psi^{\mathrm{T}}(H_0^{\mathrm{T}}+H_0^*)\psi^*\}; V]. \quad \text{(A.14)}\end{aligned}$$

By use of Eq. (5), (A.3) with $\boldsymbol{\beta}$ replacing $\boldsymbol{\alpha}$, the definitions of $\boldsymbol{\nabla}^\dagger$ and $\boldsymbol{\nabla}^{\mathrm{T}}$ (footnote 10), and Eq. (A.4) and conjugate, in the last term of Eq. (A.14) only terms with $\boldsymbol{\nabla}$ from H_0 operating on V are left, which yield, by (G-I:6) and by (7), $\frac{1}{4}(\mathbf{E}_{\parallel}\cdot\mathbf{j}+\mathbf{j}\cdot\mathbf{E}_{\parallel})$. The term in (A.14) with $[H_0; V]$ yields by (5), (G-I:6), and (A.5) the same amount. Adding (A.1), with (A.11) substituted for its last terms, to Eq. (A.14), we thus find, by Eq. (1),

$$\nabla_\mu\,{}^{\mathrm{H}}T_{\mathrm{m}}{}^{0\mu}=\mathbf{j}\cdot\mathfrak{G}+\tfrac{1}{2}(\mathbf{E}_{\parallel}\cdot\mathbf{j}+\mathbf{j}\cdot\mathbf{E}_{\parallel}), \quad \text{(A.15)}$$

which gives Eq. (10) by (G-I:44).

APPENDIX B

With the abbreviating notation of reference 1, and by Eqs. (8), (G-I:14), (G-I:22) with note between (G-I:41) and (G-I:42), Eq. (G-I:50) and conjugate, and Eq. (3), we find, all in Heisenberg representation,

$$\begin{aligned}\delta\,{}^{\mathrm{H}}T_{I'}{}^{00}&=\tfrac{1}{2}e\Re\{\psi^\dagger(\mathbf{b}\cdot\boldsymbol{\alpha})(\psi V+V\psi)\}\\ &\quad-\tfrac{1}{2}ef'(\mathbf{b}\cdot\mathbf{r}')[\boldsymbol{\nabla}'(1/r)]\\ &\qquad\cdot\Re\{\psi^\dagger(\mathbf{j}'\psi+\psi\mathbf{j}')\}, \quad \text{(B.1a)}\end{aligned}$$

$$\delta\,{}^{\mathrm{H}}T_I{}^{0k}=(\mathbf{b}\cdot\mathbf{j})\mathfrak{A}_k-\rho\delta\mathfrak{A}_k, \quad \text{(B.1b)}$$

$$\delta\,{}^{\mathrm{H}}T_I{}^{kl}=\tfrac{1}{2}\rho(b_k\mathfrak{A}_l+b_l\mathfrak{A}_k)-\tfrac{1}{2}(j_k\delta\mathfrak{A}_l+j_l\delta\mathfrak{A}_k). \quad \text{(B.1c)}$$

Temporarily putting $\mathbf{j}=\mathbf{j}_\perp+\boldsymbol{\nabla}\xi$ (with $\operatorname{div}\mathbf{j}_\perp=0$), we find by some integrations by parts, with use of (G-I:20),

$$\begin{aligned}&f'(\mathbf{b}\cdot\mathbf{r}')(\mathbf{j}'\cdot\boldsymbol{\nabla}')(1/r)\\ &\quad=-f'\xi'(\mathbf{b}\cdot\boldsymbol{\nabla}')(1/r)-f'\mathbf{b}\cdot\mathbf{j}_\perp'/r\\ &\quad=f'(\mathbf{j}_{\parallel}'-\mathbf{j}_\perp')\cdot\mathbf{b}/r. \quad \text{(B.2)}\end{aligned}$$

Further, by Eqs. (5)–(6),

$$-\Re\{\psi^\dagger\boldsymbol{\alpha}H_0\psi\}=\Re\{\psi^\dagger ihc\boldsymbol{\nabla}\psi\}-\operatorname{curl}\tfrac{1}{2}\hbar c\Re\{\psi^\dagger\boldsymbol{\sigma}\psi\}. \quad \text{(B.3)}$$

Then, by Eqs. (8), (G-I:15), (G-I:50), and (G-I:57) and their conjugates, (G-I:58), (G-I:63), (G-I:60), (G-I:20), and Eqs. (B.2), (B.3), (4), (3), and (1), one finds

$$\begin{aligned}\delta\,{}^{\mathrm{H}}T_{\mathrm{e}'}{}^{00}&=-2\textstyle\sum_k b_k\,{}^{\mathrm{H}}T_{\mathrm{m}}{}^{0k}-\tfrac{1}{2}e\Re\{\psi^\dagger(\mathbf{b}\cdot\boldsymbol{\alpha})(V\psi+\psi V)\}\\ &\quad+ef'(\mathbf{b}\cdot\mathbf{r}')[\boldsymbol{\nabla}'(1/r)]\cdot\Re\{\psi^\dagger\mathbf{j}'\psi\}. \quad \text{(B.4a)}\end{aligned}$$

By Eqs. (4), (G-I:15), (G-I:50), (G-I:51), (5), (6), (7), by relations like $\alpha_k\alpha_l+\alpha_l\alpha_k=2\delta_{kl}$ and $\sigma_{kl}\alpha_m-\alpha_m\sigma_{kl}=2i(\delta_{mk}\alpha_l-\delta_{ml}\alpha_k)=\alpha_l\sigma_{km}+\sigma_{km}\alpha_l+2\sigma_{kl}\alpha_m$, and by Eqs. (3), (4), and (1), we find

$$\begin{aligned}\delta\,{}^{\mathrm{H}}T_{\mathrm{e}}{}^{0k}&=-b_k\,{}^{\mathrm{H}}T_{\mathrm{m}}{}^{00}-\textstyle\sum_l b_l\,{}^{\mathrm{H}}T_{\mathrm{e}}{}^{kl}-\tfrac{1}{2}b_k\rho V\\ &\quad+\rho f'(\mathbf{b}\cdot(\mathfrak{F}')\nabla_k'(1/4\pi r)\\ &\quad+\tfrac{1}{2}e\Re\{\psi^\dagger f'\rho'(\mathbf{b}\cdot\mathbf{r}')[\nabla_k'(1/r)]\psi\}\\ &\qquad+\tfrac{1}{2}\textstyle\sum_l b_l(\mathfrak{A}_l j_k-\mathfrak{A}_k j_l). \quad \text{(B.4b)}\end{aligned}$$

By Eqs. (4), (G-I:15), (G-I:50), and (G-I:57) and conjugate equations, by $\alpha_k\alpha_l=\delta_{kl}+i\sigma_{kl}$, and by Eqs. (6), (7), and (G-I:7), we find

$$\begin{aligned}\delta\,{}^{\mathrm{H}}T_{\mathrm{e}}{}^{kl}&=[-b_l\,{}^{\mathrm{H}}T_{\mathrm{e}}{}^{0k}+\tfrac{1}{2}b_l\rho\mathfrak{A}_e\\ &\quad+\tfrac{1}{2}j_lf'(\mathbf{b}\cdot(\mathfrak{F}')\nabla_k'(1/4\pi r)-\tfrac{1}{2}j_lb_kV\\ &\quad+\tfrac{1}{2}ef'(\mathbf{b}\cdot\mathbf{r}')[\nabla_k'(1/r)]\Re\{\psi^\dagger\rho'\alpha_l\psi\}]\\ &\qquad+[\text{same with } k, l \text{ interchange}]. \quad \text{(B.4c)}\end{aligned}$$

Now, by (G-I:47), in Heisenberg representation

$$\begin{aligned}\delta\mathfrak{A}_k&=-f'(\mathbf{b}\cdot\mathbf{r}')(\mathbf{E}'\cdot\boldsymbol{\nabla}')\nabla_k'(1/4\pi r)\\ &=f'(\mathbf{b}\cdot\mathbf{E}')\nabla_k'(1/4\pi r)+f'(\mathbf{b}\cdot\mathbf{r}')\rho'\nabla_k'(1/r). \quad \text{(B.5)}\end{aligned}$$

By (G-I:44) and (G-I:6), the first term of the last member of (B.5) equals

$$f'(\mathbf{b}\cdot(\mathfrak{F}')\nabla_k'(1/4\pi r)+f'V'(\mathbf{b}\cdot\boldsymbol{\nabla}')\nabla_k'(1/4\pi r). \quad \text{(B.6)}$$

By (G-I:7) and (G-I:65),

$$\begin{aligned}\int' r_i'\rho'\nabla_k'(1/r) &= -\delta_{ki}\int'\rho'/r - \int'(r_i'/r)\nabla_k'\rho' \\ &= -\delta_{ki}V + \int'(r_i'/4\pi r)\triangle'\nabla_k'V' \\ &= -\delta_{ki}V + 2\int'[\nabla_k'V']\nabla_i'(1/4\pi r). \quad \text{(B.7)}\end{aligned}$$

Thence

$$\int' V'\nabla_k'\nabla_i'(1/4\pi r) = -\tfrac{1}{2}\delta_{ki}V - \tfrac{1}{2}\int' r_i'\rho'\nabla_k'(1/r), \quad \text{(B.8)}$$

so that, by (B.5) with (B.6) and (B.8),

$$\delta\mathfrak{P}_k = \int'(\mathbf{b}\cdot\mathfrak{E}')\nabla_k'(1/4\pi r) - \tfrac{1}{2}b_k V + \tfrac{1}{2}\int'(\mathbf{b}\cdot\mathbf{r}')\rho'\nabla_k'(1/r). \quad \text{(B.9)}$$

Now adding (B.1a, b, c) to (B.4a, b, c) and making use of Eqs. (8), (1), (3), (B.9), and finally of Eqs. (7), (G-I:48), and (G-I:20), we find

$$\delta\,{}^{\mathrm{H}}T_{\mathrm{m}}{}^{00} + 2\textstyle\sum_k b_k\,{}^{\mathrm{H}}T_{\mathrm{m}}{}^{0k} = \tfrac{1}{2}e\int'(\mathbf{b}\cdot\mathbf{r}')[\nabla'(1/r)]\cdot\Re\{\psi^\dagger[\mathbf{j}';\psi]\} = -\tfrac{1}{2}e\int'(\mathbf{b}\cdot\mathbf{r}')\,\delta(\mathbf{r}')\,\mathbf{j}\cdot\nabla'(1/r) = 0; \quad \text{(B.10a)}$$

$$\delta\,{}^{\mathrm{H}}T_{\mathrm{m}}{}^{0k} + b_k\,{}^{\mathrm{H}}T_{\mathrm{m}}{}^{00} + \textstyle\sum_l b_l\,{}^{\mathrm{H}}T_{\mathrm{m}}{}^{kl} = \tfrac{1}{2}e\int'(\mathbf{b}\cdot\mathbf{r}')[\nabla_k'(1/r)]\Re\{\psi^\dagger[\rho';\psi]\} = -\tfrac{1}{2}e\int'(\mathbf{b}\cdot\mathbf{r}')\,\rho\,\nabla_k'(1/r) = 0; \quad \text{(B.10b)}$$

$$\delta\,{}^{\mathrm{H}}T_{\mathrm{m}}{}^{kl} + b_l\,{}^{\mathrm{H}}T_{\mathrm{m}}{}^{0k} + b_k\,{}^{\mathrm{H}}T_{\mathrm{m}}{}^{0l} = \{\tfrac{1}{4}e\int'(\mathbf{b}\cdot\mathbf{r}')[\nabla_k'(1/r)]\Re\{\psi^\dagger\alpha_l[\rho';\psi]\}\} + [k, l \text{ interchanged}] = -\tfrac{1}{4}e\int'(\mathbf{b}\cdot\mathbf{r}')\,\delta(\mathbf{r}')\,\{j_l\nabla_k' + j_k\nabla_l'\}(1/r) = 0. \quad \text{(B.10c)}$$

PHYSICAL REVIEW VOLUME 84, NUMBER 4 NOVEMBER 15, 1951

Energy Distribution, Drift Velocity, and Temperature of Slow Electrons in Helium and Argon

DOMENICK BARBIERE
*Westinghouse Research Laboratories, East Pittsburgh, Pennsylvania**

(Received June 5, 1950)

The energy distribution, and the drift velocity and electron temperature which are closely dependent on the distribution, were calculated for slow electrons in He and A under fields ranging from $X/p=1$ to 4 volts/cm mm. The calculations were based on the theory developed by Holstein. The diffusion cross sections of the gases for electrons which account for the effect of elastic collisions were computed from the scattering data of Ramsauer and Kollath and of Normand. The effect of excitation collisions was taken into account by comparing the results for three representative values of excitation cross section: $Q_{ex}=0$ and $Q_{ex}=\infty$ which form the limiting boundaries and Q_{ex}=a constant obtained from Maier-Leibnitz. Although a considerable percentage of the electrons were to be found in the excitation region for $Q_{ex}=0$, the results for $Q_{ex}=$ constant were nearly the same as those for $Q_{ex}=\infty$. In the case of small fields, therefore, the electron energy distribution in the elastic region and related quantities may be calculated with Q_{ex} assumed infinite.

A complete set of curves are given below illustrating some of the properties of the calculated quantities. The agreement between experiment and the curves obtained with the scattering data of Ramsauer and Kollath is good, while the curves obtained from the corresponding data of Normand indicate that his cross-section values are too low.

I. INTRODUCTION

BECAUSE of the lack of a complete theory and sufficient cross-section data, the energy distribution and related parameters for electrons in gases have heretofore been calculated under various simplifying assumptions. These approximations have resulted in considerable discrepancies between the theoretical results and experiment. In the discussion below, the energy distribution, drift velocity, and electron temperature of slow electrons in helium and argon are more exactly calculated for fields up to $X/p=4$ volts/cm mm. The following factors are considered, some or all of which have not been taken into account in previous calculations: (a) an electron loses a small fraction of its energy by recoil in elastic collisions with molecules of finite mass, (b) the effect of excitation collisions cannot be neglected, (c) the elastic cross section of gases for electrons is a function of the electron energy, (d) the type of elastic cross section that should be used in computing the energy distribution is not the Ramsauer cross section but, more exactly, the diffusion cross section. The latter cross section is also referred to as the cross section for momentum transfer.

The calculations below are based on the theoretical investigations of Holstein,[1] whose work represents the most inclusive theory to date on the energy distribution of electrons. Values for the diffusion cross section could not be found in the literature and were therefore calculated from existing angular scattering data. Energy distribution, drift velocity, and electron temperature curves were obtained for three values of excitation cross section: $Q_{ex}=0$, $Q_{ex}=\infty$ and $Q_{ex}=$a reasonable constant. For the small fields considered here, the calculated curves for the latter two cases were found to be nearly coincident. As a result, for the calculation of gas parameters depending on the electron energy distribution in the non-excitation region, Q_{ex} may be

* Now with the Radiation Laboratory, Johns Hopkins University, Baltimore, Maryland.

[1] T. Holstein, Phys. Rev. **70**, 367 (1946).

assumed infinite for fields up to $X/p=4$ volts/cm mm with little error.

II. DISCUSSION OF THEORY

The physical situation considered by Holstein was that of a gas discharge region between two parallel plane electrodes with an electric field X perpendicular to the electrodes. The steady-state, homogeneous, dc solutions for the isotropic portion of the energy distribution are given by the differential equations:

$$0=\frac{4a^2}{3}\frac{d}{du}\left(u\lambda_D\frac{df}{du}\right)+\frac{2m}{M}\frac{d}{du}\left(\frac{u^2f}{\lambda_D}\right)+\sum_k(u+u_k)\lambda_k^{-1}(u+u_k)f(u+u_k) \quad (1a)$$

for $u<u_1$;

$$0=\frac{4a^2}{3}\frac{d}{du}\left(u\lambda_D\frac{df}{du}\right)+\frac{2m}{M}\frac{d}{du}\left(\frac{u^2f}{\lambda_D}\right)-\frac{uf}{\lambda_{ex}} \quad (1b)$$

for $u>u_1$, where $a=eX/m$ represents the electron acceleration in a field, X; $u=v^2$= electron velocity squared; m/M= ratio of the electronic mass to the molecular mass; $\lambda_D(u)$= the diffusion mean free path; $\lambda_k(u)$= the mean free path between those excitation collisions, which excite a gas atom to the kth excited level; $\frac{1}{2}mu_k$= the energy of the kth excited level; $\frac{1}{2}mu_1$= the energy of the first excited level; and $\lambda_{ex}=1/\sum_k\lambda_k^{-1}$= the mean free path between excitation collisions.

The complete distribution function is obtained by fitting together the solutions of Eqs. (1a) and (1b). Equation (1a) will yield the energy distribution in the elastic collision region while Eq. (1b) refers to electrons with energies above the first excitation level of the gas atoms. For the small electric fields considered here, the vast majority of the electrons will be found in the elastic collision region so that the $f(u)$ from Eq. (1a) will generally very much exceed and contribute more to the drift velocity and temperature than the $f(u)$ from Eq. (1b). Since very few electrons under small fields possess sufficient energy to cause ionization, the ionization terms in the differential equations have been neglected. The density of electrons in the energy interval defined by u and $u+du$ is proportional to $u^{\frac{1}{2}}f(u)$, and the normalized probability for finding an electron in this interval is given by

$$n(u)du=u^{\frac{1}{2}}f(u)\Big/\int_0^\infty u^{\frac{1}{2}}f(u)du.$$

Equations (1a) and (1b) represent solutions for dc fields. It was shown by Holstein[1] that when $(\omega^2\lambda_D^2/u_1)\ll 1$, the energy distribution equations for ac fields are identical with those for the dc case given above. The energy distribution, drift velocity, and electron temperature calculated from the dc Eqs. (1a) and (1b) may therefore be applied to discharges in ac fields satisfying this condition.

A number of statistical properties of a gas are closely dependent on the electron energy distribution in that gas. Among these are the electron drift velocity and electron temperature which may be calculated once the energy distribution has been determined.

The drift velocity induced in electrons by an applied electric field X is given by

$$w=-\tfrac{2}{3}(e/m)X\int_0^\infty u\lambda_D(df/du)du\Big/\int_0^\infty u^{\frac{1}{2}}fdu. \quad (2)$$

The drift velocity per unit applied field, w/X, represents the mobility of the electrons. w was calculated here from Eq. (2) for electrons in He and A up to $X/p=4$ volts/cm mm. The variation of $\lambda_D(u)$ with energy was taken into account. The drift velocity of electrons in Ne has been obtained by Druyvesteyn.[2] The Ne case is simplified by a rather flat $\lambda_D(u)$ *versus* energy curve. The drift velocity of electrons in the noble gases was measured by Townsend and Bailey[3] and R. A. Nielsen.[4] The calculated curves compare favorably with their data, and a more complete comparison will be given below.

The concept of electron temperature arose from the early erroneous assumptions that the electron energy distribution is Maxwellian. Although the concept has no place in the discussion of non-Maxwellian statistics, it finds many uses in gas discharges. Furthermore, it is capable of direct experimental determination.

In gas discharges, the electron temperature is defined as e/k times the ratio of the diffusion constant of the electrons to their mobility, where k is Boltzmann's constant. In Maxwellian statistics this ratio is equivalent to the temperature of the particles. When appropriate expressions are substituted for the diffusion constant and the mobility of the electrons, the electron temperature reduces to

$$T_e=\frac{eX}{k}\frac{D_e}{w}=-\frac{m}{2k}\int_0^\infty u\lambda_D f du\Big/\int_0^\infty u\lambda_D\frac{df}{du}du. \quad (3)$$

T_e was calculated here for He and A up to $X/p=4$ volts/cm mm. The theoretical curves agree very well with Townsend's results.[3]

The quantity $\lambda_D(u)$ appears throughout the above equations. Since curves for this cross section are not given in the literature, they were calculated for helium, neon, and argon from the angular scattering data of Ramsauer and Kollath.[5]

Introducing $\lambda_D(u)$ by way of the better known Ramsauer cross section we may write

$$1/p\lambda_R(u)=Q_R(u)=2\pi N\int_0^\pi q(u,\theta)\sin\theta d\theta, \quad (4)$$

[2] M. J. Druyvesteyn, Physica **3**, 65 (1936). Kruithoff and Druyvesteyn, Physica **4**, 450 (1937).

[3] Townsend and Bailey, Phil. Mag. **42**, 873 (1921); **43**, 594 (1922); **44**, 1033 (1922); **46**, 657 (1923).

[4] R. A. Nielsen, Phys. Rev. **50**, 950 (1936).

[5] Ramsauer and Kollath, Ann. Physik **12**, 529 (1932).

TABLE I. Comparison of the Ramsauer and diffusion cross sections. All cross sections are given in units of cm^3/cm^3 at 0°C and 1 mm Hg and were computed from the angular scattering data of Ramsauer and Kollath.

Helium				Neon				Argon			
Electron energy in ev	Ramsauer cross section	$1-\langle\cos\theta\rangle_{Av}$	Diffusion cross section	Electron energy in ev	Ramsauer cross section	$1-\langle\cos\theta\rangle_{Av}$	Diffusion cross section	Electron energy in ev	Ramsauer cross section	$1-\langle\cos\theta\rangle_{Av}$	Diffusion cross section
1.8	20.8	1.102	22.9	0.99	5.06	1.023	5.18	1.1_5	5.92	0.983	5.82
2.9	22.0	1.070	23.6	1.17	5.77	1.025	5.92	1.5	8.37	0.855	7.15
4.2	20.8	1.081	22.5	1.35	6.01	1.016	6.11	2.0	12.2	0.875	10.7
5.3_5	19.4	1.075	20.8	1.67	6.23	0.972	6.05	2.3	14.0	0.856	12.0
6.7_5	18.1	1.065	19.3	1.70	6.30	0.973	6.13	2.4_5	15.1	0.848	12.8
8.2_5	16.7	1.008	16.9	1.80	6.41	0.938	6.02	2.8	17.5	0.835	14.6
10.7_5	15.1	0.992	15.0	2.2	6.94	0.924	6.41	3.2_2	20.3	0.835	16.9
13.8	14.2	0.949	13.5	2.6	7.31	0.883	6.46	3.3	20.7	0.807	16.7
15.8	12.3	0.928	11.4	2.8	7.42	0.899	6.67	3.6	22.6	0.842	19.0
19.2	11.3	0.893	10.0	3.6	8.13	0.825	6.70	4.0	24.2	0.831	20.1
				4.9	8.91	0.798	7.11	5.0	32.6	0.857	27.9
				6.4	9.50	0.767	7.29	5.4	34.5	0.848	29.3
				7.9	10.1	0.766	7.76	6.7	45.2	0.879	39.8
				10.4	10.9	0.768	8.36	8.0	53.5	0.809	43.2
				13.1	11.5	0.782	8.99	9.0	62.5	0.833	52.1
				15.9	12.0	0.790	9.47	10.3	71.6	0.735	52.6
								12.5	78.6	0.739	58.0

where $Q_R(u)$ is the Ramsauer cross section of 1 cc of gas (usually given at 1 mm Hg and 0°C) for electrons of incident energy u, and N is the gas density in molecules per cc. The quantity $q(u, \theta)$ represents the angular scattering function for the deflection by a molecule of an electron of energy u through an angle θ. Data on $q(u, \theta)$ in the rare gases were obtained by Ramsauer and Kollath[5] for electron energies up to the first excitation level of the gases.

The diffusion cross section of 1 cc of gas is given by the somewhat similar equation

$$1/p\lambda_D(u)=Q_D(u)$$

$$=2\pi N\int_0^\pi q(u,\theta)\sin\theta(1-\cos\theta)d\theta, \quad (5)$$

whence

$$Q_D(u)/Q_R(u)=1-\langle\cos\theta\rangle_{Av}, \quad (6)$$

where

$$\langle\cos\theta\rangle_{Av}=\int_0^\pi q(u,\theta)\sin\theta\cos\theta d\theta \Big/ \int_0^\pi q(u,\theta)\sin\theta d\theta.$$

Values of $Q_R(u)$, $1-\langle\cos\theta\rangle_{Av}$, and $Q_D(u)$ for He, Ne, and A were computed from the data on $q(u, \theta)$ given by Ramsauer and Kollath and are shown in Table I. $Q_R(u)$ was also measured directly by Ramsauer and Kollath. The values calculated from Eq. (4) agree almost perfectly with their direct measurements. It can be seen from the $1-\langle\cos\theta\rangle_{Av}$ column that the deviation between the two types of cross sections can be as high as 25 percent.

Measurements of the total Ramsauer cross section, $Q_R(u)$, but not of $q(u, \theta)$, were also conducted by Normand.[6] His curves of $Q_R(u)$ display the same form as those of Ramsauer and Kollath but are displaced downward by about 20 percent, indicating a consistent source of error in one of the two experiments. For the sake of completeness, values of $Q_D(u)$ were also computed by Eq. (6) from Normand's data on $Q_R(u)$ and the $\langle\cos\theta\rangle_{Av}$ calculated from the angular scattering data of Ramsauer and Kollath. The drift velocity and electron temperature curves calculated from Normand's cross sections do not agree with experiment.

Curves for the diffusion cross section were calculated for energies up to the first excitation level (u_1) of the gas atoms. Above u_1, $Q_D(u)$ was assumed constant and equal to $Q_D(u_1)$. The differential Eqs. (1a) and (1b) for the energy distribution were solved for $Q_{ex}=0$, $Q_{ex}=\infty$ and $Q_{ex}=$ some reasonable constant. The constant chosen was $0.01\ Q_D(u_1)$ which was obtained from the curves of Maier-Leibnitz.[7]

Assuming $1/p\lambda_{ex}=Q_{ex}=0$, both Eqs. (1a) and (1b) reduce to

$$0=\frac{4a^2}{3}\frac{d}{du}\left(u\lambda_D\frac{df}{du}\right)+\frac{2m}{M}\frac{d}{du}\left(\frac{u^2f}{\lambda_D}\right) \quad (7)$$

whose solution is

$$f_1(u)=C\exp\left[-\frac{3}{4a^2}\frac{2m}{M}\int_0^u\frac{u}{\lambda_D{}^2}du\right]$$

$$=C\exp\left[-\frac{6}{(X/p)^2}\frac{m}{M}\int_0^V Q_D{}^2(V)VdV\right] \quad (8)$$

where $a=eX/300m$ with X in volts/cm; $\frac{1}{2}mu=eV/300$ with V in volts; and $(p\lambda_D)^{-1}=Q_D$ where p is the pressure in mm Hg. The energy distribution for this case is proportional to $u^{\frac{1}{2}}f_1(u)$.

Equation (8) is identical with that derived by Morse, Allis, and Lamar[8] with excitation collisions neglected.

[5] C. E. Normand, Phys. Rev. 35, 1217 (1930).

[7] H. Maier-Leibnitz, Physik 95, 499 (1935).

[8] Morse, Allis, and Lamar, Phys. Rev. 48, 412 (1935).

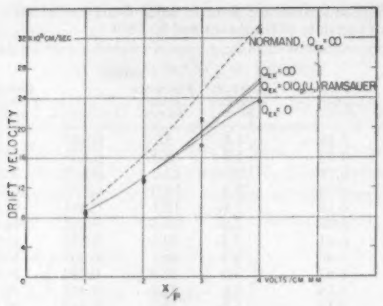

FIG. 1. Drift velocity of electrons in helium. See reference 11. Crosses are from Nielsen, and circles from Townsend and Bailey.

It was also obtained previously by Druyvesteyn[9] who assumed Q_D independent of energy.

For $Q_{ex}=\infty$, Eq. (1b) becomes meaningless and Eq. (1a) reduces to

$$\frac{4a^2}{3}u\lambda_D\frac{df}{du}+\frac{2m}{M}\frac{u^2f}{\lambda_D}=-\phi(u), \tag{9}$$

where

$$\phi(u)=\int_0^u\sum_h[(u+u_h)f(u+u_h)\lambda_h^{-1}(u+u_h)]du.$$

By standard methods one obtains the solution

$$f_2(u)=f_1(u)\left[\frac{3}{4a^2}\int_u^{u_1}\frac{\phi du}{\lambda_D f_1}\right], \tag{10}$$

where $f_1(u)$ is given by Eq. (8) and represents the solution to the homogeneous portion of Eq. (9).

The quantity $\phi(u)$ represents the contribution of electrons to the energy element around u by excitation collisions. To simplify matters it was assumed that electrons lose all their energy per excitation collision. Actually, only u_h units are lost when an atom is excited to its hth level, where $u_1\leq u_h\leq$all the energy of the electron. A few representative calculations were performed with the assumption that the electrons lose u_1 units of energy per excitation collision. It was found that the difference in results between the two extremes, i.e., a loss of u_1 units and a complete loss, was less than 2 percent in the worst case ($X/p=4$). With the complete loss assumption, ϕ becomes independent of u and may be readily obtained from Holstein's equations.[10]

For $Q_{ex}=0.01\ Q_D(u_1)$, the solution of Eq. (1a) is given by Holstein as

$$f_2(u)=f_1(u)\left[\frac{f_2'(u_1)}{f_1(u_1)}+\frac{3}{4a^2}\int_u^{u_1}\frac{\phi}{\lambda_D f_1}du\right]. \tag{11a}$$

In solving Eq. (1b) for the excitation region, it is assumed that the excitation losses very much exceed the recoil losses. The m/M term is therefore negligible, and the solution of Eq. (1b) becomes

$$f_2'(u)=Cu^{-\frac{1}{2}}e^{-\gamma u}, \tag{11b}$$

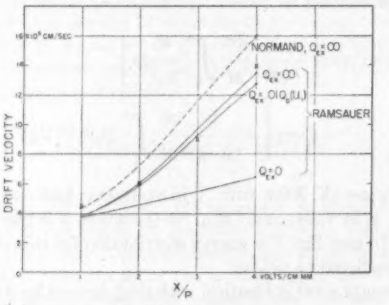

FIG. 2. Drift velocity of electrons in argon. See reference 11. Crosses are from Nielsen.

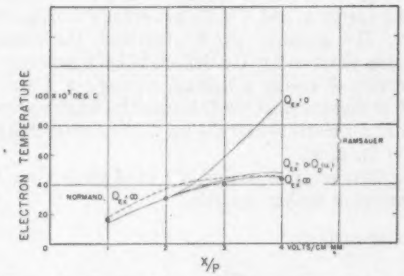

FIG. 3. Temperature of electrons in helium. See reference 11. Circles are from Townsend and Bailey.

where $\gamma=(1/2a)[3/\lambda_{ex}\lambda_D]^{\frac{1}{2}}$. For the excitation region $1/p\lambda_{ex}=0.01\ Q_D(u_1)$ and $1/p\lambda_D=Q_D(u_1)$. The constants in Eq. (11a) have been arranged so that at $u=u_1$, $f_2(u_1)=f_2'(u_1)$.

III. DISCUSSION OF RESULTS

Graphs for the energy distribution, drift velocity, and temperature of electrons in helium and argon are shown in Figs. 1 through 9.[11] Figures 1 and 2 show the drift velocity, and Figs. 3 and 4 give the electron temperature, both quantities as a function of X/p from $X/p=1$ to 4 volts/cm mm. The solid curves in Figs. 1 through 4 were computed from the elastic cross-section data of Ramsauer and Kollath, while the broken curves were obtained from the corresponding data of Normand. Figures 5 and 6 show the electron energy distribution,

[9] M. J. Druyvesteyn, Physica **10**, 69 (1930).

[10] See Sec. VII of reference 1.

[11] In Figs. 1 through 3, the solid line curves were calculated from the elastic scattering data of Ramsauer and Kollath while the broken line curves were obtained from the corresponding data of Normand. The curves in Figs. 4 through 9 were obtained from the data of Ramsauer and Kollath.

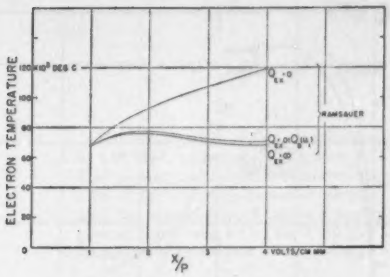

FIG. 4. Temperature of electrons in argon.

$u^{\frac{1}{2}}f(u)$, with X/p as a parameter. Figures 7 and 8 illustrate the effect of the excitation cross section on the shape of the energy distribution by comparing curves obtained for $Q_{ex}=0$, ∞ and $0.01\ Q_D(u_1)$ at $X/p=4$ volts/cm mm. Figure 9 demonstrates the effect of a variable elastic cross section on the shape of the energy distribution curve by comparing the distribution in helium where $Q_D(u)$ decreases with energy with the distribution in argon where $Q_D(u)$ increases with energy.

It is evident from the graphs that in all cases the results for $Q_{ex}=\infty$ and $Q_{ex}=0.01\ Q_D(u_1)$ are extremely close. Figures 7 and 8 indicate that although a considerable percentage of the electrons are to be found in the excitation region for $Q_{ex}=0$ at $X/p=4$, an excitation cross section of $0.01\ Q_D(u_1)$ is sufficient to drive almost all of the electrons from the excitation region producing a distribution curve for $Q_{ex}=0.01\ Q_D(u_1)$ that approaches the curve for $Q_{ex}=\infty$. Physically, it can be reasoned that when the steady state is attained in a gas discharge the energy losses sustained by electrons through the medium of collisions are replaced by gains from the electric field. However, the energy losses from excitation collisions are large so that most of the

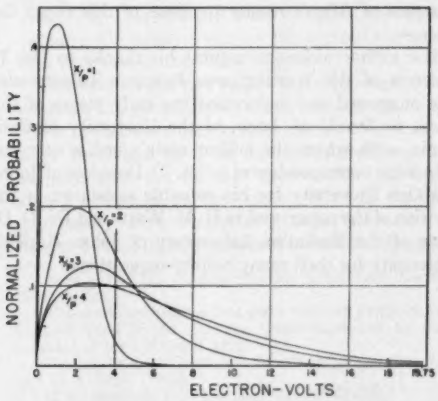

FIG. 5. Energy distribution of electrons in helium for $Q_{ex}=0.01\ Q_D(u_1)$.

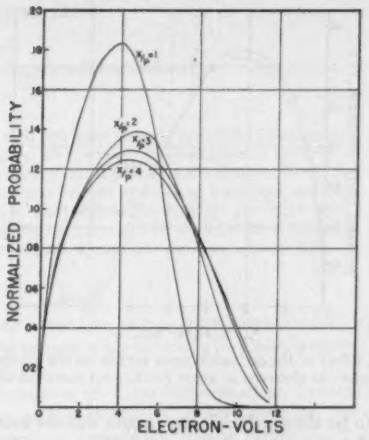

FIG. 6. Energy distribution of electrons in argon for $Q_{ex}=0.01\ Q_D(u_1)$.

electrons involved in such collisions are thrown back close to the zero energy level with very little chance, in the case of small fields, of regaining the loss. Apparently, the small values of excitation cross section chosen in these calculations to approximate the actual values in helium and argon were sufficient to create a distribution close to that of $Q_{ex}=\infty$. The discrepancy between the curves for $Q_{ex}=0.01\ Q_D(u_1)$ and $Q_{ex}=\infty$ increases with X/p. However, the difference is small up to $X/p=4$.

Also shown in Figs. 1 through 4 are the drift velocity measurements of Townsend and Bailey[3] and Nielsen,[4] and the electron temperature measurements of Townsend and Bailey.[3] The agreement between the curves computed from the data of Ramsauer and Kollath and experiment is good while Normand's curves are much too high.[12] In the case of argon, Townsend's data is too

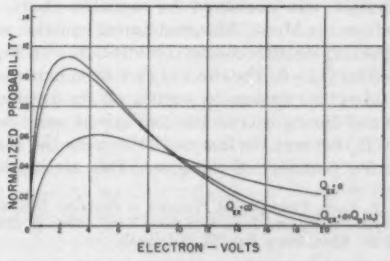

FIG. 7. Effect of the excitation cross section on the energy distribution of electrons in helium for $X/p=4$ volts/cm mm.

[12] It is interesting to note that all the quantities discussed above are a function of the product $X\lambda$. Thus, since λ (Normand) is approximately equal to 1.2λ (Ramsauer and Kollath), a result calculated from Normand's data for X should equal the one calculated from the data of Ramsauer and Kollath for $1.2X$. This fact is illustrated in Figs. 1, 2, and 3.

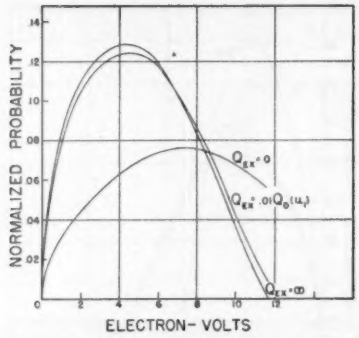

FIG. 8. Effect of the excitation cross section on the energy distribution of electrons in argon for $X/p=4$ volts/cm mm.

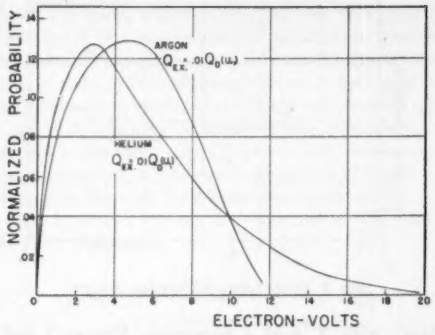

FIG. 9. A comparison of the shape of the energy distribution curves in helium and argon illustrating the effect of a variable elastic cross section, for $X/p=3$ volts/cm mm. The diffusion cross section decreases with energy in helium and increases with energy in argon.

high to be shown. In his day, argon was the most difficult of the rare gases to purify and because of its Ramsauer effect the most sensitive to impurities.

In Fig. 9 the energy distributions in helium and argon are compared, where in helium $Q_D(u)$ decreases [$\lambda_D(u)$ increases] with energy and in argon $Q_D(u)$ increases [$\lambda_D(u)$ decreases] with energy. The peak of the distribution curve, which indicates the most probable energy of the electrons, falls at a higher energy level in argon than in helium. The distribution curve in argon, however, decreases rapidly for energies above the most probable value while the downward slope in helium is considerably more gradual. Thus, we would expect a greater relative percentage of electrons at the higher energies in helium than in argon. For energies below the most probable energy peak, the distribution decreases more rapidly in helium. These effects have been observed experimentally and are very well explained in Loeb's book.[13]

A study of the effect of excitation collisions and of a variable elastic cross section on the form of the distribution law in the rare gases was made by Allen.[14] The distribution was evaluated for variable elastic free paths from the Morse, Allis, and Lamar equation which in neglecting inelastic collisions is identical with Eq. (2) derived for $Q_{ex}=0$. The effect of excitation impacts was then taken into account by cutting off the distribution curve and having it cross the zero axis at some energy value (E_1) between the first excitation potential and the ionization potential of the gases. This assumption is equivalent to setting $Q_{ex}=\infty$ for all energies beyond E_1. The exact value of E_1 was chosen by comparing the calculated results with the measured drift velocities or with the measurements of the average electron energy by Townsend and Bailey.[3] For helium, agreement was obtained for $E_1=19.7$ volts, the first excitation potential of the gas. For argon, agreement regarding the drift velocity was obtained at $E_1=11.57$ volts, the first excitation potential of the gas, but for agreement in the case of the average electron energy it was necessary to set E_1 at 15.6 volts, the ionization potential of the gas. Since Townsend's measurements in argon were often inaccurate, the former value of E_1 should be considered as the more reliable point. Thus, for both argon and helium, optimum agreement with experiment was obtained when the distribution curves were cut off at E_1, the first excitation level of the gas. The manner in which Allen accounted for the excitation collisions was, therefore, to set $Q_{ex}=\infty$. This fact is confirmed by the closeness of Allen's results to those of this paper for $Q_{ex}=\infty$.

The author wishes to express his thanks to Dr. T. Holstein of the Westinghouse Research Laboratories who suggested and supervised the early stages of the work; to Dr. L. B. Loeb, of the University of California, with whom the author maintained a very enlightening correspondence; to Dr. T. Donahue of Johns Hopkins University for his valuable assistance in the revision of the paper; and to H. M. Watts and Dr. D. D. King of the Radiation Laboratory of Johns Hopkins University for their many helpful suggestions.

[13] L. B. Loeb, *Fundamental Processes of Electrical Discharge in Gases* (John Wiley and Sons, Inc., New York, 1939), p. 214.
[14] H. W. Allen, Phys. Rev. **52**, 707 (1937).

The Radioactivity of Se^{73}

F. R. Scott*
Department of Physics, Indiana University, Bloomington, Indiana†
(Received July 16, 1951)

The disintegration of Se^{73} results in four positron groups with end-point energies and relative intensities of 1.68 Mev, 1.2 percent; 1.318 Mev, 87.4 percent; 0.750 Mev, 10.3 percent; and 0.250 Mev, 1.1 percent. Four nuclear gamma-rays are observed having energies of 67.1 kev, 361 kev, 860 kev, and 1.31 Mev. The K/L ratio of the internally converted electrons from the 67.1-kev and 361-kev gamma-ray transitions are 7.6 and 8.6, respectively. K-capture—positron branching ratios are measured as 0.45 for the 1.318-Mev positron transitions, 1.6 for the 0.750-Mev positron transition and estimated as 6 for the 0.250-Mev positron transition. Measurement of the K-Auger electrons indicates a gross K-capture—positron ratio of 0.59.

INTRODUCTION

THE radioactivity of the 7.1-hr transition from Se^{73} to As^{73} has been investigated by means of a medium sized, high resolution, magnetic spectrometer. The original interest in the problem arose from the fact that, on the basis of previously reported work,[1–3] the decay was simple with no gamma-rays. It was felt that this simple decay would provide a good test of the feasibility of measuring K-capture—positron branching ratios by means of relative Auger electron and positron intensities.

The results of the spectrometer measurements soon showed that the disintegration is complicated. The positron spectrum is found to be complex and is resolved into four groups with end-point energies of 0.250 Mev, 0.750 Mev, 1.318 Mev, and 1.68 Mev. Their relative intensities are 1.1, 10.3, 87.4, and 1.2 percent, respectively. From a consideration of an end-point energy of 1.68 Mev, a half-life of 425 minutes, and a relative intensity of 1.1 percent, the high energy transition appears to be once-forbidden with a ln ft of 7.1. The ln ft for the 1.318-Mev positron transition is 5.6, placing it in the allowed group. Little can be said about the forbiddenness of the two low energy positron groups because the half-life of their initial state is unknown. This half-life must certainly be short compared to 425 minutes because throughout the investigation only one period was observed.

Contrary to the previously reported work, measurements of the gamma-spectra indicate four gamma-rays. Their energies are 67.1 kev, 361 kev, 860 kev, and 1.31 Mev. Investigation of the internal conversion electrons suggests that the 67.1-kev gamma-ray is a magnetic 2^3-pole transition in the parent Se^{73} and the 361-kev gamma-ray is a magnetic 2^2-pole transition which follows the 1.318-Mev positron transition. The energies of the other two gamma-rays correspond to transitions to the ground state following the two low energy positron groups.

Estimates of K-capture—positron branching ratios to several of the levels in As^{73} are made by means of gamma-ray intensities. These ratios are 1.6 for the 0.750-Mev positron transition and 0.45 for the 1.318-Mev positron decay. An estimate of 6 is given for the K-capture—positron branching ratio of the 0.250 positron transition. From the intensity of the K-Auger electrons a gross ratio of 0.59 is obtained for the total number of K-captures to total number of positrons.

EXPERIMENTAL METHOD

The energy measurements were obtained with the aid of a high resolution, 180 degree focusing, 15-cm radius of curvature, shaped magnetic field spectrometer.[4]

For most measurements a 0.6-mg/cm² mica end-window counter was used as a detector. For studying the photoelectrons and the internal conversion electrons of the 67.1-kev gamma-ray and the Auger electrons, a side-window counter was employed. The window of this counter was one double layer of zapon supported by a grid of Lektromesh.[5] Because of slow diffusion of the counter gas through such a thin window (Approx. 150A thick), the 3-cm total pressure of two parts ethylene to one part argon was automatically maintained by means of a Cartesian Manostat.[6]

The Se^{73} activity was obtained by bombarding powdered and pressed germanium metal with alpha-particles in the cyclotron. The target material was dissolved in aqua regia, boiled to remove the excess nitric acid and diluted. Then selenium metal was precipitated with hydroxyamine hydrochloride similar to the method reported by the California group.[7] Three milligrams of arsenic carrier and from 60 micrograms to 400 micrograms of selenium carrier were used depending on the type of spectrometer source desired. The decay of the separated selenium activity was monitored and the

* Now at the Los Alamos Scientific Laboratory, Los Alamos, New Mexico.

† This work was assisted by a grant from the Frederick Gardner Cottrell Fund of the Research Corporation and by the joint program of the ONR and AEC.

[1] Coward, Pool, McCown, and Woodward, Phys. Rev. **73**, 1454 and **73**, 1223(A) (1948).

[2] H. H. Hopkins, Jr., Phys. Rev. **77**, 717 (1950).

[3] H. H. Hopkins, Jr., and B. B. Cunningham, Phys. Rev. **73**, 1406 (1948).

[4] J. A. Bruner and F. R. Scott, Rev. Sci. Instr. **21**, 545 (1950).

[5] Langer, Motz, and Price, Jr., Phys. Rev. **77**, 798 (1950).

[6] L. M. Langer and R. D. Moffat, Phys. Rev. **80**, 651 (1950).

[7] W. Wayne Meinke, *Chemical Procedures used in Bombardment Work at Berkeley*, AECD-2738 (1949), p. 93.

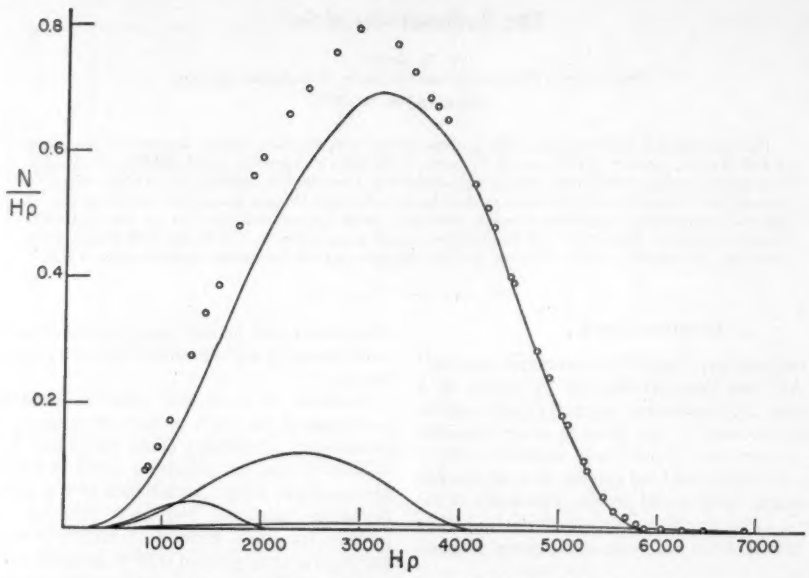

FIG. 1. Momentum distribution of the positrons of Se^{73}.

half-life was found to be 425 minutes. This period was also obtained in the spectrometer by means of repeated runs over all parts of the spectrum.

Two types of positron sources were used. A thin chemically deposited source was made by dissolving the precipitated selenium in one drop of concentrated nitric acid, evaporating almost to dryness, and placing the remaining liquid on an insulin treated zapon film.[8] The selenium was then uniformly precipitated as the metal by adding a drop of hydriodic acid. The two sources prepared in this way were 0.4 cm wide and 2 cm long with thicknesses of 0.2 mg/cm² and 0.4 mg/cm². These sources were used to investigate the positron distribution above 100 kev and the internally converted electrons from the 361-kev gamma-ray transition.

An extremely thin positron source was made by evaporation. The selenium activity obtained from the chemical separation of the target was dissolved in nitric acid, placed in a platinum boat, and treated with hydriodic acid to precipitate the selenium metal. After heating this boat under an infrared lamp only selenium metal remained. This platinum boat was then used as the filament of a high vacuum evaporator. A masked zapon film was placed three quarters of an inch from the filament. After evacuating and heating the filament, approximately one-eightieth of the activity was evaporated on to the 0.3-cm by 2.0-cm exposed zapon film area. Each of the two sources prepared in this way were estimated to be less than one microgram in weight. These sources were used in the investigation of the Auger electrons, the internally converted electrons of the 67.1-kev gamma-ray and the low energy positron distribution.

The photo- and Compton electron distributions of the gamma-rays were examined by placing a strong Se activity in a rectangular aluminum boat. A 23-mg/cm² uranium radiator, measuring 0.4 cm by 2.0 cm, covered the front face of this boat. The aluminum was not thick enough to stop all the positrons. This decreased the intensity of the annihilation photolines and Compton distribution.

RESULTS

The momentum distribution of the positrons of Se^{73} is shown in Fig. 1. The complex spectrum has been resolved into four groups on the basis of the Fermi plot shown in Fig. 2. All experimental points in Fig. 2 contain a screening correction to the coulomb wave functions,[9] and the low energy points were obtained with the thin evaporated sources and normalized to the high energy distribution.

When the positron distribution was first analyzed using data obtained with the chemically deposited sources, a residual positron distribution remained after three Fermi subtractions. Such an excess of positrons at low energy might arise from finite source thickness. Also, since all of the high energy groups had been treated as allowed transitions, the possibility existed

[8] L. M. Langer, Rev. Sci. Instr. **20**, 216 (1949).

[9] John R. Reitz, Phys. Rev. **77**, 10 (1950).

that the excess at low energy was caused by the forbidden shape of the 1.68-Mev positron group. To test the first hypothesis the low energy positrons were measured with an extremely thin evaporated source. No change was observed in the low energy positron distribution. To test the second hypothesis the Fermi analysis was repeated with the assumption that the 1.68-Mev group has an "*a*" shape.[10,11] This refinement made no difference in the resulting end-point energies and the relative intensity values given in Table I.

The distribution of the Compton and photoelectrons ejected from the uranium radiator is shown in Fig. 3. The experimental points below 200 kev were obtained with a zapon window counter and were normalized with the high energy distribution. *K* and *L* photolines can be seen which correspond to the 361-kev gamma-ray, the 511-kev annihilation radiation, and the 860-kev gamma-ray. In addition a weak Compton distribution can be seen corresponding to the 1.31-Mev gamma-ray. At low energies the three photopeaks correspond to the $L_{I,II}$, the L_{III}, and the *M* photolines of uranium resulting from the ejection of the corresponding electrons by a 67.1-kev gamma-ray.

The relative intensities of the four gamma-rays were estimated by comparing relative areas of the photolines and using Gray's formula for the variation of photoelectric cross section with energy. The intensity of the 67.1-kev gamma-ray was approximated by comparing the observed *L* lines with the *L* line of the 361-kev gamma-ray transition. The intensity of the 860-kev gamma-ray was compared to that of the 361-kev transition by means of the *K* lines and 1.31-Mev gamma-ray intensity was estimated from the Compton distribution. The energies and relative intensities of these gamma-rays are indicated in Table I.

Internal conversion electrons were found corresponding to the 67.1-kev and the 361-kev gamma-ray transitions. Figure 4 shows the *K* and *L* internally converted electrons from the 67.1-kev gamma-ray obtained from an evaporated source and using the zapon side window counter. The intensity of this source was normalized to that of the positron distribution up to 250 kev with the zapon side-window counter and then these measurements were overlapped with data using the mica end-window counter as the detector. A comparison of the two conversion lines of the 67.1-kev gamma-ray gives a K/L ratio of 7.6 and the area of the *K* line is 25.7 percent of the 1.318-Mev positron distribution.

Because of the low energy of the 67.1-kev gamma-ray, it is possible to measure the K–L energy difference between the conversion electrons accurately enough to establish the element in which the conversions occur. The measured K–L energy difference in selenium is 11.07 kev, in arsenic 10.48 kev, and in germanium 9.70 kev, as calculated from Compton and Allison.[12] The measured energy difference of the peaks of the two lines in Fig. 4 is 11.04 kev, indicating that the 67.1-kev gamma-ray transition occurs in Se^{73}.

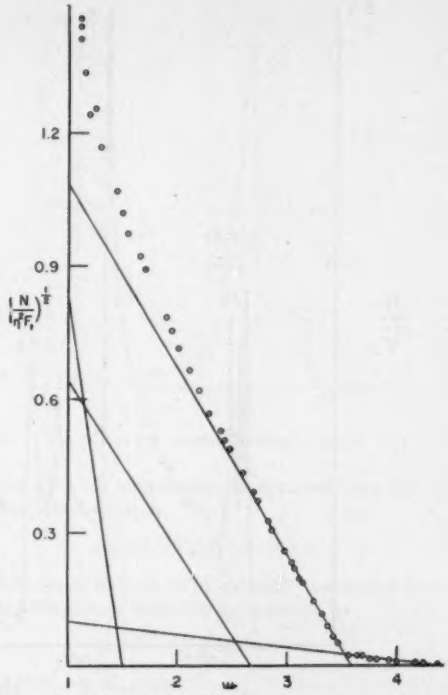

FIG. 2. Fermi plot of the positron spectrum of Se^{73}.

TABLE I. Beta- and gamma-rays of Se^{73}.

Transition	Energy in kev	Intensity (percent)
Positron 1	250	1.3
2	750	11.8
3	1318	100
4	1680	1.4
Gamma 1	67.1	9.7 (from photolines)
2	361	163
4	860	11.3 (from photolines)
5	1310	8 (from Compton electrons)
Int. conv. of gamma 1		
K	54.45	25.7
L	65.45	3.4
Int. conv. of gamma 2		
K	350.5	1.9
L	360	0.22
K-Auger electrons		
$K-2L$	9.07	38.5
$K-L-M$	10.2	

[10] E. J. Konopinski, Revs. Modern Phys. **15**, 209 (1943).
[11] L. M. Langer and H. C. Price, Phys. Rev. **76**, 641 (1949).
[12] A. Compton and S. Allison, *X-Rays in Theory and Experiment* (D. Van Nostrand Company, Inc., New York, 1935), p. 784.

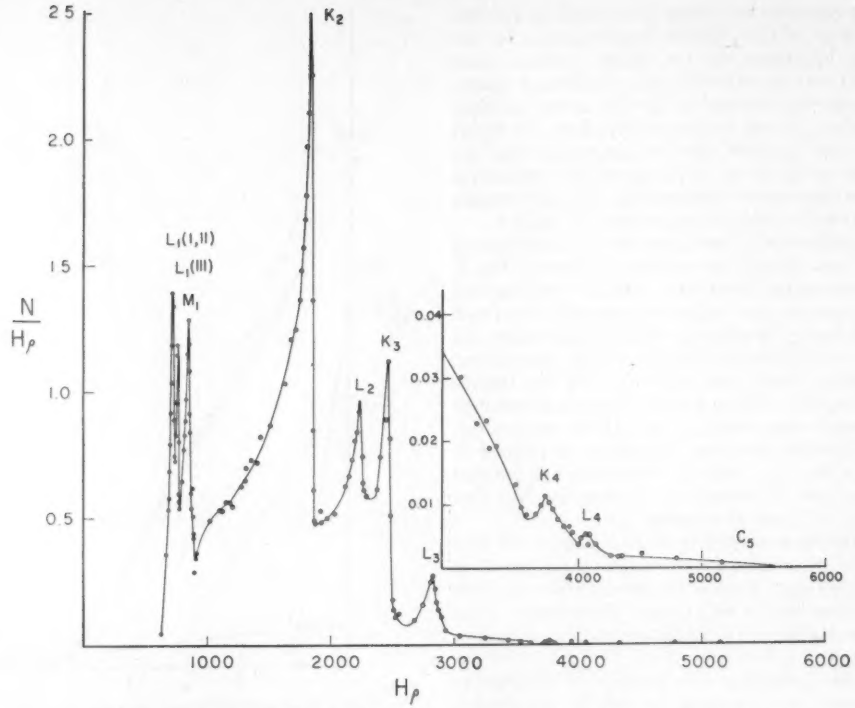

FIG. 3. Compton and photoelectrons ejected from an uranium radiator by the gamma-rays of Se^{73}.

The internally converted electrons from the 361-kev gamma-ray transition are shown in Fig. 5. These lines were obtained with the chemically deposited sources and have been normalized with the positron distribution. The K/L ratio of the areas of the two partially separated lines is 8.6, and the total area of the two lines is 2.14 percent of the 1.318-Mev positron distribution.

Figure 6 shows the K-Auger electron distribution as obtained from an evaporated source and using a zapon side-window counter. The peaks at 9.07 kev and 10.2 kev correspond to the K–$2L$ and K–L–M energies in arsenic. This is in good agreement with the values of 9.09 kev and 10.34 kev as calculated from Compton and Allison.[12] The intensity of the K-Auger electrons is 38.5 percent of the 1.318-Mev positron intensity.

The measured energies and relative intensities of the internal conversion and K-Auger electrons are given in Table I.

DISCUSSION OF RESULTS

The decay scheme of Fig. 7 is proposed for Se^{73} after the following considerations.

All the gamma-rays and all parts of the positron spectrum decay with a half-life of 425 minutes. This indicates that all of these transitions belong to the same decay. (The half-life of the ground state of Se^{73} is presumed to be very short.)

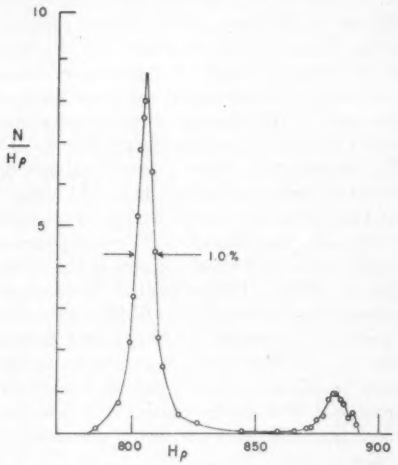

FIG. 4. Internal conversion electrons of the 67.1-kev gamma-ray of Se^{73}.

The end-point energies of 1.68 Mev and 1.318 Mev, and the relative intensities of 1.4 percent and 100 percent give ln *ft* values of 7.1 for the 1.68-Mev positron group and 5.6 for the 1.318-Mev positron group. This indicates that the high energy positron transition is once-forbidden while the intense 1.318-Mev positron transition is allowed.

The energy of the 361-kev gamma-ray equals the difference between the end-point energies of the two high energy positron groups. The K/L ratio of 8.6 for the internal conversion electrons of this gamma-ray suggests that the 361-kev gamma-ray is magnetic quadrupole radiation.[13] This would conform to a spin change of two and no parity change. This type of radiation is compatible with the forbiddenness of the two positron transitions.

The $K+L$ internal conversion coefficient for a 361-kev magnetic quadrupole gamma-ray is 0.0132 as calculated from an extrapolation[14] to $Z=33$ in Rose's tables.[15] This predicts a total relative population of 163 percent for the final state of the 1.318-Mev positron transition. This is compared with 100 percent for the positron intensity to this same level. The excess of 63 percent arises from K-capture to this level and from feeding by a 0.500 Mev cross-over gamma-ray (indicated by dotted lines in Fig. 7). The photolines of this gamma-ray are masked by that of the annihilation radiation.

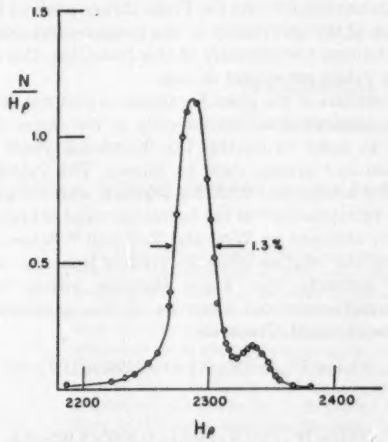

FIG. 5. Internal conversion electrons of the 361-kev gamma-ray of Se^{73}.

The intensity of the 67.1-kev gamma-ray can be estimated in the following way. The calculated ratio of the relative intensity of the 361-kev gamma-ray to that of the 67.1-kev gamma-ray, as obtained from the L photoelectron areas, is

$$N_\gamma(361)/N_\gamma(67.1)=100/6.$$

The observed ratio of the K internally converted electrons arising from these two gamma-rays is,

$$N_K(67.1)/N_K(361)=13/1.$$

Since $\beta_K=N_K/N_\gamma$, then

$$\beta_K(67.1)=\beta_K(361)\frac{N_\gamma(361)N_K(67.1)}{N_\gamma(67.1)N_K(361)},$$

and $\beta_K(67.1)$ is approximately three. Using this measured K-internal conversion coefficient, the population of the final state of the 67.1-kev gamma-ray is 37.6 percent of the 1.318-Mev positron transition. This

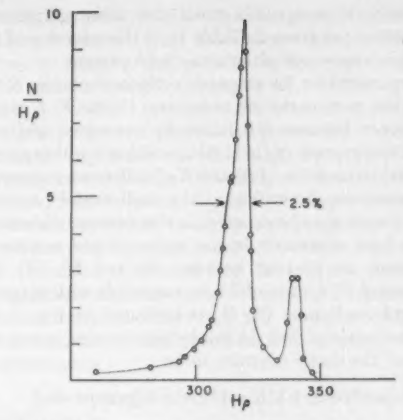

FIG. 6. K-Auger electron distribution of Se^{73}.

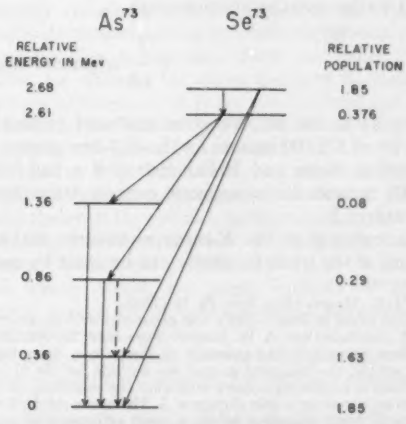

FIG. 7. Disintegration scheme for the Se^{73}—As^{73} decay.

[13] N. Tralli and I. S. Lowen, Phys. Rev. **76**, 1951 (1949).
[14] E. Segre and A. C. Helmholtz, Revs. Modern Phys. **21**, 271 (1949).
[15] Rose *et al.*, unpublished data.

intensity is compatible with the other gamma-ray intensities (as given in Table I), if the intensity of the 500-kev cross-over gamma-ray is 18 percent.

Arguments for the magnetic octipole character of the 67.1-kev gamma-ray are as follows: (1) the K–L energy difference between the internally converted electrons from this gamma-ray is 11.04 kev which is within experimental error of the 11.07 kev K–L difference measured[12] for selenium. According to the shell model[13] a metastable state may be expected in this isotope, since many have been observed[14] in the region of odd number of neutrons or protons between 38 and 50. (2) The measured K/L ratio of 7.6 is compatible with magnetic octipole radiation. (3) If, as indicated in Fig. 7, the excited state of Se^{73} decays by four modes, one would expect the decay constant to be

$$\lambda=\lambda(\text{positrons})+\lambda(K\text{-capture})+\lambda(\text{gamma-ray})+\lambda(\text{int. conv.}),$$

and if the ratio

$$\frac{N(\text{beta-decay})}{N(\text{gamma-decay})}=\frac{\lambda(\text{positrons})+\lambda(K\text{-capture})}{\lambda(\text{gamma-ray})+\lambda(\text{int. conv.})}$$

can be measured then an estimate of the mean life of the gamma-transition can be made because λ is experimentally measured. This ratio of beta-decay to gamma-decay can be obtained from the relative intensities of the 361-kev gamma-ray (excluding the 18 percent arising from the 500-kev cross-over gamma-ray) and the 67.1-kev gamma-ray. This ratio of $1.47/0.376=3.9$ closely approximates the ratio of beta-to gamma-ray intensities decaying from the excited state of selenium. Putting the decay constant λ in terms of the half-life and including the experimental ratio of beta- to gamma-decay, the half-life of the excited state of Se^{73} becomes:

$$t_{\frac{1}{2}}=\frac{1}{4.9}\cdot\frac{\ln 2}{\lambda(\text{int. conv.})+\lambda(\text{gamma-ray})}=\frac{1}{4.9}\cdot t_{\frac{1}{2}}(\text{gamma-decay}).$$

Since $t_{\frac{1}{2}}=25{,}500$ sec this gives measured gamma-ray half-life of 125,000 seconds for the 67.1-kev gamma-ray transition. Segre and Helmholtz[14] give a half-life of 50,000 seconds for a magnetic octipole transition of this energy.‡

An estimate of the K-capture—positron ratios to several of the levels in arsenic can be made by means of the relative intensities of the positron groups and the gamma-rays as given in Table I. The intensity of the 361-kev gamma-ray fed by the 1.318-Mev beta-decay is 145 percent while the intensity of the associated positron group is 100 percent. This indicated an excess of 45 percent to be accounted for by K-capture and thus gives a K-capture—positron ratio of 0.45 for the 1.318-Mev transition. This ratio compares favorably with 0.42 as predicted by the Fermi theory.[17] The sum of the intensities of the 0.860-Mev gamma-ray and the 0.500-Mev cross-over gamma-ray is in excess of the 0.750-Mev positron intensity by 18 percent of the 1.318-Mev positron intensity. Since the 0.750-Mev positron intensity is 11.8 percent of the 1.318-Mev positron intensity, this gives a K-capture—positron ratio of 1.6 for the 0.750-Mev positron transition. Theoretically, this ratio should be 2.5. In the case of the 250-kev positron transition, the estimated K-capture to positron ratio is 6, but the Fermi theory predicts 100. Because of the uncertainty in the measurement arising from the very low intensity of this transition, this discrepancy does not appear serious.

An estimate of the gross K-capture to positron decay can be obtained from the intensity of the Auger electrons. In order to do this the fluorescent yields for selenium and arsenic must be known. The values of 0.591 for arsenic and 0.620 for selenium were obtained by a Z extrapolation[18] of the fluorescent yield of krypton recently obtained by West and Rothwell.[19] Before calculating the relative gross K-captures from the total Auger intensity, the Auger electrons arising from K-internally-converted electrons of the gamma-rays must be obtained. These are

$$N_A(67.1)=W_A(\text{Se})N_K(67.1)=0.380\times 25.7=9.8$$

plus

$$N_A(361)=W_A(\text{As})N_K(361)=0.409\times 1.92=0.8,$$

where N_A is the relative number of Auger electrons arising from the K-conversion of the indicated gamma-ray, W_A is the K-Auger electron yield (one minus the K-fluorescent yield), and N_K is the relative intensity of the K-internal-conversion electrons.

When these Auger electrons are subtracted from the total Auger intensity, the remainder $N_A=0.279$ is due only to K-capture.

If this is divided by the K-Auger electron yield in arsenic the result of 63.2 percent is equal to the total relative number of K-captures as compared with the 1.318-Mev positron intensity. In terms of the total positron intensity the gross K-capture—positron ratio is 0.59.

[13] M. G. Mayer, Phys. Rev. **78**, 16 (1950).

‡ *Note added in proof:*—Since this paper was written, an article by M. Goldhaber and A. W. Sunyar (Phys. Rev. **83**, 906 (1951)) has been brought to the attention of the author. According to their article, the measured gamma-ray half-life for the 67.1-kev transition is in good agreement with what one would expect for a transition involving a spin change of 3. The measured K/L ratio for the 67.1-kev transition is not in good agreement with their values for either magnetic or electric octipole radiation.

[17] E. Feenberg and G. Trigg, Revs. Modern. Phys. **22**, 399 (1950).

[18] H. S. W. Massey and E. H. S. Burhop, Proc. Roy. Soc. (London) **A153**, 661 (1936).

[19] D. West and P. Rothwell, Phil. Mag. **41**, 873 (1950).

CONCLUSIONS

The decay of Se^{73} is complex. With the help of the Fermi theory the positron distribution has been resolved into four groups with end-point energies and relative intensities as given in Table I. Four gamma-rays have been observed. Their energies and relative intensities are given in Table I. The 67.1-kev gamma-ray has been found to be a magnetic octipole transition in the parent selenium. The 361-kev gamma-ray follows the 1.318-Mev positron group and is magnetic quadrupole radiation. The other gamma-rays and positron groups have energies and intensities compatible with the decay scheme proposed in Fig. 7.

Estimates of K-capture—positron branching ratios have been made for several of the positron transitions. For the intense 1.318-Mev positron group this ratio is 0.45 as compared to the theoretical value of 0.42. The measured ratio for the weak 0.750-Mev positron group is 1.6 and the theoretical value is 2.5, and for the very weak 0.250-Mev positron transition the measured K-capture—positron ratio is estimated as 6 and the corresponding theoretical value is 100. From the relative intensity of the K-auger electrons, a value of 0.59 was obtained from the gross ratio of K-capture to positrons.

The author wishes to express his gratitude to Professor Lawrence M. Langer for his valuable advice and encouragement. He would also like to thank Professor M. B. Sampson and the cyclotron crew for the numerous bombardments necessary for this work and Mr. E. Plassmann for his assistance in making some of the measurements.

PHYSICAL REVIEW VOLUME 84, NUMBER 4 NOVEMBER 15, 1951

A Canonical Field Theory with Spinors*

JACK HELLER,† *Polytechnic Institute of Brooklyn, Brooklyn, New York*

AND

PETER G. BERGMANN, *Polytechnic Institute of Brooklyn, Brooklyn, New York, and Syracuse University, Syracuse, New York*

(Received August 3, 1951)

In this paper, we have constructed a general field theory in covariant form which incorporates the usual covariant generalization of Dirac matrices. The field equations are derived from a lagrangian that is a second-order differential covariant (a scalar density of weight 1) constructed in the covariant spinor formalism by the same method that in riemannian geometry leads to the curvature tensor. It is possible to show that, in spite of the apparently greater wealth of geometrical elements, this theory is completely equivalent to the general theory of relativity. The field equations satisfy the usual differential identities and, in addition, "spin" identities'; there are four "strong" conservation laws which can be used to obtain equations of motion for singularities. Since we do not known at present whether the equivalence with the theory of relativity may not be lost in the process of quantization, we consider eventual quantization desirable and have, in this paper, converted the theory into the canonical form.

INTRODUCTION

IN a series of papers, Bergmann and co-workers[1–3] developed the theory of canonization of covariant field theories, in the hope that some of the difficulties in quantum field physics might be overcome by the adoption of the "best" classical (nonquantized) field theory and its subsequent quantization.

The question now arises which theory is to be considered the "best" one. We could consider Einstein's theory of gravitation (with the electromagnetic field included). In that theory the laws of physics are generally covariant, i.e., unchanged by all types of coordinate transformations for which the jacobian of the transformation is non-zero. There are other possibilities, for example, the recent theory of Einstein,[4] in which he attempts to unify the gravitational and electromagnetic fields. This theory also assumes the basic laws of physics to be generally covariant.

There are, however, indications that the basic laws of physics contain spinors as well as tensors. In the Dirac theory of the electron, anticommuting quantities arise with transformation laws different from those of tensors. The success of Dirac's theory of the electron and, among others, the ample evidence of atomic spectra, furnish strong indications that the basic laws of physics contain spinors.

In this paper we shall develop a classical field theory which is generally covariant and contains spinors. We

---

* This paper incorporates the results of the Ph.D. dissertation of the first author, accepted by the Graduate School, Polytechnic Institute of Brooklyn.

† Now at the Institute for Theoretical Physics, University of Manchester, Manchester, England.

[1] P. G. Bergmann, Phys. Rev. 75, 680 (1949).

[2] P. G. Bergmann and J. H. M. Brunings, Revs. Modern Phys. 21, 480 (1949).

[3] Bergmann, Penfield, Schiller, and Zatzkis, Phys. Rev. 80, 81 (1950).

[4] A. Einstein, *The Meaning of Relativity* (Princeton University Press, Princeton, New Jersey, 1950), third edition.

shall follow the spin algebra and analysis developed by Schrödinger,[5] Bargmann,[6] van der Waerden and Infeld,[7] Schouten,[8] Pauli,[9] and others, and then develop a lagrangian from the spin quantities. This lagrangian is constructed from a spin tensor discovered by Schrödinger.[6] Because of its relation to the Riemann-Christoffel curvature tensor, the spin lagrangian and the lagrangian of the general theory of relativity turn out to be proportional. Even though the spin vectors satisfy algebraic conditions which must be introduced into the lagrangian with undetermined multipliers, the field equations in spin form are equivalent to the field equations of the general theory of relativity. The identities due to the coordinate covariance are the same as those obtained from the general theory of relativity (the Bianchi identities). Besides, in the spin theory there is another set of identities which reflects the spin covariance. Finally, as a preliminary to quantization, we cast the theory into the canonical form.[2]

1. SPIN ALGEBRA AND ANALYSIS

We shall first summarize those results of the spin algebra and analysis necessary for our needs. Inasmuch as the spinors of Dirac and the other early workers were introduced as a half-odd representation of the lorentz group, a representation that has no analog among the representations of the full linear or even the unimodular group, we cannot expect to develop a general covariant spin algebra without sacrificing some of the formal beauty of Dirac's original theory. The loss, it turns out, consists of the complete separation of the spin transformation group from the coordinate transformation group. We write the transformation law of a spin vector γ^μ (the Dirac matrices)

$$\gamma^{\mu'}=(\partial x^{\mu'}/\partial x^\rho)S\gamma^\rho S^{-1}, \tag{1.1}$$

suppressing all spin indices. The spin transformation matrix S is invariant with respect to coordinate transformations and is composed of arbitrary scalar functions of the coordinates. We take as the fundamental relation between the covariant and contravariant spin vectors the anticommutation relation

$$\gamma_\mu\gamma^\nu+\gamma^\nu\gamma_\mu=2\delta_\mu{}^\nu E, \tag{1.2}$$

where E is the four-rowed unit matrix and γ_μ and γ^μ are two sets of four matrices each. In reliance on the "correspondence principle" with the lorentzian case, we shall also assume that each set by itself, together with all its products, forms the base of an algebra. Now we can prove, with the help of Eq. (1.2) alone, that the anticommutators of the covariant γ's as well as the anticommutators of the contravariant γ's are "c" numbers. We have

$$(\gamma_\mu\gamma_\nu+\gamma_\nu\gamma_\mu)\gamma^\rho-\gamma^\rho(\gamma_\mu\gamma_\nu+\gamma_\nu\gamma_\mu)=0, \tag{1.3}$$

i.e., the covariant anticommutators commute with every γ^ρ. Naturally, if we reverse the role of subscripts and superscripts, nothing is changed, and our assertion above is proved. We shall call one-half of each anticommutator $g_{\mu\nu}E$ and $g^{\mu\nu}E$, respectively, for example,

$$2g_{\mu\nu}E=\gamma_\mu\gamma_\nu+\gamma_\nu\gamma_\mu. \tag{1.4}$$

We need to make one further assumption in order to be able to derive all of the usual relationships, and that is

$$\gamma^\rho\gamma_\rho=4E.$$

Then, very simple calculations (not reproduced here) are needed to show that

$$g_{\mu\rho}g^{\rho\nu}=\delta_\mu{}^\nu$$

and

$$\gamma^\nu=g^{\nu\rho}\gamma_\rho, \quad \gamma_\nu=g_{\nu\rho}\gamma^\rho.$$

Since the spin vectors form a linear algebra, we can represent them as matrices. The irreducible representation is four-rowed. Schouten has shown[8] that the matrix $\gamma^1\gamma^2\gamma^3\gamma^4$, which with respect to coordinate transformations is a scalar density of weight $+1$, has as eigenvalues $i(-g)^{\frac{1}{2}}$, $-i(-g)^{\frac{1}{2}}$, and we shall, therefore, introduce a "special" spin frame in which

$$\gamma^1\gamma^2\gamma^3\gamma^4=i(-g)^{\frac{1}{2}}\mu,$$

with

$$\mu=\begin{pmatrix} I, & 0 \\ 0, & -I \end{pmatrix}, \qquad I=\begin{pmatrix} 1 & 0 \\ 0 & 1 \end{pmatrix} \tag{1.5}$$

(I stands for the two-rowed unit matrix).

In any four-rowed representation, the spin vectors, their distinct products two at a time, three at a time, four at a time, and the unit matrix form a complete base, i.e., any four-rowed matrix can be represented as a linear combination of these 16 matrices. In the "special" representation, they take the form

$$\gamma^\mu=\begin{pmatrix} 0, & \beta^\mu \\ \bar\beta^\mu, & 0 \end{pmatrix}, \tag{1.6}$$

where the β^μ and $\bar\beta^\mu$ are 2×2 matrices. From now on, we shall restrict the spin transformation matrices S to a form that will maintain the validity of Eqs. (1.5) and (1.6). The spin transformations that do this are

$$S=\begin{pmatrix} u & 0 \\ 0 & v \end{pmatrix}, \tag{1.7}$$

where u and v are arbitrary 2×2 matrices. We can restrict the spin transformations further by noting that in the Lorentz case the spin vectors are "self-adjoint." We define self-adjointness in the following way:[5] for a four-rowed matrix A its "adjoint" shall be

$$A^a=\eta A^\dagger\eta, \tag{1.8}$$

[5] E. Schrödinger, Berl. Ber. 105 (1932).
[6] V. Bargmann, Preuss, Akad. Wiss. Berlin, Ber. **25**, 346 (1932).
[7] L. Infeld and B. L. van der Waerden, Preuss. Akad. Wiss. Berlin, Ber. **9**, 380 (1933).
[8] J. A. Schouten, J. Phys. Math., 331 (1933).
[9] W. Pauli, Ann. Physik **18**, 337 (1933).

where

$$\eta=\begin{pmatrix}0 & I\\ I & 0\end{pmatrix}$$

and the dagger † denotes the hermitian adjoint. If $A^a=A$, we call A self-adjoint. From Eqs. (1.6) and (1.8) we find that

$$\beta^{a\dagger}=\beta^a, \quad \bar{\beta}^{a\dagger}=\bar{\beta}^a. \tag{1.9}$$

Since the self-adjointness of γ^μ must hold in all spin systems, we find from Eq. (1.8), subjecting the spin vectors to a spin transformation, that

$$\begin{aligned}S\gamma^\mu S^{-1}&=\eta(S\gamma^\mu S^{-1})^\dagger\eta\\ &=\eta S^{\dagger-1}\gamma^{\mu\dagger}S^\dagger\eta\\ &=\eta S^{\dagger-1}\eta\gamma^\mu\eta S^\dagger\eta.\end{aligned}$$

Thus, we must have

$$S=\eta S^{\dagger-1}\eta.$$

This can be true only if

$$S=\begin{pmatrix}s & 0\\ 0 & s^{\dagger-1}\end{pmatrix}, \tag{1.10}$$

where s is an arbitrary 2×2 matrix composed of complex scalar functions of the coordinates.

All the interesting matrices arising in the spin theory are composed either of 2×2 matrices along the diagonal or of 2×2 matrices off the diagonal.

To develop spinor analysis, we define the covariant derivative of a spin quantity in analogy to the covariant derivative of a tensor in differential geometry. If χ^Γ is a quantity with one spin index, its covariant derivative is

$$\chi^\Gamma{}_{;\tau}=\chi^\Gamma{}_{,\tau}+\Gamma_{\Sigma\tau}{}^\Gamma\chi^\Sigma$$

(all capital Greek indices are spin indices), or in matrix form

$$\chi_{;\tau}=\chi_{,\tau}+\Gamma_\tau\chi.$$

We refer to Γ_τ as the spin connection coefficients. The spin vector γ^a has two spin indices and one coordinate index. Its covariant derivative is

$$\gamma^a{}_{;\tau}=\gamma^a{}_{,\tau}+\Gamma_{\mu\tau}{}^a\gamma^\mu+\Gamma_\tau\gamma^a-\gamma^a\Gamma_\tau. \tag{1.11}$$

Pauli[9] has shown that solutions of the spin connections Γ_τ exist irrespective of the choice of affine connections $\Gamma_{\mu\tau}{}^a$. Assuming the affine connections to be symmetric in their lower indices, we find with the help of Eq. (1.4) that they are the Christoffel symbols of the second kind. We can solve for the spin connections Γ_τ, but for our present purpose these explicit expressions will not be needed. However, since the spin connection appears as a commutator in its determining Eq. (1.11), we can add to its solution, say Λ_τ, a "c" number vector $i\phi_\tau E$,

$$\Gamma_\tau=\Lambda_\tau+i\phi_\tau E. \tag{1.12}$$

Because the covariant derivative of a spin vector is spin- as well as coordinate-covariant, we find that the spin connections must satisfy a transformation law of the form

$$\Gamma_\tau'=(\partial x^\rho/\partial x^\tau)'(S\Gamma_\rho S^{-1}-S_{,\rho}S^{-1}). \tag{1.13}$$

Thus we see that Γ_τ transforms as a vector but not as a spinor.

To complete that portion of the analysis that interests us, we form with Schrödinger a spin tensor by considering the alternator of the second covariant derivative of a spin vector. We find

$$\gamma^a{}_{;\mu\nu}-\gamma^a{}_{;\nu\mu}=R_{\mu\nu\lambda}{}^\alpha\gamma^\lambda+\Phi_{\mu\nu}\gamma^a-\gamma^a\Phi_{\mu\nu}=0. \tag{1.14}$$

$R_{\mu\nu\lambda}{}^\alpha$ is the Riemann-Christoffel curvature tensor, and

$$\Phi_{\mu\nu}=\Gamma_{\mu,\nu}-\Gamma_{\nu,\mu}-\Gamma_\mu\Gamma_\nu+\Gamma_\nu\Gamma_\mu \tag{1.15}$$

is a spin tensor, i.e.,

$$\Phi_{\mu\nu}{}'=\frac{\partial x^\rho}{\partial x^{\mu'}}\frac{\partial x^\sigma}{\partial x^{\nu'}}S\Phi_{\rho\sigma}S^{-1}.$$

This spin tensor is of the second differential order in the γ^a.

2. LAGRANGIAN, FIELD EQUATIONS, AND IDENTITIES

We shall construct the field equations from a four-dimensional variational principle, where we choose as the lagrangian a linear combination of second-order scalar densities constructed from quantities that arise in the spin algebra and analysis. The resulting field equations, we shall show, are the same as those of the general theory of gravitation. Finally, we shall determine the differential identities which exist because of the coordinate and spin transformations.

The following building blocks are available for the construction of scalar densities of weight one of the second differential order: a scalar density of weight one

$$4(-g)^{\frac{1}{2}}=i\ \mathrm{tr}\{\mu\gamma^1\gamma^2\gamma^3\gamma^4\}, \tag{2.1}$$

the spin tensor $\Phi_{\mu\nu}$ (1.15), and the spin vector γ^a. From the spin tensor and spin vectors we can form the two second-order scalar matrices

$$(\gamma^\mu\gamma^\nu-\gamma^\nu\gamma^\mu)\Phi_{\mu\nu}, \quad \gamma^\mu\Phi_{\mu\nu}\gamma^\nu. \tag{2.2}$$

Taking the trace of either expression (2.2) (i.e., contracting on the spin indices) and multiplying by the scalar density (2.1), we obtain to within a numerical factor the scalar density

$$L_{(s)}=(-g)^{\frac{1}{2}}\ \mathrm{tr}\{\gamma^\mu\Phi_{\mu\nu}\gamma^\nu\}, \tag{2.3}$$

which we shall adopt as the spin lagrangian. It is possible to show that with the elements available, $L_{(s)}$ is the only scalar density of second differential order in existence. The proof will not be presented here, though. The arbitrary vector that can be added to the spin connection [see Eq. (1.12)] gives no contribution to the scalar density (2.3). In order to introduce the electromagnetic field, we must assume an electromagnetic

four vector ϕ_μ and construct a term to be added to the spin lagrangian. This term is

$$L_{(\mathrm{em})}=(-g)^{\frac{1}{2}}g^{\mu\alpha}g^{\nu\beta}(\phi_{\mu,\nu}-\phi_{\nu,\mu})(\phi_{\alpha,\beta}-\phi_{\beta,\alpha}). \quad (2.4)$$

Its treatment in what follows is the usual one and will be omitted.[10]

We shall now relate the spin lagrangian to the general theory of gravitation. By pre- and post-multiplying Eq. (1.14) by γ^μ, contracting on α and μ, adding, taking the trace, and finally multiplying through by $(-g)^{\frac{1}{2}}$, we find that

$$L_{(\mathrm{s})}=2(-g)^{\frac{1}{2}}R \quad \text{or} \quad L_{(\mathrm{s})}=2L_{(\mathrm{m})}, \quad (2.5)$$

where R is the riemann scalar curvature. Both the metric and the spin lagrangian contain second derivatives of the field variables only linearly. These terms can be converted into complete divergences, plus terms quadratic in the first derivatives of the field variables. The divergences do not contribute to the field equations, and the lagrangians in either metric or spin form may be considered as depending on the field variables and their first derivatives only. This consideration will be used to simplify the later computations.

Since $L_{(\mathrm{m})}=(-g)^{\frac{1}{2}}R$ is the lagrangian of the general theory of gravitation, the spin lagrangian (2.3) would obviously yield the same field equations were it not for the restrictions (1.3) and (1.4) on the variations of the spin vectors. These conditions can be taken into account in the hamiltonian principle by the method of undetermined multipliers.

The variational principle is, therefore,

$$\delta\int[L_{(\mathrm{s})}+\mathrm{tr}\{M_\nu{}^\mu(\gamma_\mu\gamma^\nu+\gamma^\nu\gamma_\mu)+N\gamma_\mu\gamma^\mu\}]d^4x=0, \quad (2.6)$$

where the matrices $M_\nu{}^\mu$ and N are the undetermined multipliers. The first term of Eq. (2.6) can be related to the gravitational field equations after variation with respect to the field variables, the elements of the spin vectors γ^μ. Using Eq. (2.5) and the variation of Eq. (1.4), we find, apart from discarded divergences,

$$\begin{aligned}\delta L_{(\mathrm{s})}&=\delta(2(-g)^{\frac{1}{2}}R)\\&=\tfrac{1}{2}(-g)^{\frac{1}{2}}(R_{\mu\nu}-\tfrac{1}{2}g_{\mu\nu}R)\,\mathrm{tr}\{\gamma^\mu\delta\gamma^\nu+\delta\gamma^\mu\gamma^\nu\}\\&=(-g)^{\frac{1}{2}}G_{\mu\nu}\,\mathrm{tr}\{\gamma^\mu\delta\gamma^\nu\}. \quad (2.7)\end{aligned}$$

If we denote the variations of those terms in Eqs. (2.6) which contain the undetermined multipliers by the symbol $\mathrm{tr}\{U_\mu\delta\gamma^\mu\}$, then the differential equations satisfied by solutions of the variational principle are

$$G_{\mu\nu}\gamma^\nu+U_\mu=0. \quad (2.8)$$

We shall now show that the term U_μ actually vanishes and may be omitted. Consider a solution of the field equations that would result if the variations were not subject to the algebraic restrictions (1.3), (1.4). In that case, the field equations would reduce to $G_{\mu\nu}\gamma^\nu=0$. But we know that we can construct fields of γ^μ which satisfy the algebraic restrictions (1.3), (1.4) as well as these stronger equations; in other words, we find that there are true solutions of the unrestricted variational problem which, nevertheless, are consistent with the algebraic restrictions. Hence, we can assert that among the solutions of Eqs. (2.8), with the multipliers determined subsequently by standard methods, are at least some for which the additional terms U_μ vanish. From now on, those are the only solutions we shall consider. We have not ascertained whether they are the only solutions that exist.

In the general theory of relativity we have the option of introducing a cosmological term or considering the field equations to be

$$G_{\mu\nu}=0.$$

We choose the latter, for we do not consider the cosmological term of importance, at any rate in atomic phenomena. The field equations are then

$$L_\mu\equiv G_{\mu\nu}\gamma^\nu=0. \quad (2.9)$$

In the presence of matter, the field equations are not satisfied; but rather the left-hand sides of the field equations equal expressions which represent charge, current, and mass densities, momentum densities, and stress components. Nevertheless, the left-hand sides will satisfy identities because of the following consideration. If we vary an arbitrary set of functions for the field variables infinitesimally, the lagrangian will, as a result, undergo an infinitesimal transformation of the form

$$\bar{\delta}L_{(\mathrm{s})}=\mathrm{tr}\left\{\frac{\partial L_{(\mathrm{s})}}{\partial\gamma^\mu}\bar{\delta}\gamma^\mu+\frac{\partial L_{(\mathrm{s})}}{\partial\gamma^\mu{}_{,\rho}}\bar{\delta}\gamma^\mu{}_{,\rho}\right\}. \quad (2.10)$$

If, in particular, the variation of the field variables is the result of an infinitesimal coordinate-plus-spin transformation,

$$x^{\rho'}=x^\rho+\xi^\rho, \quad (2.11)$$

$$S=E+\Sigma, \quad (2.12)$$

then the integral over the lagrangian should not change at all, except possibly as the result of the variations on the surface of the domain of integration. In other words, the variation of the lagrangian itself should be a complete divergence,

$$\bar{\delta}L_{(\mathrm{s})}=Q^\rho{}_{,\rho}.$$

If we carry out this idea, we find, first, that

$$\bar{\delta}\gamma^\mu=\xi^\mu{}_{,\rho}\gamma^\rho-\gamma^\mu{}_{,\rho}\xi^\rho+\Sigma\gamma^\mu-\gamma^\mu\Sigma$$

and, therefore,

$$\begin{aligned}Q^\rho{}_{,\rho}=\mathrm{tr}\{&L_\mu(\xi^\mu{}_{,\rho}\gamma^\rho-\gamma^\mu{}_{,\rho}\xi^\rho+\Sigma\gamma^\mu-\gamma^\mu\Sigma)\}\\&+[\mathrm{tr}\{(\partial L_{(\mathrm{s})}/\partial\gamma^\mu{}_{,\sigma})\delta\gamma^\mu\}]_\sigma,\end{aligned}$$

[10] P. G. Bergmann, *Introduction to the Theory of Relativity* (Prentice-Hall, Inc., New York, 1942).

to be satisfied identically even though the generators of the infinitesimal transformations are completely arbitrary. This condition can be satisfied only if both

$$\mathrm{tr}\{L_\mu\gamma^\mu{}_{,\nu}+(L_\nu\gamma^\mu)_{,\mu}\}\equiv 0, \tag{2.13}$$

$$L_\mu\gamma^\mu-\gamma^\mu L_\mu\equiv 0. \tag{2.14}$$

These two distinct sets of identities must hold for any lagrangian that yields convariant Euler-Lagrange equations.

The first set of identities are a result of the covariance of the field equations with respect to coordinate transformations. They are the spin form of the contracted Bianchi identities. The second set of identities are the result of the covariance of the field equations with respect to the spin transformations.

Because of the identities (2.13), we can construct a quantity whose ordinary divergence is zero. This is the "strong" form of the conservation laws. If the field equations are satisfied, we have[1]

$$t_\nu{}^\rho{}_{,\rho}=0, \quad t_\nu{}^\rho=\delta_\nu{}^\rho L_{(s)}-\mathrm{tr}\{(\partial L_{(s)}/\partial\gamma^\mu{}_{,\rho})\gamma^\mu{}_{,\nu}\}, \tag{2.15}$$

which can be verified to be equal to the relativistic expressions by means of Eq. (1.4). In the presence of matter the field equations are not satisfied, but we have instead

$$L_\mu=P_\mu.$$

The divergence of Eq. (2.15) does not vanish but is equal to $\mathrm{tr}\{P_\mu\gamma^\mu{}_{,\nu}\}$. Because of the identities (2.13), we can still form 16 quantities whose ordinary divergence is zero. We have

$$T_\nu{}^\rho{}_{,\rho}\equiv 0, \quad T_\nu{}^\rho=t_\nu{}^\rho-\mathrm{tr}\{L_\nu\gamma^\rho\}. \tag{2.16}$$

3. SPIN CONSTRAINTS AND HAMILTONIAN

In this section we construct the constraints and hamiltonian in spin form. The coordinate and parameter constraints can be formed in the same manner as they are formed in the metric case.[2] However, in the present theory there is a transformation group—the spin group—which is not present in the metric case. This group gives rise, as we have seen, to a spin identity (2.14). From this identity we shall construct the spin constraint in a manner analogous to the construction of the coordinate constraints from the contracted Bianchi identities. Knowledge of all these constraints is required for the construction of the hamiltonian.[3]

To construct the spin constraint, we consider the highest derivatives of the spin vectors in the spin identity (2.14). They are

$$\left(\frac{\partial^2 L_{(s)}}{\partial\gamma^\mu{}_{,\rho}\partial\gamma_\Sigma{}^{\Gamma_\sigma}{}_{,\sigma}}\gamma^\mu-\gamma^\mu\frac{\partial^2 L_{(s)}}{\partial\gamma^\mu{}_{,\rho}\partial\gamma_\Sigma{}^{\Gamma_\sigma}{}_{,\sigma}}\right)\gamma_\Sigma{}^{\Gamma_\sigma}{}_{,\rho\sigma},$$

where the capital Greek letters again represent spin indices. These terms must vanish for they appear by themselves. After symmetrizing with respect to ρ and σ, we have

$$\frac{\partial^2 L_{(s)}}{\partial\gamma^\mu{}_{,\rho}\partial\gamma_\Sigma{}^{\Gamma_\sigma}{}_{,\sigma}}\gamma^\mu-\gamma^\mu\frac{\partial^2 L_{(s)}}{\partial\gamma^\mu{}_{,\rho}\partial\gamma_\Sigma{}^{\Gamma_\sigma}{}_{,\sigma}}+\frac{\partial^2 L_{(s)}}{\partial\gamma^\mu{}_{,\sigma}\partial\gamma_\Sigma{}^{\Gamma_\sigma}{}_{,\rho}}\gamma^\mu-\gamma^\mu\frac{\partial^2 L_{(s)}}{\partial\gamma^\mu{}_{,\sigma}\partial\gamma_\Sigma{}^{\Gamma_\sigma}{}_{,\rho}}=0. \tag{3.1}$$

The momentum densities conjugate to the spin vectors are

$$\pi_\mu=Jt_{,\rho}(\partial L_{(s)}/\partial\gamma^\mu{}_{,\rho}). \tag{3.2}$$

Multiplying Eq. (3.1) by $Jt_{,\rho}Jt_{,\sigma}$ and introducing Eq. (3.2), we obtain

$$\frac{\partial\pi_\mu}{\partial\dot\gamma_\Sigma{}^{\Gamma_\sigma}}\gamma^\mu-\gamma^\mu\frac{\partial\pi_\mu}{\partial\dot\gamma_\Sigma{}^{\Gamma_\sigma}}=0.$$

Since the γ^μ are independent of $\dot\gamma^\nu$, we have

$$\pi_\mu\gamma^\mu-\gamma^\mu\pi_\mu=K, \tag{3.3}$$

where K is independent of "dotted" quantities. In order to evaluate K, we introduce the expression for π_μ into Eq. (3.3). From Eqs. (3.2), (2.5), and the trace of Eq. (1.4), we obtain

$$\pi_\mu=Jt_{,\rho}(\partial L_{(m)}/\partial g^{\mu\beta}{}_{,\rho})\gamma^\beta. \tag{3.4}$$

Substituting this expression into Eq. (3.3), we find

$$K=Jt_{,\rho}(\partial L_{(m)}/\partial g^{\mu\beta}{}_{,\rho})(\gamma^\beta\gamma^\mu-\gamma^\mu\gamma^\beta)=0, \tag{3.5}$$

since $\partial L_{(m)}/\partial g^{\mu\beta}{}_{,\rho}$ is a "c" number symmetric in μ and β.

In a similar manner we calculate the coordinate constraint from the contracted Bianchi identities (2.13). We find

$$Jt_{,\rho}\,\mathrm{tr}\{\gamma^\rho\pi_\mu\}=K_\mu, \tag{3.6}$$

where K_μ is independent of $\dot\gamma^\nu$. From Eq. (3.4), we obtain

$$K_\mu=Jt_{,\rho}Jt_{,\sigma}(\partial L_{(m)}/\partial g^{\mu\beta})\,\mathrm{tr}\{\gamma^\beta\gamma^\sigma\}$$
$$=4Jt_{,\rho}Jt_{,\sigma}g^{\beta\sigma}(\partial L_{(m)}/\partial g^{\mu\beta}{}_{,\rho}). \tag{3.7}$$

The metric lagrangian $L_{(m)}$, given by Eq. (2.5), contains only first derivatives of field variables. Using Eq. (2.5), we finally obtain

$$K_\mu=-\frac{(-g)^{\frac{1}{2}}}{8\pi\kappa}Jt_{,\rho}Jt_{,\sigma}\left(\delta_\mu{}^\rho g^{\alpha\beta}\left\{\begin{matrix}\sigma\\ \alpha\beta\end{matrix}\right\}-\delta_\mu{}^\rho g^{\alpha\sigma}\left\{\begin{matrix}\beta\\ \alpha\beta\end{matrix}\right\}\right.$$
$$\left.-2g^{\alpha\rho}\left\{\begin{matrix}\sigma\\ \mu\alpha\end{matrix}\right\}+\delta_\mu{}^\sigma g^{\alpha\rho}\left\{\begin{matrix}\alpha\\ \alpha\beta\end{matrix}\right\}+g^{\rho\sigma}\left\{\begin{matrix}\alpha\\ \mu\alpha\end{matrix}\right\}\right).$$

In this and the following expressions, the numerical coefficients agree with those of a recent paper concerned with purely metric space.[3] The parameter constraint[2] is

$$\mathrm{tr}\{\gamma_{\mu|\nu}\pi^\mu\}+x^\rho{}_{|\nu}\lambda_\rho=0, \tag{3.8}$$

where

$$\pi^{\mu}=g^{\mu\alpha}\pi_{\alpha}$$

and

$$\lambda_{\rho}=Jl_{,\sigma}l_{\rho}^{\sigma}. \tag{3.9}$$

The electromagnetic constraint is the same as in the metric theory:[9]

$$Jl_{,\rho}\psi^{\rho}=0,$$

where

$$\psi^{\rho}=Jl_{,\sigma}\frac{\partial L_{(em)}}{\partial\phi_{\rho,\sigma}}.$$

To construct the hamiltonian constraint, we could proceed by the straightforward method developed earlier.[3] But we can save ourselves the work of repeated transformations in the symbolic vector space by simply introducing the spin vector γ^{μ} and its canonically conjugate momentum density π_{μ} into the hamiltonian of the general theory of relativity.[3,11] In view of the fact that in a parametrized theory the hamiltonian is an expression that vanishes identically, a constraint, and since the constraints are associated with the transformation group of the theory considered, we are assured that if we can discover a constraint independent of those already enumerated in this section, then that new constraint is the hamiltonian. And naturally, the hamiltonian constraint of the general theory of relativity is an expression that will continue to vanish identically if we introduce into it the spin quantities.

The metric tensor is related to the spin vector via Eq. (1.4). We shall now calculate the metric momentum density conjugate to the metric tensor in terms of the spin momentum density conjugate to the spin vectors. The spin momentum density is

$$\pi^{\rho}=Jl_{,\rho}\frac{\partial L_{(s)}}{\partial\gamma_{\mu,\rho}}=2Jl_{,\rho}\frac{\partial L_{(m)}}{\partial g_{\alpha\beta,\sigma}}\frac{\partial g_{\alpha\beta,\sigma}}{\partial\gamma_{\mu,\rho}},$$

using Eq. (2.5) and the chain rule of differentiation. Using the trace of Eq. (1.4) we obtain

$$\pi^{\rho}=Il_{,\rho}(\partial L_{(m)}/\partial g_{\alpha\beta,\rho})\gamma_{\beta}=\pi^{\alpha\beta}\gamma_{\beta}. \tag{3.10}$$

We solve for $\pi^{\alpha\beta}$ in the usual way by pre- and post-multiplying by γ^{σ}, adding, and using Eq. (1.2). Doing this, we find

$$E\pi^{\mu\rho}=\tfrac{1}{2}(\pi^{\mu}\gamma^{\rho}+\gamma^{\rho}\pi^{\mu}). \tag{3.11}$$

Multiplying Eq. (3.11) by $g_{\mu\rho}$ and using the spin constraint (3.3), we find the relation

$$Eg_{\mu\rho}\pi^{\mu\rho}=\gamma_{\mu}\pi^{\mu}=\pi^{\mu}\gamma_{\mu}, \tag{3.12}$$

useful in the construction of the hamiltonian.

It is now a straightforward computation to arrive at the spin hamiltonian. Substituting the spin quantities for their corresponding metric quantities, we find

$$\begin{aligned}H=v^{-1}v^{\rho}v^{\sigma}\{&\tfrac{1}{2}(\lambda_{\rho}Jl_{,\sigma}+\lambda_{\sigma}Jl_{,\rho})-G_{\rho\sigma}\\&+[8\pi\kappa/(-g)^{\frac{1}{2}}X](g_{\alpha\gamma}g_{\beta\delta}+g_{\alpha\delta}g_{\beta\gamma}-g_{\alpha\beta}g_{\gamma\delta})\\&\times[\tfrac{1}{4}\operatorname{tr}\{\pi^{\alpha}\gamma^{\beta}\}Jl_{,\rho}-2G^{(\alpha\beta)}{}_{\rho}]\\&\times[\tfrac{1}{4}\operatorname{tr}\{\pi^{\gamma}\gamma^{\delta}\}Jl_{,\sigma}-2G^{(\gamma\delta)}{}_{\sigma}]-[2\pi/(-g)^{\frac{1}{2}}X]\\&\times g_{\omega\tau}(\psi^{\tau}Jl_{,\rho}-2G^{\tau}{}_{\rho})(\psi^{\omega}Jl_{,\sigma}-2G^{\omega}{}_{\sigma})\}.\end{aligned} \tag{3.13}$$

In this expression, we have used all the abbreviations introduced previously.[3]

CONCLUSION

With the setting up of the hamiltonian density (3.13), we have completed the program of this paper. We have succeeded in formulating a theory covariant both with respect to coordinate and with respect to spin transformations, in which the field equations appear as the Euler-Lagrange equations of a four-dimensional variational principle. We have furthermore found the appropriate hamiltonian form of that theory. We have omitted the explicit derivation of the secondary constraints, but the general results reported in a paper by Anderson and Bergmann[12] are applicable to this theory.

We found that this theory is completely equivalent to the general theory of relativity, in spite of the apparently greater wealth of geometric objects. In actual fact, because of the additional transformation group associated with the spinors, the supply of true geometric objects has not been increased. This result is not quite as damning as it may appear at first, for two reasons. One is that subsequent quantization of the theory may lead to an inequivalence not now apparent, just as the difference between the Dirac equations and the Klein-Gordon equation is quantum theoretical, and disappears in the classical (WBK) limit. The other reason is that the theory with spinors permits the introduction of additional geometric objects, ψ-functions, that may assume physical meaning only in the second quantization. In other words, the interaction between particles and field may be such that it can be described more adequately in terms of spinors.

We intend to continue our investigation along these lines.

[11] F. A. E. Pirani, and A. Schild, Phys. Rev. **79**, 986 (1950).

[12] J. L. Anderson and P. G. Bergmann, Phys. Rev. **83**, 1018 (1951).

The High Energy Spallation Products of Copper*

ROGER E. BATZEL, DANIEL R. MILLER, AND GLENN T. SEABORG
Department of Chemistry and Radiation Laboratory, University of California, Berkeley, California
(Received July 3, 1951)

Nuclear reactions induced in elemental copper by irradiation with charged particles accelerated to energies in the hundred-Mev range have been studied, and the reaction products cover a range from the region of the target nucleus to a region which is removed from the target nucleus by as many as forty or more nucleons. The yields of the various products were measured, and the results show that a large majority of the products result from reactions in which only a fraction of the total energy of the incident particle is left with the nucleus. The distribution of the amounts of the reaction products is in agreement with a picture of high energy nuclear reactions involving nuclear transparency and the idea that the nuclear reactions involve excitation following collisions and energy transfers between the individual nucleons in the impinging particle and the individual nucleons in the target nucleus. The results include recent work on the nuclear reactions induced by 340-Mev protons and some earlier qualitative work on the nuclear reactions induced by 190-Mev deuterons and 190- and 380-Mev helium ions.

INTRODUCTION

THE acceleration of charged particles to energies in the hundreds of Mev range by the Berkeley 184-inch cyclotron has made it possible to study nuclear reactions in which the reaction products cover a range from the region of the target nucleus to a region which is removed from the target nucleus by as many as forty or more nucleons.[1] The term "spallation" has been suggested to describe this type of transformation in which the excitation of the nucleus is degraded by emission of small nuclear fragments such as neutrons, protons, deuterons, and alpha-particles.

Some of the results of spallation reactions induced with high energy deuterons and alpha-particles have been reported previously.[1–5] The present study consists of the determination of the radioactive products formed by the irradiation of elemental copper with 340-Mev protons. The data also include the results of a cursory investigation of the products formed by the irradiation of copper with 190-Mev deuterons and 190- and 380-Mev helium ions.

The observed spallation products include some 35 nuclides from sodium through zinc and the distribution of the amounts of the reaction products formed is in general agreement with the picture of high energy nuclear reactions described by Serber.[6] The observed yields show the effects of nuclear transparency and are consistent with Serber's idea that the nuclear reactions involve excitation following collisions and energy transfers between the individual nucleons in the impinging particle and the individual nucleons in the target nucleus. As would be expected on this picture, the products which are formed by reactions requiring small amounts of excitation occur most frequently.

The spallation data from the deuteron and helium ion irradiations of copper represent the results of some early qualitative work done in 1947 and 1948. At the present time this laboratory is not planning any immediate further investigations of these spallation distributions, and the data are published here for qualitative consideration only.

Preliminary results are included which show that secondary reactions are induced in copper by nuclear fragments emitted from copper nuclei excited by bombardment with 340-Mev protons. The results show conclusively that gallium isotopes, and inconclusively that germanium isotopes, are produced by the nuclear fragments.

PROCEDURE

Irradiations with the high energy particles were carried out in the circulating beam of the 184-inch frequency modulated cyclotron. The targets consisted of 6- and 10-mil copper foil about 15 mm long and 10 mm wide. The copper strips were clamped in target holders which could be attached to the movable probe head of the cyclotron, and the bombarding energies were adjusted by fixing the radial distance of the leading edge of the target strip from the origin of the beam. Since the degradation of the energy of the high energy particles in passing through the 10-mil copper foil is small, the targets could be considered as thin targets.

Because of the fluctuations in intensity of the circulating beam, the exact amount of the irradiation of the copper target could not be determined directly. The amount of the nuclide Cu^{61} formed during any given irradiation of the copper was determined and by relating the amounts of the other nuclides formed to the amount of Cu^{61} produced, relative yields of nuclides from any series of proton, deuteron, or helium ion irradiations could be compared.

The length of the irradiations varied from ten minutes to one hour depending on the half-lives of the nuclides

* This work was performed under the auspices of the AEC.
[1] Cunningham, Hopkins, Lindner, Miller, O'Connor, Perlman, Seaborg, and Thompson, Phys. Rev. 72, 739, 740(A) (1947).
[2] Miller, Thompson, and Cunningham, Phys. Rev. 74, 347 (1948).
[3] H. H. Hopkins, Jr., Phys. Rev. 77, 717 (1950).
[4] M. Lindner and I. Perlman, Phys. Rev. 78, 499 (1950).
[5] Bartell, Helmholz, Softky, and Stewart, Phys. Rev. 80, 1006 (1950).
[6] R. Serber, Phys. Rev. 72, 1114 (1947).

which were to be studied. One approximately 30-hour proton bombardment, and one approximately 15-hour deuteron bombardment were done to determine the yields of the nuclides with very long half-lives.

An absolute cross section for the formation of the Cu^{61} from copper irradiated with 340-Mev protons was determined by irradiating a piece of 10-mil copper foil in the external beam of the 184-inch cyclotron. The beam intensity was measured directly by means of a faraday cup arrangement. In the case of the deuteron irradiation, the absolute cross section for the formation of Cu^{61} was calculated using an estimated value of one microampere for the deuteron beam intensity.

After the target was irradiated, it was dissolved and measured amounts of carriers were added to the target solution. The elemental fractions were separated by the chemical separation procedures to be discussed in the section of "Chemical Separation Procedures." For the proton irradiations, the amount of carrier remaining after the chemical separation of an elemental fraction was determined by chemical analysis and the percent of the carrier recovered was taken as a measure of the percent of the radioactive atoms of the element recovered. No correction was made for losses during the chemical separations in the cases of the deuteron and helium ion irradiations, but usually duplicate experiments were performed in the case of the deuteron study, and the higher yields were given greater statistical weight in the final average value of the yields.

Counting of the activities was done on an end-window, alcohol-quenched, argon-filled Geiger counter tube with a mica window of $\sim$3-mg/cm^2 thickness used in conjunction with a scale of 64 counting circuit. The nuclides were characterized by half-life determinations, absorption measurements, and sign of particulate radiation emitted.

A crude beta-ray spectrometer was used in the determination of the sign of the beta-particles and was especially useful where it was necessary to resolve nuclides with similar half-life but differing in sign of particulate radiation emitted.

The counting data were corrected for window and air absorption, and in the cases where the yields are based on the counting of K x-rays, corrections were made for the fluorescence yields of the x-rays. Backscattering corrections were made only in the case of the determination of the absolute cross section for the formation of the Cu^{61} from the proton irradiation of the copper. The samples from the proton irradiations were mounted on thin cover glasses or 5-mil aluminum disks, and the backscattering corrections for such backings are essentially equal and constant for the energy range of the beta-particles observed. The samples from the deuteron and helium ion irradiations were mounted on stainless steel and platinum plates, and although the backscattering corrections are not equal, no correction was applied, since the correction is not too serious and the deuteron and helium ion data are presented for qualitative consideration only. No correction was made for self-absorption and self-scattering, since the weights of the samples counted were almost negligible in all instances.

RESULTS

A. Radioactive Nuclides Identified

The characteristic activities of the nuclides discussed in this section were observed in the elemental fractions separated from the irradiated copper target. References for most of the nuclides characterized may be found in the 1948 edition of "Table of Isotopes" by Seaborg and Perlman.[7] Only in the cases where information on the nuclides was published in the literature subsequent to the data given in "Table of Isotopes" will references be cited. All activities identified in the elemental fractions are discussed below and include the results from all bombardments (190-Mev deuterons, 190- and 380-Mev helium ions, and 340-Mev protons). A check of Figs. 3, 4, and 5 and the results for 190-Mev helium ions listed in part B of this section will show which individual activities were identified in each of the elemental fractions from the different bombardments.

Germanium Fraction

The activities observed in the germanium fraction from the copper irradiated with 340-Mev protons were characteristic of the light germanium isotopes. The characteristic decay periods[8] of Ge^{69} and Ge^{67} were easily resolved, and the amount of long-lived activity remaining after the shorter lived periods had decayed was comparable with that expected for the 250-day Ge^{68}. There was also a small amount of activity which showed the characteristic decay periods of Ge^{66} and its daughter Ga^{66}. Because of the limited amounts of activity formed the nuclides were characterized solely by decay periods and chemical behavior.

Gallium Fraction

The characteristic activities of Ga^{68}, Ga^{67}, and Ga^{66} were observed in the gallium fractions separated from copper irradiated with 340-Mev protons. Cross sections were estimated for the formation of these nuclides from copper. It was assumed that Ga^{68} decays entirely by positron emission, Ga^{67} decays only by orbital electron capture (the counting efficiency of the x-rays was taken as 4 percent), and Ga^{66} decays 34 percent by orbital electron capture.[9] The cross section for the formation of Ga^{68} includes any Ga^{64} formed, since resolution of the two activities was not possible.

Zinc Fraction

The characteristic activities of Zn^{65}, Zn^{63}, and Zn^{62} were observed in zinc. The Zn^{65} was counted through

[7] G. T. Seaborg and I. Perlman, Revs. Modern Phys. **20**, 585 (1948).
[8] McCown, Woodward, and Pool, Phys. Rev. **74**, 1311 (1948).
[9] L. M. Langer and R. D. Moffat, Phys. Rev. **80**, 651 (1950).

sufficient aluminum absorber to cut out completely the particulate radiation and x-rays, and the counting efficiency of the 1.1-Mev gamma-ray was taken as one percent. The Zn^{63} was characterized by its half-life and the nuclide was assumed to decay 93 percent by positron emission and 7 percent by orbital electron capture. The Zn^{62} was assumed to decay 10 percent by positron emission and 90 percent by K-capture[10] and was counted with the 10-minute Cu^{62} daughter in equilibrium.

Copper Fraction

The activities resolved in the copper were those of Cu^{64}, Cu^{62}, Cu^{61}, and Cu^{60}. The 12.8-hour Cu^{64} was the longest lived activity identified and was assumed to have a counting efficiency of 50 percent. The 10.5-minute Cu^{62} was the shortest lived activity identified, and the nuclide was considered as decaying completely by positron emission. Cu^{61} decays 66 percent by positron emission,[11] and 66 percent was taken as the counting efficiency of the nuclide. The 25-minute Cu^{60} was resolved with precision only in the copper fractions from the 190-Mev deuteron and 380-Mev helium ion irradiations.

Nickel Fraction

The only observable activities in nickel were the 2.6-hour Ni^{65} and the 36-hour Ni^{57}. The formation of the small amount of Ni^{65} from copper irradiated with protons is probably due to the reaction $Cu^{65}(n, p)Ni^{65}$ caused by secondary neutrons and will be neglected as a spallation product from 340-Mev protons. A counting efficiency of 50 percent was used for the Ni^{65} since the nuclide decays 50 percent by positron emission and 50 percent by orbital electron capture.[12]

Cobalt Fraction

The characteristic activities of Co^{61} and Co^{55} were identified in all elemental fractions of cobalt separated. The Co^{58} and Co^{56} were identified definitely in the proton irradiations and the characteristic 72-day half-life of these activities was observed in the cobalt fraction separated from the copper irradiated with 190-Mev deuterons. The Co^{61} decayed with the characteristic 1.75-hour half-life; and since it decays by negatron (negative beta-particle) emission, no correction was necessary for the counting efficiency. The Co^{55} was easily resolvable; and since no electron capture branching has been reported, the counting efficiency was taken as 100 percent.

The fact that the Co^{58} and Co^{56} decay with equal half-lives and are both positron emitters makes their resolution difficult. The resolution of the two activities was done only for the cobalt fraction separated from the copper irradiated with 340-Mev protons. The shape of the composite positron spectrum from the cobalt fraction was determined by means of a crude beta-ray spectrometer after the 18-hour Co^{56} had been allowed to decay. The shape of the positron spectrum for a sample of pure Co^{56} which had been determined under similar conditions was available, and by subtracting the contribution of the Co^{56} positron spectrum from the composite positron spectrum, the contribution of each isotope to the total activity was obtained. The counting efficiency of the Co^{58} was taken as 15 percent and that of the Co^{56} as 100 percent.

Iron Fraction

The characteristic activities of the radionuclides Fe^{59}, Fe^{55}, Fe^{53}, and Fe^{52} were probably present in all iron fractions separated from the copper irradiated with the protons, deuterons, and helium ions. All of these activities were identified definitely only in the iron fractions separated from the copper irradiated with 340-Mev protons. The Fe^{59}, Fe^{53}, and Fe^{52} were identified in the iron fractions from the copper irradiated with deuterons, and the only yield determined for the iron from 380-Mev helium ion irradiation was the Fe^{59}. The 2.9-year Fe^{55} was assumed to decay completely by orbital electron capture[13] and a counting efficiency of 10 percent was taken for the x-rays. The Fe^{53} was assumed to decay 100 percent by positron emission. The Fe^{52} was counted in equilibrium with its 21-minute Mn^{52} daughter. By determining the amount of 21-minute Mn^{52} in equilibrium with the Fe^{52} and milking the 5.8-day Mn^{52} which grows into the iron fraction, an estimation was made of the amount of positron emission and orbital electron capture branching for the Fe^{52}. It was found that the nuclide decays approximately 65 percent by positron emission and 35 percent by orbital electron capture.

Manganese Fraction

The radionuclides Mn^{56}, Mn^{54}, Mn^{52}, and Mn^{51} were identified in manganese. The Mn^{56} was assumed to decay completely by negatron emission. The Mn^{54} was counted through sufficient aluminum absorber to cut out all the particulate radiation and x-rays, and a value of 0.8 percent was assumed as the counting efficiency of the 0.8-Mev gamma-ray. Thirty-five percent was taken as the positron branching of the 5.8-day Mn^{52}, and the yield for manganese mass number 52 is reported on the basis of this activity. The Mn^{51} was assumed to decay completely by positron emission.

Chromium Fraction

The two activities identified in chromium were those of Cr^{51} and Cr^{49}. Since the Cr^{51} decays by orbital elec-

[10] R. W. Hayward, Phys. Rev. **78**, 87(A) (1950).
[11] Owen, Cook, and Owen, Phys. Rev. **78**, 686 (1950).
[12] G. Friedlander and M. L. Perlman, Brookhaven National Laboratory Report 51 (1950), unpublished.
[13] G. L. Brownell, Massachusetts Institute of Technology Progress Report 37 (1949), unpublished.

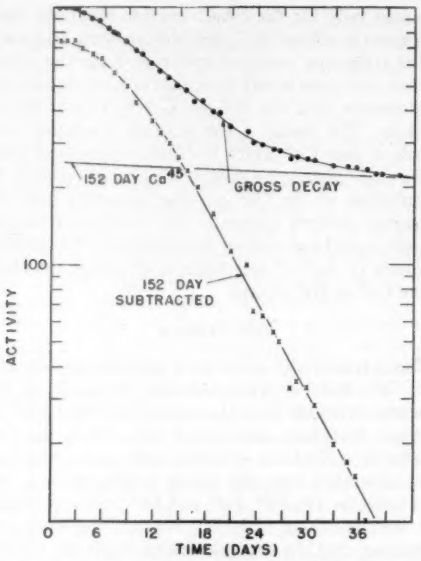

FIG. 1. Decay of calcium fraction separated from copper irradiated with 340-Mev protons.

tron capture and gamma-ray emission, the counting efficiency of this nuclide would have had to be estimated roughly, but it was possible to determine the counting efficiency directly by milking Cr^{51} from a known amount of Mn^{51} which had decayed. With the assumption that Mn^{51} decays 100 percent by positron emission, the Cr^{51} was found to have a counting efficiency of 2.6 percent when counted in a precipitate of barium chromate. The Cr^{49} was assumed to decay with no orbital electron capture branching.

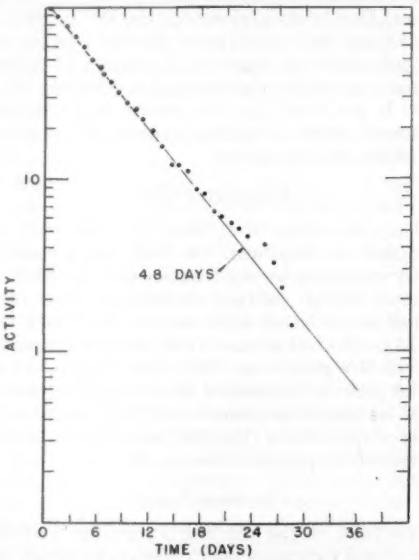

FIG. 2. Decay of calcium fraction separated from copper irradiated with 340-Mev protons counted through sufficient absorber to cut out the beta-particles of Ca^{45} and the Sc^{47} daughter.

Vanadium Fraction

The yield for vanadium is based on V^{48} which was assumed to decay 58 percent by positron emission.

Titanium Fraction

The only activity identified in titanium was that of the 3.08-hour Ti^{45} and the yield was calculated on the basis of the nuclide decaying entirely by positron emission.

Scandium Fraction

Several activities were observed in the scandium fraction separated from the copper irradiated with 340-Mev protons, and these activities were identified as belonging to Sc^{48}, Sc^{47}, Sc^{46}, Sc^{44m}, and a mixture of the 3.9-hour Sc^{44} and Sc^{43}. The 3.9-hour and 85-day activities were easily resolvable from the decay curves, but the resolution of the 2.44-day Sc^{44m}, the 3.4-day Sc^{47}, and the 44-hour Sc^{48} was more difficult. The contribution of the 2.44-day Sc^{44m}, with its 3.92-hour positron daughter in equilibrium, to the total activity was resolved approximately with the crude beta-ray spectrometer. With the positron activity resolved, the remaining activity was almost entirely that of the 3.4-day Sc^{47}, and the small amount of Sc^{48} activity resolved was so uncertain that the yield of this nuclide is not reported. The yield for Sc^{43} includes the 3.9-hour Sc^{44}, and these nuclides were assumed to decay completely by positron emission. The yield for Sc^{44} was calculated on the basis of the 2.44-day isomer.

Calcium Fraction

Only two activities were observed in the calcium fraction separated from the copper irradiated with 340-Mev protons. One was the 150-day Ca^{45} and the other was a 4.8 ± 0.2-day beta-emitter with an energy of about 1.2 Mev as determined by an aluminum absorption measurement. This activity is probably the 5.8-day calcium activity reported as Ca^{47} by Matthews and Pool.[14] The growth of a 3.4-day scandium was observed in the decay of the calcium fraction and the scandium daughter was milked from the fraction. The aluminum absorption measurement of this 3.4-day scandium daughter showed it to be the activity assigned to Sc^{47}. The decay curve of the calcium fraction is shown in Fig. 1, and Fig. 2 shows the decay of the calcium fraction counted through sufficient aluminum absorber to

[14] D. E. Matthews and M. L. Pool, Phys. Rev. **72**, 163 (1947).

cut out the beta-particles of the Ca^{45} and the Sc^{47} daughter. Thus, the decay sequence is

$$Ca^{47} \xrightarrow[4.8\ \text{days}]{\beta^-} Sc^{47} \xrightarrow[3.4\ \text{days}]{\beta^-} Ti^{47}.$$

Chlorine Fraction

The characteristic activities of Cl^{39} and Cl^{38} were identified in all the chlorine fractions separated from the irradiated copper, but Cl^{34} was identified only in the chlorine fraction separated from the copper irradiated with 340-Mev protons. The resolution of the Cl^{38} and Cl^{34} was accomplished by determining the relative amounts of positrons and negatrons present by means of the crude beta-ray spectrometer. The Cl^{39} was resolved directly from the gross decay curve. The Cl^{39}, Cl^{38}, and Cl^{34} were assumed to have counting efficiencies of 100 percent.

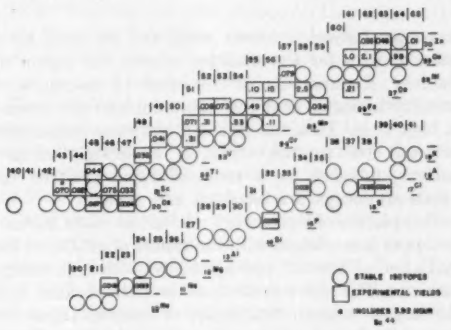

FIG. 3. Experimental yields from copper irradiated with 340-Mev protons. Yields are relative to Cu^{61}.

Phosphorus Fraction

The only activity observed in phosphorus was that of the 14.3-day P^{32}.

Sodium Fraction

Two activities were observed in the sodium fraction. The 14.8-hour Na^{24} was definitely identified, but the 2.6-year Na^{22} could be identified only on the basis of the decay during a 120-day period.

B. Yields of Spallation Products

Plots of the observed yields of the spallation products are shown in Figs. 3, 4, and 5. The yields are given relative to Cu^{61} which was arbitrarily assigned a yield of 1.0. The numbers listed for the various nuclides represent the ratios of the numbers of atoms of the particular nuclides to the number of atoms of the Cu^{61} formed in the irradiated copper, and hence the numbers represent the ratios of the cross sections for formation from elemental copper. The cross section for the formation of Cu^{61} from elemental copper irradiated with 340-Mev protons is 2.3×10^{-26} cm^2 as determined by a bombardment of copper in the external proton beam where the beam intensity was accurately measured. The cross section for formation of Cu^{61} from copper irradiated with 190-Mev deuterons is about 6×10^{-26} cm^2. This value is an average value of about six different deuteron irradiations, and the value was obtained by using an estimated value (one microampere) for the beam intensity. The cross sections for the formation of Cu^{61} from copper irradiated with 190-Mev and 380-Mev helium ions were not estimated since only one bombardment was done at each energy.

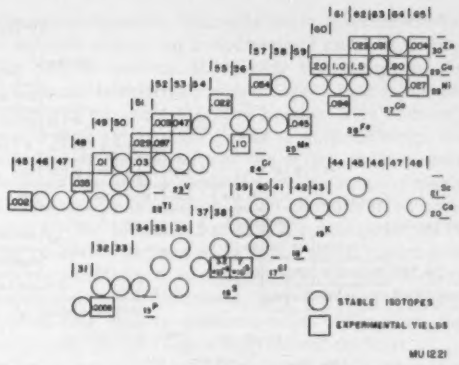

FIG. 4. Experimental yields from copper irradiated with 190-Mev deuterons. Yields are relative to Cu^{61}.

The data for the spallation products from copper irradiated with 190-Mev helium ions are not plotted since only a few values were determined. The relative yields were Cu^{61}, 1.0; Cu^{64}, 0.84; Cl^{38}, 0.0006; and no Cl^{34} was found.

The sum of the yields for the nuclides Co^{56} and Co^{58} from copper bombarded with 190-Mev deuterons was estimated to be about 1.0 on the basis of a counting efficiency of about 15 percent for the combination of

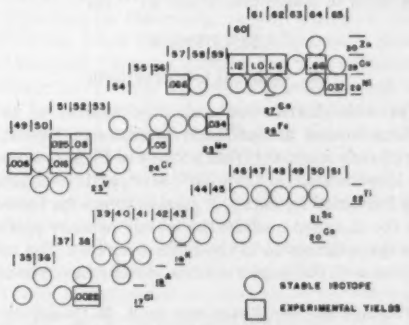

FIG. 5. Experimental yields from copper irradiated with 380-Mev helium ions. Yields are relative to Cu^{61}.

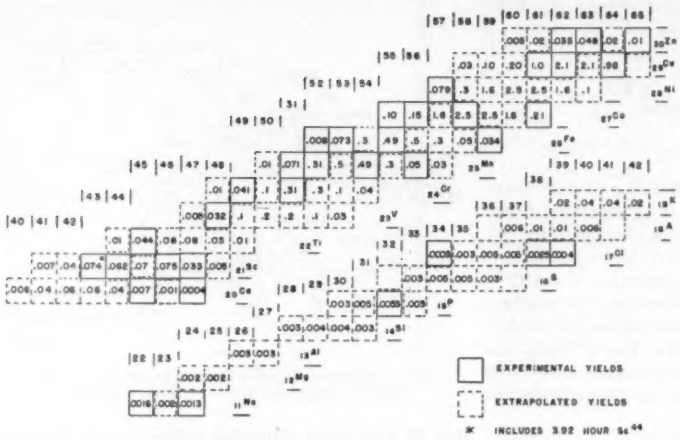

FIG. 6. Experimental, interpolated, and extrapolated yields from copper irradiated with 340-Mev protons. Yields are relative to Cu^{61}.

the activities. This is consistent with assuming that the activity is essentially all Co^{58}.

It should be emphasized that the yields for 340-Mev protons are in no way relative to the yields for 190-Mev deuterons, 190-Mev helium ions, or 380-Mev helium ions, since the cross section for formation of Cu^{61} from elemental copper is known with accuracy only in the case of the 340-Mev proton irradiations.† Many of the values for the reported relative yields are very dependent upon the counting efficiencies assumed (e.g., orbital electron capture), and when these efficiencies are better known the yields can be recalculated.

C. Yields of Secondary Reactions

The over-all or composite cross sections for formation of the gallium isotopes are as follows; Ga^{68} approximately 1×10^{-29} cm², Ga^{67} about 6×10^{-30} cm², and Ga^{66} approximately 1×10^{-29} cm².

The cross section for formation of Ge^{67}, Ge^{68}, and Ge^{69} are lower than those for the formation of the gallium isotopes, and it is estimated that these are all of the same order of magnitude, about 10^{-31} cm².

DISCUSSION

A. General Observations

The wide distribution and large number of radionuclides formed as spallation products of copper are immediately apparent from a study of Figs. 3, 4, and 5. The identification of Cu^{64}, Co^{58}, Mn^{54}, and Sc^{46}, shielded from formation by decay, is good evidence for believing that the observed nuclides are mainly primary products from the splitting up of the excited nuclues. The radionuclides with the largest neutron deficiencies or neutron excess are formed in lowest yield, and the yield for a given Z rises for the nuclides nearest the region of stability. Extrapolation of this effect to the region of stability indicates that the stable nuclides are formed in high yield. Thus the emission of almost exclusively neutrons (or protons) from a moderately excited nucleus, followed by a series of rapid positron (or negatron) decays, is a relatively rare event.

This picture of high energy nuclear reactions induced in copper is consistent with the results of studies of the spallation of arsenic[3] and antimony[4] with high energy particles. The observation that the radionuclides with the largest neutron deficiencies or neutron excess are formed in lowest yield may seem to be inconsistent with the results from studies of the spallation products from antimony irradiated with high energy particles. Lindner and Perlman[4] found that the yields of neutron deficient nuclides are larger than the yields of nuclides with an excess of neutrons. The results are consistent, however, when consideration is given to the fact that the probability of emission of charged particles from an excited nucleus is a function of the potential barrier, and is therefore a function of atomic number. The ratio of the probability of neutron emission to the probability of charged particle emission should increase with atomic number, and hence the yields of neutron deficient nuclides should rise as the atomic number of the target increases. As would be expected, however, the yields of isotopes with an excess of neutrons becomes higher than the yields for the neutron deficient isotopes of an element whenever it becomes energetically possible to form the element only by the emission of alpha-particles (or larger fragments) from the target nucleus.

The majority of the observed yield is found in the region of the target nucleus, indicating that reactions requiring much less than the maximum amount of

† *Note added in proof:* Recent work by W. B. Hutchins of this Laboratory has yielded fairly accurate values for the yield of Cu^{61} with 190-Mev deuterons (3.8×10^{-28} cm²) and with 380-Mev helium ions (about 5.2×10^{-28} cm²).

excitation available to the nucleus are more probable; this is discussed in some detail in the next section.

It should be possible, knowing the general distribution of spallation products for a given Z, to extrapolate and interpolate yields for the nuclides not directly observed as spallation products of copper. The data from the spallation of copper irradiated with 340-Mev protons have been treated in this manner, as shown in Fig. 6. It was assumed that the most probable yield for a given Z is a region 2 mass units wide and that the yields 1 mass unit on either side of this region are formed in yields about 1.5 times lower than the values in the region of the maximum yield, that spallation yields 2 mass units removed are about ten times lower than the maximum, and that yields 3 mass units removed are about a factor of 20 lower than the maximum.

A summation of these extrapolated and interpolated yields for 340-Mev protons gives a total yield relative to Cu^{61} of about 30, and using the measured value of 2.3×10^{-26} cm^2 for the cross section for formation of the Cu^{61}, the total spallation cross section for copper is about 0.7×10^{-24} cm^2. The geometrical cross section for copper is about 0.94×10^{-24} cm^2.

The difference between the observed total cross section and the geometrical cross section for copper is largely the result of the nuclear transparency for 340-Mev protons. The mean free path in nuclear matter for 340-Mev protons has been estimated to be about 4×10^{-13} cm (see part B of this section). The nuclear transparency for a given mean free path can be calculated on a geometrical basis, and if the value $R=1.37A^{\frac{1}{3}}\times10^{-13}$ cm is used for the nuclear radius (the constant 1.37 is used since this constant was used in estimating the mean free path) the calculated nuclear transparency of copper for 340-Mev protons is 20 percent. The observed transparency is 30 percent. The discrepancy between the observed and calculated transparencies probably can be explained by the approximate nature of the estimation of the total reaction cross section.

The data in Fig. 6 show that about 80 percent of the spallation yields are concentrated in the elements copper, nickel, and cobalt. Outside the immediate region of the bombarded nucleus, the yield values in the region of most probable yield for a given Z are a decreasing function of Z indicating that nuclear reactions requiring very high excitations of the nucleus are much less probable than reactions requiring perhaps some 25 to 50 Mev of excitation.

B. Mechanisms of High Energy Spallation

The accepted and experimentally supported theory of nuclear reactions at low energies (<40 Mev) involves the formation of a compound, excited nucleus;[15] the incident particle is captured by the target nucleus to form a compound nucleus with an excitation energy equal to the kinetic energy plus the binding energy of the incident particle. The excitation is then dissipated as a separate step by the evaporation of nucleons to form the product nucleus. Using only this picture of the compound nucleus, one would expect that bombardment with particles of several hundred Mev of energy would lead to very low yields of nuclides which are within a few mass units of the target nucleus, since emission of a large number of particles from the highly excited compound nucleus would be much more probable. On the contrary, however, the data presented in the preceding sections show that a large majority of the reactions induced in copper irradiated with 340-Mev protons, 190-Mev deuterons, and 190- and 380-Mev helium ions lead to products which differ from the target nucleus by a loss of only several nucleons.

Serber has suggested a mechanism which very satisfactorily explains the observed facts.[6] Irradiation with high energy protons, deuterons, and helium ions can be considered on essentially the same basis, since bombardment with 190-Mev deuterons or with 190- and 380-Mev helium ions can be regarded as a simultaneous bombardment by the several individual nucleons (neutrons and protons) making up the incident particle. The binding of the nucleons in the incident particle is important mainly in giving a spatial correlation between them. Serber points out that the collision time between a high energy incident nucleon and a nucleon in the nucleus is short compared to the time of collision of the nucleons in the nucleus, suggesting that collisions between incident nucleons and the individual nucleons in the nucleus are of primary importance.

Since the individual nucleon-nucleon collisions are important, the high energy nuclear reactions can be interpreted in terms of the high energy scattering between nucleons. Consideration of high energy scattering leads to two conclusions. First, at sufficiently high energies the nucleus becomes partially transparent to the bombarding particles, and second, the incident particle loses only a fraction of its energy in the collisions. Serber estimated that the mean kinetic energy transfer to the struck particle by a 100-Mev nucleon is about 25 Mev and that the mean free path for this 100-Mev nucleon traversing nuclear matter is about 4×10^{-13} cm. Since the struck particles have a shorter mean free path than the incident one, they will usually distribute their energy to other nucleons through collisions, but it is possible that these struck nucleons can escape from the nucleus with little or no energy loss. The subsequent behavior of the excited nucleus can be described in terms of an evaporation model, with the excitation energy dissipated by boiling off particles with several Mev of kinetic energy each.

The high spallation yields in the immediate region of the target nucleus are probably formed by reactions in which only single nucleon-nucleon collisions take place. In the case of the deuteron and helium ion yields, this means that only one of the incident nucleons undergoes a collision in these reactions. The minimum energy

[15] N. Bohr, Nature **137**, 344 (1936).

transfer from a single nucleon-nucleon collision would take place when such a collision occurs near the edge of the nucleus, and the struck nucleon escapes from the nucleus with little or no energy transfer to the nucleus.

A larger portion of the energy of the incident particle may be left with the nucleus if multiple nucleon-nucleon collisions take place. Both of the nucleons in the deuterons may undergo nucleon-nucleon collisions (or, in the case of the helium ion, two or three or four of its constituents may undergo such collisions), and each of these impinging nucleons after such collisions may either escape or collide with additional nucleons in the target nucleus. This would lead in the extreme to products resulting from nuclei excited to almost the full energy of the impinging proton, deuteron, or helium ion, amounting essentially to the formation of a compound nucleus in the ordinary sense. Thus the target may receive excitation energy from about zero up to the full energy of the projectile.

It is difficult to estimate the energetic requirements for formation of spallation products such as Cl^{38} and Na^{24}. It is apparent from energetic considerations that Cl^{38} cannot be produced in copper irradiated with 190-Mev deuterons by a reaction in which only single nucleons (neutrons and protons) are emitted. The threshold for formation of Cl^{38} from copper by the reaction $Cu^{63}(p, pn6\alpha)Cl^{38}$ in which the maximum number of alpha particles is emitted is roughly 110 Mev, but recent experimental results indicate that fragments larger than alpha-particles are emitted among the competitive products of nuclear reactions,[16–18] and the energetic requirements for these reactions are even lower than for a series of alpha-particle emissions. The observed yield for any given spallation product of copper probably actually represents the sums of the yields of several types of nuclear reactions which form the given nuclide. The fact that the observed yields for Cl^{38} from 190-Mev deuterons and 190-Mev helium ions are about a factor of six lower than those from 340-Mev protons and 380-Mev helium ions (the relative yields for chlorine from the copper irradiated with deuterons and helium ions should be accurate to at least a factor of two) indicates that nuclides in the region of Cl^{38} are probably formed mainly by reactions which require an appreciable part of the entire energy of the whole incident particle.

It is not difficult to visualize, in terms of an average energy loss of about 25 Mev per nuclear collision and a mean free path (4×10^{-13} cm) of about $\frac{3}{4}$ the nuclear radius for copper (6×10^{-13} cm) or equal to the nuclear radius as suggested by Goldberger,[19] mechanisms by which the 190-Mev deuterons, and 190- and 380-Mev helium ions might impart large portions of their total energy to the copper nucleus. It is difficult, however, to understand how a 340-Mev proton could impart large amounts of excitation to the nucleus with a fair probability if it transfers in a single nucleon-nucleon collision an average kinetic energy of only 25 Mev as would be predicted by Serber and has a mean free path about equal to the nuclear diameter for copper as estimated by Yamaguchi.[20]

In the light of some recent results of high energy scattering experiments,[21,22] it is possible to actually estimate the mean free path of 340-Mev protons in nuclear matter and to estimate the average kinetic energy loss of a 340-Mev proton in one individual collision with a nucleon in a copper nucleus and to see if the values estimated for the average kinetic energy loss and mean free path are more in line with high energy transfers having a fair probability.

The experimental data on proton-proton scattering at 340 Mev[21] show that the scattering cross section does not follow an expected $1/E$ dependence, and that the cross section is considerably higher than would be expected if it varied as $1/E$. Also the results indicate that the cross section is practically isotropic between 0° and 90° in the laboratory system. This means that high energy transfers in single proton-proton collisions have a relatively high probability. By extrapolating the data from neutron-proton scattering with 260-Mev neutrons[22] to 340 Mev and averaging the cross sections and energy transfers for $n-p$ and $p-p$ scattering over the different scattering angles, it is possible to estimate a mean energy loss for the 340-Mev protons of about 70 Mev per collision in a copper nucleus. On the basis of these scattering data the mean free path of a 340-Mev proton in nuclear matter has been estimated to be about the same as that for a 95-Mev nucleon,[23] about 4×10^{-13} cm. With the mean kinetic energy transfer per single nucleon-nucleon collision being about 70 Mev, it is not difficult to understand how large amounts of excitation are imparted to the nucleus. Incidentally, averaging in a similar manner for $n-p$ scattering with 90-Mev neutrons[24] and $p-p$ scattering with 105-Mev protons[25] gives an average energy loss for ~100-Mev protons of about 20 Mev per collision in a copper nucleus.

Recent calculations based on an evaporation model for the emission of the particles from the excited nucleus indicate that the emission of alpha-particles from the excited nucleus should be a fairly probable occurrence and that the evaporation of particles should lead to products along the region of stability.[26,27] The observed spallation yields are in agreement with these calcula-

[16] S. Wright, Phys. Rev. **77**, 742(A) (1950).
[17] L. Marquez and I. Perlman, Phys. Rev. **81**, 953 (1951).
[18] R. E. Batzel and G. T. Seaborg, Phys. Rev. **79**, 528 (1950); **82**, 607 (1951).
[19] M. L. Goldberger, Phys. Rev. **74**, 1269 (1948).
[20] Y. Fujimoto and Y. Yamaguchi, Prog. Theor. Phys. **5**, 141 (1950).
[21] O. Chamberlain and C. Wiegand, Phys. Rev. **79**, 81 (1950).
[22] Kelly, Leith, Segrè, and Wiegand, Phys. Rev. **79**, 96 (1950).
[23] S. Fernbach, private communication.
[24] Hadley, Kelly, Leith, Segrè, Wiegand, and York, Phys. Rev. **75**, 351 (1949).
[25] R. W. Birge, Phys. Rev. **80**, 490 (1950).
[26] K. J. Le Couteur, Proc. Phys. Soc. (London) **A63**, 259 (1950).
[27] Y. Yamaguchi, Prog. Theor. Phys. **5**, 142 (1950).

tions since the yields apparently do have a definite maximum of most probable yield for a given Z about 2 mass units wide and a line drawn along this region of most probable yield would be drawn through the region of stability. The very high yield of Mn^{52} compared to Fe^{52} for the isobaric pair Fe^{52}—Mn^{52}, apparent in both the 190-Mev deuteron and 340-Mev proton yields, indicates that there is a much larger difference in the yields than would be expected from the regular trends of the spallation yields, and it seems logical to explain the difference observed in terms of alpha-particles being boiled off from the excited target nucleus as suggested by Helmholz *et al.*[5] If the Fe^{52} and Mn^{52} are formed by reactions initiated by noncapture processes (processes in which the proton or the deuteron loses energy to the nucleus but is not retained by the nucleus) the reactions for the formation of Fe^{52} and Mn^{52} should, perhaps, be written $Cu^{63}(p, pp6n\alpha)Fe^{52}$ or $Cu^{63}(d, dp6n\alpha)Fe^{52}$ and $Cu^{63}(p, p3n2\alpha)Mn^{52}$ or $Cu^{63}(d, d3n2\alpha)Mn^{52}$. On this basis the yields indicate that the probability of emission of two alpha-particles plus three neutrons is much higher than that for the emission of one alpha-particle, six neutrons, and a proton. Although this effect shows up only in special cases like this where such direct comparisons can be made, it is probably a general phenomenon.

It is also possible on the basis of the spallation yields to say something about the probability of exchange reactions, for example, reactions in which the incident proton or the proton of the incident deuteron undergoes a charge exchange with a neutron in the copper nucleus and emerges as a neutron. The high yields of copper relative to the corresponding zinc isotopes indicate that these exchange reactions do not predominate.

The decreasing yields of individual nuclei far removed from the target nuclei are, of course, resulting in part from statistical considerations and the greater number of possibilities. A larger number of different combinations of emitted particles is possible from a highly excited nucleus than from a nucleus excited to a smaller extent. Thus, even if the probabilities of exciting a nucleus to say 200 and 100 Mev were the same, the yield of an individual product resulting from the higher excitation would be lower than one resulting from the lower excitation.

It is interesting to note that no observable yield of Cu^{67} was obtained from copper irradiated with 380-Mev helium ions. This nuclide can be formed only by an $(\alpha, 2p)$ reaction on Cu^{65}.

In the light of the foregoing discussion of the emission of fragments among the competitive products of spallation reactions it is possible to suggest mechanisms for the formation of the observed gallium and germanium activities. The mechanism for the formation of gallium is probably

$$_{29}Cu + p \rightarrow \text{fragments} + {}_{2}He$$

$$_{29}Cu + {}_{2}He \rightarrow {}_{31}Ga + xn,$$

and for the formation of germanium:

$$_{29}Cu + p \rightarrow \text{fragments} + {}_{3}Li$$

$$_{29}Cu + {}_{3}Li \rightarrow {}_{32}Ge + xn.$$

These mechanisms have been postulated[28, 17] previously to explain similar reactions.

CHEMICAL SEPARATION PROCEDURES

The irradiated copper foil was dissolved in hot concentrated nitric acid or hydrochloric acid and hydrogen peroxide, and milligram amounts of the elements calcium through zinc were then added to act as carrier for the elemental fractions. Known amounts of the elemental fractions to be separated were added so that a quantitative estimation of the amounts of the original carrier lost during the chemical separation procedures could be made in the case of the proton bombardment, and the macro amounts of the other elements were added to act as holdback agents. The chemical separation procedures included distillation, extraction, and precipitation operations, and these procedures were carried out usually with volumes of 5 to 15 ml.

In general the degree of radiochemical purification required depends on the relative spallation yield and the counting efficiencies of the radionuclides in the elemental fraction. If the nuclides are formed in high yield and have a high counting efficiency, the degree of radiochemical purification need not be too high, but if the spallation yields are low or the counting efficiencies are low, the degree of purification must be high.

Usually the particular elements to be investigated were separated successively from the entire dissolved target solution. Since different combinations of elements were removed in each investigation, the chemical separation procedures as a whole varied from bombardment to bombardment. The essential steps for the separation and purification of the elemental fractions were the same, and the over-all procedures differed only in the order in which the separations were used. For this reason only the important steps necessary for the chemical separation and purification of the various elemental fractions are discussed. The final precipitates, if the final step in the chemical separation procedure is a precipitation, were usually dissolved, and aliquots were taken from the solution for counting.

Germanium

The irradiated copper target was dissolved in a minimum amount of concentrated nitric acid, and 10 mg of germanium carrier was added to the solution. The solution was transferred to a glass still, and 20 ml of 6 N HCl was added. The hydrochloric acid solution was distilled until only 2 to 3 ml of solution remained in the still. The distillate was collected in a flask immersed

[28] D. H. Templeton and I. Perlman, Abstracts of Papers (Meeting of Am. Chem. Soc., Portland, Oregon, September 13–17, 1948), pp. 55–60.

in an acetone dry ice bath. Hydroxylamine hydrochloride was added to the distillate to destroy any chlorine, and hydrogen sulfide was bubbled into the cold solution to precipitate germanium sulfide. The precipitate was washed with water and then dissolved in 0.5 ml of concentrated ammonium hydroxide. The ammoniacal solution was diluted to 10 ml and transferred to a clean glass still. Ten ml of concentrated hydrochloric acid was added, and the distillation of the germanium tetrachloride was repeated. The germanium was precipitated in the final form as the sulfide and transferred to a plate for counting.

Gallium

The solution of the copper target, with 5 mg each of iron and gallium carrier added, was adjusted to 7.75 *N* in hydrochloric acid. The gallium and iron were extracted from the hydrochloric acid solution with about 20 ml of isopropyl ether. The ether layer was washed four times with 6 ml portions of 7.75 *N* HCl, and the iron and gallium were extracted from the ether layer with water. The extract was then adjusted to 1 *N* in sodium hydroxide, and the ferric hydroxide precipitate was removed by centrifugation. Two to three mg of iron carrier was added and the ferric hydroxide precipitate again removed. The sodium hydroxide solution containing the gallium was adjusted to 7.75 *N* in hydrochloric acid, and the gallium was extracted with isopropyl ether. The ether layer was washed four times with 6 ml portions of 7.75 *N* HCl and the gallium was extracted from the ether layer with water. Two to three mg of iron carrier as ferric chloride was added to the extract and the solution was adjusted to 1 *N* in sodium hydroxide. The ferric hydroxide was removed by centrifugation, and the sodium hydroxide solution was adjusted to 7.75 *N* in hydrochloric acid. The ether extraction was repeated, and the gallium was reextracted into water. Gallium hydroxide was precipitated from the water extract by adjusting the pH of the solution to about 5.5 with sodium hydroxide.

Zinc

The dissolved target solution with carriers added was adjusted to 2 *N* in hydrochloric acid and the copper precipitated as the sulfide. The hydrogen sulfide was expelled and the solution neutralized with ammonium hydroxide. The solution was then adjusted to pH 3 with dilute sulfuric acid, and the zinc was precipitated as the sulfide. The precipitate was dissolved in dilute hydrochloric acid and the hydrogen sulfide expelled by boiling. Three milligrams of iron carrier was added and the solution adjusted to 1 *N* in sodium hydroxide. The ferric hydroxide was removed by centrifugation, and the ferric hydroxide precipitation was repeated. The solution was then adjusted to 1 *N* in hydrochloric acid and the zinc precipitated by adding 4 ml of a solution of ammonium mercuric thiocyanate prepared by adding 16 g of ammonium thiocyanate and 13.5 g of mercuric chloride to 250 ml of water. The zinc mercuric thiocyanate precipitate was washed with a solution containing ammonium mercuric thiocyanate and then transferred to an aluminum plate to be dried and weighed in this form.

Copper

The dissolved target solution with carriers added was adjusted to 2 *N* in hydrochloric acid and the copper precipitated as the sulfide. The sulfide precipitate was dissolved in hot concentrated nitric acid, the sulfide expelled or oxidized, and the nitrate destroyed by boiling with concentrated hydrochloric acid. The solution containing the copper was adjusted to 0.5 *N* in hydrochloric acid, sulfur dioxide bubbled through the solution to reduce the copper, and then sodium thiocyanate added to precipitate copper as the cuprous thiocyanate. The cuprous thiocyanate was washed with water and then dissolved in nitric acid. The nitrate was again destroyed by boiling with concentrated hydrochloric acid and the solution again adjusted to 0.5 *N* in hydrochloric acid. The copper was then precipitated in the final form as the cuprous thiocyanate.

Nickel

The solution remaining, after the copper had been removed as the sulfide, was boiled to expel the hydrogen sulfide and the iron oxidized with a few drops of nitric acid. The solution was then made alkaline with ammonium hydroxide and the precipitated hydroxides removed. The precipitate was washed with a hot solution of ammonium chloride and the wash combined with the supernate from the precipitation. Three mg of iron carrier was added and the ferric hydroxide removed by centrifugation. The solution was made slightly acid with acetic acid, and 2 ml of a 1 percent alcoholic solution of dimethylglyoxime was added to precipitate the nickel as nickel dimethylglyoxime. The precipitate was washed with water and then dissolved in concentrated hydrochloric acid. One to 2 mg portions of copper, cobalt, and manganese were added to act as holdback carriers, the solution neutralized with ammonium hydroxide, and then made slightly acid with acetic acid. Dimethylglyoxime was again added to make sure that the precipitation of the nickel dimethylglyoxime was complete, and the precipitate was washed with water. The nickel was weighed as the nickel dimethylglyoxime.

Cobalt

After the copper had been removed as the sulfide, the solution was boiled to remove the hydrogen sulfide and then neutralized with potassium hydroxide. The solution was adjusted to 3 *N* in acetic acid, and 3 to 4 ml of a saturated solution of potassium nitrite acidified with acetic acid was added to the hot solution contain-

ing the cobalt. The precipitate of potassium cobaltinitrite was allowed to settle in a steam bath, removed by centrifugation, and washed with a 5 percent potassium nitrite solution acidified with acetic acid. The precipitate was dissolved in hydrochloric acid, and holdback carriers for zinc, copper, nickel, and manganese were added. The solution was then neutralized with potassium hydroxide and the cobalt again precipitated as potassium cobaltinitrite. The cobalt was weighed as the potassium cobaltinitrite.

Iron

The solution of the copper target, with 5 mg of iron carrier added, was adjusted to 7.75 *N* in hydrochloric acid and the iron extracted with isopropyl ether. The ether layer was washed four times with 6 ml portions of 7.75 *N* HCl, and the iron was extracted from the ether layer with water. The solution was made alkaline with 1 *N* NaOH and the ferric hydroxide precipitate separated by centrifugation. The precipitate was dissolved in hydrochloric acid and the iron again extracted from 7.75 *N* HCl with isopropyl ether. The ether layer was again washed with 7.75 *N* HCl and the iron extracted from the ether layer with water. The iron was analyzed by a colorimetric method.

Manganese

The solution of the target, to which 5 mg of manganese carrier and holdback carriers for the other elements had been added, was adjusted to 2 *N* in hydrochloric acid and the copper removed as the sulfide. The supernate was made alkaline with ammonium hydroxide and the alkaline sulfides precipitated. The sulfide precipitate was dissolved in concentrated nitric acid and fuming nitric acid added to make the volume up to about 5 ml. Two or three crystals of potassium chlorate were added, and the solution was boiled gently for a few minutes to precipitate manganese dioxide. The precipitate was removed by centrifugation, washed with water, and then dissolved in one drop nitric acid and one drop of hydrogen peroxide. Holdback carriers for zinc, copper, nickel, cobalt, iron, and chromium were added and the manganese was again precipitated as manganese dioxide from concentrated nitric acid. The manganese was analyzed by weighing as manganese dioxide.

Chromium

The steps for the chemical separation of chromium were the same as those given for the separation of the manganese down to the point where the manganese was first removed as manganese dioxide. At this point the chromium was in the form of the chromate and remained in the supernate after the manganese dioxide was removed by centrifugation. The nitric acid solution containing the chromate was adjusted to 0.2 *N* in nitric acid and the solution cooled in an ice bath. Two to three drops of 30 percent hydrogen peroxide were added to form the blue peroxychromic acid, and the peroxychromic acid was extracted with diethyl ether. The ether layer was washed twice with 5 ml portions of water containing a drop of nitric acid. The peroxychromic acid was removed from the ether layer by adding a solution of 0.5 *N* NaOH which breaks down the peroxychromic acid and forms the chromate. The ether was removed by evaporation, and the excess hydrogen peroxide was destroyed by boiling the solution. The solution was made slightly acid with acetic acid, and the barium was precipitated as the chromate by adding 0.5 *N* $BaCl_2$ dropwise to the hot solution of the sodium chromate. The chromium was weighed as barium chromate.

Vanadium

The vanadium was usually separated just subsequent to the extraction of the chromium as the blue peroxychromic acid as described in the preceding section on chromium. The solution containing the vanadium was almost neutralized with sodium hydroxide and then was poured into 10 ml of a hot solution of 1 *N* NaOH. The hydroxide precipitate was removed by centrifugation and then washed with 4 ml of hot 1 *N* NaOH. Two mg each of iron and titanium carrier were then added to the solution and the hydroxides precipitated. The supernatant solution containing the vanadium was boiled to reduce the volume and then made slightly acid with acetic acid. Lead acetate was added to precipitate the vanadium as lead vanadate, and the precipitate was washed with a dilute solution of lead acetate made slightly acid with acetic acid. The lead vanadate was dissolved in nitric acid and the solution adjusted to 2 *N* in nitric acid. The lead was precipitated as the sulfide, and the sulfide was expelled by boiling the solution. Five mg of chromium carrier was added and sulfur dioxide was passed through the solution to reduce the vanadium and chromium. The solution was almost neutralized with sodium hydroxide and then poured into a boiling solution of 1 *N* NaOH to precipitate the chromium hydroxide. The chromium hydroxide was removed by centrifugation, and the vanadyl ion was oxidized to the vanadate state with hydrogen peroxide. Vanadium was then precipitated as lead vanadate from a solution slightly acid with acetic acid. The vanadium was analyzed colorimetrically.

Titanium

After the copper had been removed as the sulfide, the solution with the carriers added was boiled to remove the hydrogen sulfide, and the solution was made alkaline with ammonium hydroxide to precipitate the hydroxides of iron, scandium, and titanium. The precipitate was washed with hot, dilute ammonium hydroxide and then dissolved in hydrochloric acid. The solution was then adjusted to 0.5 *N* in hydrochloric acid and scandium

precipitated as the fluoride by adding 0.3 ml of 27 *N* HF. After allowing the precipitate to settle for ten minutes on a steam bath, the scandium fluoride was removed by centrifugation, and the supernatant was made alkaline with ammonium hydroxide. The combined titanium and ferric hydroxide precipitate was removed, dissolved in nitric acid and adjusted to 1.6 *N* in nitric acid. Five ml of a solution of potassium iodate was added and the titanium separated as potassium titanium iodate. The precipitate was washed with a dilute solution of the potassium iodate. The iodate was destroyed by bubbling sulfur dioxide into the precipitate mixed with a few ml of dilute hydrochloric acid. Ammonium hydroxide was added to precipitate the titanium hydroxide; the precipitate was removed by centrifugation and then dissolved in hydrochloric acid. Five mg of scandium carrier was added, and the scandium was precipitated as scandium fluoride from a 0.5 *N* solution of hydrochloric acid as before. The titanium was again precipitated as the hydroxide and the precipitate dissolved in nitric acid. The solution was again adjusted to 1.6 *N* in nitric acid and the potassium titanium iodate again precipitated. The titanium was analyzed colorimetrically.

Scandium

The steps in the separation procedure for scandium are the same as those for titanium down to the point where the scandium fluoride is removed. The fluoride precipitate was washed with 0.5 *N* HCl containing one drop of 27 *N* HF. Sulfuric acid was used to dissolve the scandium fluoride and the fluoride ion was removed by fuming the scandium solution with a small amount of concentrated sulfuric acid. The sulfuric acid solution was made alkaline with ammonium hydroxide and the scandium hydroxide precipitate removed by centrifugation. The hydroxide was dissolved in hydrochloric acid and the solution adjusted to 0.5 *N* in hydrochloric acid. Scandium fluoride was then precipitated by adding 0.3 ml of 27 *N* HF, and the precipitate was allowed to settle on a steam bath. The precipitate was again dissolved in sulfuric acid, the hydrogen fluoride distilled, and scandium hydroxide precipitated from an alkaline ammonium hydroxide solution. The scandium was weighed as scandium oxide.

Calcium

After the copper had been removed, the solution containing 5 mg of calcium carrier and carriers for the other elements was made alkaline with ammonium hydroxide, and the alkaline sulfides and hydroxides were precipitated. Carriers for zinc through scandium were again added, and the alkaline sulfides and hydroxides were again precipitated. This last step was again repeated, and the solution was then boiled to remove the hydrogen sulfide. The solution was made slightly acid with oxalic acid, and 5 ml of 4 percent ammonium oxalate was added to precipitate calcium oxalate. The precipitate was allowed to settle on a steam bath for ten minutes, was removed by centrifugation, and washed with water containing oxalic acid and ammonium oxalate. The calcium oxalate was dissolved in concentrated nitric acid, and a few crystals of potassium chlorate were added to oxidize the oxalic acid. Three mg of iron carrier was added, and the solution was made alkaline with ammonium hydroxide. The ferric hydroxide was removed by centrifugation and the solution made acid with oxalic acid. Four ml of a solution 4 percent in ammonium oxalate was added to precipitate calcium oxalate as the final purification step, and the precipitate was allowed to settle on a steam bath. The calcium was weighed as calcium oxalate.

Chlorine

The copper was dissolved in nitric acid and 5 mg of chlorine in the form of sodium chloride was added. The solution was boiled to distill the hydrogen chloride and the gas was caught in a solution containing two to three drops of nitric acid and sufficient silver nitrate to precipitate the chlorine as silver chloride. The solution was heated almost to boiling to coagulate the precipitate, and it was removed by centrifugation. The precipitate was washed with dilute nitric acid and then dissolved in dilute ammonium hydroxide. The solution was then acidified with nitric acid and additional silver nitrate added to make sure that the precipitation of the silver chloride was complete. The chlorine was weighed as silver chloride.

Phosphorus

The copper target was dissolved in nitric acid and 5 mg of phosphorus as phosphate ion was added to the solution. Holdback carriers were also added for the other elements zinc through calcium. The solution was adjusted to 1 *N* in nitric acid and 10 ml of ammonium molybdate[29] was added to the warmed solution to precipitate ammonium phosphomolybdate. The precipitate was allowed to settle for 15 minutes, removed by centrifugation, and washed with a solution of 1 percent nitric acid. The precipitate was dissolved in ammonium hydroxide containing citrate ions to complex titanium which otherwise would form an insoluble phosphate. Hydrochloric acid was added until the precipitate that formed during neutralization dissolved with difficulty: this assured that sufficient acid had been added. Five mg each of vanadium and titanium carrier were added, and sulfur dioxide was bubbled through the solution to reduce all the vanadium to the vanadyl state. Two ml of a cold magnesium chloride mixture[30] was added, and the solution was allowed to stand for five minutes. Concentrated ammonium hydroxide was then added

[29] W. F. Scott, *Standard Methods of Chemical Analysis, I*, edited by N. H. Furman (D. Van Nostrand Company, Inc., New York, 1939), fifth edition, p. 697.

[30] Reference 29, p. 695.

equal to one-quarter of the original volume and the precipitate of magnesium ammonium phosphate was allowed to settle for 15 minutes. The precipitate was removed by centrifugation and then washed with 3 *N* NH_4OH. The precipitate was dissolved in 1 *N* HNO_3, and the phosphorus was again precipitated as the ammonium phosphomolybdate. The phosphorus was weighed as the ammonium phosphomolybdate.

Sodium

The copper was dissolved in concentrated hydrochloric acid and hydrogen peroxide, and 5 mg of sodium as sodium chloride was added as carrier. Carriers for the elements zinc through potassium were added, the solution adjusted to 2 *N* in hydrochloric acid and the copper precipitated as the sulfide. The solution was boiled to dryness to remove the excess acid, the residue dissolved, and then the solution made alkaline with ammonium hydroxide. Hydrogen sulfide was added and the sulfides and hydroxides were precipitated. Additional 3 mg portions of carriers zinc through scandium were added and precipitated. This scavenging process was repeated twice. Excess hydrochloric acid was added to the alkaline sulfide solution, the acidified solution boiled to dryness, and the ammonium chloride driven off. The residue was dissolved in water, the solution checked to make sure it was neutral, and the sodium precipitated as the sodium zinc uranyl acetate by the addition of a solution of zinc uranyl acetate.[31] Two 5-ml portions of zinc uranyl acetate were used to wash the precipitate, and the precipitate was then dissolved in absolute alcohol saturated with hydrogen chloride gas. The resulting mixture was cooled in an ice bath and the sodium chloride separated by centrifugation. The sodium chloride precipitate was washed with a 5-ml portion of an alcohol-hydrogen chloride solution. The sodium chloride was dissolved in water and the solution neutralized with potassium hydroxide. Zinc uranyl acetate was added to precipitate the sodium, the precipitate removed by centrifugation, and then washed with additional zinc uranyl acetate. The precipitate was dissolved in absolute alcohol saturated with hydrogen chloride, the mixture cooled in an ice bath, and the sodium chloride removed by centrifugation. The sodium chloride was washed with an additional portion of the ethyl alcohol-hydrogen chloride solution. The sodium was weighed as sodium chloride.

We wish to thank Mr. James T. Vale and the group operating the 184-inch cyclotron for the irradiations performed in the course of these studies.

[31] Reference 29, p. 879.

Experimental Search for the Beta-Decay of the π^+ Meson*

HELEN L. FRIEDMAN AND JAMES RAINWATER
Columbia University, New York, New York
(Received July 30, 1951)

The possibility that nuclear beta-decay is associated with the beta-decay of the meson, formed during an intermediate step, has long been of interest in the development of meson theories. To explain nuclear beta-decay, the beta-decay rate for the π-meson should be comparable to its μ-deay rate. The present investigation is an attempt to detect other than $\pi-\mu$ events for π^+ mesons which stop in G-5 400 and 600 micron emulsions. The result is one or zero $\pi-e$ event compared to 1419 $\pi-\mu$ events for mesons satisfying certain selection criteria.

A collimating exposure chamber was used in the fringing magnetic field inside the vacuum chamber of the Columbia 164-inch cyclotron to provide energy and direction selection of mesons at the photographic plate. The expected total energy spread for any point x along the plate was calculated to be about 1 Mev.

Only mesons were considered which entered the top surface of the emulsion, ended in the emulsion, and had directions and ranges within intervals including about 94 percent of the π-mesons. This procedure assured consideration of essentially all π-mesons but discriminated against μ-mesons produced by decays in flight.

I. INTRODUCTION

YUKAWA'S hypothesis[1] of the meson as a particle exchanged between nucleons in order to explain nuclear forces seemed strikingly confirmed by the discovery of particles of intermediate mass in cosmic rays.[2] The particles were observed to have a mass about 200 m_e which agrees, in order of magnitude, with the value predicted from the range of nuclear forces. Also they spontaneously decay into an electron, as first predicted by Bhabha.[3] These mesons are now called μ-mesons. However, it was gradually found that quantitative agreement between the nuclear force meson and the μ-meson of cosmic rays was lacking. Even if one adjusted the coupling constant with the nucleon field to account for nuclear forces and the coupling constant with the electron-neutrino field so as to obtain the correct results for nuclear beta-decay, then a mean lifetime of about 10^{-8} sec was predicted, whereas the observed lifetime is much larger (2×10^{-6} sec). Moreover, the experimental cross section for interaction of μ-mesons with nucleons is smaller than that required for nuclear forces by many orders of magnitude.

On the other hand the π-mesons, discovered by Powell *et al.*[4] are at least partly responsible for nuclear forces. They have been shown to interact with nucleons with about geometric cross section.[5] However, whether or not the creation and annihilation of virtual π-mesons can be used to explain nuclear beta-decay, according to the scheme: $p^+\xrightarrow{G}\pi^++n\xrightarrow{G}e^++\nu+n$ is quite another question. The theoretical investigations of this subject are summarized in the Appendix. Experimentally, one wishes to decide whether the π-meson does undergo beta-decay

$$\pi^{\pm}\xrightarrow{?}e^{\pm}+\nu$$

and if so, to determine the partial lifetime τ_e for beta-decay in terms of the known lifetime[6] $\tau\approx2.5\times10^{-8}$ sec for total decay (which is mainly, if not entirely, due to μ-decay),

$$1/\tau=(1/\tau_\mu)+(1/\tau_e).$$

(Since π^- mesons stopped in matter are trapped in atomic orbits and absorbed by the nucleus in a time short compared to 10^{-8} sec, only π^+ mesons are suitable for such an investigation.)

When photographic plates were first used to detect π^+ mesons at Berkeley[7] there was some indication that a few percent of the π^+ mesons which stopped in the C-2 emulsions used did not give rise to μ^+. The difficulties inherent in any systematic investigation of the τ_e/τ_μ ratio are twofold: (1) One must, of course, use electron

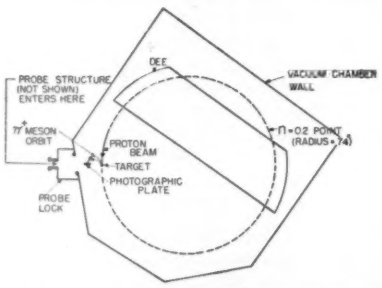

FIG. 1. Plan view of cyclotron showing π^+ meson orbits.

* Assisted by the ONR and AEC.

[1] H. Yukawa, Proc. Phys.-Math. Soc. Japan **17**, 48 (1935); H. Yukawa and S. Sakata, Math Soc. Japan **19**, 1084 (1937).

[2] C. D. Anderson and S. H. Neddermeyer, Phys. Rev. **51**, 884 (1937); J. C. Street and E. C. Stevenson, Phys. Rev. **51**, 1005(A) (1937); Nishina, Takeuchi, and Ichimiya, Phys. Rev. **52**, 1193 (1937).

[3] H. J. Bhabha, Nature **141**, 117 (1938).

[4] Lattes, Muirhead, Occhialini, and Powell, Nature **159**, 694 (1947); Lattes, Occhialini, and Powell, Nature **160**, 453, 486 (1947).

[5] Bernardini, Booth, Lederman, and Tinlot, Phys. Rev. **80**, 924 (1950); H. Bradner and B. Rankin, Phys. Rev. **80**, 916 (1950).

[6] Jacobsen, Schulz, and Steinberger, Phys. Rev. **81**, 894 (1951). References to earlier work are given here.

[7] Burfening, Gardner, and Lattes, Phys. Rev. **75**, 382 (1949).

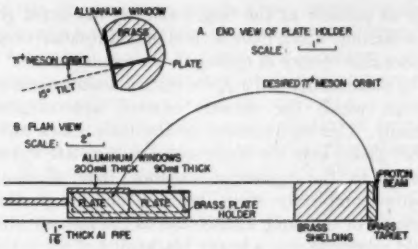

FIG. 2. Preliminary apparatus.

sensitive (G-5) emulsions to be able to detect the minimum ionization track produced by the 70-Mev electron one expects from a π^+ beta-decay. However, even so, a $\pi-\mu$ event is much more striking than a meson-electron event (for a photograph of a $\pi-\mu-e$ decay, see reference 8). In fact, it has been customary to detect positive mesons by their characteristic $\pi-\mu$ junction. Thus, unless one is careful to devise proper scanning techniques, there is danger of overlooking a greater proportion of meson-electron events than of $\pi-\mu$ events, or even of missing the meson-electron events entirely (assuming that they exist). (2) The μ meson does undergo beta-decay.

$$\mu^{\pm} \rightarrow e^{\pm} + 2\nu.$$

Thus, one must contrive means of distinguishing between the $\mu-e$ events, which one expects to be present in considerable numbers, and the $\pi-e$ events being investigated. Now a μ meson arising from a $\pi-\mu$ decay occurring when the π-meson is at rest always has 4.1-Mev kinetic energy and a residual range in G-5 emulsion of about 595μ. Thus, by the simple expedient of working with mesons of residual range considerably greater than 600μ, one can eliminate from consideration any μ-electron events arising from $\pi-\mu$ decays at rest. What remains is to discriminate between true $\pi-e$ events and $\mu-e$ events where the μ-meson is formed in a $\pi-\mu$ decay in flight. The collimating system designed to provide this discrimination and the scanning methods devised to avoid missing meson-electron events will be described in the following sections.

II. APPARATUS

The π-mesons were produced by bombarding a copper target with the 385-Mev proton beam of the Nevis 164-inch cyclotron. Positive π's emitted in the backward direction were approximately refocused in the fringing magnetic field onto an Ilford G-5 plate placed at 180° with respect to the target (see Fig. 1).

Preliminary exposures were made with the simple arrangement shown in Fig. 2. The results were unsatisfactory in two respects. (1) The background was annoyingly high so that scanning was laborious and not wholly reliable. There was the usual collection of extraneous tracks, random in orientation and randomly distributed in energy, caused by neutron and γ-ray stars, knock-on protons, etc., which one expects to find on plates exposed inside the vacuum chamber. In addition, there were numerous high energy proton tracks, all roughly parallel to each other and to the direction of the meson tracks. This particularly irritating background is caused by protons which are scattered in traversing the target and then follow trajectories such as (1) in Fig. 3. The particles spiral outward onto the plate because of the rapid decrease of magnetic field with increasing radius beyond the $n=0.2$ point. (2) The π-mesons observed at a given position x along the plate, corresponding to a given radial distance from the target in the cyclotron magnetic field, possessed no characteristic energy or entrance angle. Therefore, one could not hope to be able to distinguish between π-mesons and μ-mesons from $\pi-\mu$ decays in flight. Offhand, at a given coordinate x on the plate, one would expect, despite the smear in energies arising from the inhomogeneity of the magnetic field, that there would be a peak in the meson energy distribution at that energy which satisfied the (modified) 180° focusing condition, and also a correlation between meson energy and entrance angle. However, any such energy peaking or angular correlation is in practice obscured by the possibility of such π-meson trajectories as (2) in Fig. 3, where the meson makes a turn of 360° etc. before reaching the plate.

Thus, the "meson exposure chamber," Fig. 4, was designed with the twofold purpose in mind of cutting down background and of collimating the π-mesons. The size was limited by the requirement that the apparatus would have to fit into the probe vacuum lock and pass through the opening between the vacuum lock and the vacuum chamber. This limited the possible length and diameter to less than 14 in. and 12 in. respectively.

The copper target, which was $\frac{1}{2}$-in. thick in the beam direction and $\frac{1}{16}$-in. thick radially, was situated at $r=74$ in. and 1 in. above the median plane. This is at the $n=0.2$ point where the beam "blows up" vertically[9] due to coupling of the radial and vertical oscillations.

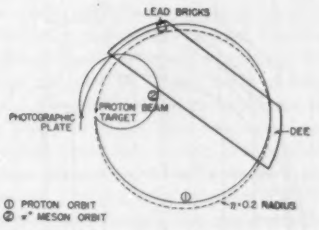

FIG. 3. Possible proton and π^+ meson orbits in the fringing magnetic field.

[8] Brown, Camerini, Fowler, Muirhead, and Powell, Nature **163**, 47 (1949).

[9] Henrich, Sewell, and Vale, Rev. Sci. Instr. **20**, 887 (1949).

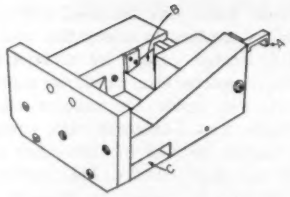

FIG. 4. Meson exposure chamber showing target A, channel B, and slot for plate holder C.

Experiment showed that the beam intensity at the target position was practically undiminished with respect to the median plane intensity. The activity of the target was found to be concentrated in a small region ($\approx\frac{1}{16}$ in.) near the bottom of the $\frac{1}{16}$-in. wide target so it acted, nearly, as a $\frac{1}{2}$-in. long line source of mesons.

Referring to Fig. 4, which shows a perspective view looking down at the exposure chamber, the metal plate on the end, to the left in the figure, was bolted onto the 4-in. probe pipe. The two bolt holes were about 1 in. above the median plane. The lower tip of the target, A, served as the source of mesons. The mesons then spiralled downwards in a roughly semicircular path through the slotted channel, B. The plate holder was inserted in the slot C. The dimensions can best be judged from Fig. 5, which shows the top view of the chamber.

For the meson orbits the important dimensions were as follows: the emulsion extended from 83-in. to 86-in. cyclotron radius and was 2.7 in. below the median plane. (The emulsions used were 1 in. by 3 in. and either 400 or 600μ thick, mounted on a glass backing of about 1.25 mm thickness.) Thus the mesons which reached the plate had to spiral down from 1 in. above the median plane to 2.7 in. below, which corresponded to an angle of dip of about 12°. This dip angle was chosen as a compromise between two opposing factors: one would like to have the plate subtend as large an effective solid angle as possible at the target and yet one must give the π-mesons, which have several mm of residual range, a reasonable chance of ending in the emulsion.

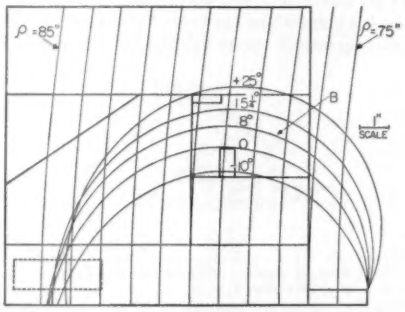

FIG. 5. Allowed and rejected orbits for 12-Mev π^+ mesons. Mesons emitted at $+25°$ and $-10°$ with respect to the proton beam direction fail to pass through the opening of channel B.

The plate holder had a $\frac{1}{16}$-in. thick aluminum window through which the mesons entered approximately normally. This was screwed to the main block and a rubber gasket kept the inside sealed so the plate was not exposed to the cyclotron vacuum. The aluminum window completely stops heavier charged particles (protons) of the same momentum as the mesons which would otherwise give a heavy blackening of the surface of the emulsion.

As can be seen from Fig. 4, there was 7 in. of copper shielding the plates from any direct radiation from the target-neutrons, γ-rays, or charged particles. (385-Mev protons have a range in copper of about 5 in.) Since only 4 to 6 in. of copper was available to shield the plates from the full energy elastically scattered protons of Fig. 3, a 6-in. thickness of lead bricks was placed inside the vacuum chamber in the position shown in Fig. 3 in order to provide additional shielding. The bricks covered a 6-in. radial distance starting just beyond the $n=0.2$ radius and a 4-in. vertical distance extending from $2\frac{1}{2}$ in. below the median plane to $1\frac{1}{2}$ in. above. Also acting to reduce background was the vertical selection imposed by the channel B in Fig. 5. Of the particles leaving the target with the correct dip angle to reach the plate, those which have longer spiral paths outside the collimating system than corresponds to a turn of about 180° are cut out, since by the time they reach the channel, they are too far below the median plane to pass through.

In order to be able to collimate the π-mesons to give optimum energy definition at the plates, accurate knowledge must be obtained of their trajectories in the fringing magnetic field of the cyclotron. To this end, trajectories of π-mesons of a given energy leaving the target at 74-in. radius, at different angles relative to the proton beam direction, were determined graphically. In Fig. 5, some of these orbits have been reproduced for a 12-Mev π-meson. Superimposed is a drawing of the collimating system, so that one can see how the edges of the collimator were located to give optimum sharpness of focus at the plate and still give a reasonable solid angle of aperture relative to the source. (A 12-Mev π has a range in copper of about 0.05 in., so the baffles were very thick compared to the meson range.)

The arc lengths of allowed meson orbits were measured, and this data as well as the known vertical drop of 3.7 in. from target to emulsion was used to adjust the height of channel B in Fig. 5, so as to pass all allowed orbits. Those mesons, on the other hand, which follow trajectories such as (2) in Fig. 3 are cut out, since they are too far below the median plane when they reach the channel to be passed.

The expected energy spread of the π-mesons reaching a given x coordinate of the plate was estimated from a consideration of the meson trajectories together with

the size of the meson source. Over the region of the plate used, a 1-Mev change in meson energy corresponds to a change in x of about 0.6 in. For the allowed orbits shown in Fig. 5, the mesons of a given energy are seen to be concentrated in a region of x of about $\frac{3}{8}$ in. (Variation in x coordinate due to both variation in entrance angle and to y coordinate are included in this estimate.) It will be remembered that the source width is $\frac{1}{16}$ in. Thus, in all, a total energy spread of about 1 Mev is expected. The expected spread in entrance angle is less than 15°.

The basis of the method is then as follows. Only mesons which enter the emulsion at about the correct direction and which have the proper residual range are considered. Most μ-mesons formed from $\pi-\mu$ decays in flight will accordingly be rejected, as discussed below. In practice, angle criteria were found useful only in the actual scanning technique finally adoped, which is discussed in Sec. III. Range criteria, however, did serve to exclude most μ-mesons. The range limits for a given x were chosen to be as narrow as possible while still including greater than 90 percent of the total π-mesons. The limits are indicated in Fig. 6 and are discussed at greater length in Sec. IV. (Note that the mesons considered in Fig. 6 have energies reduced by passage through the $\frac{1}{16}$-inch aluminum window of the plate holder.)

Once the mesons have been selected in this way, it becomes possible to distinguish between π-mesons and most μ-mesons arising from $\pi-\mu$ decays in flight. Consider a π-meson of 15 Mev decaying into a μ-meson. In the rest system of the π-meson, the μ-meson is emitted isotropically with 4.1-Mev kinetic energy. As observed in the laboratory system, however, the μ-meson is emitted at an angle to the original direction of the π-meson which can vary only from 0° up to a maximum of about 37°. The energy of the μ-meson varies from about 3 Mev for backward emission in the π-rest system, through about 15 Mev for the maximum laboratory angle case, to about 29 Mev for forward emission in the π-rest system. Thus, one expects that μ-mesons having roughly the same energy as the original π will make large angles with the original direction of the π and therefore either not get through the collimating system at all or at least enter the emulsion at an angle recognizably different from those of the accepted π-mesons. Those μ-mesons emitted in roughly the original direction of the π should have recognizably different energies and therefore residual ranges than the original π-either greater or less, corresponding to forward or backward emission in the π-rest system. Of course one cannot expect perfection. For example, a 15-Mev π headed in a direction which will not permit its passage through the collimating system, might decay in the target region to a roughly 15-Mev μ-meson which would then have the correct direction to have an allowed orbit. However, such instances will be rare and one expects on the whole good discrimination between π's and μ's from in flight $\pi-\mu$ decays. That this aim has been accomplished is shown by the results of the experiment.

III. SCANNING AND MEASUREMENTS

The scanning techniques finally used were gradually evolved over a period of months. What was required was a method of searching for events which would not be biased in favor of $\pi-\mu$ events over the less noticeable meson-electron events, and yet would not be unreasonably time consuming.

The plates obtained with the preliminary arrangement of Fig. 2 were scanned by conventional methods whereby each field of view was carefully examined throughout its depth for meson endings. Each meson found was recorded in a notebook by locating its entrance position and end with respect to cartesian coordinates and roughly drawing its trajectory. The μ-meson or electron originating from the meson ending was also drawn. Gradually, by dint of much practice, it was found possible to identify mesons well before

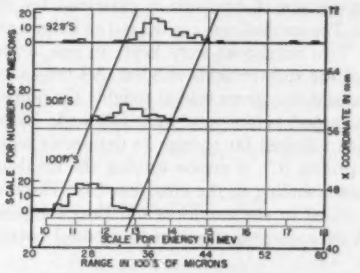

FIG. 6. Histogram of π-meson ranges and graph of accepted range limits *vs* x coordinate.

their endings by their characteristic small angle scattering. By the time scanning was begun on the plates obtained with the meson exposure chamber of Fig. 4, confidence had been built up in one's ability to recognize a meson as such and the conventional method of searching for meson endings was dropped as being prejudiced in favor of the more striking $\pi-\mu$ event.

The first new method, used on the 400 μ-plates, consisted of searching each field of view in a given column for meson trajectories. Every time a meson was found it was followed and mapped as before. Each meson was first identified when it entered the emulsion through the air surface, and then in several fields of view in each column, and also in 2 or 3 different columns, depending upon the entrance angle. This method of scanning is very thorough since each meson is identified as such several times without any reference to a $\pi-\mu$ or meson-electron event. However, the counting rate of about 10 mesons a day was too low for the method to be of practical use.

A counting rate of between 25 and 50 mesons a day was obtained with a scanning technique whereby only

TABLE I. Meson-electron events (ranges given in microns).

	x coordinate	Range	Accepted range limits
[a]1	65.0	2280	3120–4240
2	57.1	3090	2800–3900
[b]3	55.8	4180	2750–3860
4	46.0	4490	2350–3450
5	54.1	4950	2690–3790
[a]6	48.9	5770	2470–3570
[b]7	58.9	5890	2880–3990
8	48.4	6000	2450–3550
9	47.0	6350	2390–3490
10	46.7	6550	2380–3480
11	52.0	7000	2600–3700
12	51.0	7730	2560–3660
13	56.3	8880	2770–3880
14	63.3	9000	3050–4170
15	46.7	9280	2380–3480
16	62.6	9750	3030–4140
17	55.8	10,900	2750–3860

[a] No electron was observed here. However, out of 15μ-mesons arising from $\pi-\mu$ decays at rest whose endings were carefully examined for electrons, in two cases the electron was not visible. Thus, it seems reasonable that, in both cases, electrons were emitted, but at an angle unfavorable for observation.
[b] Found on 400μ-plates.

the top surface of emulsion is examined for entering mesons. The method was carried out as follows on 600μ-plates. Two notebooks were kept. In one, a plot was made of the surface fields of view. All tracks entering the emulsion in a given field at roughly the proper angle were recorded before any were followed. Each track was then followed far enough to determine whether it was a proton (C), a meson leaving the emulsion (B), or a meson ending in the emulsion (A). Those mesons which ended in the emulsion and thus comprised the desired data, were mapped in the second notebook as always.

As a check on our scanning techniques, several rows in each of the 4 plates used were scanned for $\pi-\mu$ junctions. Of the 463 π-mesons so found, only two had been missed by the top surface scanning method. Keeping in mind that any missing of events by the latter method is completely unprejudiced in favor of $\pi-\mu$ events *versus* meson-electron events, such a small fraction of events missed was considered quite satisfactory.

It was found that of the tracks entering the emulsion at approximately the correct angle, about 40 percent are mesons, of which about 40 percent end in the emulsion. The ratio $A/(C+B)$ was studied as a function of x coordinate along the plate and this study served as basis of selecting for use only the upper energy third of the plate. The area actually used extended from $x=3.5$ mm to $x=29.5$ mm (from the upper energy edge) and from $y=8.0$ mm to $y=23.0$ mm. The border was left out as being undesirable due to edge effects.

Three types of measurements were made on a sampling of the mesons which ended in the emulsion: projection on xy plane of angle of entrance, projected length of track, and vertical distance of the ending from the air or glass surface of the emulsion. The accuracy of measurement of the projected meson track lengths was about 1 percent. An attempt was made to find the true track lengths of a sample of 10 mesons by also measuring the change in z coordinate for each field of view. However, the corrections so obtained were less than 3 percent and consequently negligible for our purposes.

IV. ANALYSIS AND RESULTS

As discussed in Sec. II, it was expected that, due to focusing of the π-mesons in the fringing magnetic field of the cyclotron, each coordinate x along the plate would correspond to a reasonably definite meson energy. Originally it was thought that for a given x, finer resolution could be obtained by correlating energy with y coordinate and angle of entrance. However, straggling in range for each x was sufficiently great that no systematic variation of range with y or θ was observed, so that in practice no y or θ corrections were actually used.

The total number of $\pi-\mu$ events found was 1559, of which 264 were found on 400μ-plates, and the rest on 660μ-plates. Two corrections reducing this number were applied.

The first correction consisted in eliminating from consideration those $\pi-\mu$ events where the π-meson ended in a layer of the emulsion within 5μ[10] from the air or glass surfaces of the processed plate. The reason for applying this correction is the following one. For meson-electron events where the meson ended in the rejected layers, since the electron is easily overlooked in the process of scanning, the meson might be mistakenly classified as one leaving the emulsion. The 5μ-criterion was determined experimentally on the basis that a meson ending in the emulsion at a distance greater than 5μ from the glass or air surfaces would during the scanning be recognized as ending, with complete certainty, independently of whether or not an electron was noticed. Of a sampling of 587 $\pi-\mu$ events in the 600μ-plates, it was found that 17 mesons ended within the rejected layers. Therefore a 2.9 percent correction was applied to the 1295 $\pi-\mu$ events found in the 600μ-plates, and a $\frac{2}{3}\times 2.9$ percent correction to the 264 $\pi-\mu$ events found in the 400μ-plates, leaving 1510 mesons in all.

The second correction was concerned with range. In Fig. 6 is shown a histogram of the π-meson ranges for x coordinates corresponding to the edges of the region used, and to the center. The range spread for a given x is greater than that predicted from orbit considerations. This is due to straggling. For comparison, the variation of meson ranges for 31 mono-energetic μ's arising from the decay of a π-meson at rest has been given by Powell.[11] The straggling coefficient in percent $\delta/100=[(\Sigma(R-\bar{R})^2)/n]^{\frac{1}{2}}/\bar{R}$, where $\bar{R}$ is the mean range for n particles, is computed to be 5.1 percent for Powell's

[10] Actual thickness of rejected layer$=5\mu$ increased by a factor equal to the index of refraction of the emulsion.
[11] Lattes, Occhialini, and Powell, Proc. Phys. Soc. (London) 61, 173 (1948).

measurements on μ-mesons, whereas the theoretical[12] value is estimated to be about 6 percent. In the case of the π-mesons for x coordinate 56.1–58.1, the theoretical value is estimated to be 5.2 percent and the computed value for the 49 accepted π's is 6.8 percent. If, however, one subtracts from the computed value of $(R-\bar{R})_{\text{M}}^2$ an amount corresponding to a reasonable estimate for the expected energy spread at each x due to varying θ and due to varying y, one obtains a corrected straggling coefficient of 5 to 6 percent which agrees well with the theoretical value. This shows that the collimator worked according to theory.

Also given in Fig. 6 is a graph of accepted range limits *versus* x coordinate. Since 14 π-mesons out of a sample of 242 did not fall within the accepted limits, the total number of mesons, 1559, was reduced by a 5.8 percent correction factor. As a result of applying both corrections, the reduced number of $\pi-\mu$ events is 1419.

The accepted range limits of Fig. 6 were used to exclude all but one of the meson-electron events, as shown in Table I. Events 2 is the only meson-electron event falling within the accepted range limits, and therefore the only possible $\pi-e$ event.

As discussed in Sec. II, it is to be expected that occasionally a μ-meson of the proper range, arising from a $\pi-\mu$ decay in flight, will successfully get through the collimating system. Thus it is quite possible that event 2 is a $\mu-e$ event. It is rather gratifying, in fact, that more such events were not observed out of so large a number of total meson events. Consequently our experimental result is either zero or one $\pi\rightarrow e+\nu$ disintegration out of 1419 $\pi\rightarrow\mu+\nu$ decays.

APPENDIX. THEORETICAL ASPECTS OF THE $\pi-e$ DECAY

In what follows, it should be borne in mind that recent experimental evidence favors a pseudoscalar π-meson.[13]

Of the four possible coupling schemes recently discussed by Yukawa,[14] and illustrated in Fig. 7, in only one does nuclear beta-decay occur, according to the original Yukawa model, through the intermediate creation of a virtual π-meson, and its subsequent decay to an electron and a neutrino. Let us call this coupling scheme Model I. To obtain the correct magnitude of nuclear forces, $G^2/\hbar c\approx 0.1$. The mean lifetime τ_μ of the π-meson for μ-decay and the mean lifetime for capture of μ-mesons by nuclei are both in approximate agreement with a single choice of the coupling constant $G''[G''^2/\hbar c\approx 10^{-14}]$, as shown by Tiomno and Wheeler.[15] The coupling constant G_F' must be chosen[15] about equal

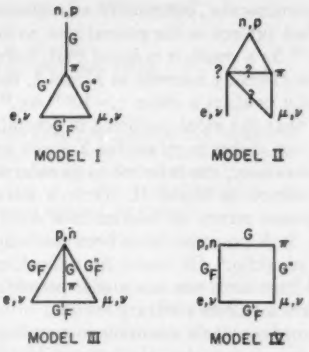

FIG. 7. Proposed coupling schemes.

to G_F in all cases except that of pseudoscalar coupling, if one is to obtain the correct lifetime for μ-meson decay. (G_F is the coupling constant for direct interaction of nucleons with the electron-neutrino system, according to the Fermi theory of nuclear beta-decay. The value of G_F is obtained, for example, from the beta-decay of the neutron ($\tau=12.5\pm 2$ min)[16].)

The only difficulty with Model I is one directly involving the $\pi-e$ decay. Thus, if one chooses G' according to the relation $G_F=GG'/k^2$ [17] where $k=m_\pi c/\hbar$ in order to account for nuclear beta-decay, one finds $G'\approx G''$, and

$$\tau_e\approx(\tau_\mu/6)(G''/G')^2 \tag{1}$$

so that the lifetime for $\pi-e$ decay is in general even shorter than that observed for $\pi-\mu$ decay, in contradiction with experiment. The one promising possibility seemed to be that of the pseudoscalar meson with pseudovector coupling. In this case one finds[18]

$$\tau_e\approx(\tau_\mu/6)(F''/F')^2(m_\mu/m_e)^2, \tag{2}$$

where the F's are pseudovector coupling constants. If one now assumes with d'Espagnat[18] that $F'\approx F''$ one obtains $\tau_e\approx 10^4\tau_\mu$ which might agree with experiment. A similar conclusion was inferred in reference 14 from the earlier calculations of Sakata.[19]

However, this peculiarity of the case of the pseudoscalar meson with pseudovector coupling does not remedy the situation.[19,20] For a self-consistent scheme, one must choose, not $F'\approx F''$, but $(m_e/m_\pi)F'=G'\approx G''=(m_\mu/m_\pi)F''$ which again yields the general result (1). In fact, if one carries through in detail the calculation of the probability $1/\tau_\beta$ for the beta-decay of a free neutron according to Model I, in the case where the intermediate

[12] M. L. Livingston and H. Bethe, Revs. Modern Phys. **9**, 284 (1937).
[13] Panofsky, Aamodt, and Hadley, Phys. Rev. **81**, 565 (1951); Brueckner, Serber, and Watson, Phys. Rev. **81**, 575 (1951); Bishop, Steinberger, and Cook, Phys. Rev. **80**, 291 (1950); Durbin, Loar, and Steinberger, Phys. Rev. **83**, 646 (1951).
[14] H. Yukawa, Revs. Modern Phys. **21**, 474 (1949).
[15] J. Tiomno and J. A. Wheeler, Revs. Modern Phys. **21**, 144, 153 (1949).
[16] Snell, Pleasanton, and McCord, Phys. Rev. **78**, 310 (1950). J. M. Robson, Phys. Rev. **78**, 311 (1950). J. M. Robson, Phys. Rev. **82**, 306 (1951).
[17] L. De Broglie, De La Mecanique Ondulatoire a la Theorie du Noyau **II**, 119 (1945).
[18] B. d'Espagnat, Compt. rend. **228**, 744 (1949).
[19] S. Sakata, Proc. Phys.-Math. Soc. Japan **23**, 291 (1941).
[20] E. C. Nelson, Phys. Rev. **60**, 830 (1941).

meson is pseudoscalar, one obtains an additional factor $(m_e/m_\pi)^2$ not present in the general case, as first shown by Nelson.[20] As a result, it is found that, instead of removing the difficulty inherent in Model I, the pseudoscalar meson predicts a value $\tau_e \approx 10^{-15}$ sec,[21] which is much less than the value predicted in general.

Thus if one wishes to retain the Yukawa scheme for nuclear beta-decay, one is forced to consider some such coupling scheme as Model II, where a virtual hypothetical meson serves as intermediate state between Fermions. Such proposals have been made by Sasaki[22] and by Caianiello.[21] Of course no difficulties are encountered here since one can assign properties to the hypothetical meson in arbitrary fashion.

If one confines one's attention to coupling schemes involving known particles, another possibility is Model III, the symmetric coupling scheme, which was proposed by Tiomno and Wheeler.[14] Here, there is direct coupling between nucleon and electron-neutrino, or between any other pair of Fermions, and the coupling constants are of the same order of magnitude in all three cases. There is no longer any direct coupling between π-meson and either electron-neutrino fields, or μ-meson-neutrino fields. However, $\pi-e$ decay and $\pi-\mu$ decay will still take place via the creation and annihilation of virtual nucleon pairs. The difficulty encountered with this model is that the probabilities for these decays are divergent with respect to the momentum of the nucleon pairs virtually created in the intermediate state.[23] On the other hand, if one makes the decay probabilities finite by some cut-off procedure, one again expects, contrary to experiment, that the lifetimes for both decay possibilities will in general have the same order of magnitude, since the coupling constants involved are of the same order of magnitude.

Detailed calculations according to the symmetric coupling scheme (Model III) have been carried out for the $\pi-e$ and $\pi-\mu$ decay rates by Steinberger[24] and by Ruderman and Finkelstein[25] using different cut-off procedures. Since the results are sensitive to the choice of cutoff employed, no conclusions can be drawn from the absolute lifetimes so calculated. However, as the same divergent integral appears in both lifetime expressions, if the integral can somewhow be made finite, the ratio of lifetimes should be independent of the method used. The results are that in some cases the decay of the π-meson by either mode is forbidden, in others that the ratio of lifetimes is about unity. Only if the π-meson is pseudoscalar, with either pseudoscalar or pseudovector coupling to nucleons, and if the nuclear beta decay coupling contains a pseudovector term do we obtain a result not in contradiction with experiment: $\tau_e/\tau_\mu \approx 10^4$. (The nuclear beta-decay coupling may also contain arbitrary amounts of scalar, vector, or tensor terms, since for these in the case of a pseudoscalar meson, the decay of the π is forbidden.) Whether or not Model III is the true coupling scheme depends on whether or not a correct calculation of τ_μ and τ_e would yield absolute results in agreement with experiment for the case of the pseudoscalar π-meson. These questions cannot be answered with existing meson theory.

An alternate possibility is Model IV, which differs from the symmetric coupling scheme in that the μ-meson-neutrino fields are now coupled to the nucleon fields only indirectly via the π-meson. Here, the $\pi-\mu$ decay takes place directly, while the $\pi-e$ decay again proceeds through intermediate virtual nucleon pairs, which again leads to divergence difficulties. It is quite conceivable that this model would yield acceptable values of τ_μ and τ_e, but again, existing meson theory is incapable of deciding.

In any event, it is quite apparent that the experimental value of the lifetime of the π-meson for beta-decay will be of vital importance in making the choice among the various possible coupling schemes.

[21] E. R. Caianiello, Phys. Rev. **81**, 625 (1951).
[22] S. Sasaki, Prog. Theor. Phys. **3**, 454 (1948).
[23] S. Sakata, Proc. Phys.-Math. Soc. Japan **23**, 283 (1941).
[24] J. Steinberger, Phys. Rev. **76**, 1180 (1949).
[25] M. Ruderman and R. Finkelstein, Phys. Rev. **76**, 1458 (1949).

The Isotope Effect in Superconductivity. I. Mercury*

C. A. Reynolds, B. Serin, and L. B. Nesbitt†
Physics Department, Rutgers University, New Brunswick, New Jersey
(Received August 3, 1951)

The critical magnetic fields of various isotopic mixtures of mercury have been measured as a function of temperature. The critical magnetic field at any temperature is found to decrease with increasing average mass, and the critical temperature also decreases with increasing mass. The relationship $M^{\frac{1}{2}}T_c=$const, connecting the critical temperature T_c and the average mass number M, is established. Conclusions are drawn concerning the specific heats of the normal and superconducting states of the isotopes.

1. INTRODUCTION

THE observation that the critical temperature of superconductors varies with isotopic mass, was made originally by workers in this laboratory[1] and by Maxwell.[2] This result has been confirmed[3–5] despite the negative results reported by earlier workers.[6,7] The experimental evidence indicates that the critical temperature, T_c, and the average isotopic mass number, M, are connected by the relation $M^{\frac{1}{2}}T_c=$const. This relation lends support to theories developed by Frohlich[8] and Bardeen[9] which take the view that superconductivity is caused fundamentally by an interaction between the electrons in a metal and the vibrations of the crystal lattice.

Because of the interest in this discovery, we have published most of our results in abbreviated form;[10–12] and it is the purpose of this paper to present the details of our experimental techniques and a compilation of the data.

2. EXPERIMENTAL APPARATUS AND METHOD

(a) Samples

The samples of mercury used in these experiments, which had isotope distributions differing from the distribution occurring in nature, were obtained from the AEC.[13] The metal had been enriched in isotopes by electromagnetic separation and was purified by triple distillation. The natural metal was purified by us by double distillation. The average mass numbers of the various samples used in the experiments are listed in Table I in Sec. III.

The samples were prepared by sealing the mercury under helium gas in thin-walled glass capillary tubes. Samples 1, 2, 3, and 4 had a diameter of about 0.5 mm and were about 3 cm long; and samples 5, 6, and 7 had the same length, but were about 0.8 mm in diameter. The wall thickness of the capillary tubing was about 0.2 mm.

(b) Apparatus

The general arrangement of the samples, the helium flask and other relevant equipment is shown in Fig. 1.

Each sample was placed in a plastic coil form 2.5 cm long and 2.5 mm in diameter. Four thousand turns of Formex coated B & S gauge No. 44 copper wire were wound on each form. Five coils, C, standing vertically,

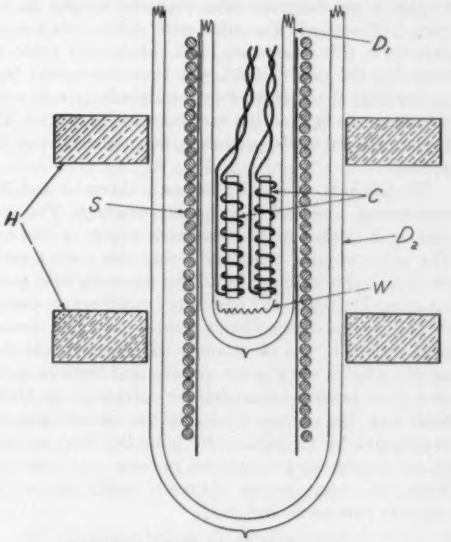

FIG. 1. The general arrangement of the apparatus. D_1 the liquid helium flask, D_2 the liquid nitrogen flask, C the sample coils, W the heater, S the solenoid, and H the Helmholtz coil.

* This work has been supported by the joint program of the ONR and AEC, the Rutgers University Research Council and by the Radio Corporation of America.

† Present address: Research Laboratory, General Electric Company, The Knolls, Schenectady, New York.

[1] Reynolds, Serin, Wright, and Nesbitt, Phys. Rev. **78**, 487 (1950).
[2] E. Maxwell, Phys. Rev. **78**, 477 (1950).
[3] E. Maxwell, Phys. Rev. **79**, 173 (1950).
[4] D. Shoenberg, *et al.*, Nature **166**, 1071 (1950).
[5] K. Mendelssohn, *et al.*, Nature **166**, 1071 (1950).
[6] H. K. Onnes and W. Tuyn, Leiden Comm. No. 160b (1922).
[7] E. Justi, Physik. Z. **42**, 325 (1941).
[8] H. Frohlich, Phys. Rev. **79**, 845 (1950).
[9] J. Bardeen, Phys. Rev. **79**, 167 (1950).
[10] Serin, Reynolds, and Nesbitt, Phys. Rev. **78**, 813 (1950).
[11] Serin, Reynolds, and Nesbitt, Phys. Rev. **80**, 761 (1950).
[12] Reynolds, Serin, and Nesbitt, Proceedings of the Low Temperature Symposium, National Bureau of Standards, March 27 to 29, 1951.
[13] The isotopes were produced by Carbide and Carbon Chemical Division, Oak Ridge National Laboratory, Y-12 Area, Oak Ridge, Tennessee; and were obtained on allocation.

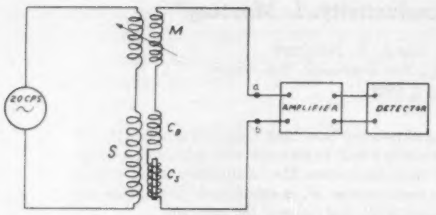

FIG. 2. Circuit for susceptibility measurement.

were arranged in a compact circle centered in the liquid helium Dewar flask, D_1. One coil was left empty. A non-inductivity wound heater coil, W, was placed below the sample coils. A solenoid, S, surrounded the helium flask, and both the flask and solenoid were centered in a second Dewar flask, D_2, which contained liquid nitrogen. The outer flask in turn was centered in a large Helmholtz coil, H.

The Helmholtz coil produced a magnetic field that was uniform to 0.1 percent over the volume occupied by the samples. A standard resistance was connected in series with the coil, so that the current flowing through the coil could be determined with an accuracy of 0.1 percent by measuring the potential drop across the resistance with a potentiometer. The flasks, solenoid and Helmholtz coil were mounted so that their common long-axis was along the direction of the earth's magnetic field. The orientation of the apparatus could be adjusted so that with the proper current flowing in the Helmholtz coil, the earth's magnetic could be canceled to give a net magnetic field over the samples of less than 0.01 oersted. The runs were made with the apparatus in this orientation, and the current value for canceling the earth's field, was then subtracted from all readings of the current in the Helmholtz coil, when the magnetic field at the samples was calculated. The Helmholtz coil could produce a maximum field of 150 oersted.

The solenoid, S, was 2.5 inches in diameter and 20.6 inches long, and had two separate windings. The samples were located at the geometric center of the coil. The outer winding consisted of fine wire and carried a small ac to provide an alternating magnetic field at the samples. The inner coil had heavy windings; it carried dc and was used when fields greater than 150 oersteds were required. The dc through the solenoid was then usually fixed at some value; and the field could be varied in a given range by changing the current in the Helmholtz coil. The current flowing in the solenoid was also determined by measuring the potential drop across a standard resistance connected in series with the coil. With this arrangement magnetic fields up to 300 oersteds were easily obtained.

(c) Critical Field Determination

The critical magnetic fields were determined by measuring the magnetic susceptibility of the samples as a function of the field. The method that we used to measure susceptibility has been carefully investigated by Shoenberg[14] and the arrangement of the components of our particular circuit is shown in Fig. 2.

The leads from each of the five coils in the helium Dewar flask were brought out of the flask through a standard multiple-connector. This arrangement permitted each sample coil C_S, in turn to be connected in series opposition to the empty coil C_B. The two coils formed the secondary of a mutual inductance, the outer winding of solenoid, S, constituting the primary. The solenoid was fed by a 20 cps alternating current signal generator; the current was adjusted to produce a magnetic field of 0.8 oersted amplitude at the samples. M is a small variable mutual inductance.

The voltage appearing across $a-b$ was amplified by a Ballantine decade amplifier and detected by a General Radio wave analyzer. The latter instrument was tuned to 20 cps and had a band width of 4 cps, thereby eliminating most noise and the extraneous 60 cps signal picked up from the power lines.

The measurements were made in the following manner. With no magnetic field in the Helmholtz coil, and the sample in the superconducting state, the mutual inductance, M, was adjusted to give a minimum signal in the detector. The magnetic field was then increased. When the field approached the critical value, the detected signal began to increase; and with a further increase in field, the signal passed through a maximum

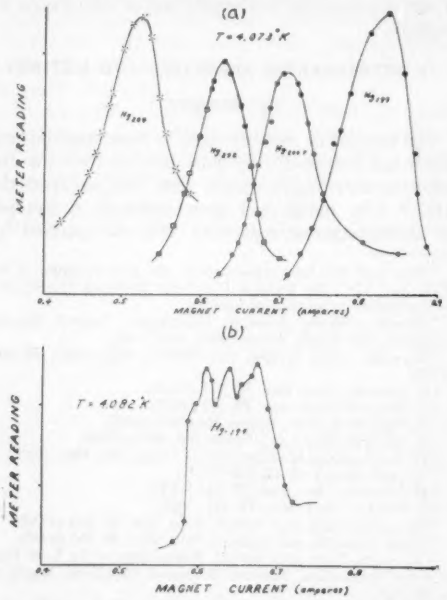

FIG. 3. Curves of detected signal *vs* current in the Helmholtz coil.

[14] D. Shoenberg, Proc. Cambridge Phil. Soc. **33**, 559 (1937).

value and finally reached a small steady value. The magnetic field value corresponding to the maximum was taken to be the critical field at a given temperature

The change in detected signal with magnetic field is the result of the transition of the sample from the superconducting state to the normal state. In the former state no magnetic field penetrates into the volume of the sample, whereas in the normal state the magnetic field passes through the whole volume. The peak signal corresponds to the magnetic field at which there is the greatest rate of change of susceptibility with field.

At 20 cps the ratio of sample radius to ac skin depth in the normal metal is less than 0.3. Thus, in these experiments there was negligible signal from the imaginary part of the susceptibility. The calculated power dissipated in the samples is also negligible.

In all the runs, we had three samples of isotopes and one sample of natural metal in the Dewar flask. At any given temperature, the critical magnetic fields of all four samples were determined as rapidly as possible. After a preliminary check that the shape of the curves of signal *versus* magnetic field were reasonably narrow and smooth, the values of the Helmholtz coil current corresponding only to the peak signal for the different samples were measured. The curve shapes were checked again in detail at three or four different temperatures.

The temperature was varied by pumping on the liquid helium bath and was kept constant by controlling the pumping speed with a Wallace and Tiernan manostat. The vapor pressure of the helium bath was measured with a mercury manometer. When the pressure was fixed, the variations were checked with a differential oil manometer. The manostat required very little manual adjustment to hold the vapor pressure constant to 1 mm of oil or about 0.1 mm of mercury. At all temperatures above 2.2°K, about 10 mw were dissipated in the heater coil to keep the liquid helium in temperature equilibrium. The vapor pressure-temperature scale used in this paper is the Mond Laboratory Scale of 1949.

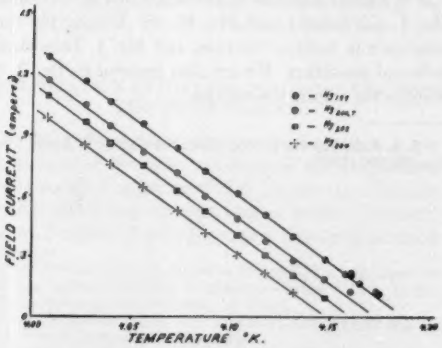

FIG. 4. Critical magnetic field *vs* absolute temperature of different isotopes.

TABLE I. The critical temperatures, T_c, as a function of average mass numbers M. Mass number 200.7 is natural mercury.

Sample No.	M	T_c °K
1	199.5	4.185
2	199.7	4.184
3	200.7	4.173
4	202.0	4.159
5	202.0	4.160
6	203.2	4.146
7	203.4	4.146

3. EXPERIMENTAL RESULTS

A typical set of curves of detected signal as a function of Helmholtz coil current are shown in Fig. 3(a). The width of the curves is about 3 oersteds, which is about twice as great as the theoretical width indicating that the width of the magnetic field transition was one or two oersteds. However, the change in critical magnetic field with average isotopic mass is clearly resolvable. There is a systematic increase in critical field with decreasing mass. The results of a series of measurements at different temperatures are shown in Fig. 4, where the critical magnetic field of each sample is plotted as a function of temperature. The critical temperatures were obtained by extrapolating these curves to zero magnetic field.

In the course of repeating the experiments we found that occasionally a sample would have a curve shape of the type shown in Fig. 3(b). In addition to being very broad, the curve has several peaks. This shape indicates that there were several jumps in susceptibility as a function of magnetic field. Behavior of this type was not the property of a particular sample, but would appear and disappear erratically in a given sample in successive runs. This behavior was traced to the procedure used in cooling the sample to liquid nitrogen temperature and in admitting liquid helium into the flask.

The procedure finally adopted was to place a small amount of liquid nitrogen in the outer shield flask.[15] The system was allowed to stand for an hour, and then small amounts of liquid nitrogen were added over the course of another hour. It was possible to get an accurate idea of the temperature of the samples during cooling by measuring the change in resistance of the copper coils surrounding them; and so bring the samples slowly through the freezing temperature of mercury. We found it important never to permit the initial blow-off of warm helium gas from the transfer tube to hit the samples. We waited until liquid helium poured from the transfer tube before placing the tube into the

[15] The helium Dewar flask had air contained between the walls at a pressure of 1 cm of Hg, permitting heat exchange with the liquid nitrogen. When liquid helium was admitted into the flask the air froze out.

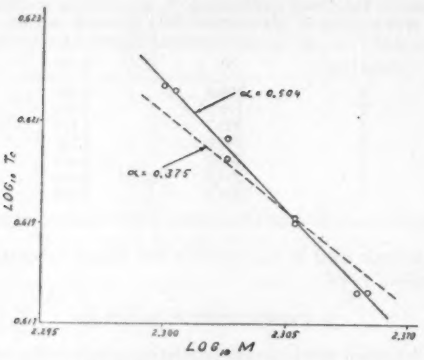

FIG. 5. $\log_{10}$ (critical temperature) vs $\log_{10}$ (average mass number).

helium flask. This procedure, which clearly produced the minimum amount of strain in the samples, resulted in consistently good curve shapes.

Omitting the occasional samples which behaved as shown in Fig. 3(b), the "isotope effect" was observed in each of our total of twelve runs on mercury.

Most of these runs were taken in the region 4.0°K to 4.2°K; however, the critical magnetic field measurements were extended down to 1.7°K in two runs. Within experimental error, the critical magnetic fields were found to be parabolic functions of the temperature. The experimental data were fitted to a parabolic relation of the form

$$H = A - BT^2, \tag{1}$$

where T is the absolute temperature. The parameters A and B were determined by the method of least squares.

In Table I we present a summary of what we consider the most reliable values of the transition temperatures of six isotopic samples of various average mass numbers and of the natural metal.

We delay giving the values of the parameters A and B until the next section.

4. DISCUSSION

Figure 5 is a plot of $\log_{10} T_c$ as a function of $\log_{10} M$. The slope of the line is -0.504. For purposes of comparison, a line of slope -0.375 is drawn, according to the suggestion of Herzfeld, Maxwell and Scott.[16] The larger negative slope clearly gives the best fit with the data, and we feel that these experiments firmly establish the relation

$$M^{\frac{1}{2}} T_c = \text{const}$$

in mercury.

Kok[17] has shown that a parabolic relation between critical magnetic field and absolute temperature follows from a specific heat relation of the form

$$C_n - C_s = \gamma T - KT^3,$$

where C_n is the specific heat per unit volume in the normal state, C_s is the specific heat per unit volume in the superconducting state and γ and K are parameters. The first term, γT, is the usual electronic specific term of the free electrons in the normal conductor. From our parameters A and B in Eq. (1), it is therefore possible to calculate γ and K for each isotope; the results are summarized in Table II. The critical fields at 0°K, H_0, obtained from Eq. (1), are also listed.

TABLE II. The critical fields, H_0 at 0°K, and the parameters γ and K, in the specific heat expression, $C_n - C_s = \gamma T - KT^3$, for various average isotopic mass numbers M. K/M is also tabulated.

M	H_0 (oersteds)	γ	K	K/M
199.5	420	1600	273	1.37
200.7	419	1600	275	1.37
202.0	417	1600	278	1.375
203.2	414	1590	278	1.37

It is fairly clear from Table II that γ is independent of M, indicating, as probably was to be expected, that the electronic specific heat in the normal state is unaffected by the mass of the lattice atoms. K, on the other hand, is approximately proportional to the lattice mass.

5. ACKNOWLEDGMENT

It is a great pleasure to thank Dr. M. P. Garfunkel, Mr. J. Gittleman, and Mr. W. H. Wright for their assistance in making the runs, and Mr. J. Teza for his technical assistance. We are also grateful to Dr. R. T. Webber for helpful discussions.

[16] Herzfeld, Maxwell, and Scott, Phys. Rev. **79**, 911 (1950).

[17] J. A. Kok, Physica **1**, 103 (1934). See also G. P. Burns, Phys. Rev. **76**, 999 (1949).

Differential Cross Section of the Reaction $He^3(d,p)He^4$ at 10.2-Mev Bombarding Energy and Search for Excited State in He^4

J. C. Allred
*Los Alamos Scientific Laboratory, University of California, Los Alamos, New Mexico, and University of Texas, Austin, Texas**

(Received August 2, 1951)

The differential cross section of the reaction $He^3(d,p)He^4$ has been measured by means of a photographic technique. The cross section shows a high degree of asymmetry and is quite similar to that previously measured for the $T(d,n)He^4$ differential cross section at 10.5 Mev. This similarity suggests equality of p-p and n-n forces. Observations of the short-range particles from bombardments of He^3 and T gases under identical conditions permit the assignment of upper limits for the reaction $He^3(d,p')He^{4*}$. At a laboratory angle of 90°, the cross section is less than 0.2×10^{-27} cm² for an excited state below 20.9 Mev.

I. INTRODUCTION

BECAUSE of the scarcity of He^3 gas in quantities sufficient for use in conventional gas targets, relatively few measurements have been made of nuclear processes in which He^3 is an initial component.[1-4] The reaction $He^3(d,p)He^4$ has associated with it the usual interest accruing to light particle reactions in that the number of nucleons, while not small, is at least not large enough to preclude the hope of theoretical investigation. Special interest attaches to this reaction, however, because of the possibility of investigating the existence of an excited state in He^4, one of the residual nuclei. In principle, one can search for such an excited state up to a fairly high energy limit, on account of the large amount of energy (18.4 Mev) available from the Q of this reaction. The existence of an excited state in He^4 would be inferred from the presence of a group of protons of energy lower than that of the proton group from the primary reaction. The energy difference of two such groups would give the excitation energy for an excited state of the He^4 nucleus.

In addition, therefore, to the measurement of the differential cross section of the $He^3(d,p)He^4$ reaction, a search was made for proton groups which would indicate level structure in He^4. Since these results were negative in the energy region investigated, it was possible only to arrive at upper limits of cross section and energy for the production of He^4 in an excited state from this reaction.

II. PURIFICATION AND HANDLING OF GAS SAMPLES; TARGET CHAMBERS

The He^3 gas samples used as the target gas were taken from samples of H^3 which had decayed a sufficient time to yield a useful quantity of He^3. In general, a tritium sample is stored in a uranium furnace as the compound UT_3. At the time of storage, such a furnace is pumped down to a low pressure (~10^{-5} mm Hg). This procedure gives reasonable assurance that gas which accumulates in the furnace on the decay of the tritium will be He^3 of extremely high purity.

In order to insure the purity of the target gas, and especially to remove traces of tritium gas, the He^3 sample is further purified by recycling over CuO at 425°C and through a trap cooled with liquid nitrogen. Traces of tritium are thus oxidized to T_2O and frozen in the cold trap. This procedure removes water vapor, CO_2, and all of the noble gases which might be present, with the exception of argon. Subsequently, the sample is recycled over Ca metal at 700°C. This procedure removes oxygen and nitrogen as the oxide and nitride, respectively. Thus, the only common gas which is not removed by the foregoing purification process is argon, which is a troublesome impurity because of its low boiling point. Argon, however, can be detected easily in the target gas because of its relatively high scattering cross section for deuterons and the fact that deuterons scattered by argon will retain a large fraction of their initial energy. Such deuterons were never observed in bombardments with thin walled targets. This evidence, combined with the initially low probability of the presence of argon as an impurity, led to the conclusion that argon contamination of the sample was extremely small.

For reasons to be discussed later, it became necessary to make bombardments with tritium as the target gas; here, a pure gas sample is somewhat easier to obtain. A uranium furnace containing tritium is pumped down to a low pressure ($<10^{-5}$ mm Hg) in order to remove traces of He^3 and inert gases. The system is then closed off and the uranium furnace heated, causing the decomposition of UT_3 and the evolution of tritium gas. The excellent "getting" properties of uranium insure that a sample thus obtained is free of oxygen and water vapor. It should be noted here that the tritium samples available were diluted to concentrations of the order of 80 percent with hydrogen. Hydrogen gas as an impurity is of no consequence in this application, and is evolved from and absorbed in the uranium along with the tritium.

The purification procedures described above are used

* Work done under the auspices of the AEC. This document is based on a doctoral dissertation submitted to the Faculty of the Graduate School of The University of Texas.

[1] Baker, Holloway, King, and Schreiber, Los Alamos Manuscript Series-2 (declassified), June, 1943.
[2] J. Hatton and G. Preston, Nature **164**, 143 (1949).
[3] Wyly, Sailor, and Ott, Phys. Rev. **76**, 1532 (1949).
[4] J. C. Allred, Phys. Rev. **77**, 753 (1950).

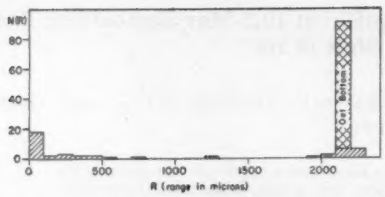

FIG. 1. Range distribution of charged particles from $He^3(d,p)He^4$ at laboratory angle of 60°. 130 tracks.

on all samples immediately before bombardment. The pressure and temperature of the sample in a standard volume are measured, and the sample transferred to a target chamber by means of a Toepler pump. Immediately after the bombardment, a similar *PVT* measurement is made on the sample, to insure that no gas has been lost. The molecular density in the target chamber is inferred from a measurement of its volume, and the measurements in the standard volume before and after each bombardment.

Two gas target chambers were used during the course of the investigation. The first of these was designed for observation of the reaction products at 90° in the laboratory system. Entrance and exit ports for the beam and two 90° windows were provided; one-mil Dural windows were used throughout. This target chamber was of standard design. The only concession to the rare gas contained was that the 0–180° axis hole was tapered, opening out toward the rear of the target, such that the volume of the target was minimized.

The second target chamber was designed to permit observation of the reaction protons over a range in the laboratory system from 20° to 160°. This target was a Dural cylinder approximately four inches long. Its maximum diameter was one inch at either end, where gasket grooves were provided for mounting the one-mil Dural windows. The central two inches of the target were of ½-inch diameter, with walls 0.005±0.0001 inch thick.

III. EXPERIMENTAL PROCEDURE

Nuclear emulsions were used to record the range and intensity distributions of the bombardment products. In conjunction with the 90° target, a single camera for each of the 90° observation ports was used, with a plate

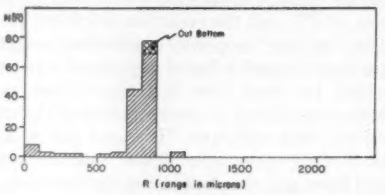

FIG. 2. Range distribution of charged particles from $He^3(d,p)He^4$ at laboratory angle of 135°. 144 tracks.

geometry essentially that described by Rosen, Tallmadge, and Williams.[5] For the angular distribution measurements, in which the wide angle Dural target was used, the detection system was the Los Alamos nuclear multiplate camera, which is described in detail elsewhere.[6] Since the analysis technique used to interpret the data has been extensively described,[7–9] only those features unique to the treatment of tracks of high energy particles will be considered here.

The externally focused deuteron beam of the 42-inch cyclotron was used to bombard the thin He^3 and *T* gas targets, the target-camera assemblies being mounted in a scattering chamber external to the water-shield walls.[10] Integrated deuteron current was measured by collection of the beam at the rear of the scattering chamber in a faraday cup connected to an electronic current integrator.

The detector geometry in both the single and multiplate cameras consists of two slits which define the reaction volume visible to the photographic plate detector. The plate is mounted so that reaction particles passing through the slit system enter the surface of the emulsion at a grazing angle. The center line of the slit system intersects the surface of the plate at about one-third of the plate length from the end of the plate nearest the slits. Tracks or particles originating in the reaction volume are distinguishable from background tracks through the following criteria: (1) They must start on the surface of the emulsion; (2) They must lie within angular limits determined by the geometry of the system; (3) They must fall within a definite length on the plate with a predictable density distribution. In most of the experiments done with this technique one has available a range criterion for tracks which should be counted; that is, one can add to the above criteria upper and lower limits for the range of a group of particles under observation.

In a sense, however, the range discrimination feature is lost in the present experiment, for at forward angles in the laboratory system the protons from $He^3(d,p)He^4$ (E_d=10.2 Mev) are so energetic that their ranges exceed the available emulsion thickness (~1800μ) at the grazing angle used. For this reason it is not possible to discriminate directly against that fraction of the particles which penetrate the slit edges but retain enough energy that their range exceeds that of the emulsion thickness at the grazing angle. Some of the tracks observed will be due to protons which scatter upward and remain in the emulsion layer for their entire range. This permits a check on the expected energy of the proton as a function of angle, and justifies a correction

[5] Rosen, Tallmadge, and Williams, Phys. Rev. **76**, 1283 (1949).
[6] Allred, Rosen, Tallmadge, and Williams, Rev. Sci. Instr. **22**, 191 (1951).
[7] Louis Rosen and J. C. Allred, Phys. Rev. **82**, 777 (1951).
[8] Allred, Phillips, and Rosen, Phys. Rev. **82**, 782 (1951).
[9] Allred, Froman, Hudson, and Rosen, Phys. Rev. **82**, 786 (1951).
[10] Curtis, Fowler, and Rosen, Rev. Sci. Instr. **20**, 388 (1949).

for slit edge penetration based on the probability that a proton will penetrate the slit edge and be degraded as compared with the probability that a proton will pass through the cone defined by the slits without degradation. This correction factor is found to be

$$(2R_a/kl)[(R_e-T)/R_e],$$

where R_a is the range of the proton in air, R_e its range in emulsion, T the emulsion thickness available, k the stopping power of the slit material relative to air, and l the distance between slits. In this experiment the largest value for this correction was 2.2 percent. It decreases with increasing angle of observation and becomes zero at 90° lab.

Though the extreme range of the high energy protons observed necessitates the correction noted above and hampers the range limit criterion which is ordinarily applied, the uniqueness of these tracks is in another sense an advantage. For, in background runs in which He^4 and T were the target gases, no tracks whatever were observed which could be confused with tracks of protons from $He^3(d,p)He^4$ when the proper criteria were applied, i.e., that the tracks start on the surface of the emulsion and proceed within defined angular limits. The characteristic low grain density of these high energy proton tracks in Ilford C-2 emulsion was an additional aid in their identification, in that this criterion permitted the immediate rejection of tracks of high grain density at their beginning.

Figures 1 and 2 show typical range *versus* number histograms at laboratory angles of 60° and 135°, respectively. Since, for the purposes of the slit penetration correction, tracks going out of the bottom of the emulsion are treated as those in the main peak, tracks out the bottom are plotted in the peak. Enough scattered tracks remain in the emulsion to indicate the range of the group. The range scale which is plotted is the projected range, measured parallel to the surface of the emulsion.

IV. RESULTS

A. Differential Cross Section

Figure 3 and Table I give the results of the differential cross section measurement *versus* center-of-mass angle. These data are to be compared with those of Wyly, Sailor, and Ott,[3] whose experimental points show a similar, but much less pronounced, asymmetry at their lower bombarding energy (3.17 Mev).

A least squares fit of the data is the following:

$$\sigma(\cos\Omega)=3.602P_4+0.787P_1+1.720P_2-0.762P_3 +1.220P_4+2.305P_5+1.479P_6.$$

Integration of this expression to give the total cross section yields a value of 45×10^{-27} cm², whereas extrapolation and integration of the experimental curve by the trapezoidal rule at 10° intervals gives 43×10^{-27} cm².

The absolute rms standard error of the data given

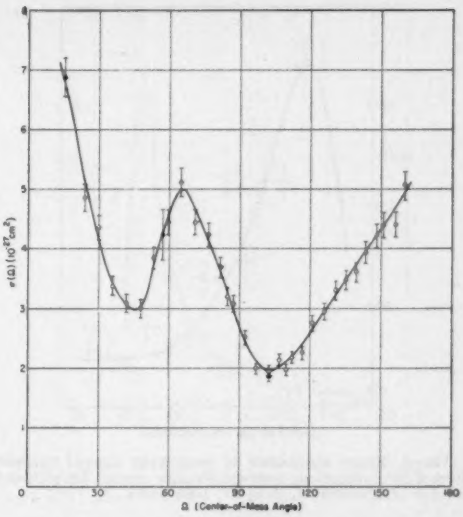

FIG. 3. Differential cross section *versus* center-of-mass angle for $He^3(d,p)He^4$ reaction at 10.2-Mev bombarding energy. Check points mentioned in the text are indicated by triangles. Errors shown represent the total rms standard error for each point.

TABLE I. Measured cross sections as function of angle in center-of-mass system for the reaction $He^3(d,p)He^4$ at 10.2-Mev bombarding energy.

Ω(c.m.) (degrees)	σ(Ω) (10^{-27} cm²/steradian)
15.5	6.88
24.3	4.85
30.2	4.35
36.3	3.38
42.0	3.09
48.1	3.02
53.6	3.84
57.5	4.22
59.7	4.44
65.0	5.11
71.0	4.44
76.7	4.23
82.0	3.68
85.0	3.20
87.3	3.08
92.5	2.51
97.4	1.99
102.7	1.96
102.7	1.87
107.2	2.14
109.7	1.97
112.5	2.18
117.1	2.25
121.9	2.75
126.4	2.95
131.0	3.30
135.1	3.47
139.7	3.61
143.5	3.93
148.1	4.21
151.9	4.39
156.3	4.40
160.0	5.05

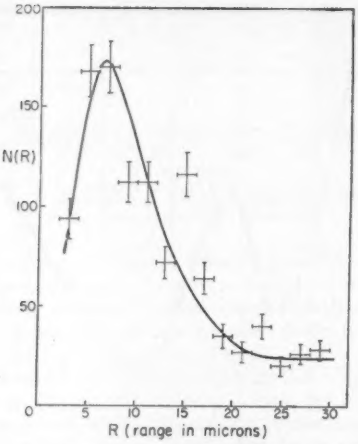

FIG. 4. Range distribution of short-range charged particles from d-He^3 interaction, observed through one-mil Dural target window at laboratory angle of 90°. 1084 tracks.

in Table I is estimated to be ±4.7 percent, apportioned as follows: statistical error, ±3.2 percent; discrimination of tracks of proper length and direction, ±2.0 percent; current integrator, ±2.5 percent; gas measurements (pressure and temperature), ±1.0 percent; and camera geometry, ±0.5 percent. It should be noted that the relative accuracy of the data is somewhat better than ±4.7 percent, since errors in the integrated current measurement and gas measurements cancel in the evaluation of relative cross-section values; this relative standard error is ±3.8 percent.

The primary data for the angular distribution measurements are those measured with the nuclear multiplate camera. The value of the cross section measured at 90° lab with the single plate camera was 1.87×10^{-27} cm². With the multiplate camera the value obtained was 1.96×10^{-27} cm². These values are consistent with the estimated error of 4.7 percent.

In a more recent experiment, whose primary purpose was the measurement of the $d-He^3$ elastic scattering differential cross section, it was possible to extend the angular range of the measurement of the $He^3(d,p)He^4$ differential cross section to a laboratory angle of 12.5° and to make a check measurement at 47.5° lab. The cross-section values obtained are in good agreement with the curve previously measured.

The walls of the wide-angle Dural gas target chamber present a thickness approximately equivalent to $(22.5/\sin\theta)$ cm air to particles originating in the reaction chamber. It can be shown that the effect of such a scatterer is to decrease the angular resolution of the measurement at angles where the second derivative of the cross section is large. A calculation has been made of this effect based on the theory of multiple scattering of Williams[11] as adapted by Dickinson and Dodder.[12] The result of this calculation shows that the cross section measured in the vicinity of the maxima and minima would be in error by the order of 1 percent, assuming that the measured shape is the correct one. This effect is therefore considered to be negligible.

Possibly the best evidence for the small effect of the target wall lies in the excellent agreement of the check data observed with thin target windows.

The energy of the deuteron beam of the cyclotron was measured by a magnetic deflection method and found to be 10.8 Mev. Correction for loss of beam energy in the target window and gas gave a value of 10.2 Mev for the beam energy at the center of the target. This energy value is assigned a standard error of ±2 percent.

B. Investigation of Existence of Excited State in He^4

Since there did not appear a well-resolved secondary proton group in the spectrum of short-range charged particles from the $He^3(d,p)He^4$ reaction products, bombardments of H^3 gas in each of the targets used for He^3 were made. The range distributions of short tracks from these bombardments were then compared in an effort to determine whether an irregularity in the He^3 distribution due to a secondary proton group might be detected. These range distributions are shown in Figs. 4 and 5.

Comparison of Figs. 4 and 5 indicates that there is no detectable low energy proton peak in the $d-He^3$ range distribution curve. In each set of curves the straggling of the particles is large, since these particles penetrated the target window at rather low energy. The number of tracks in the range 0–5 microns is too small, on account of the low detection efficiency of photographic emulsions for particles of this range. It is therefore reasonable to attribute these range distributions entirely to deuterons scattered elastically from nuclear mass 3 and to protons from the reaction $He^3(d,pn)He^3$. Energy considerations lead also to this conclusion.

From these range distribution curves it is possible to arrive at an upper limit for the cross section for production of low energy protons from the $He^3(d,p)He^4$ reaction, that is, the formation of an excited He^4 nucleus as a product particle. Referring now to Fig. 4, one may say that if there had appeared a proton group with a range of 20 microns and yield one-third as great as that of the deuteron group, it would have been detected. Comparison with the number of primary protons indicates a cross section less than 0.2×10^{-27} cm² for the production of the excited He^4 nucleus at a center-of-mass angle of 102.7°, corresponding to the 90° laboratory angle. The absence of this group of protons and of any

[11] E. J. Williams, Proc. Roy. Soc. (London) **169**, 531 (1939); Phys. Rev. **58**, 292 (1940); Revs. Modern Phys. **17**, 217 (1945).
[12] W. C. Dickinson and D. C. Dodder, LA-1182 (1950).

above it implies the absence of excited levels in He^4 below 20.9 Mev.

V. DISCUSSION

Brolley *et al.*[13] have pointed out the close similarity of the differential cross section of the $T(d,n)He^4$ reaction at 10.5-Mev bombarding energy with that of the $He^3(d,p)He^4$ reaction at 10.2 Mev in the present experiment. This result is somewhat to be expected in view of the similarity of the primary particles, and particularly because of the mirror characteristic of the two intermediate nuclei, He^5 and Li^5. There is a considerable amount of experimental and theoretical evidence that such mirror nuclei should show quite similar energy level structures.[14–16] Though the masses of these nuclei have not been measured, it seems probable, from a consideration of the near identity of the masses of H^3 (3.01695 MU) and He^3 (3.01693 MU) and the variation of the binding energy per nucleon for the stable isotopes of He and Li in the vicinity of nuclear mass 5, that the excitation energies of the compound nuclei He^5 and Li^5 do not differ by more than about 2 Mev.

It is somewhat instructive to consider the following extreme simplification. Suppose that in these two reactions each nucleon in the target nucleus interacts separately with each nucleon in the projectile nucleus. In the $d-T$ interaction, one would then observe three $n-p$, two $n-n$, and one $p-p$ interactions. For the $d-He^3$ interaction, the situation is different only in that one $n-n$ interaction is exchanged for a $p-p$ interaction. The fact that this exchange produces no extreme effect on the interactions as a whole seems good evidence for the equality of $p-p$ and $n-n$ forces, at least in the energy region in which the experimental observations were made.

The results here reported for upper limits of the excitation energy and cross section for the production of He^4 in an excited state from the $He^3(d,p)He^4$ reaction are not in disagreement with hose of Argo *et al.*,[17] who report the existence of such an excited state in the neighborhood of 21.5 Mev with an average cross section of 2×10^{-23} cm² over the energy range zero to 1.01 Mev. These data are based on observation of the $T(p,\gamma)He^4$

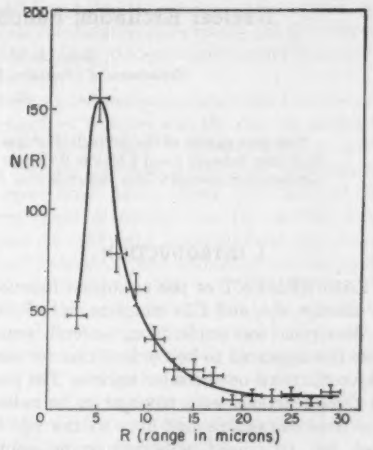

FIG. 5. Range distribution of short-range charged particles from d-T interaction, observed in identical geometry to that of Fig. 4. 474 tracks.

Benveniste and Cork[18] have recently reported an investigation of the interaction $He^4(p,p')He^{4*}$, using the proton beam of the Berkeley linear accelerator. For their 31-Mev proton energy, they set an upper limit for the differential cross section of 3×10^{-27} cm² at a laboratory angle of 45°. Their results are, again, not in disagreement with those reported here. Of interest is the fact that the inverse reaction to that here reported, $He^4(p,d)He^3$, was observed with a differential cross section of 8×10^{-27} cm² at 45° in the laboratory system.

ACKNOWLEDGMENTS

It is a pleasure to thank Dr. Louis Rosen for his supervision of this work, as well as Dr. J. L. Fowler and other members of the Los Alamos cyclotron group, who contributed helpful ideas and active assistance. Dr. E. S. Robinson, Mr. Maxwell Goldblatt, and Mr. R. M. Potter suggested the techniques for purification and handling of the gas samples. For the analysis of most of the plates, the author is indebted to Mmes. M. Bergstresser, M. Burghardt, E. Church, J. Erickson, F. Forbes, M. Gibson, O. Milligan, M. Osborn, F. Peet, A. Phillips, D. Squires, and V. Stovall.

[13] Brolley, Fowler, and Stovall, Phys. Rev. **82**, 502 (1951).
[14] L. W. Alvarez, Phys. Rev. **80**, 519 (1950).
[15] Brown, Snyder, Fowler, and Lauritsen, Phys. Rev. **82**, 159 (1951).
[16] D. R. Inglis, Phys. Rev. **82**, 181 (1951).
[17] Argo, Gittings, Hemmendinger, Jarvis, and Taschek, Phys. Rev. **78**, 691 (1950).
[18] J. Benveniste and Bruce Cork, Phys. Rev. **83**, 894 (1951).

Nuclear Excitation Functions, $Se^{82}(d,2n)Br^{82}$ and $Br^{81}(d,p)Br^{82}$

JOHN A. MISKEL* AND ARTHUR C. WAHL
Department of Chemistry, Washington University, St. Louis, Missouri†

(Received August 8, 1951)

The cross section of the $Se^{82}(d,2n)Br^{82}$ reaction was found to rise rapidly with deuteron energy, increasing from zero between 3 and 4 Mev to 0.93 barn at 9.7 Mev. The cross section of the $Br^{81}(d,p)Br^{82}$ reaction was redetermined around 9 Mev, which is near the maximum of the curve, and was found to be 0.17 barn.

I. INTRODUCTION

MEASUREMENT of the excitation functions for the d,p, d,n, and $d,2n$ reactions on Se^{82} with 10-Mev deuterons was undertaken several years ago because this appeared to be the best case for studying the three reactions on the same nucleus. The products of all three reactions were reported to be radioactive and to have reasonable half-lives so the well-known stacked foil technique[1] appeared to be applicable. Later, the discovery of the 67-second Se^{82} isomer[2] showed that resolution of the d,p and d,n yields would be very difficult, and work on these reactions was discontinued. However, work on the $d,2n$ reaction was completed and the results are described here. Also, the cross section at deuteron energies near 9 Mev of the $Br^{81}(d,p)Br^{82}$ reaction, whose excitation function had been previously measured,[1] was redetermined as a cross calibration.

II. EXPERIMENTAL PROCEDURES

Preparation of Foils

Selenium deposits of approximately 1 mg/cm² thickness were prepared by vacuum distillation of elemental selenium onto aluminum foils. The aluminum foils were about 3.6 mg/cm² thick, the thickness of each foil being determined by weighing prior to the deposition of the selenium. Seven selenium foils were obtained from each distillation by masking the aluminum foil in such a manner that seven circular selenium deposits were made. After distillation of the selenium onto the defined areas of the aluminum backing foil, the gross weight of the aluminum plus selenium was measured, and the weight of the selenium determined by difference. Individual small foils were then made by cutting out these deposits with a die. Uniform thickness of each selenium deposit was insured by the long path (~50 cm) from source to collector and the small diameter (~1.2 cm) of the deposit. The thickness of selenium obtained by weighing the individual small foils and assuming the aluminum backing to be uniform agreed with the value obtained from the weights of the large foils to within 1 percent. After being weighed, the selenium deposits were coated with zapon lacquer to prevent flaking; the thickness of the zapon was less than 0.025 mg/cm². The diameters of the deposits were determined by measurement with a comparator microscope. Each aluminum-selenium foil was then covered with a second aluminum foil of known thickness and the edges of this "sandwich" sealed with zapon.

Sodium bromide and potassium bromide deposits for the d,p reaction on bromine were prepared individually by evaporation of the salts onto half-mil aluminum in a bell-jar vacuum system. The area of a deposit was defined by a masking foil of aluminum. The aluminum collection foils were weighed before and after evaporation and the weight of salt (~1 mg/cm²) determined by difference.

Bombardment

The bombardment of a stack of foils was made in the beam defining slit system of the Washington University cyclotron. The deuteron beam at the normal target position passed through a narrow vertical slit and down an evacuated tube. Approximately 7.5 feet from the exit slit a circular $\frac{1}{8}$ inch defining slit was located. The target foils were one foot beyond this slit. The foils were mounted at the rear of a Faraday cage which could be moved in and out of the deuteron beam by means of a support rod through a Wilson seal. The deuteron current (~0.04 μa) was determined at 15-second intervals with an RCA electronic microammeter, Type WV-84A, connected to the Faraday cage. The total number of deuterons incident during a bombardment (~30 minutes) was then obtained by graphical integration of a current *vs* time plot.

The energy of the incident deuterons was determined by Grosskreutz[3] by measurement of the range of the deuterons in calibrated photographic emulsions. The energy was 9.93±0.07 Mev. The half-width of the energy spectrum was estimated to be roughly 80 kev from the distribution of deuteron track lengths after correcting for straggling in the emulsion.

The energy of the deuterons at any point in a stack of foils was obtained from the thickness of material through which the beam had passed by use of a range-energy curve for deuterons in aluminum constructed

* This paper is a portion of the dissertation presented by John A. Miskel in partial fulfilment of the requirements for the degree of Doctor of Philosophy in the Graduate School of Washington University, June 1949. AEC predoctoral fellow. Present address: Brookhaven National Laboratory, Upton, Long Island, New York.

† The cost of cyclotron operation for this work was supported by ONR.

[1] E. T. Clark and J. W. Irvine, Jr., Phys. Rev. **66**, 231 (1944).

[2] J. R. Arnold and N. Sugarman, J. Chem. Phys. **15**, 703 (1947).

[3] C. Grosskreutz (private communication).

from data given by Livingston and Bethe.[4] The relative atomic stopping power of aluminum, compared to air as 1.00, was taken as 1.50 for deuterons of 2.33 Mev. The range of deuterons in aluminum was then obtained from the range curve for deuterons in air; a correction being made for the variation of the relative atomic stopping power of aluminum with energy of the deuterons.

The stopping power of selenium per milligram thickness relative to the stopping power of aluminum was calculated to be 0.643; the relative atomic stopping power of aluminum used in the calculation was 1.50 and that of selenium was 2.82. This latter value was obtained from a smooth curve through a plot of relative atomic stopping powers measured by Mano, and reported by Livingston and Bethe,[4] against atomic number. The variation of the ratio of the relative atomic stopping power of selenium to aluminum with deuteron energy was neglected. If it is assumed that the variation of the stopping power of selenium with energy is similar to that of copper, for which data are available, the maximum error introduced by neglect of the variation is of the order of 1 percent since the selenium in a stack does only about 10 percent of the stopping.

The stopping powers of sodium bromide and potassium bromide per milligram thickness relative to aluminum were determined in a similar manner to be 0.73 and 0.725, respectively. The relative atomic stopping powers obtained from the stopping power Z curve were: sodium 1.35, potassium 1.96, and bromine 2.83.

As an over-all check on the energy determination and the range-energy relationships, the approximate range of deuterons in aluminum was measured. The deuteron current in the faraday cage was measured as various thicknesses of aluminum were placed in front of it. The mean range was found to be 101 mg/cm², which corresponds to an incident deuteron energy of 10.1 Mev, in satisfactory agreement with the value of 9.93 Mev obtained by Grosskreutz.[3]

Measurement of Activity

The activities, other than the 34-hour Br^{82}, produced by bombardment of selenium with low energy deuterons are short-lived compared to the 34-hour activity. The yield of the $Se^{82}(d,2n)Br^{82}$ reaction can therefore be determined by measurement of the activity of a selenium foil at a time sufficiently long after bombardment for the contribution of the other activities to be negligible, and extrapolation of this activity to bombardment time. The counting was done with a side window Geiger tube with a 1 mil (8.0 mg/cm²) Dural window one inch in diameter. The Geiger tube was 1.5 inches i.d. and had a 3 mil tungsten wire exposed for 3 inches. The selenium foil sandwiches were mounted on cardboard cards, covered with 3 mg/cm² of Cellophane, and placed 0.5 cm below the window when counted. In order to obtain the disintegration rate of the Br^{82}, the counter was calibrated in the empirical manner described in the next section.

The irradiated sodium or potassium bromide deposits were dissolved in water and the solution acidified with nitric acid and boiled to remove krypton activities. Silver bromide was then precipitated, digested, filtered onto tared filter paper, dried, and weighed for the chemical yield determination. The sample was then mounted on cardboard under half-mil aluminum and 3 mg/cm² Cellophane, and counted in the same geometry as the selenium foils. The counting efficiency of the silver bromide samples was found to be essentially the same as that of the selenium samples. This was to be expected since the two types of samples were very similar, the principal difference being the half-mil aluminum foil between the selenium and the cardboard. An infinity thick aluminum backing would have caused only a 10–15 percent difference.[5]

Calibration of Counter

Samples of Co^{60}, I^{131}, and P^{32} of known activity were obtained from the National Bureau of Standards and aliquots of these samples were mounted on thin zapon films and counted. A solution of RaD-E was compared with a standard RaD-E source issued by the Bureau of Standards (NBS No. 58) by mounting an aliquot of the solution on a Ag-Pd disk supplied by the Bureau and comparing the counting rates. A sample of this solution was mounted on thin zapon and counted. (The counter window was sufficiently thick to stop all RaD betas and RaF alphas.) Similarly, a UX solution was compared with weighed samples of U_3O_8, an empirically determined correction being applied for self-absorption of UX_2 radiation in the U_3O_8 samples. A 28.5 mg/cm² aluminum absorber was placed between UX samples and the window to absorb UX_1 and other soft radiations.

Aluminum absorption curves were taken with all samples and the counting rates extrapolated to zero absorber. The gamma-contributions were subtracted from the observed activities. The size of the samples was limited to 0.5 cm diameter so the counting efficiency was essentially that of a point source. It had been previously found that a point source 0.5 cm off center counted ~97 percent as efficiently as when centered. All samples mounted on zapon were thin (<2 percent of the half-thickness of the radiation in aluminum). Results of the calibration are summarized in Table I.

The low efficiency for the soft Co^{60} beta-particles is probably due to the inaccuracy of the long (about a factor of two) extrapolation to zero absorber. The intermediate 25 percent value was chosen for the moderately soft Br^{82} beta-particles because the extrapolation to zero absorber is still quite long, and similar errors may be involved. It seems unlikely that extrapolation errors

[4] M. S. Livingston and H. A. Bethe, Revs. Modern Phys. 2, 271 (1937).

[5] Conference on Absolute β Counting, Nuclear Science Series, Preliminary Report No. 8, October, 1950.

TABLE I. Beta-counting efficiencies. Thin samples mounted on thin zapon, 0.5 cm from 1.0 inch diameter window. Values corrected to zero absorber thickness.

Sample	E_{max}(Mev)	Efficiency (percent)
UX_2	2.32	34
P^{32}	1.71	30
RaE	1.17	29
I^{131}	0.60	30
Br^{82}	0.47	(25)
Co^{60}	0.31	19
Calculated		27–32[a]

[a] The larger value was calculated assuming that all betas passing through the window are counted: the smaller value was calculated by assuming that only betas passing through the window and not striking the $\frac{1}{16}$-inch counter wall supporting the window are counted.

would be any greater than for Co^{60} or any less than for I^{131}, so the 25 percent value is probably good to ±5 percent.

The actual counting rate of Br^{82} between two half-mil aluminum foils on cardboard and under 3.0 mg/cm² Cellophane was found to be 60 percent of the counting rate of Br^{82} mounted on zapon, extrapolated to zero absorber and corrected for the gamma-ray contribution. Therefore, the counting efficiency for Br^{82} radiation from the selenium or silver bromide samples was 15 percent.

III. RESULTS

Five sets of measurements of the $Se^{82}(d,2n)Br^{82}$ reaction, in which the deuteron beam current was not measured, yielded relative values of the cross section as a function of energy. Two sets of foils were used in these measurements. Two sets of measurements in which the beam current was measured gave absolute values of the cross section as a function of energy. Fresh sets of foils were used in each of these measurements. The data are plotted in Fig. 1. The relative values are normalized at the highest energy, 9.7 Mev.

Four values of the $Br^{81}(d,p)Br^{82}$ cross section were obtained from two independent runs in which the beam current was measured. These values, plotted in Fig. 1, are a little less than half those obtained by Clark and Irvine.[1] The discrepancy is probably due mainly to errors in the different methods of absolute counting. Clark and Irvine used for their absolute counting a platinum screen cathode gamma-ray counter whose

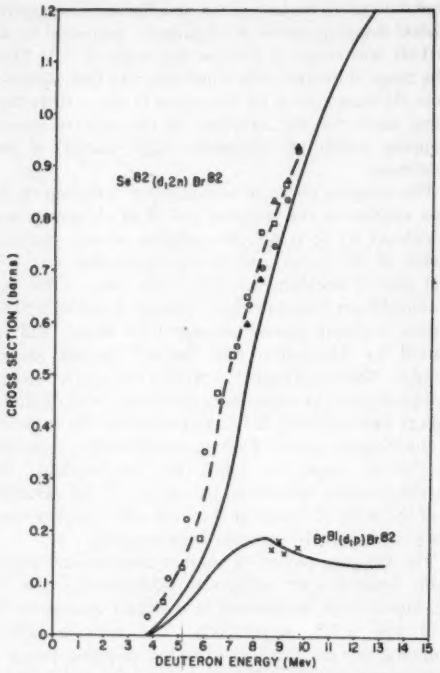

FIG. 1. Excitation functions. $Se^{82}(d,2n)Br^{82}$: △, absolute cross section measurements. ○ (average of three runs on one set of foils) and □ (average of two runs on another set of foils), relative measurements normalized to $\sigma = 9.3\times10^{-26}$ cm² at 9.7 Mev. Broken line, experimental. Solid line, theoretical for the formation of the compound nucleus [E. Konopinski and H. Bethe, Phys. Rev. **54**, 130 (1938)], with $r_0 = 1.50$ (nuclear radius $= r_0 A^{\frac{1}{3}} \times 10^{-13}$ cm), deuteron radius 1.1×10^{-13} cm, and sticking probability = 1.0. $Br^{81}(d,p)Br^{82}$: ×, absolute cross-section measurements. Solid line, Clark and Irvine (see reference 1) curve fitted to our experimental points.

efficiency as a function of gamma-ray energy had been calibrated.

The relative values of the cross sections plotted in Fig. 1 are believed to be reliable to 5 or 10 percent. The uncertainty in the absolute values may be as large as 20 or 30 percent because of uncertainties in the absolute beta-counting calibration.

Elastic Scattering of Protons from Mg^{24}

F. P. Mooring,* L. J. Koester, Jr.,† E. Goldberg, D. Saxon, and S. G. Kaufmann*‡§
University of Wisconsin, Madison, Wisconsin

(Received July 16, 1951)

The differential scattering cross section has been determined for protons scattered elastically from Mg^{24} at a laboratory angle of 164°±5°. The targets consisted of thin $Mg^{24}F_2$ films evaporated onto thick graphite. Protons scattered elastically from Mg^{24} were selected by a 90° magnetic analyzer and were counted by a proportional counter. At least nine anomalies occur in the cross section between 0.40 Mev and 3.95 Mev, indicating the excitation of nine levels of the compound nucleus, Al^{25}. At several of the resonances, competing reaction cross sections have been shown to be relatively small.

I. INTRODUCTION

THE nuclear spectroscopist has tended to neglect the elastic scattering of charged particles by atomic nuclei as a method for studying nuclear spectra. The complication of the experimental results by coulomb scattering is possibly the reason for this neglect, yet this complication by its very nature allows the nuclear physicist to obtain from scattering data information about the excited states of compound nuclei that other nuclear reactions cannot of themselves reveal. The recent experiments[1–8] at the University of Wisconsin on the elastic scattering of charged particles from nuclei have demonstrated clearly the power of this form of nuclear spectroscopy. The present report is concerned with the applications of such methods to the study of excited states of Al^{25} which are formed by protons incident on Mg^{24}.

The theory of elastic scattering of protons from nuclei with spin zero has been worked out in detail for the case of no competing reactions. (For discussions of the scattering equation see the references given in footnotes 7 and 8.) For such nuclei the theory allows one to make determinations of the angular momenta of the excited states of the compound nucleus and their parities relative to the ground state of the bombarded nucleus. One might expect the theory to be a good approximation for scattering resonances for which the elastic proton width is large compared to the sum of all other partial widths.

Mg^{24} has spin zero in the ground state and hence satisfies the first assumption of the theory. Protons with energies available from the Wisconsin electrostatic generator incident on Mg^{24} can initiate the following reactions:

$$p+Mg^{24}\rightarrow Al^{25*}\rightarrow Mg^{24}+p, \quad (1)$$

$$p+Mg^{24}\rightarrow Al^{25*}\rightarrow Mg^{24*}+p'; \quad Mg^{24*}\rightarrow Mg^{24}+h\nu, \quad (2)$$

$$p+Mg^{24}\rightarrow Al^{25*}\rightarrow Al^{25}+h\nu; \quad Al^{25}\rightarrow Mg^{25}+\beta^+. \quad (3)$$

The cross section for reaction (3) should be relatively small compared with the elastic process. As for reaction (2), only direct measurements will allow one to make any statement about the relative values of the elastic and inelastic cross sections.

Previously, little information has been available concerning the excited states of Al^{25}. Curran and Strothers[9] bombarded thin targets of non-isotopic magnesium oxide with protons in the energy range from 0.150 Mev to 1.00 Mev and counted both gamma-rays and positrons. They found the half-life of the positron activity to be approximately 7 sec. Since Al^{26} was known to have approximately a 7-sec half-life and since Al^{27} was known to be the only stable aluminum isotope, they attributed the resonances which exhibited a positron activity to the reaction $Mg^{25}(p,\gamma)Al^{26}$ and those which did not they attributed to the reaction $Mg^{26}(p,\gamma)Al^{27}$. We now know that Al^{25} has a half-life of 6.3 sec;[10] hence, one might question the assignments of Curran and Strothers, especially since Mg^{24} is the principal isotope in ordinary magnesium.

Other workers[11,12] have since studied the (p,γ) reactions of the magnesium isotopes in a manner similar to Curran and Strothers. Tangen[13] knowing that both Al^{25} and Al^{26} have about the same half-lives, assigned from intensity considerations the (p,γ) resonances at 222 kev and 417 kev to the reaction, $Mg^{24}(p,\gamma)Al^{25}$. Using

* Now at Argonne National Laboratory, Chicago, Illinois.
† AEC Predoctoral Fellow. Now at University of Illinois, Urbana, Illinois.
‡ The Mg^{24} isotope was supplied by the Y-12 Plant, Carbide and Carbon Chemicals Division, Union Carbide and Carbon Corporation, Oak Ridge, Tennessee, and was on allocation from the AEC.
§ Work supported in part by the AEC and in part by the Wisconsin Alumni Research Foundation.
[1] Bender, Shoemaker, Kaufmann, and Bouricius, Phys. Rev. 76, 273 (1949).
[2] Shoemaker, Faulkner, Kaufmann, Bouricius, and Mooring, Phys. Rev. (to be published).
[3] Gerson Goldhaber and R. M. Williamson, Phys. Rev. 82, 495 (1951).
[4] S. Bashkin and H. T. Richards (to be published).
[5] Kaufmann, Mooring, Koester, Jr., and Goldberg, paper in preparation.
[6] Laubenstein, Laubenstein, Koester, Jr., and Mobley, Phys. Rev. 84, 12 (1951).
[7] R. A. Laubenstein and M. J. W. Laubenstein, Phys. Rev. 84, 18 (1951).
[8] H. L. Jackson and A. I. Galonsky, paper in preparation.
[9] S. C. Curran and J. E. Strothers, Proc. Roy. Soc. (London) (A)172, 79 (1939).
[10] H. Bradner and J. D. Gow, Phys. Rev. 74, 1559 (1948).
[11] Hole, Holtzmark, and Tangen, Naturwiss 28, 399 (1940).
[12] R. Tangen, Kgl. Norske Videnska Selskabs Forh. Skrifter, No. I (1946).

TABLE I. Analysis of magnesium isotope.

Mass analysis			Spectroscopic analysis	
Isotope	Atom percent	Error	Element[a]	Percent
Mg^{24}	99.50	±0.02	Ag	<0.04
Mg^{25}	0.34	±0.01	Ca	<0.08
Mg^{26}	0.16	±0.01	Cu	<0.04
			Fe	<0.04
			Na	0.08
			Si	<0.05

[a] Impurities other than those listed were not detected.

isotopic targets Grotdal, *et al.*,[13] later confirmed the assignments of Tangen.

II. EXPERIMENTAL ARRANGEMENT

Monoenergetic protons produced by the Wisconsin electrostatic generator in conjunction with the 90° electrostatic analyzer, were used to bombard thin films of $Mg^{24}F_2$ evaporated onto spectroscopically pure graphite backings. Protons scattered elastically from Mg^{24} at a laboratory angle of 164°±5° were selected by a 90° magnetic analyzer[2] and were counted by a proportional counter and conventional counting circuits. The elastic scattering yield was observed as a function of incident proton energy over the energy range from approximately 0.40 Mev to 3.95 Mev. The experimental points were taken about 3 kev apart except at resonances where they were taken somewhat closer together. During the initial survey run the resolution of the 90° electrostatic analyzer was maintained at 1000. Later, for particular resonances, the resolution was raised to higher values.

The target chamber was insulated from the rest of the apparatus by Lucite spacers. Secondary electron currents were prevented from passing into or our of the target chamber by a suitably placed electron barrier maintained 300 volts negative with respect to the rest of the apparatus. A current integrator,[14] dependable to ±0.1 percent for ion beams of a few hundredths of a microampere or more, was used to determine the total proton charge incident on the target during a run.

TABLE II. Characteristics of targets.

Target No.[a]	Target material	Backing	Use	Target thickness for 1-Mev protons (kev)[b]
1	$Mg^{24}F_2$	graphite	Elastic scattering, better resolution data	1.4
3	$Mg^{24}F_2$	graphite	Elastic scattering, below 0.85 Mev	2.3
5	$Mg^{24}F_2$	graphite	Elastic scattering above 0.85 Mev	6.3
6	$Mg^{24}F_2$	1000A nickel	Inelastic scattering	10.1
7	non-isotopic magnesium	1000A nickel	Inelastic scattering	>60

[a] Targets were numbered according to position on target holder.
[b] Includes thickness of tantalum in target.

[13] Grotdal, Lönsjö, Tangen, and Bergström, Phys. Rev. **77**, 296 (1950).
[14] G. M. B. Bouricius and F. C. Shoemaker, Rev. Sci. Instr. **22**, 183 (1951).

III. TARGETS

In view of the large number of (p,γ) resonances previously seen with non-isotopic magnesium targets below 1 Mev,[9,11–13] of which only two have been identified as arising from the reaction[13] $Mg^{24}(p,\gamma)Al^{25}$, it was decided to use isotopic targets in the present experiment. The Mg^{24} isotope was obtained in the form of MgO from the Union Carbide and Carbon Corporation, Oak Ridge, Tennessee. An analysis furnished with the oxide is shown in Table I.

Because MgF_2 is easily evaporated to form uniform durable films, the MgO was converted to MgF_2. The chemistry was performed in connection with an earlier experiment.[5] The targets used during the elastic scattering runs consisted of thin $Mg^{24}F_2$ films evaporated onto thick spectroscopically pure graphite backings. Thin 1000A nickel-backed targets were used during investigations of low energy proton groups. Table II lists the characteristics of the targets used. The target material was evaporated from a tantalum boat. Hence, each target contained a small amount of tantalum which increased the absorption thickness of the targets but in no other way affected the results of the experiment.

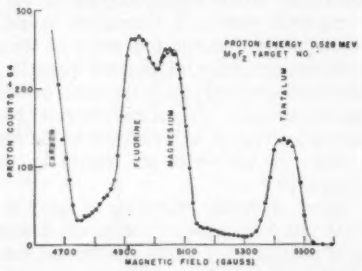

FIG. 1. Momentum analysis taken with the $Mg^{24}F_2$ target No. 3 at a proton bombarding energy of 0.528 Mev.

IV. MAGNETIC ANALYZER

A 90° magnetic analyzer[2] was used to select the proton groups scattered from the various elements in the target. Figure 1 shows a momentum analysis taken with target No. 3 at an incident proton energy of 0.528 Mev. During the elastic scattering yield measurements the field of the magnetic analyzer was adjusted to count only the protons scattered elastically from Mg^{24}. Frequent momentum analyses similar to that shown in Fig. 1 were taken throughout the experiment to insure that the field was being properly adjusted to count elastic protons from Mg^{24}.

The magnetic field was measured with a proton resonance detection unit of the type described by Knoebel

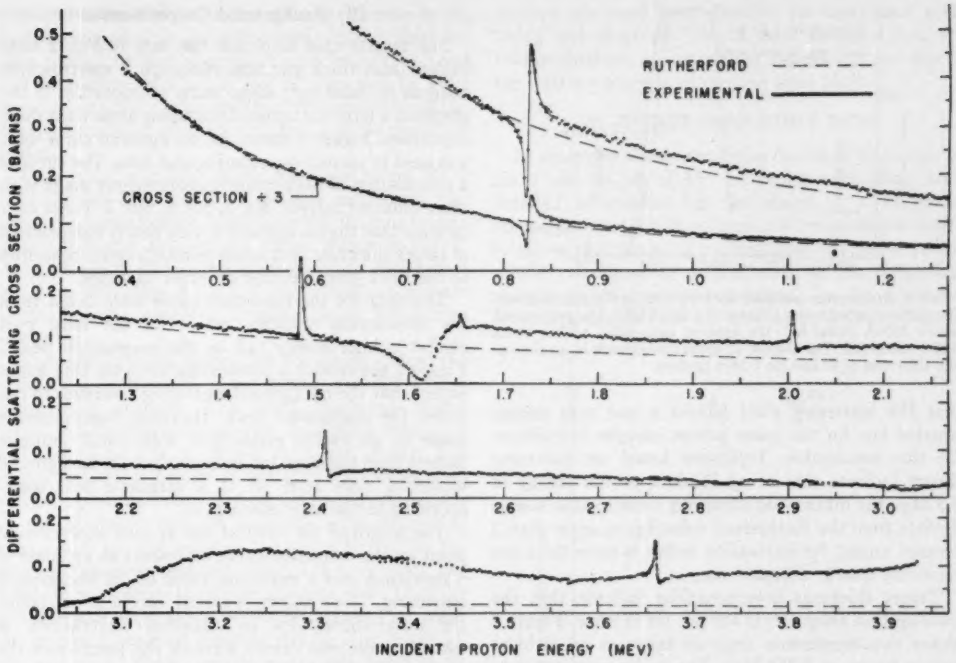

FIG. 2. Differential scattering cross section in barns per steradian for protons scattered elastically from Mg^{24} at a laboratory angle of 164°±5° as a function of incident proton energy.

and Hahn.[15] The resonant frequency of the proton resonance detector was measured with a war surplus Army Signal Corps frequency meter, BC-221-AF, the calibration of which was checked periodically against a standard 1000 kilocycle crystal. Field measurements were easily reproducible to within the 0.1 percent needed in the present experiment.

For fields above 13,000 gauss, field inhomogeneities apparently prevented a proton resonance signal large enough to be detected. Above 13,000 gauss a flip coil and fluxmeter was used to measure the magnetic field. Fortunately, the differential cross section for protons scattered elastically from Mg^{24} greatly exceeds that for protons scattered elastically from F^{19} at incident proton energies above 3.1 Mev. (Figure 2 shows a large rise in the Mg^{24} cross section at these energies.) Thus, the number of protons scattered at 164° from Mg^{24} greatly exceeded the number scattered from F^{19}. If the magnetic field became either too high or too low to count the protons scattered from Mg^{24}, a lower counting rate would occur. Hence, above a bombarding energy of 3.1 Mev, the proton counting rate could be used to indicate whether or not the magnetic field was properly adjusted.

[15] H. W. Knoebel and E. L. Hahn, *A Transition Nuclear Magnetic Resonance Detector*, Preliminary Report, University of Illinois.

V. COUNTING ARRANGEMENT

A proportional counter was used to count the charged particles. The counter consisted of a 2-in. brass cylinder with an insulated 0.005-in. molybdenum wire anode. The counter gas was a mixture of argon and 2 percent carbon dioxide.

Alpha-particles arising from the reaction $F^{19}(p,\alpha)O^{16}$ formed a background for the elastically scattered protons over much of the energy range covered. By properly adjusting the counter voltage and gas pressure a large differentiation in pulse sizes was obtained. Two similar scalers were used to record these pulses. One was biased to count all the particle pulses, while the other was biased to count only the alpha-pulses. The proton yield measurements represent the differences between the readings obtained with the two scalers.

VI. DISCUSSION OF RESULTS

(A) Cross-Section Determination

Figure 2 shows, as a function of incident proton energy, the differential scattering cross section in barns per steradian for protons scattered elastically from Mg^{24} at a laboratory angle of 164°±5°. The differential cross-section values were determined by assuming that the scattering was Rutherford below 0.8 Mev. The fact

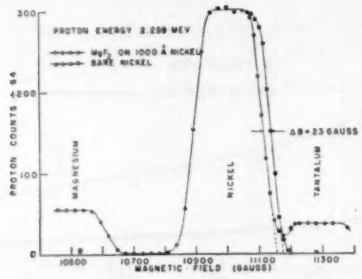

FIG. 3. Momentum analyses showing shift in the nickel group. The circles represent data taken with a thin $Mg^{24}F_2$ film evaporated onto a 1000A nickel foil; the squares, data taken with a blank 1000A nickel foil. The shift of 23 gauss corresponds to an absorption thickness of 10 kev for 1-Mev protons.

that the scattering yield follows a one over energy squared law for the lower proton energies is evidence for this assumption. Estimates based on scattering theory indicate that at an incident proton energy of 0.5 Mev the differential scattering cross section should deviate from the Rutherford value by no more than 2 percent unless the interaction radius is more than five times the usually accepted one.

Target thickness determinations indicate that the cross-section assignments are not far in error. Figure 3 shows two momentum analyses taken at an incident proton energy of 2.258 Mev. The circles represent data taken with a thin $Mg^{24}F_2$ target evaporated onto a 1000A nickel foil; the squares, data taken with a blank 1000A nickel foil. The shift of the high energy edge of the nickel group corresponds to the energy lost by a proton in passing twice through the $Mg^{24}F_2$ film. This shift at half-maximum is 23±5 gauss, which corresponds to an absorption thickness for the $Mg^{24}F_2$ film (including the tantalum impurity) of 10.1±2.2 kev for 1-Mev protons. From this one calculates for the differential scattering cross section at 1 Mev a value of 0.23±0.06 barn per steradian, whereas one gets from the assumption of Rutherford scattering at low energies a value of 0.233±0.008 barn per steradian for the cross section at 1 Mev.

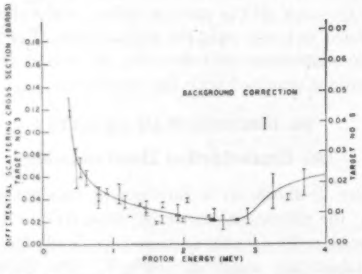

FIG. 4. Background correction curves for targets No. 3 and No. 5. The data are a compilation of background measurements made with three different graphite backings.

(B) Background Corrections

The targets used to obtain the data in Fig. 2 were backed with thick graphite. Although a spectroscopic analysis revealed only slight traces of impurities in the graphite, a large background scattering arose from these impurities. Figure 4 shows the background curve that was used to correct the experimental data. The curve is a compilation of background measurements made with three different targets, No. 1, No. 3, No. 5. These data indicate that the background is very nearly independent of target thickness, but arises primarily from impurities in the thick graphite used as target backings.

The data for the correction curve were taken from the momentum analyses, which for the most part exhibit a high energy tail on the magnesium peaks. Figure 1 shows such a momentum analysis. One might expect that the background scattering continues to rise under the magnesium peak. However, measurements made in an earlier experiment with blank graphite targets from the same lot[1] indicate that the background scattering does level off at a magnetic field corresponding to the magnesium peak.

The length of the vertical line at each experimental point on the correction curve represents an estimate of a maximum and a minimum value of the background scattering. These estimates exceed, except at one point, the uncertainties due to statistical fluctuations. A smooth curve was drawn through the points and the scattering yield measurements were corrected accordingly.

(C) Discussion of Curve

The differential scattering cross section curve (Fig. 2) shows several interesting features. At least nine different scattering anomalies occur in the cross section between 0.40 Mev and 3.95 Mev corresponding to excited states of Al^{25}. The fluctuation in the experimental points at 2.91 Mev was repeated several times and appears to be real. Above 3.7 Mev the cross section rises, probably because of the presence of a broad resonance somewhere above 3.95 Mev.

The resonance reported by Grotdal, *et al.*,[13] for an incident proton energy of 0.417 Mev was not observed in the present experiment, although the differential scattering cross-section measurements extended down to a bombarding energy of 0.396 Mev. A resonance which is markedly asymmetric, i.e., has a dip of small area compared to its rise, will usually cause an observable anomaly even though the resonance width is small compared to the spread in proton energies, whereas a narrow resonance symmetric about the Rutherford level might have been missed because of inadequate resolution. On the other hand, the resonance may occur below a bombarding energy of 0.396 Mev.

For comparison, the theoretical Rutherford cross section is shown in Fig. 2 over the entire range of bombarding energies. On the low energy side of the 0.83-Mev resonance the observed cross-section values follow

closely the expected coulomb scattering, whereas on the high energy side it is about 10 percent higher. Since the data below 0.85 Mev were taken with target No. 3 and the data above with target No. 5, there may be some question concerning the reality of this deviation. However, the available evidence indicates that the deviation is real.

Data taken with both target No. 3 and target No. 5 near the 0.83-Mev and the 1.49-Mev resonances give the same normalization factor between the two targets and lead to the cross-section values shown in Fig. 2. Also, a series of momentum analyses taken with target No. 1 on both sides of the 0.83-Mev resonance appears to confirm the observed deviation from Rutherford scattering.

The experimental points fall somewhat below the theoretical Rutherford cross section for the lowest bombarding energies. This small deviation, which becomes more pronounced with decreasing energy, is believed to be due to target thickness effects. The energy lost by a proton in the target increases with decreasing proton energy. Hence, the spread in momenta of the scattered protons increases with decreasing energy, and as a consequence the image formed by the magnetic analyzer becomes wider. For sufficiently low bombarding energies the image becomes wider than the exit slits and some of the scattered protons that enter the magnetic analyzer chamber will be intercepted by the exit slits. These considerations are believed to account for the deviation of the experimental points from the Rutherford values below 0.45 Mev.

(D) The Effect of Mg^{25} and Mg^{26}

The magnesium fluoride used in this experiment contained 99.5 percent Mg^{24}, 0.34 percent Mg^{25}, and 0.16 percent Mg^{26} (see Table I). The contaminating magnesium isotopes are believed to have had a negligible effect on the results of the present experiment. In order that the elastic scattering yield of Mg^{25} be as much as 5 percent of the yield from Mg^{24}, the differential scattering cross section of Mg^{25} must be 14.6 times that of Mg^{24}. Except possibly at resonances, it is unlikely, in view of scattering theory, that the cross section of Mg^{25} so greatly exceed that of Mg^{24}. A similar argument also holds for the effect of Mg^{26}.

(E) Evidence for Scattering from Magnesium

Early in the experiment, in order to see if the resonances being observed were caused by scattering from Mg^{24}, short yield curves of protons scattered elastically from non-isotopic magnesium, Mg^{24}, and F^{19} were taken for incident proton energies near 2.00 Mev. The results are shown in Fig. 5. A scattering resonance was observed with an ordinary magnesium metal target. With the $Mg^{24}F_2$ target, when the magnetic field was adjusted to count protons scattered elastically from Mg^{24}, a resonance was observed at the same energy and with a similar shape; but, when the field was adjusted for protons scattered from fluorine, no anomalous scattering was observed. This is good evidence that the results obtained in the present experiment are due to the elastic scattering of protons from Mg^{24}.

VII. HIGHER RESOLUTION DATA

In analyzing elastic scattering data it is important to know the shapes of the scattering anomalies, since detailed information on the shape of a scattering anomaly permits, in most cases, an unambiguous determination of the angular momentum and relative parity of the corresponding excited state of the compound nucleus. In the present experiment, the shapes of the broad resonances near 1.6 Mev and 3.1 Mev (Fig. 2)

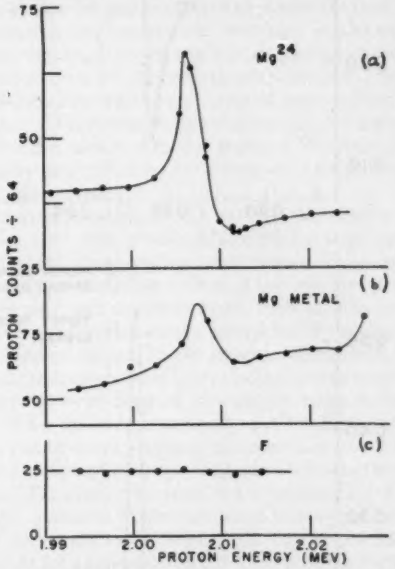

FIG. 5. Elastically scattered proton yields from (a) Mg^{24}, (b) non-isotopic magnesium metal, and (c) F^{19}, for bombarding energies near 2.000 Mev.

are though to have been little affected by target thickness and energy resolution. Except for the 3.66 Mev resonance, better resolution data were taken for all the narrow resonances. Target No. 1 was used for all of these measurements, the results of which are shown in Fig. 6. Repeated data near 2.91 Mev merely served to confirm the existence of a level in this region, and the results are not shown. Attempts to reach again energies above 3.5 Mev failed, and a pressing time schedule prevented further investigation of the 3.66-Mev level.

In each of the curves of Fig. 6 a triangle is used to represent the energy distribution in the incident proton beam. The cited proton energy spread is the ratio, in percent, of the width of the triangular distribution at half-maximum to the incident proton energy. A rec-

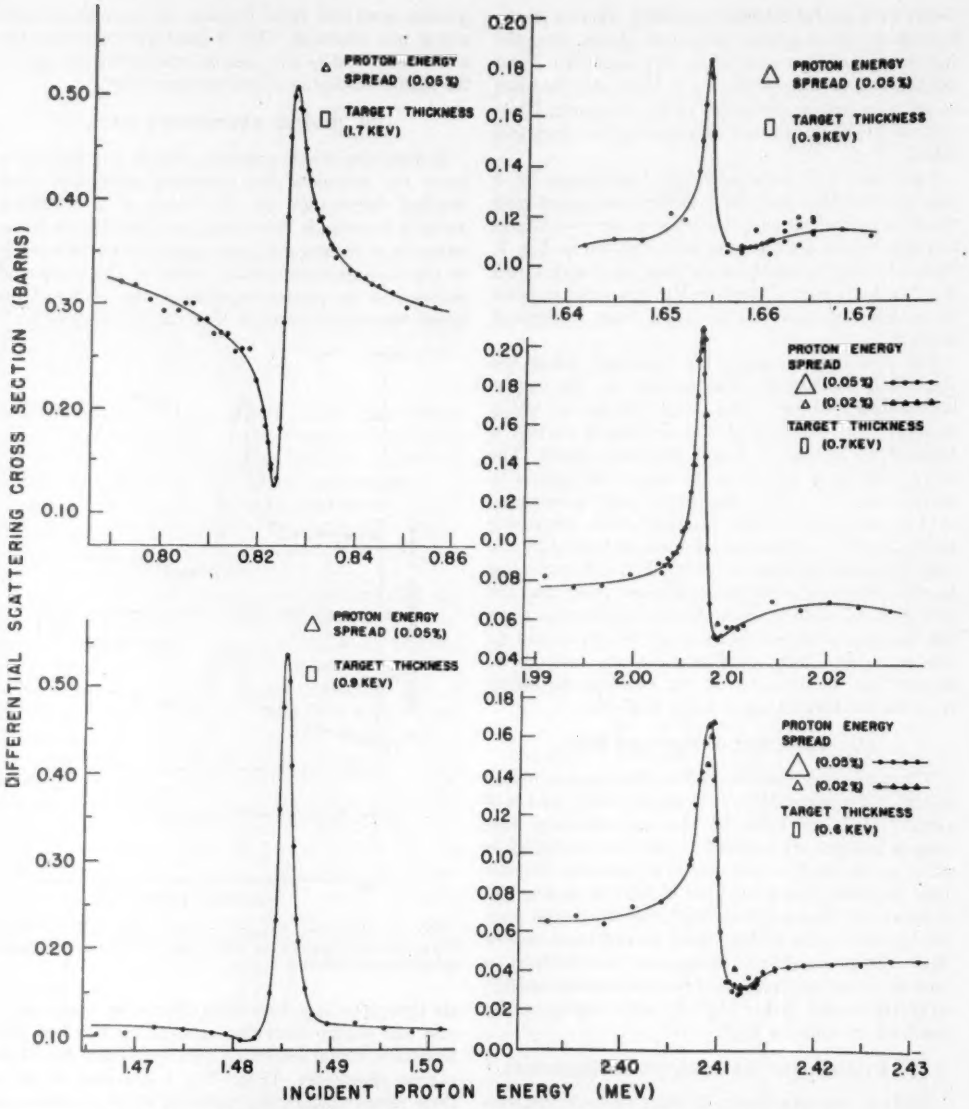
DIFFERENTIAL SCATTERING CROSS SECTION (BARNS)
INCIDENT PROTON ENERGY (MEV)
PROTON ENERGY SPREAD (0.05%)
TARGET THICKNESS (1.7 KEV)
PROTON ENERGY SPREAD (0.05%)
TARGET THICKNESS (0.9 KEV)
PROTON ENERGY SPREAD (0.05%)
PROTON ENERGY SPREAD (0.02%)
TARGET THICKNESS (0.7 KEV)
PROTON ENERGY SPREAD (0.05%)
TARGET THICKNESS (0.9 KEV)
PROTON ENERGY SPREAD (0.05%)
PROTON ENERGY SPREAD (0.02%)
TARGET THICKNESS (0.6 KEV)

FIG. 6. A compilation of the better resolution data taken with target No. 1 over narrow resonances.

tangle is used to represent the target thickness at the resonance energy. A visual comparison of the energy spread and target thickness with the widths of the peaks and dips in the cross section at resonance gives some indication of how well the shapes of these resonances have been determined. In no case can it be said that target thickness and energy spread do not have an appreciable influence upon the observed shapes of the narrow resonances. No satisfactory method of correcting elastic scattering data for target thickness and energy spread is known to the authors.

VIII. COMPETING REACTIONS

In the simple form of scattering theory one assumes that there are no reactions other than elastic scattering and that the bombarded nucleus has zero spin in the

ground state. The second of these assumptions is automatically satisfied by the choice of Mg^{24} as a target nucleus. In order to get an estimate of the relative value of the inelastic scattering cross section, momentum analyses were taken at several of the higher energy resonances. A non-isotopic magnesium metal target evaporated onto a 1000A nickel foil (target No. 7) was used in most of these measurements. For certain small regions target No. 6, a $Mg^{24}F_2$ nickel-backed target, was used.

Only at the 2.41-Mev resonance (Fig. 2) was a low energy proton group found that could be definitely attributed to the inelastic scattering of protons from Mg^{24}. At a bombarding energy of 2.416 Mev a low energy proton group was found with the magnesium metal target No. 7 at a magnetic field corresponding to the excitation of the well-known 1.38 Mev level[16] in Mg^{24}. This group persisted when the $Mg^{24}F_2$ target No. 6 was used. Short excitation curves taken for both the elastic and inelastic groups showed a resonance at the same incident proton energy. These data indicate that the low energy group is due to the inelastic scattering of protons from Mg^{24}, leaving it in the 1.38-Mev excited state. Estimates based on relative target thicknesses and observed yields indicate that at the 2.42-Mev resonance the differential inelastic scattering cross section is about 10 percent to 15 percent of the off-resonance elastic value.

Momentum analyses were also taken at the 2.01-Mev, 2.92-Mev, and the 3.1-Mev resonances. At each resonance a weak proton group was found that may be due to the inelastic scattering of protons from Mg^{24}. However, the evidence is anything but conclusive. Assuming that the observed low energy groups are inelastic proton groups from Mg^{24}, one finds that at the 2.01-Mev resonance the inelastic cross section is less than one percent of the off-resonance elastic value; at the 2.92-Mev resonance the inelastic value is about 10 percent of the off-resonance elastic value; and at the 3.1-Mev resonance the inelastic value is less than 2 percent of the elastic value at 3.25 Mev.

The level in Mg^{24} responsible for the observed low energy groups at the 2.92-Mev and the 3.1-Mev resonances, if they are indeed due to Mg^{24}, is the 1.38-Mev level. At the 2.01-Mev resonance a low energy proton group occurs at a magnetic field corresponding to the excitation of a level in magnesium 0.78 Mev above the ground state. The only reported level in any of the magnesium isotopes that can account for this level is the 0.83-Mev level in Mg^{24} observed by Mandeville.[17] The agreement is within experimental uncertainties. However, since a non-isotopic target was used for the momentum analysis at the 2.01-Mev resonance, the observed weak proton group may arise from some unknown level in either Mg^{25} or Mg^{26}.

No further investigations of the occurrence of inelastic scattering at any of the other resonances were made. Except possibly at the 2.41-Mev resonance, it is unlikely that competing processes have effects on the narrow resonances comparable to the large distortions introduced by target thickness and the spread in proton energies. For this reason, extensive measurements of the cross sections of the competing reactions did not appear profitable.

IX. CONCLUSIONS

Analyses of other elastic scattering data have recently been completed at the University of Wisconsin. By applying scattering theory to the observed differential cross section for protons scattered elastically from O^{16}, Laubenstein and Laubenstein[7] were able to infer values for the angular momenta and relative parities of several excited states of F^{17}. By analyzing the data of Goldhaber and Williamson[3] on the scattering of protons from C^{12}, Jackson and Galonsky[8] found that the angular momenta and relative parities of excited states of N^{13} appear to be uniquely determined by the shapes of the elastic scattering resonances.

The interpretation of the data in the oxygen and carbon work was greatly hampered by large uncertainties in the cross-section values introduced by experimental difficulties. The widths of the resonances were for the most part relatively large; consequently, target thickness and proton energy spread had little effect on the observed shapes. In the present experiments, it is thought that the cross-section values are known to within 10 percent over most of the energy range covered. Except for the wide resonances near 1.6 Mev and 3.1 Mev, the observed shapes of the resonances were considerably affected by target thickness and proton energy spread. For these resonances the determination of the angular momenta of the compound states may be difficult. In several cases, however, it may be possible to eliminate for a resonance all but a few possible J-values by comparing the observed shape with predicted shapes.

At the higher energies the cross section rises, indicating the presence of a wide level above 3.95 Mev that reaches down to affect the scattering at lower energies. Such a resonance will introduce interference effects that will complicate the analysis of the 3.66-Mev resonance and possibly the 3.1-Mev resonance.

No attempt has been made in this report to state accurate resonance energies since they can be determined for a scattering resonance only by a theoretical analysis of the data. The numbers cited are used merely to identify particular resonances and are not intended to indicate true resonance energies. Attempts are at present being made to interpret the data in terms of dispersion theory.

The authors would like to express their appreciation to Professor R. G. Herb for his constant interest and encouragement throughout the experiment.

[16] D. E. Alburger and E. M. Hafner, Revs. Modern Phys. 22, 406 (1950).
[17] C. E. Mandeville, Phys. Rev. 76, 436 (1949).

A Theoretical Calculation of the Inelastic Scattering of 90-Mev Neutrons by Deuterons*

GEOFFREY F. CHEW
Department of Physics, University of Illinois, Urbana, Illinois
(Received August 7, 1951)

The number and distribution of disintegration protons to be expected from the $H^2(n, p)$ reaction at 90-Mev incident neutron energy is calculated phenomenologically. No assumption about the character of nuclear forces is required, the impulse approximation allowing direct use of high energy $n-p$ and $p-p$ scattering data. Agreement with experiment is satisfactory, there being no evidence for a difference between $n-n$ and $p-p$ interactions.

INTRODUCTION

IN a previous paper,[1] hereafter referred to as I, a method has been set up for treating high energy $n-d$ inelastic scattering. The method, called the impulse approximation, requires a knowledge of the $n-p$ and $n-n$ scattering amplitudes as well as the deuteron wave functions, continuum and discrete. It does not, however, require a knowledge of the nature of nuclear forces. The first experiment on the $H^2(n, p)$ reaction at high energy has now been carried out at Berkeley by Powell and associates,[2] using the 90-Mev neutron beam from stripped deuterons. Since information is also available on $n-p$ scattering at this same energy,[3] it is possible to test some of the predictions of the impulse approximation. Such a comparison of theory with the 90-Mev experiment is carried out in this paper as a sequel to I. In part I it was also pointed out that if one is confident of the accuracy of the impulse approximation, one might derive the magnitude of the $n-n$ amplitude from the $H^2(n, p)$ experiment. This derivation will be performed here.

It is worth explaining qualitatively why the inelastic $n-d$ scattering is a more useful application of the impulse approximation than the elastic, when both are theoretically tractable by the method. The difference lies in the relative importance of interference effects. Elastic scattering is, so to speak, completely coherent. It has its origin mainly in small momentum transfers and no observation can be made to tell whether the neutron or the proton in the initial deuteron was the struck particle. Consequently there is interference between $n-p$ and $n-n$ scattered amplitudes and a knowledge of the phases is necessary to make a prediction. Such a knowledge cannot be derived directly from two-body scattering experiments, and one would have to rely on a very shaky theory. Inelastic scattering, on the other hand, tends to result from large momentum transfers, and the struck particle can often be identified because it has the higher energy. Interference effects are then much smaller, as will be seen, and the phases not important.

Gluckstern and Bethe[4] have shown by a closure argument that if one knows the fundamental forces acting, then the evaluation of the total $n-d$ cross section (elastic plus inelastic) can be carried out rather accurately without explicitly using the continuum two-particle wave functions. This simplifies the calculation enormously, but it does not circumvent the necessity of knowing the phases. These authors also discuss in a qualitative way the inelastic part of the problem. We shall often have occasion to refer to their results, many of which are independent of the nature of nuclear forces.

The formulas given in I are not evaluated exactly in this paper because of the excessive amount of computation required. The exact calculation could be performed with the aid of a computing machine if the accuracy of a future experiment should warrant it. Here varying approximations have been made which will be individually discussed as the need for them arises.

Before plunging into details, a brief discussion will first be given of those features of the problem which are understandable without reference to the theory.

A QUALITATIVE DISCUSSION OF THE INELASTIC SCATTERING PROBLEM

In most experiments on the $H^2(n, p)$ reaction, the final proton will be detected because of its charge, whereas the two neutrons will slip away unnoticed. It is therefore reasonable to categorize the possible final states according to the energy and angle of the proton. Following the classical idea that the incoming neutron may hit either the neutron or the proton making up the deuteron, but not both, it is to be expected that there will be two fairly well defined proton groups, for a fixed incident neutron energy. If the proton is hit it will tend to carry away in a predominantly forward direction an energy of the order of magnitude of the incident energy. If the neutron is hit, the proton is likely to be left behind with only the kinetic energy of zero point motion which it happened to possess at the instant of impact. This is only a few Mev and the angular distribution of these protons will tend to be spherically symmetric. The neutron-neutron collision probability therefore is largely responsible for the slow protons ob-

* Part of this work was carried out at the University of California Radiation Laboratory under the auspices of the AEC.
[1] G. F. Chew, Phys. Rev. **80**, 196 (1950).
[2] W. M. Powell, Phys. Rev. (to be published).
[3] Hadley, Kelley, Leith, Segrè, Wiegand, and York, Phys. Rev. **75**, 351 (1949).
[4] R. L. Gluckstern and H. A. Bethe, Phys. Rev. **81**, 761 (1951).

served. One might think that neutron-proton collisions in which only a small amount of momentum is transferred might contribute to the slow proton yield. They can, but only occasionally, because the deuteron tends not to disintegrate unless either a big kick is given to one of its two particles or the spin state is changed from triplet to singlet (in which it is unstable). It will be shown that the latter is unlikely as a result of $n-p$ collisions.

The fast group of protons will be even less beset by ambiguities. If one considers only those with energy above 20 Mev, there is little need to worry that they may be the residue of an $n-n$ collision, since the deuteron contains such momenta with a very small probability. Off hand one might expect these fast protons to be distributed like the recoil protons from free neutron-proton scattering. The slightly surprising result of this paper is that at small angles the intensity is sharply reduced. The reason is that exchange collisions which project the proton forward with high energy leave the incident neutron with relatively little energy. It then may find itself in a region of phase space already occupied by the second neutron, a situation forbidden by the Pauli principle.

This exclusion effect, although it is easily observable, does not produce a major decrease in the over-all inelastic cross section, being restricted to a small solid angle. A much more serious decrease in the inelastic cross section results from the reluctance of the deuteron to disintegrate when only a small amount of momentum is transferred to it either by an $n-n$ or by an $n-p$ collision.

THE ACCURACY OF THE IMPULSE APPROXIMATION

As shown by Wick and Chew,[5] the order of magnitude of the error in the impulse approximation is given by $(a/R)(1/kR)$, where a is the two particle scattering amplitude, k is the relative neutron wave number and R the deuteron "radius."† The largest and most important amplitude in this problem belongs to the triplet neutron-proton system and can be estimated from experiment[3] to be $\sim\frac{1}{4}R$. The neutron wave number is $\sim\frac{1}{4}R^{-1}$, so the order of magnitude of the error is only 6 percent. We shall, however, make approximations in the evaluation of the impulse formulae which introduce somewhat larger errors than this.

THE IMPORTANCE OF INTERFERENCE EFFECTS

Gluckstern and Bethe[4] have calculated the contribution of interference terms to the total 90-Mev neutron-deuteron cross section, using Born approximation with various conventional static potentials to obtain the phases. The most reasonable of their potentials is the half ordinary-half exchange or Serber potential for both the $n-p$ and $n-n$ interactions. This choice fits fairly well the high energy neutron-proton scattering,[3] but fails completely with the proton-proton.[6] In any case, with this assumption, they find that 16 mb out of the total of 117 mb measured by McMillan, *et al.*[7] are due to interference between neutron-neutron and neutron-proton scattered amplitudes. The elastic part of the total cross section had previously been calculated by Chew[8] with nearly identical assumptions, and he found that out of 59 mb the interference contribution was 15 mb. Too close a comparison of these numerical results is unwarranted, but it empirically apparent that the great majority of the interference contribution is associated with the elastic scattering and only a small part with the inelastic. This is not at all surprising from the qualitative arguments given in the introduction. The explanation becomes quantitative if one observes that as a function of the momentum transferred in the collision the interference term in the elastic cross section is very nearly identical to the interference term in the total cross section. Ignoring the Pauli principle and the spin dependence of the scattering, and using the closure result of Gluckstern and Bethe,[4] one finds that the interference term in the total cross section is (in the notation of I) proportional to

$$2\ \mathrm{Re}\ r_{1p}^{*}r_{12}F(q) \tag{1}$$

where

$$F(q)=\int d\tau e^{-i\mathbf{q}\cdot\mathbf{r}}\varphi_0^2(r), \tag{2}$$

the symbol $\mathbf{q}$ representing the momentum transfer, $\mathbf{k}_1-\mathbf{k}_0$. On the other hand, the interference term in the elastic part alone is proportional (with the same constant of proportionality) to

$$2\ \mathrm{Re}\ r_{1p}^{*}r_{12}S(q), \tag{3}$$

where $S(q)$ is the "sticking" factor defined in reference 8. It is given by

$$S(q)=F^2(q/2). \tag{4}$$

The functions $S(q)$ and $F(q)$ are numerically very similar, both having the maximum value unity at $q=0$ and falling off with an approximate width of 2α, if $\alpha=1/R$. For a well-known form of the deuteron wave function,[8,9]

$$\varphi_0(r)=\left[\frac{\alpha\beta(\beta+\alpha)}{2\pi(\beta-\alpha)^2}\right]^{\frac{1}{2}}\frac{(e^{-\alpha r}-e^{-\beta r})}{r},\quad(\beta=6\alpha), \tag{5}$$

the functions F and S are plotted in Fig. 1 as a function of $q/2\alpha$. The fact that for small q, S is actually somewhat larger than F seems to be a real effect; but within the accuracy of our method, we are justified in ignoring the difference between the two functions and

[5] G. C. Wick and G. F. Chew, to be published.

† By the "radius" is meant the average nucleon separation distance, 3.2×10^{-13} cm.

[6] Chamberlain, Segrè, and Wiegand, Phys. Rev. **83**, 923 (1951).

[7] Cook, McMillan, Peterson, and Sewell, Phys. Rev. **75**, 7 (1949).

[8] G. F. Chew, Phys. Rev. **74**, 809 (1948).

[9] G. F. Chew and M. L. Goldberger, Phys. Rev. **77**, 470 (1950).

therefore the interference effects in the inelastic part of the cross section.

This argument of course fails if by a spin change the deuteron is thrown into the singlet state, in which it cannot be bound. Statistical considerations give this possibility a weight of only $\frac{1}{8}$ and a more detailed consideration of the probable spin dependence of the $n-p$ interaction reveals that the chance of a final singlet state should be less than 10 percent. It therefore seems consistent, in view of experimental uncertainties,[2] to neglect all interference terms in calculating the inelastic part of the cross section. This practice will be followed here and obviates the necessity of knowing anything but the magnitudes of the $n-n$ and $n-p$ scattered amplitudes.

THE TOTAL YIELD OF FAST AND SLOW PROTONS

To calculate the total inelastic cross section, we may avail ourselves of the method of Gluckstern and Bethe.[4] These authors, by a closure argument, show that replacement of the actual final two-body wave functions by plane waves is approximately equivalent to calculating the sum of elastic and inelastic scattering. We shall therefore employ formula (21a) from I, which follows from the use of plane waves, and substitute into I-(15) and I-(16) to obtain the total cross section. The elastic part alone will then be calculated and the inelastic obtained by taking the difference. In making the subtraction it will be assumed that all interference terms (between $n-n$ and $n-p$ scattering) cancel out, the argument for this being given above. The reason for such a roundabout procedure is to avoid the two-body continuum functions, which are difficult to handle analytically.

In the notation of I, then, the total cross section is

$$\sigma_{\text{total}}=\int\int d\mathbf{k}_p d\mathbf{k}_{12}\frac{2\pi}{\hbar v_0}\{[\tfrac{3}{4}|r_{1p}{}^t|^2+\tfrac{1}{4}|r_{1p}{}^s|^2]g_0^2(\mathbf{k}_2)$$
$$+[\tfrac{3}{4}|r_{2p}{}^t|^2+\tfrac{1}{4}|r_{2p}{}^s|^2]g_0^2(\mathbf{k}_1)-2\,\mathrm{Re}g_0(\mathbf{k}_1)g_0(\mathbf{k}_2)$$
$$\times[\tfrac{3}{8}(r_{1p}{}^t)^*(r_{2p}{}^t)+\tfrac{1}{8}(r_{1p}{}^s)^*(r_{2p}{}^s)-\tfrac{1}{8}(r_{1p}{}^t)^*(r_{2p}{}^s)$$
$$-\tfrac{1}{8}(r_{1p}{}^s)^*(r_{2p}{}^t)]+[\tfrac{3}{4}|r_{12}{}^t-r_{21}{}^t|^2$$
$$+\tfrac{1}{4}|r_{12}{}^s+r_{21}{}^s|^2]g_0^2(\mathbf{k}_p)+\text{interference terms}\}$$
$$\times\delta(E_1+E_2+E_p-E_0),\quad(6)$$

with the integration to be extended over only one hemisphere of the $\mathbf{k}_{12}$ space.

If one writes down the formula for $n-p$ scattering at the same energy,

$$d\sigma_{np}/d\mathbf{k}_{1p}=\frac{2\pi}{\hbar v_0}\{\tfrac{3}{4}|r_{1p}{}^t|^2+\tfrac{1}{4}|r_{1p}{}^s|^2\}\delta(E_1+E_p-E_0)\quad(7)$$

and the formula for $n-n$ scattering,

$$d\sigma_{nn}/d\mathbf{k}_{12}=\frac{2\pi}{\hbar v_0}\{\tfrac{3}{4}|r_{12}{}^t-r_{21}{}^t|^2+\tfrac{1}{4}|r_{12}{}^s+r_{21}{}^s|^2\}$$
$$\times\delta(E_1+E_2-E_0)\quad(8)$$

then one sees that except in the third term of (6), the same combination of $n-n$ and $n-p$ scattering amplitudes occur. This third term tends to inhibit the emission of fast protons forward and represents the effect of the exclusion principle as explained in the qualitative discussion above. Its effect on the total cross section will be shown later to be about 15 percent.

Formula (6) may be rewritten in an even more significant form if a change of variables is made for the term arising from $n-p$ collisions:

$$\sigma_{\text{total}}=\frac{2\pi}{\hbar v_0}\int d\mathbf{k}_2 g_0^2(\mathbf{k}_2)\left(\frac{mk_{1p}}{2\hbar^2}\right)\int d\omega_{1p}[\tfrac{3}{4}|r_{1p}{}^t|^2$$
$$+\tfrac{1}{4}|r_{1p}{}^s|^2]+\frac{2\pi}{\hbar v_0}\int d\mathbf{k}_p g_0^2(\mathbf{k}_p)\left(\frac{mk_{12}}{4\hbar^2}\right)\int d\omega_{12}$$
$$\times[\tfrac{3}{4}|r_{12}{}^t-r_{21}{}^t|^2+\tfrac{1}{4}|r_{12}{}^s+r_{21}{}^s|^2]-\text{exclusion}$$
$$\text{principle term}+\text{interference terms}.\quad(9)$$

Carrying out the analogous operations with (7) and (8), one gets

$$\sigma_{np}{}^{\text{total}}=\frac{2\pi}{\hbar v_0}\left(\frac{mk_0}{4\hbar^2}\right)\int d\omega_{1p}[\tfrac{3}{4}|r_{1p}{}^t|^2+\tfrac{1}{4}|r_{1p}{}^s|^2]\quad(10)$$

$$\sigma_{nn}{}^{\text{total}}=\frac{2\pi}{\hbar v_0}\left(\frac{mk_0}{8\hbar^2}\right)\int d\omega_{12}[\tfrac{3}{4}|r_{12}{}^t-r_{21}{}^t|^2$$
$$+\tfrac{1}{4}|r_{12}{}^s+r_{21}{}^s|^2].\quad(11)$$

Because the energy-momentum conditions in the two-body problem differ from that in the three, the scattering amplitudes in (10) and (11) are, strictly speaking, not to be evaluated for the same magnitudes of initial and final momenta as in (9). In (10) and (11) the magnitude of both initial and final relative momenta is $k_0/2$. In (9) the initial and final relative momenta depend on the variable of integration, either k_p or k_2, but the integrands are strongly peaked around zero and at that point both initial and final relative momenta take on the value $k_0/2$. It is well within the accuracy of our method to neglect the variation of the amplitudes, giving them the value which they take on at the maximum of the integrand. If we do this and simultaneously replace k_{1p} and k_{12} by $k_0/2$, we arrive at the following very simple result, also found by previous workers[4,10] who used the Born approximation,

$$\sigma_{\text{total}}=(1-\epsilon)\sigma_{np}{}^{\text{total}}+\sigma_{nn}{}^{\text{total}}+I,\quad(12)$$

where $\epsilon\sigma_{np}{}^{\text{total}}$ is the exclusion principle correction and I represents interference terms.

The corresponding calculation of the elastic part of the cross section is made by using the deuteron wave function as both initial and final state in the overlap integrals and by calculating the density of final states for a two-body configuration rather than a three. Also

[10] F. De Hoffman, Phys. Rev. 76, 217 (1950).

the spin states must be chosen as in reference 8 rather than as in reference 1. Carrying out this program, one finds

$$\sigma_{el}=\left(\frac{2\pi}{hv_0}\right)\left(\frac{\pi m}{h^2k_0}\right)\int_0^{(16/9)k_0^2}dq^2S(q)\left\{\frac{33}{48}|r_{1p}{}^t|^2\right.$$

$$+\tfrac{3}{16}|r_{1p}{}^s|^2+\tfrac{1}{8}\,\mathrm{Re}(r_{1p}{}^s)^*(r_{1p}{}^t)+\frac{33}{48}|r_{12}{}^t-r_{21}{}^t|^2$$

$$\left.+\tfrac{3}{16}|r_{12}{}^s+r_{21}{}^s|^2+\tfrac{1}{8}\,\mathrm{Re}(r_{12}{}^s+r_{21}{}^s)^*(r_{12}{}^t-r_{21}{}^t)\right\}$$

$$+\text{interference terms}-\text{exclusion principle correction}$$

$$+\text{pickup terms.}\quad(13)$$

The interference term we shall take to be equal to I in formula (12), as explained at the beginning of this section. The exclusion principle correction is considerably smaller here than in the total cross section, since the final momenta of the two neutrons are very rarely the same when one of them is bound in a deuteron and the other free. Exclusion principle terms will be ignored. The so-called pickup terms are discussed both in reference 8 and in a paper by Goldberger and Chew.[9] They contribute only a small fraction to the elastic cross section and are experimentally distinguishable, since they are important only for values of q greater than k_0, corresponding to deuteron angles less than 41° in the laboratory system. If we agree to separate these deuterons from the rest, thus reducing the experimental elastic and total cross sections by about 4 mb, the comparison with theory becomes more correct. Henceforth the term "elastic" scattering will refer only to deuterons recoiling at angles greater than 41°. The upper limit of the integral (13) is then to be reduced to k_0^2.

The $n-p$ and $n-n$ cross sections per unit interval of q^2 are

$$d\sigma_{np}/dq^2=\left(\frac{2\pi}{hv_0}\right)\left(\frac{\pi m}{h^2k_0}\right)[\tfrac{3}{4}|r_{1p}{}^t|^2+\tfrac{1}{4}|r_{1p}{}^s|^2]\quad(14)$$

$$d\sigma_{nn}/dq^2=\left(\frac{2\pi}{hv_0}\right)\left(\frac{\pi m}{h^2k_0}\right)[\tfrac{3}{4}|r_{12}{}^t-r_{21}{}^t|^2$$

$$+\tfrac{1}{4}|r_{12}{}^s+r_{21}{}^s|^2],\quad(15)$$

so that the combination of scattering amplitudes which appears is not quite the same as in formula (13). However, the ambiguity is not great. It is almost certain that for $n-p$ scattering the triplet dominates; so that whatever the relative phases of singlet and triplet amplitudes may be, the term $(33/48)|r_{1p}{}^t|^2$ in (13) will be by far the largest. Correspondingly in (14), the term $\frac{3}{4}|r_{1p}{}^t|^2$ is most important, so in line with our previous approximations the difference between the $n-p$ terms in (13) and in (14) can be ignored. (This procedure amounts to neglecting the possibility of a final singlet deuteron state as a result of an $n-p$ collision. It would be exact if the forces were spin independent. The maximum reasonable dependence can be estimated by setting $r_{1p}{}^s=0$. In this case one would get a final singlet state one-twelfth of the time.)

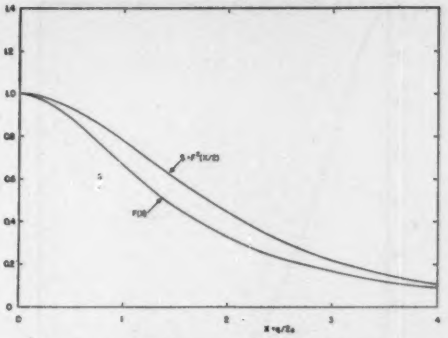

FIG. 1. The "sticking" factor S compared to the interference factor F, as a function of the momentum transfer, q.

For the $n-n$ terms we are on less sure ground. Even assuming that high energy $n-n$ and $p-p$ forces are equal, one still is uncertain about the relative importance of singlet and triplet scattering and it is possible that the cross term in (13) (between singlet and triplet $n-n$ amplitudes) might make a difference. In the frame work of our calculation, however, which assumes independent conservation of spin and orbital angular momentum, there is only one way to represent the observed isotropic nature of high energy $p-p$ scattering[6,11] and that is by a singlet interaction alone. If this is done the $n-n$ terms appearing in (13) will give three-fourths the contribution of those in (15), since the triplet scattering disappears, as does the cross term.

To make a preliminary evaluation of the integral in (13) we shall adopt what at first sight appears a rash procedure; that is, to treat the contents of the bracket as a constant. This leads to

$$\sigma_{el}=[\sigma_{np}{}^{\text{total}}+(\tfrac{3}{2})\sigma_{nn}{}^{\text{total}}]S+I,\quad(16)$$

where S is the average of the sticking factor over the interval in q^2 from 0 to k_0^2. From Fig. 1, S for 90 Mev can be computed to be 0.28 so that

$$\sigma_{el}=0.28\sigma_{np}{}^{\text{total}}+0.42\sigma_{nn}{}^{\text{total}}+I.\quad(17)$$

If $n-n$ scattering is indeed equal to $p-p$, then the above seems as sensible a procedure as any at the present time to obtain the coefficient of $\sigma_{nn}{}^{\text{total}}$, since high energy $p-p$ scattering is not only isotropic but also energy independent.[6,11] On the other hand, $n-p$ scattering is well known to have a rather strong energy and angular dependence.[3] Representing this dependence as a function of q^2, however, one finds $S=0.29$, so the effect is very small. A final check can be obtained from

[11] R. Birge, Phys. Rev. **80**, 490 (1950).

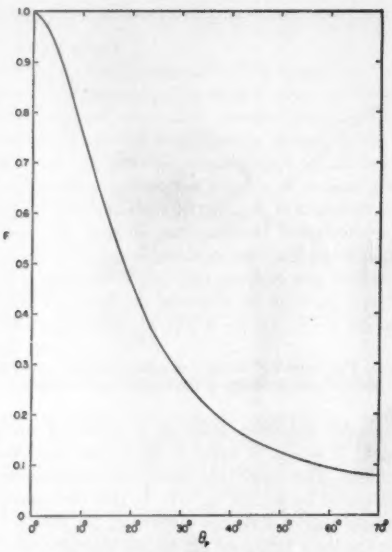

FIG. 2. The function $F(k_0 \sin\theta_p)$, which determines the reduction in the fast proton cross section owing to the exclusion principle.

the Born approximation calculation with the Serber force,[8] which also very closely gives this same result. The reason for the validity of the procedure which neglects the variation of the cross section is that most of the $n-p$ cross section is relatively isotropic, even at 90 Mev, the large variations occurring over only a small interval of q^2.

By taking the difference of formulas (12) and (17) the inelastic cross section is obtained

$$\sigma_{\text{in}}=(0.72-\epsilon)\sigma_{np}^{\text{total}}+0.58\sigma_{nn}^{\text{total}}. \tag{18}$$

To the extent to which a group of fast protons can be experimentally distinguished from a slow one, this result can be further broken down. For if

$$\sigma_{\text{in}}=\sigma_{\text{fast}}+\sigma_{\text{slow}}, \tag{19}$$

then

$$\sigma_{\text{fast}}=(0.72-\epsilon)\sigma_{np}^{\text{total}}, \tag{20}$$

and

$$\sigma_{\text{slow}}=0.58\sigma_{nn}^{\text{total}}, \tag{21}$$

according to the argument given in the introduction.

Our result for the total inelastic scattering is ambiguous only as to the magnitude of ϵ, the exclusion principle correction. If it is possible to distinguish clearly between a group of fast and a group of slow protons, the size of the slow group is connected directly by (21) to the neutron-neutron cross section. For example, Powell[2] gives 20 mb as the slow proton cross section, using 10 Mev as the dividing energy between groups. This implies a neutron-neutron cross section equal to 20 mb/0.58=35 mb±10 mb, where the uncertainty reflects theoretical as well as experimental difficulties. Such a figure is well within the limits required by equality of $n-n$ and $p-p$ interactions.[6,11]

We may at this time also compare theory with experiment for the fast group of protons. Powell gives 51 mb as the fast proton cross section, while the total neutron-proton cross section is 83 mb.[7] In the next section the exclusion principle correction ϵ will be estimated to be 0.15. Formula (20) then predicts that $\sigma_{\text{fast}}=(0.72-0.15)\times 83$ mb$=47$ mb. Agreement with experiment for both slow and fast integrated cross sections is therefore satisfactory.

If one is skeptical of the possibility of separating the fast and slow groups in this particular experiment, one may start from Powell's total inelastic cross section of 71 mb and equate this to (18). Using the known value of $\sigma_{np}^{\text{total}}$, one finds $\sigma_{nn}^{\text{total}}=[(71-47)/0.58]$ mb $=41$ mb.

Powell's measurements, however, allow a more detailed test of the theory, since they contain information about the angular distributions of the protons. Let us consider next what the impulse approximation has to say about this aspect of the experiment.

THE ANGULAR DISTRIBUTION OF THE FAST PROTONS

If one is interested only in those final states for which the proton has a high energy then the pair of particles which most strongly interact after the collision is the pair of neutrons. Therefore in formula (I-21) one must choose the upper alternative, that is, the one containing the overlap integrals I_{21}^{t} and I_{21}^{s}. We need keep only the terms generated by $n-p$ scattering, and substituting into (I-15) and (I-16) one finds the following formula for the cross section for emission of a fast proton into $d\mathbf{k}_p$.

$$\begin{aligned}d\sigma_f/d\mathbf{k}_p=(2\pi/\hbar v_0)\int d\mathbf{k}_{12}\{&|r_{1p}^{t}|^2[(33/48)|I_{21}^{t}|^2\\&+\tfrac{1}{16}|I_{21}^{s}|^2]+|r_{1p}^{s}|^2[\tfrac{3}{16}|I_{21}^{t}|^2+\tfrac{1}{16}|I_{21}^{s}|^2]\\&-\mathrm{Re}[(r_{1p}^{t})^*(r_{2p}^{t})\{(33/48)I_{21}^{s*}I_{12}^{t}-\tfrac{1}{16}I_{21}^{s*}I_{12}^{s}\}\\&+(r_{1p}^{s})^*(r_{2p}^{s})(\tfrac{3}{16}I_{21}^{t*}I_{12}^{t}-\tfrac{1}{16}I_{21}^{s*}I_{12}^{s})\\&+\tfrac{1}{16}(r_{1p}^{t*}r_{2p}^{s}+r_{1p}^{s*}r_{2p}^{t})(I_{21}^{s*}I_{12}^{s}+I_{21}^{t*}I_{12}^{t})]\\&+\tfrac{1}{8}\,\mathrm{Re}(r_{1p}^{t})^*(r_{1p}^{s})[|I_{21}^{s}|^2-|I_{21}^{t}|^2]\}\\&\times\delta(E_1+E_2+E_p-E_0).\end{aligned} \tag{22}$$

The triplet interaction between the neutrons is certainly sufficiently weak that one can replace I_{21}^{t} by $g_0(k_3)$ but the singlet interaction in the s state is by no means weak. Indeed the virtual resonance, as pointed out by Gluckstern and Bethe,[4] will reflect itself by a sharp peak in the proton spectrum near the upper limit. At a much lower energy, with a clean spectrum of incident neutrons, such a peak ought to be detectable

and will be of interest as a check on the neutron-neutron scattering length. In the Berkeley experiment, however, the neutron beam has an energy width of about 30 Mev, so that such details are entirely obscured. The shape of the proton spectrum is largely a reflection of the incident neutron spectrum.

If one does not attempt to calculate the detailed spectrum but only the total fast proton intensity at a fixed laboratory angle, then a rather simple result can be obtained, again by the use of closure. One finds for the cross section per unit solid angle in the laboratory system

$$\sigma_f(\theta_p)=\sigma_{np}(\theta_p)-F(k_0\sin\theta_p)\sigma_{ex}(\theta_p) \qquad (23)$$

where

$$\sigma_{np}(\theta_p)=\frac{2\pi}{\hbar v_0}\left(\frac{mk_0}{4\hbar^2}\right)[\tfrac{3}{4}|r_{1p}{}^t|^2+\tfrac{1}{4}|r_{1p}{}^s|^2]4\cos\theta_p$$

$$\sigma_{ex}(\theta_p)=\frac{2\pi}{\hbar v_0}\left(\frac{mk_0}{4\hbar^2}\right)[\tfrac{3}{8}|r_{1p}{}^t|^2$$

$$+\tfrac{1}{8}|r_{1p}{}^s|^2-\tfrac{1}{4}\,\mathrm{Re}r_{1p}{}^{t*}r_{1p}{}^s]4\cos\theta_p. \qquad (24)$$

In obtaining (23) the same sort of approximations were made as in obtaining (12). These approximations are harder to justify for the second term of (23) than for the first because the peak of the integrand in (22) is less sharp for the cross terms than for the direct. However, the second term represents only a relatively small correction to the first, and in any case we shall have difficulty in knowing the exact value of $\sigma_{ex}(\theta_p)$. This quantity is the cross section for the incident neutron to end up with its spin parallel to that of the other neutron. If that happens the process tends to be forbidden by the Pauli principle, the amount of "forbiddenness" depending on the momentum retained by the incident neutron, which is roughly $k_0\sin\theta_p$.

From (24) it is seen that σ_{ex} is certainly smaller than σ_{np}, but the ratio of the two is sensitive to the size and phase of $r_{1p}{}^s$. For example, if $r_{1p}{}^s=r_{1p}{}^t$ then $\sigma_{ex}=\frac{1}{2}\sigma_{np}$. On the other hand if $r_{1p}{}^s=0$, then $\sigma_{ex}=\frac{3}{8}\sigma_{np}$. These are probably the upper and lower limits. Let us assume that $\sigma_{ex}(\theta_p)=K\sigma_{np}(\theta_p)$, where K is a number which is independent of θ_p and which lies between $\frac{1}{2}$ and $\frac{3}{8}$, so that

$$\sigma_f(\theta_p)=[1-KF(k_0\sin\theta_p)]\sigma_{np}(\theta_p). \qquad (25)$$

The function, $F(k_0\sin\theta_p)$ is plotted in Fig. 2 for a 90-Mev incident neutron energy and in Fig. 3 the fast proton cross section according to (25) with $K=\frac{1}{2}, \frac{3}{8}$ is plotted and compared with experiment. The free neutron-proton cross section is also shown ($K=0$). Formula (25) must not be believed for angles greater than 60°, beyond which the proton moves so slowly that one of the neutrons has a good chance to capture it, or at least perturb it strongly. Agreement with experiment within this range is certainly satisfactory.

The value of ϵ, needed for formula (20) may be

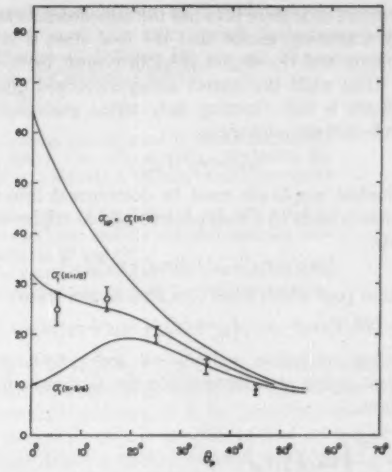

FIG. 3. The theoretical fast proton angular distribution for several different values of K, compared with experiment. (See reference 2.)

estimated by integrating the exclusion correction term, $KF(k_0\sin\theta_p)\sigma_{np}(\theta_p)$, over all angles. The result for $K=0.6$, the value which seems indicated by the forward part of the angular distribution, is $\epsilon=0.15$. Most of this (80 percent) is due to angles less than 45°.

If one is optimistic about both theory and experiment, one may say that neutron-deuteron scattering provides a new piece of information about the neutron-proton interaction which cannot be obtained from a free neutron-proton scattering experiment. The new number is K, which as we have seen depends on the ratio of singlet and triplet amplitudes. The theory at 90 Mev is too rough to make the number obtained here of real use in testing theories, but at a higher energy, say 300–400 Mev, this will no longer be the case.

THE ANGULAR DISTRIBUTION OF THE SLOW PROTONS

If the final state of the proton is a low energy one, the most strongly interacting pair of particles after the collision will in almost every case include the proton. Kinematically it is possible for the two neutrons to each have high energy and at the same time a low relative energy with respect to each other. Such a situation corresponds to a pickup process with formation of an unstable di-neutron. It will certainly occur only a very small fraction of the time, since the neutron-proton pickup, which is much more probable, amounts (experimentally) to only 4 mb. Neutron-neutron pickup will be ignored here.

It is necessary now to correct an error in part I, namely the lower alternative of (I-21), which contains terms proportional to I_{p1} and I_{p2} and which was said to be appropriate to the case now being considered.

The correct procedure is to use the same formula as for elastic scattering, except that the final state is in the continuum and the singlet possibility must be considered. Thus while the correct antisymmetrized quartet amplitude is still (keeping only terms generated by neutron-neutron scattering)

$$(r_{12}{}^t - r_{21}{}^t) I_{p1}{}^t, \tag{26}$$

the doublet amplitude must be decomposed into that part which leads to a final neutron-proton triplet state, namely

$$\tfrac{1}{4}(r_{12}{}^t - r_{21}{}^t) I_{p1}{}^t + \tfrac{3}{4}(r_{12}{}^s + r_{21}{}^s) I_{p1}{}^t \tag{27}$$

and that part which leads to a final singlet state

$$-(\sqrt{3}/4)(r_{12}{}^t - r_{21}{}^t) I_{p1}{}^s + (\sqrt{3}/4)(r_{12}{}^s + r_{21}{}^s) I_{p1}{}^s. \tag{28}$$

Setting, as before, $r_{12}{}^t = r_{21}{}^t = 0$ and $r_{12}{}^s = r_{21}{}^s = r_{nn}$, we then arrive at a formula for the slow proton distribution:

$$\frac{d\sigma^s}{d\mathbf{k}_p} = \frac{2\pi}{\hbar v_0} \int d\mathbf{k}_{12} [\tfrac{3}{4} |I_{p1}{}^t|^2 + \tfrac{1}{4} |I_{p1}{}^s|^2] |r_{nn}|^2 \delta(E_1 + E_2 + E_p - E_0), \tag{29}$$

where the integral over $d\mathbf{k}_{12}$ is to be restricted to the region $k_{1p} < k_{2p}$. Closure cannot be applied to this case and while the evaluation of (29) as it stands is a well-defined task, it is very tedious, requiring a double numerical integration for each value of $\mathbf{k}_p$. Thus to find the total number of slow protons at a fixed laboratory angle involves a triple numerical integral! The data now available do not warrant this much labor, and so far only rough approximations to (29) have been attempted. Reference to part I, Eq. (20) shows that the overlap integrals, $I_{p1}{}^t$ and $I_{p1}{}^s$, are functions of the variables, $\frac{1}{2}(\mathbf{k}_p - \mathbf{k}_1)$ and $\frac{1}{2}(\mathbf{k}_p + \mathbf{k}_1)$. Actually the dependence on the first variable is much more sensitive than on the second, and one possible approximation, described by Gluckstern and Bethe,[4] consists of neglecting the dependence on $\frac{1}{2}(\mathbf{k}_p + \mathbf{k}_1)$, giving the integrals the value they take when this vector vanishes. Because of the orthogonality of the continuum triplet $n-p$ states to the ground state, however, such an approximation neglects completely the contribution of the final triplet states. ($I_{p1}{}^t = 0$ when $\frac{1}{2}(\mathbf{k}_p + \mathbf{k}_1) = 0$.) Actually, from the closure results, we know that the triplet states contribute somewhat more than do the singlet to the total number of slow protons; so this approximation is evidently poor.

A better result can be obtained by keeping terms linear in $\frac{1}{2}(\mathbf{k}_p + \mathbf{k}_1)$, although an honest consideration of the problem shows this procedure still to be quantitatively inadequate, except for protons going backward. (From kinematic considerations, backward protons on the average involve small values of $\frac{1}{2}(\mathbf{k}_p + \mathbf{k}_1)$ and large values of $\frac{1}{2}(\mathbf{k}_p - \mathbf{k}_1)$, while the reverse is true for forward protons. This follows from the fact that the neutron, as the struck particle, generally tends to go forward.) The backward protons corresponding to a final triplet state turn out according to our rough method to be almost isotropically distributed, but the intensity increases near 90° and probably has a maximum somewhere between 45° and 90°, where it is easiest kinematically for $\frac{1}{2}(\mathbf{k}_p - \mathbf{k}_1)$ to be small. The exact position and shape of the maximum has not been determined, the approximation not being valid in this region. The protons corresponding to a singlet state are even more concentrated between 45° and 90°, as already shown by Gluckstern and Bethe,[4] so the over-all effect remains that of a maximum in this region with an isotropic backward tail. No statement can be made about the slow protons between 0° and 45° until a method of handling large values of $\frac{1}{2}(\mathbf{k}_p + \mathbf{k}_1)$ has been developed.

The experimental determination of the "slow" proton angular distribution in the forward half plane is difficult because the "fast" protons are so much more numerous there. The poor definition of the incident neutron energy thus causes trouble. In the backward half-plane, to which only $n-n$ collisions can contribute appreciably, Powell[2] finds an approximately isotropic proton distribution, in agreement with our qualitative guess. There can be no doubt from the data that the intensity of slow protons rises sharply in the forward half-plane, but the details of this part of the reaction will remain obscure until a high energy neutron beam of well defined energy is available.

SUMMARY

It has been shown explicitly that by the impulse approximation one may calculate high energy inelastic neutron-deuteron scattering with rather little ambiguity if one knows the nucleon-nucleon cross sections at the same energy. The total number of disintegration protons is particularly easy to obtain because closure may be applied. Also easily found by the same method is the angular distribution of fast forward protons. This differs from free neutron-proton exchange scattering because of the action of the Pauli principle; and the difference might conceivably be used as a measure of the spin dependence of the $n-p$ interaction at high energy. In addition, a formula has been given for the angular distribution of slow protons. This formula is discussed qualitatively but not evaluated. Comparison of the various results with the experiment of Powell at 90-Mev neutron energy shows no serious disagreement, so that one may tentatively conclude the theory to be adequate. The value of the $n-n$ cross section derived here from the experiment is consistent with the directly measured $p-p$ cross section.

The author is grateful to Professor Powell for advance communication of experimental results and thanks are due Mr. Richard Stuart and Miss Patricia Boland for assistance with numerical computations. Invaluable help was rendered by Dr. Gluckstern and Professor Bethe who kindly set to the author a preprint of their own paper on this subject.

Atomic Masses in the Region about Mass 40

T. L. Collins, Alfred O. Nier, and Walter H. Johnson, Jr.
*Department of Physics, University of Minnesota, Minneapolis, Minnesota**
(Received August 3, 1951)

The double-focusing mass spectrometer developed for the precise determination of atomic masses has been improved. A redetermination of the mass doublets $4C^{12}-S^{32}O^{16}$, $2O^{16}-S^{32}$, and $C^{12}H_4-O^{16}$ lead to the following masses: $H^1=1.008146\pm3$, $C^{12}=12.003842\pm4$, and $S^{32}=31.982236\pm7$. The relation of these results to those of other investigators is discussed.

Mass doublet comparisons between hydrocarbon fragments and S^{32}, S^{33}, S^{34}, Cl^{35}, Cl^{37}, A^{36}, A^{38}, K^{39}, K^{41}, Ca^{42}, Ca^{43}, Ca^{44}, Ca^{46}, and Sc^{45} have been made and mass values for these nuclides tabulated assuming both mass spectroscopic and nuclear reaction determined mass values for H^1 and C^{12}.

The packing fraction curve in the mass 40 region follows the general trends predicted by a formula such as that of Bohr and Wheeler, except at masses 40 and 48 where there appear to be marked discrepancies.

A DOUBLE-FOCUSING mass spectrometer has been described[1] which has proved useful for the precise measurement of atomic masses. Mass values for H^1, H^2, He^4, C^{12}, N^{14}, Ne^{20}, S^{32}, A^{36}, A^{40}, and other isotopes have been reported.[2,3] The instrument employs a 90° electrostatic analyzer followed by a 60° magnetic analyzer. Ions are produced by electron impact of gases or emitted thermionically from filaments. A small single-focusing mass spectrometer tube mounted in the same magnetic field as the main tube acts as part of a control device to compensate for fluctuations in the magnetic and electric fields in the main tube. The small tube is the input element of an inverse feedback loop which produces the stabilization.

A mass spectrum in the main tube is obtained by varying the position of a tap on a voltage divider. If Δm represents the mass difference between two ions whose masses are compared, the equation

$$\Delta m/m=(\Delta R/R)[G/(G+1)] \qquad (1)$$

gives the relation between the fractional difference in mass and the fractional shift in the resistance in the voltage divider circuit. With the apparatus as constructed, G, the open circuit gain of the feedback loop, has to be held below 100 to prevent oscillations. Because of the precise nature of the measurements, G must be measured accurately.

I. IMPROVEMENTS IN THE INSTRUMENT

A. Control System

In operation it turned out that the determination of G required as much or more effort than the measurement of $\Delta R/R$. Moreover, because of the difficulty in making the G measurements, one could not be completely certain that small systematic errors might not have been present. Accordingly, an "integral control" mechanism has now been added to the feedback circuit.† In Fig. 1 of reference 1 the output of the differential amplifier no longer goes only to the high voltage supply as shown. In addition, it is fed into the input circuit of a Brown Electronik Amplifier.[4] The output of this amplifier drives a reversible motor which has a potentiometer coupled to its shaft across which a battery is connected. The voltage between the tap and a center tap on the potentiometer is then fed into the high voltage supply, in series with the output of the differential amplifier.

In practice, the integral controller serves to hold the output of the differential amplifier at zero for slow changes in the circuit such as take place as one sweeps a mass spectrum. Thus the gain may be considered as infinite in the formula (1) above. For rapid fluctuations, due to disturbances in the circuits, the compensation is not complete, the gain remaining G.

B. Detection System

The vibrating reed electrometer previously employed has been replaced by a 10-stage electron multiplier of the Allen type.[5] The output of it is fed into an inverse feedback amplifier employing an electrometer tube for the input stage. Grid resistors up to 10^{11} ohms are employed satisfactorily, the time response of the circuit being considerably better than with the vibrating reed electrometer previously used. The increased sensitivity resulting from the use of the electron multiplier detector permits the study of rare isotopes.

C. Miscellaneous Improvements

Most of the electronic components have been rebuilt to give better regulation and more reliable performance. A description of the rebuilt apparatus will be published separately.

II. PERFORMANCE OF THE INSTRUMENT

The continuous measurement of the ion beam current allows several tests of the proper performance of the

* Research supported by joint program of ONR and AEC.
[1] A. O. Nier and T. R. Roberts, Phys. Rev. 81, 507 (1951).
[2] T. R. Roberts, Phys. Rev. 81, 624 (1951).
[3] A. O. Nier, Phys. Rev. 81, 624 (1951).
† The authors wish to express their appreciation to Professor N. B. Nichols of the Electrical Engineering Department who suggested the use of the controller.
[4] J. C. Mouzon, *Adaptability of the Measuring Circuit, Input Circuit and Amplifier of the Brown Electronic Potentiometer*, Bulletin No. B 15-10, 1948, Brown Instrument Company, Philadelphia, Pennsylvania.
[5] J. S. Allen, Rev. Sci. Instr. 12, 484 (1941); 18, 739 (1947).

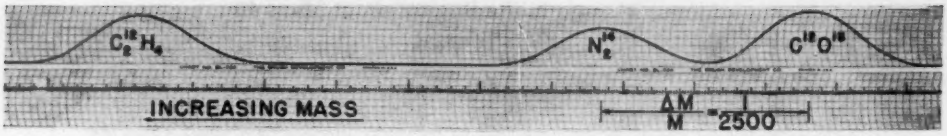

FIG. 1. Mass spectrum at mass 28 showing $(C^{12})_2H_4$, $(N^{14})_2$, and $C^{12}O^{16}$. Actually, the resolution was improved after print was made, and for most of the work in the present paper $(N^{14})_2$ and $C^{12}O^{16}$ were completely resolved.

instrument to be made periodically during runs. These tests are carried out frequently in an attempt to remove systematic errors and to improve the statistical errors.

Known possible sources of systematic error include control circuit gain not effectively infinite, leakage current to ground from the potential divider, and charge on the electrostatic analyzer plates. In general these errors will multiply the doublet difference by a constant and can be detected by measuring a known "doublet" such as $C_3H_8 - C_3H_7$ in which the difference is a hydrogen mass or 1.00814. Regular measurements are made of the hydrogen mass doublet in the region of masses being investigated. If the result is consistently in error by more than a few parts in 10^4 the measurements are discarded until a remedy is found.

We have found that an error can arise from small variations in the energy focusing of the instrument when measuring a doublet containing an ion fragment with appreciable kinetic energy from chemical binding. The energy focusing is checked by varying the 6000-v accelerating potential by about 40 volts and looking for a small shift in the position of a peak. A small movement of the whole spectrometer tube in or out of the magnetic field can correct any shift so that it is less than $\Delta M/M = 10^{-5}$. As an example, consider the measurement of the $O_2 - S$ doublet. When the S^+ ion is obtained from H_2S, almost all of the kinetic energy released in the dissociation process accompanies the light hydrogen fragments. In this case the energy focusing has little effect on doublet difference. When SO_2 is the source of S^+ ions the fragments are of equal mass and the doublet shows a strong dependence on the energy focusing. It has been found necessary to check the focusing daily, and for every new mass region, if results consistent within the statistics for each run are to be expected.

The region of good angular focusing contains the position of perfect energy focusing, and with proper adjustment the peaks have a width at half-height of $\Delta M/M = 1/4600$ (Fig. 1). The theoretical value based on slit widths alone and assuming perfect angular and energy focusing is 1/5000. We have found recently that charges on the electrostatic analyzer plates can move the energy focus position out of coincidence with the position for narrow peaks. In practice this provides a test for the accumulation of foreign material on the plates more sensitive than the hydrogen mass doublet measurement.

Statistical errors arise from noise in the electronic circuits. The stability of the control circuit is checked by tuning the spectrometer to a steep side of a peak (Fig. 2). Instability of the main amplifier and emission regulator appears as excessive fluctuation of the top of a peak. Under best conditions the noise is the shot effect of the ion beam itself. In practice statistical errors in reading the charts are not important.

III. DOUBLETS CONTAINING ELEMENTS FROM SULFUR TO SCANDIUM

Table I lists doublets containing nuclides in the neighborhood of mass 40 which we have measured recently. Three methods were used in the production of the ions. The gases SO_2, HCl, and argon were admitted to the source through capillary leaks, as were the hydrocarbons used for comparison. Potassium and calcium metals were evaporated from a small furnace and ionized by the electron beam. ScO^+ ions were obtained from a tungsten ribbon filament coated with ScO_3; the comparison peak in this case came from ethyl acetate vapor.

The peaks were matched in intensity; a run consists of at least ten consecutive tracings with alternate forward and backward sweep. Runs were taken on different days over a period of several months, and the probable errors are calculated solely from the statistics. Where necessary the doublets have been corrected for a C^{13} isotope peak on the low side of the hydrocarbon comparison. A similar correction was necessary for $S^{32}O^{17}$ and $S^{32}O^{18}$ isotope peaks under $S^{32}O^{16}$ and $S^{34}O^{16}$.

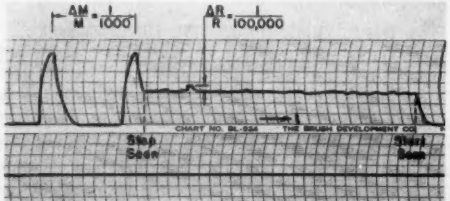

FIG. 2. Mass spectrum illustrating stability of regulating system. Mass doublet having a separation $\Delta m/m = 1/1000$ was swept from left to right. On way down and at steepest point on second peak the scanning mechanism was stopped for a period longer than required to normally scan a mass doublet. A deliberate change in $\Delta R/R$ or 1/100,000 produced a shift which may be seen on chart. Note that normal fluctuations are considerably lower than the artificial disturbance.

During these measurements six determinations were made on doublets differing by one hydrogen unit. The average value for the hydrogen mass doublet was 1.0082, a value we regard as constituting a satisfactory check of the performance of the instrument.

IV. SECONDARY STANDARD MASSES

Before the doublets can be converted to useful masses or packing fractions, it is necessary to know the masses of H^1 and C^{12}. An abundance of evidence exists indicating that masses quoted prior to 1950 are incorrect, but results of various laboratories are not consistent. At present this laboratory is concentrating on a set of doublets previously reported by Nier[3] in which carbon si determined directly from sulfur compounds. Thus, if

$$2O^{16}-S^{32}=a, \quad \text{and} \quad 4C^{12}-S^{32}O^{16}=b,$$

TABLE I. Doublets for nuclides near mass 40.

Doublet	No. of runs	Source of ions	Av. in 10^{-4} amu.	Previous work
$C_4H-S^{32}O$	4	SO_2 gas	413.85±0.46	
$C_4H_2-S^{34}O$	5	SO_2 gas	529.00±0.40	
C_4-HCl^{35}	5	HCl gas	233.41±0.44	225 ±7[a]
				246.7±1.7[b]
$C_3H_2-HCl^{37}$	5	HCl gas	420.14±0.46	412 ±7[a]
				421.7±0.9[b]
				419.8±1.1[b]
C_3-A^{36}	4	enriched A^{36}	325.01±0.33	326 ±7[a]
$H_2O-A^{36}/2$	6	enriched A^{36}	268.19±0.28	271 ±3.6[a]
				267.0±0.4[c]
$C_2H_2-A^{38}$	5	enriched A^{38}	529.10±0.40	
$C_2H_3-K^{39}$	6	K metal	599.05±0.26	
$C_2H_5-K^{41}$	5	K metal	773.61±0.33	
$C_2H_4-Ca^{42}$	3	Ca metal	882.47±0.34	
$C_2H_7-Ca^{43}$	4	Ca metal	960.40±0.52	
CO_2-Ca^{44}	7	Ca metal	346.07±0.59	
C_4-Ca^{48}	5	Ca metal	475.90±1.0	
$C_7O_3H_6-Sc^{45}O$	4	ScO_3	783.17±0.41	

[a] F. W. Aston, Proc. Roy. Soc. (London) **A163**, 391 (1937).
[b] Okuda, Ogata, Aoki, Sugawara, Phys. Rev. **58**, 578 (1940).
[c] See reference 1.

then

$$C^{12}=12+(a-b)/4.$$

Hydrogen may then be determined from any suitable hydrocarbon—oxygen doublet, in our case $C_3H_8-CO_2$, a doublet which has just twice the mass difference of the common CH_4-O doublet. Our recent results are given in Table II. The best conditions of focusing were maintained throughout this experiment, and daily measurements of a hydrogen mass doublet had an average of 1.0083. Probable errors were computed for each run; each set of runs showed internal consistency, and the quoted errors, which are purely statistical, were calculated on this basis. These doublets give the masses $H^1=1.008146\pm3$, $C^{12}=12.003842\pm4$. The differences from results previously reported by Nier can probably be attributed to the general improvement of the instrument, particularly the elimination of the gain measurement mentioned earlier.

TABLE II. Doublets determining H^1 and C^{12}.

Doublet	No. of runs	Source of ions	ΔM in 10^{-4} amu Present results	Nier[a]
C_4-SO	5	C_4H_8 SO_2	331.32±0.13	331.82±0.28
O_2-S	6	O_2 H_2S	177.64±0.07	
CO_2-CS		CO_2 CS_2		177.82±0.25
$C_3H_8-CO_2$	6	C_3H_8 CO_2	728.54±0.15	729.67±0.41

[a] See reference 3.

The recent results of several investigations are compared in Table III. Li *et al.*[6] calculated masses by means of a chain of nuclear reactions extending from H^1 to O^{16}. Ewald[7] has recently reported new values for the fundamental doublets used by earlier investigators. The results agree remarkably well considering the differences in the methods employed. However, our result for C^{12} from the very direct sulfur method is not consistent with those of Ewald[7] or Li *et al.*[6] For us to obtain $C^{12}=12.003804$, either the mass difference $4C^{12}-S^{32}O^{16}$ would have to be less than 330×10^{-4} amu, or $2O^{16}-S^{32}$ would have to be greater than 179×10^{-4} amu. Ewald[7] finds $2O^{16}-S^{32}=(177.16\pm0.20)\times10^{-4}$ amu, a good agreement with our value, but at present there are no other determinations of $4C^{12}-S^{32}O^{16}$. It is hoped that other mass spectroscopists will make a check of this important doublet.

Although our value for $C^{12}H_4-O^{16}$ is substantially higher than that of Li *et al.*,[6] and Ewald,[7] the values for H^1 obtained are in good agreement. Ogata's[8] determination for $C^{12}H_4-O^{16}$ lends support to the higher value for this doublet. Again, it is to be hoped that other independent determinations of this all-important doublet will be made. Since the disagreements in Table III do not appear to be statistical in nature, it would appear wrong to average the results in an attempt to find more accurate masses. The difficulty can be resolved only by further experimental work.‡

TABLE III. Recent determinations of secondary standards.

Mass excess in 10^{-4} amu H^1	Mass excess in 10^{-4} amu C^{12}	ΔM in 10^{-4} amu $C^{12}H_4-O^{16}$	Method	Reference
81.59±0.06	38.50±0.09	364.84±0.21	sulfur doublets	Nier[a]
81.42±0.03	38.04±0.17	363.72[b]±0.19	nuclear reactions	Li *et al.*[c]
81.41±0.02	38.07±0.11	363.71±0.12	standard doublets	Ewald[d]
		364.47±0.04		Ogata[e]
81.46±0.03	38.42±0.04	364.27±0.08	sulfur doublets	This paper

[a] See reference 3.
[b] Computed from H^1 and C^{12}.
[c] See reference 6.
[d] See reference 7.
[e] See reference 8.

[6] Li, Whaling, Fowler, and Lauritsen, Phys. Rev. **83**, 512 (1951).
[7] H. Ewald, Z. Naturforsch. **6a**, 293 (1951).
[8] K. Ogata and H. Matsuda, Phys. Rev. **83**, 180 (1951).

‡ *Note added in proof:* At the Symposium on Mass Spectroscopy, National Bureau of Standards, U.S.A., September 6–8, 1951, Ogata reported values of 177.27±0.05 and 331.27±0.07 for $2O^{16}-S^{32}$ and $4C^{12}-S^{32}O^{16}$ respectively. Mattauch and Bieri reported provisional value of 364.52±0.10 for $C^{12}H_4-O^{16}$. These new results support the values presented in this paper.

TABLE IV. Masses of nuclides from sulfur to scandium determined by mass spectroscopy.

Standards used	H^1 1.008142±3[d] C^{12} 12.003804±17[d]	H^1 1.008146±3[e] C^{12} 12.003842±4[e]
S^{32}	31.982236±7	31.982236±7
S^{33}	32.98197 ±8	32.98213 ±5
S^{34}	33.97860 ±8	33.97876 ±5
Cl^{35}	34.97993 ±7	34.98004 ±5
Cl^{37}	36.97754 ±7	36.97766 ±5
A^{36}	35.97892 ±4[a]	35.97900 ±3[a]
A^{38}	37.97479 ±7	37.97491 ±4
A^{40}	39.97502 ±4[b]	39.97513 ±3[b]
K^{39}	38.97593 ±6	38.97606 ±3
K^{41}	40.97476 ±6	40.97490 ±4
Ca^{40}	39.97534 ±9[c]	39.97545 ±9[c]
Ca^{42}	41.97202 ±6	41.97216 ±4
Ca^{43}	42.97237 ±8	42.97251 ±6
Ca^{44}	43.96920 ±6	43.96924 ±6
Ca^{46}	47.96763 ±12	47.96778 ±10
Sc^{45}	44.97000 ±6	44.97010 ±5

[a] Weighted average of the masses from the two A^{36} doublets.
[b] Weighted average from $C_2H_4-A^{40}$, $D_2O-A^{40}/2$, $Ne^{20}-A^{40}/2$ and D_2O-Ne^{20}. (A. O. Nier and T. R. Roberts, Phys. Rev. 81, 507 (1951)).
[c] From $Ca^{40}-A^{40}=3.2\pm0.8$, Nier and Roberts, see reference b.
[d] See reference 6.
[e] Values from this paper.

V. COMPUTED MASSES IN 40 REGION

The masses in Table IV have been calculated from the doublets using two sets of hydrogen and carbon masses, the values of Li *et al.*,[6] and those given in this paper. The probable errors are purely statistical, and the discrepancies in the errors come from the errors in the standards used. Thus, more consistent values for hydrogen and carbon will smaller errors are required before the full accuracy of doublets in this region can be utilized. This table also includes for completeness two nuclides computed from doublets reported previously by this laboratory. The importance of the small difference between the two sets of masses may be judged by computing the energy for the possible reaction $Ca^{42}(d,p)Ca^{44}$. Masses computed using the standards of Li *et al.* lead to $Q=2.96$ Mev, while the standards of this paper give $Q=3.20$ Mev.

TABLE V. Mass ratio Cl^{35}/Cl^{37}.

Investigations	Method	Value
Aston[a]	Mass spectroscopy	0.9459806±300
Okuda *et al.*[b]	Mass spectroscopy	0.9459452±65
Townes *et al.*[c]	Microwave (I Cl)	0.9459801±50
Gilbert *et al.*[d]	Microwave (F Cl)	0.9459775±40
Townes *et al.*[e]	Microwave (Cl CN)	0.9459906±120
Pollard[f,g]	Nuclear reaction	0.9459893±110
This paper	Mass spectroscopy	0.9459777±20

[a] F. W. Aston, Proc. Roy. Soc. (London) **A162**, 191 (1937).
[b] See reference b of Table I.
[c] Townes, Merritt, and Wright, Phys. Rev. **73**, 1334 (1948).
[d] Gilbert, Roberts, and Griswold, Phys. Rev. **76**, 1723 (1949).
[e] Townes and Shulman, reported by W. Low and C. H. Townes, Phys. Rev. **80**, 608 (1950).
[f] E. C. Pollard, Phys. Rev. **57**, 1086 (1940).
[g] J. H. Shrader and E. C. Pollard, Phys. Rev. **59**, 277 (1941).

TABLE VI. Comparison with some nuclear reactions.

	From Table IV amu	From nuclear reactions amu	Reactions used
$S^{33}-S^{32}$	0.99989±5	0.99970±2	$S^{32}(d,p)S^{33a}$
$Cl^{37}-A^{36}$	0.99866±6	0.99864±3	$Cl^{37}(p,n)A^{37b}$ $A^{36}(d,p)A^{37c}$
$A^{38}-Cl^{37}$	0.99725±6	0.99705	$Cl^{37}(n,\gamma)Cl^{38d}$ $Cl^{38}(\beta)A^{38e}$
$Ca^{42}-K^{41}$	0.99726±6	0.99720	$K^{41}(n,\gamma)K^{42d}$ $K^{42}(\beta)Ca^{42e}$

[a] Strait, Van Patter, Buechner, and Sperduto, Phys. Rev. **81**, 747 (1951).
[b] H. T. Richards and R. V. Smith, Phys. Rev. **74**, 1257 (1948).
[c] Davison, Buchanan, and Pollard, Phys. Rev. **76**, 890 (1949).
[d] Kinsey, Bartholomew, and Walker, Phys. Rev. **78**, 481 (1950) A. C. G. Mitchell, Revs. Modern Phys. **22**, 36 (1950).

In the case of Cl^{35} and Cl^{37} several independent checks of the mass ratio Cl^{35}/Cl^{37} are possible. Table V gives the comparisons. The agreement of the present results with the recent microwave and nuclear reaction values is gratifying. Differences between masses of some nuclides listed in Table IV may be compared with recent nuclear disintegration data. This is done in Table VI.

The present study constitutes the first systematic effort to determine precisely the masses of all the naturally occurring nuclides in an extended intermediate mass range. Because of their extreme rarity only S^{36}, K^{40}, and Ca^{46} had to be excluded. In Fig. 3 (solid curve) are shown the packing fractions corresponding to the atomic masses in the last column in Table IV. It is interesting to compare this with a semi-empirical mass formula such as that of Bohr and Wheeler.[9] For a precise comparison one should adjust the empirical constants in the formula to take account

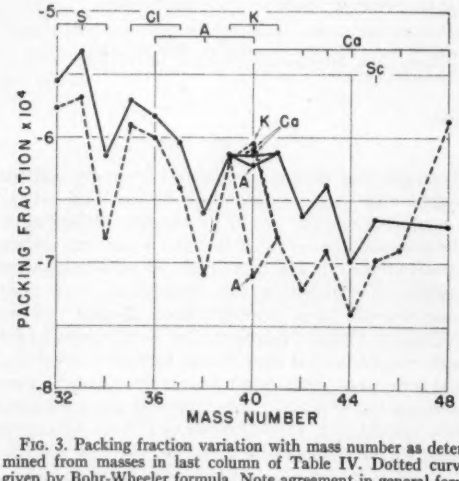

FIG. 3. Packing fraction variation with mass number as determined from masses in last column of Table IV. Dotted curve given by Bohr-Wheeler formula. Note agreement in general form except at masses 40 and 48.

[9] N. Bohr and J. A. Wheeler, Phys. Rev. **56**, 426 (1939).

of the newer experimental data. Actually our plot of the formula does take account of the newer values for the masses of the neutron and proton.

The present study is being systematically extended to higher masses. The results obtained, when supplemented by masses for the unstable isotopes in the region, will provide a large block of coherent data. Such information will make it possible to determine more precisely the numerical values for the various terms in formulas proposed for nuclear binding energies and should shed light on shell structure theories. In Fig. 3 it is interesting to note the close correspondence in undulations of the two curves and to observe the apparent discontinuities occurring at masses 40 and 48.

The authors wish to acknowledge the very able assistance of Ruth C. Boe in making many of the measurements reported here. The construction of the apparatus was aided materially by grants from the Graduate School and the Minnesota Technical Research Fund subscribed to by General Mills, Inc., *Minneapolis Star and Tribune*, Minnesota Mining and Manufacturing Company, Northern States Power Company, and Minneapolis Honeywell Regulator Company.

PHYSICAL REVIEW VOLUME 84, NUMBER 4 NOVEMBER 15, 1951

Application of the Bethe-Weiss Method to the Theory of Antiferromagnetism

YIN-YUAN LI
Department of Physics, University of Illinois, Urbana, Illinois
(Received May 31, 1951)

The P. R. Weiss method developed in the theory of ferromagnetism is applied to antiferromagnetism by introducing sublattices. Atomic lattices (spin ½ per atom) with negative Heisenberg exchange coupling J between the nearest neighbors are investigated. It has been found that two-dimensional lattices cannot sustain antiferromagnetic order. The Curie temperatures of the simple cubic and b.c.c. structure are, respectively, $2.004|J|/k$ and $3.18|J|/k$. That the f.c.c. lattice cannot be ordered by the interactions among the nearest neighbors is deduced from the disorder of a quadratic layer and the ineffectiveness of the interactions between layers in a f.c.c. lattice in producing order. This helps to understand why the ordering pattern of spins in Mn ions in MnO should be such as observed by Shull. Curves are obtained for reciprocal susceptibility and for short-range order *vs* temperature above the Curie point T_c. The experimental formula $\chi=\text{const}/(T+\theta)$ is compared with our theory. We obtain for the simple cubic and b.c.c. lattice $\theta=1.5T_c$ and $1.25T_c$ respectively if we extrapolate our theoretical curve from extremely high temperatures, and θ is slightly higher than these values if we extrapolate from the temperature range at which experimental readings are taken. This compares more favorably with the experimental data than the prediction $\theta=T_c$ of the molecular field theory. The general validity of our theory and its failure in the range of low temperatures are discussed.

I. INTRODUCTION

A MAGNETIC medium with negative exchange coupling between the neighboring atoms cannot be ferromagnetic, but under certain circumstances the spins of the neighboring atoms are ordered antiparallel at low temperatures. This ordering effect is called antiferromagnetism. Its existence was first suggested by the discovery of an anomalous specific heat in MnO near the ordering transition temperature, at which a maximum susceptibility has also been observed.[1] The latter phenomenon made possible the proper understanding of this transition. We can imagine that, as the temperature is lowered, the inner field which causes the staggering of spins becomes stronger and makes it harder for the applied field to align the spins in one direction. Quite a few substances are found to show antiferromagnetic transitions; among them are most of the ionic salts of transition metals. Theoretical interpretations of this phenomenon have been given by Néel,[2] Bitter,[3] and Van Vleck[4] using the molecular field method in which the ordering "force" is assumed to be uniquely determined by the existing degree of order over all the lattice. Increasing attention has turned to antiferromagnetism since the development of the neutron diffraction technique, which makes possible a direct investigation of the ordering pattern.[5] Using this technique, Shull *et al.*[6] have found in MnO a rather unexpected structure: The spins of Mn^{++} are ordered in such a manner that spins are lined up antiparallel in each of the four simple cubic sublattices of which the face-centered cubic lattice of Mn ions is composed. This indicates that the exchange interaction between the next-nearest neighboring Mn ions is more effective in ordering spins than that between the immediate neighboring Mn ions. A satisfying explanation of the strong exchange force between next-nearest neighbors has been offered by Anderson,[7] in which he takes into considera-

[1] See the review article, J. H. Van Vleck, Revs. Modern Phys. **17**, 27 (1945).
[2] L. Néel, Ann. phys. **17**, 64 (1932); **5**, 256 (1936).
[3] F. Bitter, Phys. Rev. **54**, 79 (1938).
[4] J. H. Van Vleck, J. Chem. Phys. **9**, 85 (1941).
[5] C. G. Shull and J. S. Smart, Phys. Rev. **76**, 1256 (1949).
[6] Shull, Strauser, and Wollan, Phys. Rev. **83**, 333 (1951).
[7] P. W. Anderson, Phys. Rev. **79**, 350 (1950).

tion the perturbation of the excited state of the O ion between two next-nearest Mn ions.

The ordering effect of antiferromagnetism is one of the so-called cooperative phenomena in which the interaction between the unit systems is vitally important. A cooperative assembly usually means a difficult problem for statistical mechanics. It is almost unnecessary to mention that an exact solution of the cooperative assembly with the Heisenberg exchange interaction is not in sight at this time, since the diagonalization of the hamiltonian of the crystal is overwhelmingly involved. In the case of a negative exchange integral even the lowest energy levels have not been worked out except for the linear chain.[8] The purpose of this work is to undertake an approximate statistical theory of antiferromagnetism, more refined than the molecular field theory. As usual, only the most important Heisenberg exchange interaction, which is not always the interaction between nearest neighbors, will be considered. We assume that the orbital moment is quenched, so that the magnetic interaction arises entirely from the spins and is isotropic. Naturally we look to the methods developed for the theory of ferromagnetism. The elegant method of Bloch's spin-waves[9] is not available in antiferromagnetism, because the lowest energy levels cannot be obtained with his scheme when they are the states of very small magnetic quantum number. The Opechowski method,[10] in which the partition function is evaluated as an expansion series of $1/T$, has been used to locate approximately the ferromagnetic Curie temperatures by making an extrapolation from the first few terms of the series expression of the reciprocal (magnetic) susceptibility, which becomes zero at the Curie point. However, for the case of antiferromagnetism the series becomes violently oscillatory, reaching $\pm\infty$ at absolute zero; hence, an extrapolation for the Curie point, at which the susceptibility reaches its maximum, cannot be effected with the terms given by Opechowski and by Zehler.[11] A few more terms can be obtained only with immense labor. The P. R. Weiss method,[12] which is the reformulation of Bethe's well-known method[13] (for the theory of superstructure in alloys), is the most convenient one to use. Consequently, we shall apply the P. R. Weiss method to the problem of antiferromagnetic transitions by introducing sublattices. A discussion of the failure of this method in the range of very low temperatures[14] will be given in a later part of this article.

II. STATISTICAL METHOD AND CURIE TEMPERATURES

As in the theory of order in binary alloys, it is convenient for the present problem to describe the long-range order in terms of sublattices. This makes the problem of antiferromagnetic transitions formally more complicated than its counterpart, the ferromagnetic case. A proper assignment of sublattices must be such that we find the lowest energy state when all the spins on each of the sublattices are perfectly aligned but antiparallelism prevails between certain different sublattices. The lattices to be considered in this section are the simple and body-centered cubic structures, the quadratic net, the honey-comb net, and the linear chain. For these we need only two equivalent sublattices; all the nearest neighbors of any site (α- or β-site) are on the other sublattice (β- or α-site). At the lowest energy state a spin is antiparallel with respect to all its nearest neighbors. In the Bethe-Weiss method the interactions in a cluster containing an arbitrary atom (the central atom) and all its immediate neighbors (the n "first shell" atoms) are treated in detail. The exchange energy of this group is diagonalized. The interaction between a first-shell atom and those outside the group is replaced by an internal field. After the assignment of sublattices we find two different kinds of clusters; one with the central atom on an α-site, and the other with the central atom on a β-site. Therefore, we must consider two different internal fields $\mathbf{H}_\alpha$ and $\mathbf{H}_\beta$ acting respectively on the first-shell spin on an α-site or a β-site. The central spin is, of course, acted upon by the applied field only, since all its neighboring interactions are accounted for. The average magnetic moment of the central atom and that of the first-shell atom can be derived from the partition function of the cluster. The self-consistency of this formulation requires that the magnetic moment of a central atom on a certain sublattice equals that of the first-shell atom on the same sublattice. These relations determine $\mathbf{H}_\alpha$ and $\mathbf{H}_\beta$. $\mathbf{H}_\alpha$ and $\mathbf{H}_\beta$ will be treated as either parallel or antiparallel to the applied field $\mathbf{H}_0$. The neglect of directional effects is not a real shortcoming except in the highly ordered states at low temperatures, but in the latter range our approximation is inadequate under any circumstance (see Sec. IV). Theoretically, the higher approximations can be obtained by taking larger clusters, i.e., including the second-shell neighboring atom, the third-shell, and so on, but the complexity of the computation increases very rapidly.

The hamiltonian of the cluster of atoms is given by

$$\mathcal{H}=-2J\sum_{i=1}^{n}\mathbf{s}_0\cdot\mathbf{s}_i-s_{0z}H_0-\sum_{i=1}^{n}s_{iz}H_f \qquad (2.1)$$

where s_z is the z-component of $\mathbf{s}$ and the direction of the applied field is taken as the z-axis. $H_f=H_\alpha$ or H_β according as the central atom of the cluster is on a β-site or an α-site. (In this article, the symbol H stands for a magnetic field in gauss multiplied by μ where μ is the product of the Bohr magneton and the Lande g-factor.) The energy states may be labeled by the quantum numbers S_1, S, and m; S is the total spin quantum

[8] L. Hulthén, Arkiv. f. Mat. Astron. Fys. **26A**, No. 11 (1938).
[9] F. Bloch, Z. Physik **61**, 206 (1930).
[10] W. Opechowski, Physica **4**, 181 (1937); **6**, 1112 (1938).
[11] V. Zehler, Naturwiss. **B5a**, 344 (1950).
[12] P. R. Weiss, Phys. Rev. **74**, 1493 (1948).
[13] H. A. Bethe, Proc. Roy. Soc. (London) **150A**, 552 (1935).
[14] P. W. Anderson, Phys. Rev. **80**, 922 (1950).

number of the cluster, S_1 that of the n outer atoms, and m the magnetic quantum number of the cluster. In what follows we shall consider only the case in which each atom as spin $\frac{1}{2}$. (The generalization to cases of higher spin is straightforward.) The partition function of the cluster of atoms has been given by P. R. Weiss:

$$P(H_0, H_f, T)=\sum_S\sum_{S_1}\omega(S_1)\sum_m \times\exp[-W(S, S_1, m)/kT], \quad (2.2)$$

where

$$\omega(S_1)=\frac{n!}{(\frac{1}{2}n+S_1)!(\frac{1}{2}n-S_1)!} - \frac{n!}{(\frac{1}{2}n+S_1+1)!(\frac{1}{2}n-S_1-1)!} \quad (2.3)$$

for $S_1<\frac{1}{2}n$, and $\omega(S_1=\frac{1}{2}n)=1$. The energy levels obtained by diagonalizing (2.1) are

$$W(S_1\pm\tfrac{1}{2}, S_1, m)=E_{(\pm)}-mH_0+e_{1(\pm)}(H_f-H_0) +e_{2(\pm)}(H_f-H_0)^2+\dots \quad (2.4)$$

with

$$E_{(+)}=-JS_1, \quad E_{(-)}=J(S_1+1),$$

$$e_{1(\pm)}=-m\left(1\mp\frac{1}{2S_1+1}\right),$$

$$e_{2(\pm)}=\mp\frac{1}{4J(2S_1+1)}\left(1-\frac{4m^2}{(2S_1+1)^2}\right),$$

$$e_{3(\pm)}=\mp\frac{m}{2J^2(2S_1+1)^3}\left(1-\frac{4m^2}{(2S_1+1)^2}\right),$$

$$e_{4(\pm)}=\pm\frac{m}{16J^3(2S_1+1)^5} \times\left(1-\frac{24m^2}{(2S_1+1)^2}+\frac{80m^4}{(2S_1+1)^4}\right). \quad (2.5)$$

The subscripts (+) and (−) stand respectively for $S=S_1+\frac{1}{2}$ and $S=S_1-\frac{1}{2}$ and the upper and lower signs in (2.5) correspond to (+) and (−) respectively. For the cluster with a central β-site, we write

$$P_\alpha=P(H_0, H_\alpha, T), \quad (2.6a)$$

and for a central α-site

$$P_\beta=P(H_0, H_\beta, T). \quad (2.6b)$$

Considering the central site, we get the average magnetic moments per atom,

$$\bar{m}_\alpha{}^e=\mu kT\partial\ln P_\beta/\partial H_0, \quad \bar{m}_\beta{}^e=\mu kT\partial\ln P_\alpha/\partial H_0 \quad (2.7)$$

for the atoms on the two sublattices. On the other hand, from the consideration of the outer atoms of the cluster, we have

$$\bar{m}_\alpha{}^e=n^{-1}\mu kT\partial\ln P_\alpha/\partial H_\alpha, \quad \bar{m}_\beta{}^e=n^{-1}\mu kT\partial\ln P_\beta/\partial H_\beta. \quad (2.8)$$

Since no distinction should be made between the central spin and one of the first shell, we must have $\bar{m}_\alpha{}^e=\bar{m}_\alpha{}^s$ and $\bar{m}_\beta{}^e=\bar{m}_\beta{}^s$. This consistency requirement gives a set of equations which relates H_α and H_β to the applied field H_0 and temperature T. They are,

$$nP_\alpha\partial P_\beta/\partial H_0-P_\beta\partial P_\alpha/\partial H_\alpha=0, \quad (2.9a)$$

$$nP_\beta\partial P_\alpha/\partial H_0-P_\alpha\partial P_\beta/\partial H_\beta=0. \quad (2.9b)$$

By exchanging the roles of H_α and H_β in (a) we get (b) and vice versa. For any given H_0 and T there is a set of solutions of (2.9) with $H_\alpha=H_\beta$ corresponding to the paramagnetic case. However, this is not always the only solution of (2.9). For a substance with negative exchange integral ($J<0$) and at sufficiently low temperatures a set of solutions with H_α different from H_β may appear to be the solution for the equilibrium state. With $H_0=0$, P_α (or P_β) is an even function of H_α (or H_β), and both $\partial P_\alpha/\partial H_0$ (or $\partial P_\beta/\partial H_0$) and $\partial P_\alpha/\partial H_\alpha$ (or $\partial P_\beta/\partial H_\beta$) are odd functions of H_α (or H_β). Consequently, $H_\beta=-H_\alpha$ offers a set of solutions for (2.9) by making them identical, giving $\bar{m}_\alpha=-\bar{m}_\beta$. Near the Curie temperature T_c the antiferromagnetic solution can be determined from

$$A+CH_\alpha{}^2=0, \quad (2.10)$$

which is obtained by putting $H_\beta=-H_\alpha\neq0$ in (2.9) and neglecting all the terms in the ascenting power series of H_α except the first two. Detailed evaluation gives

$$A=\sum_{S_1}\omega(S_1)\sum_{(\pm)}\left\{a_{0(\pm)}+\frac{a_{1(\pm)}}{kT}\right\}\exp\left[-\frac{E_{(\pm)}}{kT}\right] \quad (2.11)$$

$$C=\sum_{S_1}\omega(S_1)\sum_{(\pm)}\left\{c_{0(\pm)}+\frac{c_{1(\pm)}}{kT}+\frac{c_{2(\pm)}}{k^2T^2}+\frac{c_{3(\pm)}}{k^3T^3}\right\} \times\exp\left[-\frac{E_{(\pm)}}{kT}\right], \quad (2.12)$$

where

$$a_0=\sum_m(-2e_2),$$
$$(n-1)a_1=\sum_m\{(n-1)e_1{}^2+nme_1\},$$
$$c_0=\sum_m(-4e_4), \quad (2.13)$$
$$(n-1)c_1=\sum_m\{2(n-1)(e_2{}^2+2e_1e_3)+nme_3\},$$
$$(n-1)c_2=\sum_m\{-2(n-1)e_1{}^2e_2-nme_1e_2\},$$
$$6(n-1)c_3=\sum_m\{(n-1)e_1{}^4+nme_1{}^3\}. \quad (2.14)$$

Incidentally, we might mention that if we change the symbol n into $-n$ in the coefficients A and C of (2.10) we get Weiss' Eq. (36), the counterpart of (2.10) in the ferromagnetic case. The simple connection is an out-

TABLE I. The curie transition of different lattices. Each atom has spin $\frac{1}{2}$. The numerical values are those of $kT_c/|J|$.

Lattice	Number of nearest neighbors	Antiferromagnetism	Present method ferromagnetism[a]	Ising model[b]	Molecular field method[b]
Linear chain	2	*no* transition	*no* transition	*no* transition	1
Honey-comb net	3	*no* transition	*no* transition	0.910	1.5
Quadratic layer	4	*no* transition	*no* transition	1.44	2
Hexagonal layer	6	*no* transition[c]	*no* transition	2.47($J>0$) *no* transition ($J<0$)	transition
Simple cubic	6	2.004	1.85	2.47	3
Body-centered cubic	8	3.18	2.90	3.48	4
Face-centered cubic	12	*no* transition[c]	transition	transition	transition

[a] After P. R. Weiss.
[b] For both the antiferromagnetic and the ferromagnetic cases.
[c] See Sec. V.

come of the fact that if we put $H_a=H_\beta\neq 0$ in (2.9) our theory reduces to that of ferromagnetism.

A transition of second order takes place at a certain temperature, such that A changes sign and above this temperature (2.10) yields an imaginary value of H_a. By numerical computations using the condition $A=0$, which involves different coefficients for different lattices, we find that without the external field[15] the values of $kT_c/|J|$ for the simple cubic and b.c.c. lattices are respectively 2.004 and 3.18 and that none of the two-dimensional nets investigated show antiferromagnetism. Previously, the latter conclusion had been suggested by its counterpart in the theories of ferromagnetism.

For convenience of comparison, the results of the P. R. Weiss theory for both antiferromagnetic and ferromagnetic cases and those obtained by Van Vleck using the molecular field method are listed in Table I. Also included in Table I are the results of the present method with the Ising model. In this model spin vectors are replaced by scalars $s=\pm\frac{1}{2}$ so that

$$\mathcal{H}=-2Js_0\sum_i s_i-s_0H_0-H_f\sum_i s_i, \tag{2.15}$$

and

$$P(H_0,H_f,T)=x_0^{-1}\{x_fy^{-1}+x_f^{-1}y\}^n + x_0\{x_fy+x_f^{-1}y^{-1}\}^n, \tag{2.16}$$

with

$$x_0=\exp[H_0/2kT],\quad x_f=\exp[H_f/2kT],\quad y=\exp[J/2kT].$$

III. PHYSICAL PROPERTIES

(a) Magnetic Susceptibility

When the crystal is antiferromagnetically ordered, its magnetic susceptibility depends on the direction of the applied field with respect to the existing internal field. Our theory is not qualified to evaluate the susceptibility below the curie temperature, since from the beginning the directional effect is neglected. For the disordered state the consideration of sublattices is unnecessary, and so the formula for χ given in Weiss' article is valid for both the ferromagnetic and antiferromagnetic cases. In the present notation it reads

$$\chi=\frac{\mu^2/kT}{(n+1)P_0}\sum_{S_1}\omega(S_1)\sum_{(\pm)}\sum_m\left(m^2-\frac{H_f-H_0}{H_0}me_{1(\pm)}\right) \times\exp[-E_{(\pm)}/kT] \tag{3.1}$$

where

$$(H_f-H_0)/H_0=\{\textstyle\sum s_1\omega(S_1)\sum_{(\pm)}\sum_m \times[nm^2+(n+1)me_{1(\pm)}]\exp[-E_{(\pm)}/kT]\} \div\{\textstyle\sum s_1\omega(S_1)\sum_{(\pm)}\sum_m[nme_{1(\pm)}+(n+1) \times(e_{1(\pm)}^2-2kTe_{2(\pm)})]\exp[-E_{(\pm)}/kT]\} \tag{3.2}$$

$$P_0=P(H_0=0,\quad H_f=0,\ T). \tag{3.3}$$

χ may be written as power series in J/kT, such that

$$\chi=\frac{\mu^2}{4kT}\left\{1+\sum_{r=1}^{\infty}\frac{B_r}{(kT/J)^r}\right\}. \tag{3.4}$$

Both P. R. Weiss and Opechowski have found $B_1=\frac{1}{2}n$ and $B_2=\frac{1}{2}n(\frac{1}{2}n-1)$ for all the lattice structures under consideration. The coefficients of the higher terms are not functions only of n. By detailed calculations we get for the simple cubic lattice

$$\chi=\frac{\mu^2}{4kT}\left\{1+\frac{3}{kT/J}+\frac{6}{(kT/J)^2} +\frac{2579}{224(kT/J)^3}+\frac{10725}{448(kT/J)^4}+\cdots\right\}, \tag{3.5}$$

with the coefficients of the third and higher powers slightly different from those in the series,

$$\chi=\frac{\mu^2}{4kT}\left\{1+\frac{3}{kT/J}+\frac{6}{(kT/J)^2} +\frac{11}{(kT/J)^3}+\frac{165}{8(kT/J)^4}+\cdots\right\}, \tag{3.6}$$

[15] In general, the Curie temperature is a function of H_0 and can be determined by using (2.9). The calculation for the case of non-vanishing applied field is much too involved. However, that T_c should decrease as H_0 is increased is shown qualitatively in a previous note (Y. Y. Li, Phys. Rev. **80**, 457 (1950)) by drawing an analogy with the well-developed theory of Ising model.

obtained by Opechowski and by Zehler (see Sec. IV). For extremely high temperatures, we may take only the first two terms in the series and rewrite in the form of the modified Curie's law

$$\chi=\mu^2/4k(T\pm T'), \tag{3.7}$$

with

$$T'=n|J|/2k, \tag{3.8}$$

where the upper sign is for antiferromagnetism. The molecular field theory gives this formula as its prediction of susceptibility for any temperature above the Curie point. This is equivalent to the neglect of all the terms except the first two in (3.4).

It is customary for experimentalists to fit their data taken at temperatures above the Curie point with the formula $\chi=\text{const}/(T\pm\theta)$. If we compare this formula with (3.7) we simply get $\theta=T'$. However, this is an extrapolation from the range of extremely high temperatures and is not in conformity with the ordinary experimental practice, in which the data are taken from temperatures immediately above T_c to those of several times T_c in the absolute scale. Therefore, in order to obtain a theoretical value of θ, the so-called "paramagnetic critical temperature," we should effect a linear extrapolation from the theoretical curve $1/\chi$ against T in the range $T=2T_c$ to $3T_c$. The tangent of this section of the curve is then extended to meet the abscissa at $-\theta$ in the case of antiferromagnetism. Table II shows the ratios of θ/T_c and T'/T_c for both antiferromagnetism and ferromagnetism. The values obtained with the molecular field theory are also included. We see that in the antiferromagnetic case $\theta>T'$ noticeably, but in the ferromagnetic case $\theta<T'$ and is only slightly higher than T_c. In general, an experimentalist would notice that, as the temperature goes higher, the value of θ in his empirical expression must be shifted in order to obtain the best fit for his data when they are taken over a wide range of temperatures; in the ferromagnetic case θ increases with increasing temperature, but in the antiferromagnetic case θ decreases. This difference is an outcome of the fact that the tangent of extrapolation meets the T-axis at a point immediately above T_c in the ferromagnetic case, but the intersection is on the negative T-axis in the antiferromagnetic case. Experimentally, it is found that for various antiferromagnetic salts θ/T_c ranges from 1.4 to 5.0, though for the iron group θ is only higher than T_c by only a few percent. These results agree nicely with our theory. The well-known prediction $\theta=T_c$ is a consequence of the simple theory of the molecular field method. Therefore, it is not essential to include the next-nearest interactions in order to explain the appreciable deviation of θ from T_c,[16,17] though it may be required for getting better quantitative agreement with experimental data.

The quantity χ is calculated numerically from (3.1)

[16] L. Néel, Ann phys. 3, 137 (1948).
[17] P. W. Anderson, Phys. Rev. 79, 705 (1950).

TABLE II. The paramagnetic critical temperatures for two cubic lattices.

		The present method: Antiferromagnetism	The present method: Ferromagnetism[a]	Molecular field method[b]
simple cubic	θ/T_c	1.7	1.1	1
	T'/T_c	1.50	1.62	1
b.c.c.	θ/T_c	1.5	1.05	1
	T'/T_c	1.26	1.38	1

[a] After P. R. Weiss.
[b] For both antiferromagnetism and ferromagnetism.

for the simple cubic lattice and is presented in Fig. 1 with $\chi(T_c)/\chi$ against T/T_c. At the Curie point we have $\chi(T_c)=3.63\ 10^{-2}\mu^2/|J|$. Our curve is concave upward, instead of being a straight line as required by the modified curie's law. The experimental data of Bizette *et al.*[18] on MnO are also presented for comparison. The Mn ions in the f.c.c. lattice are ordered on four superimposed simple cubic lattices, and therefore it seems legitimate to compare their data with our calculation for a simple cubic lattice, if we identify our J with the exchange coupling between two next-nearest Mn ions. The Mn ion has a spin 5/2 instead of $\frac{1}{2}$. In making the comparison we assume that the spin quantum number per atom does not have much influence on the behavior of $\chi/\chi(T_c)$, though it has a great effect on the value of χ itself. Figure 1 evidently shows that our calculated curve is much nearer to the experimental one than is that of the molecular field theory, although the present theory must still be regarded as only a fair approximation in the temperature range directly above the Curie point.

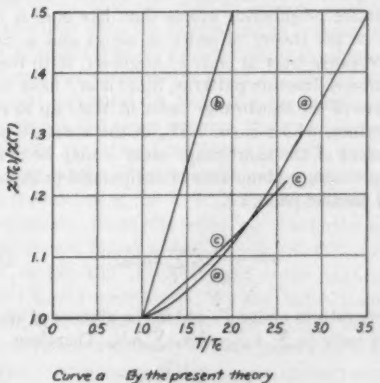

FIG. 1. Reciprocal susceptibility vs temperature.

[18] Bizette, Squire, and Tsai, Compt. rend. 207, 449 (1938).

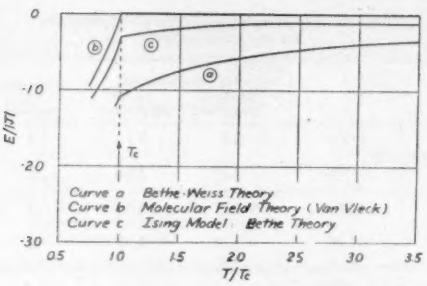

FIG. 2. Energy *vs* temperature for a simple cubic lattice.

(b) Energy and Short-Range Order

It is trivial to verify that Weiss' formula for ϵ, the energy per atom, when $H_0=0$, is unchanged by the introduction of sublattices. We have

$$\epsilon=-J\langle \mathbf{s}_0\cdot\textstyle\sum_i \mathbf{s}_i\rangle_{Av}$$
$$=\{\textstyle\sum_{S_1}\omega(S_1)\sum_{(\pm)}\sum_m E_{(\pm)}$$
$$\times\exp -W(S_1\pm\tfrac{1}{2}, S_1, m, H_f)/kT\}/2P. \quad (3.9)$$

With $T\gtrsim T_c$ the above formula reduces to

$$\epsilon=-\frac{|J|}{P_0}\sum_{S_1}\omega(S_1)S_1(S_1+1)$$
$$\times\left\{\exp-\frac{E_{(-)}}{kT}-\exp-\frac{E_{(+)}}{kT}\right\}. \quad (3.10)$$

Figure 2 shows ϵ *versus* the temperature for a simple cubic lattice.

As the energy decreases with the temperature, more antiparallel pairs are formed at the expense of the parallel pairs. The very similar situation of finding more unlike neighboring atoms than like ones is well-known in the theory of order in alloys and is called the *short-range order* or *order of neighbors*. With the use of neutron diffraction patterns, Shull *et al.*[6] have found evidences of the short-range order in MnO up to room temperature, which is *ca.* $2.5T_c$ in the absolute scale. The degree of the short-range order σ may be defined as the percentage abundance of antiparallel pairs minus that of parallel pairs, i.e.,

$$\sigma=-\frac{4}{n}\langle s_{0z}\sum_i s_{iz}\rangle_{Av}. \quad (3.11)$$

At temperatures above T_c and in the absence of applied field we have $\langle s_{0z}\sum_i s_{iz}\rangle_{Av}=\frac{1}{3}\langle \mathbf{s}_0\cdot\sum_i \mathbf{s}_i\rangle_{Av}$. Therefore

$$\epsilon=-\tfrac{3}{4}n|J|\sigma. \quad (3.12)$$

The corresponding relation for the Ising coupling reads

$$\epsilon=-\tfrac{1}{4}n|J|\sigma. \quad (3.13)$$

From (3.12) the σ *vs* T curves (Fig. 3) are calculated for the two cubic lattices with $J<0$. Table III is compiled for comparison between different theories and models. We see that the values of $\sigma(T_c)$ obtained by using the Ising model are quite close to our results, but it is not so for $\epsilon(T_c)$. The equation for σ the short-range order of parallel spins in the ferromagnetic case is different from (3.12) only by a negative sign.

In (3.9) H_f vanishes at T_c but not its derivative with respect to temperature, so our theory gives a jump of the specific heat at T_c. Using Weiss' formula we obtain for a simple cubic lattice the discontinuity of specific heat at T_c

$$\Delta c=1.0k. \quad (3.14)$$

Millar[19] measured the specific heat of MnO. From his data we have

$$\Delta c=50k. \quad (3.15)$$

A close agreement between (3.14) and (3.15) is not expected, since the MnO have a spin 5/2 in contradiction to our assumption of $\frac{1}{2}$, and we have neglected the interactions other than the most important ones. Besides, the result of an exact solution,[20] or of even a better approximation, might yield a quite different value for Δc. However, we notice that Millar's value of Δc is exceptionally large as compared with the specific heat jump found in other second-order transitions such as order-disorder transitions in alloys (say, β-brass). We should like to point out certain complications which are profoundly associated with the antiferromagnetic transition. First of all, the appearance in the lattice of a periodic change of spin directions gives a new characteristic behavior to the electrostatic interaction and influences the wave functions of the crystal. We can make it clear by considering the Hartree-Fock equation, following the interpretation given by Slater.[21] At the ordered states ρ_+ and ρ_-, the densities of electrons with $+$ and $-$ spins respectively, are two different periodic functions with a period twice the crystal spacing. Ac-

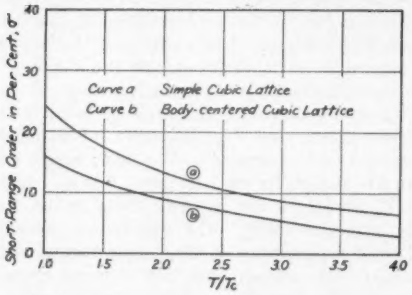

FIG. 3. Short-range order above Curie temperature.

[19] R. W. Millar, J. Am. Chem. Soc. **50**, 1875 (1928).
[20] L. Onsager, Phys. Rev. **65**, 117 (1944); this exact solution of the two-dimensional Ising problem gives an infinite specific heat at T_c instead of a finite discontinuity of specific heat as shown by the approximate solutions.
[21] J. C. Slater, Phys. Rev. **81**, 385 (1951).

cordingly, we have two different periodic potentials for each electron; one is the ionic potential and the other is the electronic interaction corrected by the so-called Fermi or exchange hole. The latter potential depends on the long-range order and is different for electrons with opposite spins mostly by a phase shift of a half period.[32] In the Heisenberg approximation, the wave functions and the integral J must change appreciably as the order of antiparallelism increases. For simplicity of manipulation, J is assumed in our theory to be a constant, which is certainly not true even when the thermal change of lattice spacing is considered. (The variation of J with the degree of antiparallel order is more profound than with the thermal expansion.) At the Curie point the rate of change of J with temperature reaches its maximum because here we have the highest rate of the increase of order as temperature is lowered. Our theory has neglected this effect, as well as its contribution to the jump of specific heat. Furthermore, the recent observations of a slight change of crystal symmetry and space parameters in the vicinity of T_c of most antiferromagnetic salts[33] add one more complication to the transition and its specific heat. As pointed out by Greenwald and Smart, the change of crystal symmetry is connected with the change of J.

IV. LIMITATION OF THE METHOD

Before we proceed to treat more complicated lattices, we must discuss the valldity of our method and its limitations. Bethe's theory of atomic order in alloys, as shown by Fowler and Guggenheim,[34] has its sound origin in the customary statistical mechanics as an approximate evaluation of the grand partition function of the whole crystal. In the problem of atomic interactions in alloys or of the Ising coupling, the states of the cluster can be simply stated as n_A atoms of one kind and $n-n_A$ of another kind around the central one, and the interaction of these atoms with the rest of the crystal can be brought in by introducing the factors $\xi_A^{n_A}$ and $\xi_B^{n-n_A}$ (only one of ξ_A and ξ_B is independent). It is evident that the use of the inner fields H_f in Sec. II for the Ising problem is nothing more than writing ξ as $\exp H_f/2kT$ (see Eq. (2.16)). In dealing with the problem of the Heisenberg exchange couplings, we cannot rejoice in the simplicity of scalar quantities; for different eigenstates, different parameters are needed to adjust the ordering effect of the rest of the crystal to the cluster. These parameters are somehow related to each other, but their inter-relations are by no means known. This situation forces us to make a reasonable assumption that the interaction between the cluster and the rest of the crystal is $-S_{1z}(H_f-H_0)$, which sounds so natural from the viewpoint of the molecular field. It becomes clear that besides inheriting Bethe's approximation in statistics, the P. R. Weiss method contains an assumption which does not have a sound basis in the quantum-mechanical treatment. Therefore, we can hardly expect P. R. Weiss' theory to yield results for the true exchange coupling case as good as those given by Bethe's theory for the Ising problem. It is in the lowest temperature range that the theory meets its failure, as can be easily seen from the behavior at extremely low temperatures of several equations in the preceding section. Anderson[14] has made this point clear by a comparison with Bloch's theory. In the latter theory, the dominant states at lowest temperatures are certain spin-waves with rather long wavelength, but the cluster considered in Weiss' theory can accommodate only the shortest spin-waves. Anderson shows that in the extremely low temperature range the second-order perturbation of the ordering field H_f offsets the ferromagnetism even for ferromagnetic lattices. With numerical calculations, he finds the existence of an anti-Curie point at a temperature about 1/7 of that of the Curie point computed by Weiss for the simple cubic lattice; only in the range between these two temperatures should the crystal be ferromagnetic, if Weiss' theory were correct. These remarks remain true for the present application of the P. R. Weiss method to antiferromagnetism. From the equation $A=0$, the anti-Curie points are found at $0.981|J|/k$ and $0.714|J|/k$ for the simple and body-centered cubic (antiferromagnetic) lattice respectively. We also notice from A, as a function of T, that half-way between the Curie and anti-Curie points the theory already shows its failure. For higher temperatures, however, the thermal excitation then outweighs the improper influence of H_f.

On the other hand, the justification of our theory in the range of higher temperatures can be inferred by a comparison with the Opechowski theory. In the latter, the free energy function is written in the form of an

TABLE III. Short-range order and energy at T_c.

		The present method			Molecular field method[a]
		Antiferromagnetic	Ferromagnetic	Ising model[a]	
simple cubic	$\sigma(T_c)$	0.242	0.175	0.200	0
	$\epsilon(\infty)-\epsilon(T_c)$	$1.09\|J\|$	$0.788J$	$0.300\|J\|$	0
b.c.c.	$\sigma(T_c)$	0.159	0.130	0.143	0
	$\epsilon(\infty)-\epsilon(T_c)$	$0.954\|J\|$	$0.779J$	$0.286\|J\|$	0

[a] For both the antiferromagnetic and ferromagnetic cases.

On the other hand, the justification of our theory in the range of higher temperatures can be inferred by a comparison with the Opechowski theory. In the latter, the free energy function is written in the form of an

[32] When we use the "band" approximation, the effect of the superstructure of antiparallel spins within the atomic lattice would split one energy band into two, which may overlap. This situation, however, could not occur in the case of ferromagnetic order in which spins are lined up simply in a certain direction without periodic variation. See the recent article by J. C. Slater, Phys. Rev. 82, 538 (1951).

[33] S. Greenwald and J. S. Smart, Nature 166, 523 (1950); J. S. Smart and S. Greenwald, Phys. Rev. 82, 113 (1951).

[34] R. H. Fowler and E. A. Guggenheim, *Statistical Thermodynamics* (Cambridge University Press, London, 1939), Chapter 13.

infinite power series of J/kT,

$$F/N=-(kT/J)\ln(2\cosh H_0/kT)$$
$$+\sum_{r=1}^{\infty} A_r/(kT/J)^{r-1} \quad (4.1)$$

where A_r is the coefficient of N in the expression

$$[(-1)^{r+1}/r!]\,\mathrm{spur}[\epsilon_0{}^r\exp(-\epsilon_H/kT)]/\mathrm{spur}$$
$$\times[\exp(-\epsilon_H/kT)] \quad (4.2)$$

$$\epsilon_0=-2J\sum_{j,k}(\mathbf{s}_j\cdot\mathbf{s}_k) \quad (4.3)$$

$$\epsilon_H=-H_0\sum_j(\mathbf{s}_j)_z \quad (4.4)$$

with j summed over all the N atoms in the assembly and k over all the nearest neighbors of the j-th atom. Only the first four coefficients $A_1,\cdots,A_4$ have been worked out. The longest chain of connected spins $(\mathbf{s}_{j_1}\cdot\mathbf{s}_{j_2})\,(\mathbf{s}_{j_2}\cdot\mathbf{s}_{j_3})\cdots(\mathbf{s}_{j_r}\cdot\mathbf{s}_{j_{r+1}})$ involved in the calculation of A_r contains $r+1$ spins (see Table I and II of the article by Opechowski). Our center-and-the-first-shell cluster can take in only the two-spin and three-spin chains. Consequently, when we expand the closed expression of our theory into the power series of J/kT, we obtain for A_1 and A_2 in the free energy function and for B_1 and B_2 in χ the same values as by the Opechowski theory. Furthermore, our first approximation, in which the smallest Bethe cluster includes all but one of the configurations involved in the calculation of A_3 in the Opechowski series, gives a very accurate value for B_3 in the series of χ (3.5). As the power of J/kT in the series goes higher, the fact that our clusters no longer contain the configurations of spin groups involved in the correct evaluation of the coefficient of $(J/kT)^r$ becomes worse, and so the accuracy of the coefficient given by our theory decreases. (B_4 in (3.5) is 15 percent higher than the correct value.) In general, if a central atom and its first r shells are taken as the Bethe cluster, we should expect to get the correct value for $B_1, B_2,\cdots, B_{r+1}$ in χ and a very accurate B_{r+2}. For the diamond lattice the first approximation of the Bethe-Weiss theory produces the same result as for the quadratic layer. However, the second approximation (with a center-and-the-first-two-shells cluster) would correctly give different results for these two lattices. In parallel, the Opechowski theory gives the same values of A_1 and A_2 but different A_r ($r\geqslant 3$) for these two lattices. The advantage of our method lies in its ability to obtain approximately closed expressions for the thermodynamic functions instead of the finite number of terms of an infinite series obtained by the Opechowski theory, leaving the coefficients of all the higher powers of J/kT unknown. Both theories cannot produce dependable results for very low temperatures, since then the very high powers of $1/T$ become important. It is beyond any doubt that, in the temperature range around the Curie points of the cubic lattices, the Bethe-Weiss method gives at least semi-quantitatively correct results (see reference 14).

V. HEXAGONAL LAYER AND FACE-CENTERED CUBIC LATTICE

In this section we shall treat the hexagonal layer and f.c.c. structures, in which we find nearest interactions among the first-shell spins. The work will be presented rather briefly, since it involves no complications beyond that just mentioned. The hexagonal layer (triangular net) has a coordination number 6, as does the simple cubic lattice, but each of the 6 nearest neighboring spins has two nearest neighbors to itself. Even if we adopt the Ising model this lattice sustains no antiferromagnetic ordering, as has been shown by Wannier[35] who obtained an exact solution. In our approximate method, the proper assignment of sublattices has alternate rows of α- and β-sites (Fig. 4). When all the spins in each sublattice are aligned and those in different sublattices are antiparallel to these, we have a maximum number of antiparallel paired spins and the lowest energy. As shown by Wannier, the lowest energy state of a triangular net of Ising spins can be arranged not only in the above manner, but also in many quite different ways. Our assignment of sublattices, perhaps, has an effect of over emphasizing the possibility of ordering. The cluster which we consider in detail has a central α- (or β-) site, and four β- (or α-) sites and two α- (or β-) sites in the first shell. With the Ising model, the present method obtains the same conclusion as the exact solution of Wannier. The details of its derivation are not given, since they are very similar to the following consideration for the case of the Heisenberg exchange coupling. We have the hamiltonian

$$\mathcal{H}=-2J(\mathbf{s}_0\cdot\textstyle\sum_i\mathbf{s}_i+\mathbf{s}_1\cdot\mathbf{s}_2+\mathbf{s}_2\cdot\mathbf{s}_3+\cdots+\mathbf{s}_6\cdot\mathbf{s}_1)$$
$$-H_{12}\tau_2-H_{11}\tau_1-H_0s_{0z}, \quad (5.1)$$

where

$$\tau_1=s_{2z}+s_{5z}, \quad (5.2a)$$

and

$$\tau_2=s_{1z}+s_{3z}+s_{4z}+s_{6z}. \quad (5.2b)$$

H_{11} stands for $H_{\alpha\alpha}$ or $H_{\beta\beta}$ and H_{12} for $H_{\alpha\beta}$ or $H_{\beta\alpha}$; $H_{\alpha\beta}$ is the internal field acting on the spin of a β-site in the shell of an α-centered cluster, and similarly we have $H_{\beta\alpha}$, $H_{\alpha\alpha}$, and $H_{\beta\beta}$. The eigenfunctions of $(\mathbf{s}_1\cdot\mathbf{s}_2+\cdots+\mathbf{s}_6\cdot\mathbf{s}_1)$ and the expectation values of τ_1 and τ_2 are given in the Appendix. The diagonalization of the perturbing part $-2J\mathbf{s}_0\cdot\sum_i\mathbf{s}_i-H_{12}\tau_2-H_{11}\tau_1-H_0s_{0z}$ is similar to that carried out in a previous section. The energy levels of $\mathcal{H}$ are now

$$W(S_1\pm\tfrac{1}{2},\,S_1,\,j,\,m)=E_j(S_1)+E_{(\pm)}-mH_0$$
$$+e_{1(\pm)}X_j(S_1)+e_{2(\pm)}X_j^2(S_1)+\cdots, \quad (5.3)$$

[35] G. H. Wannier, Phys. Rev. **79**, 357 (1950); see also G. F. Newell, Phys. Rev. **79**, 876 (1950); R. M. F. Houtappel, Physica **16**, 425 (1950).

with

$$X_j(S_1)=d_j(S_1)(H_{11}-H_0)+(1-d_j(S_1))(H_{12}-H_0), \quad (5.4)$$

where $E_{(\pm)}$ and $e_{(\pm)}$'s are as defined above. $E_j(S_1)$ and $d=\tau_1/\tau_1+\tau_2$ are given in Table V of the Appendix. The index j refers to the different eigenstates listed in Table V. With these data the partition functions for an α-centered and a β-centered cluster,

$$P_\alpha=P(H_0, H_{\alpha\beta}, H_{\alpha\alpha}, T) \text{ and } P_\beta=P(H_0, H_{\beta\alpha}, H_{\beta\beta}, T),$$

can be written. The condition of self-consistency requires

$$m_\alpha{}^c=m_\alpha{}^{(\alpha)}=m_\alpha{}^{(\beta)}, \quad (5.5a)$$

$$m_\beta{}^c=m_\beta{}^{(\beta)}=m_\beta{}^{(\alpha)}, \quad (5.5b)$$

where $m_\beta{}^{(\alpha)}$ is the average magnetic moment of the first-shell spins on β-sites in an α-centered cluster. These quantities can be derived easily from the respective partition functions. It can be shown that, when $H_0=0$, the possible antiferromagnetic solution with $H_{\alpha\alpha}=-H_{\beta\beta}(=H_1)$ and $H_{\alpha\beta}=-H_{\beta\alpha}(=H_2)$ sends (5.5a) into (5.5b) and vice versa. The internal field intensities are to be determined by equations

$$F(H_1, H_2, T)=0, \quad G(H_1, H_2, T)=0 \quad (5.6)$$

obtained from (5.5). H_1 and H_2 can apparently take small but nonvanishing values near a temperature T_1 which is determined by the equation

$$\partial(F, G)/\partial(H_1, H_2)=0; \quad (5.7)$$

at this temperature $H_1=H_2=0$ is a double solution. We find by actual calculations that the only solution of (5.7) is $T_1=0$, and above zero temperature there is no nonvanishing solution for H_1 and H_2. So we conclude that the hexagonal layer does not sustain an antiferromagnetic order. As an immediate consequence of this, we may point out that the spin superlattice of the cations in the salt of $FeCl_2$ group should conform with the "superexchange" interaction between the next-nearest neighboring cations which are separated by anions, since the nearest neighbors of cations form hexagonal layers. A neutron diffraction experiment could easily reveal this.

Finally, we come to the problem of a f.c.c. lattice with negative exchange coupling. With the Ising model we can show that antiparallel order exists at low temperatures and the transition is one of the first order with a latent heat.[26] We have no reason to believe this conclusion would hold for the quantum-mechanical exchange. To follow our treatment, we need first to solve the problem of exchange energy of 12 electrons in the first-shell atoms of the cluster. There are accordingly 924 S_1-states ($S_1=6, 5, 4, \cdots, 0$). The work would be immensely laborious. So we decided to resort to an argument which makes use of the result we have obtained for the simpler lattices. The f.c.c. lattice may be viewed as consisting of quadratic layers. Since a quadratic layer with the Heisenberg coupling does not sustain antiferromagnetism, the ordering in a f.c.c. lattice can only be effected by the interactions among the spins on neighboring layers. For any atom there are four nearest neighbors in the next layer. When they are ordered, two spins are opposite to the others. Therefore, we cannot count on their total effect on their common neighbor in the next layer (i.e., on the interaction between layers) to produce order. We may safely conclude that an antiferromagnetic transition does not occur in a f.c.c. lattice. (On the other hand, the same argument shows that, either with the Ising model or in the molecular field theory, the f.c.c. lattice should sustain antiferromagnetism, because then each quadratic layer does so.) This offers an explanation for the fact that the f.c.c. lattice of manganous ions in MnO is not ordered in a superlattice corresponding to the nearest interactions, but is found to show ordered structure agreeing with the superexchange interaction between next-nearest neighbors. The above argument, which was hinted at by Anderson in his articles,[7,17] is very useful if not rigorous. It applies to the hexagonal layer as well. The latter may be considered as made of linear chains; each spin has two neighbors in the next chain. When they are ordered, one of the two neighbors is opposite the other. (See Fig. 4: sites 1, 0, and 4 are on one chain and so forth.) Therefore, the ordering cannot be effected by the coupling between chains. Since a linear chain cannot be ordered regardless of the interaction (Ising type or quantum-mechanical), the hexagonal layer must not sustain antiferromagnetism.

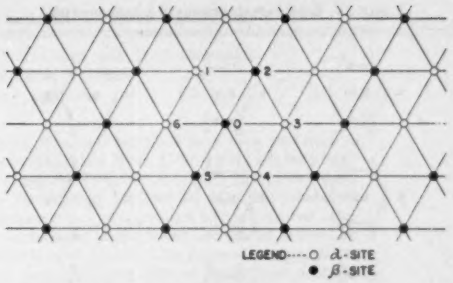

FIG. 4. Hexagonal layer decomposed into two sublattices. (At the center a Bethe cluster is indicated by labeling the sites as shown.)

ACKNOWLEDGMENTS

The author is deeply indebted to Dr. P. W. Anderson who has kindly made several very helpful suggestions and critiques. He also wishes gratefully to acknowledge the generous encouragement given by Professors F. Seitz and J. H. Van Vleck and the interesting discussions with Dr. F. Fumi.

[26] Y. Y. Li, Phys. Rev. **80**, 457 (1950).

TABLE IV. Bond eigenfunctions of a benzene ring.

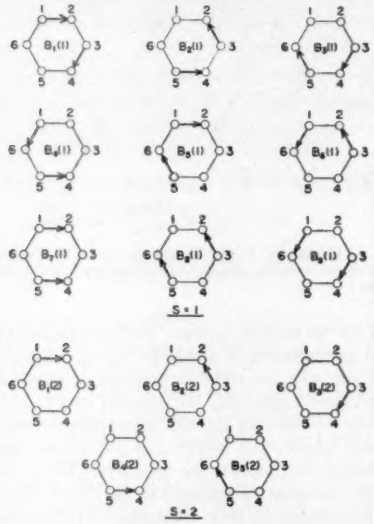

APPENDIX: THE ENERGY LEVELS AND EXPECTATION VALUES OF THE FIRST-SHELL OF A BETHE CLUSTER OF A HEXAGONAL LAYER

The 6 atoms in the first shell of our cluster form a benzene ring, the exchange energy of which has been obtained by Serber[37] using algebraic methods. Unfortunately, we need not only the energy levels but also the expectation values of τ_1 and τ_2. Therefore, we must obtain the eigenfunctions of the energy states. The method of achieving this aim has been well developed by Eyring *et al.*[38] The calculations are cut short by using some knowledge of the theory of groups. The six-atom configuration as 20 S_1-states: One with $S_1=3$, five with $S_1=2$, nine with $S_1=1$, and five with $S_1=0$, and so the same numbers of bond eigenfunctions corresponding to these are used. They are listed in the following table. Each S_1-state is $(2S_1+1)$ fold degenerate. When the z-component of S_1 is $+1$, the function $B_1(2)$ listed in Table IV is actually $B_1(S_1=2)=(a_1u_1{}^+b_2u_2{}^- - a_2u_2{}^+b_1u_1{}^-)c_3u_3{}^+d_4u_4{}^+e_5u_5{}^+f_6u_6{}^- +$all possible terms of different permutations among the functions of the atoms 3, 4, 5, and 6, where a, b, c, d, e, and f are the orbital functions. The bond (indicated by an arrow in Table IV) between two electrons requires their taking only antiparallel spins in each term of $B(S_1)$. Following the method of Eyring *et al.*, we have found the eigenfunctions of the exchange energy $-2J(\mathbf{s}_1\cdot\mathbf{s}_2+\cdots+\mathbf{s}_6\cdot\mathbf{s}_1)$ and the expectations of τ_1 and τ_2 as given in Table V. Those for $S_1=0$ states are not shown there, since they are not involved in our calculations. The energy level agrees, of course, with Serber's value except for a shift of the zero level. The eigenfunctions of a degenerate level are chosen, such that they are also eigenfunctions of both τ_1 and τ_2.

TABLE V. The eigenfunctions of a benzene ring.

S_1	$\psi_f(S_1)$	$E_f(S_1)/J$	$d_f(S_1)$
3	$\psi(3)=B(3)$	−3.00	1/3
2	$\psi_1(2)=B_1(2)+B_3(2)+B_5(2)$	1.00	1/3
	$\psi_2(2)=B_1(2)-B_3(2)-B_4(2)+B_5(2)$	0.00	1/2
	$\psi_3(2)=B_1(2)+B_3(2)-B_4(2)-B_5(2)$	0.00	1/2
	$\psi_4(2)=B_1(2)-B_3(2)+B_4(2)-B_5(2)$	−2.00	1/2
	$\psi_5(2)=B_1(2)-3B_2(2)+4B_3(2)-3B_4(2)+B_5(2)$	−2.00	1/6
1	$\psi_1(1)=f_1(1)-1.235f_5(1)$	4.236	1/3
	$\psi_2(1)=f_1(1)+3.236f_5(1)$	0.236	1/3
	$\psi_3(1)=B_1(1)-B_3(1)-B_4(1)+B_5(1)$	2.00	1/2
	$\psi_4(1)=B_1(1)+2B_2(1)+B_3(1)-B_4(1)-2B_5(1)-B_6(1)$	2.00	1/6
	$\psi_5(1)=f_3(1)-1.561f_7(1)$	2.561	0.4500
	$\psi_6(1)=f_3(1)+1.561f_7(1)$	2.561	0.2167
	$\psi_7(1)=f_4(1)+2.562f_7(1)$	1.561	0.4934
	$\psi_8(1)=f_4(1)-2.562f_7(1)$	1.561	0.1733
	$\psi_9(1)=B_1(1)-B_3(1)+B_5(1)-B_4(1)+B_5(1)-B_6(1)$	−1.00	1/3

with
$f_1(1)=B_1(1)+B_2(1)+B_3(1)+B_4(1)+B_5(1)+B_6(1)$
$f_2(1)=2\{B_1(1)+B_3(1)+B_5(1)\}$
$f_3(1)=B_1(1)-B_3(1)$
$f_4(1)=B_1(1)+B_3(1)-2B_5(1)$
$f_7(1)=B_1(1)-B_3(1)+B_4(1)-B_5(1)$
$f_8(1)=B_1(1)-2B_2(1)+B_3(1)+B_4(1)-2B_5(1)+B_6(1)$.

[37] R. Serber, J. Chem. Phys. **2**, 697 (1934).

[38] Eyring, Frost, and Turkevich, J. Chem. Phys. **2**, 777 (1934); Eyring, Walter, and Kimball, *Quantum Chemistry* (John Wiley and Sons, Inc., New York, 1944).

Electrostatic Analysis of Nuclear Reaction Energies*

R. M. WILLIAMSON,† C. P. BROWNE,‡ D. S. CRAIG, AND D. J. DONAHUE
University of Wisconsin, Madison, Wisconsin
(Received August 6, 1951)

Electrostatic analyzers for incident and product particles of nuclear reactions have been employed to measure the following ground-state Q values: $Li^6(p, He^3)\alpha$ (4.024±0.005 Mev), $Li^7(d, p)Li^8$ (−0.192±0.001 Mev), $Be^9(p, d)Be^8$ (0.558±0.002 Mev), $Be^9(p, \alpha)Li^6$ (2.123±0.004 Mev), $Be^9(d, Li^7)\alpha$ (7.159±0.009 Mev). Absolute energy calibration was based on a $Li^7(p, n)Be^7$ threshold of 1.882±0.002 Mev. No systematic differences appear between these data and other measurements employing magnetic analysis and other absolute energy calibrations. Data taken on the inelastic scattering of both protons and deuterons from Li^7 result in a value of 0.4780±0.0012 Mev for the first excited level of lithium. This figure overlaps previous gamma-ray measurements based on the 411.2-kev gamma from Au^{198}. The yield of alphas from deuteron bombardment of tritium absorbed in zirconium showed that the number of absorbed tritium atoms decreased rapidly near the surface of the zirconium. From this data, a lower limit of 17.578−0.030 Mev may be given the $T(d, \alpha)n$ Q value.

I. INTRODUCTION

RECENT refinements in the energy analysis of nuclear reaction particles have made it possible to obtain reaction Q values accurate to a few kilovolts. Ground-state Q values may be compared with mass spectrographic doublets, which are measured to the same order of accuracy for stable light atoms. Sufficient nuclear data is now published[1–4] to establish a table of nuclear masses[2] based on O^{16} for all elements lighter than neon. A comparison of this table with the most recent mass spectrographic data of Nier[5] and Roberts[6] indicates differences several times quoted errors.

Most of the previously reported nuclear data has been obtained by magnetic analysis based on absolute alpha-particle energy measurements,[7,8] the F^{19} $(p, \alpha\gamma)$ resonance energy,[9] and the proton moment.[10] Equipment developed at Wisconsin, consisting of a cylindrical electrostatic analyzer[11] for incident particles and a spherical electrostatic analyzer[12] for product particles, has been used to remeasure ground-state Q values of lithium and beryllium reactions in order to check for the presence of systematic errors in the nuclear data. In this work, absolute energy calibration was based on a $Li^7(p, n)Be^7$ threshold of 1.882±0.002 Mev.[9,13,14]

As a further comparison of absolute energy calibrations, the 478-kev excited level[15] in Li^7 was investigated by inelastic scattering of protons and deuterons. Gammas from this level to the ground state have been measured in several laboratories relative to the 411.2 ±0.1-kev gamma from Au^{198}, measured absolutely by DuMond.[16]

II. PROCEDURE

Incident beam energies (T_1) were obtained by calibrating the cylindrical electrostatic analyzer against the $Li(p, n)$ threshold. The spherical analyzer[12] was then calibrated using particles of known energy (T_2) elastically scattered from thick platinum. Product particle yields from thick targets of lithium, beryllium, and tritium then gave T_3 for the various reactions. Q is calculated from T_1, T_2, and θ, which is a known constant of the spherical analyzer.

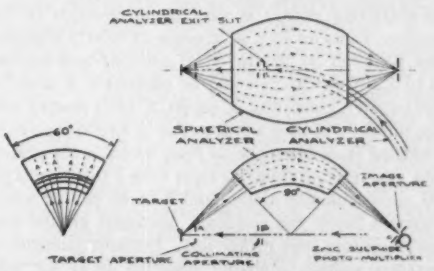

FIG. 1. Schematic drawing showing the arrangement of the two analyzers and the paths of the particles.

* Supported by the Wisconsin Alumni Research Foundation and the AEC.

† Now at Duke University, Durham, North Carolina.

‡ Now at Massachusetts Institute of Technology, Cambridge, Massachusetts.

[1] Strait, Van Patter, Buechner, and Sperduto, Phys. Rev. **81**, 747 (1951).

[2] Li, Whaling, Fowler, and Lauritsen, Phys. Rev. **83**, 512 (1951); A. H. Wapstra, Phys. Rev. **82**, 756 (1951).

[3] L. del Rosario, Phys. Rev. **74**, 304 (1948).

[4] Collins, McKenzie, and Ramm, Nature **167**, 682 (1951).

[5] A. O. Nier, Phys. Rev. **81**, 624 (1951).

[6] T. R. Roberts, Phys. Rev. **81**, 624 (1951).

[7] W. B. Lewis and B. V. Bowden, Proc. Roy. Soc. (London) **A145**, 250 (1934).

[8] G. H. Briggs, Proc. Roy. Soc. (London) **A157**, 183 (1936).

[9] Herb, Snowdon, and Sala, Phys. Rev. **75**, 246 (1949).

[10] Thomas, Driscoll, and Hipple, Phys. Rev. **78**, 787 (1950).

[11] Warren, Powell, and Herb, Rev. Sci. Instr. **18**, 559 (1947).

[12] Browne, Craig, and Williamson, Rev. Sci. Instr. (to be published).

[13] Shoup, Jennings, and Jones, Phys. Rev. **76**, 502 (1949).

[14] W. J. Sturm, Phys. Rev. **83**, 542 (1951). Sturm has measured the energy of RaC′ and Po alphas in terms of the $Li(p, n)$ threshold.

[15] Brown, Snyder, Fowler, and Lauritsen, Phys. Rev. **82**, 159 (1951)—contains a complete summary of all data on Li^7.

[16] DuMond, Lind, and Watson, Phys. Rev. **73**, 1392 (1948).

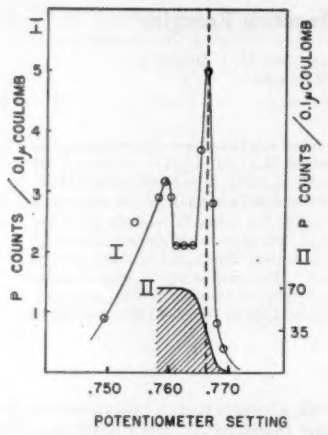

FIG. 2. Curve I shows protons scattered elastically from carbon in an evaporated beryllium target. The peak at 0.766 coincides with the half yield point of Curve II and represents surface carbon buildup. The peak at 0.759 is from carbon between the evaporation and the nickel backing foil. Curve II shows protons scattered elastically from thick soot. A potentiometer setting of 1.0 corresponds to about 1.0 Mev/charge in particle energy.

The path of the particles through the two analyzers is illustrated in Fig. 1. Bombarding particles from a pressure electrostatic generator emerged from the cylindrical analyzer with an energy spread of ± 0.06 percent. Spherical analyzer collimating and detector slit diameters of 1 and 2 mm, corresponding to resolutions of 0.15 percent and 0.24 percent in T_2, were used. Beam currents of 1/20 to 1/10 microampere were obtained. The mean angle θ between T_1 and T_2 was 134°31.5′, while the range of angle θ of particles accepted by the spherical analyzer was $\pm 12'$. The mean angle was obtained[12] by direct measurement and by observation of protons scattered from deuterons, since the scattering energy is very angle sensitive in this reaction. Particles in a solid angle of 0.0025 steradian were accepted by the spherical analyzer and energies up to 1.2 Mev/charge could be measured. A scintillation counter, consisting of an RCA 1*P*21 dusted with zinc sulfide, was used for detection of product particles —ranging from mass one to mass seven in the present data. Background counting rates were 1 to 2 counts per 100 microcoulombs above, and 5 to 40 per 10 microcoulombs below the elastically scattered groups from thin beryllium and nickel foils. Incident particles of degraded energy, probably resulting from slit edge scattering or inhomogeneities in the foils, were the cause of the higher counting background below elastically scattered groups.

Lithium was evaporated in the target chamber onto 4 micro-inch nickel foils.[17] Both 10 micro-inch beryllium foils (obtained from Dr. Hugh Bradner, University of California) and beryllium evaporations on 4 micro-inch nickel foils were used. Platinum foils were found to be very stable targets and were used for most of the calibration data. Targets were constantly heated to 200°C to prevent condensation of oil vapor. One water-cooled and one liquid-air-cooled baffle between the oil diffusion pump and the system reduced the amount of vapor present.

The use of thin nickel target backings allowed the observation of elastically scattered particles from carbon as one check on taget contamination. A thick soot target was used to check the carbon scattering cross section at 135° for 1-Mev incident protons (see Fig. 2). The value $d\sigma/d\Omega = 2.2\times10^{-25}$ cm²/steradian was the basis for the calculations of amounts of carbon contamination. All contamination checks were made near this bombarding energy, which is in a nonresonant region of the scattering yield curve.[18]

Both lithium and beryllium evaporations showed a constant distribution of carbon through the evaporations (see Fig. 1, Curve I). The surface carbon buildup was easily discernable as a superimposed thin target yield whose peak corresponded to the mean energy of scattering from pure carbon.

Prolonged bombardments of bare nickel foil showed that oxygen buildup was small compared to carbon. The oxygen scattering cross section at 165° may be obtained from the data of Laubenstein *et al.*[19] Lithium targets were found to oxidize almost immediately after evaporation in the target chamber and beryllium targets contained small amounts of oxygen distributed through the thickness of the evaporation.

The position of the elastic scattering edges from lithium and beryllium also served as a check on the surface condition of these targets. In the case of lithium targets, the half yield point of either the product particle edge or the elastic scattering edge could be observed before and after re-evaporation for shift due to contamination.

Our experience was that the rate of contamination buildup was not a predictable function of bombarding time. The buildup seemed to be greater for the 4-micro-inch foils than for the 0.002″ platinum. The scattering edge from 0.002″ platinum showed no contamination shift greater than 0.03 percent during 6-hour bombardment with 1-Mev protons. No data from targets evaporated on 4-micro-inch nickel showed more than 3×10^{16} carbon atoms/cm² after four hours bombardment. This corresponds to 0.1 percent energy loss in one traversal of a 300-kev proton. Most of the particle edges were taken in two hours or less and none of our light particle data required contamination correction, while the corrections to heavy particle data were considerably less than calibration uncertainties. Much of

[17] S. Bashkin and G. Goldhaber, Rev. Sci. Instr. **22**, 112 (1951).

[18] G. Goldhaber and R. M. Williamson, Phys. Rev. **82**, 495 (1951).

[19] Laubenstein, Laubenstein, Koester, and Mobley, Phys. Rev. **84**, 12 (1951).

the data reported by other laboratories[1,2,18] contain contamination corrections greater than calibration errors.

The choice of target thickness lay between targets either thick or thin compared to the spherical analyzer resolution. T_2, the mean product particle energy, is the "half yield" point of a thick target edge and the peak of a thin target yield curve. Platinum scattering data showed that thin target peak yields less than $\frac{1}{4}$ of the thick target yield coincided with the half yield point of the thick target edge. Because of the higher counting rates involved, thick targets were used for most of the reactions. Further advantages are: evaporation thickness is noncritical, re-evaporation leaves the shape of the edge unchanged, survey points need not be as closely spaced, and unbacked foils may be used.

For some reactions, the change in product particle energy over the $\pm 12'$ acceptance angle of the spherical analyzer was sufficient to decrease the slope of the thick target edge. Both scattering data and line shape calculations[20] showed the $Li^7(d, d)Li^7$ edge slope to be $\frac{3}{4}$ that of the platinum scattering edge. Calibrations based on half yield points of these edges were in good agreement. An analysis of line shape showed that all other sources of line width which depend on the source of the observed particles have a negligible effect on the shape of the edges. Extrapolated end points could be used in calibration if the scattering data and the reaction data involved the same $dT_2/d\theta$. This procedure was followed for Li^{7*} and $T(d, \alpha)n$.

First-order relativistic corrections, $(1+T/2E)$, were applied to the calibration of both analyzers so that T_1 and T_2 were relativistically correct (E is the rest mass of the particle). These then have to be converted to relativistic momenta, P_1 and P_2, in order to solve for P_3, the momentum of the recoil nucleus, and hence T_3 and Q. The difference between classical and relativistic treatment at this step is more than academic for the $T(d, \alpha)n$ reaction, being -133 kev in Q. This correction for the $Be^9(d, Li^7)\alpha$ Q is -3.4 kev, while the remaining reactions are changed less than 1-kev. This same consideration enters into the calculation of elastic scattering ratios. The effect is negligible for 1-Mev protons scattered from platinum, but is $-1/2000$ in the scattered energy of 2.5-Mev deuterons on Li^7. When the bombarding particles were HH^+ ions, a correction of 1/3674 (energy of the H) was made for the fraction of the kinetic energy carried by the electrons.

III. ERRORS

The following sources of systematic errors and the bases for their estimated magnitudes are considered.

(*A*) *Absolute energy calibration of both analyzers* is based on the value 1.882 ± 0.002 Mev for the $Li(p, n)$ threshold.[9] The effect on Q is always 0.1 percent of Q.

(*B*) *Analyzer angle* (θ) is $134°31.5' \pm 3'$.[12] This uncertainty has no effect on the spherical analyzer calibration since the elastic scattering ratio of protons and deuterons on platinum is insensitive to changes in angle. The effect of the 3′ angle uncertainty is calculated for each Q.

(*C*) *The relative calibration of the spherical analyzer with respect to the cylindrical analyzer* was determined by a series of 30 platinum scattering edges taken at various bombarding energies over the course of 24 days. The extreme fluctuation of calibration points over this period was ± 0.1 percent. However, no points adjacent in time to a reaction differ by more than ± 0.05 percent. Both electrical tests of the high voltage power supply control circuits and checks on the position of the platinum edge showed no systematic sources of irreproducibility greater than ± 0.02 percent in test periods of several hours. Proton scattering tests between 1 and 2 Mev in T_1 and $\frac{1}{2}$ and 1 Mev in T_2 showed the combined effects of analyzer magnetic fields and power supply nonlinearity to be less than 0.02 percent. The source of the long period instability was not located and a systematic calibration uncertainty of 0.07 percent is attached to T_2 and ± 0.03 percent to T_1. Since Q is more sensitive to errors in T_2 than to errors in T_1, this is a safe assignment.

(*D*) *Uncertainties in nuclear mass values*[2,5,6] are negligible in all of the reactions reported.

The following statistical errors are considered.

(*E*) *Product particle edge.* The uncertainty in the graphical location of the center of the product particle edges is given for each reaction in Results.

(*F*) *Calibration particle edges.* Statistics on these edges are small compared to the total systematic calibration uncertainty.

Two methods of combining estimated errors are commonly quoted in current literature. The term "probable error" generally refers to the practice of taking the square root of the sum of the squared statistical and systematic errors. The term "limit of error" or "uncertainty" generally implies addition of the magnitudes of the systematic errors and the total statistical error. Current ground-state Q values[1,2] are generally quoted with "probable errors." This convention seems most consistent with the least squares treatment of ground state Q values used in calculating a table of masses.[2] "Limit of error" would appear to be the more useful convention when measurements of the same quantity are compared in order to locate discrepancies greater than quoted errors. In order that data from a large number of sources may be treated consistently, it is desirable to consider treatment of errors in some detail.

Table I shows the magnitude of the errors involved in one of the runs of the $Be^9(p, \alpha)Li^6$ reaction. The total limit of error minus the error of absolute calibration is given as the "limit of error of measurement"—dQ_m. This allows the comparison of our data with other data

[20] R. M. Williamson, thesis, University of Wisconsin (1951).

TABLE I. Calculation of errors for $Be^9(p, \alpha)Li^6$. For this run $T_1 = 2.5554$, $T_2 = 1.9280$, $Q = 2.1239$. All energies are given in Mev.

Source of error	Magnitude	Error in Q Mev
Relative calibration of analyzers	±0.03 percent T_1 ±0.07 percent T_2	0.0005 0.0025
Analyzer angle	±3′	0.0009
Alpha-edge statistics (Fig. 2)	±0.0008 Mev	0.0015
Absolute calibration	±0.1 percent Q	0.0021
limit of error of measurement (dQ_m)		0.0054
total limit of error		0.0075
total probable error		0.0037

employing the same absolute calibration. Also, since the error in Q due to uncertainty in angle is small compared to the relative calibration errors of our data, dQ_m is a good measure of our estimates of statistical and relative calibration uncertainties when different runs of the same reaction are compared. Our final values are a weighted average of the runs taken and the final errors are the errors of the best runs.

IV. RESULTS

For each reaction reported, the following paragraphs give; bombarding energies, observed particles and edge statistics, target condition, Q values resulting from each run, average Q, error of measurement (dQ_m), and total errors. Figures 3, 4, 5, and 6 show some of the reaction data and the counting rates and backgrounds involved. The bases of the triangles in the upper right corner of these plots represent twice the spherical analyzer resolution. A potentiometer setting of 1.0 corresponds to about 1.0 Mev/charge in product particle energy.

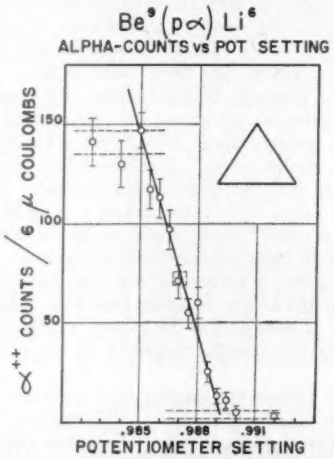

FIG. 3. Doubly ionized alphas from $Be^9(p, \alpha)Li^6$. The bombarding energy is 2.555 Mev.

$Li^6(p, \alpha)He^3$

The yield of He^{3++} from natural lithium targets was sufficient to locate edges to ±3/10,000 in about 2 hours bombarding time. Further evaporation of lithium at the end of this time caused no appreciable change of counting rate at the center of the He^3 edge. The scattering yield from carbon also showed the effect of contamination to be less than the uncertainty of the edge.

No. of runs	T_1 Mev	Q Mev	dQ_m
2	0.939	4.0220	0.0051
1	0.601	4.0265	0.0048

Average Q 4.024±0.009 limit of error
±0.005 probable error.

$Li^7(d, p)Li^8$

One proton edge was located to ±4/5000 when lithium was bombarded with 1.291-Mev deuterons. Deuterons scattered from Li^7 were observed in their calculated position at the end of the bombarding period and further evaporation of lithium did not shift this edge. Since the (d, p) reaction is less sensitive to contamination than elastic scattering, no correction to the Q values is required. The limit of error in the resulting Q of −0.192 Mev is ±0.0016 Mev; the probable error is ±0.001 Mev.

$Be^9(p, d)Be^8$

Data from both beryllium evaporations and beryllium foil targets are given below. No contamination corrections were necessary.

No. of runs	T_1 Mev	Q Mev	dQ_m
4	0.600	0.5587	0.002
1	0.732	0.5582	0.002
1	0.850	0.5584	0.002
2	1.100	0.5563	0.002

Average Q 0.558±0.0025 limit of error
±0.002 probable error.

$Be^9(p, \alpha)Li^6$

Doubly charged alphas were observed from beryllium bombarded at widely differing proton energies. The Q's resulting from observation of doubly and triply ionized Li^6 are increased 0.002 Mev because of contamination observed by scattering from carbon; the correction to the alpha-edges is negligible. Statistics on the alpha-edges were ±5/10,000, on the Li^6 edges ±15/10,000.

No. of runs	T_1 Mev	Q Mev	dQ_m
2	0.368	2.1238	0.004 alpha
4	0.601	2.1223	0.004 alpha
1	2.349	2.1231	0.0054 alpha
1	2.555	2.1239	0.0054 alpha (Fig. 3)
1	2.349	2.113	0.0075 Li^{6++} (Fig. 4)
1	2.349	2.117	0.0075 Li^{6+++}

Average Q 2.123±0.006 limit of error
±0.004 probable error.

$Be^9(d, \alpha)Li^7$

Doubly ionized Li^7 was counted from an evaporated beryllium target bombarded with 0.660-Mev deuterons. The alpha-edge was above the limiting energy of the spherical analyzer. Statistics on the Li^7 edge were $\pm 7/10{,}000$ and the position of elastically scattered deuterons indicated contamination effects to be negligible. Q was found to be 7.159 ± 0.017 limit of error, ± 0.009 probable error.

$T(d, \alpha)n$

Zirconium evaporated onto 0.010″ tungsten was loaded with tritium. (We are indebted to Dr. C. K. Bockelman for these targets.) Similarly shaped particle edges were obtained at bombarding energies of 0.800 and 1.000 Mev in the expected position for doubly

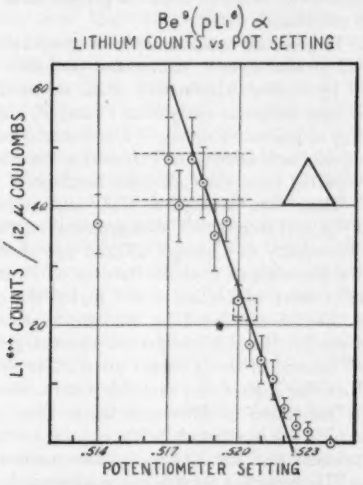

FIG. 4. Doubly ionized Li^6 from $Be^9(p, Li^6)\alpha$. The bombarding energy is 2.349 Mev.

charged alphas from the $T(d, \alpha)n$ reaction. The counting rate deep in the target was about that expected for the tritium/zirconium ratio of 1/1 which was indicated by tritium beta-activity. However, the number of tritium atoms was found to decrease rapidly near the surface of the zirconium. The maximum alpha-yield occurred 80 kev below cutoff instead of 8 kev, as expected for 2-Mev alphas from a uniform tritium target. Scraping the surface of the zirconium had no effect on the shape of the alpha-edge. Time was not available for further target development and the results of this data can only put a lower limit on the $T(d, \alpha)n$ Q value.

The extrapolated end point of deuterons elastically scattered from Li^7 was used in calibration. $dT_2/d\theta$ is the same for this scattering reaction as for the $T(d, \alpha)n$ reaction and the extrapolated cutoffs should bear the same ratio to the mean energies. Because of the non-uniform tritium target the experimental curve for the

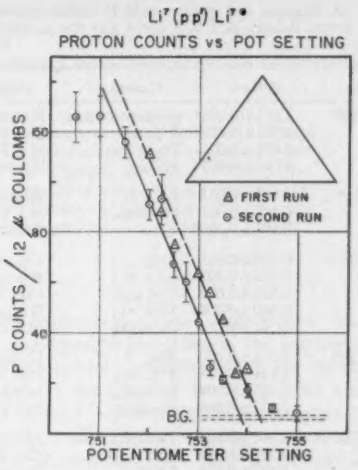

FIG. 5. Protons from $Li^7(p, p')Li^{7*}$ (478 kev). The bombarding energy is 1.812 Mev.

$T(d, \alpha)n$ reaction has a slope much less than expected. Q can be given as $17.578 - 0.030$ Mev. This does not disagree with the mass value of Li and Whaling,[2] from which Q is 17.576 ± 0.018 Mev.

Li^{7*}

The 0.478-Mev level in Li^7 was investigated by the inelastic scattering of both protons and deuterons. Within the sum of the limits of error of the two measurements (± 0.0017 Mev), the two reactions involve the same level. Alternate edges of elastically and inelastically scattered particles were taken and found to reproduce to better than $\pm 4/10{,}000$ (see Figs. 5 and 6).

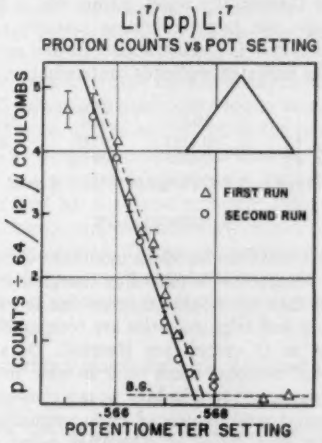

FIG. 6. Elastically scattered protons from Li^7 bombarded at 0.9051 Mev. The first and second runs follow the first and second runs, respectively, of Fig. 4.

TABLE II. Summary of ground-state Q values quoted with probable errors. References 1, 2, 3, and 4 give the publications of all data.

Reaction	Q(Mev)	Calibration	Laboratory
$Li^6(p, \alpha)He^3$	4.015±0.006[a]	proton moment	Birmingham[d]
	4.017±0.012	$F(p, \alpha\gamma)$	Cal. Tech.[e]
	4.021±0.006	Po alpha	M.I.T.[f]
	4.024±0.005	$Li(p, n)$	Wisconsin
$Li^7(d, p)Li^8$	−0.192±0.001	$Li(p, n)$	Wisconsin
	−0.188±0.007	Po alpha	M.I.T.[f]
	−0.187±0.010[b]		Cambridge[g]
$Be^9(p, d)Be^8$	0.541±0.003	Abs.	Chicago[h]
	0.558±0.002	$Li(p, n)$	Wisconsin
	0.558±0.003	$F(p, \alpha\gamma)$	Cal. Tech.[e]
	0.560±0.004[c]	$Li(p, n)$	Wisconsin[i]
	0.562±0.004	Po alpha	M.I.T.[f]
$Be^9(p, \alpha)Li^6$	2.074±0.030	Abs.	Chicago[j]
	2.121±0.007	$F(p, \alpha\gamma)$	Cal. Tech.[e]
	2.123±0.004	$Li(p, n)$	Wisconsin
	2.142±0.006	Po alpha	M.I.T.[f]
$Be^9(d, \alpha)Li^7$	7.150±0.008	Po alpha	M.I.T.[f]
	7.151±0.010	ThC′ alpha	Cal. Tech.[k]
	7.159±0.009	$Li(p, n)$	Wisconsin

[a] Limit of error.
[b] Recoil angle of Li^8.
[c] From photodisintegration thresholds of D and Be^9.
[d] See reference 4.
[e] Tollestrup, Fowler, and Lauritsen, Phys. Rev. 76, 428 (1949).
[f] See reference 1.
[g] E. B. Paul, Phil. Mag. 41, 942 (1950).
[h] See references 3 and 13.
[i] R. C. Mobley and R. A. Laubenstein, Phys. Rev. 80, 309 (1950).
[j] See references 3 and 20.
[k] See reference 2.

The elastic scattering edge was taken as the spherical analyzer calibration and the added fluctuations of the elastic and inelastic scattering edges was taken as the error in T_2. None of this fluctuation was attributed to the cylindrical analyzer. Since Q is more sensitive to dT_2 than to dT_1, this is a safe assignment. Extrapolated end points of the two edges could be compared since the slopes are theoretically equal. Errors due to both analyzer angle and target condition partially cancel in the calculation of Q. Carbon scattering and re-evaporation checks indicated negligible contamination effect.

	Q Mev	dQ_m Mev	T_1 Mev
$Li^7(p, p')$	−0.4782	0.0007	1.812
$Li^7(d, d')$	−0.4775	0.0010	2.495

Average Q −0.4780±0.0012 limit of error.

V. DISCUSSION

From the reactions for which more than one edge was taken at comparable bombarding energies, it may be concluded that the estimated errors due to calibration uncertainty and edge statistics are comparable to the variations in Q values (see Results). Data on the $Be^9(p, \alpha)Li^6$ reaction taken over a wide interval of proton energy, 0.37 to 2.55 Mev, give a combined check on the correct measurement of angle, estimation of contamination, and choice of calibration point. The observation of Li^{6++} and Li^{6+++} from this same reaction serves to verify the above considerations and previous estimates[12] of spherical analyzer magnetic field. No closed cycles can be given from the present data as an internal consistency check.

TABLE III. Measurements of the excitation energy of Li^{7*} (478 kev).

Calibration	Reaction	Energy (kev)	Laboratory[b]
Au^{198} gamma	$Be^7(K)$	478.5±0.5	Wash. Univ.
Au^{198} gamma	$Be^7(K)$	476.6±0.8	Cal. Tech.
Au^{198} gamma	$Li^7(p, p')$	478.3±0.6[a]	Cal. Tech.
Au^{198} gamma	$Li^8(d, p')Li^{7*}$	478.5±1.0[a]	Cal. Tech.
Au^{198} gamma	$B^{10}(n, \alpha')Li^{7*}$	478.5±1.5	Chalk River
$Li(p, n)$	$Li^7(p, p')$	478.2±1.2	Wisconsin
$Li(p, n)$	$Li^7(d, d')$	477.5±1.5	Wisconsin
$F(p, \alpha\gamma)$	$Li^7(p, p')$	479.0±1.0	Cal. Tech.
Po alpha	$Be^9(d, \alpha')Li^{7*}$	482±3	M.I.T.

[a] No correction for Doppler shifts.
[b] Reference 15 contains a complete list of measurements of this level.

Table II gives all measurements of comparable accuracy of ground-state Q values and probable errors reported by various laboratories. Data reported from *MIT*[1] is from magnetic analysis of T_1 and T_2 based on the energy of polonium alphas.[7,8] Electrostatic analysis of T_1 and magnetic analysis of T_2 is used in the measurements reported from the California Institute of Technology.[2] Their data is based on ThC′ alpha-energy[7,8] or the $F^{19}(p, \alpha\gamma)$ resonance.[9] Measurements carried out at the University of Chicago[3] utilized one absolutely calibrated electrostatic analyzer for data on T_1 and T_2. The recent work of Collins *et al.*,[3] makes use of one annular magnet calibrated by the proton resonance method against the absolute proton moment given by Hipple.[10] Several of the Q values listed differ by more than twice the sum of the probable errors. However, the only indication of differences larger than quoted errors which are systematic with respect to type of absolute calibration are the Chicago measurements.[21]

Table III shows the most accurate observations[15] of the 478-kev level in Li^7. Here again the errors of comparison appear to mask hidden systematic errors in the comparison or absolute measurements involved. Hence it is not possible to decrease the $Li^7(p, n)$ quoted error[9] by a comparison of inelastic scattering data with gamma-ray data based on the absolute measurement by DuMond[16] of the Au^{198} gamma. Sturm[14] has measured the energies of Po and RaC′ alphas with a cylindrical analyzer[11] calibrated against the $Li^7(p, n)$ threshold. Collins[4] has measured Po and ThC′ alphas in an annular magnet calibrated with respect to the proton moment given by Hipple.[10] These more direct comparisons of absolute calibrations also suggest no errors greater than the present errors of measurements in reaction data.

We wish to thank Professor H. T. Richards for suggesting this work and for many helpful discussions of it, and Mr. R. E. Benenson and Mr. K. W. Jones for their help in the experimental work.

[21] More recent Chicago work reported at the Washington 1951 meeting gives values agreeing with those of the other laboratories.

Hamiltonians without Parametrization*

ROBERT H. PENFIELD†
Syracuse University, Syracuse, New York
(Received July 2, 1951)

Theories which are covariant with respect to transformation groups involving arbitrary functions cannot be of the Cauchy-Kowalewski type. Therefore, it would appear that such theories cannot be cast into a hamiltonian formalism. However, a hamiltonian function can be formed although it is, to a certain extent, arbitrary. This lack of uniqueness is an immediate consequence of the covariance requirements. The adoption of a particular hamiltonian function destroys the covariance of the theory. This situation is similar to the introduction of "cordinate conditions" in the theory of gravitation or the use of the Lorentz gauge condition in electrodynamics.

I. INTRODUCTION

THE development of a covariant field theory in the hamiltonian form has to overcome the difficulty that the usual (lagrangian) field equations do not permit the unique determination of a particular solution by suitable initial conditions on a (space-like) hypersurface, inasmuch as from any one solution formally different ones may be obtained by a coordinate transformation confined to a bounded domain, but with arbitrary generating functions, while on the other hand, in the typical hamiltonian theory the equations are solved with respect to the time derivatives of all the variables, and as a result, the equations are a typical Cauchy-Kowalewski system; if the initial conditions are properly set, the solution is unique. The first successful attempt to solve the problem was made by Rosenfeld[1] although the Lagrangian considered by him has a much more simple transformation law than those to be considered in this paper. Dirac[2] and after him Schild and Pirani[3] have solved this apparent contradiction by retaining in the expression for the hamiltonian some of the velocities, so that some of the usual canonical equations reduce to empty relations. The Syracuse group[4–6] has taken a different approach, by constructing a hamiltonian which, while free of velocities, contains a certain number of arbitrary functions. Choice of these functions in a particular calculation amounts to the adoption of so-called coordinate conditions in the usual formalism.

Originally, the Syracuse method included the adoption of a system of supplementary coordinates, the so-called parameters. Their introduction leads to certain homogeneity properties in the lagrangian and in the momentum densities which are utilized to construct the hamiltonian. In the present paper, a different method will be presented. Parameters are not introduced at all, but instead, by means of a transformation of variables, the time derivatives of the variables are separated into two sets, such that one set of "velocities" can be expressed uniquely in terms of the canonical variables ("coordinates" and "momentum densities"), while the velocities of the other set are completely arbitrary. The corresponding momentum densities then turn out to satisfy certain relationships not involving velocities, and these relationships correspond exactly to the "constraints" of the earlier Syracuse papers and will again be called "constraints." When the customary expression for the hamiltonian is written out, the velocities are then multiplied by expressions which vanish because of the constraints, and thus these terms may be omitted. The constraints then form a set of conditions which must be satisfied on the initial hypersurface, while the canonical equations must be satisfied throughout space-time.

As far as subsequent quantization is concerned, it appears now as if the new formalism will be considerably simpler to work with than the parameter formalism, at least in the absence of particles. Whether results of the two approaches will be equivalent in the presence of matter, only future investigations will show.

In the sections that follow the new method will be developed first for a general covariant theory with a quadratic lagrangian, without reference to a particular type of physical field. The general result will then be applied to the case of Einstein's theory of gravitation, for the case of combined gravitational and electromagnetic fields.

II. THE FIELD VARIABLES AND THE LAGRANGIAN

The exact nature of the field variables will be left unspecified and denoted by y_A $(A=1, \cdots, N)$, where N is the number of algebraically independent components. It will be assumed that the field equations can

* This work was supported by a contract with the ONR. This paper contains the prncipal resuilts of a Ph.D. thesis accepted by the Graduate School of Syracuse University.
† Now at Harpur College, Endicott, New York.
[1] L. Rosenfeld, Ann. Physik **5**, 113 (1930).
[2] P. A. M. Dirac, Can. J. Math. **2**, 129 (1950).
[3] A. Schild and F. A. E. Pirani, Phys. Rev. **79**, 986 (1950).
[4] P. G. Bergmann, Phys. Rev. **75**, 680 (1949). Equations in this paper will be referred to by I plus the number of the equation e.g., (I-3.6).
[5] P. G. Bergmann and J. H. M. Brunings, Revs. Modern Phys. **21**, 480 (1949).
[6] Bergmann, Penfield, Schiller, and Zatzkis, Phys. Rev. **80**, 81 (1950), Equations in this paper will be referred to by III plus the number of the equation e.g., (III-7.5).

be derived from a variational principle of the form

$$\delta I=0, \quad I=\int_V L(y_A, y_{A,\rho})d^4x,$$

where

$$L=\Lambda^{A\rho B\sigma}y_{A,\rho}y_{B,\sigma}, \tag{1}$$

and

$$\Lambda^{A\rho B\sigma}=\Lambda^{A\rho B\sigma}(y_C).$$

The coefficients $\Lambda^{A\rho B\sigma}$ have the following symmetry property:

$$\Lambda^{A\rho B\sigma}=\Lambda^{B\sigma A\rho}. \tag{2}$$

The field equations which result from a variation of the Lagrangian (1) will be denoted by L^A,

$$\begin{aligned} L^A&\equiv\partial L/\partial y_A-(\partial L/\partial y_{A,\rho})_{,\rho}=0, \\ L^A&\equiv(\Lambda^{A\rho B\sigma}+\Lambda^{A\sigma B\rho})y_{B,\sigma\rho}+\cdots. \end{aligned} \tag{3}$$

Regardless of whether the field equations are satisfied or not, L^A will be used for the left-hand side of these equations.

With respect to infinitesimal coordinate transformations, the field variables will be assumed to transform according to the law (I-2.3)

$$\bar{\delta}y_A=F_{A\mu}{}^{B\nu}\xi^\mu{}_{,\nu}y_B-y_{A,\mu}\xi^\mu. \tag{4}$$

The four functions ξ^μ represent the infinitesimal changes of the coordinate values of a fixed world point. The $F_{A\mu}{}^{B\nu}$ are numbers which depend on the type of field variables which represent the field, independent of the coordinate system used and of the coordinate values themselves. Lastly, the $\bar{\delta}y_A$ are the changes produced in the field variables y_A as a function of their arguments as a result of the infinitesimal coordinate transformation.

To assure covariant field equations from the variational principle, it is required that (I-2.5)

$$\bar{\delta}L=Q^\mu{}_{,\mu}. \tag{5}$$

As a consequence of this requirement and the assumed transformation law for the y_A, one obtains four identities (I-3.3)

$$(F_{A\mu}{}^{B\nu}y_BL^A)_{,\nu}+y_{A,\mu}L^A\equiv 0. \tag{6}$$

By substituting L^A, Eq. (3), into the above identities, the terms containing second derivatives will lead to third derivatives, and these must cancel each other. It follows that the coefficients $\Lambda^{A\rho B\sigma}$ must satisfy the identities (I-3.6)

$$(F_{A\mu}{}^{B\nu}L^{AC\rho\sigma}+F_{A\mu}{}^{B\sigma}L^{AC\nu\rho}+F_{A\mu}{}^{B\rho}L^{AC\sigma\nu})y_B\equiv 0, \tag{7}$$

where

$$L^{AC\rho\sigma}=\Lambda^{A\rho C\sigma}+\Lambda^{A\sigma C\rho}.$$

In what follows, $4N$ of these identities are of special interest, those in which ρ, σ, and ν all equal to 4, (I-3.7)

$$F_{A\mu}{}^{B4}y_BL^{AC4}=2F_{A\mu}{}^{B4}y_B\Lambda^{A4C4}\equiv 0. \tag{8}$$

Also, from Eq. (1),

$$\Lambda^{A4C4}=\tfrac{1}{2}\partial^2L/\partial\dot{y}_A\partial\dot{y}_B, \tag{9}$$

where

$$\dot{y}_A=y_{A,4}.$$

Consequently, the matrix Λ^{A4C4} is a singular matrix because it has four nonvanishing, linearly independent null vectors, $F_{A\mu}{}^{B4}y_B$. In other words, its determinant must vanish. Now Λ^{A4B4} is just the matrix of the coefficients of these second "time" derivatives in the field equations. Therefore, the Euler-Lagrange equations cannot be solved with respect to all the second "time" derivatives. The requirement of covariant field equations forces the matrix Λ^{A4C4} to be singular; that is, its determinant is zero. Since this matrix has four linearly independent null vectors, its rank will in general be $N-4$ unless the lagrangian has other special invariance properties, *viz.*, the guage invariance of electromagnetism. In such cases, its rank will be even lower. Each arbitrary function involved in the transformation group with respect to which the field equations are covariant reduces the rank of the singular matrix Λ^{A4C4} by one.

III. THE MOMENTUM DENSITY AND THE CONSTRAINTS

The momentum densities are introduced by the usual definition

$$\pi^A=\partial L/\partial\dot{y}_A. \tag{10}$$

From Eq. (1), it follows that

$$\pi^A=2\Lambda^{A4B\sigma}y_{B,\sigma}.$$

However, the momentum densities thus defined will not be algebraically independent of each other because, from Eqs. (8) and (9), the functional determinant or jacobian between the "new" and "old" variables, in this case between π^A and $\dot{y}_A$, vanishes.

$$J=|\partial\pi^A/\partial\dot{y}_B|=|\partial^2L/\partial\dot{y}_A\partial\dot{y}_B|\equiv 0. \tag{11}$$

Therefore, it would appear impossible that one could solve for the "velocities," $\dot{y}_A$, in terms of the momentum densities, π^A, in the usual manner. Since the momentum densities are not algebraically independent, they must satisfy a number of algebraic relationships which are free of $\dot{y}_A$. As is apparent from above, these relationships or "constraints" are a consequence of our covariance requirement. If the theory contains any other invariance properties in addition to the coordinate invariance, there will be other constraints. The number of constraints will always be equal to the number of arbitrary functions involved in the transformation group with respect to which the field equations are covariant. In the case of coordinate covariance, there are four arbitrary functions in the transformation group, and consequently, there are four constraints among the momenta π^A. In the case of electromagnetism, the gauge

group involves one arbitrary function, and one additional constraint arises from this special invariance. In Eq. (10), we can separate derivatives with respect to x^4 from the other derivatives, and get[7]

$$\pi^A = 2\Lambda^{A4B\nu} y_{B,\nu} + 2\Lambda^{A4B4}\dot{y}_B. \tag{12}$$

We have already shown that the matrix Λ^{A4B4} is a singular matrix, with at least four independent null vectors. Since $F_{A\mu}{}^{B4}y_B$ are four null vectors of the matrix Λ^{A4B4}, $(\mu=1, \cdots, 4)$, multiplication of Eq. (12) by $F_{A\mu}{}^{B4}y_B$ yield four relationships which are free of "velocities" and which have the form,

$$F_{A\mu}{}^{B4}y_B(\pi^A - 2\Lambda^{A4C\nu}y_{C,\nu}) = 0. \tag{13}$$

These four constraints we shall call the *coordinate constraints*. As was mentioned before, the existence of constraints is a direct consequence of covariance requirements, since the matrix, Λ^{A4B4}, is singular for this reason. In what follows it will be assumed that there are w arbitrary and consequently w null vectors to the singular matrix Λ^{A4B4} and w constraints, $(w \geqslant 4)$. The null vectors form a linear manifold. That is, any linear combination of null vectors is again a null vector, and any null vector multiplied by a constant is again a null vector.

IV. THE TRANSFORMATION AND THE HAMILTONIAN

We shall now proceed to construct hamiltonians for covariant field theories whose lagrangian density is homogeneous, quadratic function of the first derivatives of the field variables. The form of the hamiltonian for such lagrangians will be obtained explicitly. The method makes use of the fact that the theory can be made invariant under transformations in the $\dot{y}_A$ space which bring the singular matrix Λ^{A4B4} to a form in which its last w rows and columns are filled with zeros. Such a matrix will be termed a "bordered" matrix. The $N-w$ sub-matrix which results will be a nonsingular matrix having a definite inverse. Then, it will be possible to solve for some of the transformed velocities in terms of the transformed momenta. If the hamiltonian is then formed by the usual means, the "velocities" which could not be expressed in terms of momenta can be eliminated by the constraint conditions. The hamiltonian so formed will then depend intimately on the constraints and cannot be freed from the constraints without re-introducing the velocities.

The transformation matrices, which accomplish the bordering of the matrix Λ^{A4B4}, are to a large extent arbitrary. The last w rows of the transformation matrix (D) are filled with the w independent null vectors, while the first $N-w$ rows are arbitrary except that they must be linearly independent of the null vectors in order that the transformation matrix D should be nonsingular.

[7] In this paper Greek indexes run from one to four and Latin indexes from one to three.

The algebraic constrains between the canonical variables must hold for any combination of the field variables consistent with the expression (10) for the momentum densities. Therefore, the $\dot{y}_A$ will be considered as the coordinates of a symbolical "vector space" and the functions, π^A, are then specific first-degree homogeneous functions of the coordinates in that vector space. In any transformation of the y_A into new y_A with nonvanishing jacobian, the "coordinates" of our vector space (the $\dot{y}_A$) will undergo a linear transformation, and the momentum densities will transform contragradiently to them. The $\dot{y}_A$ will be referred to as "coordinates," and all quantities with the same transformation law will be called "contravariant vectors." The π^A form a "covariant vector," the matrix Λ^{A4B4} a "covariant symmetric tensor," and the lagrangian is a "scalar." Therefore, the hamiltonian as it is usually defined,

$$H = -L + \dot{y}_A\pi^A, \quad A=1, \cdots, N, \tag{14}$$

is also a "scalar." If one considers the non-singular transformation matrix $D^{-1A}{}_B$, then the coordinates $\dot{y}_A$ transform according to the law

$$\dot{y}_B{}' = \dot{y}_A D^{-1A}{}_B, \tag{15}$$

and other important quantities according to the laws

$$\begin{gathered}(\Lambda^{A4B4})' = \Lambda^{C4D4}D^A{}_C D^B{}_D, \\ \{\Lambda^{A\nu B4}y_{A,\nu}\}' = (\Lambda^{A\nu C4}y_{A,\nu})D^B{}_C, \\ \pi'^A = D^A{}_B\pi^B, \quad V'_{AS} = V_{BS}D^{-1B}{}_A, \\ S = 1, \cdots, w.\end{gathered} \tag{16}$$

V_{AS} represents the null vectors of Λ^{A4B4}. This transformation procedure is similar to that carried out in III.

As indicated previously, the D matrix must be chosen in such a way that the new matrix, Λ'^{A4B4} of Eq. (16), becomes a matrix in which the last w rows and columns are filled with zeros. That is, the matrix Λ'^{A4B4} must be "bordered" with zeros. The matrix will have this structure if the last w rows of the D matrix are chosen as the w null vectors of Λ'^{A4B4} and if the first $N-w$ rows are any arbitrary set of vectors, not containing velocities, which are linearly independent of the null vectors. A D matrix so determined will be a non-singular matrix which has a unique inverse D^{-1}. The D and D^{-1} matrices have the following structure:

$$D = \begin{array}{c} \\ N-w \\ w \end{array} \begin{array}{c} \overset{N}{} \\ \left[\begin{array}{c} D^{A^*}{}_A \\ \hline D^S{}_A \end{array}\right. \end{array}, \quad \begin{array}{l} A=1, \cdots, N \\ A^*=1, \cdots, N-w \\ S=(N-w+1), \cdots, N \end{array} \tag{17}$$

$$D^{-1} = \begin{array}{c} \\ N \end{array} \begin{array}{c} \overset{N-w \qquad w}{} \\ \left[\begin{array}{c|c} D^{-1A}{}_{A^*} & D^{-1A}{}_S \end{array}\right. \end{array}.$$

If the only invariance properties of the theory are coordinate invariance, the rectangular matrix $D^S{}_A$ is given by

$$D^S{}_A = D_{\mu A} = F_{A\mu}{}^{B4} y_B. \tag{18}$$

From Eq. (16),

$$\Lambda'^{S4B4} = \Lambda^{C4D4} D^S{}_C D^B{}_D = 0 \tag{19}$$

because $D^S{}_C$ is a rectangular array of null vectors of Λ^{C4D4}. Moreover, the matrix

$$\Lambda'^{A^*4B^*4} = \Lambda^{C4D4} D^{A^*}{}_C D^{B^*}{}_D, \tag{20}$$

is a nonsingular matrix because $D^{A^*}{}_C$ is a rectangular array of vectors which are linearly independent of the null vectors. However, $\Lambda'^{A^*4B^*4}$ is not determined uniquely until the rectangular matrix $D^{A^*}{}_C$ has been chosen. If the inverse of $\Lambda'^{A^*4B^*4}$ is denoted by $G_{A^*4B^*4}$, then

$$\Lambda'^{A^*4B^*4} G_{B^*4C^*4} = \delta^{A^*}{}_{C^*}. \tag{21}$$

Therefore, the Λ'^{A4B4} matrix has the form

$$\Lambda'^{A4B4} = \begin{array}{c} \\ N-w \\ w \end{array} \begin{array}{c} \begin{array}{cc} N-w & w \end{array} \\ \left[\begin{array}{c|c} \Lambda'^{A^*4B^*4} & 0 \\ \hline 0 & 0 \end{array}\right] \end{array}, \tag{22}$$

and the new lagrangian density has the form,

$$L = L' = (\Lambda^{AnBm} y_{A,n} y_{B,m})' + 2(\Lambda^{AnB4} y_{A,n})' \dot{y}'_B + \Lambda'^{A4B4} \dot{y}'_A \dot{y}'_B. \tag{23}$$

The new momentum densities, calculated from either the new lagrangian density or from the transformation Eq. (16), are

$$\pi'^A = 2(\Lambda^{A4Bn} y_{B,n})' + 2\Lambda'^{A4B4} \dot{y}'_B. \tag{24}$$

Because of the special form of Λ'^{A4B4},

$$\Lambda'^{A4B4} \dot{y}'_B = \Lambda'^{A4B^*4} \dot{y}'_{B^*}. \tag{25}$$

If the components of π'^A in the null space are separated from the other components,

$$\pi'^{A^*} = 2(\Lambda^{A^*4Bn} y_{B,n})' + 2\Lambda'^{A^*4B^*4} \dot{y}'_{B^*}, \tag{26}$$

and,

$$\pi'^S = 2(\Lambda^{S4Bn} y_{B,n})'. \tag{27}$$

Equation (27) is the expression for the constraints in the new coordinate system.

Equation (26) can be solved for the $\dot{y}'_{B^*}$ by multiplication by $G_{A^*4B^*4}$ to obtain

$$\dot{y}'_{A^*} = G_{A^*4B^*4} (\tfrac{1}{2}\pi'^{B^*} - (\Lambda^{B^*4Cn} y_{C,n})'), \tag{28}$$

by using condition (21). The matrix $G_{A^*4B^*4}$ is arbitrary until the form of the rectangular matrix $D^{A^*}{}_C$ has been chosen.

It will be shown, by properly using the constraints [Eq. (27)], that a hamiltonian density can be found in the new space by the usual methods. However, the hamiltonian density so determined is not unique, and, in fact, an infinity of hamiltonians can be found. The hamiltonian density in the original space can then be found by use of the transformation equations for the momentum densities and "tensors." The fact that the hamiltonian is not uniquely determined is not surprising because, the covariant Euler-Lagrange equations cannot be solved with respect to the highest "time" derivatives. Therefore, the continuation of the solutions in "time" is not unique. However, the canonical equations, by their very nature, are solved with respect to the highest "time" derivatives. Yet the hamiltonian formalism is equivalent to that of Lagrange. The apparent contradiction finds its explanation in the fact that the hamiltonian is not uniquely determined. Therefore, the continuation in "time" would not be unique with given initial conditions, and the apparent contradiction is thereby resolved.

The hamiltonian density is usually defined as,

$$H = -L + \dot{y}_A \pi^A. \tag{29}$$

Since the hamiltonian density is a scalar under the "coordinate" transformation described above in the $\dot{y}_A$ vector space,

$$H = H' = -L' + \dot{y}'_A \pi'^A. \tag{30}$$

If the expression for L' [Eq. (23)] is substituted in the above expression for H', one obtains, after separating derivatives with respect to x^4 from the other derivatives and using the fact that Λ'^{A4B4} is a "bordered" matrix,

$$H' = -(\Lambda^{AnBm} y_{A,n} y_{B,m})' - \Lambda'^{A^*4B^*4} \dot{y}'_{A^*} \dot{y}'_{B^*} + (\pi'^{A^*} - 2(\Lambda^{A^*4Bm} y_{B,m})') \dot{y}'_{A^*} + (\pi'^S - 2(\Lambda^{S4Bm} y_{B,m})') \dot{y}'_S, \tag{31}$$

where A^*, A, and S have the same meaning as before. The coefficient of the $\dot{y}'_S$ term vanishes because of the constraints [Eq. (27)]. The fact that the "velocities" $\dot{y}'_S$ drop our of the hamiltonian is very fortunate since we cannot express them in terms of the canonical variables π^A, y_A, and $y_{A,n}$. The "velocities" $\dot{y}'_{A^*}$, on the other hand, can be expressed in terms of the canonical variables [Eq. (28)], and thus we can form a hamiltonian altogether free of "velocities." However, this hamiltonian depends on the constraints in such a manner that it cannot exist unless the constraints are satisfied. From the expression for $\dot{y}'_{A^*}$ [Eq. (28)], the hamiltonian becomes

$$H' = -(\Lambda^{AnBm} y_{A,n} y_{B,m})' + G_{A^*4B^*4} (\tfrac{1}{2}\pi'^{A^*} - (\Lambda^{A^*4Am} y_{A,m})') \times (\tfrac{1}{2}\pi'^{B^*} - (\Lambda^{B^*4Bn} y_{B,n})') \tag{32}$$

after using Eq. (21). However, this expression is not the only hamiltonian which can be obtained. We can add to the above hamiltonian any algebraic combina-

tion of the constraints [Eq. (27)] with unknown coefficients which are free of "velocities." Therefore, the hamiltonian can be written in the form

$$H'=H'_1+K_S(y'_A, y'_{A,n}, \pi'^A)(\pi'^S-2(\Lambda^{SkBm}y_{B,m})'), \quad (33)$$

where H'_1 is the hamiltonian of Eq. (32).

If one expresses the primed quantities in the hamiltonian in terms of the unprimed quantities by means of Eqs. (16), the hamiltonian

$$H=-\Lambda^{AnBm}y_{A,n}y_{B,m}+G_{A^*kB^*l}D^{A^*}{}_AD^{B^*}{}_B \times(\tfrac{1}{2}\pi^A-\Lambda^{AkCn}y_{C,n})(\tfrac{1}{2}\pi^B-\Lambda^{BlDm}y_{D,m}), \quad (34)$$

which results contains the original canonical variables π^A, y_A, and $y_{A,n}$. The choice of the rectangular matrix $D^{A^*}{}_A$ has no effect on the final form of H except to permit the addition of linear and quadratic combinations of the coordinate constraints (13). Therefore, the hamiltonian (34) possesses exactly the degree of arbitrariness required by the general theory.

In III a similar hamiltonian to the expression (34) was obtained which we shall call the p-hamiltonian. We can make the p-hamiltonian identical with the expression (34). First we must set the arbitrary function v^ρ in III equal to $\delta_4{}^\rho$; then, remembering that the integral over all space of the momentum density λ_4 (III-7.5) is a constant of the motion,—the "time" derivatives of λ_4 can be expressed as a surface integral which vanishes when the surface boundaries are at infinity—we shall drop the term containing λ-quantities. The remaining terms in (III-7.5) are then identical with the expression (34).

The canonical field equations take the form

$$\dot{y}_A=\partial H/\partial\pi^A-(\partial H/\partial\pi^A{}_{,n})_{,n}\equiv\delta H/\delta\pi^A,$$

and,

$$\dot{\pi}^A=-\partial H/\partial y_A+(\partial H/\partial y_{A,n})_{,n}\equiv-\delta H/\delta y_A. \quad (35)$$

The time derivative of any functional of the canonical variables

$$\mathfrak{F}=\int_V F(y_A, y_{A,n}, \pi^B, \pi^B{}_{,n})d^3x,$$

can be given the form,

$$\dot{\mathfrak{F}}=\int_V\left(\frac{\partial F}{\partial y_A}\frac{\delta H}{\delta\pi^A}+\frac{\partial F}{\partial y_{A,n}}\left(\frac{\delta H}{\delta\pi^A}\right)_{,n}-\frac{\partial F}{\partial\pi^A}\frac{\delta H}{\delta y_A}-\frac{\partial F}{\partial\pi^A{}_{,n}}\left(\frac{\delta H}{\delta y_A}\right)_{,n}\right)d^3x.$$

If a total divergence term is separated from this expression, this term makes no contribution since it can be converted by Gauss theorem into a surface integral which vanishes when surface integral which vanishes when surface boundaries are at infinity. The remaining terms have the form

$$\dot{\mathfrak{F}}=\int_V(F, H)d^3x,$$

where (F, H) is the "Poisson bracket" between F and H and stands for

$$(F, H)=\frac{\delta F}{\delta y_A}\frac{\delta H}{\delta\pi^A}-\frac{\delta F}{\delta\pi^A}\frac{\delta H}{\delta y_A}.$$

This "Poisson bracket" is very useful when passage to the quantum theory is desired.

V. THE LAGRANGIAN OF RELATIVITY WITH ELECTROMAGNETIC FIELD

The lagrangian density of the general theory of relativity has the following structure if the electromagnetic field is included

$$L=L_{grav}+L_{el},$$

where L_{grav} and L_{el} have the same form as in III.

The appropriate values for the constant coefficient $F^{B\gamma}{}_{A\beta}$, if one considers as the basic field variables the $g_{\alpha\nu}$ and ϕ_ν, are given in III. The $g_{\alpha\nu}$ are the symmetric components of the covariant metric tensor and the ϕ_μ are the four electromagnetic potentials. This lagrangian density contains the field variables and their first derivatives only. Moreover, the lagrangian is also homogeneous quadratic in the first derivatives of the field variables. Therefore, the theory of the earlier parts of this paper applies to the case of gravitation with electromagnetic field.

The lagrangian density can be rewritten to demonstrate this quadratic structure. Renaming dummy indexes and factoring we get,

$$L=\Lambda^{(\alpha\beta)\rho(\gamma\delta)\sigma}g_{\alpha\beta,\rho}g_{\gamma\delta,\sigma}+Y^{\mu\rho\nu\sigma}\phi_{\mu,\rho}\phi_{\nu,\sigma}, \quad (36)$$

where $\Lambda^{(\alpha\beta)\rho(\gamma\delta)\sigma}$ and $Y^{\mu\rho\nu\sigma}$ with their symmetry properties are given in III. From Eq. (8) it can be shown that

$$\Lambda^{\beta\tau\rho\upsilon\sigma\upsilon}+\Lambda^{\beta\tau\sigma\upsilon\rho\upsilon}+\Lambda^{\beta\tau\upsilon\sigma\rho\upsilon}+\Lambda^{\beta\sigma\rho\upsilon\upsilon\tau}+\Lambda^{\beta\rho\sigma\upsilon\upsilon\tau}+\Lambda^{\beta\rho\upsilon\sigma\upsilon\tau}\equiv 0. \quad (37)$$

If $\rho=\sigma=\nu=4$ in Eq. (37), one sees that

$$\Lambda^{4\beta4\gamma44}=\Lambda^{\gamma44\beta44}\equiv 0, \quad (38)$$

and

$$Y^{\mu444}=Y^{44\mu4}\equiv 0, \quad (39)$$

hold. Therefore, the singular matrices $\Lambda^{\alpha\beta4\gamma44}$ and $Y^{\mu4\nu4}$ have the important property of being "bordered"; that is, they have their zeros in the last rows and columns. Consequently, it is not necessary to make any transformations to bring them into this form. The submatrices Λ^{ab4mn4} and $Y^{\mu4\nu4}$ are nonsingular matrices and have unique inverses.

From Eq. (9) the null vectors of this matrix are

$$-(g_{\mu\alpha}\delta_\beta{}^4+g_{\mu\beta}\delta_\alpha{}^4)-\phi_\mu\delta_\alpha{}^4, \qquad \begin{matrix}\mu=1,\cdots,4\\ \alpha,\beta=1,\cdots,4\end{matrix} \tag{40}$$

when substitution for $F_{(\alpha\beta)\mu}{}^{(\gamma\delta)4}$ and $F_{\alpha\mu}{}^{\gamma 4}$ is made. Since the null vectors form a linear manifold, linear combinations of these null vectors are again null vectors. Therefore, multiplication of Eq. (40) by $g^{\mu\gamma}$ will give null vectors

$$-(\delta_\alpha{}^\gamma\delta_\beta{}^4+\delta_\beta{}^\gamma\delta_\alpha{}^4)-\phi^\gamma\delta_\alpha{}^4, \qquad \begin{matrix}\gamma=1,\cdots,4\\ \alpha,\beta=1,\cdots,4\end{matrix} \tag{41}$$

where γ indicates the null vector in question and $(\alpha\beta)$ and α indicate the components of the null vector. Written out they become,

$$\begin{matrix}(0\,0\,0\,0\,0\,0, & -1 & 0 & 0 & 0, & 0\,0\,0 & -\phi^1)\\ (0\,0\,0\,0\,0\,0, & 0 & -1 & 0 & 0, & 0\,0\,0 & -\phi^2)\\ (0\,0\,0\,0\,0\,0, & 0 & 0 & -1 & 0, & 0\,0\,0 & -\phi^3)\\ (0\,0\,0\,0\,0\,0, & 0 & 0 & 0 & -1, & 0\,0\,0 & -\phi^4).\end{matrix} \tag{42}$$

A fifth null vector of Λ^{44B4} independent of those above is,

$$(0\,0\,0\,0\,0\,0,\ 0\,0\,0\,0,\ 0\,0\,0\ x), \tag{43}$$

where x is any nonvanishing quantity.

Because of the special structure of the Λ^{44B4} matrix in the case of gravitation with electromagnetic field, the whole development from this point on becomes identical with the primed vector spaced introduced in the general theory of Sec. IV.

The inverses to the nonsingular matrices Λ^{ab4mn4} and Y^{r4s4} must be calculated. The inverse matrices are defined by the equations

$$G_{kl4ab4}\Lambda^{ab4mn4}=\tfrac{1}{2}(\delta_k{}^m\delta_l{}^n+\delta_l{}^m\delta_k{}^n), \tag{44}$$

and,

$$G_{k4s4}Y^{s4n4}=\delta_k{}^n.$$

These inverses were found by the method of "building blocks" similar to that in III. They are

$$G_{kl4mn4}=[2/(-g)^{\frac{1}{2}}g^{44}](g_{km}g_{ln}+g_{kn}g_{lm}-g_{kl}g_{mn}), \tag{45}$$

and

$$G_{k4n4}=-[2/(-g)^{\frac{1}{2}}g^{44}]g_{kn}.$$

VI. THE MOMENTUM DENSITIES AND CONSTRAINTS

The momentum densities are defined by the usual definition which, in this case, become

$$\pi^{\alpha\beta}=\partial L/\partial\dot{g}_{\alpha\beta} \quad \text{and} \quad \psi^\mu=\partial L/\partial\dot{\phi}_\mu,$$

where

$\pi^{\alpha\beta}$ = gravitational momentum densities

and

ψ^μ = electromagnetic momentum densities.

If the lagrangian is supplied with Eq. (36), we find

$$\pi^{\alpha\beta}=2\Lambda^{\alpha\beta4\gamma\delta n}g_{\gamma\delta,n}+2\Lambda^{\alpha\beta4\gamma\delta4}\dot{g}_{\gamma\delta}, \tag{46}$$

and,

$$\psi^\mu=2Y^{\mu4\nu n}\phi_{\nu,n}+2Y^{\mu4\nu4}\phi_\nu.$$

Because of the special structure of the matrices $\Lambda^{\alpha\beta4\gamma\delta4}$ and $Y^{\mu4\nu4}$ the constraints can be written down at once. They are the coordinate constraints

$$\pi^{4\beta}=2\Lambda^{4\beta4\gamma\delta n}g_{\gamma\delta,n}, \tag{47}$$

and the gauge constraint,

$$\psi^4=0. \tag{48}$$

Substitution for $\Lambda^{4\beta4\gamma\delta n}$ gives,

$$\pi^{4\beta}=\tfrac{1}{4}(-g)^{\frac{1}{2}}[2g^{47}(g^{4\beta}g^{\delta n}-g^{\beta n}g^{4\delta})+g^{\gamma\delta}(g^{44}g^{\beta n}-g^{4n}g^{4\beta})]g_{\gamma\delta,n}. \tag{49}$$

As for the remaining momentum densities, we have,

$$\pi^{ab}=2\Lambda^{ab4\gamma\delta n}g_{\gamma\delta,n}+2\Lambda^{ab4mn4}\dot{g}_{mn}, \tag{50}$$

and,

$$\psi^m=2Y^{m4\nu n}\phi_{\nu,n}+2Y^{m4\nu4}\phi_\nu. \tag{51}$$

If the $g^{\mu\nu}$ are replaced by the $\mathfrak{g}^{\mu\nu}$, the electric momenta reduce to the expressions usually given for these momenta.[8]

Multiplication of Eqs. (50) and (51) by G_{ab4mn4} and G_{n4m4}, respectively, gives

$$\dot{g}_{mn}=G_{mnab4}(\tfrac{1}{2}\pi^{ab}-\Lambda^{ab4\gamma\delta n}g_{\gamma\delta,n}), \tag{52}$$

and

$$\dot{\phi}_n=G_{n4m4}(\tfrac{1}{2}\psi^m-Y^{m4\nu}\phi_{\nu,\nu}). \tag{53}$$

VII. THE HAMILTONIAN DENSITY OF RELATIVITY WITH ELECTROMAGNETIC FIELD

The hamiltonian is formed according to the expression (41) which was derived in Sec. IV. If the gravitational part is separated from the electric part,

$$\begin{aligned}H'=H=&-\Lambda^{\alpha\beta n\gamma\delta m}g_{\alpha\beta,n}g_{\gamma\delta,m}\\ &+G_{ab4kl4}(\tfrac{1}{2}\pi^{ab}-\Lambda^{ab4\gamma\delta m}g_{\gamma\delta,m})(\tfrac{1}{2}\pi^{kl}-\Lambda^{kl4\omega\tau n}g_{\omega\tau,n})\\ &-Y^{\mu n\nu m}\phi_{\mu,n}\phi_{\nu,m}+G_{k4l4}(\tfrac{1}{2}\psi^k-Y^{k4\nu m}\phi_{\nu,m})\\ &\times(\tfrac{1}{2}\psi^l-Y^{l4\mu n}\phi_{\mu,n}).\end{aligned} \tag{54}$$

This expression may appear unduly lengthy. But the reader should bear in mind that the ordinary concise expressions for such quantities as the Riemann-Christoffel curvature tensor in the ordinary theory of relativity appear brief only because of the adoption of abbreviating notations—the Christoffel symbols and Einstein's summation convention. We have not used here Christoffel symbols, and in indicating sums, we had in many cases separated the index 4 from the spatial indices. Thus, actually, the present expression

[8] See for instance, L. Schiff, *Quantum Mechanics* (McGraw-Hill Book Company, Inc., New York, 1949), p. 404, Eq. (48.4).

is probably not longer than those current in general relativity.

In the case of special relativity ($g_{\mu\nu}=n_{\mu\nu}$) this hamiltonian reduces to the hamiltonian usually given for the electromagnetic field.

VIII. CONCLUSION

A hamiltonian formalism in nonrelativistic dynamics determines uniquely the state of a dynamical system for all instants $-\infty \leqslant t \leqslant \infty$ if the values of the momenta and coordinates are given at one instant t_0. An "instant" is here defined according to Dirac[1] to be a space-like hypersurface at a given time t. A hamiltonian formalism which satisfies the principle of general covariance with respect to arbitrary coordinate transformations must still show how the dynamical variables vary from instant to instant. However, in a covariant theory the instant can be varied arbitrarily in four different ways, and the hamilton equations of motion must always apply. Therefore, the field variables cannot be determined uniquely as functions of the independent variables, and the arbitrariness in their determination is exactly given by the four arbitrary coefficients of the constraints (13). This arbitrariness is then incorporated in the arbitrariness of the rectangular matrices $D^{A*}{}_{A}$. If the hamiltonian formalism is covariant with respect to other transformations like the guage transformation of electromagnetism, other arbitrary functions will occur in the hamiltonian to allow for the freedom of adding an arbitrary gradient to the field variables after their initial values have been fixed. This arbitrary function, in the case of electromagnetism, will be the arbitrary coefficient of the gauge constraint (46). If the arbitrary coefficient of all the constraints are chosen, this is equivalent to the adoption of particular gauge and coordinate conditions.

These comments apply equally to the parameter-hamiltonian developed in III and the formalism presented in this paper. The chief difference between the two methods of constructing a hamiltonian lies in the use of "parameters" in III. The parameters are an auxiliary coordinate system which is introduced alongside the usual coordinates x^k. The purpose of the parameters is twofold. Prior to quantization, the parameters enable us to prescribe the motion of any singularities at will in terms of the parameters and, thus, to restrict the domain of integration of the lagrangian density to regions free of singularities. In the quantized theory, then, the coordinates, including the coordinates of any singularities of the field (particles) appear as q-numbers, while the parameters remain c-numbers. In this formalism, on the other hand, there is only one system of coordinates used, and we succeed in constructing the hamiltonian function without recourse to the homogeneity properties characteristic of the parameter formalism. In the unquantized theory and in the absence of singularities, the two systems of equations must lead to identical results; the treatment of singularities in this formalism must await subsequent investigations. In the quantized theory, we cannot expect the coordinates to appear as q-numbers, they will remain in the c-number-field on which the field variables are defined.

While the parameter formalism may possibly afford a more direct access to the operators representing the dynamical variables of particles, the present formalism is simpler in every other respect. It should, therefore, facilitate the comparison of the covariant formalism with other theories (such as quantum electrodynamics) which lack full covariance, but which have been investigated more fully in the past. Thus, for many purposes the present formalism constitutes a bridge between the covariant and more conventional theories, and we expect that the two formalisms now available will supplement each other in future investigations.

It is a particular pleasure to thank Dr. Peter G. Bergmann for suggesting the problem and for his guidance and encouragement throughout my work. I wish to thank Dr. William Fredrickson, Dr. Charles Loewner, and Dr. Henry Zatzkis for many valuable discussions.

A Canonical Transformation in the Theory of Particles of Arbitrary Spin

W. A. HEPNER
Department of Mathematics, Imperial College of Science, London, England
(Received July 26, 1951)

Canonical transformation between the β-operators and certain components of the spin-tensor yields explicit expressions for the latter. The transformation is used to deduce general consequences that simplify the derivation of commutation relations. It can also be applied with advantage to construct free particle solutions of the wave equation.

BHABHA'S theories of the equations of particles of arbitrary spin[1,2] all rest on a basic assumption about the explicit expression for the relativistic skew-symmetric spin-tensor $t_{\mu\nu}$. A possible set of "five-dimensional" theories is based on the assumption that $t_{\mu\nu}=\beta_\mu\beta_\nu-\beta_\nu\beta_\mu$. In the following paper details of a different approach[3] are presented. It is shown that a certain symmetry in the equations expressing the relativistic covariance of the linear first-order wave equation suggests the existence of a canonical transformation between three components $t_{\mu\nu}$ and three β_λ. An almost obvious specialization of this canonical transformation leads to the above expression for $t_{\mu\nu}$ as a result. Conversely it can be shown that within the frame work of Bhabha's "five-dimensional" theories the canonical transformation always exists; it simply corresponds to a rotation through the angle $\pi/2$ in the (x_k, x_μ) plane. Leaving aside the problem of other possible transformations leading to different expressions for $t_{\mu\nu}$ (which may yield the equations of Dirac, Fierz, and Pauli for higher spins, or the symmetric equation of the meson suggested by Eliezer[4] and considered by Bhabha[2]), the implications and applications of this particular transformation, and others related to it by covariance, are studied. Hitherto awkwardly derived results, such as the equality of the characteristic equations of the spin operators σ_k and the β_λ, or the imitation by two or three σ_k of the algebraic relations of the β_λ, are here deduced as almost immediate consequences. Furthermore, by way of illustration, the equations of the Dirac electron and the Duffin-Kemmer meson are derived in but a few lines. Finally, taking the case of a particle of spin $\frac{3}{2}$ as an example, it is shown that the canonical transformation also provides an elegant method for obtaining free particle solutions of the wave equation.

A. THE CANONICAL TRANSFORMATION

The condition that the linear first-order wave equation be covariant under Lorentz transformations requires that the components of the skew-symmetric tensor $t_{\lambda\nu}$ formed by the generators of the Lorentz group satisfy the commutation relation

$$[\beta_\mu, t_{\lambda\nu}]=\delta_{\lambda\mu}\beta_\nu-\delta_{\nu\mu}\beta_\lambda, \quad (\lambda, \mu, \nu=1, \cdots 4), \quad (1)$$

where $[A, B]\equiv AB-BA$. On the other hand, the generators of the Lorentz group satisfy the commutation relation

$$[t_{\mu\nu}, t_{\rho\sigma}]=-\delta_{\mu\rho}t_{\nu\sigma}-\delta_{\nu\sigma}t_{\mu\rho}. \quad (2)$$

Defining

$$\sigma_k=-it_{lm}, \quad \gamma_k=-it_{4k}, \quad (k, l, m=1, 2, 3 \text{ cyclic}), \quad (3)$$

(1) and (2) give the following two sets of equations:

$$\begin{aligned} &\text{(a) } [\beta_k, \sigma_k]=0, && \text{(d) } [\beta_k, \gamma_l]=0,\\ &\text{(b) } [\beta_k, \sigma_l]=i\beta_m, && \text{(e) } [\beta_k, \gamma_k]=i\beta_4, \\ &\text{(c) } [\beta_4, \sigma_k]=0, && \text{(f) } [\beta_4, \gamma_k]=-i\beta_k, \end{aligned} \quad (4)$$

and

$$\begin{aligned} &\text{(a) } [\gamma_k, \sigma_k]=0, && \text{(b) } [\gamma_k, \sigma_l]=i\gamma_m, \\ &\text{(c) } [\gamma_k, \gamma_l]=i\sigma_m, && \text{(d) } [\sigma_k, \sigma_l]=i\sigma_m. \end{aligned} \quad (5)$$

Furthermore, if the wave equation is to be covariant under reflections, there exist four operators η_μ such that

$$\eta_\mu^2=1, \quad \eta_\mu\beta_\nu+\beta_\nu\eta_\mu=0, \quad (\mu\neq\nu), \quad \eta_\mu\beta_\mu=\beta_\mu\eta_\mu, \quad (6)$$

i.e., in particular,

$$\eta_4\beta_k+\beta_k\eta_4=0, \quad \eta_4\beta_4=\beta_4\eta_4. \quad (6a)$$

It is noteworthy that from Eqs. (4) it can be derived (see Appendix I) that the three operators γ_k, too, satisfy

$$\eta_4\gamma_k+\gamma_k\eta_4=0, \quad (7a)$$

and that

$$\eta_4\sigma_k=\sigma_k\eta_4. \quad (7b)$$

Now in addition to this similarity between Eqs. (6a) and (7a), it is remarkable that Eqs. (5a) and (5b), too, differ from (4a) and (4b) merely by having γ_k and γ_m in place of β_k and β_m. This suggests the possibility of a canonical transformation

$$\gamma_k=gS\beta_kS^{-1}, \quad (8)$$

where

$$S\sigma_k=\sigma_kS, \quad (9a)$$

and where g is an ordinary constant. In addition assume that S commutes with β_4:

$$S\beta_4=\beta_4S. \quad (9b)$$

Substituting (8) in (4d) gives

$$S^{-1}\gamma_kSS\beta_lS^{-1}-S\beta_lS^{-1}S^{-1}\gamma_kS=0,$$

[1] H. J. Bhabha, Revs. Modern Phys. **17**, 200 (1945).
[2] H. J. Bhabha, Revs. Modern Phys. **21**, 451 (1949).
[3] W. A. Hepner, Phys. Rev. **81**, 290 (1951); **82**, 447 (1951).
[4] C. J. Eliezer, Nature **159**, 60 (1947).

whence, multiplying by S^{-1} on the left and by S on the right,

$$(S^{-1})^2\gamma_k S^2\beta_l-\beta_l(S^{-1})^2\gamma_k S^2=0.$$

Adding

$$\gamma_k\beta_l-\beta_l\gamma_k=0, \tag{4d}$$

one obtains

$$\beta_l[(S^{-1})^2\gamma_k S^2+\gamma_k]-[(S^{-1})^2\gamma_k S^2+\gamma_k]\beta_l=0. \tag{10a}$$

Similarly, using (8) and (9b), one obtains from (4e)

$$\beta_k[(S^{-1})^2\gamma_k S^2+\gamma_k]-[(S^{-1})^2\gamma_k S^2+\gamma_k]\beta_k=0. \tag{10b}$$

Finally, multiplying (4f) by $(S^{-1})^2$ on the left and by S^2 on the right, and adding (4f), one obtains

$$\beta_4[(S^{-1})^2\gamma_k S^2+\gamma_k]-[(S^{-1})^2\gamma_k S^2+\gamma_k]\beta_4 =-i[(S^{-1})^2\beta_k S^2+\beta_k]. \tag{10c}$$

It can now easily be seen that a consistent solution is obtained assuming

$$\beta_k S^2+S^2\beta_k=0. \tag{11}$$

For Eqs. (10) then merely say that the operators $(S^{-1})^2\gamma_k S^2+\gamma_k$ commute with all four β_μ, and hence with all the elements of the group or algebra composed of the β_μ and their products. The operators $(S^{-1})^2\gamma_k S^2+\gamma_k$ must therefore be multiples of the unit operator. Since, from (5b),

$$\text{spur}(S^{-1})^2\gamma_k S^2=\text{spur}\gamma_k=0, \tag{12}$$

one obtains

$$(S^{-1})^2\gamma_k S^2+\gamma_k=0, \tag{13}$$

i.e.,

$$S^2\gamma_k+\gamma_k S^2=0, \tag{14}$$

which, according to (8), is in agreement with the assumption (11). From (11) and (9b) it can therefore be deduced that a consistent solution is obtained if S^2 is a numerical multiple of the operator η_4 defined in (6a).

Applying the transformation (8) and (9) to (4f) and (5c), one now obtains

$$\gamma_k=-ig^2(\beta_4\beta_k-\beta_k\beta_4), \quad \sigma_m=-ig^2(\beta_k\beta_l-\beta_l\beta_k), \tag{15a}$$

i.e.,

$$I_{\mu\nu}=g^2(\beta_\mu\beta_\nu-\beta_\nu\beta_\mu). \tag{15b}$$

This expression for $I_{\mu\nu}$ forms the starting point of Bhabha's theory of particles of arbitrary spin; here it is obtained as a result of the canonical transformation (8), (9).

Conversely, it can be shown that within the framework of Bhabha's theory the S-transformation satisfying (8), (9), (11) always exists. For in Bhabha's theory Eqs. (15) together with Eqs. (1) and (2) are interpreted as the commutation relations of the components of an angular momentum tensor I^{KL} in five dimensions ($K, L=1, \cdots 5$), with $g\beta_k=I^{k5}$. This means that to every Lorentz transformation in five dimensions specified by $x_K'=a_K{}^L x_L$ there corresponds an operator T such that

$$TI^{MN}T^{-1}=a_K{}^M a_L{}^N I^{KL}=I'^{MN}. \tag{16}$$

Now consider the particular transformation representing a rotation through the angle $\pi/2$ in the (x_4, x_5) plane:

$$x_k'=x_k, \quad x_4'=x_5, \quad x_5'=-x_4,$$

i.e.,

$$a_1{}^1=a_2{}^2=a_3{}^3=1, \quad a_4{}^5=-a_5{}^4=1.$$

Equation (16) now gives

$$TI^{15}T^{-1}=gT\beta_1T^{-1}=a_K{}^1a_L{}^5I^{KL}=a_1{}^1a_4{}^5I^{14}=\gamma_1,$$

$$TI^{45}T^{-1}=gT\beta_4T^{-1}=a_K{}^4a_L{}^5I^{KL}=a_5{}^4a_4{}^5I^{54}=g\beta_4,$$

and

$$TI^{14}T^{-1}=T\gamma_1T^{-1}=a_K{}^1a_L{}^4I^{KL}=a_1{}^1a_5{}^4I^{15}=-g\beta_1,$$

$$T\sigma_1T^{-1}=\sigma_1,$$

and similarly for β_2, β_3, γ_2, γ_3, and σ_2, σ_3. Hence T is identical with the S-transformation specified by (8), (9), and (11).

It can also be shown that, if the expressions (15) are to hold, then the transformation specified by (8) and (11) is the only one such that S commutes with β_4. For from (4f) one obtains by canonical transformation, using (8) and (9b),

$$-i\gamma_k=g^2\beta_4S^2\beta_k(S^{-1})^2-g^2S^2\beta_k(S^{-1})^2\beta_4.$$

Hence, if (15) is to hold, then

$$-ig^2(\beta_4\beta_k-\beta_k\beta_4)=ig^2[\beta_4S^2\beta_k(S^{-1})^2-S^2\beta_k(S^{-1})^2\beta_4],$$

i.e.,

$$\beta_4[S^2\beta_k(S^{-1})^2+\beta_k]=[S^2\beta_k(S^{-1})^2+\beta_k]\beta_4.$$

Similarly, by canonical transformation of (10a) and (10b) one obtains, respectively,

$$S\beta_kS^{-1}[S^2\beta_k(S^{-1})^2+\beta_k]=[S^2\beta_k(S^{-1})^2+\beta_k]S\beta_kS^{-1},$$

$$S\beta_kS^{-1}[S^2\beta_k(S^{-1})^2+\beta_k]=[S^2\beta_k(S^{-1})^2+\beta_k]S\beta_kS^{-1}.$$

These equations show that the operators $S^2\beta_k(S^{-1})^2+\beta_k$ commute with β_4 and with the three γ_l. But since, in virtue of (4f), β_l can be expressed in terms of β_4 and γ_l, it follows that $S^2\beta_k(S^{-1})^2+\beta_k$ is a constant multiple of the unit operator. Since $\text{spur}\beta_k=0$, it follows that the constant is zero, i.e., (11) must hold.

Assuming, as is compatible with Eqs. (8), (9), and (11), that S depends on β_4 only, an expression for S can easily be given. Since S^2 anticommutes with the three β_k and commutes with β_4, S^4 can be represented by the unit operator. Now it is shown below that the characteristic values of $g\beta_4$ and σ_k must be the same, *viz.*, either the integers $-n, \cdots 0, \cdots +n$, for integral spin, or the half-integers $-n, \cdots -\frac{1}{2}, +\frac{1}{2}, \cdots +n$, for half-integral spin. It is therefore possible to represent S^4 by

$$S^4=\exp(2\pi ig\beta_4), \tag{17a}$$

this operator being equal to $+1$ for integral spin and to -1 for half-integral spin. Hence S and S^{-1} can be represented by

$$S=\exp(\tfrac{1}{2}i\pi g\beta_4), \quad S^{-1}=\exp(-\tfrac{1}{2}i\pi g\beta_4), \quad (17b)$$

showing that S is unitary if β_4 is hermitian. It is clear that S can be expanded into a polynomial of degree $2n$ in $g\beta_4$, the $2n+1$ coefficients being determined by (17b), using the $2n+1$ eigenvalues of $g\beta_4$.

In Appendix II it is shown that, as is to be expected from relativistic covariance, the transformation (8), (9) is not the only one that leads to (15). More generally, there are four transformations S_μ such that $[S_\mu, \beta_\mu]=0$, $S_\mu^2\beta_\nu+\beta_\nu S_\mu^2=0$ $(\nu\neq\mu)$; they correspond, in Bhabha's five-dimensional scheme, to rotations through the angle $\pi/2$ in the (x_μ, x_5) plane. Finally, it is interesting to note another possibility leading yet again to the expressions (15), *viz.*, (see Appendix III)

$$S_\mu\beta_\mu+\beta_\mu S_\mu=0, \quad [S_\mu^2, \beta_\lambda]=0.$$

These four transformations correspond to rotation through the angle $\pi/2$ in the (x_μ, x_5) plane and reflection of x_5.

B. APPLICATIONS OF THE CANONICAL TRANSFORMATION

(i) Some Consequences

The existence of the transformation (8), (9) has numerous immediate consequences that hitherto have been derived only by laborious calculations, using the expressions (15). For example, it follows immediately that the characteristic equation of σ_k, which determines the eigenvalues of the spin components, is also the characteristic equation of $g\beta_\mu$. For owing to the complete parity of the four β_μ, the characteristic equations of γ_k and σ_k are the same, and the characteristic equation of γ_k transforms into that for $g\beta_k$. Furthermore, it is now obvious that the four operators γ_k and $g\beta_4$ satisfy the same algebraic relations as the four β_μ.

Similarly, it is now easy to see why the three operators σ_k satisfy commutation relations of three operators $g\beta_k$. Regarding relations involving only two different σ's this is now almost self-evident; for owing to the complete parity of all four β's and in virtue of the equivalent structure of two σ's on the one hand and two γ's on the other, the relations between two γ's will also be satisfied by two σ's, and the relations between two γ's are satisfied by two $g\beta$'s. Now the relations between three different $g\beta$'s are obtained from (see 5c) (5a)

$$[[\gamma_k, \gamma_l], \gamma_m]=0, \quad (18a)$$

by canonical transformation, after suitable reductions with the help of the characteristic equations and the relations involving only two different γ's. Since, according to (5d), the three σ's, too, satisfy

$$[[\sigma_k, \sigma_l], \sigma_m]=0, \quad (18b)$$

it follows that the resulting equation for three σ's, after similar suitable reductions with the help of the characteristic equations and the relations involving only two different σ's, will be the same as for three $g\beta$'s. The converse is not true; owing to the different structure of the sets of three σ's and three γ's, an equation between three σ's, for example (5d), need not be satisfied by three $g\beta$'s.

(ii) Derivation of Commutation Relations for Spin ½ and Spin 1

Substituting (15) in (1), and using the result that $g\beta_\mu$ and σ_k satisfy the same characteristic equation, the commutation relations of the β's can now be derived in a few lines. Putting $\lambda=\mu\neq\nu$, one obtains

$$\beta_\mu^2\beta_\nu+\beta_\nu\beta_\mu^2-2\beta_\mu\beta_\nu\beta_\mu=(1/g^2)\beta_\nu, \quad (\mu\neq\nu), \quad (19)$$

whatever the value of the spin.

(a) *Dirac's Commutation Relations*

For spin ½ the characteristic equation of σ_k is given by

$$(\sigma_k-\tfrac{1}{2})(\sigma_k+\tfrac{1}{2})=0, \quad (20)$$

whence also

$$(g\beta_\mu)^2=\tfrac{1}{4}. \quad (21a)$$

Hence (19) becomes

$$\beta_\mu\beta_\nu\beta_\mu=-(1/4g^2)\beta_\nu,$$

whence, multiplying by β_μ and using (21a),

$$\beta_\mu\beta_\nu+\beta_\nu\beta_\mu=0, \quad (\mu\neq\nu). \quad (21b)$$

Since the numerical factor g can be absorbed in the mass constant, its value can be freely adjusted. Without loss of generality one may therefore put $g^2=\frac{1}{4}$, so that

$$\beta_\mu^2=1. \quad (21c)$$

Equations (21) are identical with Dirac's commutation relations for the electron. The expressions (17b) now give

$$S=(1-i\beta_4)/\sqrt{2}, \quad S^{-1}=(1+i\beta_4)/\sqrt{2}; \qquad S^2=-i\beta_4=-i\eta_4. \quad (22)$$

(b) *The Duffin-Kemmer Relations*

For spin 1 the characteristic equation of σ_k is given by

$$(\sigma_k-1)\sigma_k(\sigma_k+1)=0, \quad (23)$$

whence also

$$\beta_\mu^3=(1/g^2)\beta_\mu. \quad (24)$$

Hence, multiplying (19) by β_μ on both sides, one obtains

$$2\beta_\mu^2\beta_\nu\beta_\mu^2=(1/g^2)\beta_\mu\beta_\nu\beta_\mu, \quad (25)$$

whence again

$$(1/g^2)\beta_\mu^2\beta_\nu\beta_\mu^2=(2/g^4)\beta_\mu\beta_\nu\beta_\mu, \quad (26)$$

and therefore

$$\beta_\mu\beta_\nu\beta_\mu=0, \quad (\mu\neq\nu). \tag{27}$$

Taking $\mu\neq\lambda$, $\nu\neq\lambda$, $\mu\neq\nu$, and using (15b), (1) gives

$$\beta_\mu\beta_\lambda\beta_\nu+\beta_\nu\beta_\lambda\beta_\mu=\beta_\mu\beta_\nu\beta_\lambda+\beta_\lambda\beta_\nu\beta_\mu, \tag{28}$$

whence, multiplying by β_λ^2 on the right and using (27) and (19),

$$\beta_\mu\beta_\nu\beta_\lambda+\beta_\lambda\beta_\nu\beta_\mu=0. \tag{29}$$

Putting $g^2=1$, Eqs. (19), (24), (27), (29) are identical with the Duffin-Kemmer commutation relations for the meson of spin 1. The expressions (17b) now give

$$S=1-i\beta_4-\beta_4^2, \quad S^{-1}=1+i\beta_4-\beta_4^2; \tag{30a}$$

$$S^2=1-2\beta_4^2=\eta_4. \tag{30b}$$

(iii) Derivation of Solutions of the Wave Equation by Lorentz Transformation

Apart from making the derivation of commutation relations much simpler, the knowledge of the existence of the canonical transformation (8), (9) is of great help in finding solutions of the wave equation. Instead of solving a system of n simultaneous linear equations, where n is the degree of the matrix representation, the idea is to construct the solutions from the obvious elementary solutions in the rest system (all but one spinor components vanish) by Lorentz transformation, the procedure being greatly simplified by an application of the canonical transformation (8). This method also facilitates the finding of that combination of solutions that is also eigensolution of certain operators, as is frequently desirable. It is best to demonstrate the method for a particular case, say Bhabha's equation[5] for a particle of spin $\frac{3}{2}$. In this case the canonical transformation (8), (9) holds true with

$$S=\frac{1}{2\sqrt{2}}\left(\frac{5}{2}-\frac{13}{3}i\beta_4-2\beta_4^2+\frac{4}{3}i\beta_4^3\right),$$

$$S^{-1}=\frac{1}{2\sqrt{2}}\left(\frac{5}{2}+\frac{13}{3}i\beta_4-2\beta_4^2-\frac{4}{3}i\beta_4^3\right),$$

$$S^2=i\eta_4=-\tfrac{1}{3}i(7\beta_4-4\beta_4^3);$$

but the explicit expressions will not be required in the following. Designating the four-vector of momentum by $\mathbf{p}$, $(p_4=i\omega)$, and the position vector of the world point by $\mathbf{x}$, $(x_4=il)$, consider the plane wave solutions

$$\psi=U\exp(i\mathbf{p}\cdot\mathbf{x}). \tag{31}$$

The (16-component or 20-component) spinor amplitude U satisfies

$$(ip_\mu\beta_\mu+\kappa)U=0. \tag{32}$$

Taking the direction of x_1 in the direction of the three-vector with components p_1, p_2, p_3, and writing $p_1=p$, (32) becomes

$$(ip\beta_1-\omega\beta_4+\kappa)U=0. \tag{33}$$

The solutions U of these equations for given p can be obtained from the elementary solutions U_0 for $p=0$, $(\omega=\omega_0)$, by the Lorentz transformation

$$U=TU_0, \quad U_0=T^{-1}U, \tag{34}$$

where

$$(-\omega_0\beta_4+\kappa)U_0=0, \tag{35a}$$

i.e.,

$$(-\omega_0\beta_4+\kappa)T^{-1}U=0. \tag{35b}$$

Multiplying (35b) on the left by T and using (33), one obtains

$$-\omega_0T\beta_4T^{-1}U+\kappa U$$
$$=-\omega_0T\beta_4T^{-1}U-ip\beta_1U+\omega\beta_4U=0. \tag{36a}$$

Hence T satisfies the equation

$$T\beta_4=(\omega/\omega_0)\beta_4T-i(p/\omega_0)\beta_1T. \tag{36b}$$

It is natural to assume that T can be expressed in terms of powers of the operator γ_1, this being the generator of translations in the x_1-direction. Now the components of the spin satisfy the characteristic equation of fourth order

$$(\sigma_k-\tfrac{3}{2})(\sigma_k-\tfrac{1}{2})(\sigma_k+\tfrac{1}{2})(\sigma_k+\tfrac{3}{2})=0. \tag{37}$$

Since γ_1 satisfies the same equation, T can be represented by

$$T=1+A\gamma_1+B\gamma_1^2+C\gamma_1^3, \tag{38}$$

where A, B, C are ordinary constants.

A considerable simplification can now be effected by substituting (38) not in (36b) but in the canonically transformed equation

$$STS^{-1}\beta_4=(\omega/\omega_0)\beta_4STS^{-1}-i(p/\omega_0)S\beta_1S^{-1}STS^{-1}, \tag{39}$$

where S satisfies (8), (9), (11). Since $S\gamma_1S^{-1}=S^2\beta_1(S^{-1})^2=-\beta_1$, the awkward terms γ_1^2 and γ_1^3 in T are now simply transformed into β_1^2 and $-\beta_1^3$, (39) thus giving

$$\beta_4-A\beta_1\beta_4+B\beta_1^2\beta_4-C\beta_1^3\beta_4$$
$$=(\omega/\omega_0)(\beta_4-A\beta_4\beta_1+B\beta_4\beta_1^2-C\beta_4\beta_1^3)$$
$$-i(p/\omega_0)(\gamma_1-A\gamma_1\beta_1+B\gamma_1\beta_1^2-C\gamma_1\beta_1^3). \tag{40}$$

Using the direct product representation[6] $\beta=\xi\times\eta$, (40) can be written in the form

$$(a_1\xi_4+b_1\xi_1\xi_4+c_1\xi_4\xi_1)\eta_4$$
$$+(a_2\xi_4+b_2\xi_1\xi_4+c_2\xi_4\xi_1)\eta_1\eta_4=0, \tag{41}$$

where the constants a, b, c, involve the coefficients A, B, C. Now η_4 and $\eta_1\eta_4$ are independent operators, and so are ξ_4, $\xi_1\xi_4$, $\xi_4\xi_1$. Hence $a=b=c=0$, which gives six linear equations for the coefficients A, B, C. The solu-

[5] H. J. Bhabha, Proc. Indian Acad. Sci. (A) **21**, 241 (1945).

[6] Madhavarao, Thiruvenkatachar, and Venkatachaliengar, Proc. Roy. Soc. (London) **187**, 385 (1946).

tion is

$$A=-\frac{2}{3}\frac{p}{\omega+\omega_0}\frac{\omega-13\omega_0}{5\omega_0-\omega},\quad B=4\frac{\omega-\omega_0}{5\omega_0-\omega},\qquad C=-\frac{8}{3}\frac{p}{\omega+\omega_0}\frac{\omega-\omega_0}{5\omega_0-\omega}, \tag{42a}$$

providing that

$$\omega^2=\omega_0^2+p^2. \tag{42b}$$

In the general case, for motion in any direction with momentum components p_1, p_2, p_3, the transformation T is obtained by simply replacing in (38) γ_1 by $(p_1\gamma_1+p_2\gamma_2+p_3\gamma_3)/p$, where $p^2=p_1^2+p_2^2+p_3^2$.

The solution U can now easily be constructed from (34), (38), (42). This method has the particular advantage that if, as is often desirable, the solutions are to be eigensolutions of the component of the spin-vector in the direction of p (σ_1 in the above case) it is easier to construct first the corresponding eigensolutions U_0 in the rest system. Since γ_1 commutes with σ_1, the transformed solutions $U=TU_0$ are then still eigensolutions of σ_1.

APPENDIX I

Multiplying Eqs. (4d), (e), (f) by η_4 on the left and right, and using (6a), one obtains, adding respectively (4d), (e), (f),

$$\beta_\lambda(\eta_4\gamma_k\eta_4+\gamma_k)-(\eta_4\gamma_k\eta_4+\gamma_k)\beta_\lambda=0,$$

valid for all four β_λ. The operator $\eta_4\gamma_k\eta_4+\gamma_k$ thus commutes with all the elements of the algebra and must therefore be a multiple of the unit operator, say $a1$. But since $\eta_4=\eta_4^{-1}$, and since, from (5b), spur $\gamma_k=0$, it follows that $a\text{spur}1=0$, whence $a=0$.

Similarly, it follows from (4a), (b), (c) that $\eta_4\sigma_k=\sigma_k\eta_4$.

APPENDIX II

In the transformation (8), (9) the role of β_4 differs from that of the three other β_k in that S commutes with β_4 and with the three components $t_{\mu\nu}$ for which both $\mu\neq4$ and $\nu\neq4$, while the three t_{k4} are transformed into β_k. Owing to the relativistic covariance, there is of course no real distinction of β_4, and in fact any other β can play the same role. It is instructive to see how, despite the altered correspondence between Eqs. (4) and (5), the expressions (15) are again obtained if, say, β_3 is chosen to play that role. Thus, in place of (8), (9), consider the transformation characterized by

$$[S,\beta_k]=0,\quad [S,t_{\mu\nu}]=0 \text{ if both } \mu\neq3 \text{ and } \nu\neq3,\qquad t_{13}\to\beta_1,\quad t_{23}\to\beta_2,\quad t_{43}\to\beta_4; \tag{A1}$$

i.e.,

$$[S,\beta_4]=[S,\gamma_1]=[S,\gamma_2]=[S,\sigma_3]=0,\qquad \sigma_3=S\beta_1S^{-1},\quad \sigma_1=-S\beta_2S^{-1},\quad \gamma_3=-S\beta_4S^{-1}. \tag{A2}$$

Now from (4b)

$$\beta_1\sigma_2-\sigma_2\beta_1=i\beta_3,$$

whence, multiplying by S^{-1} on the left and S on the right, and using (A2),

$$\beta_1(S^{-1})^2\sigma_2S^2-(S^{-1})^2\sigma_2S^2\beta_1=-i\beta_3.$$

Hence

$$\beta_1[\sigma_2+(S^{-1})^2\sigma_2S^2]-[\sigma_2+(S^{-1})^2\sigma_2S^2]\beta_1=0. \tag{A3}$$

Similarly, canonical transformation of

$$\beta_1\sigma_1-\sigma_1\beta_1=0$$

gives

$$\beta_1(S^{-1})^2\sigma_2S^2-(S^{-1})^2\sigma_2S^2\beta_2=0.$$

Adding

$$\beta_2\sigma_2-\sigma_2\beta_2=0,$$

one obtains

$$\beta_1[\sigma_2+(S^{-1})^2\sigma_2S^2]-[\sigma_2+(S^{-1})^2\sigma_2S^2]\beta_2=0. \tag{A4}$$

Again, by canonical transformation of

$$\beta_1\gamma_2-\gamma_2\beta_1=0$$

one has

$$\beta_4(S^{-1})^2\sigma_2S^2-(S^{-1})^2\sigma_2S^2\beta_4=0.$$

Adding

$$\beta_4\sigma_2-\sigma_2\beta_4=0,$$

one obtains

$$\beta_4[\sigma_2+(S^{-1})^2\sigma_2S^2]-[\sigma_2+(S^{-1})^2\sigma_2S^2]\beta_4=0. \tag{A5}$$

Finally, by canonical transformation of

$$\beta_2\sigma_2-\sigma_2\beta_2=-i\beta_1$$

one obtains

$$\beta_2[\sigma_2+(S^{-1})^2\sigma_2S^2]-[\sigma_2+(S^{-1})^2\sigma_2S^2]\beta_2=-i[\beta_1+(S^{-1})^2\beta_1S^2]. \tag{A6}$$

Hence, assuming that β_1 anticommutes with S^2, one now derives, since spur$\sigma_2=0$,

$$\sigma_2S^2+S^2\sigma_2=0, \tag{A7}$$

which, because of $\sigma_2=S\beta_1S^{-1}$, is consistent with the assumption.

Similarly one finds that, if β_2 and β_4 anticommute with S^2, then

$$\sigma_1S^2+S^2\sigma_1=0,\quad \gamma_2S^2+S^2\gamma_2=0, \tag{A8}$$

in agreement with (A2). It can therefore be deduced that, apart from a constant factor, S^2 is identical with the operator η_2 defined in (6). The expression for S can be obtained from (17) by replacing β_4 by β_2.

It now remains to show that the expressions (15) still hold true. Indeed from

$$i\sigma_3=\sigma_1\sigma_2-\sigma_2\sigma_1$$

one now obtains by the canonical transformation (A2)

$$i\sigma_3=\beta_1\beta_2-\beta_2\beta_1. \tag{A9a}$$

Similarly, from

$$\begin{aligned}&\text{(b)}\quad -i\beta_3=\sigma_1\beta_2-\beta_2\sigma_1,\\ &\text{(c)}\quad i\beta_3=\sigma_2\beta_1-\beta_1\sigma_2,\\ &\text{(d)}\quad i\gamma_1=\sigma_2\gamma_3-\gamma_3\sigma_2,\\ &\text{(e)}\quad i\gamma_2=\gamma_3\sigma_1-\sigma_1\gamma_3,\\ &\text{(f)}\quad -i\beta_4=\gamma_3\beta_2-\beta_2\gamma_3,\end{aligned} \tag{A9}$$

the old expressions (15) for σ_1, σ_2, γ_1, γ_2, γ_3 are obtained, respectively, by the canonical transformation (A2).

APPENDIX III

Consider the transformation

$$\gamma_k=S\beta_kS^{-1},\quad S\beta_4=-\beta_4S. \tag{B1}$$

From Eqs. (4d), (e), (f) one derives by a now familiar procedure

$$[\beta_k,\Gamma_l]=0,\quad [\beta_k,\Gamma_k]=0,\qquad [\beta_4,\Gamma_k]=-i[\beta_k-(S^{-1})^2\beta_kS^2], \tag{B2}$$

where

$$\Gamma_k\equiv\gamma_k-(S^{-1})^2\gamma_kS^2.$$

A consistent solution can be obtained assuming

$$S^2\beta_k=\beta_kS^2,\quad \text{i.e.,}\quad S^2\gamma_k=\gamma_kS^2. \tag{B3}$$

Multiplying (4f) by S on the left and by S^{-1} on the right, and using (B1), one obtains

$$\gamma_k=-i(\beta_4\beta_k-\beta_k\beta_4).$$

To obtain the expression for σ_n note that from (4a), (b), (c) one now derives by canonical transformation

$$[\gamma_k,\Sigma_k]=0,\quad [\gamma_k,\Sigma_l]=0,\quad [\beta_4,\Sigma_k]=0, \tag{B4}$$

where

$$\Sigma_k = \sigma_k - S\sigma_k S^{-1}.$$

Owing to (4f) this means that the operator Σ_k commutes with the four β_μ; it is therefore a multiple of the unit operator. Since, from (5d), spur$\sigma_k=0$, it follows that

$$S\sigma_k = \sigma_k S. \tag{B5}$$

Hence by canonical transformation of (5c) one obtains

$$i\sigma_m = \beta_k\beta_l - \beta_l\beta_k.$$

The canonical transformation under consideration is characterized by

$$\beta_k \to \gamma_k, \quad \gamma_k \to \beta_k, \quad \sigma_k \to \sigma_k, \quad \beta_4 \to -\beta_4. \tag{B6}$$

In Bhabha's five-dimensional scheme, using (16), this corresponds to the transformation

$$x_k' = x_k, \quad x_4' = x_4, \quad x_5' = x_5,$$

i.e.,

$$a_1^1 = a_2^2 = a_3^3 = 1, \quad a_4^4 = a_5^4 = 1. \tag{B7}$$

This describes a rotation through the angle $\pi/2$ in the (x_4, x_5) plane, and reflection of x_5.

Owing to the relativistic covariance it is clear that any other β_k can play the role of β_4. Hence there are four transformations S_μ such that

$$S_\mu\beta_\mu + \beta_\mu S_\mu = 0, \quad [S_\mu^2, \beta_\lambda] = 0. \tag{B8}$$

It is interesting to note that S_μ^2 is now a multiple of the unit operator.

PHYSICAL REVIEW VOLUME 84, NUMBER 4 NOVEMBER 15, 1951

Energy Release in the Disintegration of Be⁸

RICHARD R. CARLSON
Department of Physics and Institute for Nuclear Studies, University of Chicago, Chicago, Illinois
(Received July 26, 1950)

Thin beryllium targets were bombarded with 400-kev protons and the energy spectra of the particles given off at 90 degrees to the beam direction were observed with a cylindrical electrostatic analyzer. The beryllium was evaporated onto a nickel backing which was thin enough to confine the elastically scattered protons to a narrow energy range. At energies below that of the elastically scattered protons, peaks were observed in the energy spectra which corresponded to the maximum alpha-particle energy in the continuous energy distribution of alpha-particles resulting from the breakup of Be⁸. The position of these maxima give a value for the energy release in the disintegration of 77.5±4 kev.

INTRODUCTION

THE nucleus Be⁸ occurs as a compound state, or an intermediate product, in a large number of nuclear reactions.[1] In cases where the ground state is involved, there is evidence that alpha-decay occurs.[2] The result of the early work on this problem was the conclusion that the ground state of Be⁸ was unstable against alpha-decay by about 125 kev. The conclusion, as to the instability of Be⁸, is bolstered by the fact that naturally occurring beryllium contains no detectable amount of mass eight isotope.[3] Recently, a measurement of the half-life for this decay was made by measuring the track lengths of fragments of oxygen nuclei in an emulsion when the emulsion had been exposed to energetic gamma-radiation.[4] Some of these fragments were identified as Be⁸ nuclei. The half-life was found to be $(5\pm1)\times10^{-14}$ second. This value corresponds to an energy of the order of 100 kev which is available for decay into two alpha-particles, assuming the latter have zero angular momentum.[5] Two recent direct measurements of the energy release give values of 103±10 kev,[6] and 89±4 kev.[7]

The method used in the present experiment, consisted in bombarding an evaporated beryllium target with protons. This results in the reactions,

$$Be^9 + H^1 \to Li^6 + He^4 + Q_1, \tag{1}$$

$$Be^9 + H^1 \to Be^8 + He^2 + Q_2, \tag{2}$$

$$Be^8 \to He^4 + He^4 + Q_3, \tag{3}$$

where Q_1, Q_2, and Q_3 refer to the energy releases. Previous work has shown that the alpha-particles from reaction (3) have less energy than the elastically scattered protons at bombardment energies above 240 kev, where sufficient yields for our measurements may be expected.[7,8] In the present work, a backing of nickel foil was used, which was thin enough to confine the elastically scattered protons to a narrow range of energies, thus permitting alpha-particles to be observed without serious interference. An electrostatic analyzer was used to separate particles of different energy-to-charge ratio. In previous work with these reactions,

[1] Hornyak, Lauritsen, Morrison, and Fowler, Revs. Modern Phys. 22, 309 (1950).
[2] Oliphant, Kempton, and Rutherford, Proc. Roy. Soc. (London) 150, 241 (1935); O. Laaf, Ann. Phys. 32, 743 (1938); K. Fink, Ann. Phys. 34, 717 (1939); J. Wheeler, Phys. Rev. 59, 27 (1941). Wheeler summarizes the earlier work and corrects some mistakes in analysis.
[3] A. Nier, Phys. Rev. 52, 933 (1937).
[4] C. Miller and A. Cameron, Phys. Rev. 81, 316 (1951).
[5] H. Bethe, Revs. Modern Phys. 9, 167 (1937).
[6] A. Hemmendinger, Phys. Rev. 75, 1267 (1949).
[7] Tollestrup, Fowler, and Lauritsen, Phys. Rev. 76, 428 (1949).
[8] L. del Rosario, Phys. Rev. 74, 304 (1948).

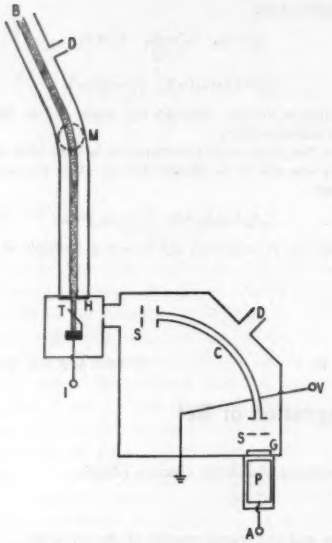

FIG. 1. Schematic diagram of experimental arrangement. A, connection to counting equipment; B, beam from kevatron; C, electrostatic analyzer plates; D, connection to diffusion pump; G, glass disk with zinc sulfide screen; H, $\frac{1}{4}$-inch collimating hole; I, connection to beam current integrator; M, magnetic field; P, photomultiplier tube; S, 0.1-cm slit; T, target; V, connection to high voltage.

particles of different momentum-to-charge ratio were separated and singly charged alpha-particles from the breakup of Be^8 were observed with doubly charged lithium ions from the competing reaction being partially superposed.[7] Foils were used to separate the two ions. No stopping foils were used in the present arrangement.

In the course of this work, the lithium and deuterium ions, from the reactions indicated above, were observed and their energies measured. These measurements led to values for Q_1 and Q_2. A great deal of work has been done on the measurement of these Q values and the values obtained here are of interest mainly in that they confirm the presently accepted results.[7–9]

DESCRIPTION OF THE APPARATUS

Figure 1 is a schematic diagram of the experimental arrangement. The various items are described below.

The source of the proton beam was the University of Chicago 400-kilovolt Cockroft-Walton accelerator, or kevatron. The kevatron beam was first magnetically analyzed and the proton component directed down a one meter tube to the target. A $\frac{1}{4}$-inch diameter collimating hole limited the beam cross section in front of the target. A beam current of the order of two microamperes on the target was usually used. The current was monitored by a beam current integrator of conventional design. Since the target and backing together were too thin to stop the beam, a piece of $\frac{1}{4}$-inch thick metal was mounted behind the target and both were connected electrically to the integrator. The target assembly could be rotated and moved along the axis coincident with the beam direction through a Wilson seal. By using this freedom of motion and a window looking into the target chamber, the position of the beam spot on the target was brought opposite the analyzer entrance. The positioning was checked by making sure it maximized the counting rate due to scattered protons. The direction of entrance to the analyzer was defined by the 0.1-cm slit and window as shown in the schematic; a finite acceptance angle of approximately 0.020 radian is also defined by the geometry of the layout. The angle between the beam and the direction of entrance to the analyzer was known to be 90 degrees to an accuracy of 0.5 degree, or 0.009 radian, from the accurate machining of the analyzer and target chamber parts.

The electrostatic analyzer used in this experiment has been described in the literature.[10] Briefly, it is of the cylindrical type with an average radius of 15 cm, spacing of 0.5 cm, and a deflection angle of 90 degrees. Voltages up to 50 kilovolts have been applied across the analyzer plates and for such voltages protons of 750-kev energy are focused. From the calibration experiments carried out in this laboratory, the analyzer constant for the arrangement employed was known to be 15.78_8. The constant is the ratio of the energy in kilovolts per charge (in units of the electronic charge) of the ion focused to the voltage across the analyzer plates in kilovolts.

A scintillation screen was used to detect particles which managed to traverse the analyzer. The screen was made by putting a thin coating of activated zinc sulfide powder on a glass disk.[11] The scintillations were detected by an RCA 5819 photomultiplier tube using 900 volts of batteries for the voltage supply. Batteries were found necessary for adequate stability. The pulse output of the photomultiplier tube was fed through a preamplifier to an amplifier and thence to a discriminator and scalar; all were of the type described by Elmore and Sands.[12] An amplifier gain of about 320 was used throughout the entire work. With the arrangement used, it was found that, for voltages on the

[9] R. Döpel, Z. Physik. **91**, 796 (1934); F. Kirchner and H. Neuert, Physik. Z. **36**, 54 (1935); B. Zyprich, Z. Physik. **96**, 337 (1935); R. Döpel, Z. Physik. **104**, 666 (1937); F. Kirchner and H. Neuert, Physik. Z. **38**, 969 (1937); J. Allen, Phys. Rev. **51**, 182 (1937); Williams, Haxby, and Shepherd, Phys. Rev. **52**, 1031 (1937); G. Hatch, Phys. Rev. **54**, 165 (1938); Allison, Skaggs, and Smith, Phys. Rev. **54**, 171 (1938); L. Skaggs, Phys. Rev. **56**, 24 (1939); Allison, Graves, Skaggs, and Smith, Phys. Rev. **57**, 550 (1940); Strait, Van Patter, Buechner, and Sperduto, Phys. Rev. **81**, 747 (1951).

[10] Allison, Frankel, Hall, Montague, Morrish, and Warshaw, Rev. Sci. Instr. **20**, 735 (1949).

[11] Patterson Type "D" Powder, E. I. du Pont Company.

[12] W. Elmore and M. Sands, *Electronics* (McGraw-Hill Book Publishing Company, Inc., New York, 1949).

Schmidt discriminator of 30 volts and over, the background counting rate was negligible.

The vacuum in the accelerator tube was maintained by an oil diffusion pump system. Liquid air traps between the pumps and the accelerator tube were used to keep oil vapor out of the tube during the time that measurements were made. To reduce the amount of oil deposition inside the accelerator tube, the connection between the pumping system and the accelerator tube was partly closed by a vane between runs. The problem of oil deposition on targets is acute in this experiment, since, as it will appear later, deposition is an important source of error for which very little can be done in the way of correction. To reduce the chance of oil deposition as much as possible, a liquid-air trap was placed on the vacuum pump used to rough-out the target chamber. Also, the target chamber was closed off from the accelerator tube and the analyzer between runs. The electrostatic analyzer had its own oil diffusion pump system and liquid air trap which was kept filled whenever the analyzer was open to the target chamber.

ENERGY MEASUREMENTS

The energy of the particles, which came off the target at right angles to the beam direction, was measured with the electrostatic analyzer. The voltage across the analyzer plates was measured by draining a small current through a 50 megohm stack of wirewound (Taylor) resistors of 0.1 percent precision. The drain was of the order of 200 microamperes. The meter, which was used to measure the drain, had an accuracy of 0.25 percent.

The voltage applied across the analyzer plates was obtained from a half-wave rectifier using 60-cycle, 110-volt input. A variac was used to vary the input to the step-up transformer of the rectifier; a Sola transformer was used to smooth out the line voltage fluctuations. A 0.05-microfarad condenser was used to reduce the ripple to 0.66 percent at the voltages used here.

From the calibration experiments, the analyzer constant was known to an accuracy of 0.1 percent; the analyzer resolution was known to be 0.33 percent. The analyzer had a triangular energy "window." That is to say, a monoenergetic group of particles would produce a triangular shaped energy spectrum with the maximum at the true energy and a width, at half-maximum, of 1/300 of the true energy if the voltage across the analyzer plates were perfectly steady. Actually there is a sawtooth ripple of 0.66 percent in the voltage. This causes the analyzer window to become roughly gaussian in shape with a width at half-maximum equal to the ripple. The effective window shape is drawn in Fig. 4B.

Including all the sources of inaccuracy discussed above, it is estimated that energy measurements with the analyzer on a monoenergetic group of particles could be made with an accuracy of 0.75 percent.

The accelerating voltage for the bombarding proton beam was measured by draining a small current from the high voltage point of the kevatron through a resistor of approximately 6.6×10^9 ohms. A Sola constant voltage transformer was used in the input to the kevatron. It is estimated that the kevatron accelerating voltage was maintained constant to within one part in five hundred from readings on the current drain. Previous work in this laboratory, by Morrish, showed that the kevatron has a total voltage fluctuation due to ripple of 2.1-kilovolts for a voltage of 330 kilovolts.[13] This was determined by measuring the energy spectrum of an H_2 beam sent directly into an electrostatic analyzer which had a voltage regulation better than that used in this experiment. A simplified analysis of the Cockroft-Walton circuit gives the ripple as 270 volts per 100 microamperes drain. This implies a drain of about 800 microamperes at a voltage of 330 kilovolts. Half of this is taken by the beam and the resistor drain. The remainder may be accounted for by leakage down supports, the glass accelerator tube, and tubes of kerosene coolant used in the ion source, and by corona loss.

As a result of the above mentioned work, a calibration table of the kevatron voltage against the current drain through the resistor stack was obtained. It is estimated that this table gives the accelerating voltage on the kevatron to an accuracy of one percent. For an accuracy of 0.1 percent, the calibration of the resistor stack against the electrostatic deflector must be carried out simultaneously with the measurement. An accuracy of one percent is quite adequate for the present work since an error of one percent in the bombarding energy contributes an error of a few tenths of a kilovolt in a total error of several kilovolts in the value of Q_3.

TARGET CHARACTERISTICS

The targets used in this experiment were prepared by vacuum evaporation, in the manner described by J. Strong, of beryllium onto thin nickel foils.[14] From the geometry of the evaporation set-up, the amount of beryllium put on the target was roughly estimated to be less than 0.005 mg/cm^2. The nickel foils were obtained commercially in the form of ½-inch squares.[15] The nickel had a nominal thickness of 1000 angstroms and was backed by copper of 2500-angstroms thickness. The manufacturer estimates the nickel thickness to be within ±20 percent of the nominal value. From evidence discussed below, this would seem to be true of the average thickness. However, from the method of manufacture—electrodeposition of nickel upon a mandrel followed by electrodeposition of copper onto the nickel—one might expect thick spots in the foil. From evidence considered in the discussion of results, this would seem to be true also. The foils are quite sturdy in the form in which they are supplied; however,

[13] A. H. Morrish, Phys. Rev. **76**, 1651 (1949).
[14] J. Strong, *Procedures in Experimental Physics* (Prentice-Hall Company, New York, 1938).
[15] Chromium Corporation of America, Waterbury, Connecticut.

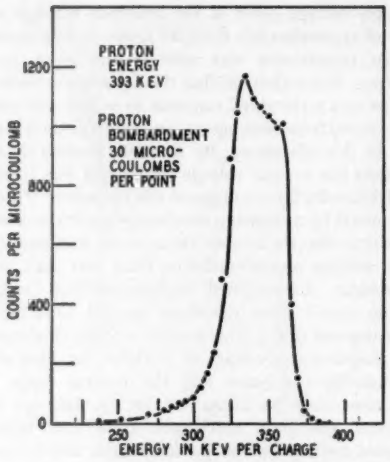

FIG. 2. Energy spectrum of elastically scattered protons.

any misuse will show up later as tears in the nickel. The nickel foil, with its backing on, was mounted in a holder. The assembly was dipped in a solution made up of roughly 50 percent concentrated ammonium hydroxide and 50 percent trichloroacetic acid by weight. The percentages are not critical. The copper dissolves in a few minutes whereas the nickel is unaffected. After stripping, the nickel foil was washed in two baths of distilled water for several hours. It is quite delicate at this stage and a jig is useful for handling purposes. Once the copper backing was stripped off, the foil was never removed from the holder. Bashkin and Goldhaber have recently described procedures of handling thin nickel foils quite similar to those used here.[16]

Figure 2 shows the energy spectrum obtained when 393-kev protons were elastically scattered at 90 degrees off one of the targets. Variation in detector efficiency and analyzer resolution with energy cannot modify the energy spectrum appreciably over the width of the scattered proton peak; consequently, the width at half-maximum should give the energy lost by protons in traveling through the foil a distance of $2\sqrt{2}$ times the foil thickness. The factor $2\sqrt{2}$ enters because the foil

TABLE I. Nuclear masses used in the calculations.

Nucleus	Symbol	Mass[a] (mass units on the physical scale)
H^1	M_p	1.008
H^2	M_d	2.015
He^4	M_α	4.004
Li^8	M_{Li}	6.017
Be^8	M_{Be}	8.008
He^9	M_t	9.015

[a] See reference 18.

[16] S. Bashkin and G. Goldhaber, Rev. Sci. Instr. 22, 112 (1951).

was mounted so that the beryllium covered surface faced the analyzer entrance and the oncoming protons, and the perpendicular to this surface bisected the 90-degree angle between the beam direction and the direction of those particles entering the analyzer. The energy loss in this case was 41 kev. Using S. D. Warshaw's results on the rate of loss of energy by protons traversing various materials,[17] the estimated thickness of the nickel in this foil is 0.072 mg/cm^2 or 810 angstroms.

In Fig. 2, at an energy of 334 kev, there is a rise superimposed upon the main peak. This rise occurs at the place one would expect to find protons scattered by a carbon layer. This assignment is reasonable since the energy spectrum shown in Fig. 2 was measured on a target which had been subjected to about 25-microampere-hours of bombardment and exposed to untrapped diffusion pumps. Measurements of the energy of the alpha-particles from the breakup of Be^8 were never made under these circumstances; liquid air traps were always kept filled and targets were discarded for measurement purposes after about 6-microampere-hours bombardment, all of which was done in one run. The thickness of the carbon layer indicated in Fig. 2 may be calculated by using the fact that the position of the peak caused by scattering from nickel is lower than the expected value by 17 kev. Again using Warshaw's data, the beryllium layer can account for no more than 6 kev loss, leaving 11 kev to be lost in carbon by the protons in getting down to the top nickel layer and in getting out again. This gives the carbon thickness as about 0.01 mg/cm^2. The protons scattered from the beryllium layer should, in Fig. 2, appear on the steep, low energy side of the peak scattered by nickel. The beryllium layer is so thin and its atomic number is so low that the protons it scatters are obscured in the rapidly falling slope of the nickel peak. For lower bombardment energies, peaks due to scattering from beryllium were observed.

FORMULAS FOR ENERGY RELEASES

For the nonrelativistic velocities involved in this experiment and for 90-degree observation, the laws of conservation of energy and momentum give the following formulas:

$$Q_1=(1+M_{Li}/M_\alpha)E_{Li}-(1-M_p/M_\alpha)E_p, \quad (4)$$

$$Q_2=(1+M_d/M_{Be})E_d-(1-M_p/M_{Be})E_p, \quad (5)$$

where "E" refers to the energy and "M" refers to the mass of the ion indicated by the subscript, whose meaning is indicated in Table I.

Neglecting for the moment the energy loss of the ions in the target material, Be^8 nuclei will give rise to a continuous distribution of alpha-particles with energies ranging from zero on up to a maximum value, E_α. The origin of the continuous distribution lies in the fact that

[17] S. D. Warshaw, Phys. Rev. 76, 1759 (1949).

the alpha-particles are emitted in all directions with respect to the Be^8 nuclei, which may have any direction in the laboratory. From Fig. 3, which is a scale drawing of the velocity vectors involved in reactions (2) and (3), it may be seen that the maximum observed alpha-particle velocity, for 90-degree observation of the distribution, is given by,

$$v_\alpha^2=(v_{Be}+v_\alpha')^2-v_{c.m.}^2, \tag{6}$$

where v_α is the observed alpha-particle velocity in the laboratory, v_{Be} is the velocity of the Be^8 ion in the center-of-mass system, v_α' is the velocity of the alpha-particle with respect to the Be^8 ion, and $v_{c.m.}$ is the velocity of the center of mass. If one substitutes the energies of the particles into Eq. (6) and solves for the energy release in the Be^8 breakup, one obtains,

$$\begin{aligned}Q_2=2[&\{E_\alpha+E_pM_pM_\alpha/(M_p+M_t)^2\}^{\frac{1}{2}}\\&-\{Q_2M_dM_\alpha/M_{Be}(M_{Be}+M_d)\\&+E_pM_dM_\alpha M_t/M_{Be}(M_{Be}+M_d)(M_t+M_p)\}^{\frac{1}{2}}]^2.\end{aligned} \tag{7}$$

Table I gives the values of the masses used in formulas (4), (5), and (7).[18] Exact values of for the masses have been used in these formulas but no corrections for relativistic effects have been made. This was considered justified since the Be^8 nucleus, which gives off the alpha-particle, has a velocity of 1.9×10^8 cm/sec in the laboratory and the alpha-particle, a velocity of 1.4×10^8 cm/sec with respect to the Be^8 nucleus. For these velocities, relativistic correction terms would be of the order of 0.01 percent and, consequently, negligible.

For observations taken at angles deviating from $\frac{1}{2}\pi$ radians by a small amount ϵ, corrections to formulas (4) and (5) become,

$$\Delta Q_1=(4E_{Li}E_pM_{Li}M_p/M_\alpha^2)^{\frac{1}{2}}\epsilon, \tag{8}$$

$$\Delta Q_2=(4E_dE_pM_dM_p/M_{Be}^2)^{\frac{1}{2}}\epsilon, \tag{9}$$

respectively. Corrections to formula (7) may be made by noticing that, to the first order in ϵ,

$$E_\alpha'=E_\alpha+\{4E_\alpha E_pM_\alpha M_p/(M_t+M_p)^2\}^{\frac{1}{2}}\epsilon, \tag{10}$$

where E_α' is the maximum alpha-particle energy at an angle to the beam of $\frac{1}{2}\pi-\epsilon$ radians. If we replace E_α by E_α' in the second term on the right, substitute into formula (7), and expand to the first order in ϵ, we get a correction to Q_2 as follows

$$\Delta Q_2=(1-1/S)\{4E_\alpha'E_pM_\alpha M_p/(M_t+M_p)^2\}^{\frac{1}{2}}\epsilon, \tag{11}$$

$$\begin{aligned}S=\{&E_\alpha'+E_pM_\alpha M_p/(M_t+M_p)^2\}^{\frac{1}{2}}\\&\times\{[Q_2+E_pM_t/(M_t+M_p)]\\&\times[M_dM_\alpha/M_{Be}(M_{Be}+M_d)]\}^{-\frac{1}{2}}.\end{aligned} \tag{12}$$

These corrections are of interest because the finite acceptance angle of the analyzer introduces a spread in the energy spectra and because deviation of the mean entrance angle from 90-degrees introduces a systematic source of error. It turns out that the spread due to the acceptance angle is comparable to that due to the analyzer ripple and, therefore, adds to the probable error. If the machining of the analyzer and target chamber parts was as good as claimed, there should be no systematic error of any importance arising from lack of knowledge of the mean entrance angle. Evidence in favor of this conclusion will be considered in the discussion of results obtained.

In order to estimate the effects of errors in the values of E_{Li}, E_α, E_d, E_p, and Q_2 on the values of Q_1, Q_2, and Q_3, the following formula was used

$$P_f^2=\sum_i(\partial f(x_i)/\partial x_i)^2P_i^2, \tag{13}$$

where P_f denotes the probable error in a quantity "f," which is a function of certain other quantities "x_i" which have probable errors P_i.[19] Application of formula

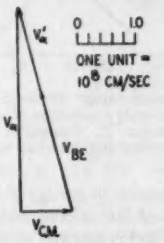

FIG. 3. Vector diagram of the velocities involved in reactions (2) and (3) under the conditions leading to maximum energy of the alpha-particles at 90-degrees to the proton beam. $v_{c.m.}$ refers to the velocity of the center-of-mass system (B^{10}); v_{Be} refers to the velocity of the Be^8 ion in this center-of-mass system; v_α' refers to the velocity of the alpha-particle, from the breakup of Be^8, with respect to the Be^8 ion; v_α refers to the velocity of the observed alpha-particle.

(13) to Q_2 gives,

$$\begin{aligned}P_2=2(S-1)\{&[P_\alpha/S]^2+[P_2M_dM_\alpha/M_{Be}(M_{Be}+M_d)]^2\\&+[M_dM_\alpha M_t/M_{Be}(M_{Be}+M_d)(M_t+M_p)\\&-M_pM_\alpha/(M_p+M_t)S]^2P_p^2\}^{\frac{1}{2}},\end{aligned} \tag{14}$$

$$\begin{aligned}P_3=2(S-1)\{&(P_\alpha/S)^2+(P_2/10)^2\\&+(9-4/S)^2(P_p/100)^2\}^{\frac{1}{2}},\end{aligned}$$

where P_α, P_2, and P_p are the probable errors in E_α, Q_2, and E_p, respectively.

ALPHA-PARTICLE DISTRIBUTION IN ENERGY

The experimentally observed energy spectrum will be influenced by various factors and some analysis is necessary to obtain the relation of the experimental observations to the nascent energy spectrum. First of all, if we consider a system in which the center of mass of the bombarding proton and the beryllium target nucleus is

[18] H. Bethe, *Elementary Nuclear Theory* (John Wiley and Sons, Inc., New York, 1947).

[19] H. Margenau and G. Murphy, *The Mathematics of Physics and Chemistry* (D. Van Nostrand Company, Inc., New York, 1943).

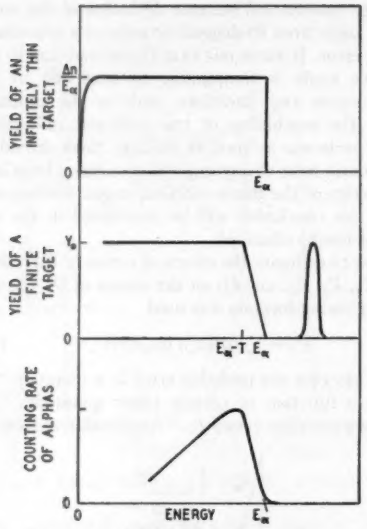

FIG. 4. A. Calculated energy spectrum of an infinitely thin target. B. Calculated energy spectrum of a finite target and the analyzer energy window. C. Calculated energy spectrum as modified by the analyzing and detecting equipment.

at rest, the distribution in energy of the alpha-particles from the breakup of Be^8 is constant. This rests on the assumptions that Be^8 is emitted with equal probability in all directions in the center of mass system and that alpha-particles are emitted isotropically with respect to the Be^8. The first assumption has been directly verified by measurements on the angular distribution of the deuterons.[20] The second assumption is quite reasonable since the ground state of Be^8 is supposed to have zero angular momentum causing the alpha-particles to be emitted in an s-state.[1] Making these assumptions, one finds $P(\mathbf{v})$, the probability of a given velocity $\mathbf{v}$, for an alpha-particle, per unit volume of velocity space, to be,

$$P(\mathbf{v}) = \text{constant}/v. \tag{15}$$

Thus,

$$P(E)dEd\omega = P(v)v^2dvd\omega, \quad P(E) = \text{constant}, \tag{16}$$

where $P(E)$ is the probability per unit solid angle $d\omega$, of finding alpha-particles of energy E, in the center-of-mass system of the B^{10} compound nucleus. In the laboratory system of coordinates, one finds the corresponding quantities to be,

$$P(\mathbf{v}') = P(\mathbf{v}), \tag{17}$$

where $P(\mathbf{v}')$ is the probability of a given velocity $\mathbf{v}'$ in the laboratory, per unit volume of velocity space, for an alpha-particle, and $\mathbf{v}$ and $\mathbf{v}'$ refer to the same point in velocity space with the prime referring to the laboratory system; thus,

$$P(E')dE'd\omega' = P(\mathbf{v}')v'^2dv'd\omega' = \text{constant}\ (v'/v)(v'dv')d\omega', \tag{18}$$

$$P(E') = \text{constant}(v'/v).$$

For 90-degree observation of alpha-particles, the resulting distribution is drawn in Fig. 4A for proton bombarding energies in our range.

For an infinitely thin target, the yield curve of Fig. 4A may be approximated by a step function and its area by a rectangle since it is the shape near E_α that is of interest; this gives,

$$\Delta n = \int_0^{E_\alpha} Y(E)dE = 2\sigma F\Delta N, \qquad \text{Yield, } Y(E) = (\Delta n/E_\alpha), \tag{19}$$

where E_α is the maximum alpha-particle energy, Δn is the total number of alpha-particles produced, σ is the cross section, F is the proton flux, and ΔN is the number of target nuclei. For thicker targets one must sum the contributions of many such layers to obtain the yield of alpha-particles of energy E',

$$Y(E') = \int_{E'}^{E_\alpha} dn/E = \int_{E'}^{E_\alpha} 2\sigma FdN/E, \tag{20}$$

$$dN = \text{constant}(dE/L), \tag{21}$$

where L is the rate of loss of energy of emergent ions in the target. If we assume that our target thickness to entrant and emergent ions is small compared to E_α, as it always was, σ and L may be taken as constants over the range of integration and the yield curve looks as shown in Fig. 4B. Over energies from E_α down to $E_\alpha - T$, where T is the sum of the thicknesses of the target to entrant and emergent ions, the yield curve is approximately,

$$Y(E') = Y_0(E_\alpha - E')/T. \tag{22}$$

One effect of the analyzer energy window will be to round the edges of the distribution as finally observed. If the target thickness is less than the window width, the leading edge of the observed distribution will rise to maximum value in a distance equal to the window width. The point E_α will correspond to the half-maximum value on the leading edge of the observed distribution in this case. If the target thickness is greater than the window width, the leading edge becomes rounded at the foot and the peak but retains a linear section. The point E_α will correspond to the extrapolated end point of the linear section of the observed leading edge in this case.

Since the analyzer window energy width is proportional to the energy of the focused ions, the trailing edge of the observed distribution will fall off with the

[20] Neuendorffer, Inglis, and Hanna, Phys. Rev. 82, 75 (1951).

energy. This effect will be emphasized by the decrease in detector sensitivity with the energy of the focused ions and by the reduced number of charged particles emerging from the target with energies in the lower ranges of the distribution. The predicted form of the curve of counting rate against energy for the alpha-particles from the breakup of Be^8 is shown in Fig. 4C.

The high energy side of the curve in Fig. 4C is not appreciably dependent on the value assumed for the spin of Be^8. The possible higher values of 2, 4, etc., result in fewer alpha-particles being emitted at right angles to the direction of motion of the Be^8 nucleus but this only affects the alpha-particle spectrum for energies in the middle of the allowed range. The high energy side of the curve in Fig. 4C is not appreciably affected by the width of the ground state of Be^8, either, since estimates show that the latter is much less than the width of the analyzer energy window.[3,4]

The kevatron ripple does not affect the above analysis since, as an examination of formula (7) shows,

$$dE_\alpha/dE_p=\{M_dM_tM_\alpha/M_{Be}(M_{Be}+M_d)(M_t+M_p)\}S - M_pM_\alpha/(M_p+M_t)^2. \quad (23)$$

With the bombarding energies used in this experiment, dE_α/dE_p is approximately 0.11.

The thickness of a target in the above discussion depends on the relation of the width of the analyzer energy window to the loss of energy of the emergent ions in traversing the beryllium target. The emergent ions in reaction (3) would be Be^8 ions, if their lifetime has the value mentioned in the Introduction, since the beryllium target was no more than 250 angstroms thick and the Be^8 ions should travel about 1000 angstroms before decaying. The emergent ions would be the observed alpha-particles, if the Be^8 lifetime were much shorter than the above value. In either case, the emergent ions will lose considerably more energy in any contaminating surface layer on the target than the entrant protons will lose. The latter loss is relatively small and not of great importance since the alpha-particle energy does not depend on the bombarding energy very strongly, as is shown in formula (23). The former loss is of considerable importance, however, since any loss of energy by the emerging ions is directly reflected in the value of the energy release. This is the reason that oil deposition on the target is an important source of error.

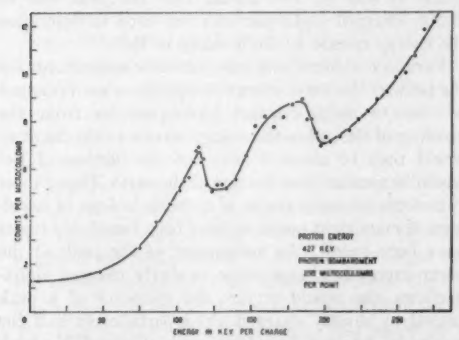

FIG. 5. Observed energy spectrum for 427-kev proton bombardment. The group of particles with an upper energy edge slightly above 200 kev consists of protons from the breakup of stray hydrogen molecular ions striking the target. The doubly-charged alpha-particles from the disintegration of Be^8 have an upper energy edge of 235 kev and appear at an energy-to-charge value of 117 kev per charge.

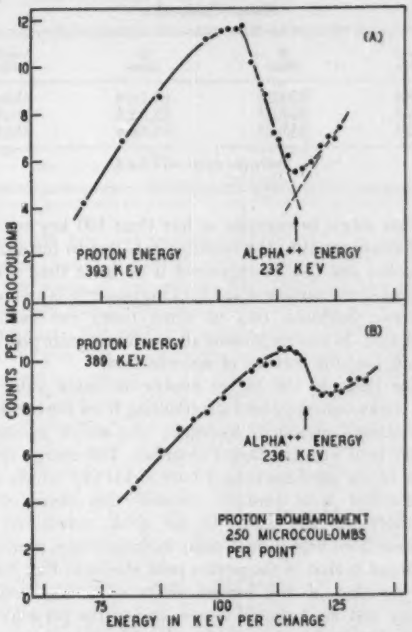

FIG. 6. A. Observed energy spectrum of 393-kev proton bombardment. The doubly-charged alpha-particles from the breakup of Be^8 appear at an energy-to-charge ratio of 116 kev per charge. The target was thick to emergent ions. B. Observed energy spectrum for 389-kev proton bombardment. The double-charged alpha-particles from the breakup of Be^8 appear at an energy-to-charge ratio of 118-kev per charge. The rise occurs in the width of the analyzer energy window. This puts an upper limit on the width of the ground state of Be^8 of 3 kev.

DISCUSSION OF RESULTS

The energy spectrum of the particles obtained by bombarding one of the targets with 427-kev protons is shown in Fig. 5. Only that portion of the spectrum well below the peak due to scattered protons is shown. To understand the difference between this curve and the one in Fig. 4C, one must realize that, while the average thickness of the nickel backing is small enough to confine the elastically scattered protons to a narrow energy band, there is a long tail on the low energy side, probably caused by thick spots on the foil. This tail

TABLE II. Results.

E_p (kev)	E (kev)	Q_2 (kev)	Beryllium thickness
389±4	236±5	80.1±4	thin
393±4	232±5	75.8±4	thick
427±4	235±5	76.5±4	thick
Average value = 77.5±4			

reaches down to energies of less than 100 kev with a magnitude equal to the counting rate due to the alpha-particles, and can be explained if no more than a few percent of the surface of the backing material is assumed to have thickness two to three times the average thickness. As was mentioned above, this is quite possible considering the method of manufacture.

The peak at the higher energy-to-charge value in Fig. 5 was caused by protons resulting from the breakup of scattered molecular hydrogen ions which managed to get bent into the target chamber. The energy spectrum of the particles from a bare nickel foil, which was bombarded with protons, showed this same peak. Furthermore, the width of the peak, attributed to protons from broken molecular hydrogen ions, is about the same as that of the proton peak shown in Fig. 2 and the position of the former shifts with bombarding energy just as it should if it is due to the presence of molecular hydrogen ions in the beam striking the target. The conclusion is that, in the magnetic analysis of the kevatron beam which was about 60 percent molecular hydrogen ion, the imperfect focusing of the beam and the inhomogeneity of the resolving magnetic field allowed a small amount of molecular ion beam to accompany the proton beam down to the target. From the relative heights of the peaks due to scattered protons and scattered molecules, one can say that about 0.1 percent of the beam striking the target was molecular hydrogen.

The peak at the lower energy-to-charge value in Fig. 5 was attributed to doubly-charged alpha-particles from the breakup of Be^8. Figure 6 shows this peak as obtained on two other targets. No peak was obtained, which corresponded to the peak at the lower energy-to-charge value in Figs. 5 and 6, where a bare nickel foil was used as a target with a bombarding energy for protons equal to that used in obtaining the data shown in Fig. 6A.

TABLE III. Energy release in $Be^9(p,\alpha)Li^8$ from observed energies of Li^{6++} particles.

E_p (kev)	Number of determinations averaged	E_{Li} (kev)	Q_1 (Mev)	Beryllium thickness
269±3	4	928±8	2.121±0.020	thin
331±3	3	948±9	2.125±0.023	thin
334±3	8	954±6	2.137±0.014	thick
Weighted average value = 2.130±0.010				

In Figs. 5 and 6A the alpha-particle peak was obtained from thick targets and, in Fig. 6B, it was obtained from a thin target. For a thick target, the proper way to locate the point E_a is to extrapolate the linear portion of the leading edge of the peak down to a zero counting rate for doubly-charged alpha-particles. The latter is obtained by extrapolation of the falling curve upon which the rise due to doubly-charged alpha-particles is superimposed. These operations have been indicated in Fig. 6. For the data obtained from the thin target, the point E_a was located by taking it as the position at which half the maximum value of the rise was achieved. The results obtained from the data in Figs. 5 and 6 are listed in Table II. The average of three measurements gives the energy release in the breakup of Be^8 as 77.5 kev.

The fact that data were obtained from a target which was thin to the emergent ions implies that the width of the ground state of Be^8 must be less than the width of the analyzer energy window. An upper limit of 3 kev is thereby placed on the width of the ground state of Be^8.

The basis of the assignment of the lower peak to alpha-particles from the breakup of Be^8 was the smallness of the shift in the position of E_a with the shift in proton bombarding energy. Formula (23) shows this to be a characteristic of the alpha-particles from the breakup. A second reason was the shape of the peak in Fig. 6A. It is quite distinctive and closely approaches the predicted shape for the alpha-particle distribution. Third, there were indications of a peak in the energy spectrum at an energy-to-charge value which was twice that of the lower peak. The singly-charged alpha-particles from the breakup of Be^8 could have caused these peaks. The number of elastically scattered protons was rising rather sharply at this position and could easily obscure a peak due to the singly-charged alpha-particles. It was for this reason that the peak due to doubly-charged alpha-particles was used to determine the energy release in the breakup of Be^8.

Various considerations rule out other assignments for the peak at the lower energy-to-charge value. It cannot be due to singly-charged alpha-particles from the breakup of Be^8, since the energy release in the breakup would then be about 6 kev, and the lifetime of Be^8 would be greater than the age of the earth. Under these circumstances some traces of a stable isotope of beryllium of mass eight ought to have been found. No traces have been found.[8] An assignment of the peak at the lower energy-to-charge value to singly charged alpha-particles also would require the existence of a peak caused by doubly charged alpha-particles at half the energy-to-charge value of the peak observed. No peak was observed at the latter value. The observed peak cannot be the result of a group of particles from either reaction (1), or (2), because the positions in the energy spectrum of the various ions produced are well known and do not fall near the peak in question.[8] Particles

from reaction similar to (1) and (2), in which one of the product ions is left in an excited state, could not cause the peak in question because they would all require larger shifts in the peak position, with changes in the bombarding energy, than the shifts which were observed.

The presence of the elastically scattered protons was a source of trouble in the determination of the point E_a from the peak due to the doubly-charged alpha-particles since they obscured the high energy side of the peak. The scattering from the molecular ion beam was a similar source of trouble. Targets, which had a relatively large number of thick spots in their backing, would have the peaks due to alpha-particles superposed on a large counting rate due to elastically scattered protons and elastically scattered molecular hydrogen ions. The data were discarded for purposes of determining the point E_a in these cases. Out of seven targets, on which observations were made, four proved useless for this reason. In the case of those targets which provided useful data, it is felt that the point E_a was determined with a probable error of 2.0 percent. This estimate of the probable error P_a, for use in Eq. (14), was obtained by combining the inherent error in the measurement of the energy of a mono-energetic group of particles with the analyzer, the error caused by the finite acceptance angle of the analyzer, and the error caused by the uncertainty in the location of the point E_a.

In all of the runs to determine the energy release in the Be^8 breakup, there was the danger that carbon would accumulate on the target and slow down the emerging ions. Knowledge of the carbon thickness would be of no help since the energy loss rate and the state of charge of the emergent ions of reaction (3) are not known as functions of the energy. To overcome this difficulty, only fresh targets were used and the position of the peak due to doubly charged Li^6 ions from reaction (1) was determined just before and just after a measurement. In all of the cases reported here, no change of any significance was found. Since Li^6 is a fairly heavy nucleus, it was felt that any carbon accumulation which did not affect it, would not affect the emergent ions of reaction (3).

Considerable data on reaction (1) were compiled in the course of the work. These data are listed in Table III together with estimated errors. The significant points on the peaks caused by Li^6 ions were taken to be the maximum point for the thin targets and the half-maximum point on the leading edge for the thick targets. The classification, as thick or thin, was made on the basis of the Li^{6++} peak shape but it always coincided with the classification made on the basis of the shape of the rises caused by the alpha-particles from Be^8. In observing these lithium peaks, a bombarding energy near 331 kev was usually used to take advantage of the resonance in reaction (1) at this energy.[21]

TABLE IV. Energy release in $Be^8(p,d)Be^8$ from observed deuteron energies.

E_p (kev)	E_d (kev)	Q_2 (kev)	Beryllium thickness
202±2	587±6	558±8	thin
202±2	587±6	558±8	thin
202±2	587±6	558±8	thin
202±2	586±6	557±8	thin
Average value = 558±5			

On some of the targets, the peaks in the energy spectrum due to deuterons from reaction (2) were also observed. The deuteron peaks were observed in the same runs that measurements were made to determine the energy release in the breakup. The targets, from which these peaks were obtained, were thick to the emergent ions of reaction (3) and to the Li^6 ions; however, because of their lower energy loss rate, the yield for deuterons was characteristic of a thin target. The results are contained in Table IV. The value of Q_2, which was used in formula (7), was the average value indicated in the table, 558 kev, with a probable error P_2, equal to 0.7 percent.

The values of Q_1 and Q_2, which were mentioned above, agree quite well with the presently accepted values of 2.12 Mev and 560 kev, respectively.[1] Some confidence that serious errors of a systematic nature were not overlooked may be obtained from this agreement. One source of systematic error which such agreement limits is that arising from a deviation of the mean analyzer entrance angle from 90-degrees. From the extent of the agreement between the value of Q_1 obtained here and that presently accepted, it may be seen from formula (8) that the deviation could not be more than 0.016 radian. The correction to Q_3 is less than a kilovolt, therefore, on this account. A kilovolt has been added to the probable error in Q_3, as calculated from formula (14), to cover this correction. The probable error in Q_3 was calculated with values of 2.0 percent, 0.7 percent, and 1.0 percent for P_a, P_2, and P_p, respectively. The final estimated probable error in Q_3 is 4 kev, which gives the energy release in the breakup of Be^8 as 77.5±4 kev.

ACKNOWLEDGMENTS

The author would like to take this opportunity to thank Professor S. K. Allison for suggesting this problem and for his advice and assistance throughout the course of the work. In addition, he would like to thank the other members of the laboratory, D. Bushnell, H. Casson, H. Kanner, and F. Ribe, for their kind assistance; in particular, he would like to thank H. Kanner for many helpful suggestions.

[21] Thomas, Rubin, Fowler, and Lauritsen, Phys. Rev. 75, 1612 (1949).

The Adiabatic Elastic Constants of Rock Salt*

W. C. Overton, Jr.,† and R. T. Swim‡
Rice Institute, Houston, Texas

(Received June 4, 1951)

The velocities of propagation of 10-Mc/sec longitudinal and transverse sound waves in single crystals of rock salt have been measured over the temperature range from 60°K to 300°K by means of the ultrasonic pulse method. From these velocities the adiabatic elastic constants have been calculated, with the results that $c_{11}=4.828\pm0.015$, $c_{44}=1.273\pm0.005$, and $c_{12}=1.276\pm0.025$ at 300°K in units of dyne/cm$^2\times10^{11}$. The values of these elastic constants extrapolated to absolute zero temperature are, in these units, 5.750, 1.327, and 0.986, respectively. The adiabatic compressibility has been calculated from c_{11} and c_{12} and is 4.07×10^{-12} cm^2/dyne at 300°K. The Debye characteristic temperature is computed to be 292.6 ± 0.5°K at $T=0$°K.

INTRODUCTION

THE ultrasonic pulse method has been used to measure the velocity of 10-Mc/sec sound waves in single crystals of rock salt at temperatures from 60°K to 300°K. From the knowledge of the velocity of propagation of longitudinal and transverse waves in the medium, the adiabatic elastic constants c_{11}, c_{44}, and c_{12} may be calculated. The ultrasonic pulse method of determination of mechanical properties of solids,[1–3] made practicable by the development of electrical circuits for pulsing, has certain advantages over the previously used methods.[4,5] Perhaps the most important of these is the fact that the velocity of propagation of sound waves in the medium may be calculated directly from experimentally observed quantities. Since the piezoelectric quartz crystal employed to generate the acoustic pulses is many wavelengths in diameter at high frequencies, the acoustic waves propagated by the crystal are essentially traveling plane wave pulses. Using an oscilloscope such as the Du Mont 256-D, direct measurement of the time required for the pulses to travel twice the length of the specimen is possible, which allows immediate calculation of the wave velocity. From this velocity and the density of the medium the elastic constants may be calculated.

EXPERIMENTAL

The specimens of NaCl employed are single crystals, free from flaws and impurities, obtained from the Harshaw Chemical Company, and are in the form of cylinders approximately three centimeters in diameter. Two rock salt crystals are used in the experiments: one cut so that the end faces of the cylinder are parallel to the (0, 0, 1) crystalline plane, the other with end faces parallel to the (0, 1, 1) plane, where 0 and 1 are Miller indices. The lengths of the crystals are about 6.6 and 12.7 cm, respectively. The advantage in the use of single crystals is that no extraneous effects are introduced due to scattering and reflections of the sound pulses by the grain structure present in polycrystalline specimens. The end faces of the specimens have been carefully ground and polished so that they are both flat and parallel; the lengths of the specimens are thus constant over the area of the faces to ±0.0004 inch. Furthermore, any focusing of the sound beam caused by curvature of the reflecting faces is minimized.

It has been determined experimentally that the quartz transducer must be physically bonded to the specimen in order to obtain the intelligible echoes necessary for precise velocity measurements. If the quartz is merely pressed against the end face of the specimen, the contact is not sufficiently good to allow transmission of the acoustic pulse to the specimen without undesirable pulse distortion. In the measurements on rock salt the choice of the cement used to bind the quartz to the specimen must be made according to the temperature range over which the measurements are to be made. The reason for this is that as the temperature is lowered, differential thermal contraction between the quartz, the binder, and the rock salt may result in one of two effects, either of which renders further measurements impossible. The first of these is the cracking of the binding layer, so that the quartz is no longer in contact with the rock salt. The second is that stresses introduced in the quartz crystal may deform it and hence change its piezoelectric properties, with the result that intelligible echoes are no longer received. Both phenomena have been observed, and in one instance the thermal stress was sufficiently large to cleave the specimen very slightly.

It has been found that ordinary stopcock grease serves as an adequate binder for the quartz transducer in the temperature range from room temperature to 160°K, but below this temperature the binding layer cracks because of thermal stresses. For measurements below 160°K an organic mixture,[6] consisting of ethyl ether, ethyl alcohol, and isopentane, has been employed as a binder. This mixture is applied at a temperature

* This project was supported by the ONR.
† Now with The Field Research Laboratories, Magnolia Petrolium Company, Dallas, Texas.
‡ Magnolia Petrolium Company Fellow.
[1] H. B. Huntington, Phys. Rev. **72**, 321 (1947).
[2] J. K. Galt, Phys. Rev. **73**, 1460 (1948).
[3] W. C. Overton, Jr., J. Chem. Phys. **18**, 113 (1950).
[4] L. Balamuth, Phys. Rev. **45**, 715 (1934).
[5] F. C. Rose, Phys. Rev. **49**, 50 (1936).
[6] G. N. Lewis and M. Kasha, J. Am. Chem. Soc. **66**, 2100 (1944).

of about 125°K, and with it measurements may be made from 110°K to 60°K. The substitution of pentane for isopentane in this organic binder allows measurements to be made at temperatures as high as 140°K, although the thermal contraction of the medium is greater at lower temperatures than that of the mixture using isopentane. At temperatures below about 50°K the differential contraction between the transducer, the binder, and the rock salt is sufficient to deform physically the transducer. The result of this is a radical alteration in the electrical and acoustical properties of the quartz crystal, and the pulses are so distorted that accurate measurements are impossible. At the present time no binder has been found which will allow measurements to be carried out below this temperature on rock salt.

In the determination of the round-trip travel time of the pulses in the specimen some ten readings are made of the position in time of the leading edge of each echo occurring in the first 100 microseconds after the initial pulse, and an average taken. Then the differences between the times of occurrence of successive echoes give the desired travel time, which in general has an average deviation of ±0.03 microsecond. It is to be noted that although the acoustic pulses may be reflected at grain boundaries in the binder and at the faces of the transducer as well as at the faces of the specimen, measurements at the leading edges of the echoes insure that the distance travelled by the pulses, corresponding to the measured time, is wholly within the specimen.[7] Temperatures are measured with a copper-constantan thermocouple and a helium gas constant volume thermometer. Although there are temperature gradients during measurements at temperatures above 80°K, the rate of cooling of the specimen may be regulated so that the temperature is constant to within one degree during a given measurement. These temperature gradients were not sufficiently large to cause any noticeable pulse distortion. Figure 1 shows the cryostat used in these measurements. The Dewar flask A surrounds the apparatus and serves both as a container for the liquid refrigerant and as a shield against external thermal radiation. In addition another Dewar flask surrounds flask A and is filled with liquid nitrogen for refrigeration purposes. The specimen is held in the brass can B, and layers of paper are used as a sound absorbing medium between the specimen and the can. The rock salt crystal may be raised and lowered and rotated by means of the stainless steel rod C. The leads of the copper-constantan thermocouple thermometer D are soldered to the can, giving good thermal contact with the specimen. The glass capillary E is used for the application of the quartz-to-specimen binder for temperatures below 140°K, and may be

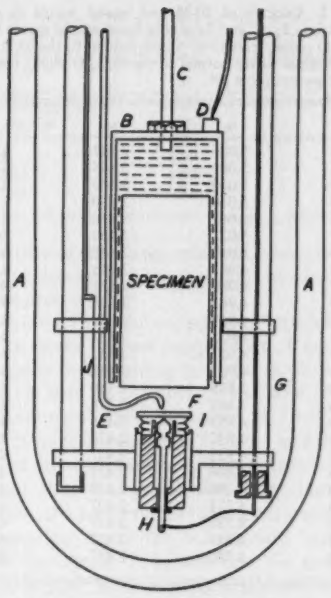

FIG. 1. Cryostat used for low temperature ultrasonic measurements.

rotated from above. The rf pulses to the quartz crystal F are brought down by the coaxial line G, which consists of a stainless steel tube and an inner copper conductor. The electrical contacts to the transducer are the spring-loaded plunger H and the stack of steel disc springs supporting a brass contact I. J is the bulb of the helium gas constant volume thermometer.

In order to calculate the velocity of propagation of elastic waves in a solid, the length of the specimen must be known accurately. This in turn requires knowledge of the temperature dependence of the linear coefficient of thermal expansion, which in the case of NaCl has not been determined experimentally over the temperature interval under consideration. However, it may be calculated from available data in two independent ways. Also the temperature dependence of the density of rock salt must be known in order to calculate the elastic constants. Grüneisen[8] has shown that the ratio α/c_p where α is the linear coefficient of thermal expansion and c_p the specific heat at constant pressure, is independent of temperature for many solids. Using published values of α and c_p at 0°C, α has been calculated from the temperature variation of c_p.[9] From this knowledge of α the volume coefficient of thermal expansion is determined, which allows calculation of the temperature dependence of the density, assuming a

[7] In this connection Lazarus (see reference 13) reports the necessity of a correction to the observed travel time. However, Huntington (see reference 1) maintains that according to the above discussion no such correction is necessary.

[8] E. Grüneisen, Ann. Physik 26, 211 (1908).

[9] *International Critical Tables* (McGraw-Hill Book Company, Inc., New York, 1928), Vol. 3, p. 43.

TABLE I. Velocity of 10-Mc/sec sound waves in rock salt. The subscripts 1_1, t_1, and 1_2 denote longitudinal waves normal to the (0, 0, 1) plane, transverse waves normal to the (0, 0, 1) plane, and longitudinal waves normal to the (0, 1, 1) plane, respectively. The units are cm/sec$\times 10^5$.

T	c_{11}	c_{t_1}	c_{12}
60	5.086	2.447	4.602
70	5.081	2.448	4.596
80	5.070	2.449	4.590
90	5.056	2.450	4.584
100	5.042	2.450	4.578
110	5.027	2.450	4.572
120	5.012	2.448	4.568
130	4.997	2.445	4.562
140	4.980	2.441	4.556
150	4.965	2.438	4.550
160	4.949	2.435	4.544
170	4.933	2.433	4.538
180	4.917	2.432	4.532
190	4.901	2.431	4.526
200	4.885	2.430	4.520
210	4.869	2.429	4.514
220	4.853	2.428	4.508
230	4.837	2.428	4.502
240	4.822	2.427	4.498
250	4.806	2.427	4.492
260	4.790	2.427	4.488
270	4.774	2.427	4.483
280	4.758	2.427	4.479
290	4.741	2.427	4.476
300	4.726	2.427	4.473

cube of unit volume at 0°C. The second method of calculation employs the use of the empirical relation between density and temperature for NaCl,[10] which is

$$\rho(t)=2.1680(1-1.12\times10^{-4}t-5\times10^{-8}t^2),$$

TABLE II. Adiabatic elastic constants and compressibility of rock salt. The units of the elastic constants are dyne/cm$^2\times10^{11}$ and of the compressibility are cm^2/dyne$\times10^{-13}$.

T	c_{11}	c_{44}	c_{12}	k_s
0	5.750	1.327	0.986	3.89
60	5.730	1.327	0.986	3.90
70	5.713	1.327	0.986	3.91
80	5.685	1.327	0.986	3.92
90	5.649	1.326	0.986	3.94
100	5.613	1.325	0.992	3.95
110	5.575	1.324	1.001	3.97
120	5.535	1.321	1.017	3.97
130	5.496	1.316	1.034	3.97
140	5.456	1.310	1.052	3.97
150	5.415	1.306	1.069	3.97
160	5.376	1.302	1.082	3.98
170	5.336	1.298	1.098	3.98
180	5.296	1.295	1.110	4.00
190	5.256	1.293	1.122	4.00
200	5.216	1.290	1.134	4.01
210	5.177	1.288	1.143	4.02
220	5.137	1.286	1.155	4.03
230	5.097	1.284	1.169	4.05
240	5.059	1.282	1.181	4.05
250	5.020	1.281	1.190	4.06
260	4.981	1.279	1.205	4.06
270	4.942	1.277	1.222	4.07
280	4.904	1.276	1.236	4.07
290	4.864	1.275	1.258	4.07
300	4.828	1.273	1.276	4.07
Uncertainty:	±0.015	±0.005	±0.025	±0.03

[10] A. Henglein, Z. physik Chem. **115**, 97 (1925).

where t represents the centigrade temperature. The density is calculated directly from this, and upon application of the above relation to a unit cube of rock salt at 0°C the linear coefficient of thermal expansion may be calculated. In either case the length is computed by numerical integration of the relation

$$L(T)=L(T_0)\left[1+\int_{T_0}^{T}\alpha(T)dT\right].$$

The values of the lengths of the specimens obtained by these two independent methods differ by not more than one part in 3000.

RESULTS

The velocity of propagation of the sound waves is calculated for each of the two determinations of the

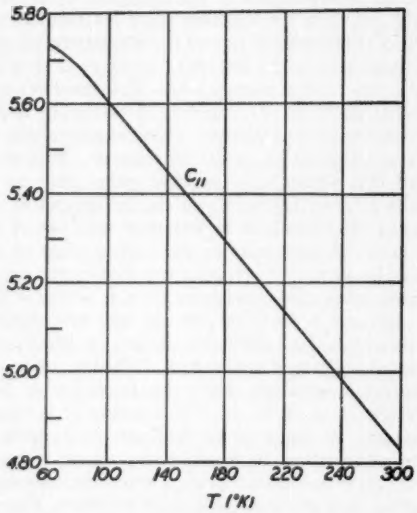

FIG. 2. Elastic constant c_{11} of rock salt in units of dyne/cm$^2\times10^{11}$.

length, and the curves of the experimental results are smoothed. Table I gives the velocities measured in this experiment, determined by the algebraic mean of the smoothed values calculated by each of the above methods.

In the case of a cubic crystal such as NaCl rotational and reflectional symmetries require that there be only three independent, nonzero elastic constants, which are c_{11}, c_{44}, and c_{12}. It may be shown[11] that the following relations hold for cubic crystals, where ρ is the density and c the wave velocity:

longitudinal waves normal to the (0, 0, 1) plane,

$$\rho c^2=c_{11};$$

[11] A. E. H. Love, *The Mathematical Theory of Elasticity* (Dover Publications, Inc., New York, 1944), pp. 295–299.

transverse waves normal to the (0, 0, 1) plane,

$$\rho c^2 = c_{44};$$

longitudinal waves normal to the (0, 1, 1) plane,

$$\rho c^2 = \tfrac{1}{2}(c_{11}+c_{12}+2c_{44}).$$

In the calculation of the elastic constants one value of ρc^2 is determined from the density and velocity calculated according to Grüneisen's theory and another from the empirical relation for the density, and an average of the two is taken. These two values of ρc^2 never differ by more than one part in 2500, which is well within the total uncertainty of 0.4 percent in the values of this quantity. Table II gives the values of the adiabatic elastic constants as functions of temperature, and also the adiabatic compressibility, which is

$$k_s = 3/(c_{11}+2c_{12}).$$

The greater uncertainty in c_{12} is due to the contributions

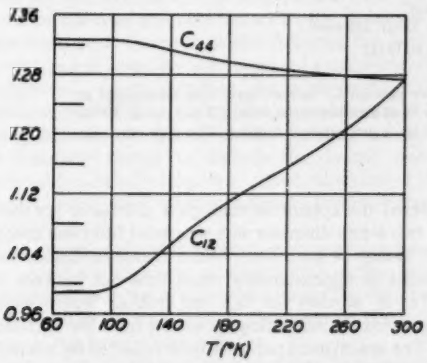

FIG. 3. Elastic constants c_{44} and c_{12} of rock salt in units of dyne/cm$^2\times 10^{11}$.

of the uncertainties of c_{11} and c_{44}. The values of these quantities at absolute zero are determined by extrapolation of the results at higher temperatures. Figures 2 and 3 give the plots of the elastic constants as functions of temperature.

DISCUSSION

The adiabatic elastic constants of rock salt have been determined previously in this temperature range by Rose[1] and Durand,[12] both of whom used the composite oscillator method. Also these quantities have been measured at room temperature by Huntington,[1] Galt,[2] and Lazarus,[13] using the ultrasonic pulse technique. A comparison of the values obtained here with these previous results at room temperature is given in Table III. It is to be noted that in the present work c_{12} is smaller than c_{44}, except at room temperature, showing

[12] M. A. Durand, Phys. Rev. **50**, 449 (1936).
[13] D. Lazarus, Phys. Rev. **76**, 545 (1949).

TABLE III. Elastic constants of rock salt measured at room temperature in units of dyne/cm$^2\times 10^{11}$.

	c_{11}	c_{44}	c_{12}
Overton and Swim	4.86	1.27	1.28
Huntington	4.85	1.26	1.23
Galt	4.87	1.26	1.24
Rose	4.96	1.27	1.30
Durand	4.99	1.27	1.31
Lazarus	4.91	1.28	1.23

the invalidity of the cauchy relations, which require the equality of these two elastic constants in a cubic lattice at all temperatures.

It is evident from the experimental results that the elastic constants become independent of temperature at a temperature depending upon the particular elastic constant. It is to be expected that c_{ij} as a function of temperature should have zero slope at $T=0$°K as can be seen from the strain-energy function and the Nernst theorem of thermodynamics. A more detailed consideration of the strain-energy function shows that $\partial c_{ij}/\partial T$ may vanish at a temperature considerably greater than zero, dependent upon the temperature variation of strain in the crystal. It follows that the temperature at which $\partial c_{ij}/\partial T$ becomes zero is not necessarily the same for all of the elastic constants, as is also shown by the experimental results. Consideration of the strain-energy function also leads to the possibility of the existence of inflection points in the curves of the elastic constants *vs* temperature, which are experimentally found to occur. The hump in the curve of c_{12} *vs* temperature in the region between 120° and 220°K, although generally within the experimental error of the measurement, is due to the inflection of c_{44} in this temperature region. In the relation used to calculate c_{12}, $c_{12}=2\rho c^2-c_{11}-2c_{44}$, ρc^2 and c_{11} are linear functions of temperature over this interval, whereas c_{44} undergoes the abovementioned inflection.

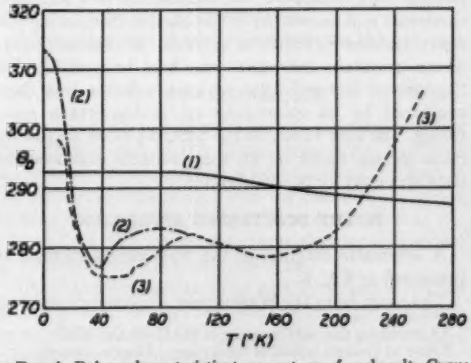

FIG. 4. Debye characteristic temperature of rock salt. Curve (1) is due to Overton and Swim, (2) to Kellermann, and (3) to Clusium, Goldmann, and Perlick.

From the values of the elastic constants obtained here the Debye characteristic temperature θ_D has been computed as a function of temperature, and as is to be expected, is constant over a wide temperature range. The computed values of θ_D are shown in Fig. 4, together with the results obtained by Kellermann[14] from a theoretical analysis of the NaCl lattice vibrations and with those obtained by Clusius, Goldmann, and Perlick[15] from specific heat measurements. Comparison of the three curves shows that the inadequacy of the Debye theory in providing an accurate description of the properties of the crystal may be attributed to the choice of the distribution function for the frequencies, rather than to anomalous behavior of the elastic constants. The value of θ_D at absolute zero temperature is 292.6±0.5°K.

[14] E. W. Kellermann, Trans. Roy. Soc. (London) **A238**, 513 (1940); Proc. Roy. Soc. (London) **A178**, 17 (1941).
[15] Clusius, Goldmann, and Perlick, Z. Naturforsch. **4A**, 424 (1949).

ACKNOWLEDGMENT

The authors are indebted to Professors W. V. Houston and C. F. Squire for helpful discussions concerning this work.

PHYSICAL REVIEW VOLUME 84, NUMBER 4 NOVEMBER 15, 1951

Scattering of Protons by Alpha-Particles*

C. H. BRADEN†
Washington University, St. Louis, Missouri
(Received August 6, 1951)

Differential scattering cross sections for 5.10±0.10-Mev protons by helium have been determined at laboratory angles from 30° to 150°. Probable errors in the cross sections varied from 2.4 percent at 30° to 4.1 percent at 150°. The scattered protons were detected by a proportional counter. The apparatus was calibrated by a study of proton-proton scattering.

I. INTRODUCTION

THE scattering of protons by helium has previously been studied at energies up to 3.6 Mev.[1] In the present work the scattering of 5.10-Mev protons by helium has been studied at laboratory angles of 30°, 45°, 60°, 75° 58′, and 150°. The effect of a slight variation in energy on the scattering cross section at 30° was investigated.

The determination of absolute scattering cross sections is usually complicated by difficulties in measuring certain geometrical constants of the apparatus. In the present work, moreover, the capacitance of a standard condenser and associated circuit used in integrating the beam current presents a problem in measurement. These uncertain constants were here lumped into an "apparatus factor." This apparatus factor was then evaluated by an experiment on proton-proton scattering. The best value for the proton-proton scattering cross section based on all the available experimental data was used for this calibration.

II. THE SCATTERING APPARATUS

A schematic diagram of the scattering apparatus is presented as Fig. 1.

The beam from the Washington University cyclotron entered the apparatus through a collimator consisting of two 4-mm diameter slits separated from one another by about 34 cm. Four 6-mm diameter baffles were spaced at approximately equal intervals between the slits. A window of 0.25-mil rubber hydrochloride separated the scattering apparatus from the cyclotron.

The unscattered particles were collected by a faraday cage. The faraday cage, maintained at a pressure of about 4×10^{-6} mm of Hg, was separated from the scattering gas by a window of 0.5-mil polyethylene.[2] The charge was accumulated on a 1μf polystyrene condenser made by John E. Fast and Company of Chicago, Illinois. This condenser showed no appreciable leakage or polarization. The voltage across the condenser was measured by a null method using a Compton electrometer as the null indicator. The error in the charge measurement was estimated to be ±0.2 percent, the largest part of this error being due to slight drifts in the electrometer zero.

The scattered protons were defined by a slit system consisting of two 2-mm×4-mm slits spaced about 8.5 cm apart. The distance from the center of the scattering volume to the second slit, the counter slit, differed slightly at the various angles. All the data were normalized to a distance of 16.15 cm. Uncertainty in this distance contributed an estimated ±0.6 percent error to the final cross sections. The proton-proton

* Assisted by the joint program of the ONR and AEC.
† Now at Georgia School of Technology, Atlanta, Georgia.
[1] Freier, Lampi, Sleator, and Williams, Phys. Rev. **75**, 1345 (1949); N. P. Heydenburg and N. F. Ramsey, Phys. Rev. **60**, 42 (1941).
[2] The 0.5-mil and 0.25-mil polyethylene used in this work was kindly furnished by the Du Pont Company.

calibration procedure did not eliminate this one geometrical source of error, because some of the angles studied in the proton-alpha work could not be studied in the proton-proton work. The calibration procedure eliminated only those errors which remained constant at the various scattering angles, e.g., the slit sizes and distance between slits.

The slit system provided an angular resolution of about $\pm 1° 40'$ at all the angles studied (i.e., $\theta''-\theta=\theta$, $-\theta'=1° 40'$, where θ'', θ, and θ' are indicated in Fig. 1).

The scattered particles were detected by a proportional counter having an inside diameter of 1.50 inches, an inside length of five inches, and a center conductor of 10-mil tungsten wire. A potential difference of 1080 volts was used, corresponding to a filling of 19 cm of Hg of argon and one cm of Hg of carbon dioxide. The counter window was of 0.25-mil polyethylene.

The largest possible pulses are produced when the particle to be counted just stops in the counter. In order to secure this optimum pulse size, slowing foils appropriate to the type and angle of scattering under study were inserted at the counter slit. Securing the largest possible pulses from the counter served to minimize the background counts caused by stray neutrons in the cyclotron room. The neutron-induced counts were of all sizes, hence the use of a discriminator circuit with level set just low enough to include the desired pulses eliminated all small background pulses. Shielding of the counter by the use of borax and paraffin further reduced the background.

The slowing foils used to obtain optimum size pulses also served to eliminate all counts due to the recoil alpha-particles in the proton-alpha work. The thickness of the slowing foil used was, at the least, six times the range of the recoil alpha-particles.

The counter pulses were first amplified by an Atomic Instrument Company model 205-A preamplifier, next conducted through 150 feet of coaxial cable to the control room, and thereupon fed to an Atomic Instrument Company model 204-B amplifier and discriminator. The output pulses from the discriminator were counted by a Nuclear Instrument Company scaling circuit.

The scattering angle to be studied was selected by attaching the counter and associated slit system to any one of the five ports located in the walls of the gas chamber. These ports were accurately placed to within about 10′ of arc. The system could be pumped out within one hour after changing angle. It was not necessary to admit air to the counter during the change.

The pressure of the scattering gas was determined by a U-tube manometer filled with Apiezon oil B. One side of the manometer was always connected to the pumps. The error introduced by inaccurate readings of this manometer was estimated to be ± 0.3 percent. Gas pressures of about 2.2 cm of Hg were used in the work. One series of runs was taken with about half the normal

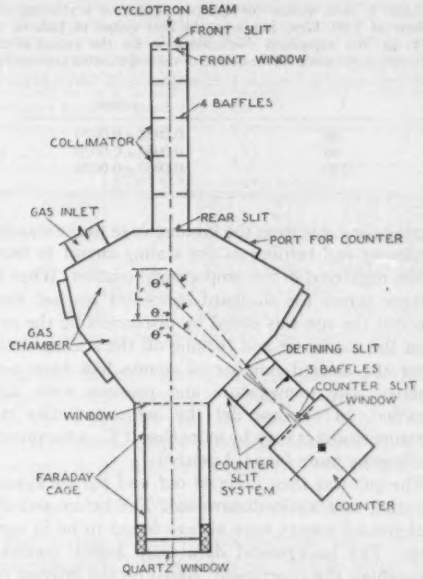

FIG. 1. Schematic diagram of the scattering apparatus (top view).

pressure. The data so obtained were consistent with those at the higher pressures usually used.

The temperature of the scattering gas was measured by a thermometer located some distance from the chamber. This thermometer was found to read within 0.5°C of another thermometer placed at the chamber. Making a liberal allowance for possible error due to poor ventilation with resultant fluctuations in the temperature, it is felt that a precision of ± 0.7 percent may safely be assigned to this measurement.

The calibration procedure used made it necessary to obtain only relative temperature and pressure measurements of high precision. It was necessary to know the absolute values only approximately.

All vacuum seals in the system were made by the use of O rings.

III. RUN PROCEDURE

The chamber was pumped out to a pressure of less than 4×10^{-5} mm of Hg. A background run was then made in which all conditions were identical to those in the scattering runs except that the chamber contained no gas. The background counts were determined at the pulse height discriminator settings that were expected to be correct for the scattering runs.

The chamber was then filled with hydrogen or helium of 99.5 percent purity, furnished in standard cylinders by the Ohio Chemical Company. The gas pressure and temperature were recorded.

The scattering data were then taken in a succession of runs. A run was commenced by simultaneously con-

TABLE I. Best values for the proton-proton scattering cross sections at 5.10 Mev, based on the best values of Jackson and Blatt for the expansion coefficients. θ Rs the center-of-mass scattering angle and σ Rs the center-of-mass scattering cross section.

θ	σ(barn)
60°	0.0955±0.0020
90°	0.0982±0.0020
120°	0.0955±0.0020

necting the cable from the faraday cage to the standard condenser and turning on the scaling circuit to record pulses registered in the proportional counter. When the voltage across the standard condenser reached about one volt the run was ended by disconnecting the cable from the condenser and turning off the scaling circuit. After the desired number of counts had been accumulated, the temperature and pressure were again recorded. In no case did the before-and-after temperature readings vary by more than 2°C, or the pressure readings by more than 0.3 percent.

The gas was then pumped out and the background counting rate again determined. The before-and-after background counts were always found to be in agreement. The background data were highly consistent throughout the experiment. Based on the internal consistency of the data and the number of background counts recorded, it is felt that the probable error in the background correction is not more than ±10 percent.

The scattering data were corrected for the background counts and then normalized to uniform conditions of temperature and pressure, to 1 volt on the standard condenser, to a distance of 16.15 cm from the scattering center to the counter slit, and multiplied by the sine of the scattering angle. This latter factor arises from the increase in length of the scattering region (see Fig. 1) as the scattering angle becomes smaller.

IV. CALIBRATION USING PROTON-PROTON SCATTERING

Jackson and Blatt[3] have given a thorough analysis of the low energy proton-proton scattering data. They give an expansion in terms of the incident proton energy (the expansion for K in their paper) from which the phase shift and thus the scattering cross sections may be determined. They also give the best experimentally determined values for the two arbitrary constants in the expansion for K. Four recent precision experiments[4] on proton-proton scattering have been treated according to the method of Jackson and Blatt and all found to be in excellent agreement with their best values, the probable errors in the experiments overlapping the values given by Jackson and Blatt. Further, no systematic trend away from the Jackson and Blatt values is indicated.

The best proton-proton scattering cross sections at 5.10 Mev have, accordingly, been determined from Jackson and Blatt's best values for the expansion coefficients. These best cross sections at the angles of interest are listed in Table I. The errors quoted are based on the limits of error assigned by Jackson and Blatt to the best values for the expansion coefficients. These error limits are consistent with the additional data mentioned above.

The observed counts are given by

$$N_n = G\sigma,$$

where N_n is the number of observed counts corrected for background and normalized to uniform conditions of temperature, pressure, voltage on the condenser, value of $\sin\theta = 1$, and distance from counter slit to scattering region of 16.15 cm; σ is the differential scattering cross section in the laboratory; and G is the apparatus factor involving various geometrical factors, the capacitance of the standard condenser, the temperature and pressure of the scattering gas, and certain physical constants.

Proton-proton scattering was studied at laboratory angles of 30°, 45°, and 60°. Over 30,000 counts were recorded. The average apparatus factor, the value used in all later calculations, was found to be 1043×10^{24} cm^{-2} (±2 percent). The probable error includes errors in the measurement of voltage, pressure, temperature, distance from counter slit to scattering volume, scattering angle, the statistical probable error in the number of counts observed, and the estimated probable error in the background correction. The ratio of real counts to background counts was 11:1 at 60°, 25:1 at 45°, and 29:1 at 30°.

G was also calculated on the basis of direct measurements of all the factors involved and found to be 1016×10^{24} cm^{-2} (±5 percent). This satisfactory agreement between the two independent determinations of G serves as a check on any gross errors in the experimental procedure.

V. RESULTS OF THE PROTON-ALPHA SCATTERING

The scattering of 5.10±0.10-Mev protons by alpha-particles was studied at five angles. The cyclotron beam was then slowed down to 4.80±0.10 Mev by interposing a 1-mil aluminum foil ahead of the collimator. Data were taken at an angle of 30° with this lower energy beam of protons.

The normalized and corrected proton-alpha data along with the differential scattering cross sections are listed in Table II. The probable errors quoted for N_n include errors in the measurement of pressure, temperature, voltage on the standard condenser, the distance from the counter slit to the scattering volume, the scattering angle, the statistical probable error in the observed counts, and the probable error in the back-

[3] Jackson and Blatt, Revs. Modern Phys. 22, 77 (1950).
[4] Bondelid, Ph.D. thesis, Washington University, 1950; Mather, Phys. Rev. 82, 133 (1951); Meagher, Phys. Rev. 78, 666 (1950). Meagher's results are listed by Jackson and Blatt, although excluded from their evaluation of the best values for the expansion coefficients; Zimmerman and Kruger, Phys. Rev. 83, 218 (1951).

ground correction. The probable errors quoted for the scattering cross sections include the error in N_a and the ± 2 percent probable error in the proton-proton scattering value for G. It should be noted that the G for proton-alpha scattering is one-half the G for proton-proton scattering, because helium is a monatomic gas while hydrogen is a diatomic gas.

VI. IMPURITY SCATTERING

Impurity scattering is not believed to affect the results of this work seriously. No evidence of the building up of impurities in the gas chamber was noted. Neither an increase in pressure with time nor a change in the observed counts with time were noticed. In the worst case, proton-proton scattering at 30°, a 1-percent contaminant of air would have produced only about a 1-percent error in the observed number of counts. Moreover, tests were conducted showing that particles scattered from a heavy impurity were counted with poor efficiency, the counts from a 5-percent impurity of argon not being distinguishable from the background. This discrimination against impurity counts is a property of the proportional counter used as the detector. The impurity-scattered particles have a higher energy than the particles scattered by helium or hydrogen. These higher energy particles produce smaller pulses in the counter than the real counts. The discriminator level that is correct for the desired counts, therefore, cuts out most of the impurity-scattering events.

The 0.5-percent impurity possible in the scattering gas according to the supplier's information can cause the pressure used to be incorrect. The quoted probable errors in N_a and the scattering cross sections include a ± 0.5-percent allowance for an error in the pressure due to the presence of impurities.

VII. ENERGY OF THE CYCLOTRON BEAM

The value of the energy of the cyclotron beam used in this work is based on several independent determinations.[8] Most of these determinations were based on the measurement of track lengths in photographic emulsions. It is thought that the quoted limits of error include all the seemingly reasonable measurements that have been brought to the attention of the author.

TABLE II. The results of the proton-alpha scattering work. θ is the scattering angle in the laboratory system, n is the number of counts observed, R is the ratio of the number of genuine counts to the number of background counts, N_a is the observed number of counts corrected for background and normalized to uniform conditions, and σ is the differential scattering cross section in the laboratory system expressed in barns.

θ	n	R	N_a	σ
		5.10±0.10-Mev protons incident		
30°	13,000	70	328.0 (±1.3%)	0.628 (±2.4%)
45°	7000	25	197.3 (±1.6%)	0.378 (±2.6%)
60°	3600	10	106.3 (±2.2%)	0.204 (±3.0%)
75°58′	2000	7	58.4 (±2.8%)	0.112 (±3.4%)
150°	1600	4	17.2 (±3.6%)	0.033 (±4.1%)
		4.80±0.10-Mev protons incident		
30°	11,000	15	333.2 (±1.5%)	0.638 (±2.5%)

VIII. ACKNOWLEDGMENTS

The author wishes to acknowledge the help and encouragement of Professor R. N. Varney. Suggestions of Professor A. L. Hughes, Professor F. B. Shull, and Professor J. Townsend have proved very helpful. The excellent machine work necessary for the satisfactory operation of the apparatus was performed by Mr. J. W. Boyle and Mr. O. W. Meyer under the direction of Mr. O. Retzloff. Mr. Retzloff also furnished valuable assistance in the design of many of the mechanical details of the apparatus. The author wishes to express his gratitude to Mr. A. A. Schulke, Mr. A. B. Phillips, and the other members of the cyclotron staff for their fine cooperation throughout the work. Mr. S. M. Carter and Mr. A. G. Ford assisted in the testing of the apparatus and in the taking of much of the data.

[8] Mather, see reference 4; Bondelid, Ph.D. thesis, Washington University, 1950; Shull and Keller, private communication.

Multiple Scattering in a Semi-Infinite Medium*

JOHN W. WEYMOUTH†
Department of Physics, University of California, Berkeley, California
(Received July 17, 1951)

The Boltzmann equation for the multiple scattering of charged particles is solved for a semi-infinite medium by means of the Laplace transformation. The sources are isotropic and distributed throughout the medium, corresponding to a thick layer of electron emitting atoms. The solution is obtained as a series in spherical harmonics and is carried as far as the P_2 coefficient. In order to obtain a solution it is necessary to assume that the transport mean free path λ is not a function of energy. As a particular evaluation of the solution the flux on the surface is examined and modified to correct for the energy dependence of λ by comparing with the corresponding solution of the age diffusion equation. The resulting spectrum is compared with an experimental case of 301.3-kev photoelectrons produced in a thick thorium converter. Using the experimental spectrometer resolution of 1.5 percent the theoretical spectrum is integrated over the window curve and a shift of the peak from the edge of the primary spectrum of 4.3 kev is obtained. Considering the errors involved this compares favorably with the experimental peak shift of 3.5 kev for a converter thickness of 25 mg/cm².

I. INTRODUCTION

IN the study of multiple scattering of charged particles much has been done within the limits of the small angle approximation, that is, by exploiting the fact that the scattering is predominantly forward. However, little has been done to include the effect of the wide angle scattering in the transport process and it is precisely this effect that must be considered if any knowledge of backscattering is to be obtained.

Goudsmit and Saunderson[1] have developed the theory for the angular distribution without the small angle limitation but this does not include the spatial distribution. Snyder and Scott[2] studied the integro-differential Boltzmann equation but again the small angle approximation was made. Lewis[3] studied the Boltzmann equation in an infinite medium and obtained the Goudsmit and Saunderson angular distribution. In addition he developed a method for obtaining the moments of the spatial distribution.

The purpose of this paper is to study the solution of the Boltzmann equation in the presence of boundaries and thereby to gain some information on the backscattering. In particular, the multiple scattering in a semi-infinite medium is examined. The method, depending on an expansion in spherical harmonics, is not well suited for such situations as incident beams but converges rapidly for spherically symmetric sources. The main difficulty with the method is that the scattering cross section is not allowed to vary as a function of the velocity. Within this limitation the energy loss is treated by considering the energy as a function of the residual range of the particle.

The general method for solution of the Boltzmann equation in a semi-infinite medium is outlined in Section II. In Sections III and IV the problem is solved for a uniform distribution of spherically symmetric sources and the flux at the surface is calculated. In Section V an estimation is made of the correction due to the variation of the cross section with velocity. This corrected flux is applied in Section VI to an experimental example of the energy spectrum of a thick source of electron emitters.

II. GENERAL METHOD

A. Transport Equation

We consider the distribution function $f(x, s, \mathbf{v})$ in the semi-infinite medium, where x is the perpendicular distance in from the surface, s the distance the particle has traveled, and $\mathbf{v}$ a unit vector designating the direction of motion. This function satisfies the transport equation

$$\partial f/\partial s+u\partial f/\partial x=N\int[f(x, s, \mathbf{v}')-f(x, s, \mathbf{v})]\sigma(\mathbf{v}\cdot\mathbf{v}')d\mathbf{v}', \quad (1)$$

where N is the number of scattering centers per unit volume, $u=\cos\theta$ relative to the x axis, and $\sigma(\mathbf{v})$ is the differential scattering cross section. The source is treated as an "initial" condition.

The procedure followed to solve the transport equation is to expand $f(x, s, \mathbf{v})$ in Legendre polynomials and to solve the resulting system of equations by means of the Laplace transformation. Since the angular dependence of f is only through $\cos\theta$ we can let

$$f(x, s, \mathbf{v})=\sum_l(2l+1)f_l(x, s)P_l(u).$$

Putting this into (1) and operating with $\int_{-1}^{+1}P_{l'}du$ we get

$$2\frac{\partial f_{l'}}{\partial s}+\sum_l(2l+1)\frac{\partial f_l}{\partial x}\int_{-1}^{1}P_{l'}uP_l du=N\sum_l(2l+1)f_l\int_{-1}^{1}\int P_{l'}(u)\times[P_l(u')-P_l(u)]\sigma(\mathbf{v}\cdot\mathbf{v}')d\mathbf{v}'du.$$

* Submitted in partial fulfillment of the requirements for the degree of Doctor of Philosophy at the University of California.
† Now at the Physics Department, University of San Francisco, San Francisco, California.
[1] S. Goudsmit and J. L. Saunderson, Phys. Rev. **57**, 24 (1940). and **58**, 36 (1940).
[2] H. Snyder and W. T. Scott, Phys. Rev. **76**, 220 (1949).
[3] H. W. Lewis, Phys. Rev. **78**, 526 (1950).

Using the recurrence relation for $uP_{l'}$ in the second term we obtain, for this term

$$(2l+1)\int_{-1}^{1} P_{l'}uP_l du = 2\left\{\frac{l'+1}{2l'+1}\delta_{l,l'+1}+\frac{l'}{2l'+1}\delta_{l,l'-1}\right\}.$$

For the right-hand side expand the cross section

$$\sigma(u)=\sum_n (2n+1)c_n P_n(u),$$

with

$$c_n=\tfrac{1}{2}\int_{-1}^{1} P_n\sigma du,$$

so this term becomes, using the addition theorem for $P_n(u)$,

$$2\pi N\sum_l\sum_n (2l+1)(2n+1)f_l c_n \int_{-1}^{1}\int_{-1}^{1} P_{l'}(u) \times[P_l(u')-P_l(u)]P_n(u)P_n(u')du\,du' = 8\pi N f_{l'}(c_{l'}-c_0).$$

If we define

$$\kappa_l(s)=2\pi N\int_{-1}^{1}\sigma(u)[1-P_l(u)]du,$$

then Eq. (1) becomes

$$(2l+1)\left(\frac{\partial}{\partial s}+\kappa_l(s)\right)f_l(x,s) + \frac{\partial}{\partial x}[(l+1)f_{l+1}(x,s)+lf_{l-1}(x,s)]=0. \quad (2)$$

In this problem the explicit form of the κ_l is determined by the fact that we use the scattering cross section for the screened coulomb potential $V=(Ze/r)e^{-r/a}$, that is

$$\sigma(u)=C/(1-u+2\psi)^2, \quad (3)$$

where $C=(Z^2e^4)/(m^2v^4)$ and $\psi=\hbar^2/(2amv)^2$, v being the velocity of the scattered particle. For the cases we consider here ψ is small, so for moderate values of l we have[4]

$$l=0, \quad \kappa_l\equiv 0$$

$$l\neq 0, \quad \kappa_l\approx \pi NCl(l+1)\left[\ln\frac{1}{\psi}+1-2\sum_{m=1}^{l}\frac{1}{m}\right]. \quad (4)$$

We will first assume that σ is not a function of energy, then later study the modification due to energy dependence.

[4] See reference 3, p. 528.

B. Solution by Laplace Transformation

To solve the system of differential Eq. (2) we make the Laplace transformations

$$h_l(y,t)=\int_0^\infty\int_0^\infty f_l(x,s)e^{-sy}e^{-st}dxds.$$

Thus integrating (2) over x and s we get the system of equations (κ_l are now constants)

$$(2l+1)(t+\kappa_l)h_l(y,t)+y[(l+1)h_{l+1}(y,t)+lh_{l-1}(y,t)] = (l+1)\eta_{l+1}(t)+l\eta_{l-1}(t)+(2l+1)\gamma_l(y), \quad (5)$$

where the transform of the distribution function at the boundary and at the "initial time" are given by

$$\eta_l(t)=\int_0^\infty f_l(0,s)e^{-st}ds, \quad \gamma_l(y)=\int_0^\infty f_l(x,0)e^{-sx}dx. \quad (6)$$

The method of solution of the system (5) was suggested by a procedure applied to neutron diffusion[5] as well as a similar treatment of Chandrasekhar[6] on solar radiation. To simplify the equations we take s and x in units of the transport mean free path $1/\kappa_1$. Utilizing the relation (4) for the κ_l we make the approximation

$$\kappa_l/\kappa_1\approx\tfrac{1}{2}l(l+1).$$

Then Eq. (5) becomes

$$lyh_{l-1}(y,t)+\alpha_l(t)h_l(y,t)+(l+1)yh_{l+1}(y,t) = (l+1)\eta_{l+1}(t)+l\eta_{l-1}(t)+(2l+1)\gamma_l(y), \quad (7)$$

where $\alpha_l(t)=(2l+1)[t+\frac{1}{2}l(l+1)]$. The approximation used is to assume that the expansion in Legendre polynominals converges rapidly enough so that the series may be cut off after the nth polynomial (this is called the P_n approximation). For the problem worked out here this assumption seems to be quite good, as will be seen below.

The determinant of the system (7) in the P_n approximation is:

$$D=\begin{vmatrix} \alpha_0 & y & 0 & 0 & \cdots & 0 \\ y & \alpha_1 & 2y & 0 & \cdots & 0 \\ 0 & 2y & \alpha_2 & 3y & \cdots & 0 \\ 0 & 0 & 3y & \alpha_3 & \cdots & 0 \\ \cdot & \cdot & \cdot & \cdot & & \cdot \\ \cdot & \cdot & \cdot & \cdot & & \cdot \\ \cdot & \cdot & \cdot & \cdot & & \cdot \\ 0 & 0 & 0 & 0 & \cdots & \alpha_n \end{vmatrix}$$

If we define D_l as the determinant D with the lth column replaced by the inhomogeneous terms in (7), then

$$h_l(y,t)=D_l(y,t)/D(y,t).$$

We will first consider the inverse transformation in the variable y. If $I_l(x,t)$ is the function obtained in this

[5] See R. E. Marshak, Revs. Modern Phys. 19, 222 (1947).
[6] S. Chandrasekhar, Astrophys. J. 99, 180 (1944).

transformation, then

$$I_l(x, t)=(1/2\pi i)\int_C h_l(y, t)e^{xy}dy, \tag{8}$$

where C is the usual Laplace contour [parallel to the imaginary axis and to the right of the singularities of $h_l(y)$]. This integration is easily carried out since $h_l(y)$ contains only simple poles. The only poles that might occur in the numerator $D_l(y)$ are due to the functions $\gamma_l(y)$ in the inhomogeneous terms. If the x dependence of the source is restricted to $\delta(x)$ or to a constant (i.e., surface or thick sources) then the $\gamma_l(y)$ will have at most a simple pole at $y=0$. Such terms can be separated out by breaking up the inhomogeneous terms in the following manner. Let

$$c_l(y, t)\equiv(l+1)\eta_{l+1}(t)+l\eta_{l-1}(t)+(2l+1)\gamma_l(y)$$
$$=\psi_l(t)+b_l/y. \tag{9}$$

Then D_l can be broken up also, $D_l=D_l^{\phi}+D_l^{b}$, where only D_l^{b} contains any poles that are in D_l. The only term in D_l^{b} for which b_l/y has no factor y, and therefore the only term retaining the pole, is the diagonal product

$$\alpha_0\alpha_1\cdots\alpha_{l-1}(b_l/y)\alpha_{l+1}\cdots\alpha_n.$$

Since $D(0)=\alpha_0\alpha_1\cdots\alpha_n$, the residue of this term in h_l contributes b_l/α_l to the integral. The remaining contributions come from the roots y_i of $D(y)$. Therefore we can write

$$I_l(x, t)=\sum_i\left\{\frac{D_l(y_i)e^{xy_i}}{[D(y)/(y-y_i)]_{y=y_i}}\right\}+\frac{b_l}{\alpha_l}.$$

Since $D(y)$ can be written in the form

$$D(y)=a-by^2+cy^4-\cdots(-)^{k/2}dy^k, \quad k=n+1 \text{ if } n \text{ odd}$$
$$=n \text{ if } n \text{ even},$$

the roots of $D(y)$ occur in pairs $y_i=\pm y_r$. Therefore we can write

$$D(y)=a\prod_{r=1}^{k/2}\left(1-\frac{y^2}{y_r^2}\right), \quad a=\alpha_0\alpha_1\cdots\alpha_n.$$

The denominator then becomes

$$\left[\frac{D(y)}{y-y_i}\right]=\pm\frac{2a}{y_r}\prod_{s\neq r}\left(1-\frac{y_r^2}{y_s^2}\right),$$

with the $(+)$ sign if $y_i=-y_r$ and the $(-)$ sign if $y_i=+y_r$. Therefore the y integration gives

$$I_l(x, t)=\sum_{r=1}^{k/2}\frac{y_r}{2a\prod_{s\neq r}\left(1-\frac{y_r^2}{y_s^2}\right)}$$
$$\times\{-D_l(+y_r)e^{xy_r}+D_l(-y_r)e^{-xy_r}\}+\frac{b_l}{\alpha_l}. \tag{10}$$

The final inverse transformation then yields the solution

$$f_l(x, s)=(1/2\pi i)\int_C I_l(x, t)e^{st}dt. \tag{11}$$

C. Boundary Conditions

In order to perform the integration in Eq. (11) it is necessary to determine the $\eta_l(t)$. This is done by imposing boundary conditions at $x=0$ and $x\to\infty$. The conditions used are

$$f(x, s, u)=0, \quad \begin{cases}x=0\\ u>0\end{cases} \quad (\text{all } s), \tag{12}$$

$f(x, s, u)$ bounded as $x\to\infty$.

From the first condition it follows that

$$\int_0^1 P_l(u)f(x=0, s, u)du=0, \quad \text{all } l. \tag{13}$$

In the P_n approximation this condition is applied to all l up to some value $m<n$ determined by restrictions discussed below. This is equivalent to saying each moment of u up to u^m vanishes for $u>0$. Since $f=\sum_k(2k+1)f_kP_k$ this condition becomes,

$$\text{at} \quad x=0, \quad f_l+\sum_{k\neq l}f_k(2k+1)\int_0^1 P_lP_k du=0,$$
$$l=0, 1, \cdots, m. \tag{14}$$

Performing the Laplace transformation in s (Eq. (6)) this condition becomes

$$\eta_l(t)+\sum_{k\neq l}\eta_k(t)(2k+1)\int_0^1 P_lP_k du=0. \tag{15}$$

These conditions give $m+1$ linear relations among the η_l. The number of these relations that can be used are restricted by (1) the conditions imposed at infinity and (2) an additional condition that exists among the η_l when the number of differential equations used is odd (n even).

(1) *Restrictions Imposed at Infinity*

We will now show that the conditions at infinity give as many relations among the η_l as there are pairs of roots of $D(y)$. The condition at infinity requires that $f_l(x, s)$ be bounded. Therefore the transform of f_l in x, $I_l(y, t)$, must be bounded. Looking at Eq. (10) we see that this means

$$D_l(+y_r)=0, \quad l=0, 1, \cdots, n;$$
$$r=1, \cdots, \tfrac{1}{2}(n+1) \quad \text{for } n \text{ odd} \tag{16}$$
$$=1, \cdots, \tfrac{1}{2}n \quad \text{for } n \text{ even}.$$

Each equation in (16) gives a relation among the η_l, but we must determine how many are independent.

For a given root y_r consider the equation $D_l=0$ as a set of $n+1$ homogeneous equations in the terms c_l as defined in (9). For instance, the first equation of this set is:

$$D_0=\begin{vmatrix} c_0 & y_r & 0 & \cdots & 0 \\ c_1 & \alpha_1 & 2y_r & \cdots & 0 \\ c_2 & 2y_r & \alpha_2 & \cdots & 0 \\ \cdot & \cdot & \cdot & & \cdot \\ \cdot & \cdot & \cdot & & \cdot \\ \cdot & \cdot & \cdot & & \cdot \\ c_n & 0 & 0 & \cdots & \alpha_n \end{vmatrix}=0. \tag{17}$$

It can be seen that the coefficient of c_l in this equation is the cofactor of the corresponding term in $D(y_r)$. Since interchanging the rows and columns of D leaves it unchanged, we see that the determinant of the coefficients of the c_l, which we will call $\Delta(y_r)$, is formed by replacing each element of $D(y_r)$ by its cofactor; that is Δ is the adjoint of D, or $\Delta=D'$. Now if M is a minor of D of dimensions m and M' the corresponding minor of D', then[7]

$$M'=(D)^{m-1}\times(\text{algebraic complement of } M).$$

Since $D(y_r)=0$ then any minor, M', equals zero unless $m=1$. Therefore the rank of Δ is one. Thus there is one independent relation among the c_l. The same argument holds for all the roots y_r. Therefore there are as many relations among the c_l, and consequently among the η_l, as there are pairs of roots[8] y_r. In the P_n approximation this number is $\frac{1}{2}(n+1)$ if n is odd and $\frac{1}{2}n$ if n is even.

(2) *Restriction Imposed for n Even*

In the P_n approximation the first and the last differential equation of the set each contain only one x derivitive. Thus when the number of equations used is odd (n even) the last equation can be combined with all the preceding equations for which l is even so as to eliminate all the x derivatives in the sub-set. This means that in the x, l space there exists one algebraic relation among the $I_l(x, l)$ where l is even. At $x=0$ this gives one relation among the η_l. This can be seen in the P_2 approximation carried out below.

From this and the discussion above it follows that the number of relations (15) that must be used is $(n+1)-\frac{1}{2}(n+1)=\frac{1}{2}(n+1)$ if n is odd and $(n+1)-\frac{1}{2}n-1=\frac{1}{2}n$ if n is even.

III. P_1 APPROXIMATION

A. Solution of Equations

We now proceed to study a specific problem in the P_1 approximation. This is to find the distribution function for a thick layer of beta-emitting sources. We therefore treat this as a semi-infinite medium with the initial condition

$$\begin{aligned} f(x, s, u)&=0, \quad x<0 \\ &=A, \quad x>0 \end{aligned} \quad \text{at} \quad s=0. \tag{18}$$

This represents a spherically symmetric emission of A electrons per unit volume, per unit solid angle throughout the medium.

The system (2), in this approximation, becomes

$$\begin{aligned} \partial f_0/\partial s+\partial f_1/\partial x&=0, \\ 3(\partial/\partial s+1)f_1+\partial f_0/\partial x&=0. \end{aligned} \tag{19}$$

From Eq. (6) the initial condition (18) becomes

$$\gamma_l=(A/y)\delta_{l0}. \tag{20}$$

Therefore the transformed system (7) is

$$lh_0+yh_1=\eta_1+A/y, \quad yh_0+\alpha_1h_1=\eta_0, \tag{21}$$

where $\alpha_1=3(l+1)$. The determinant

$$D(y)=l\alpha_1-y^2 \tag{22}$$

has roots $y=\pm y_1$ where

$$y_1=(l\alpha_1)^{\frac{1}{2}}. \tag{23}$$

From Eq. (10) and the condition at $x\to\infty$ (Eq. 16) the transforms in s are

$$\begin{aligned} I_0(x, l)&=\frac{1}{2y_1}\left(\alpha_1\eta_1-\frac{\alpha_1A}{y_1}+y_1\eta_0\right)e^{-xy_1}+\frac{A}{l}, \\ I_1(x, l)&=\frac{1}{2y_1}(l\eta_0+y_1\eta_1-A)e^{-xy_1}. \end{aligned} \tag{24}$$

From the previous discussion it is apparent that only one of the conditions (15) between the η_l can be used. The one chosen is for $l=1$, that is

$$\eta_1+\tfrac{1}{2}\eta_0=0.$$

This is the relation resulting from the condition that the net incoming current vanishes. Using this relation to eliminate η_1 and using relation (16) for $x\to\infty$, we get

$$D_0(y_1)\equiv\alpha_1(A/y_1-\tfrac{1}{2}\eta_0)-\eta_0y_1=0.$$

Then

$$\eta_0=-2\eta_1=2A/(2l+y_1).$$

Substituting these into (24), the solutions become

$$\begin{aligned} f_0(x, s)&=A-\frac{A}{2\pi i}\int_C\left[\frac{3(l+1)}{l}\right]^{\frac{1}{2}}\frac{e^{-xy_1+sl}}{2l+[3l(l+1)]^{\frac{1}{2}}}dl, \\ f_1(x, s)&=\frac{-A}{2\pi i}\int_C\frac{e^{-xy_1+sl}}{2l+[3l(l+1)]^{\frac{1}{2}}}dl. \end{aligned} \tag{25}$$

It will be noticed that the solutions give a more general initial situation than was imposed. That is, since $y_1\to l\sqrt{3}$ for large l, the contours must be closed to the right if $\sqrt{3}x>s$ and the integrals contribute nothing.

[7] M. Bôcher, *Introduction to Higher Algebra* (Macmillan Company, New York, 1947), p. 31.

[8] Assuming that there are no accidental relations $y_r=y_{r'}$.

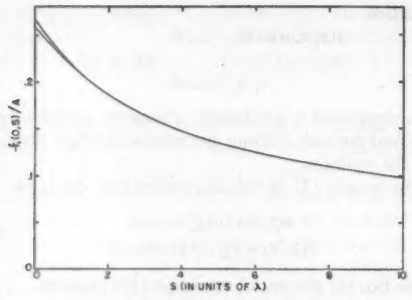

FIG. 1. Theoretical electron flux $f_1(0, s)$ at surface of semi-infinite medium in P_1 and P_2 approximations. The P_2 approximation gives the lower curve for small values of s.

Thus the initial condition is for $s<\sqrt{3}x$ rather than just for $s=0$. This is what should be expected since the initial distribution is unaffected until s is large enough for the particle to reach the surface. The same condition holds in the P_2 approximation as will be seen below. However, in higher approximations, there will be a series of such integrals each arising from an additional root y_r and each contributing when s is greater than some value of x determined by the value of y_r for large t.

B. Current at the Boundary

For a specific evaluation of these solutions we consider the net flux at the boundary, that is

$$f_1(0, s)=-\frac{A}{2\pi i}\int_C \frac{e^{st}dt}{2t_+[3t(t+1)]^{\frac{1}{2}}}. \tag{26}$$

A cut is placed between the branch points $t=0$ and $t=-1$, and the contour is closed to the left about these points. The integrand may be rationalized and written as follows

$$f_1(0, s)=-\frac{A}{2\pi i}\int_C \frac{2t-[3t(t+1)]^{\frac{1}{2}}}{t(t-3)}e^{st}dt.$$

Since $t=3$ is a root of the numerator it is not a pole and thus the first term contributes nothing. The second term can be written as two integrals along the cut and combined to give (for convenience we replace t by $-t$)

$$f_1(0, s)=-\frac{A}{\pi}\int_0^1 \left[\frac{3(1-t)}{t}\right]^{\frac{1}{2}}\frac{e^{-st}}{(t+3)}dt. \tag{27}$$

This is evaluated in the appendix and plotted in Fig. 1.

IV. P_2 APPROXIMATION

A. Solution of Equations

We now carry the same problem to the next approximation. The system (2) of equations is now

$$\begin{aligned}&\partial f_0/\partial s+\partial f_1/\partial x=0,\\ &3(\partial/\partial s+1)f_1+\partial f_0/\partial x+2\partial f_2/\partial x=0,\\ &5(\partial/\partial s+3)f_2+2\partial f_1/\partial x=0,\end{aligned} \tag{28}$$

The transformed system, with the same initial conditions as above, is

$$\begin{aligned}th_0+yh_1&=\eta_1+A/y,\\ yh_0+\alpha_1h_1+2yh_2&=\eta_0+2\eta_2,\\ 2yh_1+\alpha_2h_2&=2\eta_2.\end{aligned} \tag{29}$$

The roots $y=\pm y_1$ of the determinant of this system are

$$y_1=[t\alpha_1\alpha_2/(4t+\alpha_2)]^{\frac{1}{2}}. \tag{30}$$

The transforms in s are (using conditions (16))

$$\begin{aligned}I_0(x, t)&=\tfrac{1}{2}\left[\frac{\alpha_2(\eta_0-A/t+2\eta_2)}{4t+\alpha_2}+\frac{y_1\eta_1}{t}\right]e^{-xy_1}+\frac{A}{t},\\ I_1(x, t)&=\tfrac{1}{2}\left[\eta_1+\frac{\alpha_2t(\eta_0-A/t+2\eta_2)}{y_1(4t+\alpha_2)}\right]e^{-xy_1},\\ I_2(x, t)&=\left[\frac{t(\eta_0-A/t+2\eta_2)}{4t+\alpha_2}+\frac{\eta_1y_1}{\alpha_2}\right]e^{-xy_1}.\end{aligned} \tag{31}$$

For the relations among the η_i there is first the relation (16) due to the condition at $x\to\infty$. This is

$$(4t+\alpha_2)y_1\eta_1-\alpha_2t(\eta_0-A/t+2\eta_2)=0.$$

The relation due to the use of an odd number of equations as discussed above can be seen by considering the first and third of the Eqs. (28) in the x, t space:

$$tI_0+\partial I_1/\partial x=A,\quad \alpha_2I_2+2\partial I_1/\partial x=0.$$

Therefore at $x=0$, we have

$$2t\eta_0-\alpha_2\eta_2=2A.$$

The third relation to be used is one of the conditions (15) and as before the condition for $l=1$ is chosen. This is

$$4\eta_0+8\eta_1+5\eta_2=0.$$

Solving for the η_i from these three equations gives

$$\begin{aligned}\eta_0(t)&=A(4\alpha_2+5y_1)/W,\\ \eta_1(t)&=-2A\alpha_2/W,\\ \eta_2(t)&=-4Ay_1/W,\end{aligned}$$

where $W=2\alpha_2y_1+t(4\alpha_2+5y_1)$. Putting these into (31) gives

$$\begin{aligned}f_0(x, s)&=A-\frac{2A}{2\pi i}\int_C\frac{\alpha_2y_1e^{-xy_1+st}}{tW}dt,\\ f_1(x, s)&=-\frac{2A}{2\pi i}\int_C\frac{\alpha_2e^{-xy_1+st}}{W}dt,\\ f_2(x, s)&=-\frac{4A}{2\pi i}\int_C\frac{y_1e^{-xy_1+st}}{W}dt.\end{aligned} \tag{32}$$

B. Current at the Boundary

As before we evaluate this solution for a special case, that is the flux at the boundary

$$f_1(0,s)=-\frac{2A}{2\pi i}\int_C \frac{\alpha_2 e^{st}dt}{2\alpha_2 y_1+t(4\alpha_2+5y_1)}. \quad (33)$$

For large s the integral can be evaluated for $t\to 0$. This gives

$$f_1(0,s)\approx -\frac{A}{2\pi i}\int_C \frac{e^{st}}{(3t)^{\frac{1}{2}}}dt=-\frac{A}{(3\pi s)^{\frac{1}{2}}},$$

which is the same result that is obtained in the P_1 approximation [see (26) or compare with the leading term in (A1)].

For small s the integral is treated as follows. The integrand is rationalized [using y_1 given by (30)] giving

$$\frac{(4t+\alpha_2)^{\frac{1}{2}}[(t\alpha_1\alpha_2)^{\frac{1}{2}}(2\alpha_2+5t)-4\alpha_2 t(4t+\alpha_2)^{\frac{1}{2}}]e^{st}}{t[\alpha_1(2\alpha_2+5t)^2-16\alpha_2 t(4t+\alpha_2)]}.$$

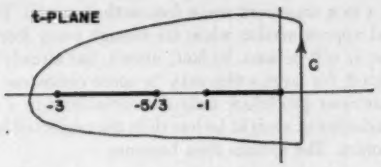

FIG. 2. Contour in t-plane for P_2 approximation.

The denominator can be rewritten, expanding the α_i and collecting terms in t, to give

$$15t(-3t^2+t^2+120t+180).$$

The roots of this polynomial are

$$t_1=-1.6305,\quad t_2=-5.1633,\quad t_3=7.1271. \quad (34)$$

All of these as well as $t=0$ are roots of the numerator, therefore there are no poles. Expanding the numerator, we get

$$f_1(0,s)=\frac{1}{2\pi i}\left(\frac{2A}{15}\right)\int_C \frac{15(t+2)[45t(t+1)(t+3)(3t+5)]^{\frac{1}{2}}-60t(t+3)(3t+5)}{t(t-t_1)(t-t_2)(t-t_3)}e^{st}dt,$$

with the contour as shown in Fig. 2. The second term contributes nothing so we can write

$$f_1(0,s)=\frac{2A(15)^{\frac{1}{2}}}{2\pi i}\int_C \times\frac{(t+2)[(t+1)(t+3)(t+5/3)]^{\frac{1}{2}}}{t^{\frac{1}{2}}(t-t_1)(t-t_2)(t-t_3)}e^{st}dt. \quad (35)$$

Integrating along the cuts gives

$$f_1(0,s)=\frac{2A(15)^{\frac{1}{2}}}{\pi}[P(s)+Q(s)], \quad (36)$$

where

$$P(s)=-i\int_0^{-1}\frac{(t+2)[(t+1)(t+3)(t+5/3)]^{\frac{1}{2}}}{t^{\frac{1}{2}}(t-t_1)(t-t_2)(t-t_3)}e^{st}dt,$$

$$Q(s)=-i\int_{-5/3}^{-3}\frac{(t+2)[(t+1)(t+3)(t+5/3)]^{\frac{1}{2}}}{t^{\frac{1}{2}}(t-t_1)(t-t_2)(t-t_3)}e^{st}dt.$$

These are evaluated in the appendix and plotted in Fig. 1.

Figure 1 illustrates the behaviour of the convergence of the polynomial expansion. For large s the main contribution in the t integral comes from the singularities near the origin and, as was seen above, this brings the higher approximation into agreement with the lower one. However for s small the singularities away from the origin contribute. These arise in the higher approximation because more terms α_l are involved in the roots of $D(\gamma)$. This is to be expected since the P_1 approximation gives the diffusion approximation (see next section) and therefore should give good results when s is sufficiently far from the source. The next approximation, involving the next spherical harmonic, is then the improvement on this and one should expect P_2 to deviate most from P_1 for small s, that is before the diffusion region is reached.

From an elementary calculation (see appendix) it can be shown that f_1 should approach the value $\frac{1}{4}A$ as s approaches zero. It can be seen from Fig. 1 that P_2 improves on P_1 in this respect deviating from the correct end point by only about 3 percent.

V. ENERGY DEPENDENCE

The s dependence of the distribution function can be related to the energy through the empirical range-energy relation and thus the energy dependence may be obtained. However our treatment of the Boltzmann equation did not include the energy dependence of the cross section and therefore of the variation in the mean free path. No satisfactory way was found to take account of this in the solution of the Boltzmann equation. However a rough estimate of this effect on the spectrum at the surface may be obtained by use of the age equation employed in neutron diffusion.[9] Solutions for this for constant and for variable cross section are compared with the previous solution and an estimate is then made of the necessary correction.

We now consider the cross section as a function of s. Starting with the system of Eqs. (19) of the P_1 approximation the additional approximation is made that $\partial f_1/\partial s$ is small (that is, that the fractional change of f_1

[9] See R. E. Marshak, Revs. Modern Phys. 19, 212 (1947).

along s in a transport mean free path is small). This is a good approximation when far enough away from the source, as will be seen. In fact, since f_2 has already been neglected, for large s this may be more consistent than the previous procedure near discontinuities in x since the variation in s might be less than the neglected higher harmonics. The system then becomes

$$\begin{aligned}\partial f_0/\partial s+\partial f_1/\partial x&=0,\\ 3\kappa_1(s)f_1+\partial f_0/\partial x&=0.\end{aligned}\tag{37}$$

Eliminating f_1 and defining the age variable

$$\tau(s)=\int_0^s ds/\kappa_1(s),$$

we get the age diffusion equation

$$\partial f_0/\partial\tau=\tfrac{1}{3}\partial^2 f_0/\partial x^2.\tag{38}$$

The boundary condition can be obtained by utilizing the relation existing between f_0 and f_1 in the P_1 approximation as a condition for no returning current, that is

$$f_0=-2f_1.$$

Combining with the second of (37) gives

$$\partial f_0/\partial x=-\tfrac{3}{2}\kappa_1(s)f_0,\quad\text{at}\quad x=0.\tag{39}$$

The initial condition is given by

$$f_0=A,\quad\text{at}\quad\tau=0.$$

To solve this problem with this boundary condition is difficult. However, since $\kappa_1(s)$ is slowly varying in s under certain conditions (e.g., large Z of the scatterer, not too large s) we make the approximation that in the boundary condition κ_1 is constant, that is $\kappa_1=\kappa_1(0)$. This then is the heat problem of a constant initial temperature and radiation at the surface into zero temperature.[10] The solution is

$$f_0=A\left\{\operatorname{erf}\left[x\left(\frac{3}{4\tau}\right)^{\frac{1}{2}}\right]+e^{\frac{1}{2}x+\frac{3}{4}\tau}\operatorname{erfc}\left[x\left(\frac{3}{4\tau}\right)^{\frac{1}{2}}+\left(\frac{3\tau}{4}\right)^{\frac{1}{2}}\right]\right\}.\tag{40}$$

The current at $x=0$ is given by

$$f_1=-\frac{1}{3\kappa_1(s)}\left(\frac{\partial f_0}{\partial x}\right)_{x=0}=-\frac{A}{2\kappa_1(s)}e^{\frac{3}{4}\tau(s)}\operatorname{erfc}(\tfrac{3}{4}\tau(s)).\tag{41}$$

VI. COMPARISON WITH EXPERIMENT

The experimental situation with which the above results could best be compared would be the energy spectrum of an internal conversion line produced in a thick layer of fairly heavy material and measured with an instrument of known resolving power. Such data were not found. We shall, therefore, compare results with the data of Hornyak, Lauritsen, and Rasmussen[11] on the photoelectron spectrum of the 411-kev gamma-radiation of Au^{198} converted in thorium (301.3-kev maximum electron energy).

To make the comparison for this case it is first necessary to estimate the energy-dependence correction to the derived spectrum as discussed in section V above. Then the corrected spectrum in s must be transformed to a function of energy. The resulting spectrum is then integrated with the known window curve of the spectrometer to get the spectrum as it appears experimentally.

A. Correction for Energy Dependence

We now evaluate $f_1(0, s)$ in Eq. (41). Over the range of s considered here the transport mean free path $1/\kappa_1(s)=\lambda(s)$ does not vary much in s so we can write

$$\lambda(s)=\lambda(0)\left[1+\frac{1}{\lambda(0)}\left(\frac{d\lambda}{dE}\frac{dE}{ds}\right)_{E=E_{\max}}s\right].\tag{42}$$

For $d\lambda/dE$ we use the relativistic form of (4)

$$\kappa_1=\frac{2\pi NZ^2e^4}{(mc^2)^2(\gamma-\gamma^{-1})^2}\left[\ln\frac{1}{\psi}-1\right],$$

where

$$\psi=h^2/[4a^2m^2c^2(\gamma^2-1)],\quad\gamma=(1-v^2/c^2)^{-\frac{1}{2}}.$$

For this case, the kinetic energy is 301.3 kev, $A=232$, and $Z=90$. Then $\lambda(0)=11.63$ mg/cm² and $d\lambda/dE=0.0602$ mg/cm² kev). For the factor dE/ds we will use the energy loss relation:

$$-\frac{dE}{dx}=\frac{2\pi NZe^4}{mc^2(\gamma-\gamma^{-1})}\times\left[\ln\frac{(mc^2)^2}{2I^2}+\ln(\gamma^2-1)(\gamma-1)-\left(\frac{2}{\gamma}-\frac{1}{\gamma^2}\right)\ln 2+\frac{1}{\gamma^2}\right].$$

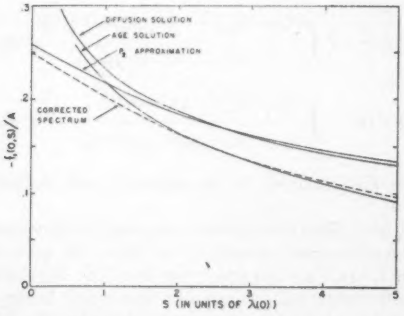

FIG. 3. Theoretical primary spectrum $f_1(0, s)$ corrected for energy dependence for case of 301.3-kev photoelectrons produced in thorium.

[10] See Carslaw and Jaeger, *Conduction of Heat in Solids*, (Oxford University Press, London, 1946), p. 51.

[11] Hornyak, Lauritsen, and Rasmussen, Phys. Rev. **76**, 731 (1949).

For the average ionization potential I/Z we will use the value of 9.6 ev determined for uranium by Segrè and Bakker.[12] This gives, at 301.3 kev

$$dE/dx = -1.145 \text{ kev}/(\text{mg}/\text{cm}^2). \quad (43)$$

Since s is measured in units of $\lambda(0)$, Eq. (42) becomes

$$\lambda(s)/\lambda(0) = 1 - 0.0688s. \quad (44)$$

Using this, the age solution (41) is calculated and plotted in Fig. 3. From this solution the correction to the P_2 solution is then extrapolated to the correct end point.

B. Integration over Window Curve

In order to obtain the resultant spectrum we integrate the primary spectrum over the window curve which we take to be gaussian. The resulting distribution is

$$N(E) = \int_0^{E_m} f(E_m - E') \times \exp[-(E'-E)^2/(aE')^2]dE', \quad (45)$$

where f is the primary spectrum with maximum energy E_m and a is determined by the resolution of the spectrometer. In this calculation we use for the resolution a width of 1.5 percent at half-maximum.[13] This gives $a = 9.0 \times 10^{-3}$.

To facilitate the integration we notice that the main contribution comes from the region $E' = E$ to $E' - E = aE'$ and since a is small, we have

$$(E'-E)/E \ll 1.$$

The denominator in the exponential can then be written

$$(aE')^{-2} = (aE)^{-2}[1 - 2(E'-E)/E].$$

Placing this into (45) and expanding the exponential due to the last term we get

$$N(E) = \int_0^{E_m} f(E_m - E) \exp[-(E'-E)^2/(aE)^2] \times [1 + 2(E'-E)^3/a^3E^3]dE'. \quad (46)$$

Over the range of integration a linear approximation for the primary spectrum can be used, so that

$$f(E_m - E) = f(E_m) - (df/dE)_{E_m}(E_m - E).$$

In terms of s we have

$$\frac{df}{dE} = \frac{df}{ds}\frac{ds}{dE} = \frac{1}{\lambda(0)}\frac{df}{ds}\frac{dx}{dE},$$

[12] E. Segrè and C. J. Bakker, Phys. Rev. 81, 489 (1951).
[13] Hornyak *et al.*, see reference 11, p. 732.

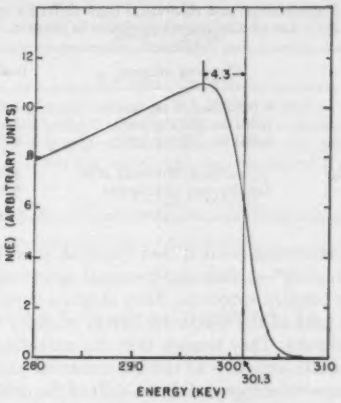

FIG. 4. Theoretical spectrum of 411-kev radiation from Au^{198} converted in thick Th foil (301.3-kev maximum energy of photoelectron). 1.5 percent resolution of spectrometer.

where df/ds is determined by the extrapolated curve in Fig. 3, and dE/dx is given by (43). Thus we can write (taking $df/ds = 0.0470$)

$$f(E_m - E) = A - B(E_m - E) \quad (47)$$

with $A = 0.250$ and $B = 0.00353$. Integrating (46) gives

$$N(E) = aE\{\tfrac{1}{2}(A - By)\pi^{\frac{1}{2}}[1 + \text{erf}(y/aE)] - a[(A - By)(1 + [y/aE]^2) + \tfrac{1}{2}EB]\exp[-(y/aE)^2]\}, \quad (48)$$

where $y = E_m - E$. This is plotted in Fig. 4.

C. Discussion of Results

Perhaps the most interesting result of the calculations in the previous section is the peak shift, that is the shift in the maximum of the spectrum from that of the primary spectrum. The above theoretical calculation gives a value of about 4.3 kev. Hornyak, *et al.* give, for a converter thickness of 0.0005 inch (16 mg/cm²), a value of 3.2 kev. For thicker converters their data indicates the results in Table I. The value for 0.001 inches is taken from a plotted spectrum in their article and has the most uncertainty. They also make a theoretical estimation of the upper limit, i.e., for an infinitely thick converter.

One of the largest sources of error in our calculations is the estimation for the energy dependence correction. An error in the slope df/ds of 10 percent results in an error in the peak shift of about 5 percent. Another source of difference is that the photoelectrons are not produced isotropically, although there will be some averaging out due to the angular distribution of the incident gamma-rays. With this in mind, we see that the peak shift comparison, although not conclusive, seems to give fairly good agreement.

TABLE I. Experimental and theoretical peak shifts for spectra of 301.3-kev photoelectrons produced in thorium.

	Converter thickness	Peak shift
Exp.	0.0005 in. (16 mg/cm²)	3.2 kev
	0.001 in. (25 mg/cm²)	3.5 kev
	0.003 in. (78 mg/cm²)	3.8 kev
Theor.	upper limit, Hornyak *et al.*	4.3 kev
	infinite, our calculation	4.3 kev

One interesting point is that Hornyak *et al.* perform an "unfolding" of their experimental spectrum to obtain the primary spectrum. They obtain a curve with a marked peak at the maximum energy in sharp contrast to our results. They remark that the unfolding operation is quite sensitive to the experimental position of the maximum energy and that a shift of the order of the probable error results in a much smoother curve—a curve which would be in much better agreement with our results.

One more remark can be made and that concerns the effect of a finite width source. It was noticed in the solutions in Secs. III and IV that, for a given depth x, the initial solution is undisturbed until $s=\sqrt{3}x$. (As was pointed out in Sec. III this is only true in the P_1 and P_2 approximations and is an oversimplification.) Therefore, for a finite thickness, the spectrum will be unaltered until $s=\sqrt{3}l$, where l is the width of the slab.[14] To estimate the value of l below which the peak will be changed from its limiting position, we note that the window curve has a half-width of about 4.5 kev. Adding this to the limiting peak shift, we get 8.8 kev. If the primary spectrum is altered below this value then the peak will be changed. This corresponds to a value of l of about 4.4 mg/cm². Hornyak, *et al.*, note that the peak position is changed most when going from a converter of 7 mg/cm² to one of 16 mg/cm² and thereafter the change is small. Thus our results give a value of the right order of magnitude.

ACKNOWLEDGMENTS

The author wishes to express his thanks to Professor H. W. Lewis for suggesting the problem and for guidance and discussion on the method. The author also wishes to thank Professor R. Serber for many fruitful discussions and further guidance.

TABLE II. Coordinates and weights for Gauss quadrature of the integral $\int_{-1}^{1}(1-x^2)^{-\frac{1}{2}}P(x)dx$ for $n=3$ and $m=5$.

$x_1=-0.8660$	$a_1=1.0472$
$x_2=0$	$a_2=1.0472$
$x_3=+0.8660$	$a_3=1.0472$

[14] The solution of the problem for a finite slab in the P_1 approximation can be obtained as a series containing the semi-infinite solution plus integrals that are nonvanishing when $s>\sqrt{3}l$, $s>2\sqrt{3}l$, $s>3\sqrt{3}l$, etc.

VII. APPENDIX

A. Evaluation of $f_1(0,s)$ in P_1 Approximation

From Eq. (27) we had

$$f_1(0,s)=-\frac{A}{\pi}\int_0^1\left[\frac{3(1-t)}{t}\right]\frac{e^{-st}}{(t+3)}dt.$$

For large s the main contribution comes from near $t=0$ so the coefficient of e^{-st} in the integrand can be expanded in powers of t and the integral evaluated term by term. This gives

$$f_1(0,s)=-\frac{A}{\pi\sqrt{3}}\left(\frac{1}{s^{\frac{1}{2}}}\gamma(\tfrac{1}{2},s)-\frac{5}{6}\frac{1}{s^{\frac{3}{2}}}\gamma(\tfrac{3}{2},s)+\frac{11}{72}\frac{1}{s^{5/2}}\gamma(5/2,s)\right), \quad \text{(A1)}$$

where $\gamma(n,s)$ is the incomplete gamma-function.

For small s the integrand is rewritten by the substitution $t=(1+u)/2$

$$f_1(0,s)=-\frac{A\sqrt{3}e^{-s/2}}{\pi}\int_{-1}^{1}\frac{(1-u)e^{-su/2}}{(1-u^2)^{\frac{1}{2}}(u+7)}du. \quad \text{(A2)}$$

The integral is written in this form in order to facilitate numerical integration by Gauss' method.[15]

We will briefly examine the Gauss method. For an integral of the form

$$\int_a^b P(x)w(x)dx \quad \text{(A3)}$$

where $w(x)$ is some known function and $P(x)$ is a polynomial of degree m in x, it is possible to construct a quadrature formula using n values of $P(x)$ at points x_i with weights a_i so that the integral is given exactly by

$$\int_a^b P(x)w(x)dx=\sum_{i=1}^{n}a_iP(x_i) \quad \text{(A4)}$$

with $n=\frac{1}{2}(m+1)$. For the integral (A2) it is convenient to take

$$w(u)=(1-u^2)^{-\frac{1}{2}}.$$

If the a_i and the x_i are determined for $n=3$, the error involved can be estimated by examining the expansion of $e^{-(su)/2}$ up to and including $(su)^5$.[5] The error at the extremes of the interval will be small if $s^6/6!<1$ or $s\sim 3$. Thus the error of the quadrature will be small for values of s somewhat over $s=3$. We therefore take $n=3$ and $m=5$. The points and weights determined for this case are given in Table II. Using these values the integral (A2) is evaluated and plotted in Fig. 1.

B. Evaluation of $f_1(0,s)$ in P_2 Approximation

For the evaluation of the integrals (36) we will use the same procedure as before for small s. For the integral $P(s)$ we make the transformation $t=(u-1)/2$. Then

$$P(s)=e^{-s/2}\int_{-1}^{1}\frac{(u+3)(u+1)[(u+5)(u+7/3)]^{\frac{1}{2}}e^{su/2}}{(1-u^2)^{\frac{1}{2}}(u-u_1)(u-u_2)(u-u_3)}du,$$

where $u_1=-2.2610$, $u_2=-9.3266$, $u_3=15.2542$. This method, with weights and divisions for a polynomial of fifth degree, still gives good results for this integral. The worst factor in the integrand, $(u+2.2610)^{-1}$, approximated by a polynomial of second degree only has an error of 8.5 percent at the end points $u=\pm 1$.

For the evaluation of $Q(s)$ let $t=(2v-7)/3$. Then

$$Q(s)=\frac{e^{-7s/3}}{\sqrt{2}}\int_{-1}^{1}\frac{(2v-1)(1-v^2)(2-v)^{\frac{1}{2}}e^{2vs/3}}{(1-v^2)^{\frac{1}{2}}(7-2v)^{\frac{1}{2}}(v-v_1)(v-v_2)(v-v_3)}dv,$$

where $v_1=1.0542$, $v_2=-4.2449$, $v_3=14.191$. To assume that the coefficient of $(1-v^2)^{-\frac{1}{2}}$ in this case approximates a fifth-order polynomial seems questionable because of the factor $(v-1.0542)^{-1}$ near the limits $v=\pm 1$. However, (a) the main contribution to the

[15] See S. Chandrasekhar, *Radiative Transfer* (Oxford University Press, London, 1950), p. 57.

integral comes from the central part of the interval because of the factor $(1-v^2)$, (b) the factor $e^{-(1+v)/s}$ rapidly reduces the contribution of Q to f_1 for larger s, and (c) even for $s=0$ the contribution of Q to f_1 is only about 4 percent. Therefore it seems justified to use this more convenient method in this case also. Integral (36) is plotted in Fig. 1.

C. End-Point Calculation

In this section we calculate the value of $f_1(s, x)$ at the boundary $x=0$ when $s\to 0$ by simply considering the distribution $f(s, x, u)$ before many collisions have occurred. The density and the current for a given distance s, integrated over unit volume, are given by

$$D=\int f(s, x, u)d\Omega=2\pi\int_{-1}^{1}fdu$$

$$J=\int uf d\Omega=2\pi\int_{-1}^{1}ufdu.$$

Since

$$f_1=\tfrac{1}{2}\int_{-1}^{1}P_1 f du$$

we have

$$D=4\pi f_0,\quad J=4\pi f_1.$$

The number of particles that go a distance s without a collision is given by the kernel $e^{-s}/(4\pi s^2)$. If we consider a distance s sufficiently small so that the initial, spherically symmetric distribution with density $D=4\pi A$ is undisturbed, then the current is given by

$$J=-\int\frac{e^{-s}}{4\pi s^2}4\pi A\cos\vartheta s^2 d\Omega$$

(negative since current is out). At $x=0$ this is

$$J=-2\pi A e^{-s}\int_0^1 u du=-\pi A e^{-s}.$$

In the limit as $s\to 0$, $J=-A\pi$ and therefore $f_1=-\frac{1}{4}A$.

PHYSICAL REVIEW VOLUME 84, NUMBER 4 NOVEMBER 15, 1951

Total Cross Section of Nitrogen for Fast Neutrons*

C. H. JOHNSON,† B. PETREE,‡ AND R. K. ADAIR
University of Wisconsin, Madison, Wisconsin

(Received July 30, 1951)

The total neutron cross section of nitrogen has been measured for neutron energies from 0.15 to 1.45 Mev. Resonances in the total cross section are observed at 0.433, 0.640, 1.00, 1.12, 1.35, and 1.45 Mev. The second, third, and last of these resonances correspond in energy to resonances observed in the disintegration of nitrogen. Application of the nuclear dispersion theory indicates that the resonances at 0.64 and 1.00 Mev are caused by neutrons of zero orbital angular momentum forming compound states of spin $\frac{1}{2}$ and $\frac{3}{2}$, respectively. An experiment is proposed which would, in conjunction with these measurements, determine the relative parity of C^{14} and N^{14}.

I. PROCEDURE AND RESULTS

FOR the interpretation of previously published results on the disintegration of nitrogen by fast neutrons,[1] a knowledge of the total neutron cross section of nitrogen is desirable. A preliminary measurement[2] of this cross section in which NaN_3 was used as the scattering material showed a resonance at 440 kev, the same energy at which a prominent resonance occurs in oxygen. It was, therefore, suspected that the NaN_3 might have contained some water. Furthermore, it was desirable to use nitrogen combined with elements having no resonances in the range of neutron energies considered.

In the present measurements aminotetrazole (N_5CH_3) was used. It had been purified by recrystallization, and the water of crystallization was driven off quantitatively by heating.[3] Sufficient carbon was added to give a mixture with the empirical formula $N_{10}(CH_2)_3$. The effect of the nitrogen was observed by comparing the neutron attenuation produced by the mixture with that of a polythene sample having the same number of carbon and hydrogen atoms as the mixture. The cross section of nitrogen was determined in a simple transmission experiment,[4] assuming exponential attenuation of the neutron flux by nitrogen. Corrections were applied for the background of neutrons scattered from the walls and the floor and for scattering by nitrogen into the detector.

In the lower portion of Fig. 1 the observed total cross section of nitrogen is shown as a function of neutron energy. Points were taken at intervals less than the neutron energy spread except in the energy range from 0.7 to 0.9 Mev where the NaN_3 data had shown no resonances. Cross sections given in Fig. 1 agree with those previously obtained using NaN_3. The results also agree with the observations of Frisch[5] for neutron energies below 0.4 Mev, but not for neutron energies from 0.5 to 0.8 Mev.

In the upper part of Fig. 1 is plotted the sum of the $N(n, p)$ and $N(n, \alpha)$ cross sections previously reported.[1]

* Work supported by the AEC and the Wisconsin Alumni Research Foundation.

† Now at Oak Ridge National Laboratory.

‡ Now at National Bureau of Standards.

[1] C. H. Johnson and H. H. Barschall, Phys. Rev. **80**, 818 (1950).

[2] Bockelman, Adair, Barschall, and Sala, Phys. Rev. **75**, 336 (1949).

[3] Johannes Thiele, Ann. Chem. **270**, 54 (1892).

[4] Adair, Barschall, Bockelman, and Sala, Phys. Rev. **75**, 1124 (1949).

[5] R. K. Adair, Revs. Modern Phys. **22**, 249 (1950).

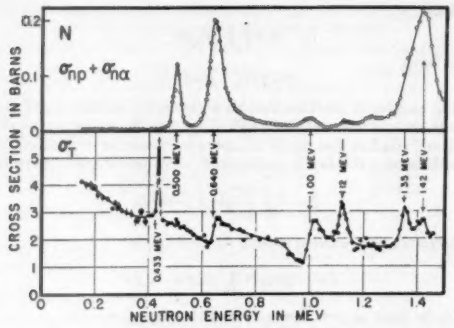

FIG. 1. Neutron cross sections of nitrogen as a function of neutron energy. The upper curve shows the sum of the (n, p) and (n, α) cross sections. The lower curve represents the total cross section.

Resonant energies are shown with arrows indicating that the resonances were observed in one or both curves. These energies have an uncertainty of less than 10 kev for neutron energies below 1 Mev and less than 20 kev for higher energies.

II. DISCUSSION

S-Levels

Of the several total cross-section resonances shown in Fig. 1, only those at 0.64 and 1.00 Mev are sufficiently broad relative to the neutron energy spread, and sufficiently isolated from other levels that their magnitude gives definite information on the spin of the compound state involved. In addition, these resonances exhibit pronounced minima which, at these neutron energies, can only be interpreted in terms of interference between resonance and potential scattering for neutrons of zero orbital angular momentum. Since the spin of nitrogen is 1, s-neutrons may form compound states of spin $\frac{1}{2}$ or $\frac{3}{2}$. In the following discussion, the Breit-Wigner theory as presented by Feshbach *et al.*,[6] and Wigner and Eisenbud[7] is applied to describe the 0.64- and 1.00-Mev resonances as resulting from neutrons of zero orbital angular momentum forming states of spin $\frac{1}{2}$ and $\frac{3}{2}$, respectively.

Assuming that inelastic scattering and radiative capture of neutrons may be neglected,[1] the total cross section is the sum of the cross sections for the (n, p) and (n, α) reactions and for elastic scattering. At an energy E near an isolated s-resonance at energy E_r, the elastic scattering cross section consists of a small background of scattering for neutrons of angular momentum $l>0$ and the s-neutron contribution, which may be written:

$$\sigma_0=4\pi k^{-2}\left\{g_J\left|\frac{\frac{1}{2}\Gamma_n}{E-E_r+\frac{1}{2}i\Gamma}-e^{-ikR}\sin\delta_0\right|^2+(1-g_J)\sin^2\delta_0\right\}. \quad (1)$$

In this expression Γ_n and Γ are the neutron width and total width, k is the neutron wave number in the center-of-mass system, δ_0 is the phase shift for s-wave potential scattering, J is the spin of the compound nucleus, and $g_J=(2J+1)/6$ for nitrogen. The first of the two terms in Eq. (1) represents the interference of part of the potential scattering with the resonance contribution, and the other term is the remainder of the s-neutron potential scattering.

The following lettered paragraphs refer to Table I, which was prepared to aid in the description of the 0.64- and 1.00-Mev resonances in terms of Eq. (1).

(a) Maximum and minimum scattering cross sections were obtained at each resonance by subtracting the reaction cross section from the total cross section. A correction was made for the effect of the lower energy neutron group which has been observed in the $Li^7(p, n)$ reaction. Intensities of this neutron group were previously determined;[1] the correction is negligible at the 640-kev resonance.

(b) Assignment of total angular momentum J: According to Eq. (1) the variation in cross section at a scattering resonance is within the range of values from

$$(\Gamma_n/\Gamma)[(\Gamma_n/\Gamma)4\pi k^{-2}g_J]$$

for $\delta_0=0$, to

$$(2-\Gamma_n/\Gamma)[(\Gamma_n/\Gamma)4\pi k^{-2}g_J] \quad (2)$$

for $\delta_0=-\pi/2$. In the present case $\delta_0\cong-\pi/4$ so that the difference between the maximum and minimum cross section at a resonance is very nearly $(\Gamma_n/\Gamma)\times(4\pi k^{-2}g_J)$. For each possible value of J this theoretical difference, $\sigma_{max}-\sigma_{min}$ was found using the observed reaction cross section to determine Γ_n/Γ. The experimentally observed $\sigma_{max}-\sigma_{min}$ for the 0.64- and 1.00-Mev resonances are consistent with the theoretical value for $J=\frac{1}{2}$ and $J=\frac{3}{2}$, respectively. The small discrepancy in cross section with these assignments of J-values is mostly attributed to the effect of the neutron energy spread.

(c) To a good approximation the dip in cross section given by Eq. (1) is $4\pi k^{-2}\sin^2\delta_0$. An estimate of the radius R of interaction of the neutron and nitrogen may be obtained from the dip in cross section because $\delta_0\cong-kR$. Radii estimated in this manner for the two levels are consistent with each other and also with radii estimated for other light nuclei.

(d) At each minimum the cross section should consist of (1) that part of the s-potential scattering that does not interfere with the resonance, (2) potential scattering for higher l-values, and (3) other resonance con-

[6] Feshbach, Peaslee, and Weisskopf, Phys. Rev. 71, 142 (1947).
[7] E. P. Wigner and L. Eisenbud, Phys. Rev. 72, 29 (1947).

tributions. Table I shows the approximate potential scattering for $l \neq 0$ plus the expected residual s-potential scattering, which is equal to $(g_J^{-1}-1)$ times the dip in cross section. This sum agrees within 0.2 or 0.3 barn with the observed minimum cross section; the 0.2- or 0.3-barn difference is attributed to the effects of neutron energy spread and contributions of other resonances.

(e) In the measurement of the disintegration cross section, resonance energy, and total width were determined from the energy at the peak and its width at half-maximum. Values of Γ and E_r must be found indirectly from the total cross section using the observed δ_0 and the neutron energies at the maximum and minimum in cross section. At the 1.00-Mev resonance $\Gamma_n \cong \Gamma$ so that Γ and E_r are readily computed using Eq. (1); however, at the 0.64-Mev resonance, where the observed reaction cross section indicates $\Gamma_n \doteq 0.85\Gamma$, a graphical solution of Eq. (1) in the complex plane was convenient. Table I shows agreement of resonance energies found in the two experiments. The observed level widths are larger as determined from disintegration experiments, presumably because the neutron energy spread was about 30 kev for the disintegration measurements and only 10 kev for the total cross-section measurements.

TABLE I. S-neutron resonances in nitrogen.

		640-kev resonance	1000-kev resonance
a. Observed scattering cross section	σ min.	1.65 barns at 620 kev	0.95 barn at 975 kev
	σ max.	2.65 barns at 620 kev	2.65 barns at 1020 kev
b. $\sigma_{max}-\sigma_{min}$		1.0 b	1.7 b
$(\Gamma_n/\Gamma)4\pi\lambda^{-2}g_{1/2}$		1.3 b	1.0 b
$(\Gamma_n/\Gamma)4\pi\lambda^{-2}g_{1/2}$		2.9 b	2.0 b
Assigned J-value		1/2	3/2
c. Observed dip in σ		0.7 b	1.0 b
δ_0 from dip in σ		0.73	−0.79
$R=-\delta_0/k$		4.4×10^{-13} cm	3.9×10^{-13} cm
d.[a] $\sigma_{l=1}=4\pi\lambda^{-2}(2l+1)\sin^2\delta_1$		0.06 b	0.14 b
$(g_J^{-1}-1)$(dip) $+\sigma_{l=1}$		1.46 b	0.64 b
e. Γ (from scattering curve)		40 kev	45 kev
Γ (from σ_{np} curve)		55 kev	60 kev
E_r (from scattering curve)		640 kev	998 kev
E_r (from σ_{np} curve)		640 kev	995 kev

[a] The expression for p-wave potential scattering may be found in reference 6.

Other States

Other isolated resonances in the total cross section appear at 0.433 and 1.12 Mev. The absence of a dip preceding these peaks indicates that they are formed by neutrons of $l>0$. Since the 0.433-Mev resonance is scarcely broader than the neutron energy spread, the peak cross section can only place a lower limit on the resonance cross section. Accordingly, an application of the Breit-Wigner formula to this level indicates $J>\frac{1}{2}$. The magnitude of the 1.12-Mev resonance is only well enough defined to indicate that either $J=3/2$ or $J=5/2$.

The relative magnitude of the total, the (n, p) and the (n, α) resonance cross sections gives the relative probabilities or widths for the emission of neutrons, protons, and alpha-particles from the compound nucleus; thus, the presence of several total cross-section resonances in Fig. 1 without corresponding resonances in $\sigma_{np}+\sigma_{n\alpha}$, indicates that these resonances neutron emission strongly predominates over charged particle emission. The reverse situation is observed at the 0.5-Mev resonance.

The partial width for emission of a particle can be written as $\Gamma=2k\gamma^2/(F_l^2(a)+G_l^2(a))$ where k is the wave number of the particle and F and G are the regular and irregular solutions of the radial wave equation[8] outside of the range of nuclear forces, evaluated at a, the reaction radius. The reduced widths, γ^2, are expected to be of the same magnitude for the different states and for the emission of the various particles. In the previous discussion the resonances in (n, p) and (n, α) cross sections were described with quantum numbers such that much of the variation in emission probabilities was attributed to the variation in the wave numbers and the barrier penetration factors $1/(F_l^2(a)+G_l^2(a))$, whereas the reduced widths remained within what were considered reasonable limits. In a similar manner the isolated resonances in the total cross section and reaction cross section in Fig. 1 have been described using quantum numbers chosen to minimize the deviation of the reduced widths from the values found for the neutron at the two s-resonances. In this description it was found that the reduced widths must vary by a factor of from 20 to 30 depending on the relative parity assumed for the nuclei. Since the quantum numbers were assigned with the view of minimizing this variance, 20 to 30 must be considered a lower limit. In general, the results of such considerations are sensitive to the choice of a, the reaction radius.

Since for a particular value of Γ the reduced width depends on the angular momentum of the particle emitted, one might expect to learn the angular momentum of the interacting particles and hence the parities of the nuclei involved by studying the relative emission probabilities. However, the large variation in the nuclear matrix elements, the γ^2, seems to preclude this possibility.

Average spacing of the resonances is about 200 kev. This spacing is somewhat less than that found by scattering neutrons of these energies from the neighboring nuclei, C^{12} and O^{16}.[5] The difference in spacing may be attributed primarily to the difference in excitation energies of the various compound nuclei; neutrons incident on N^{14} form N^{15} with excitation energy about 11 Mev above the N^{15} ground state, whereas neutrons incident on C^{12} or O^{16} form compound nuclei of only about 5-Mev excitation.

[8] Bloch, Hull, Broyles, Bouricius, Freeman, and Breit, Phys. Rev. 80, 553 (1950).

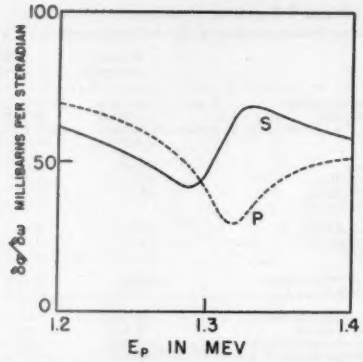

FIG. 2. Differential scattering cross section calculated from Eq. (3) for protons scattered through 180° by C^{14}. Values of Γ, Γ_p, and E_r were determined from the results shown in Fig. 1. The solid curve was found for s-protons, whereas the dotted curve presents results for p-protons. An experimental observation of the proton scattering should indicate the correct curve and thereby allow an assignment of the relative parities of C^{14} and N^{14}.

III. THE RELATIVE PARITIES OF C^{14} AND N^{14}

Most nuclear models predict that C^{14} and N^{14} have the same parity whereas the $C^{14}-N^{14}$ beta-decay is more readily explained if they have opposite parity. Gerjuoy[9] has suggested methods for determining the relative parities of these nuclei. While the present experiments do not allow a determination of the relative parities, they suggest another method which may have some experimental advantages.

The total cross-section measurements indicate that the 0.64-Mev level is excited by s-neutrons. The proton emitted by this state must have $l=0$ if the $N^{14}-C^{14}$ parities are the same, and $l=1$ if their parities differ. An observation of the protons scattered by C^{14} at this resonance should reveal the orbital angular momentum of the protons contributing to this level.

The differential cross section for the scattering of protons by C^{14} at this resonance can be calculated for either value of the relative parities using the values of Γ, Γ_p, and E_r determined from the $N^{14}(n,n)$ and $N^{14}(n,p)$ measurements. Neglecting the nuclear potential scattering for particles of angular momentum greater than zero, and assuming that the widths will remain nearly constant over the width of the resonance, we use the results of nuclear dispersion theory[8,9] and write:

$$d\sigma/d\Omega=(1/k_p^2)(|-\eta/2\,\csc^2\tfrac{1}{2}\vartheta\,\exp i\eta\ln\csc^2\tfrac{1}{2}\vartheta+e^{i\delta_0}\sin\delta_0+A(\Gamma_p/\Gamma)e^{i\delta_r}\sin\delta_r|^2+|B(\Gamma_p/\Gamma)e^{i\delta_r}\sin\delta_r|^2), \quad (3)$$

where $\eta=6e^2/\hbar v$ and $\delta_0=-\tan^{-1}(F_0(a)/G_0(a))$, $F_0(a)$ and $G_0(a)$ signifying the regular and irregular solutions of the radial part of the coulomb wave equation, evaluated at a, the reaction radius. If C^{14} and N^{14} have the same parity, the level will be excited by s-wave protons and $A=e^{2i\delta_0}$, $B=0$. If the nuclei have different parity, the state will be reached by p-protons and $A=[(1+i\eta)/(1-i\eta)]\cos\vartheta$, $B=\sin\vartheta$. The δ_r in either case will be equal to $\tan^{-1}[\Gamma/2(E_r-E)]$.

Some recent measurements of the scattering of protons by various nuclei as a function of proton energy have been made at angles near 180°. The results of such a measurement on C^{14} at this resonance will depend strongly on the angular momentum of the proton exciting this state, and hence on the relative parity of the two nuclei. Figure 2 shows the differential scattering cross section at 180° of protons on C^{14} near this resonance as calculated from Eq. (3) for these two parities. The shape of the curves is dependent almost entirely on the value of η and is quite insensitive to the values of the parameters Γ, Γ_p, and a. Since η is a function only of the proton energy it is quite accurately known. It therefore seems likely that a measurement of the scattering might, with little ambiguity, determine the relative parities of these nuclei.

The authors are indebted to Professor H. H. Barschall and Professor E. P. Wigner for the benefit of discussions on the performance and interpretation of the experiment.

[9] E. Gerjuoy, Phys. Rev. 81, 62 (1951).

A Phenomenological Treatment of Photomeson Production from Deuterons

G. F. CHEW
*Brookhaven National Laboratory, Upton, Long Island, New York** and *University of Illinois, Urbana, Illinois*

AND

H. W. LEWIS
University of California, Berkeley, California

(Received August 10, 1951)

A phenomenological treatment of charged and neutral photomeson production from deuterons is presented which is independent of the details of the meson theory. It is shown that an experimental comparison of the deuteron and proton cross sections can be used to determine the nucleon spin flip probability.

I. INTRODUCTION

THE available experimental information about π-mesons produced by γ-rays incident on free protons[1] is not at present satisfactorily interpretable theoretically, even though this is one of the simplest meson reactions. The difficulty lies in current meson theory which is incapable of making quantitative predictions so long as the meson-nucleon coupling is not weak. For photomeson reactions in light complex nuclei, nevertheless,[2] it is possible to make a phenomenological analysis based on the impulse approximation. This paper presents such a treatment for the special case of the deuteron. The method is expected to be applicable no matter what theory of mesons and their coupling to nucleons finally turns out to be correct.

The production of mesons by photons on deuterium as contrasted to that from free protons is of interest because of the information it gives about the dependence of the reaction on the charge and spin of nucleons. The charge dependence is manifested in the positive-negative ratio, since only the neutron can serve as a source of negative mesons and only the proton for positives. The spin dependence, on the other hand, shows up in the relative number of positive mesons emitted from a proton bound in a deuteron compared to the number emitted when the proton is free. Feshbach and Lax[3,4] have pointed out that unless the proton spin changes in the emission process, the deuteron cross section for positive photomeson production will be diminished relative to the free proton cross section. This is because in the former case there are two neutrons left in a triplet spin state, and due to the Pauli principle they can have only odd orbital angular momentum. For γ-ray energies presently available from synchrotrons and betatrons, the relative energy of the two neutrons is likely to be of the order of 15 Mev, or even less when the meson is emitted forward. The exclusion of S states therefore can reduce the available phase space considerably. It will be shown in this paper that the exclusion principle effect may be expressed in terms of the spin change probability without reference to meson theory. The conclusion reached therefore, is that the ratio of deuteron to proton cross sections can be used as a direct and quantitative measure of the nucleon spin flip probability.

Neutral photomeson production from deuterons will also be considered. Both neutron and proton can act as source in this case, so there will be interference effects. These will be of the same order of magnitude as the exclusion principle effect in the charged meson production but of a sign which depends on the detailed meson theory.

II. GENERAL CONSIDERATIONS FOR CHARGED MESON PRODUCTION

The fundamental assumption of the impulse approximation[2] is that the meson production "amplitudes" from the various nucleons (in this case two) are linearly superposable to form the production amplitude for the whole nucleus. This is an assumption analogous to the use of Born approximation in the scattering of x-rays by many electron systems or the Fermi approximation in the scattering of slow neutrons by crystals. Sufficient conditions for validity[2] are: (1) Small individual amplitudes in comparison to the distance between sources. (2) Long mean free paths for both incoming and outgoing particles in comparison to the over-all dimensions of the system. (3) A "collision time" short compared to the period of the nuclear system. These conditions are well satisfied for our case. The smallness of the fine structure constant guarantees the small amplitudes and long photon mean free path. The condition on the outgoing meson mean free path can, in the case of the deuteron, be restated as a requirement that the meson-nucleon scattering cross section be small compared to the cross-sectional area of the deuteron. The latter is $\sim 10^{-24}$ cm^2, whereas the meson-nucleon cross section[5] is only $\sim 10^{-26}$ cm^2. The collision time seems certain to be sufficiently small, since the average extent to which energy

* Research carried out at Brookhaven National Laboratory under the auspices of the AEC.

[1] J. Steinberger and A. S. Bishop, Phys. Rev. **78**, 494 (1950); Bishop, Steinberger, and Cook, Phys. Rev. **80**, 291 (1950); Steinberger, Panofsky, and Steller, Phys. Rev. **78**, 802 (1950).

[2] G. F. Chew and G. C. Wick (to be published).

[3] H. Feshbach and M. Lax, Phys. Rev. **76**, 134 (1949).

[4] M. Lax and H. Feshbach, Phys. Rev. **81**, 189 (1951).

[5] Chedester, Isaacs, Sachs, and Steinberger, Phys. Rev. **82**, 958 (1951).

conservation is violated in the intermediate states must be of the order of the meson rest energy.

An additional possibility arises, when we consider nucleons bound in a nucleus, which could still invalidate the use of the superposition approximation. Strong nuclear forces may actually modify the character of the individual scattering centers. In other words, the charge-current distribution of meson-nucleon field which we call a free proton may become polarized when that "proton" is inside a complex nucleus, leading to "exchange" currents which have an electromagnetic interaction absent for free nucleons. This possibility is ignored in the present paper on the qualitative grounds that the deuteron is so weakly bound that the meson "clouds" surrounding the individual neutron and proton overlap only slightly. The question is receiving further study.

It will be sufficient to restrict consideration to nucleon recoil velocities which are small compared to the velocity of light, since for larger recoils the deuteron will behave simply as a pair of free nucleons. The outgoing meson, however, must be treated relativistically. Using units in which $\hbar=c=1$, and the meson rest mass is also unity, the incident photon energy will be denoted by ν_0, and its momentum by ν, the emitted meson energy and momentum by μ_0 and μ. We assume the deuteron to be initially at rest with binding energy $-\epsilon_i$ and represent the total momentum of the recoiling nucleon system by $\mathbf{D}$ and the internal (relative) energy by ϵ_f. The initial energy of the system as a whole is then $\nu_0+2M+\epsilon_i$, and the final energy is $\mu_0+2M+D^2/4M+\epsilon_f$. The neutron-proton mass difference will be ignored. Thus the cross section for meson emission into the momentum interval $d\boldsymbol{\mu}$, while the nucleus recoils into the interval $d\mathbf{D}$ and the internal state f, may be expressed in the form

$$d\sigma_f/d\boldsymbol{\mu}d\mathbf{D}=(2\pi)^{-2}|Q_f|^2\delta(\mu_0+\epsilon+D^2/4M-\nu_0) \quad (1)$$

where Q_f is the appropriate element of the scattering matrix, and $\epsilon=\epsilon_f-\epsilon_i$. According to our fundamental assumption, the scattering matrix is to be approximated by

$$T=T_1+T_2,$$

where T_j is the part of the scattering matrix which describes the photoproduction of, let us say, a positive meson by the jth nucleon acting alone. (The positive and negative meson production problems are obviously symmetrical.) The dependence of T_j on the nucleon position $\mathbf{r}_j$, spin $\boldsymbol{\sigma}_j$, and isotopic spin $\boldsymbol{\tau}_j$, may be made explicit by writing

$$T_j=(\boldsymbol{\sigma}_j\cdot\mathbf{K}+L)\exp[i(\mathbf{v}-\boldsymbol{\mu})\cdot\mathbf{r}_j]\tau_j^+. \quad (2)$$

This form is required by momentum conservation and the properties of the Pauli spin operator. If $\mathbf{K}$ and L are allowed to depend on the momenta of photon, meson, and nucleon, as well as on the polarization of the photon, then the form is completely general. (Even though we are treating the meson spin as if it were zero, most of the important results do not actually depend on this point.)

$|Q_f|^2$ must be summed over the final and averaged over the initial spin and isotopic spin states. The initial deuteron is a spin triplet and an isotopic spin singlet

$$|i\rangle=2^{-\frac{1}{2}}[p(1)n(2)-p(2)n(1)]^3\chi_m(2\pi)^{-\frac{1}{2}}u_i(\rho), \quad (3)$$

where $\boldsymbol{\rho}=\mathbf{r}_1-\mathbf{r}_2$ is the relative coordinate and ${}^3\chi_m$ is the triplet spin function, m being the z component of the total spin. The small amount of spin-orbit coupling in the deuteron is being neglected.

The final state consists of two neutrons, an isotopic triplet, with asymptotic relative momentum $\mathbf{k}_f$, so that $\epsilon_f=k_f^2/M$. The Pauli principle requires separate consideration of the two final states: one that is symmetric and one that is antisymmetric in space.

$$|f_e\rangle=(2\pi)^{-\frac{1}{2}}n(1)n(2)^1\chi_0\,u_{f,e}(\rho)\exp(i\mathbf{D}\cdot\mathbf{R}), \quad (4a)$$

$$|f_0\rangle=(2\pi)^{-\frac{1}{2}}n(1)n(2)^3\chi_m u_{f,o}(\rho)\exp(i\mathbf{D}\cdot\mathbf{R}). \quad (4b)$$

$\mathbf{R}=\frac{1}{2}(\mathbf{r}_1+\mathbf{r}_2)$ is the center-of-mass coordinate. We now introduce (2), (4a) or (4b) into Q_f. The integration over $\mathbf{R}$ leads to a momentum conservation requirement that only final states with $\mathbf{D}=\mathbf{v}-\boldsymbol{\mu}$ be allowed, and the matrix elements for the symmetric and antisymmetric cases become respectively (with the momentum delta-function factored out)

$$Q_{f,e}=2^{-\frac{1}{2}}\langle{}^1\chi_0|\,\mathbf{K}\cdot(\boldsymbol{\sigma}_1-\boldsymbol{\sigma}_2)|\,{}^3\chi_m\rangle E_f, \quad (5a)$$

$$Q_{f,o}=2^{-\frac{1}{2}}\langle{}^3\chi_m|\,\mathbf{K}\cdot(\boldsymbol{\sigma}_1+\boldsymbol{\sigma}_2)+2L|\,{}^3\chi_m\rangle O_f, \quad (5b)$$

where

$$E_f=\int u_{f,e}{}^*(\rho)\exp(i\mathbf{k}_0\cdot\boldsymbol{\rho})u_i(\rho)d\boldsymbol{\rho}, \quad (6a)$$

$$O_f=\int u_{f,o}{}^*(\rho)\exp(i\mathbf{k}_0\cdot\boldsymbol{\rho})u_i(\rho)d\boldsymbol{\rho}, \quad (6b)$$

if $\mathbf{k}_0=\frac{1}{2}\mathbf{D}$.

Since the final states u_f are either even or odd, it is conventional to extend any integrations which may be done only over half of $\mathbf{k}_f$ space, providing the normalization of the final states is taken to be:

$$\int u_{f,e}{}^*(\rho)u_{f',e}(\rho)d\boldsymbol{\rho}=\delta(\mathbf{k}_f-\mathbf{k}_f')+\delta(\mathbf{k}_f+\mathbf{k}_f')$$

$$\int u_{f,o}{}^*(\rho)u_{f',o}(\rho)d\boldsymbol{\rho}=\delta(\mathbf{k}_f-\mathbf{k}_f')-\delta(\mathbf{k}_f+\mathbf{k}_f').$$

One may already see from (5) that only $\mathbf{K}$ is effective in changing the spin state of the deuteron. It is also clear from (6) that O_f approaches zero at threshold ($k_f=0$) and also whenever the nuclear recoil is zero ($k_0=0$). Under either of these circumstances, then, the spin flip term will dominate.

In obtaining (5), the assumption has been made that **K** and L depend only on $\mathbf{v}$ and $\mathbf{y}$ and not at all on the nucleon momenta. For charged meson production, where the nucleon currents are relatively unimportant, this is certainly justified, and even for neutral production, it is not unreasonable. This is because the final momentum of the struck particle is usually not far from the value $\mathbf{D}=\mathbf{v}-\mathbf{y}$ which it would assume if the proton were free and at rest. One can understand **K** and L to be evaluated for zero initial nucleon momentum and a final nucleon momentum equal to $\mathbf{v}-\mathbf{y}$ and need neglect only the relatively small fluctuations about these values.

The expressions (5a) and (5b) are to be squared, summed over final nuclear spins and averaged over initial nuclear spins and photon polarizations. This yields

$$\langle|Q_f|^2\rangle_{Av}=\tfrac{2}{3}\langle|\mathbf{K}^2|\rangle_{Av}|E_f|^2 +[4/3\langle|\mathbf{K}^2|\rangle_{Av}+2|L^2|]\langle|O_f|^2\rangle_{Av} \quad (7)$$

with conservation of momentum understood. To go further we must decide what distribution function we should like to have. One may ask for the total number of mesons at a given angle, as a function of angle, or perhaps also the spectrum of mesons at each angle. For certain experiments one might even be interested in the distribution of nucleon recoils. The most natural theoretical distribution parameter turns out to be the square of the nuclear recoil, that is, D^2. We shall first discuss the distribution in this quantity and then show that it has a rather close connection to the meson angular distribution.

III. THE DISTRIBUTION OF NUCLEAR RECOILS

If the momentum conservation condition is used to eliminate the meson momentum as a degree of freedom in (1), the distribution of nuclear recoils is obtained:

$$d\sigma_f/d\mathbf{D}=(2\pi)^{-2}\langle|Q_f|^2\rangle_{Av}\delta(\mu_0+\epsilon+D^2/4M-\nu_0) \quad (8)$$

where

$$\mu_0=((\mathbf{v}-\mathbf{D})^2+1)^{\frac{1}{2}}=(\nu_0^2+D^2-2\nu_0 D\cos\theta_D+1)^{\frac{1}{2}}.$$

The energy delta-function may next be used to eliminate θ_D, the angle between $\mathbf{v}$ and $\mathbf{D}$, leaving as free variables the magnitude of $\mathbf{D}$ and the azimuth of $\mathbf{D}$ with respect to $\mathbf{v}$. The cross section obviously does not depend on this angle for an unpolarized beam of photons, so we end up with the distribution in D^2 for a given final nuclear state f,

$$d\sigma_f/dD^2=(2\pi)^{-1}\langle|Q_f|^2\rangle_{Av}(\nu_0-\epsilon-D^2/4M)/2\nu_0. \quad (9)$$

The limits on D^2 are determined by the equation,

$$(\nu_0-\epsilon-D^2/4M)^2=(\nu_0-D)^2+1, \quad (10)$$

which may be solved to give the maximum value of k_f^2 for a given value of D,

$$k_m^2=M[\nu_0-((\nu_0-D)^2+1)^{\frac{1}{2}}]-(\alpha^2+k_0^2), \qquad \alpha^2=-M\epsilon_i. \quad (11)$$

In Fig. 1, a plot is made of k_m^2 as a function of D^2 for several values of ν_0.

From a general point of view, the problem is now solved. Using the ground-state deuteron wave function and the continuum wave functions of the di-neutron, the overlap integrals E_f and O_f may be evaluated. The matrix elements K and L are to be given by the meson theory. From a practical point of view, however, it is important to make further approximations, both to avoid excessive lator and to circumvent the present lack of a reliable meson theory.

A study of the matrix elements Q_f reveals that for a recoil, $D=2k_0$, the important final nuclear states are restricted to a range of energies whose half-width is of the order $3\alpha k_0/M$, while from (11), it is seen that k_0 cannot be greater than ν_0. The average energy transfer, ϵ, corresponding to a recoil, D, is approximately $D^2/4M$. (This last point can be understood qualitatively by going to the limit $\alpha=0$, so that the proton behaves as if completely free, absorbing the entire recoil.) Now in

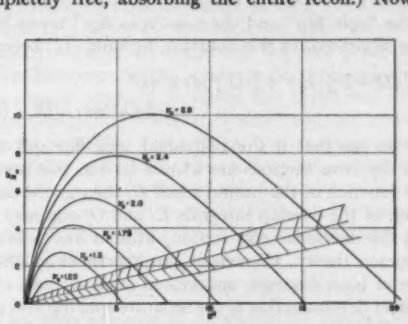

FIG. 1. A diagram of k_m^2, the upper limit of k_f^2, as a function of ν_0 and D^2. The shaded region includes the most important contributions.

(9), the only dependence on f, except for the matrix element Q_f, occurs in the term, ϵ. If the variation in ϵ is only $\sim 3(\alpha/M)\nu_0$ for a given value of D, the variation may be neglected, since $\alpha/M\approx 1/20$. Inserting (7) and replacing by its approximate average, $D^2/4M$, one may rewrite (9) as

$$d\sigma_f/dD^2=(2\pi)^{-1}\{2(\tfrac{1}{3}|E_f|^2+\tfrac{2}{3}|O_f|^2)\langle|\mathbf{K}^2|\rangle_{Av} +2|O_f|^2\langle|L|^2\rangle_{Av}\}(\nu_0-D^2/2M)/2\nu_0. \quad (12)$$

The matrix elements **K** and L depend on the final nuclear state through their dependence on the meson momentum $\mathbf{y}=\mathbf{v}-\mathbf{D}$ (which depends on the angle θ_D and thus on ϵ_f). We shall assume, however, that the variation is small over the range of directions of D which can occur with appreciable probability for a given magnitude D. This assumption is more difficult to justify quantitatively than the preceding one and will be better for some meson theories than for others. It leaves only E_f and O_f as functions of the final nuclear state f, and formula (12) should now be compared

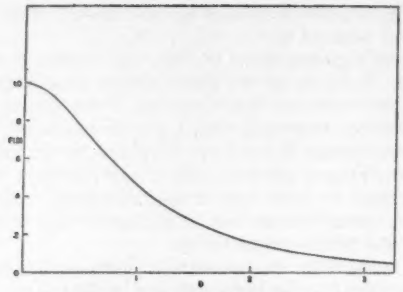

FIG. 2. The exclusion principle function $F(D)$ according to formula (A3).

with the corresponding formula for a free proton,

$$d\sigma_p/dD^2=(2\pi)^{-1}\{\langle|\mathbf{K}^2|\rangle_{av}+\langle|L|^2\rangle_{av}\}(\nu_0-D^2/2M)/2\nu_0$$
$$=d\sigma_K/dD^2+d\sigma_L/dD^2. \quad (13)$$

The "spin flip" and the non-"spin flip" terms have been separated. In this notation, formula (12) becomes

$$d\sigma_f/dD^2=2(\tfrac{1}{3}|E_f|^2+\tfrac{2}{3}|O_f|^2)d\sigma_K/dD^2$$
$$+2|O_f|^2d\sigma_L/dD^2, \quad (12')$$

and we see that if the individual spin flip and non-spin flip cross sections are known for the free proton, as a function of the proton recoil D, then by the calculation of the overlap integrals E_f and O_f one may obtain the deuteron cross section, without any reference to meson theory. Conversely, an experimental knowledge of both deuteron and proton cross sections allow a direct determination of the separate spin flip and non-spin flip terms, since these terms occur with different weights in the two processes.

The evaluation of E_f and O_f, once the deuteron and di-neutron wave functions are known, is straightforward but tedious. In a forthcoming paper, Feshbach, Goldberger, and Villars[6] will describe the calculation and present some results, using the wave functions of the Hulthèn potential. A principal feature which can be obtained only from such a calculation is the "resonance" in the cross section due to the "almost binding" of the singlet di-neutron. This causes E_f to increase sharply for values of ϵ_f less than 1 Mev, the effect being spectacular for small values of D. Unless the spin flip term, $d\sigma_K/dD^2$, is very small, this resonance will dominate the behavior of the cross section near threshold.

The existence of the neutron-neutron interaction, which tends to favor final states with low values of ϵ_f, actually helps make valid a very useful further approximation. Suppose one wishes to know the total cross section for a given recoil D, but for all allowable final states f. If the sum is extended to all values of k_f (i.e., ϵ_f), even those not allowed by the energy conservation condition (11) (see Fig. 1), then one is in a position to employ closure theorems. This overestimates the cross section, but if the energetic upper limit on ϵ_f is sufficiently greater than the "average" final nuclear energy, $D^2/4M$, the contribution from the forbidden states will not be important. The $n-n$ interaction helps keep the spread in energies ϵ_f on the low side of the above value.

The closure theorems which we need may be stated in the following form,

$$\int u_{f,e}^*(\rho)u_{f,e}(\rho')d\mathbf{k}_f=\delta(\rho-\rho')+\delta(\rho+\rho'),$$

$$\int u_{f,o}^*(\rho)u_{f,o}(\rho')d\mathbf{k}_f=\delta(\rho-\rho')-\delta(\rho+\rho_i).$$

Applying these formulas to (12') in summing over all states f (which means integrating over half of $\mathbf{k}_f$ space), we find

$$d\sigma/dD^2\approx[1-\tfrac{1}{3}F(D)]d\sigma_K/dD^2$$
$$+[1-F(D)]d\sigma_L/dD^2, \quad (14)$$

where

$$F(D)=\int \exp(i\mathbf{D}\cdot\rho)u_i^2(\rho)d\rho. \quad (15)$$

The result (14) is extremely instructive in showing the effect of the exclusion principle. The function $F(D)$ (plotted in Fig. 2, for the Hulthèn deuteron function [see Appendix]) is equal to unity when $D=0$ and falls off with increasing D at a rate determined by the zero point motion of the deuteron. It reaches its half-maximum near $D=1$. For small D the non-spin flip term is thus suppressed, while $\frac{2}{3}$ of the spin flip contribution is allowed. Experiments designed to measure the nucleon spin dependence of the photomeson production clearly must concentrate on small values of D. For large values, F approaches zero and no new information from the deuteron can be obtained.

For large ν_0 the limits on the allowable range of D for the deuteron can be shown to effectively approach those for the proton. Thus the obvious requirement that deuteron and proton total cross sections shall asymptotically become equal as $\nu_0\to\infty$ is satisfied by (14), because the fraction of the total range of D^2 where $F(D)$ is significant becomes smaller and smaller as ν_0 increases. However, that portion of the range where $D\gtrsim 1$ will always have a substantially smaller cross section for the deuteron than for the proton, regardless of the size of ν_0.

It is unfortunate that the nuclear recoil D is not always an easily measurable quantity, since in comparing the properties of complex nuclei to those of free nucleons in high energy reactions, it is by far the most significant single parameter. In charged meson production experiments, the most easily measured quantities

[6] Feshbach, Goldberger, and Villars, private communication.

happen to be the energy and angle of the emitted meson. Before considering the theoretical distribution in these variables from a systematic standpoint, it should be pointed out that the total number of mesons emitted at a fixed laboratory angle is closely, although not exactly, related to the number of nuclear recoils of a given magnitude. Thus the results of this section may be applied roughly to the meson angular distribution.

The general connection between the meson angle, θ_μ, the nuclear recoil, D, and the nuclear excitation energy, ϵ, is as follows:

$$\cos\theta_\mu=\frac{\nu_0^2+(\nu_0-\epsilon-D^2/4M)^2-1-D^2}{2\nu_0[(\nu_0-\epsilon-D^2/4M)^2-1]^{\frac{1}{2}}}. \quad (16)$$

Except very close to threshold, we may argue, as we did for (9), that formula (17) is well approximated by replacing ϵ by $D^2/4M$. One may therefore use the approximate relation,

$$\cos\theta_\mu\approx\frac{\nu_0^2+(\nu_0-D^2/2M)^2-1-D^2}{2\nu_0[(\nu_0-D^2/2M)^2-1]^{\frac{1}{2}}}, \quad (17)$$

to connect a nuclear recoil D with a meson angle θ_μ. Since this connection is the same as for a free proton, it follows that a formula of the type (14) applies roughly for the meson angular distribution as well as for the distribution of recoils. In other words, if we write the cross section for meson production into the solid angle $d\Omega_\mu$, from a free proton at rest, as

$$d\sigma_p/d\Omega_\mu=d\sigma_K/d\Omega_\mu+d\sigma_L/d\Omega_\mu, \quad (18)$$

separating the spin flip and non-spin flip terms as before, then the corresponding deuteron cross section in the closure approximation is

$$d\sigma/d\Omega_\mu=[1-\tfrac{1}{3}F(D)]d\sigma_K/d\Omega_\mu +[1-F(D)]d\sigma_L/d\Omega_\mu, \quad (19)$$

where D is connected to θ_μ through (17).

The relationship (17) is plotted in Fig. 3 for several values of ν_0. It is seen that, in general, small angles of meson emission correspond to small values of the nuclear recoil and therefore to a large exclusion principle effect. It follows that experiments to determine the nucleon spin dependence must be done at small angles of meson emission.

Nearly all the approximations made in evaluating formula (9) can be systematically improved by a method due to Placzek.[7] This consists of an expansion in powers of $\epsilon-D^2/4M$, of which the zero'th order terms are the results given here by our closure approximation. This approach also yields the total cross section in a simple form. A subsequent paper will discuss the "Placzek corrections" to the closure approximation.

[7] G. Placzek, private communication.

IV. THE ENERGY AND ANGULAR DISTRIBUTION OF CHARGED MESONS

If one eliminates from (1) the nucleon recoil D and fixes the final state f by energy conservation, then the distribution of final meson momenta $\mathfrak{y}$ is obtained. After the same approximations which led to (9), one finds

$$d\sigma/d\mathfrak{y}=(2\pi)^{-2}\{(\tfrac{1}{3}I_e+\tfrac{2}{3}I_o)\langle|\mathbf{K}^2|\rangle_{Av}+I_o\langle|L|^2\rangle_{Av}\},$$

where

$$I_e=\int d\mathbf{k}_f|E_f|^2\delta(\mu_0+\epsilon+(\mathfrak{v}-\mathfrak{y})^2/4M-\nu_0),$$
$$I_o=\int d\mathbf{k}_f|O_f|^2\delta(\mu_0+\epsilon+(\mathfrak{v}-\mathfrak{y})^2/4M-\nu_0). \quad (20)$$

The integrals I_e and I_o can be carried out for the Hulthèn wave functions,[6] but the results are so cumbersome that they have been evaluated at only a few selected points. In a paper by Feshbach and Lax[8] a tractable result is obtained by neglecting the final state interaction between the two neutron. As explained above, this cannot properly represent the upper end of the meson spectrum, where ϵ_f is small and the neutrons interact strongly. For large ϵ_f the approximation is presumably adequate. For reasons of economy we shall here go no further in the discussion of this approach to the meson energy distribution but refer the reader to the work of Feshbach and Lax, who have studied it thoroughly.

V. NEUTRAL MESON PRODUCTION

The phenomenological treatment of neutral meson production is similar to that for charged meson produc-

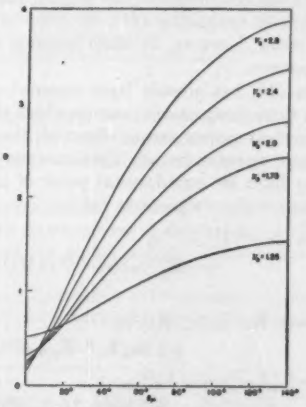

FIG. 3. The relationship between the recoil, D, of a free nucleon and the angle of meson emission, θ_μ (in the laboratory system), for various values of ν_0. Except quite close to threshold, this relationship is also approximately true for deuteron recoils.

[8] H. Feshbach and M. Lax (to be published).

tion. All arguments used for the charged meson case apply equally well here, with the possible exception of the assumption that the matrix elements do not vary in an important way with the nucleon momenta. The cross section in the laboratory system takes the form,

$$d\sigma_{f,o}/d\mathbf{y}d\mathbf{D}=(2\pi)^{-2}|Q_f|^2\delta(\mu_0+\epsilon+D^2/4M-\nu_0), \quad (21)$$

where

$$\begin{aligned} Q_f&=\langle f|\,T_n+T_p\,|i\rangle,\\ T_n&=(\boldsymbol{\sigma}_n\cdot\mathbf{K}_n+L_n)\exp[i(\mathbf{v}-\mathbf{y})\cdot\mathbf{r}_n], \quad (22)\\ T_p&=(\boldsymbol{\sigma}_p\cdot\mathbf{K}_p+L_p)\exp[i(\mathbf{v}-\mathbf{y})\cdot\mathbf{r}_p]. \end{aligned}$$

The notation permits the matrix elements for meson production on free neutron targets to differ from those with free proton targets. The final relative energy ϵ_f of the neutron proton pair takes the value k_f^2/M, if the two particles recede with relative momentum k_f, and the value $+\epsilon_i$, if the final state is the unmodified deuteron bound state.

For neutral meson production, the distribution of nuclear recoils may actually be experimentally observable. In any case one can arrive at a formula, analogous to (12):

$$d\sigma_{f,o}/dD^2=(2\pi)^{-1}\{\tfrac{2}{3}\langle|\mathbf{A}_f|^2\rangle_{Av}+\langle|B_f|^2\rangle_{Av}+\tfrac{1}{3}\langle|\mathbf{C}_f|^2\rangle_{Av}\}(\nu_0-D^2/2M)/2\nu_0, \quad (23)$$

where

$$\begin{aligned} \mathbf{A}_f&=(u_f^3(\boldsymbol{\rho}),[\mathbf{K}_n\exp(i\mathbf{k}_0\cdot\boldsymbol{\rho})+\mathbf{K}_p\exp(-i\mathbf{k}_0\cdot\boldsymbol{\rho})]u_i(\rho))\\ B_f&=(u_f^3(\rho),[L_n\exp(i\mathbf{k}_0\cdot\boldsymbol{\rho})+L_p\exp(-i\mathbf{k}_0\cdot\boldsymbol{\rho})]u_i(\rho))\\ \mathbf{C}_f&=(u_f^1(\rho),[\mathbf{K}_n\exp(i\mathbf{k}_0\cdot\boldsymbol{\rho})-\mathbf{K}_p\exp(-i\mathbf{k}_0\cdot\boldsymbol{\rho})]u_i(\rho)). \end{aligned} \quad (24)$$

By expressing the deuteron wave functions u_i, u_f^1, and u_f^3 in momentum space, a dependence of $\mathbf{K}_{n,p}$ and $L_{n,p}$ on the nucleon momenta can in principle be taken into account in evaluating (24). In order to obtain a tractable result, however, we shall continue to neglect this dependence.

Formula (23) has already been summed over final spins, but there is one special case in which the spin of the final nuclear system can be observed, that is, when the deuteron remains bound. This case may be very interesting from an experimental point of view, so a formula is now given separately for it:

$$d\sigma_{00}/dD^2=(2\pi)^{-1}\{\tfrac{2}{3}\langle|A_0|^2\rangle_{Av}+\langle|B_0|^2\rangle_{Av}\}(\nu_0-D^2/4M)/2\nu_0, \quad (25)$$

where

$$\begin{aligned} \langle|A_0|^2\rangle_{Av}&=(\langle|\mathbf{K}_n|^2\rangle_{Av}+\langle|\mathbf{K}_p|^2\rangle_{Av}\\ &\quad+2\,\mathrm{Re}\langle\mathbf{K}_n^*\cdot\mathbf{K}_p\rangle_{Av})F^2(k_0)\\ \langle|B_0|^2\rangle_{Av}&=(\langle|L_n|^2\rangle_{Av}+\langle|L_p|^2\rangle_{Av}\\ &\quad+2\,\mathrm{Re}\langle L_n^*L_p\rangle_{Av})F^2(k_0). \end{aligned} \quad (26)$$

Interference effects in (25) obviously may be strong, and the result cannot be completely expressed in terms of the free proton and free neutron cross sections since it depends on the relative phases of $\mathbf{K}_n$ to $\mathbf{K}_p$ and L_n to L_p. Notice that again the important parameter is $k_0=D/2$. The "elastic" meson production falls off rapidly as the nuclear recoil becomes large.

As before, we may use closure to obtain the total cross section, "elastic" plus "inelastic" for a given recoil D. The formula analogous to (14) is

$$\frac{d\sigma_0}{dD^2}\approx\frac{1}{2\pi}\{\langle|\mathbf{K}_n^2|\rangle_{Av}+\langle|\mathbf{K}_n^2|\rangle_{Av}+\langle|L_n|^2\rangle_{Av}+\langle|L_p|^2\rangle_{Av}+2F(D)\,\mathrm{Re}[\tfrac{1}{3}\langle\mathbf{K}_n^*\cdot\mathbf{K}_p\rangle_{Av}+\langle L_n^*L_p\rangle_{Av}]\}\times\frac{\nu_0-D^2/2M}{2\nu_0}, \quad (27)$$

which is seen to be the free proton cross section plus the free neutron cross section plus interference terms, whose importance depends on the size of D.

Interpretation of neutral meson production from deuterons is complicated by the interference terms, but there is the advantage that for the "elastic" part, which under certain conditions will not be at all negligible, the calculation of the nuclear overlap integrals can be carried out without approximation. Experimentalists are recommended to concentrate on this part of the investigation.

VI. CONCLUSIONS

The photoproduction of mesons in deuterium has been discussed phenomenologically on the basis of the following assumptions. (1) The production "matrix" is the sum of the free neutron and proton production matrices, evaluated between initial and final nuclear states. (2) The matrix elements, except for the momentum conservation factor, do not vary appreciably from their value in free nucleon photoproduction. It has been shown that the result for charged mesons is then expressible in terms of the free nucleon spin flip and non-spin flip meson production cross sections and certain overlap integrals which have nothing to do with meson theory. These integrals can be evaluated if the deuteron bound state wave function and the di-neutron continuum wave functions are given. Neutral meson production from deuterium involves the same integrals but also interference terms, the size of which do depend on meson theory.

Exact evaluation of the nuclear overlap integrals is in general tedious, but an approximation has been described which should be adequate to give the meson angular distribution except near threshold. Near threshold the final state nuclear interaction dominates the behavior of the cross section. In one special case, the "elastic" production of neutrals, the influence of the interaction is easily calculable. In other cases, when the final state is in the continuum, the formulas are complicated, but have been evaluated in a few cases by another group of workers.

In general, two-body effects are important when the nuclear recoil is of the same order or smaller than the momenta occurring in the zero point motion of the deuteron. This means that if information on the nucleon spin dependence of the matrix elements is to be derived from a comparison of deuteron and proton cross sections, the measurement must be carried out at small angles of meson emission and not too high an incident photon energy.

ACKNOWLEDGMENT

Close communication with H. Feshbach and M. Lax, who are also publishing a paper on this subject, was of great assistance to the authors. Much of the contents of the two papers is similar, and indeed an effort was made to employ the same notation. However, the Feshbach-Lax paper will be seen to emphasize different distribution variables than are here employed. For example they give the differential meson energy distribution, but do not obtain the total intensity at a given angle in a closed form. Also, since the validity of the different approximations made in the two papers is not entirely clear, it was felt worthwhile to publish the two separately.

APPENDIX

The Hulthèn Wave Function for the Ground State of the Deuteron

A convenient representation of the deuteron ground state is given by the Hulthèn function,

$$u_t(\rho)=\left[\frac{\alpha}{2\pi(1-\alpha\rho_1)}\right]^{\frac{1}{2}}\frac{(e^{-\alpha\rho}-e^{-\beta\rho})}{\rho}, \tag{A1}$$

where ρ_1 is the triplet neutron-proton effective range (1.74×10^{-13} cm), connected to the parameter, β, by the relation $\rho_1=4/(\alpha+\beta)-1/\beta$. The corresponding momentum space wave function is

$$c(\mathbf{k})=\left[\frac{\alpha}{\pi^2(1-\alpha\rho_1)}\right]^{\frac{1}{2}}\frac{(\beta^2-\alpha^2)}{(\alpha^2+k^2)(\beta^2+k^2)}. \tag{A2}$$

The Integral $F(k)$

From (15) and (A1), one easily finds

$$F(k)=\int\exp(i\mathbf{k}\cdot\boldsymbol{\rho})u_t^2(\rho)d\boldsymbol{\rho}=\frac{1}{1-\alpha\rho_1}\left(\frac{2\alpha}{k}\right)\times\left\{\tan^{-1}\left(\frac{k}{2\alpha}\right)+\tan^{-1}\left(\frac{k}{2\beta}\right)-2\tan^{-1}\left(\frac{k}{\alpha+\beta}\right)\right\}. \tag{A3}$$

PHYSICAL REVIEW VOLUME 84, NUMBER 4 NOVEMBER 15, 1951

Half-Life and Alpha-Particle Energy of U^{236}

A. H. Jaffey, H. Diamond, A. Hirsch, and J. Mech
Argonne National Laboratory, Chicago, Illinois

(Received August 9, 1951)

Several samples containing U^{236} were examined for measurement of the specific activity and the alpha-particle energy. The samples contained U^{234}, U^{235}, U^{236}, and U^{238}, the isotopic composition being known from mass spectrometer data. The samples were "weighed" through fission counting comparison with standards containing known amounts of pure U^{235}. The alpha-activity due to U^{236} was determined by ionization chamber energy analysis. The same instrument was used for the energy determination.

The half-life of U^{236} was found to be 2.46×10^7 years and the alpha-particle energy 4.499 Mev.

WORK at Los Alamos[1] in 1943 showed that some of the neutrons absorbed by U^{235} led to capture rather than to fission, with the presumable formation of the isotope U^{236}. It was later observed in highly irradiated U^{235} both mass-spectrographically[2] and with the alpha-energy pulse analyzer.[3] From the alpha-activity detected with the latter instrument, from the U^{235} capture cross section, and from the estimated neutron flux, the half-life was calculated to be approximately 2×10^7 years. The measured alpha-particle energy was 4.5 Mev.

U^{236} has been prepared recently in a more concentrated form by extensive neutron-irradiation of U^{235} followed by electromagnetic separation. Several of these samples have been made available,[4] which has made it possible for us to make more accurate measurements of both the half-life and alpha-particle energy of U^{236}.

The determination of the U^{236} specific activity involved the measurement of the weight of U^{236} in each sample and the alpha-particle disintegration rate due

TABLE I. Composition of U^{236} samples (mole percent).

Sample no.	U^{234}	U^{235}	U^{236}	U^{238}
I	0.3	59.0±0.20	22.15±0.25	18.55±0.25
II	0.4	54.5±0.24	22.0±0.30	23.1±0.30
III	0.65±0.02	58.58±0.19	37.62±0.18	3.17±0.03

[1] Unpublished Los Alamos work.
[2] D. Williams and P. Yuster, Los Alamos Report LAMS-195 (1945) (unpublished).
[3] Ghiorso, Brittain, Manning, and Seaborg, Phys. Rev. 82, 558 (1951).
[4] We are indebted for these samples to Dr. R. S. Livingston of the Electromagnetic Research Laboratory, Carbide and Carbon Chemicals Division, Oak Ridge, Tennessee.

TABLE II. Half-life values from three samples containing U^{236}.

Sample	Half-life value
I	$(2.43_7 \pm 0.03_4) \times 10^7$ years
II	$2.45_3 \pm 0.02_8$
III	$2.48_0 \pm 0.04_5$
Average	$2.45_7 \times 10^7$ years

TABLE III. Alpha-energy standards.

Nuclide	Energy, Mev	Nuclide	Energy, Mev
Po^{210}	5.298[a]	Pu^{238}	5.493[b]
Pu^{239}	5.140[b]	U^{234}	4.763[c,d]

[a] G. T. Seaborg and I. Perlman, Revs. Modern Phys. 20, 633 (1948).
[b] W. P. Jesse and H. Forstat, Phys. Rev. 73, 926 (1948).
[c] Clark, Spencer-Palmer, and Woodward, British Report-522, October 10, 1944 (unpublished).
[d] See reference 8.

to it. To determine the weight of U^{236}, relative concentrations of the uranium isotopes were measured by mass-spectrometric analysis[5] (Table I), and the absolute weight of uranium in each sample was determined indirectly by counting neutron-induced fissions. Although the sample weight could be determined, in principle, by weighing techniques, the samples were too small for good purification and accurate weighing to be done conveniently, and fission counting was used instead. Since the U^{235} concentrations were known, the total uranium weight could be determined by comparing the fission rates with that of a sample containing a known amount of U^{235}. The comparisons were made in a 2π ion chamber imbedded in paraffin using a one-gram Ra–Be sample as neutron source. To minimize effects of sample thickness, the fission counting rates were determined as a function of pulse height and extrapolated to zero pulse height. In addition, small corrections were made for the fission fragments totally absorbed in the sample.

To determine the U^{236} alpha-activity, collimated samples were measured in a grid-type ionization chamber associated with a 48-channel pulse height analyzer.[6] The pulse analysis results determined the fraction of the total alpha-activity which was due to U^{236}. The total alpha-activity was measured in a 2π argon-CO_2 pulse ionization chamber, and the counting rate determined by extrapolating the counting-rate curve to zero pulse-height. The counting efficiency of 51.3 percent was evaluated by measuring several alpha-emitting samples in the argon-CO_2 counter and also in a calibrated low geometry counter (geometry calculated from dimensions), where effects of sample backscattering were negligible.[7]

The results from the three samples are shown in Table II. The errors include standard deviations of the mass spectrometric measurements and pulse analyses, and estimated errors in extrapolating alpha and fission counting plateaus to zero pulse height and in the use of 51.3 percent counting efficiency.

The energy of the U^{236} alpha-particle was measured in the grid-type ionization chamber (with pulse-analyzer)[6] relative to standard samples containing alpha-emitters of known energy. Pu^{238}, Pu^{239}, Po^{210}, and U^{234} were used as the reference standards, the U^{234} being present in the U^{236}-containing sample. The samples were collimated to reduce effects of sample self-absorption and alpha-backscattering. The energies used are given in Table III. It was assumed that the energy-ionization curve was linear over the region considered. This assumption has been shown to be true in argon (the gas used in this chamber).[8,9] Since no attempt was made to measure the position of zero pulse height, the U^{236} energy was really determined relative to that of U^{234}, the other standards being used to determine the slope of the pulse height *versus* energy curve. Thus, an error in the U^{234} energy used will be reflected in an almost equal systematic error in the U^{236} alpha-energy. However, errors due to peak shifts from sample self-absorption are almost canceled, since the U^{234} peak is shifted by almost the same amount as the U^{236} peak. The average of nine measurements resulted in an alpha-particle energy value of 4.499 ± 0.004 Mev (mean deviation).

[5] We wish to thank M. G. Inghram and D. C. Hess (Argonne National Laboratory) and R. F. Hibbs (Y-12 Chemical Division Assay Laboratory, Carbide and Carbon Chemicals Corporation, Oak Ridge, Tennessee) for mass spectrographic analyses of the uranium samples.

[6] Ghiorso, Jaffey, Robinson, and Weissbourd, *The Transuranium Elements* (McGraw-Hill Book Company, Inc., New York, 1949), Paper No. 16.8, National Nuclear Energy Series, Vol. 14B, Division IV.

[7] A. H. Jaffey, "Radiochemical assay by alpha and fission measurements," National Nuclear Energy Series, Vol. 14A, Division IV, Chapter 16 (to be published).

[8] W. P. Jesse and J. Sadauskis, Phys. Rev. 78, 1 (1950).

[9] Jesse, Forstat, and Sadauskis, Phys. Rev. 77, 782 (1950).

The Magnetic Susceptibility of Zinc at Liquid Nitrogen Temperatures*

J. W. McCLURE† AND J. A. MARCUS
Department of Physics, Northwestern University, Evanston, Illinois

(Received July 20, 1951)

The magnetic susceptibility of zinc parallel to the hexagonal axis, χ_3, has been observed to be field dependent up to 85°K. The behavior of χ_3 at liquid nitrogen temperatures somewhat resembles the de Haas-van Alphen effect with the amplitude of oscillation sharply decreased and the maxima and minima displaced in field strength. The value about which χ_3 oscillates appears to be a constant approximately equal to -0.180×10^{-6} up to at least 63°K. Addition of 0.016 percent copper does not significantly change the results.

I. INTRODUCTION

PERIODIC variations of the magnetic susceptibility of bismuth with magnetic field strength were discovered at low temperatures by de Haas and van Alphen in 1930.[1] This phenomenon, called the de Haas-van Alphen effect, was found in zinc at liquid hydrogen temperatures in 1947.[2] The effect in zinc was further investigated at liquid helium temperatures by Mackinnon[3] and Sydoriak and Robinson.[4] It was previously found that the susceptibility was field dependent up to 64°K.[2] The present work consists of a more accurate investigation of the field dependence in the liquid nitrogen range.

The theory of the effect has been studied near absolute zero by Peierls,[5] Blackman,[6] Landau,[7,8] and Shoenberg[9] with some success but it is still unsatisfactory. As yet there is no theory covering the range of the present measurements.

II. PROCEDURE

In zinc the susceptibility parallel to the hexagonal axis, χ_3, is field dependent while the susceptibility perpendicular to the hexagonal axis, χ_1, is independent of the field strength except for field strengths greater than 9.5 kilogauss at liquid helium temperatures.[10] Also, χ_1 is independent of the temperature and equal to -0.150×10^{-6} up to about 100°K. Thus a convenient and sensitive procedure was to measure the differential susceptibility, $\Delta\chi=\chi_3-\chi_1$, using a torsion method. The specimen, a single crystal, was suspended in a uniform magnetic field and the resultant torque measured with a torsion balance, employing electromagnetic damping. This method allowed measurements of $\Delta\chi$ to an accuracy of one to three percent. The field strength was measured with a fluxmeter with an approximate error of 0.1 kilogauss. The temperature was measured with a thermocouple with an accuracy of about 1°K. After proper precautions were taken, no trace of ferromagnetic impurities was detected in either the specimen or the balance.

TABLE I. Values of magnetic susceptibility of zinc parallel to the hexagonal axis, χ_3, for low values of the magnetic field strength.

Temperature (degrees Kelvin)	$-\chi_3\times10^6$	Source
4.2	0.180	Sydoriak and Robinson[a]
14	0.182	Marcus[b]
20	0.176	Marcus
54	0.179	Present work
63	0.179	Present work
77	0.184	Present work
85	0.189	Present work

[a] See reference 4. [b] See reference 2.

III. RESULTS

Measurements were made on two specimens, both single crystals. One was of New Jersey Superpure zinc (99.999 percent purity) weighing 0.7650 g and the other was of zinc containing 0.016 atomic percent copper weighing 0.6932 g. The discrepancies between the two sets of measurements were of order of experimental error, indicating that, in contrast to

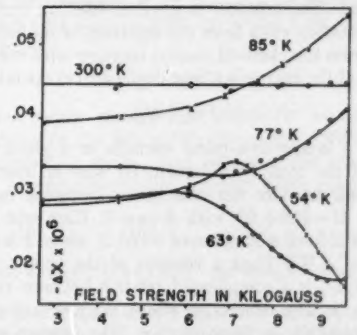

FIG. 1. Differential susceptibility of zinc, $\Delta\chi$, *versus* magnetic field strength in the direction of the hexagonal axis.

* Part of the work herein contained formed a portion of a thesis submitted by one of the authors (J. W. M.) in partial fulfillment of the requirements for the degree of Master of Science in Physics at Northwestern University.

† Now at the University of Chicago, Chicago, Illinois.

[1] W. J. de Haas and P. M. van Alphen, Comm. Phys. Lab. Univ. Leiden no. 212a (1930).

[2] J. A. Marcus, Phys. Rev. **71**, 559 (1947); **76**, 413, 621 (1949).

[3] L. Mackinnon, Proc. Phys. Soc. (London) **62B**, 170 (1949).

[4] S. Sydoriak and J. Robinson, Phys. Rev. **75**, 118 (1949).

[5] R. Peierls, Z. Physik. **80**, 763; **81**, 186 (1933).

[6] M. Blackman, Proc. Roy. Soc. (London) **A 166**, 1 (1938).

[7] L. Landau, private communication to Shoenberg, see reference 8.

[8] D. Shoenberg, Proc. Roy. Soc. (London) **A 170**, 341 (1939).

[9] D. Shoenberg, Nature **166**, 652 (1950).

[10] Verkin, Lazarev, and Rudenko, Dokl. Akad. Nauk. SSSR **73** (no. 1), 59 (1950).

bismuth, small amounts of nonferromagnetic impurities do not appreciably effect the field dependence.

In Fig. 1 $\Delta\chi$ is plotted against the component of the magnetic field strength in the direction of the hexagonal axis for the five temperatures investigated. It is seen that the field dependence persists up to at least 85°K. The variation of χ_3 with field strength in the region investigated is of order 0.01×10^{-6} while it is of order 0.05×10^{-6} at 20°K and 0.25×10^{-6} at 4°K. At 85°K χ_3 is of order 0.20×10^{-6} and $\Delta\chi$ is of order 0.05×10^{-6}. Thus at 85°K the variation is χ_3 in about 5 percent while the variation in $\Delta\chi$ is about 20 percent. As previous work at this temperature was done using the body force method, which gives a direct measurement of χ_3, it is not surprising that field dependence was not observed.

It would be desirable to have more data at higher field strengths to see if χ_3 performs the oscillations characteristic of the de Haas-van Alphen effect. Note that, in contrast to the effect at hydrogen and helium temperatures, the maxima and minima do not occur at the same field strengths for different temperatures. It would also be desirable to have more data between 85°K and 300°K in order to determine the point at which the field dependence disappears.

At helium temperatures χ_3 oscillates about the value which it approaches for low field strengths. Table I lists the average values of χ_3 found by other investigators and the low field (2.7 kilogauss) values found in the present work. It is seen that the low field value of χ_3 is approximately constant up to at least 63°K.

PHYSICAL REVIEW VOLUME 84, NUMBER 4 NOVEMBER 15, 1951

A Note on the Quantum Rule of the Harmonic Oscillator

L. M. YANG
University of Edinburgh, Edinburgh, Scotland
(Received February 3, 1951)

The purpose of the present note is to show, with the aid of an elementary example, that the commutation rules, which are usually given the rule of postulates in quantum mechanics, are in fact not arbitrary, provided that a more stringent definition of the Hilbert space and a strict expansion theorem are adopted.

I. INTRODUCTION

IN this note the following problem, which has been recently treated by Wigner,[1] is considered again. In the formulation of quantum mechanics, one often wonders whether it is possible to reverse the ordinary procedure, in which the commutation relations are first postulated as a generalization of the classical poisson bracket and then the equations of motion are deduced. The problem is whether one can derive the commutation rules from the equation of motion taken over from the classical theory, together with the postulate that the energy is a time displacement operator, i.e.,

$$\dot{f}=[f, H], \tag{1}$$

where f is any dynamical variable of a given system and H the total hamiltonian. By way of illustration, we shall consider the case of an harmonic oscillator where $H=\frac{1}{2}(x^2+\dot{x}^2)$ with $\hbar=\omega=1$. Here one notices that H is itself a function of x and $\dot{x}$, where $\dot{x}$ is defined by $\dot{x}=[x, H]$. Thus a relation of the type (1), with $f=f(x, \dot{x})$, is a complicated relation between the commutators. The conclusion which Wigner arrived at in this example is negative; i.e., the correct solution $[x, \dot{x}]=1$ does not follow uniquely. It will be shown in the present note that by properly formulating the conditions, including a more stringent definition of Hilbert space and a strict expansion theorem, the commutation rule will follow uniquely, though with less stringent definitions other solutions cannot be excluded.

It must be stressed that whether or not a state is physically permissible, cannot be seen clearly without referring to a special representation. Hence, it is the suitable boundary conditions in a special representation, laid down on physical grounds and in general being different for different systems, that serves to restrict wave functions to a certain special type, to include at the same time all permissible ones, and thereby to mark precisely the complete Hilbert space in which the state of the system is depicted and its operators apply.

For the oscillator one requires that the eigenvalues of x and $\dot{x}$ form continuous spectra and extend from $-\infty$ to $+\infty$, and that H be positive definite.[2] These restrictions do not suffice to mark completely the appropriate Hilbert space. For this purpose one has to impose restrictions on the energy eigenfunctions $\psi_n(x)$. Here we have, as is obvious on physical grounds, a natural boundary condition, i.e., $\psi_n(x)\to0$ as $x\to\pm\infty$ for all n.

[1] E. P. Wigner, Phys. Rev. 77, 711 (1950).

[2] It is then sufficient to deduce that H is discrete [see (10)].

We summarize the conditions for the deduction of the commutation rule in the case of the harmonic oscillator.

(a) Hamiltonian $H=\frac{1}{2}(x^2+\dot{x}^2)$

(b) Equation of motion $\ddot{x}+x=0$

(c) The complete Hilbert space for the system defined by the complete set of energy eigenfunctions $\psi_n(x)$ satisfying the boundary condition that $\psi_n(x)\to 0$ as $x\to\pm\infty$ $(-\infty<x<+\infty)$

(d) Superposition principle in the Hilbert space defined in (c). By (c) and (d) we require that any physically admissible state represented by a wave function satisfying the boundary condition in (c) shall be expansible in terms of the set of energy eigenfunctions. Here we need the stringent definition of the expansion theorem; for an arbitrary admissible wave function $f(x)$, we require that the expansion

$$\sum_{n=0}^{\infty} a_n\psi_n(x)$$

converges absolutely and uniformly to $f(x)$. If a less stringent definition is adopted, namely,

$$\sum_{n=0}^{\infty} a_n\psi_n(x)$$

converges to $f(x)$ only in the mean

$$\lim_{N\to\infty}\int_{-\infty}^{+\infty}|f(x)-\sum_{n=0}^{N}a_n\psi_n(x)|^2dx=0,$$

then we cannot rule out other possibilities than $[x,\dot{x}]=1$. These conclusions, however, cannot be reached without referring to the x-representation where a natural boundary condition can be laid down.

II. DEDUCTION OF THE COMMUTATION RULE

From (1) and (a) with $f=x$, it follows that

$$\dot{x}=[x,\tfrac{1}{2}\dot{x}^2]=\tfrac{1}{2}(\dot{x}[x,\dot{x}]+[x,\dot{x}]\dot{x}).$$

Introducing $S=[x,\dot{x}]-1$, one has

$$\{S,\dot{x}\}=0, \tag{2}$$

where the curly bracket is the anti-commutator. From (1) and (b), one has similarly

$$\{S,x\}=0. \tag{3}$$

From (2) and (3), it can easily be shown that

$$[S^2,x]=[S^2,\dot{x}]=0,\quad [S,H]=0$$

which shows that S is a constant of motion, and that S^2 is a real numerical constant.

In the x-representation, (2) becomes $(x'+x')\times\langle x'|S|x''\rangle=0$. Hence it follows that

$$\langle x'|S|x''\rangle=c(x')\delta(x'+x'') \tag{4}$$

where $c(x')$ is an arbitrary function of x', and the hermitian property of S requires that $c(x')=c^*(-x')$. Hence in the x-representation one can write

$$S=c(x)R, \tag{5}$$

where R is the reflection operator defined by

$$R|x\rangle=|-x\rangle. \tag{6}$$

From this representation of S, one obtains the explicit operational form of $\dot{x}$;

$$\dot{x}=-i\frac{d}{dx}+g(x)+i\frac{c(x)}{2x}R, \tag{7}$$

where $g(x)$ is real. It can be shown that the term $g(x)$ can be removed by properly choosing the phase factor in the x-representation. Using a star to denote the operator in the new representation, one has

$$\left(\frac{d}{dx}\right)^*=e^{-iv}\frac{d}{dx}e^{iv}=\frac{d}{dx}+i\frac{dy}{dx}$$

$$R^*=e^{-iv}Re^{iv}=e^{-2iv_-}R$$

where y is a real function of x, and y_- is the odd part of y. If for y one chooses $y=\int^x g(x)dx$, (7) becomes

$$\dot{x}=-i\left(\frac{d}{dx}\right)^*+i\frac{c'(x)}{2x}R^*,\quad c'(x)=c(x)e^{2iv_-}.$$

Dropping the stars and the dash, and with the help of (2), one can show that $c(x)$ is a numerical constant, thus obtaining

$$\dot{x}=-i\frac{d}{dx}+\frac{ic}{2x}R. \tag{8}$$

The next step is to set up the symbolic energy eigenstates by using the variables $\eta=(\dot{x}+ix)/\sqrt{2}$ and $\eta^*=(\dot{x}-ix)/\sqrt{2}$.[3] Following a similar argument to that usually used in the treatment of the harmonic oscillator, it can be shown that starting from the lowest state $|0\rangle$ characterized by

$$\eta^*|0\rangle=0 \tag{9}$$

one can obtain the excited states by successively multiplying on the left of $|0\rangle$, the energy difference of two neighboring states being always 1. The scheme of energy eigenstates and their corresponding eigenvalues are

$$\left.\begin{array}{cccccc} |0\rangle & , & \eta|0\rangle & , & \eta^2|0\rangle & , \cdots \\ \frac{1}{2}(1+cR_0), & & \frac{1}{2}(3+cR_0), & & \frac{1}{2}(5+cR_0), & \cdots \end{array}\right\} \tag{10}$$

where c is a real constant so far undetermined and R_0 is the eigenvalue of R in the ground state, being either 1 or -1. The condition that H is positive definite

[3] See P. A. M. Dirac, *The Principles of Quantum Mechanics* (Clarendon Press, Oxford, 1947), 3rd edition.

requires that

$$cR_0 \geq -1. \tag{11}$$

By using the result of (8) and (9), it is possible to investigate the ground state of the oscillator. For

$$\left\langle x\left|\frac{1}{\sqrt{2}}(\dot{x}-ix)\right|0\right\rangle=\left\langle x\left|\frac{i}{\sqrt{2}}\left(-\frac{d}{dx}+\frac{c}{2x}R-x\right)\right|0\right\rangle$$

or, writing $\psi_0(x)=\langle x|0\rangle$

$$\left(\frac{d}{dx}+x\right)\psi_0(x)=\frac{c}{2x}\psi_0(-x). \tag{12}$$

Here the condition (c) is used. It follows that the admissible solutions can be written in the form

$$\psi_0^{(\tau)}(x)=b_\tau x^\tau \exp(-x^2/2) \tag{13}$$

where $\tau=(-1)^{n/2}c/2$ and $b_\tau=(2^{\tau+1}/1\cdot 3\cdot 5\cdot(2\tau-1)\sqrt{\pi})^{\frac{1}{2}}$ is a normalizing constant. It should be noted that (12) is an eigenvalue problem; there exist solutions of (12) only for certain values of c. The spectrum of c and the corresponding ones of cR_0 and τ allowed by (11) are

$$\left.\begin{array}{lccccccc} c=0 & -2 & 4 & -6 & 8 & \cdots \\ cR_0=0 & 2 & 4 & 6 & +8 & \cdots \\ \tau=0 & 1 & 2 & 3 & 4 & \cdots \end{array}\right\} \tag{14}$$

The wave function of the nth excited state for any τ follows from (8) and (10)

$$\begin{aligned}\psi_n^{(\tau)}(x)&=\langle x|\eta^n|0\rangle \\ &=\left(\frac{i}{\sqrt{2}}\right)^n\left(-\frac{d}{dx}+x+\frac{c}{2x}R\right)^n\psi_0^{(\tau)}(x)N_n^{(\tau)}\end{aligned} \tag{15}$$

where $N_n^{(\tau)}$ is a normalizing factor

$$N_n^{(\tau)}=\underbrace{\{(1+2\tau)2(3+2\tau)4\cdots\}}_{n\text{ factors}}^{-\frac{1}{2}}.$$

Substituting (13) in (15) one obtains

$$\begin{aligned}\psi_n^{(\tau)}(x)=&\left(\frac{i}{\sqrt{2}}\right)^n N_n^{(\tau)}b_\tau x^\tau e^{x^2/2} \\ &\times\underbrace{\{\cdots(D+2\tau/x)D(D+2\tau/x)D\}}_{n\text{ factors}}e^{-x^2}.\end{aligned} \tag{16}$$

It becomes clear that for even n the lowest power in x in the expression (16) is always x^τ, and for odd n it is $x^{\tau+1}$, irrespective of the value of τ. The set $\psi_n^{(\tau)}(x)$ with $\tau\neq 0$ will vanish at $x=0$ for all n. That these sets with $\tau\neq 0$ do not meet our requirement (d) is obvious, when one considers the expansion of a permissible wave function that is finite at the origin, such as $\exp(-x^2/2)$.

$$\exp(-x^2/2)=\sum_{n=0}^{\infty}a_n^{(\tau)}\psi_n^{(\tau)} \tag{17}$$

where

$$\begin{aligned}a_n^{(\tau)}=&\left(\frac{i}{\sqrt{2}}\right)^n N_n^{(\tau)}b_\tau \\ &\times\int_{-\infty}^{\infty}x^\tau\underbrace{\{\cdots(D+2\tau/x)D(D+2\tau/x)D\}}_{n\text{ factors}}\exp(-x^2dx),\end{aligned}$$

which is zero when $(n+\tau)$ is odd, and finite when $(n+\tau)$ is even. The expansion in (17), therefore, ceases to hold at $x=0$, though they can be shown to converge in the mean. We have seen now that only the set $\psi_n^{(0)}$ meets all four requirements and that S must be a null operator.

III. DISCUSSION

It is seen that the deduction of the commutation rule in the case of the harmonic oscillator requires in particular "a suitable boundary condition to mark the appropriate Hilbert space" and "the strict expansion theorem." It is difficult to say that such a stringent expansion theorem should be rigidly followed in quantum mechanics. But once this is adopted, it has been found that this formulation of the quantum rule seems to hold for any nonrelativistic particle with a reasonable potential function expressible as a power series in x. A possible application of the present formulation is its connection with the second quantization of Bose particles. If the lagrangian of the field contains derivatives of the field variables higher than the second, it is no longer possible to derive the hamiltonian from the lagrangian as an explicit function of pairs of conjugate variables, but the former can only be brought into the form $\sum_\mu \psi_\mu^* F(D', D)\psi_\mu$ where ψ_μ are the field variables, D and D' operate on ψ_μ and ψ_μ^*, respectively, such that $D\psi_\mu=\dot{\psi}_\mu$ and $\psi_\mu^* D'=\dot{\psi}_\mu^*$, and F is an arbitrary function of D' and D. The definition $\dot{\psi}_\mu=[\psi_\mu, H]$ together with the equation of motion derived from the lagrangian is all that is needed to obtain quantization; any guess of the commutation rules among the field variables and their derivatives is redundant and may be quite wrong.

The writer wishes to express his sincere thanks to Professor M. Born for his advice and interest, and to Dr. K. C. Cheng for useful discussions.

Intensities of Heavy Cosmic-Ray Primaries by Pulse Ionization Chamber Measurements

JAMES A. VAN ALLEN*
State University of Iowa, Iowa City, Iowa and Applied Physics Laboratory, John Hopkins University, Silver Spring, Maryland
(Received August 2, 1951)

The results of two rocket flights of electron collection, pulse ionization chambers above the atmosphere are summarized and discussed. It is shown that the data provide limiting information on the absolute intensities of the heavy nuclei in the primary cosmic radiation. Additional confidence in the photographic emulsion estimates of these intensities by other workers is provided by the consistency of their results with the entirely independent ionization chamber measurements.

I. INTRODUCTION

THERE have been reported previously[1] the results of the flight of a bundle of four pulse ionization chambers above the appreciable atmosphere by means of a V-2 rocket (flight and data therefrom referred to by I). The present paper contains the results of a subsequent such flight (V-2 No. 48, fired on February 17, 1949) of an identical single ionization chamber arranged in the rocket in an environment much freer of surrounding material (referred to by II). The geomagnetic latitude of the flight was again 41°N (White Sands Proving Ground, New Mexico). It is shown how these ionization chamber measurements can be interpreted to provide limiting information on the absolute intensities of heavy nuclei in the primary cosmic-ray beam above the atmosphere. Related balloon flight data have been reported by Coor,[2] Whyte,[3] and McClure and Pomerantz.[3a]

II. EXPERIMENTAL

The ionization chambers and associated amplifiers used in both I[1] and II were made to be substantially identical to those of Bridge and Rossi,[4] with their kind assistance in matters of constructional detail, circuit diagrams, etc. The filling was argon at 5 atmospheres absolute pressure at 25°C purified over hot metallic calcium. The chambers were used throughout these investigations in a soldered off condition. They were found to retain their "electron collection" characteristics for at least two years. In our laboratory tests the ionization chamber-amplifier system was found to perform in the manner thoroughly described in reference 4. Hence, no further description is given here. An additional calibration feature in our ionization chambers was an arrangement of the thin polonium α-particle source so that it could be exposed to the active volume of the chamber only as desired. This made possible the use of a sufficiently strong source to give a significant over-all calibration of the system during selected intervals in the very brief time of a rocket flight without masking cosmic-ray bursts during the major portion of the flight.

The output of the fast amplifier was fed through a simple pulse stretcher to the Naval Research Laboratory pulse-time radio telemetering system, which was carried in the rocket for transmitting flight data to a ground receiving, decoding, and recording station. The ionization chamber record was thus finally obtained on the photographic film record of a fast string oscillograph, the film speed being about 7.5 cm/sec. The actual data reduction was done from a photographic print of the original record, the height of each pulse being measured individually and tabulated. In both flights I and II very clear records were obtained for the flight duration reported. The characteristic and easily recognizable pulse shape from the electronic pulse stretcher provided additional assurance of validity. A step-by-step calibration of the entire electronic system including the radio link and the ground station was made by an artificial pulse generator which gave pulses of known absolute height to the central wire of the ionization chamber. This calibration was made only prior to the flight. Laboratory experience with the system and special care in providing rocket-borne power supplies of considerably excess capacity were relied upon for maintenance of this calibration during flight. The extrapolated integral pulse amplitude of the Po—α distribution corresponded to 4.1 millivolts input to the amplifier for the chambers of flight I and 4.45 millivolts for flight II. This is not, of course, a fundamental quantity since it depends not only on the energy delivered to the central wire of the chamber from the collection of ionization electrons in the chamber but also on the electrostatic capacity of the central wire, the input capacity of the first tube of the amplifier, and the connecting lead. However, it is gratifying to note the satisfactory agreement with that to be expected from a crude measurement of the total input capacity and with that obtained by Bridge (private communication).

Because of the microphonism in the system during the noisy propulsion period of the rocket and because of the brief time involved in traversing the appreciable atmosphere (about 70 seconds), very little information of value was obtained within the atmosphere. It was only possible to discern a very rapid increase in burst

* Fellow of John Simon Guggenheim Memorial Foundation at Brookhaven National Laboratory, Upton, New York, summer, 1951.

[1] H. E. Tatel and J. A. Van Allen, Phys. Rev. 73, 87 (1948).

[2] T. Coor, Jr., Phys. Rev. 82, 478 (1951) and doctoral dissertation, Princeton University, August, 1948.

[3] G. N. Whyte, Phys. Rev. 82, 204 (1951).

[3a] G. W. McClure and M. Pomerantz, Phys. Rev. 79, 911 (1950).

[4] See, in particular, Bridge, Hazen, Rossi, and Williams, Phys. Rev. 74, 1083 (1948).

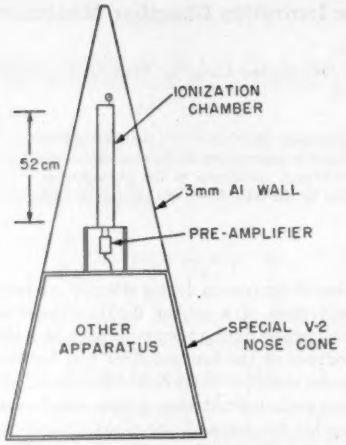

FIG. 1. Schematic arrangement of ionization chamber in nose of rocket in flight II.

rate with increasing altitude, being particularly marked above about 20 km. After the propulsion period, the noise level of the output fell to its typical laboratory level, or perhaps a bit less. There was no significant variation of burst rate above 40 km. *Rocket data in this paper are only those recorded in the "plateau" region above 40 km.* In flight I, 150 seconds of such data-time were obtained; in flight II, 238 seconds.

The physical arrangement of the four ionization chambers in flight I was such[1] that a typical particle trajectory traversed approximately 15 g/cm² of brass and iron before encountering the active volume of a chamber. In addition, a disk of lead occupied a restricted region forward of the bundle of chambers. (This situation does not, of course, correspond to the balloon situation at an atmospheric depth of 15 g/cm² where there is a considerably greater path length through the atmosphere of the trajectories of most primaries.)

The single chamber in flight II was located in the isolated forward tip of the 3-mm-thick aluminum nose cone of the rocket. It was mounted on light fiber supports and was well separated from other material. These precautions were taken in order to expose the chamber to the primary cosmic-ray beam with as little intervening material as reasonably practical. Figure 1 shows the arrangement schematically. An average primary traversed 4 g/cm² of brass and aluminum in reaching the active volume of the chamber.

III. IONIZATION CHAMBER BURST DATA OF FLIGHTS I AND II

The data of flight I are described in reference 1, to which the reader is referred.

In flight II, a clear telemetering record was obtained for 238 seconds at altitudes above 40 kilometers. Individual burst heights were measured and tabulated, as previously described. Figure 2 is a log-log plot of the observed number of bursts in the 238-second period as a function of ionization chamber output in millivolts. The plot is an integral one, each point representing the number of bursts observed to have height in excess of the plotted abscissa of the point. The vertical bars are of length twice the statistical probable error. Abscissas are accurate to ±0.1 millivolt. The extrapolated integral pulse height of the calibrating Po−α source is shown by the arrow at 4.45 millivolts.

For purposes of interpretation the smooth fitted curves to the data of flights I and II were replotted on a comparable basis. The ordinates of points on the curve of Fig. 2 of reference one were multiplied by the relative time-of-observation factor 238/150. A common scale of abscissa in units of one Po−α was established by using the respective polonium α-particle calibrations. Normalization was thus made on an absolute, not an arbitrary, basis. The resulting replot is shown in Fig. 3. Note that a semilogarithmic plot has been chosen for subsequent convenience of interpretation.

Curve III is discussed subsequently (Sec. V).

IV. BASIS FOR INTERPRETATION OF DATA

A. Causes of Bursts of Ionization

As originally pointed out by Coor[2] the bursts of ionization in a thin-walled chamber above the atmosphere are due to only two principal causes:

(a) Passage through the gas of the chamber of the charged products of nuclear disintegrations ("stars") produced by the primary radiation in the walls and gas of the chamber and in other material in the immediate environment.

(b) Direct traversals of charged primary particles without nuclear interactions. As will be shown later, the simultaneous passage of about sixty minimum ionizing singly-charged particles with a path length of one diameter of the chamber is required to yield a burst of

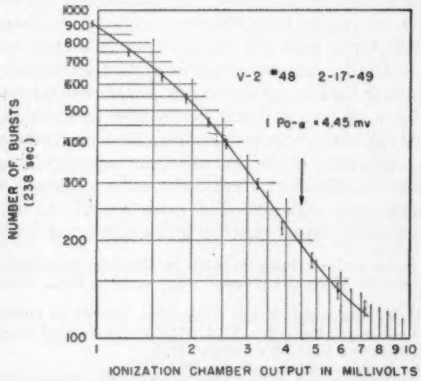

FIG. 2. Experimental integral burst height distribution above the atmosphere (flight II).

ionization equal to 1.0 Po$-\alpha$. Since the noise level of the system limited satisfactory pulse-height measurements to about 0.2 Po$-\alpha$, it is evident that our system was effective in recording direct traversals of only primaries having Z at least as great as 3.

B. Geomagnetic Considerations

At the geomagnetic latitude of flights I and II (41°N) the geomagnetic cutoff for primary charged particles is at least as great as $r_0=0.284$ störmers[5] in the vertical direction. With sufficient accuracy for present purposes this may be taken as the same over the upper hemisphere. The corresponding cut-off momentum p_0 is given by

$$p_0=59.4Zr_0^{-2}\ \text{Bev}/c. \quad (1)$$

Thus, p_0c/mc^2 is equal to 4.8 for protons and approximately 2.4 for all heavier (stripped) nuclei for which the atomic weight $A\approx 2Z$; mc^2 denotes the rest mass of the nucleus in question in units of Bev. Assuming a reasonable momentum spectrum of primaries and referring to Rossi and Greisen[6] it is seen that the expected rate of loss of energy by ionization is about 5 percent greater than minimum. This simplifying fact is applicable to all primary (stripped) nuclei at this latitude.

C. Distribution of Burst Heights due to Direct Traversals

Our ionization chamber can be idealized as being a cylinder of effective length (L) 52.0 cm and effective radius (R) 3.8 cm. The central wire is 0.032 cm in radius (a). The length/diameter ratio $(L/2R)=6.84$.

The first problem is to obtain the expected distribution of path lengths through this cylindrical chamber when exposed in a field of radiation, isotropic over one hemisphere, zero over the other—a satisfactory approximation for the present purpose. The integral path length distribution for a cylinder of diameter $2R$ and length infinite is found to be

$$G(l)=(2l/\pi R)\int_0^K[(2R/l)^2-\sin^2\theta]^{\frac{1}{2}}\sin^2\theta d\theta, \quad (2)$$

where K is arc $\sin(2R/l)$ or $\pi/2$, whichever is smaller. $G(l)$ is the expected fraction of path lengths greater than l, the length of that portion of the particle trajectory which lies within the boundaries of the cylinder. The integral on the right-hand side of Eq. (2) has been evaluated graphically. $G(l)$ is plotted as a function of $l/2R$ in Fig. 4. For $l/2R\gg 1$, Eq. (2) has the asymptotic form,

$$G(l)=0.25(l/2R)^{-2}. \quad (3)$$

Thus, it is seen that, for a chamber of infinite length, less than one traversal of a thousand has a path length longer than $l/2R=6.84$. Therefore, Eq. (2) can be accurately applied to the chamber used.

It is shown in reference 4 that if N ion pairs are produced in a localized group at distance r from the axis of a cylindrical electron collection ionization chamber, then the output voltage of the electron pulse is proportional to

$$Ne[\ln(r/a)/\ln(R/a)], \quad (4)$$

e being the electronic charge and a the radius of the central wire of the chamber. In the present case $R/a=120$. From a plot of function (4) and from consideration of the details of the derivation of Eq. (2), it was estimated that a gross factor of 0.9 could be satisfactorily applied to the pulse height expected from a path length, l occurring near the wall of the chamber to obtain the pulse height resulting from an average actual traversal, l.

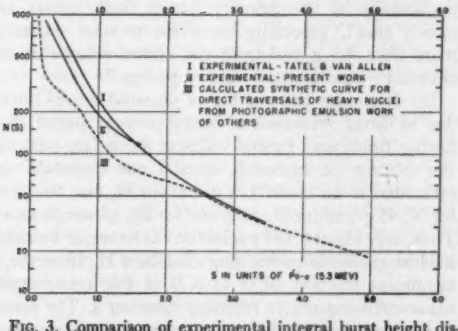
I EXPERIMENTAL - TATEL & VAN ALLEN
II EXPERIMENTAL - PRESENT WORK
III CALCULATED SYNTHETIC CURVE FOR DIRECT TRAVERSALS OF HEAVY NUCLEI FROM PHOTOGRAPHIC EMULSION WORK OF OTHERS
S IN UNITS OF Po-α (5.3 MEV)

FIG. 3. Comparison of experimental integral burst height distributions of flights I and II with each other (curves I and II, respectively) and with synthetic curve III, which shows the distribution expected from direct traversals of heavy primaries with intensities derived from Minnesota-Rochester emulsion data at other latitudes. Curves I, II, and III are independently on an absolute basis.

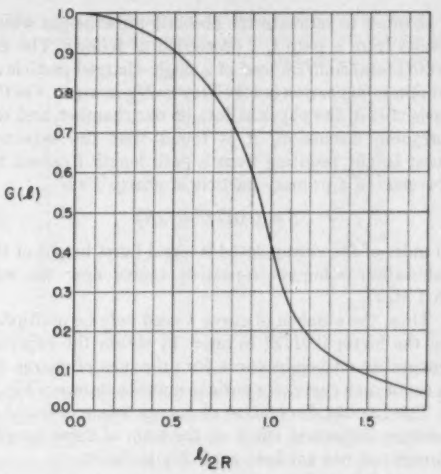

FIG. 4. The integral distribution of path length l through an infinitely long cylinder of radius R. Hemispherically isotropic directional intensity assumed.

[5] R. A. Alpher, J. Geophysical Research 55, 437 (1950).
[6] B. Rossi and K. Greisen, Revs. Modern Phys. 13, 240 (1941).

In order to estimate the absolute pulse height which results from a path l, I proceeded as follows. The expected total collision loss[6] of a singly-charged particle at minimum ionization is 1.49 Mev cm²/g in argon. On the basis of this, the physical data on our chamber, and the foregoing discussion, it is found that the expected burst height resulting from a path length l caused by traversal of a primary particle of charge Ze is

$$S=(0.017Z^2)(l/2R) \tag{5}$$

in units of the extrapolated integral burst height of the calibration polonium α-particle source near the wall (5.3 Mev).

Thus, the abscissa of curve 4 need only be multiplied by the factor $0.017Z^2$ in order to obtain the expected integral burst height curve for primaries of charge Ze. A set of such curves for various nuclei is shown in Fig. 5. The Landau fluctuation of energy loss was found to have no important effect on the form of these integral curves and has not been explicitly included.

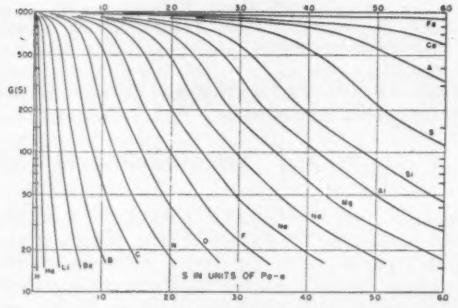

FIG. 5. Expected integral burst height curves for direct traversals of various nuclei through our ionization chamber. Scale of ordinates is arbitrary.

The total number of traversals per second through a cylinder of length L, radius R, exposed to a hemispherically isotropic directional intensity j, is

$$\pi^2RLj(1+R/L). \tag{6}$$

For the chamber used in this work (6) becomes $2092\,j$, where j is in units of (sec cm² steradian)$^{-1}$.

In the flight time of 238 seconds there will occur

$$4.98\times10^5\,j_Z \tag{7}$$

traversals of nuclei of charge Ze, whose absolute directional intensity is j_Z. Each of the relative pulse-height curves of Fig. 5 can be converted to an absolute basis by normalizing the intercept at $S=0$ to the value given by (7) for any assumed or known j_Z.

Such a curve is to be understood to represent the expected absolute number of bursts of height greater than S (occurring in our ionization chamber in 238 seconds) as a function of S, due to exposure to a hemispherically isotropic beam of primaries of charge Ze, directional intensity j_Z.

V. INTERPRETATION

A. Consideration of Fig. 3

Referring to the experimental curves I and II in Fig. 3, it is seen that II is markedly lower than I in the region of small bursts, i.e., $S<1.0$ Po$-\alpha$. From crude quantitative estimates it appears that this difference can be attributed in a reasonable way to a lesser number of nuclear stars produced in the vicinity of the chamber in flight II than in flight I. As pointed out in Sec. II, the environment of the chamber in flight II was much freer of surrounding material and, in fact, approached free space conditions. It seems impractical to account for the difference in the observed numbers of small bursts in a precise way due to the detailed complexity of the environment of chamber I and due to meager knowledge of the energy distribution, angular distribution, and nature of the secondaries emerging from the collision process.

The less rapid fall-off of curve II then curve I in the region $1.1<S<1.6$ appears to be definite (see plot of raw data in Fig. 2) and significant. Unfortunately, the choice of amplification in flight II was such as to favor measurements of smaller bursts. The amplitude limitations of the telemetering system did not permit height measurement of bursts larger than 1.6 Po$-\alpha$; they could be only counted and tabulated as being larger than this.

As will appear later, a large portion of these observed bursts of ionization was due to direct traversals of heavy primaries (see paragraph IV, A). The primary radiation passed through about 4 g/cm² of material to reach chamber II and about 15 g/cm² of material to reach chambers I. The additional material has two effects:

(a) Increases the number of bursts due to nuclear stars, mainly caused by H and He, due to their preponderance in the primary beam. Such bursts are mostly small,[2] especially those due to stars occurring more than 0.5 g/cm² from the active volume of the chamber—absorption of "heavy prongs."

(b) Decreases the number of (mostly larger) bursts due to direct traversals of heavy primary nuclei. Following Bradt and Peters[7] collision mean free paths in the mixture of materials around our chambers are estimated to be about 100 g/cm² for H, He; 60 g/cm² for N; 45 g/cm² for Si; 35 g/cm² for Fe, as sample cases. Thus, only about 0.1 of nuclei even as heavy as Fe suffer nuclear collisions in reaching chambers II. However, a significant fraction (0.35 to 0.2) of the heavy nuclei make collisions before reaching chamber I. The secondaries from such a collision will in general make a much smaller bursts of ionization in the chamber than would the unaffected primary, due to absorption of heavy prongs in intervening material, angular dispersal of intermediate energy secondaries, and a considerably

[7] H. L. Bradt and B. Peters, Phys. Rev. 77, 54 (1950).

lower value of $\sum_i Z_i^2$ for the energetic secondaries as compared to Z^2 for the primary.

For these reasons, curve II is the truer one to use in considerations of the composition of the primary beam. For $S>1.6$ Po$-\alpha$, curve I contains our only experimental data and will be used in this region of burst heights; but it must be expected that the portion of it due to direct traversals of heavy primaries is low by approximately 20 to 35 percent.

The foregoing appears to yield a reasonably satisfactory understanding of the comparative results from I and II. In the following, curve II is used for $S<1.6$ Po$-\alpha$, curve I is used (with the foregoing reservation) for $S>1.6$ Po$-\alpha$.

B. *A Priori* Upper Limits on Absolute Intensities of Primary Nuclei

The ionization chamber curves I–II can be immediately used to place upper limits on the absolute intensities of primary nuclei of various Z. This is done by comparing the differentiated versions of the curves of Fig. 5 (broadened by the Landau fluctuation) with corresponding differences from the experimental data. The crude results of this process are cited in Table I.[8]

TABLE I. *A priori* upper limits.

Element	$10^4 \times j_Z$(sec cm^2 sterad)$^{-1}$
H, He, Li, Be, B	No significant upper limit
C+N+O	10
$Z\geq 10$	3

C. Upper Limits Using Universal Abundances of Brown

An interesting analysis can be made by assuming that the primary cosmic-ray beam consists of a mixture of elements in accordance with the universal relative abundances of Brown.[9] Tables III and IV of reference 9 have been simplified for the present purpose (see Table II).

By superposition of curves of our Fig. 5, adjusted to the relative abundances of Table II, a synthetic curve is obtained which represents on an arbitrary scale of ordinates the expected burst height distribution in a chamber of the size of the one used but of zero wall thickness (no stars!). Normalization of this composite curve to the observed total primary intensity[10] at geomagnetic latitude 41°,

$$\sum_1^{\infty} j_Z = 730\times 10^{-4} \text{ (sec cm}^2 \text{ steradian)}^{-1},$$

yields values of j_Z lower by an order of magnitude for

TABLE II. Simplification of universal abundances of brown.

Z	Element	Relative atomic abundance (Si = 10,000)
1	H	3.5×10^5
2	He	3.5×10^7
6	C	8.0×10^4
7	N	1.6×10^5
8	O	2.2×10^5
10	Ne	3.7×10^4
12	Mg	8.9×10^3
14	Si	1.0×10^4
16	S	3.5×10^3
18	A	1.0×10^3
20	Ca	6.7×10^2
26	Fe	1.83×10^4
28	Ni	1.34×10^3

$Z\geq 6$ than those found by photographic emulsions flown in balloons. This clearly shows that the primary cosmic-ray beam does not exhibit nearly as high a $(H+He)/(Z\geq 6)$ abundance ratio as is indicated by astrophysical evidence on the chemical composition of universal matter. It might be taken to cast doubt on the astrophysical basis for the abundance of hydrogen and helium relative to heavier elements, if it were not for the fact that too little is known of the origin and propagation of cosmic rays to lead to the conclusion that the cosmic-ray beam should be a typical chemical sample of the universe—much less that the magnetic rigidity (momentum/charge ratio) spectrum of all nuclei should be the same, so that the chemical composition would be independent of geomagnetic latitude.

Results of some interest are obtained, however, if H and He in Table II be ignored and the residual synthetic burst height curve (Fig. 6) be placed at its maximum permissable height with respect to the experimental curves I–II of Fig. 3. This residual synthetic curve has a suggestive resemblance to I–II and yields the upper limits to the absolute intensities of elements of $Z\geq 6$ in the Brown mixture (see Table III). It may be noted that

$$j_6+j_7+j_8=6\times 10^{-4} \text{ (sec cm}^2 \text{ steradian)}^{-1} \quad (8)$$

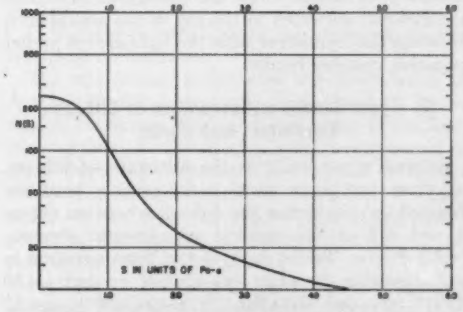

FIG. 6. Expected integral burst height curve for direct traversals of mixture of nuclei of $Z\geq 6$ in the relative abundances given by Brown. Scale of ordinates is arbitrary.

[8] Compare E. P. Ney and D. M. Thon, Phys. Rev. **81**, 1068, 1069 (1951).
[9] H. Brown, Revs. Modern Phys. **21**, 625 (1949).
[10] J. A. Van Allen and S. F. Singer, Phys. Rev. **78**, 819 (1950).

TABLE III. Upper intensity limits using Brown mixture for $Z \geq 6$.

Z	Element	$10^4 \times j_Z$ (sec cm² steradian)$^{-1}$
6	C	1.0
7	N	2.1
8	O	2.9
10	Ne	0.5
12	Mg	0.12
14	Si	0.13
16	S	0.05
18	A	0.01
20	Ca	0.01
26	Fe	0.24
28	Ni	0.02

for the C, N, O group; and that

$$\sum_{10}^{\infty} j_Z = 1.1 \times 10^{-4} \qquad (9)$$

for the $Z \geq 10$ elements.

D. Comparison with Results of Photographic Emulsion Workers

Estimates of the absolute intensities of heavy nuclei in the primary beam have been made by other workers[7,11] using balloon-borne photographic emulsions at latitudes 55°N, 51°N, and 30°N. Since about the same relative intensities of the various components were obtained by the two groups of workers at the widely different latitudes, an interpolated set of intensities at 41°N has been tentatively adopted by assuming an average set of relative intensities and by equating the total intensity to the rocket value 730×10^{-4} (sec cm² steradian)$^{-1}$ at 41°N. (Intensities of C, N, O were arbitrarily taken to be equal.) Table IV lists the results.

The dashed curve III in Fig. 3 is the synthetic burst height curve obtained from Table IV in the manner previously described.

It should be particularly noted that curve III is on an absolute scale entirely independent of the experimental burst height curve. Thus, it is seen that the interpolated photographic emulsion data of Table IV, deduced from records within the atmosphere at various latitudes and corrected to the top of the atmosphere, are altogether consistent with the independent rocket ionization chamber results.

E. Upper Limits on Intensities of Lithium, Beryllium, and Boron

Extreme upper limits on the intensities of lithium, beryllium, and boron nuclei in the primary beam are obtained by considering the difference between curves II and III at the smallest experimental abscissa, $S = 0.2$ Po$-\alpha$. Taking each of the three elements in turn, assuming the other two absent, we find $j_3 < 80 \times 10^{-4}$ (sec cm² steradian)$^{-1}$; $j_4 < 14 \times 10^{-4}$; $j_5 < 12 \times 10^{-4}$. Or assuming all three elements present simultaneously with equal intensities (in addition, of course, to the elements of Table IV) we find

$$j_Z < 6 \times 10^{-4}, \quad Z = 3, 4, 5$$

or

$$\sum_{3}^{5} j_Z < 18 \times 10^{-4}.$$

It may be worth recalling that these results come from an ionization chamber above the appreciable atmosphere with effective wall thickness 4 g/cm² of brass and aluminum. The intensity figures given in this paragraph are nonetheless extreme upper limits since it will be shown in the next paragraph that even under these conditions the entire difference between curves II and III of Fig. 3 can be attributed in a reasonable way to nuclear stars ("wall effect").

Thus, no argument can be given for the existence of Li, Be, and B in the primary cosmic-ray beam at 41°N with *any appreciable intensity*.

F. Difference Between Curves II and III in Fig. 3

Finally, the difference between curves II and III at the smallest observed pulse height, $S = 0.2$ Po$-\alpha$, is seen to be 540 bursts compared to a total of some 36,000-particle traversals (mostly H and He). By detailed numerical calculation the weighted average thickness of material traversed by a particle in reaching the active volume of the ionization chamber was found to be 4 g/cm² of brass and aluminum. The process of averaging is justified by the fact that the greatest thickness is a small fraction of a mean free path for nuclear interaction. Thus it is found that the mean free path of the primary radiation for producing a burst of ionization greater than 0.2 Po$-\alpha$ (1.1 Mev) in the walls and immediate surroundings of our chamber is about 270 g/cm². This is seen to be reasonable by comparison with the mean free path corresponding to geometrical cross section—about 100 g/cm².

In the thick "walled" chamber (curve I) there is an "excess" of 640 bursts larger than 0.32 Po$-\alpha$. The resulting higher value of experimental mean free path corresponding to the "wall" thickness of 15 g/cm² is presumably due to the larger value of S, to geometrical

TABLE IV. Intensities at 41°N, from references 7, 10, and 11.

Element	Relative intensity		Absolute intensity	
H	4000		582×10^{-4} (sec cm² steradian)$^{-1}$	
He	950		138	
C	11	33	1.6	4.8
N	11		1.6	
O	11		1.6	
Na, Mg, Al, Si	6.0	9.3	0.88	1.4
S, A, Ca	2.3		0.34	
Fe	1.0		0.14	
			730	Total

[11] Ney, Oppenheimer, and Freier, Proceedings Echo Lake Cosmic-Ray Symposium, June 23–28, 1949, Paper No. 59, p. 229.

considerations (angular dispersal of secondaries), and to absorption of lower energy secondaries from nuclear events occurring in the more distant portions of the environment, which account for the major portion of the 15 g/cm².

If the albedo radiation above the atmosphere is also of star-producing character then the afore-quoted experimental mean free paths become considerably larger. At any rate there is seen to be no difficulty in accounting for the difference between curves II and III in a crude quantitative way.

The conclusions of Tatel and Van Allen[1] must be modified in the light of the present analysis. Thus, there are only some 45 bursts larger than 1.5 Po$-\alpha$ (8 Mev) which are attributable to stars in the wall of chamber II. This corresponds to a zero pressure intercept on the upper curve of Fig. 3 of reference one of only 680 bursts/hour—considerably lower than the raw value of 1850 bursts-hour. Therefore, a transition flattening of the curve near the top of the atmosphere is indicated in preference to the rapid fall-off of the originally reported raw data. This is in harmony with the recent definitive measurements of Whyte[3] at lower latitudes, who shows that ionization chamber bursts lower in the atmosphere are the result not only of residual primaries, as suggested in reference one, but also of secondary nucleons in the nucleonic cascade. There is now, of course, a large body of evidence leading to this expectation.

The number of star-generated bursts of height $S>1.6$ Po$-\alpha$ (difference between curves I and III) is of uncertain magnitude due to important upward corrections of curve I to account for collision and resulting burst height degeneration of heavy nuclei in the thick surroundings of chamber I (see paragraph V-A).

VI. FURTHER POTENTIALITIES OF THE IONIZATION CHAMBER METHOD

The way in which ionization chamber measurements above the atmosphere can be interpreted to yield limiting information on the intensities of heavy nuclei in the primary cosmic radiation has been emphasized. It appears, however, that the same technique can be used to not only limit but also *determine* the values of these intensities. Certain improvements in arrangement of apparatus are needed in order to accomplish this—

(a) Better collimation of the measured beam to reduce the geometrical spread in path length. The intrinsic Landau fluctuation of energy loss places a limit to profitable collimation. It appears that the resolution in Z can be made similar to that of the photographic emulsion,[7,12,13] with much less laborious data reduction.

(b) Further reduction of effective wall thickness of the ionization chamber in order to reduce the number of bursts due to nuclear stars. A wall thickness of less than 0.7 g/cm² of brass is readily possible.

The ionization chamber technique is well adapted to measurements at various geomagnetic latitudes for the purpose of obtaining the momentum spectrum of heavy primaries—

(a) The data can be transmitted by radio telemetering. This obviates the necessity of physical recovery and the very considerable attendant difficulties at other than well-established bases of operation.

(b) The large geometrical factor of an ionization chamber makes it possible to obtain satisfactory measurements with only a relatively short time at "altitude."

(c) Directional intensity measurements can be restricted to the near vertical direction. If balloon flights are used, there is a considerable reduction in the uncertainty in the correction to the top of the atmosphere as compared with correction of the omnidirectional intensity.

The scintillator technique of Ney and Thon[8] is the same in principle as that of the ionization chamber. It has less noise level limitation for the measurement of small bursts; but it appears very difficult to reduce the effect of nuclear disintegrations in the apparatus, due to their occurrence in the detector itself and due to the intrinsic necessity of a sizeable amount of solid (or liquid) material as the detector.

VII. CONCLUSIONS

A. Using data from two rocket flights of pulse ionization chambers above the atmosphere, it has been shown how limiting information on the absolute intensities of the heavy nuclei in the primary cosmic-ray beam can be obtained in a manner entirely independent of previously used photographic emulsion methods.

B. Additional confidence is given to the photographic emulsion results of other workers by the consistency of their results with those of the ionization chamber method.

C. Further potentialities of the ionization chamber technique are indicated.

The experimental rocket work was conducted at the Applied Physics Laboratory, Johns Hopkins University, Silver Spring, Maryland, and at the White Sands Proving Ground, New Mexico, with the support of the Navy Bureau of Ordnance. The author is particularly indebted to his colleagues at the A.P.L., L. W. Fraser and R. O. Ostrander, for a large share of the work in preparing the apparatus, conducting flight II, and reading the telemetering record.

He is also indebted to the John Simon Guggenheim Memorial Foundation for personal support and to the Brookhaven National Laboratory for its hospitality.

[12] H. L. Bradt and B. Peters, Phys. Rev. 80, 943 (1950).
[13] Dainton, Fowler, and Kent, Phil. Mag. 42, 317 (1951).

The Effect of Inhomogeneities on the Electrical Properties of Diamond

A. J. AHEARN
Bell Telephone Laboratories, Murray Hill, New Jersey
(Received August 1, 1951)

To account for the non-uniformities in the electrical properties of diamond, particularly those observed in bombardment conduction, the proposal is made that the well-known lattice imperfections are not distributed homogeneously in the physical crystal, and that the resulting fluctuations in the height of the energy bands relative to the Fermi level might produce interspersed "pools of mobile charge" separated by barriers within the diamond. These pools and barriers should lead to dielectric losses at high frequencies. A single conducting channel, in series with a barrier, could be represented by a series resistance R_s and capacity C_s or by the equivalent parallel resistance R_p and capacity C_p.

With some, but not all, diamonds measurable dielectric losses at 70 mc/sec were observed. R_p varied from 5×10^9 ohms, the limit of measurement, to 4×10^8 ohms. Furthermore, the proposed model suggests that, in some cases, these barriers might be sufficiently lowered to establish a dc conducting channel all the way through a crystal. With a few of the lossy diamonds precisely this phenomenon of "high conduction" has been observed, in which a resistance of the order of a megohm is obtained with a dc voltage applied. This current appears abruptly in time but it lags behind the application of the voltage. This lag is influenced by irradiation with light or alpha-particles or by previous treatment.

The proposed pools of mobile charge are a sufficient but not necessary description of the dielectric loss observations, but the high conduction phenomenon lends further support to this idea of conducting channels with barriers in lossy diamonds. Such localized conducting channels would introduce inhomogeneities into an otherwise uniform electric field applied across an insulator. In bombardment conduction, measurements of counting efficiency could be very sensitive to field inhomogeneities.

Under alpha-particle bombardment a large variation in counting efficiency over the surface of typical diamonds is shown. In a group of 20 diamonds, most of those that exhibited definite losses also had high ($\geq$25 percent) counting efficiencies in some region, and the majority of the remainder had low counting efficiencies. These experiments lend further support to the suggestion that inhomogeneous fields at least partially account for the inhomogeneities in bombardment conduction.

Serious errors in the normal estimates of range and mobility of electrons or holes in insulators can be introduced by neglecting these field inhomogeneities.

1. INTRODUCTION

IN studying the properties of diamond only the ideal valence bonded diamond structure which is perfectly periodic and perfectly uniform is usually considered. However, the literature contains many examples of inhomogeneities in the electrical and optical properties of diamond. They appear not only as variations from specimen to specimen but also as variations within small specimens.[1–6]

This paper reports experiments which show inhomogeneities in bombardment conduction and other electrical properties of diamond. When a potential difference is applied across a diamond of a given thickness one usually assumes that the field is the same at all points within the diamond. However, the experiments lead to the conclusion that in many diamonds this probably is not true; that on the contrary, the field may vary considerably from point to point. Consequently in certain regions, most of the potential drop may be localized within a distance small compared with the crystal thickness. In many cases this region where the potential drop is localized may be at or near the crystal surface. This paper presents the results of three different and independent experiments, none of which prove the validity of this conclusion but all of which strongly suggest that these field inhomogeneities frequently do occur. They are thought to be the result of an electrical conductivity that varies from region to region in the diamond.

2. DIELECTRIC LOSS EXPERIMENTS

2a. Introduction

The ideas that led to these experiments are as follows. Assume that the physical crystal contains lattice imperfections and chemical impurities and that they are not homogeneously distributed through the crystal. Wannier[7] and also James[8] showed that in an insulator, fluctuations in the height of the conduction and filled band relative to the Fermi level would be introduced by localized lattice imperfections. In extreme cases electrons would be introduced into the hollows of the conduction band or holes into the hills of the filled band depending on the sign of the charge of the imperfections. Thus there is the possibility of "pools of mobile charge" or "conducting channels" within the insulator and separated by barriers, and in the simplest case these channels and barriers could in turn be represented by a resistance R_s in series with a capacity C_s. Furthermore in an ac field, dielectric losses should appear and should depend on the frequency in a predictable way. The model of a series resistance and capacity R_s and C_s to represent the proposed conducting channels and barriers is equivalent to the parallel combination R_p and C_p (see Fig. 1) where R_p varies with the frequency f

[1] G. R. Rendall, Proc. Indian Acad. Sci. **19A**, 293 (1944); **24A**, 168 (1946).
[2] D. E. Blackwell and G. B. B. M. Sutherland, J. Chim. Phys. **46**, No. 1–2, 9–15 (1949).
[3] Robertson, Fox, and Martin, Trans. Roy. Soc. (London) **232A**, 463 (1934).
[4] C. V. Raman, Proc. Indian Acad. Sci. **19A**, 199 (1944).
[5] A. J. Ahearn, Phys. Rev. **73**, 1113 (1948).
[6] K. Achyuthan, Proc. Indian Acad. Sci. **24A**, 162 (1946).
[7] G. H. Wannier, Phys. Rev. **76**, 438 (1949).
[8] H. M. James, Science **110**, 254 (1949).

as follows.

$$R_p = R_s[1+1/(2\pi f R_s C_s)^2]. \quad (1)$$

This suggests measurements of dielectric loss in diamonds.

2b. Results

Typical results for one diamond are shown in Fig. 1. The experimental points give the measured values of R_p as a function of the frequency of the electric field. The data satisfy a straight line of slope -1.1 up to about 20 mc/sec. Above this frequency the vast majority of the points fall above this line indicating the approach of R_p to R_s which is independent of f. The dashed line represents Eq. (1) fitted to the experimental data. Considering the simplicity of the model represented by the dashed line, this fit is not bad. Perhaps the equivalent series resistance and capacitance consists of two or more such arrays with different time constants.

Losses like this were observed with about 13 out of a group of 20 diamonds studied. R_p at 70 mc/sec varied from 5×10^6 to 4×10^5 ohms. No losses[9] could be detected with the other 7 diamonds. Probe tests with some diamonds showed that at least a substantial part of the loss was localized within a small region of the crystal.

As most models of dielectric loss lead to a relation of this type, an explanation in terms of conducting channels and barriers is not unique. However, further experimental evidence presented in Sec. 3 suggests that this explanation is at least a reasonable one.

3. HIGH CONDUCTION EXPERIMENTS

3a. Introduction

The experimental support for the proposed conducting channels given by the dielectric loss measurements leads to the following possibility. Wannier and James pointed out that the aforementioned fluctuations in the band structure tend to be smoothed out when electron hole pairs are introduced as in photoconduction or bombardment conduction. This introduces the possibility that in this smoothing process a channel through the crystal might be established along which the conduction band approaches sufficiently to the Fermi level of the conducting electrode at the cathode insulator interface to allow electrons to pass from one electrode into the insulator crystal and out through the other.

This suggests that in extreme cases, a diamond crystal might pass a dc current far greater than that which is characteristic of the low intrinsic conductivity of diamond. Precisely this "high conduction" phenomenon was observed as described below.

3b. Results

In this section data and observations are presented on the high conduction current that appears in a few of the diamonds in which dielectric losses appear. Thus far this high conduction phenomenon has not been observed with diamonds in which no dielectric losses were observed. After a dc field of 10,000 to 20,000 volts/cm is applied to some of these lossy diamonds the resistance drops abruptly from the order of 10^{13} ohms to the order of a megohm. This occurs in some specimens even though they are in complete darkness. Once this high conduction current is initiated, it can be maintained with any specimen in complete darkness merely by maintaining a minimum field of several thousand V/cm.

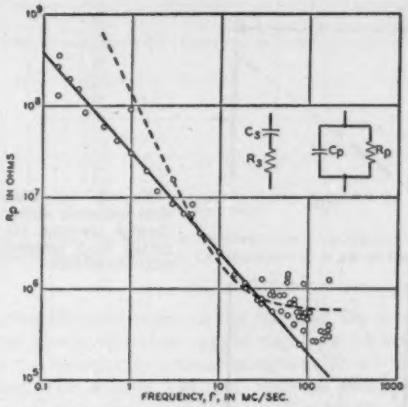

FIG. 1. Dielectric loss in diamond. Equivalent parallel resistance vs frequency of ac field.

Figure 2 shows how this high conduction current for a given diamond varies with the dc voltage. The points scatter widely. The current varies rapidly with voltage, dropping to zero at three to four hundred volts. Data for other diamonds are only qualitatively like this. For instance, in other specimens the current might persist to a lower voltage and might rise more rapidly or less rapidly with increasing voltage.

One of the characteristic features of this phenomenon is that while it appears abruptly there is a time lag or delay between the setting up of the necessary external conditions and this abrupt appearance. In some cases time lags of many minutes occurred. There is considerable variation in the amount and kind of external stimulation that is necessary to initiate high conduc-

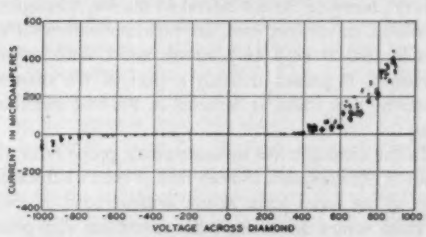

FIG. 2. High conduction in diamond. Dc current vs voltage.

[9] This indicates that negligible electrode losses are involved in these tests.

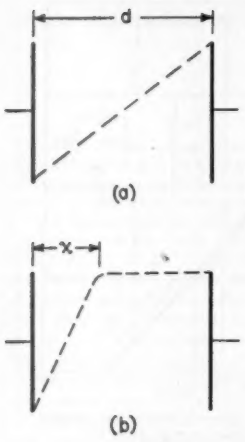

FIG. 3. (a) Potential drop uniformly distributed through insulator. (b) Potential drop concentrated near one surface.

tion. After the application of a field of 10,000 to 20,000 volts/cm, high conduction appears in some diamonds even though they are in total darkness. With other diamonds, bombardment with polonium alpha-particles or with white light while this field is applied, is necessary to establish this high conduction. With other lossy diamonds it was never observed. The time lags of many minutes already mentioned were observed under alpha-bombardment with a diamond in a high vacuum. This clearly demonstrates that we are dealing neither with a surface leakage nor a gas discharge. The time lag does suggest that an activation process is necessary to establish this dc conducting channel all the way through the crystal.

This high conduction current is not a case of dielectric breakdown since there appears to be no permanent change in the diamond. When the voltage is reduced to zero for more than a few seconds, the high conduction current does not reappear as soon as the voltage is turned on; it reappears only after the usual time lag.

This high conduction current is quite localized. This was first revealed by a minute fluorescent spot on the diamond and was later confirmed with a probe electrode. Many of the diamonds on which this report is based, have one or more internal cracks or flaws which in general, however, do not extend all the way through the specimen. In one specimen, this high conduction current was located at such an internal crack. With another specimen, it passed through a part of the diamond where no flaw could be detected at 200-fold magnification.

In the dielectric loss measurements, probe tests with some of the diamonds showed that at least a substantial part of the losses occur in the neighborhood of cracks in these stones. However, other specimens with prominent cracks were loss free.

4. ALPHA-BOMBARDMENT CONDUCTION EXPERIMENTS

4a. Introduction

The dielectric loss measurements lend support to the general idea of conducting channels with interspersed barriers. Furthermore, the measurements indicate that the series resistance R_s is as low as the order of a megohm. The high conduction experiments furnish additional support not only to the general idea of conducting channels but also to the megohm value by demonstrating that such values can be obtained sometimes in dc experiments. Now such localized conducting channels would introduce appreciable inhomogeneities in an electric field applied across a diamond.

The effect of these field inhomogeneities on measurements of bombardment conduction is shown in Fig. 3. In the usual analysis, a potential V applied to an insulator of thickness d is assumed to give the uniform field indicated by the potential distribution shown by the dashed line in the upper sketch in Fig. 3. When an electron is released by impact of an alpha-particle the conduction is determined by the range ω. The quantity measured by the amplifier is the normalized range Ω. It is proportional to the fraction of the anode cathode voltage that is traversed by the electron and is given by the relation

$$\Omega = \omega/d = \mu FT/d = \mu TV/d^2, \qquad (2)$$

where μ is the mobility, F is the applied field, T is the free time in conduction band, and V is the potential applied.

Thus an electron released near the cathode must travel completely through the crystal to the anode in order to produce the optimum response in the amplifier.

Suppose now that in some region of this crystal there is one of the proposed conducting channels and

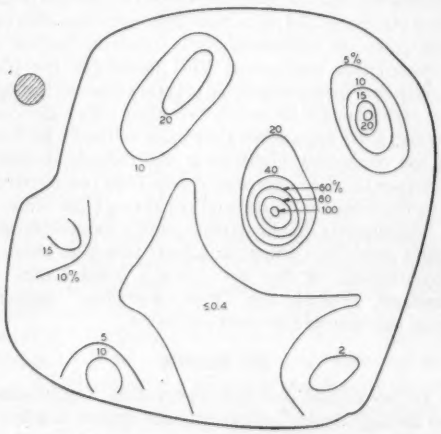

FIG. 4. Alpha-conduction in diamond. Counting efficiency inhomogeneities for electron pulses.

that in its neighborhood the potential distribution is altered to that indicated in the lower sketch of Fig. 3. Here most of the potential drop is localized in a layer of thickness x at the surface of the diamond. An electron released near the surface need only have a range ω equal to x in order to produce the optimum response in the amplifier. Moreover, in this region the field acting on the electron is substantially larger than in the above uniform field case. Consequently Eq. (2) becomes

$$\Omega=\omega/x=\mu TF/x=\mu TV/d^2(d/x)^2. \qquad (3)$$

Thus the quantity which the amplifier measures is magnified by the square of the factor d/x introduced by this field inhomogeneity. Therefore in alpha-bombardment conduction, a measurement of counting efficiency (in which all values of Ω above some preset value are registered) would be very sensitive to field inhomogeneities. It should be high when the field near the bombarded surface is high and when the field is low the counting efficiency should be low. This leads to measurements of counting efficiency in alpha-bombardment conduction, the details of which are described in the sections immediately following.

4b. Results

Some of the results were shown in Fig. 4. Here a diamond (9*B*) is manually scanned with a narrow beam of alpha-particles, the diameter of which is shown by the shaded disk. The contour lines show how the counting efficiency varies in different parts of the crystal. Here the electrode at the bombarded face is the cathode. Consequently the current pulses initiated by the alphas are electron pulses.

These scanning experiments revealed a wide range of counting efficiencies. In Fig. 4 the values vary from zero to 100 percent. With only minor exceptions, the same relative peaks and valleys of Fig. 4 appeared in the same positions when positive hole pulses were counted. The spread in this case was from zero to 71 percent. Figure 4 clearly demonstates that the over-all response is largely contributed by a very localized area. A large internal crack is located in this region of the diamond and it is here that the dielectric loss and high conduction current are located.

Variations in counting efficiency like those shown in Fig. 4 are not exceptional; they are the general rule. Field inhomogeneities could constitute an important factor[10] in accounting for these variations by assuming that the peaks of high counting efficiency are regions where the field is high and that at the region of zero counting efficiency the field is very low.

Measurements of counting efficiency and dielectric loss on about twenty diamonds are shown in Fig. 5. The value plotted on the ordinate is that of the highest

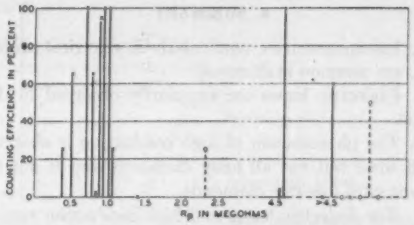

FIG. 5. Alpha-conduction in diamond. Counting efficiency vs equivalent parallel resistance. (× measured C.E., 0 estimated C.E.)

counting efficiency region of the diamond. On the abscissas R_p the equivalent parallel resistance calculated from the dielectric loss measurements at 70 mc/sec is plotted. The smallest loss that could be detected in these experiments corresponds to $R_p=5\times10^6$ ohms approximately. Consequently the points to the right of this value are for diamonds in which no loss was observed.

The large majority of the diamonds showing measurable losses have a relatively high counting efficiency. Similarly the large majority of those that show no dielectric loss have zero counting efficiency. Among the lossy diamonds an enhanced field could account for the high counting efficiency cases and a depressed field could explain the low ones. Among the diamonds with which losses were not detected there are a couple of exceptions to the general rule of zero counting efficiency. This probably indicates another factor favorably affecting the bombardment conduction in these cases. The over-all correlation between losses and counting efficiency suggests that inhomogeneous fields occur and account at least in part for these observed counting efficiency variations, variations that appear not only from specimen to specimen but also in different parts of a given specimen.

F. FIELD INHOMOGENEITIES AND MEASUREMENTS OF RANGE AND MOBILITY IN DIAMOND

None of these experiments on dielectric loss, high conduction and bombardment conduction prove the existence of the proposed field inhomogeneities but all of them suggest that such inhomogeneities do frequently occur in diamond. Such field variations would have an important influence on determinations of the numerical values of the range ω and the mobility μ of electrons or holes in insulators like diamond. This is best shown by referring to Fig. 3 and Eqs. (2) and (3) of Sec. 4. In the homogeneous field case shown in Fig. 3 a calculation of range ω using Eq. (2) would be in error by the factor $(d/x)^2$. Thus serious errors in the normal estimates for the values of range and mobility of electrons and holes in insulators can be introduced by neglecting these field inhomogeneities.

[10] Inhomogeneities in the density of electron traps or positive hole traps may still be an important factor influencing counting efficiency variations.

6. SUMMARY

1. Inhomogeneities, particularly in electrical properties, are common in diamond.

2. Dielectric losses are frequently observed in diamond.

3. The phenomenon of high conduction is observed with some but not all lossy diamonds and is not observed with loss free diamonds.

4. The dielectric losses and high conduction suggest that conducting channels frequently occur. Such channels would introduce inhomogeneities in an electric field applied across an insulator.

5. In alpha-bombardment conduction the variation in counting efficiency in different regions of a given diamond are readily explained in terms of field inhomogeneities.

6. Most diamonds that exhibit definite losses have a high counting efficiency in some region. Most of the loss free diamonds have very low counting efficiencies. This suggests that inhomogeneous fields at least partially account for variations in bombardment conduction.

7. Serious errors in the normal estimates of range and mobility of electrons or holes in insulators can be introduced by neglecting these field inhomogeneities.

The careful assistance of Mr. R. A. Maher has been a great help in carrying on this work for which the author is very grateful. Many thanks are tendered to Dr. K. G. McKay for invaluable assistance particularly in the interpretation of data.

PHYSICAL REVIEW VOLUME 84, NUMBER 4 NOVEMBER 15, 1951

Experiments with Audiofrequencies on Superconductors*

B. SERIN, C. A. REYNOLDS, J. R. FELDMEIER,† AND M. P. GARFUNKEL‡
Physics Department, Rutgers University, New Brunswick, New Jersey
(Received August 3, 1951)

Experiments are described in which alternating and direct currents are superimposed on tin wires in the superconducting state. As the amplitude of the ac is increased, the average PD goes through a maximum and approaches an asymptotic value. The experimental curves agree with calculated curves for low frequency ac (<50 cycles/sec). However, as the frequency is increased the curves change in character. The maxima increase in height and occur at large values of the ac. It is shown that this anomalous behavior can be traced to the ac skin effect, and it is concluded that experiments of this type are not suitable for a determination of the relaxation time in the phase transition from the superconducting to the normal states.

1. INTRODUCTION

LAZAREV, Galkin, and Khothevich[1] have studied the behavior of thallium wires carrying high frequency alternating currents of such amplitude as to induce a phase transition between the superconducting and the normal states. The general concept of the experiment is found in the earlier work of Silsbee, Brickwedde, and Scott.[2] It consists in superimposing direct and alternating currents on a superconductor and measuring the average potential difference as a function of the amplitude of the ac. Lasarev and co-workers believed that a study of this relationship at low and at high frequencies could be used to determine the relaxation time in the phase transition of a superconductor. Recently, Pippard[3] has shown theoretically that it is reasonable to expect that the kinetics of the phase transition is basically governed by the electromagnetic effects accompanying the penetration of the magnetic field into the normal conducting metal.

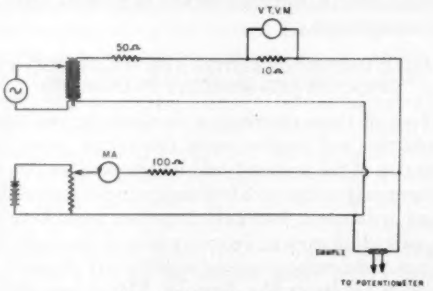

FIG. 1. Measuring circuit.

We have repeated the experiments of Lasarev *et al.*, with tin wires and have found that at quite low frequencies the electromagnetic effects, which can be represented by the usual ac skin penetration, greatly influence the experimental results, thereby making dubious an interpretation in terms of a relaxation time. The bulk of this paper is devoted to presenting the

* This work has been supported by the joint program of the ONR and AEC, the Rutgers University Research Council, and the Radio Corporation of America.

† Associated with us during 1947 and 1948. Now at College of Saint Thomas, St. Paul, Minnesota.

‡ Present address: Westinghouse Research Laboratory, East Pittsburgh, Pennsylvania.

[1] Lasarev, Galkin, and Khothevich, Compt. rend. acad. sci. U.R.S.S. 55, 805 (1947).

[2] Silsbee, Brickwedde, and Scott, J. Research Natl. Bur. Standards 20, 109 (1938).

[3] A. B. Pippard, Phil. Mag. 41, 243 (1950).

experimental results, to supplement the brief reports already presented.[4]

2. APPARATUS

The circuit used to provide the superimposed alternating and direct currents is shown in Fig. 1. The alternating current was supplied by a Hewlett-Packard audiofrequency oscillator capable of delivering 5 watts into a matched load, and the magnitude of the current was measured by a Ballantine electronic voltmeter shunted by a standard resistance provided with the voltmeter.

The potential differences developed across the wires were measured with a Rubicon microvolt potentiometer and a Rubicon galvanometer having a sensitivity of 5.7×10^{-8} v/mm and a period of 9.2 sec. Because of the long period of the galvanometer, its reading equalled the average PD across the sample. All measurements were made to an absolute accuracy of about one percent.

The samples and liquid helium were contained in a Dewar flask surrounded by a shield flask containing liquid air. The Dewars were surrounded by a Helmholtz coil which cancelled the earth's magnetic field, so that the net magnetic field at the samples was less than 0.01 oersted.

TABLE I. Sample diameters and resistivities at room temperature and at 4.2°K.

Sample	Description	Diameter (cm)	Resistivity at 300°K (ohm cm)	Resistance (4.2°K) / Resistance (300°K)
A	pure, grown	0.0200	11.85×10^{-6}	1.57×10^{-4}
B	0.01 percent Pb	0.0189	10.65	7.04
C_1	0.05 percent Pb	0.0193	14.2	22.6
C_2	C_1, grown	0.0193	11.3	28.3
D	pure, grown	0.0104	11.7	2.01

The temperature of the liquid helium bath was controlled by controlling the pumping rate with a Wallace and Tiernan manostat to maintain the vapor pressure constant. About 10 mw were dissipated in a heater coil to keep the liquid in thermal equilibrium. We estimate that the temperature of the helium was kept constant to at least 0.0005°K. The vapor pressure-temperature scale used in this paper is the Mond Laboratory scale of 1949.

3. PRELIMINARY RESULTS

The general results to be expected in this experiment may be deduced if it is recalled that resistance reappears in a superconducting wire when the magnitude of the current in the wire is such that the magnetic field at the surface due to the current equals the critical magnetic field for destruction of the superconducting state.[5]

[4] (a) Serin, Feldmeier, and Garfunkel, Phys. Rev. **76**, 167 (1949), (b) Serin, Reynolds, and Garfunkel, Phys. Rev. **79**, 211 (1950).

[5] Burton, Grayson-Smith, and Wilhelm, *Phenomena at the Temperature of Liquid Helium* (Reinhold Publishing Company, New York, 1940), pp. 98–101.

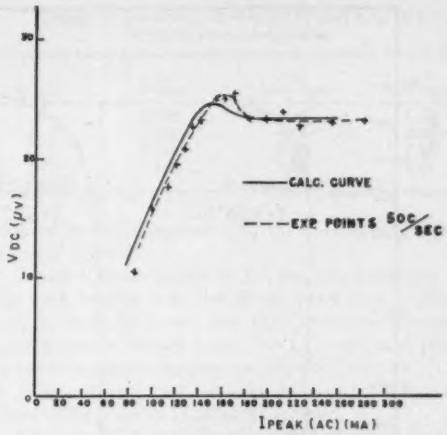

FIG. 2. Comparison of experimental and calculated curves of average PD *vs* ac amplitude.

This phenomenon is called the Silsbee effect. For simplicity of the initial argument, we assume that when the current reaches this critical value, I_c, the resistance is abruptly restored to its value in the normal state, R_n. Thus, if we superimpose alternating and direct currents on a superconductor, there will be no potential difference as long as the total current is always less than I_c. As the amplitude of the alternating current is increased, there will be first a positive potential difference during part of the positive half-cycle of the ac, whose average value will increase with increasing amplitude. With still further increase in amplitude, a negative potential difference during the negative half-cycle will set in so that the average value of the potential difference over a cycle will pass through a maximum and approach an asymptotic value.

An exact treatment may be made from the experimentally measured relationship between resistance and

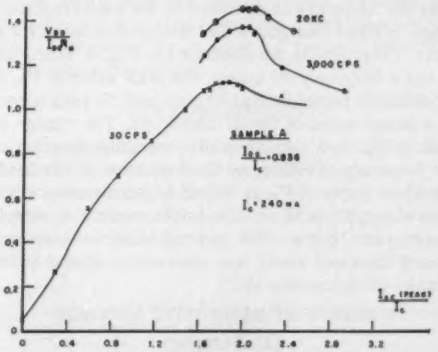

FIG. 3. Normalized curves of average PD *vs* ac at three different frequencies for sample *A*.

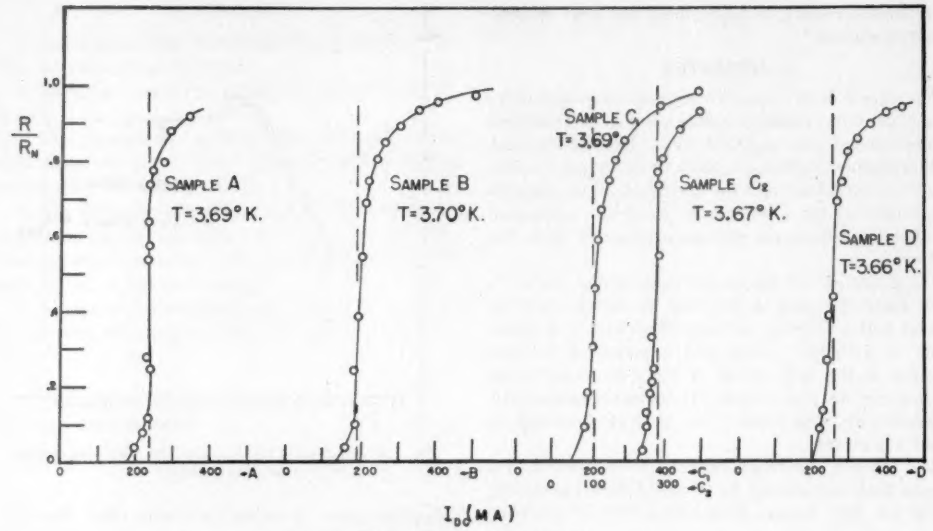

FIG. 4. Curves of Silsbee effect.

direct current (see Fig. 4). It is assumed in the presence of alternating and direct currents, the resistance at any time is the same as for a direct current equal in magnitude to the instantaneous sum of the applied ac and dc values. The PD at any time is then the product of the instantaneous resistance and its corresponding current value. This PD when averaged over a cycle of the alternating current should give the measured value.

As may be seen from Fig. 2, the agreement between the experimental results and the above picture is quite good for low frequency. The experimental points were taken with 50 c/sec ac on a polycrystalline tin wire about 10^{-2} cm in diameter and 8 cm long. The calculated curve was obtained by numerical integration as outlined above. In this paper the measured value of the average PD across the sample is denoted by V_{dc}.

As the frequency is increased in the audiofrequency range, marked changes in the measured values of V_{dc} occur. These effects are illustrated in Fig. 3. When the ac has a frequency 20 kc/sec, the peak value of V_{dc} is considerably higher than at 30 c/sec and the peak occurs at a larger value of the ac amplitude. The change in peak height is a monotonically increasing function of the frequency. Further, as the frequency is increased, the whole curve of V_{dc} is shifted in the direction of increased amplitude of ac. The details concerning sample A are given below. The general behavior with frequency discussed above was observed in a total of ten samples of high purity tin.

4. EFFECT OF RESISTIVITY AND SIZE

(a) Samples

The pertinent data concerning the five samples to be discussed are contained in Table I.

Samples A, B, C_1, and C_2 were prepared by first drawing the capillaries, choosing those which deviated by less than 1 percent in diameter over their length and then filling with tin. Sample D was made by drawing the tin in soft glass. Samples A and D were prepared from 99.993 percent tin. Lead impurity was purposely added to samples B, C_1, and C_2 to increase the low temperature resistivity. The designation "grown" in the second column indicates that the samples were withdrawn slowly from an oven kept above the melting temperature of tin and hence are presumably single crystals. Sample C_2 is the same as sample C_1, except that it was grown and then remeasured.

The diameters of the capillaries were measured with a microscope and the lengths, which were about 6.3 cm, with a traveling microscope. The room temperature

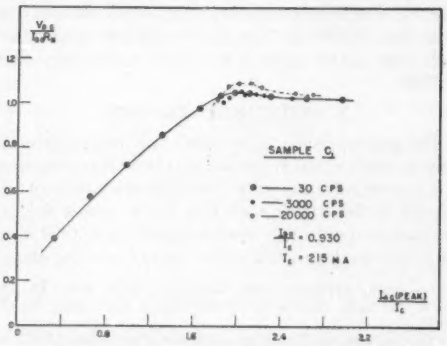

FIG. 5. Normalized curves of average PD as ac at three different frequencies for sample C_1.

value of the resistivity of the pure samples agrees quite well with the accepted value.

The glass was left on the samples except at the ends where it was chipped off. The samples were then mounted between small brass clamps which served as current and potential leads.

(b) Results of Measurement

The curves of the Silsbee effect for the samples are shown in Fig. 4. The sharp jump to about 0.8 of the normal value of resistance is evident in the pure, grown samples A and D and in C_2 which was also grown.

The alternating current data for samples A and C_1 are shown in Figs. 3 and 5 respectively. It is to be noted that the greatest deviations are shown by sample A the pure, grown sample, whereas sample C_1, the most impure sample shows no appreciable deviation. Because of this behavior, C_1, was grown and then remeasured, but there was no change in the character of the curves. Samples D and B have deviations intermediate between those of A and C_1.

It is clear from these measurements, that deviations from low frequency behavior are a property of the sample and not of our measuring equipment. Further these deviations depend on the normal resistivity of the sample and on its diameter.

The curves in Figs. 3 and 5, have been normalized. V_{dc} was divided by the asymptotic value of V_{dc}, given by the product of the direct current and the resistance of the wire when in the normal state. The amplitude of the ac was divided by the value of the critical current, I_c.

5. DISCUSSION

In attempting to interpret these data, we are impressed by the extremely large ratio of the sample radius, r, to the usual ac skin depth, d, computed using the resistivity of the normal state. The values of this ratio at several frequencies for the various sample are given in Table II.

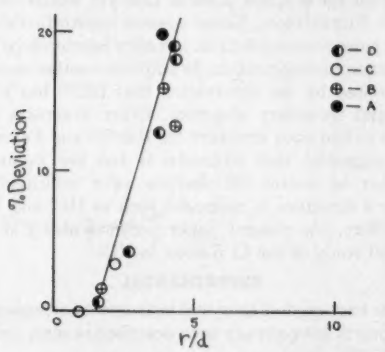

FIG. 6. Deviation of peak heights from 30 c/sec peak height as a function of ratio of sample radius to skin depth.

TABLE II. The ratio, r/d, of sample radius to ac skin depth at various frequencies.

Sample	r/d 30 c/sec	r/d 3000 c/sec	r/d 20,000 c/sec
A	0.390	3.90	9.24
B	0.168	1.68	4.32
C_1	0.082	0.82	2.13
D	0.165	1.65	4.26

Figure 6 shows a plot of the percent deviations of the peak heights from the 30 cps value as a function r/d. It is to be noted that the deviations increases approximately linearly once $r/d > 1.75$, and that there is good correlation among the different samples. It is to be appreciated that the same value of r/d occurs at different frequencies in different samples.

The correlation with the skin depth shown in Fig. 6, shows that the electrodynamic effects discussed earlier appreciably affect the measurements.

The problem involved with these samples is much more complicated than the skin effect problem in an ordinary conductor. For our case, the problem is a nonlinear one, involving a moving boundary between a region of normal conductivity and an intermediate state region whose ac properties are unknown. However, for sufficiently large ac, and sufficiently large values of r/d, we expect the usual type of calculation to be applicable during an appreciable fraction of a cycle. Hence we would expect an increase at higher frequencies in the value of the ac resistivity over the dc values, and thus deviations of the general character that we have observed. These results probably explain the "enhanced Silsbee effect" reported by Lebacqz and Andrews.[6]

However, it is just the difficulties of interpretation that we wish to emphasize. They become even worse in the megacycle region where r/d becomes extremely large. We feel that as long as the detailed consequences of the electromagnetic effects cannot be separated from effects due to relaxation time, experiments of this type are unsuited for determining the relaxation time for the phase transition.

ACKNOWLEDGMENT

In conclusion, we wish to thank Mr. J. Teza and Mr. L. B. Nesbitt for their technical assistance.

We are especially indebted to Professor F. G. Dunnington for his encouragement and for help in continuing these investigations while one of the authors (B.S.) was ill.

[6] J. V. Lebacqz and D. H. Andrews, *Proceedings of the National Electronics Conference*, Vol. 4, 11 (1948).

The K X-Ray Absorption Structure of Cl_2 and HCl

S. T. Stephenson, R. Krogstad, and W. Nelson
*Washington State College, Pullman, Washington**

(Received August 6, 1951)

The fine structure on the short wavelength side of the K x-ray absorption edge of chlorine in Cl_2 and in HCl has been measured with a vacuum double crystal spectrometer using Geiger counter registration. Pronounced structure was obtained which agreed well with structure previously detected using lower resolution and photographic registration. However, the structure does not agree with the theory. Some reasons for the discrepancy in terms of the optical levels and the different types of binding in the two cases are discussed.

INTRODUCTION

THERE is a fine structure to be observed on the short wavelength side of the x-ray absorption edges of certain gases. For monatomic gases and vapors this structure is limited to a region within the ionization potential of the atom of next higher atomic number and is brought about when an electron, removed from some inner shell in the absorption process, goes into one of the optical levels for a final state. For molecular gases and vapors one finds, however, an extended fine structure which may reach out several hundred volts on the short wavelength side of the edge and which can be ascribed to final energy states characteristic of the molecule caused by the scattering of the ejected electron by the neighboring atom or atoms in the molecule.

The best known polyatomic molecule from an extended fine structure point of view is $GeCl_4$. The theory for this molecule has been worked out[1–3] and measurements have been made both by photographic[4,5] and by double crystal spectrometer[6–8] methods. The double crystal method with its greater resolution brought out certain discrepancies between theory and experiment both as to position and intensity of the structure near the edge. Now it would seem that the best chance of obtaining agreement between theory and experiment in extended fine structure would come for the simplest possible case for which such extended structure is expected, namely, the case of the diatomic molecule; for this purpose, bromine and chlorine offer the best possibilities. The K absorption edge of Br_2 and the region adjacent to it on the short wavelength side have been studied thoroughly and with high resolution.[9–11] It may be regarded as well established that there is a very pronounced absorption minimum on the high energy side of the edge extending from about 2 volts to 12 volts with the actual minimum about 5–6 volts from the edge. There is no structure of magnitude greater than experimental error at distances further from the edge. The theory of secondary fine structure as applied to this particular molecule[12] gives the position of the first minimum of the absorption coefficient with acceptable accuracy but predicts this structure to be less pronounced than is actually the experimental case. The theory also predicts structure still further from the edge which is not observed at all. One reason for the lack of agreement may be that the scattering fields and phases have not been worked out in detail for bromine, hence approximate expressions derived from krypton were used in the calculations.

The most accurate application of the theory should be in the case of chlorine for which the fields and phases have been worked out[2] in detail. However, predictions concerning the structure[12,13] do not agree with the only experimental work on Cl_2.[14] Since the experiments were carried out with a photographic spectrograph of only 18 cm radius, the resolution was not as great as one would hope for. Therefore, it was thought worthwhile to study the K absorption edge of Cl_2 using a vacuum double crystal Geiger counter spectrometer to insure high resolution, thus rendering feasible an accurate and independent comparison between theory and experiment for the simplest possible case yet worked out in detail. Furthermore, Geiger counter registration should yield more accurate data on intensity relationships than photographic registration. In addition another question was raised by the observation that HCl[14] has a pronounced secondary structure. Other observers have failed to find such structure for HBr[10,11] and Peterson[12] has suggested that hydrogen is too low in atomic number to scatter the electron wave sufficiently to cause a structure in molecules such as HCl and HBr. Therefore, the present paper presents also a double crystal study of the Cl K-edge in HCl.

EXPERIMENTAL

The vacuum double crystal instrument and associated equipment have already been described in some detail.[15]

* This work was supported in part by the ONR.

[1] R. de L. Kronig, Z. Physik **75**, 468 (1932).
[2] Hartee, Kronig, and Peterson, Physica **1**, 895 (1934).
[3] E. M. Corson, Phys. Rev. **70**, 645 (1946).
[4] D. Coster and G. H. Klamer, Physica **1**, 889 (1934).
[5] T. Drynski and R. Smoluchowski, Physica **6**, 929 (1939).
[6] C. H. Shaw, Phys. Rev. **70**, 643 (1946).
[7] S. T. Stephenson, Phys. Rev. **71**, 84 (1947).
[8] H. Glaser, Phys. Rev. **82**, 616 (1951).
[9] S. T. Stephenson, Phys. Rev. **50**, 790 (1936).
[10] B. Cioffari, Phys. Rev. **51**, 630 (1937).
[11] C. H. Shaw, Phys. Rev. **57**, 877 (1940).
[12] T. M. Snyder and C. H. Shaw, Phys. Rev. **57**, 881 (1940).
[13] H. Peterson, Z. Physik **80**, 258 (1933); **76**, 768 (1932).
[14] A. E. Lindh and A. Nilsson, Arkiv. Mat, Astron. Fysik, **29A** 27, 1 (1943).
[15] S. T. Stephenson and F. W. Mason, Phys. Rev. **75**, 1711 (1949).

The double crystal arrangement is of the Ross[16] type using calcite crystals whose faces had been lightly etched with HCl. These crystals gave a (1, −1) rocking curve having a full width at half-maximum of 50 seconds at the wavelength of the chlorine *K*-edge. The scales on crystal *B* do not allow absolute determinations of wavelength but relative settings may be made to 10 seconds of arc. X-ray intensities were measured with a Geiger counter having a Cellophane covered window; the counters were filled with neon to 9 cm pressure and with 1 cm of alcohol vapor. The counting rates varied from 23 counts per second on the low absorption side to 9 counts per second on the high absorption side including a natural count of 0.8 count per second. From 5000 to 10,000 counts were taken at each point in a run and three different runs were made on Cl_2 and three on HCl in the final studies.

Many preliminary runs were made while testing absorption cells and using gases of different degrees of purity. The cells finally used were glass bubbles blown out as thin as could be done without collapsing mechanically and having a diameter of 4 to 5 cm. These bubbles were fastened to an all glass system using three stopcocks in such a way that the bubble could be pumped down with the spectrometer system and then sealed off from the bell jar. The gas was then admitted from a glass vessel previously filled with Cl_2 or HCl, the relative

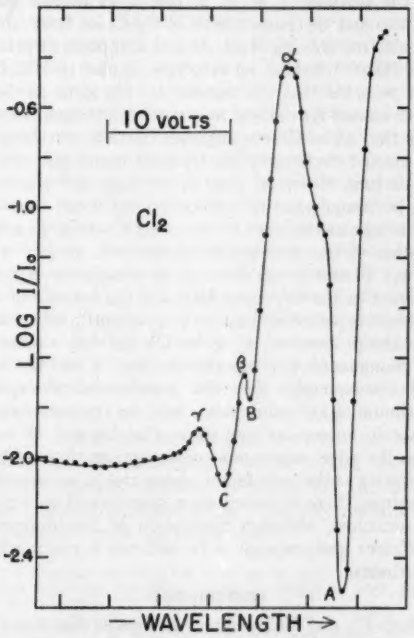

FIG. 1. *K* x-ray absorption edge of chlorine in Cl_2.

[16] P. A. Ross, Rev. Sci. Instr. 3, 253 (1932).

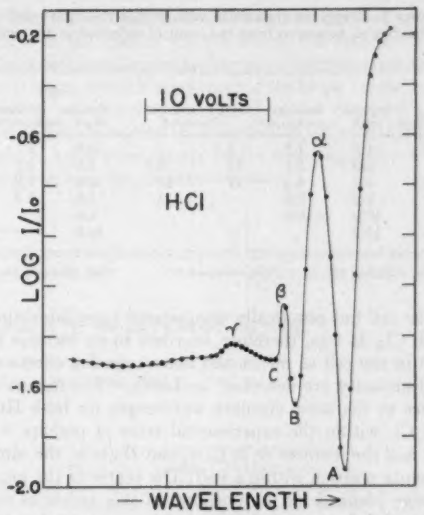

FIG. 2. *K* x-ray absorption edge of chlorine in HCl.

volumes of the vessel and the bubble having been calculated so that the final pressure in the bubble was about 10 cm. The bubbles would withstand this pressure indefinitely but, of course, shattered immediately if for any reason, in preparation, the pressure outside the bubble exceeded that inside. The gases were taken from cylinders freshly obtained from The Matheson Company and having a purity of 99.8 percent. These gases were entirely satisfactory. One has to be particularly careful about HCl as an impurity in Cl_2. In the runs on Cl_2 the increase of an HCl impurity could be noted after several hours of operation, and this was ascribed to reaction of the Cl_2 with residual water vapor on the walls of the glass container and with the grease on the three small bore stopcocks which were used. Blank runs of the background were made without any gas in the glass bubble.

The x-ray tube was operated at 5.5 kv and 250 ma. The target was a tungsten button in a hollow copper block through which the cooling water circulated. In order to prevent reflected electrons from passing out of the x-ray tube into the bell jar, the hole in the x-ray tube was covered by a grid fastened electrically to the cathode support. The power supply, pumping system and other details are as previously described[15] except that the glass bell jar has been replaced with a steel bell jar.

RESULTS

A typical individual run over Cl_2 is shown in Fig. 1, and a typical run for HCl is given in Fig. 2. The structure feature in Cl_2 between *A* and α comes at the same position as the main *K*-edge of HCl. This feature became more and more pronounced as long as the Cl_2 was left

TABLE I. Energy separations in volts of fine structure maxima and minima as measured from the point of inflection of the main edge.

Structure	Cl_2 Present work	Cl_2 Previous experiment[a]	Cl_2 Theory[b,c]		HCl Present work	HCl Previous experiment[a]
A	1.2	1.1	3.5		0.8	1.1
α	6.0	5.1	12	6.5	3.0	3.1
B	8.6	8.3	17	13	4.8	4.8
β	9.2	9.0		23	5.8	5.7
C	10.6	10.6			6.6	
γ	13.2				10.0	

[a] See reference 14. [b] See reference 12. [c] See reference 13.

in the cell but practically disappeared upon admitting fresh Cl_2. It was, therefore, ascribed to an increase of HCl in the cell as mentioned above; similar effects of HCl impurity are described by Lindh.[14] The feature α comes at the same absolute wavelength for both HCl and Cl_2 within the experimental error of perhaps 0.5 volt and the features B, β, C, γ, and D are at the same absolute position within a volt. The center of the main K-edge (defined for the purposes of this article as the point of inflection of the edge of longest wavelength) for HCl was shifted $3.0^{\pm 0.5}$ volts to a shorter wavelength than the Cl_2 K-edge. Lindh's[14] value for the shift was 2.6 volts.

The distances in volts from the center of the main edge of the structure observed are presented in Table I together with other experimental results and theoretical predictions.

DISCUSSION

It is apparent at once after inspecting Table I that the present experimental results with a double crystal x-ray spectrometer and Geiger counter registration are in excellent agreement with the single crystal results using photographic registration, although comparison of Figs. 1 and 2 with Lindh's[14] work indicates that the double crystal spectrometer gives better resolution. It is also apparent that there is no agreement between theory and experiment.

The situation from the standpoint of theory within 10 to 15 volts of the main K-edge is really quite complicated in the case of a molecule as can be seen from the following considerations: 1. Certainly the atomic optical levels are important in this region giving rise to a structure which, in the case of monatomic gases, can be related to the optical levels of the atom of atomic number one greater. Thus argon[17] shows a structure characteristic of the atomic levels; however, krypton[11] does not show such a structure because of the increased width of the K level, the closeness of the optical levels one to another, and the poorer energy resolution obtainable in this wavelength region. 2. In a molecule the atomic optical levels are changed by the presence of the other atom or atoms in the molecule; just what these changes are would be very difficult to calculate. No doubt the effect of the H atom in HCl which is chiefly heteropolar in character would be quite different from the effect of a Cl atom in Cl_2 which is homopolar. 3. At some energy, which should really characterize the series limit for the molecular-atomic optical levels, the electrons become essentially free, and for this and larger energies scattering of the ejected electron by the neighboring atom or atoms becomes the main consideration in the calculation of extended structure. But the position of this series limit is not readily calculable as indicated under 2.

HCl (Fig. 2) shows a pronounced structure, and yet one supposes that any scattering of the ejected electron by the H atom would be so small as to give rise to no extended structure from this source. Consequently all the structure must be ascribed to atomic levels essentially like those of argon but modified by the presence of the H atom. A comparison of the structure with the known optical atomic energy states of argon shows no detailed agreement, so the presence of the H atom must cause considerable modification. During the course of a private conversation on this topic, Parratt pointed out that if the structure close to the edge, as obtained in HCl, is characteristic of the chlorine ion rather than the molecule, it might bear some relation to the close-in structure of the chlorine ion in KCl.[18] A comparison does in fact show remarkable agreement for the features A, α, B, β, and C as though these features may be characteristic of the Cl ion from which a K electron is being lifted. At first it appears surprising that HBr[10,11] yielded no structure similar to HCl but it is probable that the reasons are the same as those which caused Kr to show no structure although A does.

In the case of Cl_2 one supposes that the scattering of the ejected electron by the Cl atom would give rise to a structure. However, close to the edge this structure will be complicated by atomic optical levels modified by homopolar binding with the other Cl atom. Thus the position of the absorption maxima and minima with respect to the initial increase in absorption is quite different in the two cases HCl and Cl_2 because of the different types of binding. It is quite pertinent to note that the pronounced A, α, for Cl_2 are very similar to the pronounced A, α reported for Br_2,[9–11] and for N_2[19] and consequently that the pronounced absorption maximum A and minimum α may be characteristic of diatomic homopolar molecules. Out beyond 15 volts from the edge, where one could suppose that electron scattering is the only factor giving rise to an extended structure, there is no structure pronounced enough to be measured, although fluctuation of the absorption coefficient great enough to be detected is predicted by the theory.

CONCLUSION

Both Cl_2 and HCl yield a pronounced fine structure close to the edge, for which earlier measurements with

[17] L. G. Parratt, Phys. Rev. **56**, 295 (1939).

[18] J. W. Trischka, Phys. Rev. **67**, 318 (1945).

[19] J. A. Prins, Physica **1**, 1174 (1934).

photographic registration have been checked with higher resolution and Geiger counter registration of intensities. This structure is all so close to the edge as to be affected by, if not governed entirely by, atomic optical levels modified by heteropolar (HCl) and homopolar (Cl_2) binding. Extended structure solely dependent upon electron scattering was not observed.

There is no agreement between theory and experiment in the case of Cl_2 for which the best chance of checking theory and experiment is expected. This serves to point up other discrepancies cited in the Introduction and to indicate that the theory of the structure to be found for absorption in molecular gases, within several tens of volts immediately on the short wavelength side of the main edge, is unsatisfactory.

PHYSICAL REVIEW VOLUME 84, NUMBER 4 NOVEMBER 15, 1951

A Note on the Propagation of Excitation in an Idealized Crystal*†

WILLIAM R. HELLER AND ALMA MARCUS
Physics Department, University of Illinois, Urbana, Illinois
(Received August 3, 1951)

It is shown that, in insulators, overlapping of the electronic wave functions of near-by crystal constituents is not necessary for effective transfer of excitation energy by the "exciton" mechanism. The electromagnetic interaction of the "virtual" dipoles of the transition is sufficient to give rise to such transfer characterized in cubic crystals by a wave number **k**, and an anisotropic effective mass, given in order of magnitude by the ratio electronic mass/oscillator strength of transition. Implications and limitations of the calculation are discussed.

I. INTRODUCTION

DURING the past year, a basic advance has been made in the understanding of the processes of migration of energy in ionic crystals,[1] through the experimental work of Apker and Taft. Although these workers dealt with photoelectric emission, an inescapable conclusion from their results is that part of the emitted electrons derive their energy only by some intermediate transfer process from the energy of the incident photons. Since the energy distribution of this group of electrons (called the *S*-group by Apker and Taft) does not display the characteristics one would expect if the electrons were directly released by absorption of light, one is led to the hypothesis that, in an intermediate stage, the energy is carried by what have been called "excitons." These entities were first introduced as a theoretical concept by Frenkel,[2] and signify a moving state of electronic excitation energy in the lattice. That electronic states of this kind must in general be characterized by a wave number, rather than by a label corresponding to the atom on which they reside, is a consequence of the strong coupling between adjacent constituents of the lattice; in the alkali halides the participating units may presumably be considered to be the halide ions.

An important purpose of the present paper is to show that the use of the term "exciton" (for electronic excitation energy traveling in an insulating solid) is appropriate to a situation in which there is "strong coupling" of any type between an excited atom and its neighbors. In particular, appreciable overlapping of their electronic wave functions is not necessary to insure "strong coupling" of the crystal constituents. It will be seen as a principal result, that energy transfer by electromagnetic "near zone" interactions may take place very quickly in certain crystals.[3] Thus, because of this interaction alone, one must characterize the wave functions of the excitation by a wave number (and hence one is obliged to use the term exciton), rather than view the excitation as well localized on single atoms or molecules. This does not require the appearance of a new band in the spectrum of atoms when they are placed into condensed systems. The structure in absorption spectra due to the doublet levels characteristic of the bromide and iodide ions, for example, is observed also in the solid state. The work of the present paper demonstrates that one has every reason to believe that these levels become typical exciton levels when the ions mentioned are made the anions of ionic crystals.

Further discussion of the implications of our calculation will be given in later publications. The authors wish to thank Professor Frederick Seitz for suggesting that a suitably simplified model of an insulating crystal

* A preliminary report of this work was given at the New York meeting of the American Physical Society, February, 1951, Phys. Rev. **82**, 315 (1951).
† Supported by the ONR.
[1] L. Apker and E. Taft, Phys. Rev. **82**, 814 (1951); **81**, 698 (1951); **72**, 964 (1950); M. Hebb, Phys. Rev. **81**, 702 (1951).
[2] J. Frenkel, Phys. Rev. **37**, 17 (1931); **37**, 1276 (1931); Physik. Z. Sowjetunion **9**, 158 (1936).
[3] This is analogous to the mechanism of "sensitized fluorescence" in gases. G. Cario and J. Franck, Z. Physik **17**, 202 (1923), and many later papers.

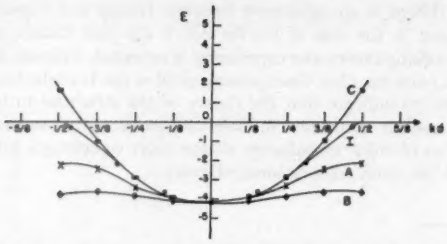

FIG. 1. Dependence of exciton energy on wave numbers for $(\mathbf{\mu}, \mathbf{k})=90°$, in a face-centered crystal. Ordinate: $(E_k{}^n-E_{JJ}{}^n)/|\mathbf{\mu}|^2 s^3=E$. Abscissa: $|\mathbf{k}|d$, where $d=(2s_0)^{-\frac{1}{3}}$. I: Integral Approximation (same for all directions of k). A: $\mathbf{k}$ in 100 direction. B: $\mathbf{k}$ in 110 direction. C: $\mathbf{k}$ in 111 direction.

be chosen, with the problem of electromagnetic "near zone" exciton propagation in mind.

II. CALCULATIONS AND CONCLUSIONS

A suitable framework for this study was proposed long ago by Frenkel[2] and Peierls,[4] but they do not appear to have emphasized the relative importance of the electromagnetic coupling between atoms. This leads to several important conclusions which are discussed in the latter part of this section, and form the principal content of the present work.

We consider a cubic crystal of effectively infinite size, on the lattice sites of which are arranged identical one-electron atoms, whose thermal vibration we shall leave out of the computation. As a starting approximation, we may take a determinant wave function of all the atoms, which ignores spin effects and neglects the overlapping of the ground-state wave functions on different atoms. This does not mean that exchange effects are to be totally ignored, as we shall see, and hence does not exclude the kind of band formation characteristic of a quantum theoretical approach (although we do assume that the effects of overlap, and hence exchange, on the normalization, are secondary).

As a convenience we shall assume that the ground-state atomic functions are S-type, and that the corresponding excited state wave functions have P-character. Since the lattice has cubic symmetry, we need not concern ourselves with the orbital degeneracy of the excited state; (i.e., it is not lifted by the cubic symmetry), this has an important corollary the fact the state may in principle have an arbitrary direction of polarization.

Thus the ground-state wave function is[5]

$$\Psi_0=\frac{1}{\sqrt{N!}}\begin{vmatrix}\psi_1{}^0(\mathbf{r}_1) & \cdots & \psi_1{}^0(\mathbf{r}_N)\\ \cdot & & \cdot\\ \cdot & & \cdot\\ \psi_N{}^0(\mathbf{r}_1) & \cdots & \psi_N{}^0(\mathbf{r}_N)\end{vmatrix}$$

and a typical zero'th order excited state wave function will be

$$\Psi_J{}^n=\frac{1}{\sqrt{N!}}\begin{vmatrix}\psi_1{}^0(\mathbf{r}_1) & \cdots & \psi_1{}^0(\mathbf{r}_N)\\ \cdot & & \cdot\\ \cdot & & \cdot\\ \psi_J{}^n(\mathbf{r}_1) & \cdots & \psi_J{}^n(\mathbf{r}_N)\\ \cdot & & \cdot\\ \cdot & & \cdot\\ \psi_N{}^0(\mathbf{r}_1) & \cdots & \psi_N{}^0(\mathbf{r}_N)\end{vmatrix}.$$

Here the superscript n refers to the nth excited atomic state of energy ϵ_n, the subscript labels the nucleus involved, the vector argument refers to the electron in question. The energy corresponding to Ψ_0, is found to be:

$$E^0=N\epsilon_0-\tfrac{1}{2}e^2\sum_{I,J}{}'\int\psi_I{}^0(\mathbf{r}_1)\psi_J{}^0(\mathbf{r}_2)\times\frac{1}{r_{12}}\psi_I{}^0(\mathbf{r}_2)\psi_J{}^0(\mathbf{r}_1)d\tau_1d\tau_2. \quad (1)$$

where the prime acts to exclude the case in which $I=J$. Consistently with the assumption that no overlapping of the ground-state wave function takes place, we have neglected here the total coulomb interaction of neighboring atoms. We have used the hamiltonian

$$H=\sum_I H_I+\sum_{I,J}{}'H_{IJ}$$

$$H_I=\frac{-e^2}{r_{iI}}-\frac{\hbar^2}{2m_{e1}}\nabla_i^2,\quad H_{IJ}=\sum_{I,J}{}'\frac{e^2}{R_{IJ}}-\sum_{i,I}\frac{e^2}{r_{jI}}+\sum_{i,j}{}'\frac{e^2}{r_{ij}},$$

where ∇_i^2 refers to the ith electron, associated with the Ith atom, and the small letters refer to the electrons, the large to the nuclei.

The energy of the excited state wave function $\Psi_J{}^n$ is computed to be

$$E_{JJ}{}^n=N\epsilon_0+\epsilon_n-\epsilon_0-e^2\sum_{L\neq 0}\times\int\psi_{L+J}{}^0(\mathbf{r}_2)\psi_{L+J}{}^0(\mathbf{r}_1)\frac{1}{r_{12}}\psi_J{}^n(\mathbf{r}_1)\psi_J{}^n(\mathbf{r}_2)d\tau_1d\tau_2$$
$$-\frac{e^2}{2}\sum_{\substack{I\neq M\\ I\neq J\\ J\neq M}}{}''\int\psi_I{}^0(\mathbf{r}_1)\psi_M{}^0(\mathbf{r}_2)\times\frac{1}{r_{12}}\psi_I{}^0(\mathbf{r}_2)\psi_M{}^0(\mathbf{r}_1)d\tau_1d\tau_2. \quad (2)$$

Here ϵ_0= energy of the isolated atom in its ground state, ϵ_n= energy of the isolated atom in its excited state, and N= total number of atoms or electrons. The excited state wave functions do not diagonalize the hamiltonian, and, of course, are degenerate. The off-diagonal

[4] R. Peierls, Ann. Physik **13**, 905 (1932).

[5] For a brief summary of Peierls' and Frenkel's work, see F. Seitz, *Modern Theory of Solids* (McGraw-Hill Book Company, Inc., New York, 1940), pp. 415–417.

matrix elements are typified by E_{JL},

$$E_{JL}=\int\cdots\int_{i=1,\cdots,N}\Psi_J^n H\Psi_L^n d\tau_1\cdots d\tau_N.$$

These reduce to

$$E_{JL}=e^2\int\psi_J^n(\mathbf{r}_1)\psi_L^0(\mathbf{r}_2)\frac{1}{r_{12}}\psi_J^0(\mathbf{r}_1)\psi_L^n(\mathbf{r}_2)d\tau_1 d\tau_2 \quad \text{"coulomb"}$$

$$-e^2\int\psi_J^n(\mathbf{r}_1)\psi_L^0(\mathbf{r}_2)\frac{1}{r_{12}}\psi_J^n(\mathbf{r}_2)\psi_L^0(\mathbf{r}_1)d\tau_1 d\tau_2. \quad \text{"exchange"} \quad (3)$$

In order to obtain a correct zero'th order wave function from the degenerate set Ψ_J^n, the following linear combination is chosen

$$\Psi_{\mathbf{k}}^n=1/\sqrt{N}\sum_J\exp(2\pi i\mathbf{k}\cdot\mathbf{r}_J)\Psi_J^n.$$

It may be verified that the off-diagonal matrix elements of two wave functions with quantum numbers $\mathbf{k}$ and $\mathbf{k}'$ do indeed vanish, if one uses the δ-function relation:

$$\sum_J\exp[2\pi i(\mathbf{k}-\mathbf{k}')\cdot\mathbf{r}_J]=\delta_{\mathbf{k}-\mathbf{k}',0}.$$

The new diagonal energy is found to be

$$E_{\mathbf{k}}^n=E_{JJ}^n+\sum_L{}'E_{JL}\exp[2\pi i\mathbf{k}\cdot(\mathbf{r}_J-\mathbf{r}_L)]. \quad (4)$$

The prime signifies that $J\neq L$, and the sum is to be taken over all lattice points.

It is at this stage of the calculation, we wish to stress, that previous treatments diverge in emphasis, as well as in the physical conclusions drawn. In order to evaluate the lattice sum in Eq. (4), it is expedient to examine the terms in the expression (3) for E_{JL}, as functions of lattice parameter. For convenience we proceed in reverse order; i.e., we shall first consider the "exchange" term. This will depend exponentially on lattice parameter, somewhat in the fashion $(e^2/R)\times\exp(-2R/a)$ where a=equivalent Bohr radius of the excitation; R=nearest neighbor distance. Hence, only the nearest neighbors, if we consider the important lower excited states, will contribute to the lattice sum. Furthermore, even this contribution will be small, because of the exponential dependence, at a density characteristic of many ionic and molecular crystals. Further discussion will be given this term later. The other term in E_{JL}, the coulomb part, is nothing more than an expression for the interaction of two charge clouds, each with density equal to the product of the excited and ground-state wave functions of an isolated atom. Such an integral can be expanded in the lattice parameter, or, more conveniently, in the distance between the atoms R. One obtains

$$\frac{Q_1Q_2}{R}+\left(\frac{Q_1\mathbf{R}\cdot\boldsymbol{\mu}_2}{R^3}-\frac{Q_2\mathbf{R}\cdot\boldsymbol{\mu}_1}{R^3}\right)$$

$$-\left(\frac{\boldsymbol{\mu}_1\cdot\boldsymbol{\mu}_2}{R^5}(\mathbf{R})\cdot(-\mathbf{R})-3\frac{(\boldsymbol{\mu}_1\cdot\mathbf{R})(\boldsymbol{\mu}_2\cdot\mathbf{R})}{R^5}\right)+\cdots.$$

Here

$$Q_1=\int\psi_J^n(\mathbf{r}_1)\psi_J^0(\mathbf{r}_1)d\tau_1,\quad Q_2=\int\psi_L^n(\mathbf{r}_2)\psi_L^0(\mathbf{r}_2)d\tau_2$$

$$\boldsymbol{\mu}_1=e\int\psi_J^n(\mathbf{r}_1)[\mathbf{r}_1-\mathbf{r}_J]\psi_J^0(\mathbf{r}_1)d\tau_1,$$

$$\boldsymbol{\mu}_2=e\int\psi_L^n(\mathbf{r}_2)[\mathbf{r}_2-\mathbf{r}_L]\psi_L^0(\mathbf{r}_2)d\tau_2.$$

Thus the first two terms cancel, and we are left with the third term. Because we have neglected thermal effects, the vectors $\boldsymbol{\mu}_1$, $\boldsymbol{\mu}_2$ have the same direction and magnitude for all atoms, and hence the final expression for the lattice sum of the coulomb parts of the original off diagonal matrix element is

$$\sum_L{}'E_{JL}=-|\boldsymbol{\mu}|^2\sum_L{}'\left(\frac{3\cos^2(\boldsymbol{\mu},\mathbf{r}_J-\mathbf{r}_L)-1}{|\mathbf{r}_L-\mathbf{r}_J|^3}\right)$$

$$\times\exp[2\pi i\mathbf{k}\cdot(\mathbf{r}_J-\mathbf{r}_L)].$$

Note that the contributions of distant neighbors, especially for $|\mathbf{k}|\approx 0$, cannot be neglected, as previous treatments have done.[2,4,5]

It remains to consider the relative magnitude of the coulomb and exchange terms. A rough idea may be obtained by considering the excitation of the lowest level (exciton level) in an alkali halide. The excitation may be regarded as characteristic of the halide ion lattice, and thus R may be chosen to be the nearest like neighbor distance, for purposes of comparison. When this is done, and an oscillator strength of order unity is assigned to the dipole transition represented by $|\boldsymbol{\mu}|$, one sees that the relative order of magnitude is about

$$\frac{\exp(-2R/a)/R}{a^3/R^3}\quad\frac{\exp[-(2)(3.14)\sqrt{2}/(1.5)]}{((1.5)/(3.14)\sqrt{2})^3}$$

a number of the order of 1/10. A more precise comparison will certainly not invert the relative importance of the two terms.[6] It is seen that the dipole-dipole term is

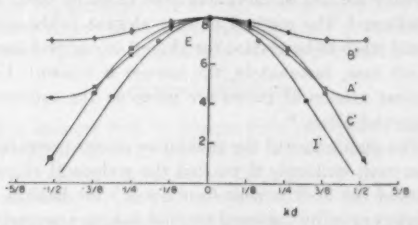

FIG. 2. Dependence of exciton energy on wave number for $(\boldsymbol{\mu},\mathbf{k})=0°$, in a face-centered crystal. The symbols have the same meaning as in Fig. 1.

[6] The writers are indebted to Dr. D. Dexter for making available to us his results on the "spread" of exciton wave functions in NaCl. See Phys. Rev. **83**, 435 (1951). It is shown there that most of the charge density of the excited state is concentrated on the Cl^- ion (not on the Na^+ ions as is commonly supposed).

the important one. The sum, when carried out for $|\mathbf{k}|\approx 0$ (i.e., $|\mathbf{k}|R \ll 1$) is nothing more than the interaction energy of a lattice of static dipoles of magnitude $|\mathfrak{p}|$. If we neglect the contribution of outer surface (depolarization) terms, and replace the summation by an integral, both of these operations being permissible when $|\mathbf{k}|\approx 0$ (i.e., of order $1/\lambda_{op}$) we obtain

$$E_k{}^n = E_{JJ}{}^n + 8\pi/3 P_2(\cos(\mathfrak{p},\mathbf{k}))n_0|\mathfrak{p}|^2\{j_0(\rho)-j_2(\rho)\},$$

where P_2 is the Legendre polynomial of order two, n_0 the density of atoms and j_0 and j_2 are spherical bessel functions[7] of argument $\rho = 2\pi|\mathbf{k}|R_0$, where R_0 is determined by the condition that $(4\pi/3)R_0{}^3 = 1/n_0$.

It should be specifically mentioned that the summation method used breaks down when $|\mathbf{k}|$ precisely equals zero, because then the outer surface terms are just as important as contributions from nearest neighbors. In practice, however, $|\mathbf{k}|$ never exactly equals zero (except possibly when, under the influence of lattice polarization, the exciton may become trapped. Our treatment is not appropriate for such situations). This result applies to any centro-symmetric cubic lattice, but the integral is a good approximation only for $|\mathbf{k}|$ small, but not zero. It is to be noted that if $|\mathbf{k}|\to 0$, $(\mathfrak{p},\mathbf{k}) = 90°$, we obtain a factor $4\pi/3$ which bears a strong resemblance to the Lorentz-Lorenz polarization contribution. The relevance of this fact for a consideration of the problem of "local fields" is discussed in a paper by Heller and Dexter.[8] Figures 1 and 2 illustrate the goodness of approximation of the integral to the sum for the particular directions relative to the cubic axes (in a face-centered crystal) which are indicated. It is to be stressed that the angle $(\mathfrak{p},\mathbf{k})$ is completely arbitrary, and thus that anisotropy of exciton motion may be expected even in a cubic lattice. Although only the state $(\mathfrak{p},\mathbf{k}) = 90°$ will be excited by light waves if the simultaneous creation of phonons is neglected, others may arise through interaction with lattice modes, and during creation of excitons by α-particles or β-rays.

The sums were carried out by use of an extension of Ewald's method of theta-functions given by Born and Bradburn.[9] The method is very elegant (although it would have to be revised for $|\mathbf{k}| = 0$ in our problem in which case, fortunately, the answer is known). Convenient numerical tables are given in the articles of Born and Misra.[10]

The significance of the qualitative results presented is seen most strikingly if we find the reciprocal effective mass of the exciton near (but not at) the base of the energy curve, by the usual method, taking a second derivative. This gives

$$\left(\frac{1}{m_{eff}}\right)_{|\mathbf{k}|\approx 0} = \left(\frac{1}{\hbar^2}\frac{\partial^2 E}{\partial k^2}\right)_{|\mathbf{k}|\approx 0}$$

$$= \frac{8\pi}{3} P_2(\cos(\mathfrak{p},\mathbf{k}))\frac{|\mathfrak{p}^2|}{\hbar^2} n_0(j_0'' - j_2'')_{|\mathbf{k}|=0}(2\pi R_0)^2$$

$$= \frac{8\pi}{3} P_2(\cos(\mathfrak{p},\mathbf{k}))\frac{|\mathfrak{p}|^2}{\hbar^2} n_0 \cdot 4\pi^2 R_0{}^2(-\tfrac{1}{5}).$$

Changing to the oscillator strength f_{n0} by use of the relation:

$$f_{n0} = \frac{(\epsilon_n - \epsilon_0)m_{el}|\mathfrak{p}|^2}{3\hbar^2 e^2}$$

one has

$$\left(\frac{1}{m_{eff}}\right)_{|\mathbf{k}|\approx 0} = -\frac{16\pi}{3\times 15}\left(\frac{3}{4\pi}\right)^{\frac{1}{3}} P_2(\cos(\mathfrak{p},\mathbf{k})) \times \left(\frac{e^2 n_0{}^{\frac{1}{3}}}{\epsilon_n - \epsilon_0}\right)\cdot\frac{f_{n0}}{m_{el}}.$$

In other words, the effective mass will be positive or negative depending upon the relative orientation of $\mathfrak{p}$ and $\mathbf{k}$ (and, incidentally, the effective mass can become infinite for certain relative orientations), but, in general we may say that $m_{exciton} \sim (m_{electron}/f_{n0})(R_0/a)$, and is positive when the exciton is created by light (since $P_2(\cos 90°) = -\frac{1}{2}$). Thus the smaller the oscillator strength, the slower is the propagation of excitation, for a given kinetic energy of the exciton.

These findings should be compared with Foerster's[11] result that the speed of migration of excitation from one molecule to another in a dilute solution of dye molecules varies as the inverse sixth power of the mean separation. Our picture of exciton migration deals with a different limiting case, that in which the density is so high that the stationary states cannot be well approximated by imagining only one atom excited at a time. Thus, throughout the region of high concentration, the appropriate model is much more like that of the electron wave packets in metals, in which collisions (changing $\mathbf{k}$ and, in general, $\mathfrak{p}$) will take place during the lifetime of the excitation. This approach suggests that a typical "maximum diffusion distance" of an exciton wave packet will be given by d, where

$$d \leq (\langle v^2_{\text{thermal}}\rangle \tau_{\text{thermal}}\tau_{\text{opt}})^{\frac{1}{2}} \approx (10^{14}\times 10^{-14}\times 10^{-8})^{\frac{1}{2}} = 10^{-4}\text{ cm},$$

although the total path length covered may be of the order of centimeters. Of course a competing process, such as creation of F-centers, may rob the exciton of its energy long before the optical lifetime is up.

[7] P. M. Morse, *Vibration and Sound* (McGraw-Hill Book Company, Inc., New York, 1948), second edition, p. 316.
[8] W. R. Heller and D. L. Dexter (to be published).
[9] M. Born and M. Bradburn, Proc. Cambridge Phil. Soc. **39**, 104 (1943).
[10] R. D. Misra, Proc. Cambridge Phil. Soc. **36**, 173 (1940); M. Born and R. D. Misra, Proc. Cambridge Phil. Soc. **36**, 466 (1940).
[11] T. Foerster, Ann. Physik **2**, 55 (1948), and references to earlier work there given.

It is interesting to realize that the lattice sum which leads to the main conclusions is a very sensitive function (for $|\mathbf{k}| \approx 0$) of the distant configuration of atoms. This implies that if the crystal has dimensions of the order of the diffusion distance or smaller, one may notice peculiar effects (due to the consequent anisotropy and increase in magnitude of the effective mass) in fluorescence or other phenomena associated with energy transfer by this mechanism. It was pointed out to the authors[12] that Vavilov[13] has observed unusually well developed luminescence phenomena in very fine capillaries, using dye solutions which do not display such effects in bulk. The fact that the atoms in solution are not arranged in a cubic lattice should not change the qualitative prediction.

One may emphasize that all our conclusions follow from the premise that there is only a small amount of actual overlapping of the excited state wave functions of the electrons. While this premise will not hold in some cases (obviously not in the case of strong valence bonds between the crystal constituents) it should be qualitatively appropriate in certain ionic and molecular crystals in which the electronic wave functions are large at the sites of relatively widely spaced crystal constituents and small in between them. Qualitatively similar conclusions should hold for pure liquids and solutions in both the solid and liquid states, since the only difference will lie in the random arrangement of the excited atoms or molecules in these systems.

An important point to be settled before the present results can be applied to actual crystals is that of the effect of lattice vibrations on the calculations. Reasoning from an argument based on the use of the customary plots of total energy *versus* nuclear configuration coordinate, one might expect that "resonant transfer" of electromagnetic energy must await a favorably similar disposition of the configuration coordinates of a neighboring atom. But, as was stressed in Peierls' fundamental paper,[4] such curves are appropriate only when the energy levels of the electronic system are very widely spaced relative to the interaction energy with the important lattice vibrations. Otherwise, (as is the case for strong coupling) the adiabatic approximation on which the use of the energy curves is based, must break down, and, in fact, one should solve the problem of the states generated by the "mixture" of the two quasi-continuous spectra of the excitons and of the phonons.

Difficult as this is, one sees that such a mixture will allow the resonant interaction to have its effect without waiting, so to speak, because the nuclear displacement coordinates no longer correspond to precise points on the curve of total energy. We may thus see that the resonant near-zone interaction should make possible a well-developed band structure with its quantum-mechanical implications as regards the nonlocalization of energy, even when the lattice vibrations are taken into account. A criterion, then, which allows us to reason as in this paper, without taking specific account of the lattice vibrations, is simply that the band widths due to electromagnetic coupling be large (and hence that the spacing between levels be small) compared to the lattice vibration energies which are relevant for the particular electronic transitions. In ionic lattices this criterion should be satisfied, if f_{n0} is not much less than 1, at practically all temperatures. In molecular crystals however, especially for small oscillator strengths and at low temperatures the argument based on energy curves may apply; the excitation mass will then be limited to values effectively of the order of nuclear masses, i.e., propagation will be relatively slow.

[12] In private conversation with Mr. E. Jacobs and Professor E. Rabinowitch.

[13] S. Vavilov, Doklady Akad. Nauk. S.S.S.R. **67**, 811 (1949).

SUMMARY

It is shown that overlapping of electronic wave functions on nearby atoms or molecules in crystals is not necessary for effective transfer of excitation energy by the exciton mechanism. This is due to the fact that the principal interaction, varying as $1/R^3$, is characteristic of electromagnetic oscillators in their quasi-static zone. For an idealized cubic crystal, the results are obtained that anisotropy exists, in general, in the motion of excitons, and that the effective mass of an exciton corresponding to a dipole transition is given in order of magnitude by

$$m_{eff} \sim (m_{el}/f_{n0})(R_0/a),$$

where m_{el} = mass of electron, f_{n0} = oscillator strength of corresponding isolated atomic transition, a = equivalent Bohr radius of internal exciton orbit in crystal $R_0 = (\frac{3}{4}\pi n_0)^{\frac{1}{3}}$, and n_0 = atomic density.

The qualitative conclusion is pointed out that for sample dimensions small relative to the "diffusion distance" of an exciton, one should observe characteristic changes in the effective mass. Also, the whole discussion should have qualitative value for energy transfer in liquids or concentrated solutions, under suitable restrictions, although the atomic arrangement here has no long range order. A discussion is given of the effect on the results of accounting for lattice vibrations.

ACKNOWLEDGMENT

The authors wish to express their particular thanks to Professor F. Seitz and to Dr. David Dexter for a number of very stimulating discussions of the work. In addition, we wish to thank Dr. Paul Marcus for calling our attention to the work of Born and his collaborators. Drs. Apker, Taft and Hebb were very kind and helpful in discussing their results both before and after publication. One of us (Alma Marcus) is indebted to the University of Illinois for the grant of a fellowship during the tenure of which the work was completed.

The Effect of a Magnetic Field on Electrons in a Periodic Potential

J. M. LUTTINGER
Department of Physics, University of Wisconsin, Madison, Wisconsin
(Received June 25, 1951)

A theorem due to Wannier for treating the motion of electrons in a perturbed periodic field is generalized to include the effect of a slowly varying magnetic field. It is shown that the problem reduces to that of solving an effective Schrödinger equation, which is known as soon as we have solved the problem without perturbing fields.

I. INTRODUCTION

RECENTLY Slater[1] has revived interest in a theorem due to Wannier[2] which enables one to study the behavior of electrons in a perturbed periodic potential. This theorem may be stated as follows: Say the energy for the unperturbed periodic potential as a function of the quasi-momentum $\mathbf{p}'$ is known, and is given by $E_0(\mathbf{p}')$. Let the perturbing potential be $e\varphi(\mathbf{r})$, where $\varphi(\mathbf{r})$ is a function which does not change appreciably over one lattice spacing (for example, the potential of an applied electric field). Then the allowed energies E of the perturbed problem are given approximately by solving the equation

$$\{E_0(-i\hbar\nabla)+e\varphi(\mathbf{r})\}\psi(\mathbf{r})=E\psi(\mathbf{r}). \tag{1}$$

The operator $E_0(-i\hbar\nabla)$ is the same function of $-i\hbar\partial/\partial x$, $-i\hbar\partial/\partial y$, $-i\hbar\partial/\partial z$ as it was of p_x', p_y', p_z'.

The question now arises as to what modifications of (1) are necessary when an external magnetic field is also imposed. This problem has been studied and to some degree solved by Peierls,[3] in connection with his investigation of the diamagnetism of strongly bound electrons in metals. Our results will be a simplification and generalization of those of Peierls.

The simplest modification of (1) consistent with the requirements of gauge invariance[4] would be obtained by replacing $-i\hbar\nabla$ by $-i\hbar\nabla-(e/c)\mathbf{A}$, where $\mathbf{A}$ is the vector potential of the magnetic field. It is by no means clear that these are the only terms which arise, for one could add to the resulting hamiltonian any terms which depend on the magnetic field only, and which would therefore be automatically gauge invariant. It is the purpose of this paper to show that in fact no such extra terms occur, and, therefore, that the energy levels in the presence of a magnetic field are approximately given by

$$\{E_0[-ie\nabla-(e/c)\mathbf{A}]+e\varphi\}\psi=E\psi. \tag{2}$$

II. EFFECT OF A SLOWLY VARYING MAGNETIC FIELD

Let the hamiltonian of the electron in the unperturbed periodic lattice be given by $\mathcal{H}_0=\mathbf{p}^2/2m+V(\mathbf{r})$, $V(\mathbf{r})$ being the periodic potential. We will assume that we can solve this unperturbed problem; that is, we can obtain the energy as a function of the quasi-momentum $\mathbf{p}'$. Let this energy by $E_0(\mathbf{p}')$, and let the corresponding normalized Bloch function be $\psi_{\mathbf{p}'}(\mathbf{r})$, i.e.,

$$\mathcal{H}_0\psi_{\mathbf{p}'}(\mathbf{r})=E_0(\mathbf{p}')\psi_{\mathbf{p}'}(\mathbf{r}).$$

Now let us construct the Wannier localized atomic functions $a(\mathbf{r}-\mathbf{Q}_k)$,[5] where $\mathbf{Q}_k$ is the vector to the kth lattice point. These functions are defined as

$$a(\mathbf{r}-\mathbf{Q}_k)=\frac{1}{\sqrt{N}}\sum_{\mathbf{p}'}\exp\left[-\frac{i\mathbf{p}'\cdot\mathbf{Q}_k}{\hbar}\right]\psi_{\mathbf{p}'}(\mathbf{r}) \tag{3}$$

where the summation on $\mathbf{p}'$ is extended over all N levels of the band in question, N being the number of atoms in the lattice. One may easily show[1] that these functions are orthonormal,

$$(a(\mathbf{r}-\mathbf{Q}_k),\quad a(\mathbf{r}-\mathbf{Q}_l))=\delta_{kl}. \tag{4}$$

We used the standard notation (ψ_1, ψ_2) for the scalar product of the functions ψ_1 and ψ_2,

$$(\psi_1, \psi_2)=\int\int\int dxdydz(\psi_1^*\psi_2).$$

Further they have the property that they are localized[2] about the point $\mathbf{Q}_k$: they drop off rapidly as we move away from $\mathbf{Q}_k$. It is these properties that make them so useful in discussing the perturbed periodic lattice. In the presence of a perturbing electric and magnetic field the hamiltonian $\mathcal{H}$ takes the form

$$\mathcal{H}=(\mathbf{p}-e\mathbf{A}/c)^2/2m+V(\mathbf{r})+e\varphi(\mathbf{r}),$$

$\mathbf{A}$ being the vector potential of the perturbing magnetic field. We want to solve the Schrödinger equation

$$\mathcal{H}\psi=i\hbar\partial\psi/\partial t.$$

For the case of no magnetic field Slater (see reference 1) shows that it is convenient to expand ψ in terms of the Wannier functions, that is to put

$$\psi=\textstyle\sum_m\Psi(\mathbf{Q}_m)a(\mathbf{r}-\mathbf{Q}_m) \tag{5}$$

$\Psi(\mathbf{Q}_m)$ being coefficients to be determined. Here the

[1] J. C. Slater, Phys. Rev. **76**, 1592 (1949).
[2] G. H. Wannier, Phys. Rev. **52**, 191 (1937).
[3] R. Peierls, Z. Physik **80**, 763 (1933).
[4] The requirements of gauge invariance for velocity dependent operators have been investigated by R. G. Sachs and N. Austern, Phys. Rev. **81**, 705 (1951).
[5] We shall follow most of the notation of Slater, see reference 1, Appendix I.

summation is extended over all the points in the lattice. Such an expansion is always possible as long as we assume that the electric and magnetic fields are weak enough so that we may neglect contributions from different bands. According to well known calculations of Zener[6] this is usually an excellent approximation, and we shall assume it throughout this paper. A little consideration shows, however, that the expansion (5) is no longer quite suitable when a magnetic field is present. This is because of the perturbing term of the form $\mathbf{A}\cdot\mathbf{p}$ in $\mathcal{H}$. This term contains a derivative operator, and the method used by Slater is only directly applicable to perturbing terms which are functions of the coordinates alone. By suitably modifying the expansion (5), we shall be able to use most of the apparatus of Slater's proof. Let us replace (5) by

$$\psi=\sum_m \Psi(\mathbf{Q}_m)\exp\{(ie/\hbar c)G_m\}a(\mathbf{r}-\mathbf{Q}_m), \qquad (6)$$

where

$$G_m\equiv\int_{\mathbf{Q}_m}^{\mathbf{r}}\mathbf{A}(\xi)d\xi,$$

the integral being taken along the straight line path joining $\mathbf{Q}_m$ to $\mathbf{r}$. The exponential term has the effect of approximately removing the troublesome $\mathbf{A}\cdot\mathbf{p}$ term. One may write G_m in another form, which is convenient for calculation:

$$G_m=\int_0^1 d\lambda(\mathbf{r}-\mathbf{Q}_m)\cdot\mathbf{A}(\mathbf{Q}_m+\lambda(\mathbf{r}-\mathbf{Q}_m)). \qquad (7)$$

Equation (7) is obtained simply by parametrizing the line integral in the original definition of G_m.

We must now calculate $\mathcal{H}\psi$. Using the notation

$$\Psi(\mathbf{Q}_m)=\Psi_m,\quad a(\mathbf{r}-\mathbf{Q}_m)=a_m,$$

we have

$$\begin{aligned}\mathcal{H}\psi&=\mathcal{H}\sum_m\Psi_m\exp\{(ie/\hbar c)G_m\}a_m\\&=\sum_m\Psi_m[(\mathbf{p}-e\mathbf{A}/c)^2/2m+V+e\varphi]\exp\{(ie/\hbar c)G_m\}a_m\\&=\sum_m\Psi_m\exp\{(ie/\hbar c)G_m\}\\&\quad\times\left(\frac{[\mathbf{p}-(e/c)(\mathbf{A}-\nabla G_m)]^2}{2m}+V+e\varphi\right)a_m.\end{aligned}$$

It is a straightforward matter to compute ∇G_m (see Appendix I). One obtains

$$\nabla G_m=\mathbf{A}(\mathbf{r})+\int_0^1\lambda d\lambda\,(\mathbf{r}-\mathbf{Q}_m)\times\mathbf{H}(\mathbf{Q}_m+\lambda(\mathbf{r}-\mathbf{Q}_m)).$$

$\mathbf{H}(\xi)$ is the magnetic field at the point ξ, $\mathbf{H}(\xi)=\nabla_\xi\times\mathbf{A}(\xi)$.

[6] C. Zener, Proc. Roy. Soc. (London) A145, 523 (1934).

Thus

$$\mathcal{H}\psi=\sum_m\Psi_m\exp\{(ie/\hbar c)G_m\}\times\left[\frac{\left[\mathbf{p}+(e/c)\int_0^1 d\lambda\lambda(\mathbf{r}-\mathbf{Q}_m)\times\mathbf{H}\right]^2}{2m}+V+e\varphi\right]a_m.$$

We may now invoke (following Slater) the localization of the a_m. This allows us to put $\mathbf{r}\cong\mathbf{Q}_m$ in the operator on a_m, as long as the electric and magnetic fields are not too rapidly varying.[7] When we do this we obtain very simply

$$\mathcal{H}\psi=\sum_m\Psi_m\exp\{(ie/\hbar c)G_m\}[p^2/2m+V+e\varphi(\mathbf{Q}_m)]a_m,$$

or,

$$\mathcal{H}\psi=\sum_m\Psi_m\exp\{(ie/\hbar c)G_m\}[\mathcal{H}_0+e\varphi(\mathbf{Q}_m)]a_m. \qquad (8)$$

To complete the evaluation of the right-hand side of (8) we must have $\mathcal{H}_0a_m$. This is easily accomplished as follows: Using (3),

$$\begin{aligned}\mathcal{H}_0a_m&=N^{-\frac{1}{2}}\sum_{p'}\mathcal{H}_0\exp\{-i\mathbf{p}'\cdot\mathbf{Q}_m/\hbar\}\psi_{p'}\\&=N^{-\frac{1}{2}}\sum_{p'}E_0(\mathbf{p}')\exp\{-i\mathbf{p}'\cdot\mathbf{Q}_m/\hbar\}\psi_{p'}.\end{aligned}$$

Expressing $\psi_{p'}$ in terms of the a_m we have

$$\psi_{p'}=N^{-\frac{1}{2}}\sum_l\exp\{i\mathbf{p}'\cdot\mathbf{Q}_l/\hbar\}a_l,$$

so that we have finally

$$\mathcal{H}_0a_m=N^{-1}\sum_l\sum_{p'}E_0(\mathbf{p}')\exp\{i\mathbf{p}'\cdot(\mathbf{Q}_l-\mathbf{Q}_m)/\hbar\}a_l. \qquad (9)$$

Now as is well known $E_0(\mathbf{p}')$ is a periodic function of $\mathbf{p}'$, having the periodicity of the reciprocal lattice. Thus we may expand

$$E_0(p')=\sum_s B_s\exp\{-i\mathbf{p}'\cdot\mathbf{Q}_s/\hbar\}. \qquad (10)$$

Using (10) in (9) we obtain

$$\begin{aligned}\mathcal{H}_0a_m&=N^{-1}\sum_{l,s}\sum_{p'}B_s\exp\{ip'(\mathbf{Q}_l-\mathbf{Q}_s-\mathbf{Q}_m/\hbar\}a_l\\&=\sum_{l,s}B_s\delta_{l,m+s}a_l\end{aligned}$$

or

$$\mathcal{H}_0a_m=\sum_s B_s a_{m+s}. \qquad (11)$$

Substitution of (11) into (8) then yields

$$\mathcal{H}\psi=\sum_m\Psi_m\exp\{(ie/\hbar c)G_m\}[\sum_s B_s a_{m+s}+e\varphi(\mathbf{Q}_m)a_m].$$

If we replace $m+s$ by m' in the first term in the square bracket, we obtain (on dropping the prime)

$$\mathcal{H}\psi=\sum_m a_m[\sum_s B_s\Psi(\mathbf{Q}_m-\mathbf{Q}_s)\exp\{(ie/\hbar c)G_{m-s}\}+e\varphi(\mathbf{Q}_m)\Psi(\mathbf{Q}_m)\exp\{(ie/\hbar c)G_m\}]. \qquad (12)$$

Equation (12) may be put in a more elegant form if we make use of the well-known operator identity

$$\Psi(\mathbf{Q}_m-\mathbf{Q}_s)=\exp\{-\mathbf{Q}_s\cdot\nabla_m\}\Psi(\mathbf{Q}_m)$$

[7] Unfortunately it seems rather difficult within this formalism to make an estimate of the error involved here, and therefore it is impossible to say exactly what the conditions are under which the theorem to be proved is valid. This is so even without the presence of the magnetic field.

where ∇_m is the gradient operation with respect to the position vector $\mathbf{Q}_m$. Using this, (12) takes the form

$$\mathcal{H}\psi=\sum_m a_m[\sum_s B_s \exp\{(ie/\hbar c)G_{m-s}\}\exp\{-\mathbf{Q}_s\cdot\nabla_m\} + e\varphi(\mathbf{Q}_m)\exp\{(ie/\hbar c)G_m\}]\Psi(\mathbf{Q}_m).$$

Now this equation may further be simplified by using once again the localization of the a_m. This tells us that in G_{m-s}, and in G_m we can put $\mathbf{r}\cong\mathbf{Q}_m$. We have

$$G_m(\mathbf{r}=\mathbf{Q}_m)=0$$

$$G_{m-s}(\mathbf{r}=\mathbf{Q}_m)=\int_0^1 d\lambda\,\mathbf{Q}_s\cdot\mathbf{A}(\mathbf{Q}_m-(1-\lambda)\mathbf{Q}_s) = \int_0^1 d\lambda\,\mathbf{Q}_s\cdot\mathbf{A}(\mathbf{Q}_m-\lambda\mathbf{Q}_s).$$

Substituting, we obtain

$$\mathcal{H}\psi=\sum_m a_m\Big[\sum_s B_s \exp\Big\{(ie/\hbar c)\times\int_0^1 d\lambda\,\mathbf{Q}_s\cdot\mathbf{A}(\mathbf{Q}_m-\lambda\mathbf{Q}_s)\Big\}\exp\{-\mathbf{Q}_s\cdot\nabla_m\} + e\varphi(\mathbf{Q}_m)\Big]\Psi(\mathbf{Q}_m).$$

We now make use of the operator identity (for a proof, see Appendix II)

$$\exp\Big\{(ie/\hbar c)\int_0^1 d\lambda\,\mathbf{Q}_s\cdot\mathbf{A}(\mathbf{Q}_m-\lambda\mathbf{Q}_s)\Big\}\exp\{-\mathbf{Q}_s\cdot\nabla_m\} = \exp\{-\mathbf{Q}_s\cdot[\nabla_m-(ie/\hbar c)\mathbf{A}(\mathbf{Q}_m)]\} = \exp\{-i\mathbf{Q}_s\cdot[\mathbf{p}_m-(e/c)\mathbf{A}_m]/\hbar\},$$

where $\mathbf{p}_m\equiv-i\hbar\nabla_m$. Thus

$$\mathcal{H}\psi=\sum_m a_m[\sum_s B_s \exp\{-i\mathbf{Q}_s\cdot[\mathbf{p}_m-(e/c)\mathbf{A}(\mathbf{Q}_m)]/\hbar\} + e\varphi(\mathbf{Q}_m)]\Psi(\mathbf{Q}_m). \quad (13)$$

However, using (10) we see that the summation over s is easily performed:

$$\sum_s B_s \exp\{-i\mathbf{Q}_s\cdot[\mathbf{p}_m-(e/c)\mathbf{A}(\mathbf{Q}_m)]/\hbar\} = E_0[\mathbf{p}_m-(e/c)\mathbf{A}(\mathbf{Q}_m)], \quad (14)$$

where $E_0[\mathbf{p}_m-(e/c)\mathbf{A}(\mathbf{Q}_m)]$ is the same function[8] of $\mathbf{p}_m-(e/c)A(\mathbf{Q}_m)$ as $E_0(\mathbf{p}')$ is of $\mathbf{p}'$. Using (14), we may rewrite (13) as

$$\mathcal{H}\psi=\sum_m a_m\{E_0[\mathbf{p}_m-(e/c)\mathbf{A}(\mathbf{Q}_m)]+e\varphi(\mathbf{Q}_m)\}\Psi(\mathbf{Q}_m). \quad (15)$$

[8] Since $A(\mathbf{Q}_m)$ does not commute with $\mathbf{p}_m$, there may be some ambiguity in the ordering of the factors in $E_0(\mathbf{p}_m-(e/c)\mathbf{A}(\mathbf{Q}_m))$. In such cases the order is uniquely determined by returning to the expansion (14).

The Schrödinger equation reads

$$\mathcal{H}\psi=i\hbar\partial\psi/\partial t = i\hbar\sum_m a_m \exp\{(ie/\hbar c)G_m\}\dot{\Psi}(\mathbf{Q}_m) - (e/c)\sum_m \dot{G}_m a_m\Psi(\mathbf{Q}_m)\cong i\hbar\sum_m a_m\dot{\Psi}(\mathbf{Q}_m),$$

on using once again the localization of the a_m. Using (15), we obtain

$$\sum_m a_m\{E_0[\mathbf{p}_m-(e/c)\mathbf{A}(\mathbf{Q}_m)]+e\varphi(\mathbf{Q}_m)\}\Psi(\mathbf{Q}_m) = i\hbar\sum_m a_m\dot{\Psi}(\mathbf{Q}_m).$$

Finally, taking the scalar product of both sides with a_l, and using the orthonormality of the a_k, we obtain

$$\{E_0[\mathbf{p}_m-(e/c)\mathbf{A}(\mathbf{Q}_m)]+e\varphi(\mathbf{Q}_m)\}\Psi(\mathbf{Q}_m)=i\hbar\dot{\Psi}(\mathbf{Q}_m), \quad (2')$$

The eigenvalue problem associated with Eq. (2') is identical (apart from notation) with Eq. (2), so that we have proven that for fields which vary slowly enough approximate eigenvalues of the energy may be obtained by solving (2).

III. THE MOTION OF WAVE PACKETS

Following Slater[1] we can also investigate the motion of wave packets of electrons in the perturbed lattice. If we construct our wave packets from the solutions of (2), then we know (Ehrenfest's theorem) that the center of gravity of such a wave packet moves according to the classical canonical equations. In our case this hamiltonian is

$$\mathcal{H}=E_0[\mathbf{p}-(e/c)\mathbf{A}]+e\varphi.$$

The equations of motion are therefore

$$dx/dt=v_x=\partial\mathcal{H}/\partial p_x, \text{ etc.},$$

and

$$dp_x/dt=-\partial\mathcal{H}/\partial x, \text{ etc.}$$

Let us use the notation

$$\mathbf{P}=\mathbf{p}-(e/c)\mathbf{A}.$$

Then

$$v_x=\partial\mathcal{H}/\partial p_x=\partial E_0(\mathbf{P})/\partial p_x=\partial E_0(\mathbf{P})/\partial P_x,$$

or

$$\mathbf{v}=\nabla_P E_0(\mathbf{P}). \quad (16)$$

The other canonical equation gives

$$\frac{dp_x}{dt}=-\frac{\partial}{\partial x}[E_0(\mathbf{P})+e\varphi] = -e\frac{\partial\varphi}{\partial x}-\left(\frac{\partial E_0}{\partial P_x}\frac{\partial P_x}{\partial x}+\frac{\partial E_0}{\partial P_y}\frac{\partial P_y}{\partial x}+\frac{\partial E_0}{\partial P_z}\frac{\partial P_z}{\partial x}\right) = -e\frac{\partial\varphi}{\partial x}+\frac{e}{c}\left(v_x\frac{\partial A_x}{\partial x}+v_y\frac{\partial A_y}{\partial x}+v_z\frac{\partial A_z}{\partial x}\right).$$

From this we can construct the equation of motion

for P_x:

$$\frac{dP_x}{dt}=\frac{dp_x}{dt}-\frac{e}{c}\frac{dA_x}{dt}$$

$$=\frac{dp_x}{dt}-\frac{e}{c}\left(\frac{\partial A_x}{\partial t}+\frac{\partial A_x}{\partial x}v_x+\frac{\partial A_x}{\partial y}v_y+\frac{\partial A_x}{\partial z}v_z\right)$$

$$=e\left[-\frac{\partial\varphi}{\partial x}-\frac{1}{c}\frac{\partial A_x}{\partial t}+\frac{1}{c}\left(v_y\left(\frac{\partial A_y}{\partial x}-\frac{\partial A_x}{\partial y}\right)-v_z\left(\frac{\partial A_z}{\partial x}-\frac{\partial A_x}{\partial z}\right)\right)\right].$$

Using the defining equations for the electric and magnetic fields

$$\mathbf{E}=-\nabla\varphi-(1/c)\partial\mathbf{A}/\partial t$$
$$\mathbf{H}=\nabla\times\mathbf{A},$$

we obtain

$$dP_x/dt=e[E_x+(1/c)(v\times H)_x]$$

of finally,

$$d\mathbf{P}/dt=e[\mathbf{E}+(1/c)(\mathbf{v}\times\mathbf{H})]. \tag{17}$$

Equations (16) and (17) are actually well known,[9] though the derivations previously given differ considerably from the one presented here.

In conclusion I should like to express my warmest thanks to Professor R. G. Sachs and to Professor J. Powell for many stimulating and helpful discussions.

APPENDIX I

We must construct the gradient of G_m.

$$\nabla G_m=\int_0^1 d\lambda\nabla[(\mathbf{r}-\mathbf{Q}_m)\cdot\mathbf{A}(\mathbf{Q}_m+\lambda(\mathbf{r}-\mathbf{Q}_m))]$$

$$=\int_0^1 d\lambda[(\mathbf{r}-\mathbf{Q}_m)\times(\nabla\times\mathbf{A})+\mathbf{A}\times(\nabla\times(\mathbf{r}-\mathbf{Q}_m))+(\mathbf{A}\cdot\nabla)(\mathbf{r}-\mathbf{Q}_m)+((\mathbf{r}-\mathbf{Q}_m)\cdot\nabla)\mathbf{A}],$$

by a well-known expansion in vector analysis. Using

$$\nabla\times\mathbf{A}[\mathbf{Q}_m+\lambda(\mathbf{r}-\mathbf{Q}_m)]=\lambda\mathbf{H}[\mathbf{Q}_m+\lambda(\mathbf{r}-\mathbf{Q}_m)]$$
$$\nabla\times\mathbf{r}=0,\quad(\mathbf{A}\cdot\nabla)\mathbf{r}=\mathbf{A},$$

we get

$$\nabla G_m=\int_0^1 d\lambda[\lambda(\mathbf{r}-\mathbf{Q}_m)\times\mathbf{H}+\mathbf{A}+((\mathbf{r}-\mathbf{Q}_m)\cdot\nabla)\mathbf{A}].$$

However, integrating by parts gives

$$\int_0^1 A(\mathbf{Q}_m+\lambda(\mathbf{r}-\mathbf{Q}_m))d\lambda=\lambda A(\mathbf{Q}_m+\lambda(\mathbf{r}-\mathbf{Q}_m))\Big|_0^1$$
$$-\int_0^1 d\lambda\cdot\lambda\cdot\frac{d}{d\lambda}\mathbf{A}(\mathbf{Q}_m+\lambda(\mathbf{r}-\mathbf{Q}_m))$$
$$=\mathbf{A}(\mathbf{r})-\int_0^1 d\lambda((\mathbf{r}-\mathbf{Q}_m)\cdot\nabla)\mathbf{A}.$$

Inserting this in our original expression we obtain

$$\nabla G_m=\mathbf{A}(\mathbf{r})+\int_0^1 d\lambda\cdot\lambda\cdot(\mathbf{r}-\mathbf{Q}_m)\times\mathbf{H}(\mathbf{Q}_m+\lambda(\mathbf{r}-\mathbf{Q}_m)),$$

which is the required result.

APPENDIX II

We wish to establish the identity[10]

$$\exp\{-\mathbf{Q}\cdot(\nabla-(ie/\hbar c)\mathbf{A})\}$$
$$=\exp\left\{(ie/\hbar c)\int_0^1 d\lambda\mathbf{Q}\cdot\mathbf{A}(\mathbf{r}-\lambda\mathbf{Q})\right\}\exp\{-\mathbf{Q}\cdot\nabla\}.$$

To do this, let us define an operator $F(\eta)$ as follows:

$$F(\eta)=\exp\left\{(ie/\hbar c)\int_0^\eta d\lambda\mathbf{Q}\cdot\mathbf{A}(\mathbf{r}-\lambda\mathbf{Q})\right\}\exp\{-\eta\mathbf{Q}\cdot\nabla\}.$$

Then

$$dF/d\eta=\exp\left\{(ie/\hbar c)\int_0^\eta d\lambda\mathbf{Q}\cdot\mathbf{A}(\mathbf{r}-\lambda\mathbf{Q})\right\}\times[(ie/\hbar c)\mathbf{Q}\cdot\mathbf{A}(\mathbf{r}-\lambda\mathbf{Q})]\exp\{-\eta\mathbf{Q}\cdot\nabla\}$$
$$+\exp\left\{(ie/\hbar c)\int_0^\eta\mathbf{Q}\cdot\mathbf{A}(\mathbf{r}-\lambda\mathbf{Q})d\lambda\right\}\times\exp\{-\eta\mathbf{Q}\cdot\nabla\}(-\mathbf{Q}\cdot\nabla).$$

But

$$(ie/\hbar c)\mathbf{Q}\cdot\mathbf{A}(\mathbf{r}-\eta\mathbf{Q})\exp\{\eta\mathbf{Q}\cdot\nabla\}=\exp\{-\eta\mathbf{Q}\cdot\nabla\}(ie/\hbar c)\mathbf{Q}\cdot\mathbf{A}(\mathbf{r}),$$

since $\exp\{-\eta\mathbf{Q}\cdot\nabla\}$ is just the displacement operator for the displacement $-\eta\mathbf{Q}$. Therefore, we obtain

$$dF/d\eta=F(\eta)[-\mathbf{Q}\cdot\nabla+(ie/\hbar c)\mathbf{Q}\cdot\mathbf{A}(\mathbf{r})]=F(\eta)[-\mathbf{Q}\cdot(\nabla-(ie/\hbar c)\mathbf{A})].$$

This is a differential equation for $F(\eta)$, and may be integrated at once, giving

$$F(\eta)=\exp\{-\eta\mathbf{Q}\cdot(\nabla-(ie/\hbar c)\mathbf{A})\}$$

(the constant of integration being fixed by the condition $F(0)=1$, which follows from the original definition of F). If we set $\eta=1$ in this expression we obtain the identity in question.

[9] A. H. Wilson, *Theory of Metals* (Cambridge University Press, London, 1935), p. 61 ff., and W. Shockley, *Electrons and Holes in Semi-Conductors* (D. Van Nostrand Company, Inc., New York, 1950), p. 424 ff. The form in which we have given these equations is that of Shockley, who makes extensive application of them in the theory of semiconductors. A discussion of the range of validity of these equations is also to be found in Shockley's book.

[10] This identity is given in a slightly different form, and with an entirely different proof in R. G. Sachs, Phys. Rev. 74, 433 (1948), Sec. IV.

Note on the Interaction of an Electron and a Lattice Oscillator*

E. P. Gross
Laboratory for Insulation Research, Massachusetts Institute of Technology, Cambridge, Massachusetts
(Received July 30, 1951)

The interaction of an electron and a lattice oscillator is studied for an interaction energy of a special type linear in the oscillator coordinates and momenta. The energy values and eigenfunctions for arbitrary coupling strength are found by solving a three-term recurrence relation. A plot of energy *vs* total momentum of electron plus oscillator reveals the role of degeneracies of states involving different numbers of quanta in the oscillator. As the frequency of the oscillator tends to zero, one finds the bandlike spectrum characteristic of an electron moving in a periodic potential. With increasing total momentum the electron makes Bragg reflections, transferring quanta of energy and momentum to the oscillator, and remaining bounded in velocity. For strong coupling the state of minimum energy is one of nonzero total momentum. For sufficiently strong coupling, regions of small effective electron mass cease to exist.

I. INTRODUCTION

In recent months increased attention has been directed to the interaction of electrons with the lattice vibrations of crystals.[1–4] In many cases as, for example, the motion of electrons in polar lattices the electron lattice interaction is so strong that ordinary perturbation methods are inadequate. The present note is concerned with the exact treatment of a very simple system: An electron interacting with a single lattice oscillator for a special form of interaction. The lattice oscillator is characterized by an angular frequency ω and a propagation vector $\mathbf{k}$, i.e., is a traveling wave. As the first of several main points we shall find the energy values and eigenfunctions of the system of electron plus oscillator and study the lowest state in detail. The energy is a function of three parameters: the total momentum of the system, the strength of interaction, and the ratio $(\hbar k)^2/m\hbar\omega$. By studying the energy values and eigenfunctions as a function of total momentum and interaction strength one can see the role of states in which many quanta are present in the oscillator and the effect on the effective mass of the electron. Second, the exact probability of scattering can be computed and compared with the results given by time-dependent perturbation theory. Third, we shall study the limit of zero frequency when the phase velocity (ω/k) of the wave tends to zero. The traveling wave then becomes stationary and, provided one can neglect the recoil motion of the oscillator, one has exactly the problem of an electron in a periodic potential with its characteristic band-energy spectrum. If a small electric field acts, continually imparting momentum to the electron, Bragg reflections occur in which momentum is transferred to the system providing the periodic potential, and the electron remains bounded in velocity and energy. For the case treated here it is interesting to understand in detail the momentum transfer process.

We adopt the notation used by Fröhlich[5] in the discussion of the motion of electrons in a polar lattice. A system consisting of one electron interacting with a set of oscillators in a polar crystal is governed by the approximate hamiltonian

$$\mathcal{H}=\frac{p^2}{2m}+\sum_k g_k\left(X_k\sin\mathbf{k}\cdot\mathbf{q}+\frac{Y_k}{M\omega}\cos\mathbf{k}\cdot\mathbf{q}\right)+\sum_k\left(\frac{M\omega^2}{2}X_k^2+\frac{Y_k^2}{2M}\right).$$

Here p_x, p_y, p_z are the canonical momenta and q_x, q_y, q_z the canonical coordinates of the electron, X_k and Y_k are canonical coordinates and momenta of a lattice oscillator with propagation vector $\mathbf{k}$ and frequency $\omega(\mathbf{k})$. M depends on the mass of the ions giving rise to the lattice vibration. The sum over k goes over all lattice vibrations and has a natural cutoff for wavelengths of the order of the lattice spacing. The coupling constant for the case of a polar crystal is approximately $g_k=4\pi e/k$. The form of interaction used here differs from that occurring in metals, being characteristic of the long-range coulomb forces due to the ionic nature of the constituents of a polar lattice, but is general in that it is linear in the oscillator coordinates and momenta. We are not concerned with the accuracy with which the above hamiltonian describes the actual situation in a polar crystal, but merely take advantage of the fact that the type of interaction term allows one to make an exact treatment of the interaction of an electron with one oscillator.

II. MOMENTUM INTEGRAL AND WAVE FUNCTION COEFFICIENTS

We now study the interaction of an electron with a radiation oscillator the direction of propagation of which coincides with that of the electron and with a hamiltonian

$$\mathcal{H}=p^2/2m+g_k(X_k\sin kq+(Y_k/m\omega)\cos kq)+\tfrac{1}{2}(M\omega^2X_k^2+Y_k^2/M). \quad (1)$$

* Sponsored by the ONR, the Army Signal Corps, and the Air Force under ONR contract.

[1] H. Fröhlich, Phys. Rev. **79**, 845 (1950).
[2] J. Bardeen, Phys. Rev. **79**, 167 (1950); **80**, 567 (1950).
[3] Fröhlich, Pelzer, and Zienau, Phil. Mag. **41**, 221 (1950).
[4] T. Muto and S. Ôyama, Prog. Theor. Phys. **5**, 833 (1950).
[5] H. Fröhlich, Proc. Roy. Soc. (London) **A160**, 230 (1937).

Since this is a system of two degrees of freedom, one additional integral of motion will suffice to determine the motion. Let us consider the operator

$$\Lambda=p+\tfrac{1}{2}(k/\omega)(M\omega^2X_k^2+Y_k^2/M),$$

which is the total momentum of the system. We form the Poisson bracket $[\Lambda, \mathfrak{H}]$ and with the help of the relations $[p, f(q)]=-i\hbar\partial f/\partial q$, $[q, f(p)]=+i\hbar\partial f/\partial p$, which hold for any pair of canonical variables, we verify that $[\Lambda, \mathfrak{H}]=0$, so that the total momentum Λ is an integral of motion. As a result the eigenfunctions of $\mathfrak{H}$ must simultaneously be eigenfunctions of Λ. Let the eigenvalues of Λ be λ, and the eigenfunctions be $\psi_\lambda(X_k, q)$. Now Λ is highly degenerate in the sense that a given value λ of total momentum has an eigenfunction which is an arbitrary linear combination of states corresponding to distribution of the given momentum in different ways on the electron and phonons. The coefficients in the Λ eigenfunctions must be so chosen that the ψ_λ's are simultaneously eigenfunctions of $\mathfrak{H}$.

The eigenfunctions of Λ are determined from

$$\Lambda\psi_\lambda=\left\{p+\frac{1}{2}\frac{k}{\omega}\left(M\omega^2X_k^2+\frac{Y_k^2}{M}\right)\right\}\psi_\lambda=\lambda\psi_\lambda(X_k, q). \quad (2)$$

Since Λ is the sum of operators for each of the degrees of freedom we may look for separable solutions, and it may be verified that the most general eigenfunction of Λ belonging to a total momentum λ is

$$\psi_\lambda=\exp\left[\frac{i}{\hbar}\left(\lambda-\frac{\hbar k}{2}\right)q\right]\sum_{n=0}^{\infty}a_n^\lambda e^{-in\hbar q}\phi_n^\lambda(X_k). \quad (3)$$

The a_n^λ are arbitrary complex numbers and the ϕ_n^λ are oscillator wave functions

$$\phi_n^\lambda=\left(\frac{(M\omega/\pi\hbar)^{\frac{1}{2}}}{2^n n!}\right)^{\frac{1}{2}}H_n\left[\left(\frac{M\omega}{\hbar}\right)^{\frac{1}{2}}X_k\right]$$
$$\times\exp[-(M\omega/2\hbar)X_k^2]j^n. \quad (4)$$

We adopt periodic boundary conditions and normalize the wave function over a box of unit length so that

$$\sum_{n=0}^{\infty}a_n^{*\lambda}a_n^\lambda=1.$$

For a given λ there are states where the electron has a negative momentum and many quanta are excited. Our treatment places no restrictions on λ so that it may range quasi-continuously from $-\infty$ to $+\infty$. The a_n^λ are found by satisfying the Schrödinger equation $\mathfrak{H}\psi_\lambda=E\psi_\lambda$. Operating on ψ_λ with the interaction part of the hamiltonian we find

$$g_k\left(X_k\sin kq+\frac{Y_k}{M\omega}\cos kq\right)\psi_\lambda$$
$$=g_k\left(\frac{\hbar}{2M\omega}\right)^{\frac{1}{2}}\exp\left[\frac{i}{\hbar}\left(\lambda-\frac{\hbar k}{2}\right)q\right]$$
$$\times\sum_{n=0}^{\infty}[a_{n+1}^\lambda(n+1)^{\frac{1}{2}}+a_{n-1}^\lambda n^{\frac{1}{2}}]e^{-in\hbar q}\phi_n^\lambda, \quad (5)$$

where the coefficient $a_{-1}^\lambda=0$. The result of satisfying the Schrödinger equation $\mathfrak{H}\psi_\lambda=E\psi_\lambda$ is, therefore,

$$\sum_{n=0}^{\infty}\left[\left\{(n+\tfrac{1}{2})\hbar\omega-E+\frac{(\lambda-\frac{1}{2}\hbar k-n\hbar k)^2}{2m}\right\}a_n^\lambda\right.$$
$$\left.+g_k\left(\frac{\hbar}{2M\omega}\right)^{\frac{1}{2}}\{a_{n+1}^\lambda(n+1)^{\frac{1}{2}}+a_{n-1}^\lambda n^{\frac{1}{2}}\}\right]e^{-in\hbar q}\phi_n(X_k)=0.$$

Multiplying both sides by $e^{in\hbar q}\phi_n$ and integrating over q and X_k one obtains the recurrence relation

$$\left\{(n+\tfrac{1}{2})\hbar\omega-E+\frac{(\lambda-\frac{1}{2}\hbar k-n\hbar k)^2}{2m}\right\}a_n^\lambda$$
$$+g_k\left(\frac{\hbar}{2M\omega}\right)^{\frac{1}{2}}[a_{n+1}^\lambda(n+1)^{\frac{1}{2}}+a_{n-1}^\lambda n^{\frac{1}{2}}]=0, \quad (6)$$

where $n=0, 1, 2, \cdots$, and $a_{-1}^\lambda=0$.

For the case of zero interaction we set $g_k=0$, and find

$$E_{n\lambda}^0=(n+\tfrac{1}{2})\hbar\omega+(\lambda-\tfrac{1}{2}\hbar k-n\hbar k)^2/2m, \text{ or } a_n^\lambda=0. \quad (7)$$

The energy levels are specified by two quantum numbers: n which is discrete and λ which is continuous. The spectrum consists of continua which overlap over a portion of their ranges. When $n=0$ we have $E=\frac{1}{2}\hbar\omega+(\lambda-\frac{1}{2}\hbar k)^2/2m$ and $\psi_\lambda^0=a_0^\lambda\exp[i/\hbar(\lambda-\hbar k/2)q]\phi_0(X_k)$ while for $n=1$ we have $E=3\hbar\omega/2+(\lambda-3\hbar k/2)^2/2m$

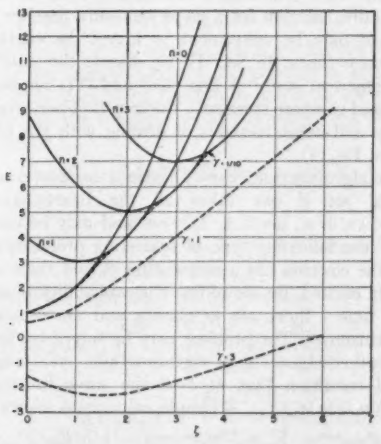

FIG. 1. Energy vs momentum for $\alpha=1$. The quantities α and γ are defined by the equations $\frac{1}{2}\hbar\omega\alpha^2=(\hbar k)^2/2m$ and $\frac{1}{2}\hbar\omega\gamma=g_k(\hbar/2M\omega)^{\frac{1}{2}}$.

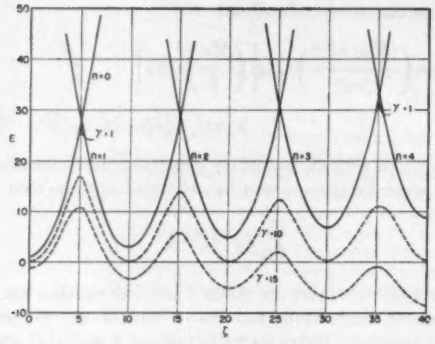

FIG. 2. Energy *vs* momentum for $\alpha=10$.

and $\psi_\lambda{}^1=\exp[i(\lambda-3\hbar k/2)q]a_1{}^\lambda\phi_1(X_k)$. The chief features of the energy spectrum for zero interaction may be illustrated by plotting E *vs* $\lambda-\hbar k/2$, one curve for each n value. This is done in Figs. 1 and 2 for different values of the ratio $(\hbar k)^2/m\hbar\omega$, using reduced units [see Eq. (8)]. Each curve is a parabola symmetric about the value $n\hbar k$ and has its minimum at that value. Two curves intersect at some value of ζ, so that for larger values of ζ the curve for the lower n value lies higher while for smaller ζ values it lies lower. It will be seen that the introduction of interaction removes the intersection of the curves in a way analogous to the removal of intersections of potential curves in the theory of molecules. The lowest curve to the right of the intersection point has a wave function similar to that of the higher curve before interaction was introduced. For sufficiently strong interaction even portions of the lowest curve near the minimum have several quantum terms in their wave functions. (Near the intersection points the effective mass of the electron is altered.)

III. ENERGY SPECTRUM AND SCATTERING PROBABILITY

We note that to deal with the case of finite interaction in the present method one must study the three-term recurrence relation Eq. (6). The energy values are the roots of an infinite determinant. After these have been determined one may find the corresponding ratios of the coefficients $a_n{}^\lambda$. The use of continued-fraction methods will permit us to find numerically the spectrum and the wave functions to any desired accuracy.

To study the recurrence relations we will put

$$(\hbar k)^2/2m=\tfrac{1}{2}\alpha^2\hbar\omega, \quad g_k(\hbar/2M\omega)^{\frac{1}{2}}=\tfrac{1}{2}\gamma\hbar\omega \tag{8}$$

and express all energies in units of $\hbar\omega/2$. Then with $\eta^2=\lambda^2/(2m\hbar\omega/2)$ and $\zeta=\eta-\alpha/2$

$$\{(2n+1)-E+(\zeta-n\alpha)^2\}a_n{}^\lambda +\gamma[a_{n+1}{}^\lambda(n+1)^{\frac{1}{2}}+a_{n-1}{}^\lambda n^{\frac{1}{2}}]=0. \tag{9}$$

Let us put $v_0=a_1/a_0$, $v_1=a_2/a_1\cdots v_r=a_{r+1}/a_r$. Noting that $v_0v_1=a_2/a_0$, we have for the $n=1$ equation

$$v_0{}^\lambda=-\gamma/[\{3-E+(\zeta-\alpha)^2\}+\gamma v_1\sqrt{2}]. \tag{10}$$

We find for the general term

$$v_{r-1}{}^\lambda=-\gamma r^{\frac{1}{2}}/[\{(2r+1)-E+(\zeta-r\alpha)^2+\gamma v_r{}^\lambda(r+1)^{\frac{1}{2}}]. \tag{11}$$

This last equation can be used to find $v_0{}^\lambda$ in terms of some v_r with r very large as a continued fraction. Inspection of Eq. (11) shows that there is a solution of the recurrence relation for which $v_r\to 0$ as $r\to\infty$. An expression for the energy spectrum is found by obtaining an independent equation for $v_0{}^\lambda$ and comparing with Eq. (10). One finds, using the $r=0$ equation of the recurrence relation,

$$v_0{}^\lambda=-(1-E+\zeta^2)/\gamma. \tag{12}$$

Hence the energy spectrum can be computed from

$$1-E+\zeta^2=\frac{\gamma^2}{3-E+(\zeta-\alpha)^2}\dotplus\frac{\gamma^2\cdot 2}{5-E+(\zeta-2\alpha)^2} \dotplus\frac{\gamma^2\cdot 3}{7-E+(\zeta-3\alpha)^2}\dotplus\frac{\gamma^2\cdot 4}{9-E+(\zeta-4\alpha)^2}\dotplus\cdots, \tag{13}$$

where we use the notation

$$\frac{1}{a}\dotplus\frac{1}{b}\dotplus\frac{1}{c}\equiv\cfrac{1}{a-\cfrac{1}{b-\cfrac{1}{c}}}.$$

Equation (13) has infinitely many roots representing the eigenvalues of ground and excited states for a given value of λ. We thus see that we should actually write $E_{\lambda\mu}$ and $\psi_{\lambda\mu}$ for the eigenvalues and eigenfunctions. To find the root which goes continuously to the zero interaction solution for a given quantum number n as $\gamma\to 0$, it may be convenient to invert the continued fraction n times. In Sec. IV we discuss the results of the numerical study of Eqs. (13) and (11) for several cases and compare them with the results of perturbation theory and other methods of dealing with the hamiltonian, Eq. (1).

The eigenfunctions Eq. (3) form a complete, orthonormal set if one takes all the functions with $-\infty<\lambda<+\infty$, $\mu=0, 1, 2, \cdots\infty$ and may be used to study the following type of scattering problem: If at $t=0$ the electron has a momentum p_0 and there are n quanta excited, we are to find the probability that at a later time t there are m quanta and an electron of momentum p_1. The problem may be solved by finding a linear combination of eigenfunctions satisfying the initial condition that at $t=0$ the wave function is $\exp[i(p_0/\hbar)q]\phi_n(X_k)$. A simple calculation shows that

$$P_{mp_1{}^{np_0}}=|\textstyle\sum_\mu a_n{}^{*\lambda\mu}a_m{}^{\lambda\mu}\exp[-(1/\hbar)E_{\lambda\mu}t]|^2, \tag{14}$$

where λ is fixed by specifying the initial state and p_0 and p_1 are linked by the law of conservation of momen-

tum $\lambda=p_0+n\hbar k=p_1+m\hbar k$. In Figs. 1 and 2 this means that only vertical transitions are permitted.

IV. DISCUSSION OF CASES

(1) Case of Infinite Wavelength, $\alpha=0$

As a first example, let us treat the limiting case $\alpha=0$, where it is possible to find exact expressions for the energy levels and wave functions for arbitrary strength of interaction. The main result is that all the energy levels are shifted by the same amount, which depends on the strength of interaction, while the wave functions are multiplied by a phase factor. Since the shapes of the energy-*vs*-momentum curves are unaltered, the effective mass and average velocity[6] remain that of a free electron. These results occur because one is dealing with the case $\hbar k=0$, or zero phonon recoil momentum. With the help of the exact wave functions the probabilities of occurrence of scattering processes are evaluated and compared with the time-dependent perturbation theory. For small values of the coupling constant the latter gives accurate results, but for stronger coupling it overestimates the scattering probability.

a. Exact Energy Values and Eigenfunctions

Let us take the limit $k\to 0$, assuming that g_k remains finite. The hamiltonian becomes

$$\mathcal{H}=p^2/2m+g_k(Y_k/M\omega)+\tfrac{1}{2}(M\omega^2X_k^2+Y_k^2/M). \quad (15)$$

The eigenfunctions and energy values of the system are

$$\psi_{n\lambda}=\exp\left(-\frac{i}{\hbar}\lambda q-i\frac{g_k}{\hbar\omega}X_k\right)H_n\left[\left(\frac{M\omega}{\hbar}\right)^{\frac{1}{2}}X_k\right]\times\exp\left(-\frac{M\omega}{2\hbar}X_k^2\right)\left[\frac{(M\omega/2\hbar)^{\frac{1}{2}}}{2^n n!}\right]^{\frac{1}{2}}(i)^n, \quad (16)$$

$$E_{n\lambda}=\hbar^2\lambda^2/2m+(n+\tfrac{1}{2})\hbar\omega-g_k^2/2M\omega^2. \quad (17)$$

In units of $\hbar\omega/2$ the expression is $E_{n\lambda}=E_{n\lambda}{}^0-\gamma^2/2$, the interaction causing a constant depression of energy.

In order to interpret these wave functions, we expand in terms of the complete set of wave functions without interaction .

$$\psi_{n\lambda}=\sum_{n'\lambda'}(n\lambda|a|n'\lambda')\phi_{n'}\exp[-i(\lambda'/\hbar)q].$$

We find

$$(n\lambda|a|n'\lambda')=\int_{-\infty}^{+\infty}\int_{-\infty}^{+\infty}\phi_{n'}{}^*\exp(i\lambda' q/\hbar)\psi_{n\lambda}dqdX_k.$$

Inserting $\psi_{n\lambda}$ from Eq. (16) there results

$$(n\lambda|a|n'\lambda')=\delta_{\lambda\lambda'}\int_{-\infty}^{+\infty}\exp\left[-i\frac{g_k}{\hbar\omega}X_k-\frac{M\omega}{\hbar}X_k^2\right]\times H_nH_{n'}dX_k\frac{(M\omega/\pi\hbar)^{\frac{1}{2}}}{(2^n n!2^{n'}n'')^{\frac{1}{2}}}=\delta_{\lambda\lambda'}a_{nn'}, \quad (18)$$

where $\delta_{\lambda\lambda'}$ is the Kronecker delta. The $a_{nn'}$ may be evaluated by using the generating function for the Hermite polynomials. One finds for the lowest coefficients

$$\begin{aligned}
&a_{00}=\exp(-\gamma^2/8),\quad a_{01}=-\tfrac{1}{2}i\gamma\exp(-\gamma^2/8),\\
&a_{02}=-(\gamma^2/4\sqrt{2})\exp(-\gamma^2/8);\\
&a_{11}=(4-\gamma^2)/4\exp(-\gamma^2/8),\\
&a_{03}=(i\gamma^2/8\sqrt{3})\exp(-\gamma^2/8),\\
&a_{12}=[i(\gamma^3-8\gamma)/8\sqrt{2}]\exp(-\gamma^2/8),\\
&a_{00}=(\gamma^4/32\sqrt{6})\exp(-\gamma^2/8),\\
&a_{13}+[(\gamma^4-12\gamma^2)/16\sqrt{6}]\exp(-\gamma^2/8). \quad (19)
\end{aligned}$$

It is to be noted, in addition, that the relation $a_{mn}=a_{nm}$ is valid.

b. Time-Dependent Processes

The preceding formulas for the energy values and eigenfunctions may be also derived from stationary-state perturbation theory, if the perturbation theory is carried out to arbitrarily high accuracy. The factor $\exp(-\gamma^2/8)$ will enter if one takes care to normalize the perturbed wave functions. However, the time-dependent perturbation theory becomes very unwieldy in the higher approximations.

Using Eqs. (14) and (17) we compute

$$P_{0\lambda}{}^{0\lambda}=|\textstyle\sum_\mu|a_0{}^{\lambda\mu}|^2e^{-i\omega\mu t}|^2. \quad (20)$$

Inserting the values of $a_0{}^{\lambda\mu}$ given in Eq. (19), we find

$$P_{0\lambda}{}^{0\lambda}=\left|1+\frac{\gamma^2}{4}e^{-i\omega t}+\frac{\gamma^4}{32}e^{-2i\omega t}+\frac{\gamma^6e^{-3i\omega t}}{48\cdot 8}+\frac{\gamma^8e^{-4i\omega t}}{6\cdot 64\cdot 16}\right|^2\times\exp(-\gamma^2/2). \quad (21)$$

If $\gamma\ll 2$ we can keep only terms up to γ^2. Then

$$P_{0\lambda}{}^{0\lambda}\simeq 1-\tfrac{1}{2}\gamma^2(1-\cos\omega t). \quad (22)$$

Now $P_{0\lambda}{}^{0\lambda}$ is the probability that a system which has been observed to have zero quanta at time $t=0$ will have zero quanta at time t. This probability is less than unity and oscillates about the average value $1-\gamma^2/2$. If γ becomes of the order unity, the probability becomes small. The first approximation in time-dependent perturbation theory gives the same result as the exact probability expanded to order γ^2.

With the help of Eq. (21) we may find the probability $P_{0\lambda}{}^{0\lambda}$ to order γ^4. The result is

$$P_{0\lambda}{}^{0\lambda}=\left(1-\frac{\gamma^2}{2}+\frac{3}{16}\gamma^4\right)+\left(\frac{\gamma^2}{2}-\frac{\gamma^4}{4}\right)\cos\omega t+\frac{\gamma^4}{16}\cos 2\omega t. \quad (23)$$

We thus see that the nonfluctuating part of $P_{0\lambda}{}^{0\lambda}$ has

[6] With the help of methods used in the theory of electron motion in a periodic potential one may show that the mean electron velocity is given by $\bar{V}=\partial E/\partial\lambda$.

been increased to $(1-\frac{1}{2}\gamma^2+\frac{3}{16}\gamma^4)$, In general, the nonfluctuating part is

$$\exp(-\gamma^2/2)\left\{1+\left(\frac{\gamma^2}{4}\right)^2+\left(\frac{\gamma^4}{32}\right)^2+\left(\frac{\gamma^6}{8\cdot 48}\right)^2+\left(\frac{\gamma^8}{6\cdot 16\cdot 64}\right)^2+\cdots\right\}.$$

For $\gamma^2=4$ we find $e^{-2}\{1+1+(\frac{1}{2})^2+(\frac{1}{6})^2+\cdots\}\simeq 0.28$.

(2) Case of Intermediate α, $\alpha=1$

In Fig. 1 we have plotted, for several strengths of interaction, the energy curves obtained by solving Eq. (13). For weak interaction ($\gamma=\frac{1}{10}$) it is seen that the energy remains very close to the zero-quantum curve, giving an effective mass close to the free electron mass. Near the first intersection point, anomalies in average velocity and effective mass occur. The electron velocity decreases rapidly, and the electron has a negative and very small effective mass in this region. Beyond this region, as the total momentum increases, the velocity increases again since the electron must follow the one-quantum curve. The coefficients in the wave function are plotted in Figs. 3 and 4, where one sees the gradual increase of coefficients representing the many-quanta terms.

The moderate interaction curve ($\gamma=1$) starts at $\zeta=0$ with a small curvature, i.e., a large effective mass. As λ increases the curvature approaches zero and the electron velocity remains constant indicating practically infinite electron mass. We note that the region of small effective mass is no longer present. The momentum delivered to the electron is continuously transferred to the oscillators as shown by the increasing values of the higher coefficients, so that the electron velocity cannot increase. One sees from the wave-function curves that at $\zeta=0$ there is a greater contribution from a_1 coefficient than for the weak interaction case. The curves rise slowly showing that at any given value of ζ many of the coefficients are appreciable. As the interaction becomes stronger ($\gamma=3$) another feature comes into play. The absolute minimum, i.e., the most stable state of the system occurs at a nonzero value of λ. On either side the effective mass is very large.

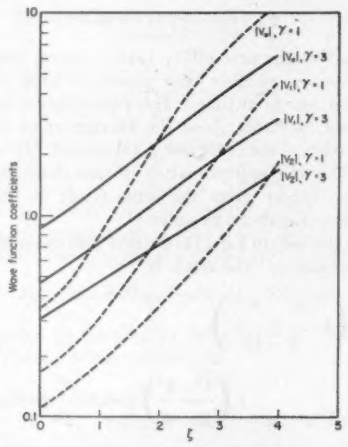

FIG. 3. Wave functions for $\alpha=1$.

The foregoing discussion is concerned with the stationary states. If, however, a sizable electric field is applied so that λ increases steadily and rapidly, there is an appreciable probability that an electron will jump to an excited-state curve.[7] If a transition takes place, the velocity does not experience anomalies and the electron continues to behave as a free particle. For weak interaction the probability of a transition is high.

Let us now compare the foregoing results with those obtained by applying second-order perturbation theory. If one is far from an intersection point, one expects to obtain accurate results for weak interaction. Consider the region between $\zeta=0$ and the first intersection point where the lowest energy curve is close to the zero-quantum curve. Second-order perturbation theory gives for the energy

$$E_0=1+\zeta^2-\gamma^2/(2-2\zeta\alpha+\alpha^2). \tag{24}$$

We find for $\zeta=0$, $\alpha=1$

$\gamma=1$, $|\delta E|=\frac{1}{3}$, as compared to $\frac{1}{8}$ for the exact theory;

$\gamma=3$, $|\delta E|=3$, as compared to 2.6;

$\gamma=5$, $|\delta E|=8.3$, as compared to 6.2.

We thus see that, for increasing interaction, perturbation theory predicts a shift proportional to γ^2, whereas, in reality, a saturation sets in. The accuracy depends, however, on the values of ζ and α. The perturbation expression is valid for strong interactions if $\alpha\gg 1$.

As ζ increases we come near the intersection point, the perturbation treatment breaks down, and one must first remove the degeneracy of the zero and one-quantum curves. Beyond the intersection point perturbation theory applied to the one-quantum curve gives sensible results for weak interactions.

Fröhlich, Pelzer, and Zienau,[8] in their discussion of the lowest levels of an electron interacting with the optical modes of a polar lattice, use a variational method to obtain results considerably more accurate than the perturbation theory. They take a trial wave-function involving the first two terms of our series Eq. (3) and choose the ratio a_1/a_0 so as to obtain the lowest value possible. It is clear from our results that this choice is adequate to handle the anomalies occurring near the intersection point. This method is, in fact, just the procedure which would be employed to remove the degeneracy. From Fig. 3 we see, however, for strong

[7] This probability can be computed using methods developed by W. V. Houston, Phys. Rev. 57, 184 (1940).

interaction ($\gamma=3$), the coefficient a_2 is large even at $\zeta=0$, so that this method will then give inaccurate results. A technique similar to that employed by Fröhlich, Pelzer, and Zienau could be used to handle the degeneracies at higher values of ζ.

(3) Case of the Transition to Periodic Potential, $\alpha\to\infty$

Let us now pass to the limit $\hbar\omega\to 0$, keeping $\hbar k$ finite. We also let the mass of the particles giving rise to the oscillation tend to infinity in such a way that $g_k(\hbar/2M\omega)^{\frac{1}{2}}$ remains finite. The recurrence relation Eq. (6) becomes

$$\left\{\frac{[\lambda-(n+\tfrac{1}{2})\hbar k]^2}{2m}-E\right\}a_n^{\lambda}+g_k\left(\frac{\hbar}{2M\omega}\right)^{\frac{1}{2}}[a_{n+1}^{\lambda}(n+1)^{\frac{1}{2}}+a_{n-1}^{\lambda}(n)^{\frac{1}{2}}]=0. \quad (25)$$

This three-term recurrence form is similar to that arising in the solution of Mathieu's equation and gives the same band-type spectrum. The quantity k takes the place of $2\pi/a$ where a is the lattice spacing in the periodic potential problem. The difference is that here values of λ differing by $\hbar k$ do have physical significance, corresponding to different values for the total momentum of the system. For the case where $\hbar\omega$ is small but not zero, the energy oscillates but slowly rises as the total momentum increases. If a weak electric field is applied, imparting momentum to the electron, one can say that a Bragg reflection occurs each time the total momentum passes a maximum. The electron transfers momentum and energy to the oscillators. These relations may be seen from Fig. 2. For small $\hbar\omega$ the curves for zero interaction representing different numbers of quanta in the oscillators have very nearly the same minimum values of energy. Interaction removes the crossing of curves and we find our bandlike spectrum.

As noted in case (2) perturbation theory is valid here unless one goes to extremely strong interactions (measured in units of $\hbar\omega/2$). That is, if one considers two oscillators of the same ω, the one of short wavelength satisfies perturbation theory for stronger interactions.

V. RESUMÉ

The lattice oscillator is characterized by an angular frequency ω and a propagation vector k. In the limit of zero frequency and finite k the phase velocity ω/k tends to zero and one obtains the solution of the problem of an electron moving in a periodic potential. For zero interaction between electron and oscillator the total energy is $E=(n+\frac{1}{2})\hbar\omega+p^2/2m$. Here n is the number of quanta in the oscillator and p in the momentum of the electron. Introducing the total momentum λ of the system, we have $p=\lambda-(n+\frac{1}{2})\hbar k$ and

$$E=(n+\tfrac{1}{2})\hbar\omega+\{\lambda-(n+\tfrac{1}{2})\hbar k\}^2/2m.$$

The energy thus depends on two quantum numbers, λ which is continuous, and n which is discrete. One plots E *vs* λ with one curve for each value of n. (See Figs. 1 and 2.) Although the plots differ, depending on the values of k and ω, a general feature is the intersection of curves. For values of λ less than that at the point of intersection, the curve representing n quanta lies lower than the curve for $n+1$, while beyond the intersection point the reverse is true. Thus the lowest energy state becomes that in which successively more quanta occupy the oscillator. Introduction of interaction removes the degeneracy and results in continuous curves but the same qualitative features remain. For moderate interactions the lowest energy curve has the shape of the asymptote of the zero energy curves. This means that the energy does not rise as rapidly as the zero quantum curve and results in a high effective electron mass.

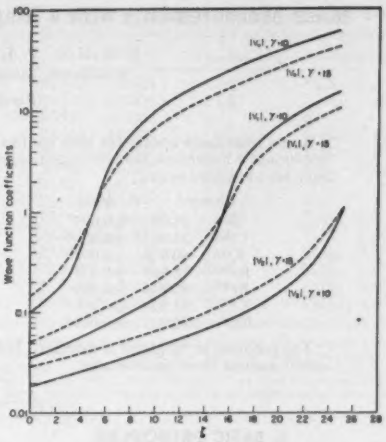

FIG. 4. Wave functions for $\alpha=10$.

If one examines the curves of Fig. 3, which are for the low frequency case, one sees that removal of degeneracy leads to a bandlike spectrum with energy slowly rising as the total momentum increases. The physical interpretation is that the electron makes Bragg reflections giving up a quantum of energy and momentum to the oscillator so that, as the total momentum increases, the electron velocity remains bounded, but more and more momentum and energy are present in the oscillator.

ACKNOWLEDGMENT

The author is grateful to Professor A. von Hippel for his helpful interest in this work and to Professor J. C. Slater for several stimulating discussions.

Mass Measurements with a Magnetic Time-of-Flight Mass Spectrometer*

E. E. Hays, P. I. Richards, and S. A. Goudsmit
Brookhaven National Laboratory, Upton, New York

(Received August 6, 1951)

A new mass spectrometer has been used to measure the time of flight of ions for a number of complete revolutions in a magnetic field. This spectrometer is especially suitable for heavy masses; the following results have been obtained so far:

Element	Mass		Element	Mass	
S^{32}	31.983	±0.001	Rb^{87}	86.9295	±0.0020
Cl^{35}	34.9805	±0.0005	I^{127}	126.9415	±0.0025
K^{41}	40.975	±0.002	Xe^{129}	128.9455	±0.0015
Br^{79}	78.944	±0.001	Xe^{130}	129.945	±0.002
Br^{81}	80.943	±0.001	Xe^{131}	130.944	±0.002
Kr^{84}	83.938	±0.001	Xe^{132}	131.945	±0.002
Rb^{85}	84.931	±0.0015	Xe^{134}	133.947	±0.002

The precision as tabulated is estimated from the consistency between independent runs. The "probable error" is about three times smaller.

I. BASIC PRINCIPLES

A MASS spectrometer[1] has been constructed which measures the time of flight of ions describing a number of revolutions in a uniform magnetic field. For N revolutions in a homogeneous field of H gauss the time of flight T is given by

$$T=652NM/H \quad \mu\text{sec}. \tag{1}$$

The mass M is in amu.[2] Conventional mass spectrometers decrease in accuracy with increasing mass. In the time-of-flight spectrometer, the mass-time proportionality and the time-measuring equipment give an essentially constant precision for all masses. In our particular instrument this accuracy is one or two millimass units.

In the present apparatus a pulsed ion source is placed about 12 cm above an ion detector in a vertical magnetic field of about 450 gauss. Some ions leave the source with a vertical velocity component, and travel in a helix, reaching the ion detector after one, two, three, or more revolutions, depending on the initial vertical velocity. Because of the finite size of source and detector only a limited number of revolutions can be observed; ions moving on a helix with a small pitch are intercepted by the rear structure of the source after a single revolution. In the present apparatus about 12 revolutions can be recorded with sufficient intensity for measurement It must be noted that heat motion of the ions in the source is sufficient to give them the required vertical components of velocity; a special deflecting field is not necessary.

The ion detector records pulses received after one to about fifteen revolutions. The time interval usually measured is between the second and ninth pulse, giving $N=7$ in Eq. (1). The field is chosen so that this time interval corresponds to about 10 μsec per mass unit; thus H is about 450 gauss. Since the time intervals can be measured to 0.01 μsec, this yields a mass determination with a precision of 0.001 atomic mass unit.

For complete revolutions in a perfectly uniform magnetic field, the time of flight is entirely independent of direction and magnitude of the initial velocity of the ions; ions with different velocities move along different paths. In addition to this time focusing, the field produces a space focusing: after each revolution the ions focus along a field line passing through source. These focusing characteristics are very advantageous for the intensities of the higher orders of revolution. The focusing properties offer also the advantage that this spectrometer does not require narrow defining slits. However, it is actually necessary to restrict the circular path of the ions somewhat by means of baffles. One reason for this limitation is that ions traveling on small circles have a very low kinetic energy, and are easily scattered. For a radius of R cm the kinetic energy E is

$$E=H^2R^2/(144)^2M \text{ ev}. \tag{2}$$

With our radius of 12.5 cm and our magnetic field $H=450$, this gives $E\sim 10$ ev for $M=150$. This energy decreases with the square of decreasing radii.

From Eq. (1) it seems at first advisable to use as small a field H as possible in order to increase the time T and thus the accuracy of the measurement. However Eq. (2) shows that the energy of the ions is proportional to H^2 and a weaker field means slower ions and more scattering resulting in lower intensity and decreased sharpness of the recorded pulses. In fact, for heavy ions a field of 450 gauss mentioned above gives suitable pulses only up to about six revolutions in our present apparatus. Increasing the field to about 600 gauss im-

* Work performed at the Brookhaven National Laboratory, under the auspices of the AEC.

[1] S. A. Goudsmit, Phys. Rev. **74**, 1537 (1948).

[2] In all formulas, we shall express time in microseconds, length in centimeters, mass in atomic mass units ($O^{16}=16.0000$), and kinetic energy E in electron volts. In these units a very convenient approximation, correct to three percent, is $E=\frac{1}{2}Mv^2$ (v in cm/μsec). If in addition H is in gauss and electric field F in volts/cm, the force on a singly charged ion is $\mathbf{F}+(\mathbf{v}\times\mathbf{H})/100$ and its momentum $p=H\rho/100$. All equations will be written for singly charged particles but can easily be modified for higher ionizations.

proves the higher orders considerably and allows measuring to about the 12th order.

II. DEVIATIONS FROM LINEARITY

According to Eq. (1) the time interval is proportional to the mass of the ion.[3] In an ideal case it would only be necessary to compare the time for an unknown mass with that for a standard ion. Unfortunately, small perturbing electric fields, discussed in more detail below, cause slight deviations from linearity. Moreover, these fields, which are caused by deposits on the wall of the vacuum chamber, are slowly varying with time. Instead of Eq. (1) we must now write

$$T = aM(1+\epsilon M). \tag{3}$$

The coefficient ϵ has been less than 10^{-6} in our work. It is therefore necessary to measure simultaneously the time of flight for two standards and the unknown mass. As standards we have selected a number of suitable hydrocarbons. By observing how the time ratio of the two standards differs from their known mass ratio, the quadratic correction is obtained and can be applied to the unknown mass. By choosing one of the two standards near the unknown mass the correction due to nonlinearity can be made small; it usually amounts to a few milli-mass-units. We have checked this method by measuring three known hydrocarbons and found agreement within our limits of precision.

Since changes in standards occur from time to time it is useful to know how this affects the evaluation of the masses. If A and B are the present values for the masses of the standards and δA and δB some future corrections, the correction δM in the mass M is given by

$$\delta M/M = (\delta A/A)(M-B)/(A-B) + (\delta B/B)(M-A)/(B-A). \tag{4}$$

In the foregoing expression it is usually sufficient to use mass numbers instead of the actual masses.

III. RESULTS

Table I gives a list of masses measured with the new spectrometer, together with the reference standards used in each case. It must be noted that the indicated limits of accuracy are estimated from the consistency of a number of independent measurements. If we apply the usual procedure of determining the "probable error," these limits of accuracy would be about three times smaller; we prefer however the more conservative values. Under favorable conditions of low pressure, steadiness of field, negligible surface potentials and good intensity, the present apparatus can measure to 0.001 amu, which accuracy we have reached in a few cases. We doubt, however, that even with the best performance of the present instrument it is possible to go much beyond this limit. For Cl the precision is higher because we measured the ion CCl_3^+.

[3] Actually this is true for a fixed path in a magnetic field of arbitrary shape.

TABLE I. Masses measured with new spectrometer.

Element	Mass[a]		Measured ion	Standards[b]	
S^{32}	31.983	±0.001	CS_2^+	C_2H_{12}	C_3H_6O
Cl^{35}	34.9805	±0.0005	CCl_3^+	C_3H_{12}	C_4H_{10}
K^{41}	40.975	±0.002	K^+	K^{39}	
Br^{79}	78.944	±0.001	$C_3H_4Br^+$	C_6H_6	C_7H_{10}
Br^{81}	80.943	±0.001	$C_3H_4Br^+$	C_6H_6	C_7H_8
Kr^{84}	83.938	±0.001	Kr^+	C_6H_6	C_7H_8
Rb^{85}	84.931	±0.0015	Rb^+	C_6H_{12}	
Rb^{87}	86.9295	±0.0020	Rb^+	Rb^{85}	
I^{127}	126.9415	±0.0025[c]	CH_2I^+	C_6H_{12}	$CCl_2^{35}Cl^{37}$
Xe^{129}	128.9455	±0.0015	Xe^+	C_6H_6	C_7H_{12}
Xe^{130}	129.945	±0.002	Xe^+	C_7H_{12}	Xe^{129}
Xe^{131}	130.944	±0.002	Xe^+	C_7H_{12}	Xe^{129}
Xe^{132}	131.945	±0.002	Xe^+	C_8H_{12}	Xe^{129}
Xe^{134}	133.947	±0.002	Xe^+	C_8H_{12}	Xe^{129}

[a] The precision as tabulated is estimated from the consistency between independent runs. The "probable error" is about three times smaller.
[b] Basic values used are H = 1.0081386, C = 12.003895 from K. Bainbridge, Phys. Rev. 81, 146 (1951). For Cl^{35} and Cl^{37} we used the values derived by Henry Motz (private communication) from disintegration data, namely, 34.97996, 36.97769.
[c] Preliminary value.

IV. SHORT DESCRIPTION OF APPARATUS

The magnet consists of a brass sphere of 20-in. inner diameter, wound with coils in such a way as to produce a homogeneous field over the whole volume inside the sphere. It was designed and constructed several years ago by E. U. Condon and J. A. Hipple, at that time on the staff of the Westinghouse Research Laboratories. We are very fortunate to have obtained this magnet on a loan from Westinghouse. The field has been tested with a proton probe, and by means of small shims the homogeneity has been improved over a cylindrical shell of about 5-in. radius, 5-in. height, and about ½-in. thickness. Submarine batteries furnish a current of 20 amperes at 48 volts, to give a field of 400 gauss. The two halves of the sphere can be connected in parallel and the field increased up to about 800 gauss with present equipment.

A cylindrical vacuum chamber is built inside the sphere and is provided with a removable gold-plated liner to reduce the effect of contact and surface potentials. Shields surround the source and detector so that the ion beam sees only the gold plated surfaces. A few baffles restrict the ions to a helical path lying on a cylinder of 5-in. radius and a width of about ¼ in. The pressure during measurements is 1 to 5×10^{-6} mm Hg.

As detector for the ion pulses one can use a simple Faraday cage or a scintillation detector.[4] By far the best detector is an electron multiplier especially designed for this purpose by Smith and described in detail elsewhere.[5]

V. THE ION SOURCE

The ion source is of conventional design. An electron beam, collimated by the magnetic field, ionizes vapor in the small source chamber of about 3-mm depth by ½-in. square. In some of the sources the rear wall is a hot filament on which salts can be deposited to produce

[4] E. E. Hays and P. I. Richards, Rev. Sci. Instr. 21, 99 (1950).
[5] L. G. Smith, Rev. Sci. Instr. 22, 166 (1951).

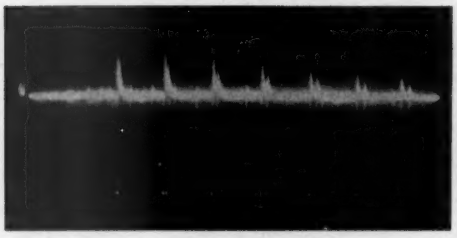

FIG. 1. The second to eighth order of rubidium isotopes 85 and 87 displayed on a 1000 μsec sweep. The deflections are downward and saturated; the upward pulses are amplifier kickbacks. The first order is very weak. The background shows weak pulses due to other alkali ions; the fifth order of Cs lies just before the eighth order of Rb.

alkali ions. The voltage of the ionizing electron beam is variable, but the best ion pulses are obtained with energies of 10 to 20 volts at 0.5 milliamp.

The front plate of the source, containing a $\frac{1}{16}$-in. exit slit, is insulated from the rest of the structure and can be given pulses up to 600 volts and lasting $\frac{1}{4}$ μsec, $\frac{1}{2}$ μsec or longer. An important feature of the source is the following: because of the short duration of the pulse, heavy ions reach the exit slit after the pulse has stopped. In this manner ions heavier than a certain mass (depending upon pulse voltage, pulse duration and source depth) will not receive the full energy but all will obtain the same momentum. All ions therefore follow the same helical paths in the magnetic field and can be made to move in paths determined by the baffles. Thus ions of a large range of masses can be observed and measured simultaneously; it is not necessary to readjust the source parameters for each mass. This obviously facilitates relative measurements and increases reliability and accuracy.

Since the radius is restricted by baffles to the value R, ions below a certain mass cannot be observed. The maximum energy ions can get is equal to the pulse voltage; the smallest observable mass can thus be obtained from Eq. (2) by putting E equal to the pulse voltage. If no baffles are used all masses can be recorded, as the lighter ions move then on smaller radii.

VI. MEASURING TECHNIQUE

A most essential part of the apparatus is, of course, the time-measuring equipment. It follows the principle of Loran[6] navigation receivers and has been adapted to our needs by the Electronics Division of Brookhaven National Laboratory where it was designed by W. Higinbotham.

The essential features are the following. One scope displays the whole sweep; Figs. 1–3 show examples of various displays. Two separately movable electronic markers select two pulses, which then appear on two separate fast traces on a second scope. By turning the dials which control the markers the two pulses on the second scope can be made to coincide. The dial setting then reads directly the time interval between the two pulses. In order to facilitate the measurements, the two traces on the fast scope can be separated or made to coincide at will, and the relative amplification of the two pulses can be varied so as to make them look more alike. In this way good pulses can be matched to 0.01 μsec even if they are as long as a $\frac{1}{2}$ μsec. Figure 4 shows an example; this picture shows the fastest sweeps of about 2 μsec which are used for precision measurements. Experience proves that a skilled observer can match to almost 0.01 μsec even those pulses which fluctuate considerably in intensity. The sweep repetition rate is about 300/sec and is not critical.

FIG. 2. The eighth order of Rb^{85} and Rb^{87} on a delayed sweep of 25 μsec at about 950 μsec from the start. The separation is 22 μsec.

The organic standards and unknown mass are introduced into the source simultaneously through suitable leaks. A reading consists in matching say the second and tenth pulses of each ion, using the same pair of orders for the standards and the unknown. In order to eliminate the effect of slow drifts in the magnetic field, readings are taken in a symmetrical order.[7] If A and B denote the standards and M the mass to be determined, the order of measurement is, for example,

$$M\,A\,B\,B\,A\,M\,M\,A\,B\,B\,A\,M\cdots.$$

Not only does this procedure eliminate slow drift by averaging, but inspection of individual sequences also gives an indication of sudden variations so that consistent runs may be selected. Each reading takes about a minute, a run about ten minutes.

VII. THE PULSE LENGTH

The magnetic field does not necessarily have to be homogeneous. Particles following the same orbits have equal momenta in any magnetic field, and the time of travel between two points is proportional to the mass. It is of course advantageous that the field be homogeneous, since the beam defining slits can then be wide and full use made of space focusing properties. Nonhomogeneity lengthens the pulses and decreases the accuracy of pulse matching, unless the slits are made very narrow.

[6] See "Loran," Vol. 4 of *Massachusetts Institute of Technology Radiation Lab Services* (McGraw-Hill Book Company, Inc., New York, 1949).

[7] We are currently installing a regulator for the magnetic field.

Observations indicate that the minimum length recorded depends primarily upon the depth of the source. The pulse leaving the source is a small cloud of ions of about 0.3 cm thickness along its path. This cloud spreads out vertically and also perpendicularly to its path, but after every complete revolution its dimension along its path is ideally again 0.3 cm. The recorded over-all pulse duration τ is thus given by the time it takes for this cloud to enter the detector. Denoting the length of the cloud by s, and the time for one revolution by T, we have

$$\tau=(s/2\pi R)T\sim 100sM/HR\ \mu\text{sec}; \qquad (5)$$

thus the pulse duration increases with the mass. For $M=150$, $H=450$ gauss, $R=12.5$ cm, and $s=0.3$ cm we find $\tau=0.8$ μsec. The observed values of the base width of the pulses agree well with the computation; the recorded pulses are perhaps somewhat narrower. We have not succeeded in constructing shallower sources to reduce the size of the pulse below 0.3 cm.

Equation (5) gives another reason for using baffles to eliminate ions moving on small circles. The relative size of ion cloud to path length would be large and produce long pulses.

VIII. INTENSITY

The intensities of the various orders can be computed by assuming that the vertical velocity components of

FIG. 3. The eighth order of xenon isotopes 128, 129, 130, 131, 132, 134, and 136 on a sweep of about 90 μsec delayed about 1050 μsec from the start. The separation between consecutive isotopes is about eight μsec.

the ions obey a Maxwell distribution corresponding to an absolute temperature θ. We call a the height of the exit slit of the source, assuming for simplicity that it equals the entrance slit of the detector, and we denote by l the vertical distance between them. A simple geometrical consideration gives for the fraction I of ions that reach the detector after N revolutions

$$I=0.067aH/N(M\theta)^{\frac{1}{2}}\exp(-0.0142l^2H^2/N^2M\theta). \qquad (6)$$

Note that even when the exponential factor is negligible the intensity decreases only with the first power of the number of revolutions. This is due to the space focusing. The intensity has a maximum for the order N near the value

$$N_{\max}=(0.0284l^2H^2/M\theta)^{\frac{1}{2}}. \qquad (7)$$

Since $l=12$ cm one finds, for a temperature of 1000°K and a field of 450 gauss, that the third order will be the strongest for $M=100$. It also becomes clear why for large l the first order is very weak. For the order of maximum intensity Eq. (6) gives $I\sim a/4l$, or about 2 percent for $a=1$ cm. However, in reality it is probably much smaller since Eq. (6) is based on idealized and simplified assumptions.

Formula (6) does not take into account the decrease in intensity due to scattering. This would add another exponential factor with a negative exponent proportional to the path traversed, or to N, the number of revolutions.

IX. SCATTERING

An advantageous feature is that single scattering of the ions does not in general lengthen the recorded pulse; it merely removes ions from the pulsed beam. The change in direction and energy experienced in a collision with residual gas molecules usually causes a change in path such that the scattered ions cannot reach the entrance slit of the detector. If the scattering happens to occur near 180° from source and detector, the approximate 180° focusing invalidates this statement, but such occurrences are rare. If the pressure is so high that multiple scattering takes place, the pulses are lengthened and considerably weakened. It is indeed comforting that under favorable operating conditions the pulses of the various orders are quite similar, an important factor in accurate pulse matching.

Whether a scattered ion will reach the detector depends on where in its path the deflection occurred. The change in arrival time caused by the scattering is also a function of the position and the amount of deflection. A detailed theoretical treatment, though elementary, would be uselessly complex. We shall merely state that geometrical consideration shows that a deflection by a

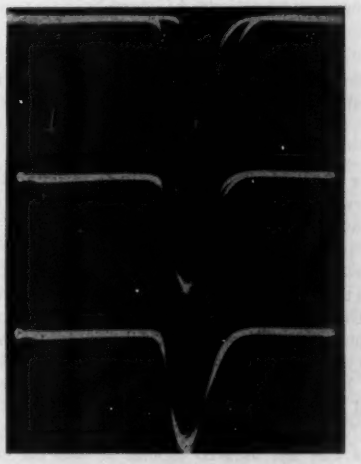

FIG. 4. Pulse matching. In the top picture the shift is 0.1 μsec, in the middle picture it is 0.02 μsec, and in the bottom picture the pulses are matched. The sweep is 2 μsec.

small angle ϕ causes, on the average, a change $\phi T_1/2\pi$ in arrival time. In order to keep the pulses sharp we want this change to be less than $\frac{1}{4}$ μsec or

$$\phi < H/400M \text{ radians.} \tag{8}$$

The gas scattering will be primarily due to dipole moments induced in residual gas molecules by the moving ions. In this case the potential energy will be of the form k/r^4. The value of k depends upon the polarizability of the gas molecules and is of the order of 10^{-31} ev cm^4. For organic molecules such as pump oil or our standards, the value k may be several times larger. The probability that an ion experiences a deflection larger than a small angle ϕ can be expressed in terms of a cross section σ. A straight-forward application of mechanics shows that

$$\sigma^2 \sim 100k/\tfrac{1}{2}Mv^2\phi. \tag{9}$$

With the help of Eqs. (2) and (8) we find

$$\sigma \sim 3\times 10^4 k^{\frac{1}{2}} M/RH^{\frac{1}{2}}. \tag{10}$$

With k at least 10^{-31} ev cm^4, this shows that for $M=150$, $H=450$ gauss, $R=12.5$ cm, the value of σ is at least 1.2×10^{-14} cm^2. At a pressure of 5×10^{-6} mm Hg this results in a mean free path L such that

$$L < 350 \text{ cm.} \tag{11}$$

This is almost doubled if we increase the field from 450 gauss to 600 gauss.

X. SURFACE POTENTIALS

If surface potentials cause a radial component of electric field averaging F volts/cm, the time of flight T is changed by an amount ΔT given by

$$\Delta T/T \sim 10^4 FM/H^2R. \tag{12}$$

Combining this with Eqs. (1) and (3) gives for the correction coefficient ϵ

$$\epsilon = 10^4 F/H^2R. \tag{13}$$

Since ϵ was found to be less than 10^{-5} it indicates that the average perturbing field F is less than 2 mv/cm (indicating potentials of the order of 20 mv).

If surface potentials produced a fairly uniform field they would not cause serious difficulties even if the field varied slowly in time. We have, however, some evidence that these fields are probably irregularly distributed and thus cause deflections of the ions similar to scattering. It is not possible to give an *a priori* estimate of this effect but it is considerably reduced by occasional careful cleaning of the gold-plated liner. This "scattering" probably behaves as if it were caused by fixed dipoles and not induced dipoles as was the case for molecular scattering. If that is so, the mean free path is proportional to $E\phi = H^2R^2/M^2$. The disturbing effects will decrease rapidly with increasing the magnetic field.

XI. LIMITATIONS IN PRECISION

It has not been ascertained whether surface potentials or gas scattering determine the mean free path in the present apparatus. Considering the latter only, it is possible to study the limit of precision of which this type of mass spectrometer is capable without making radical changes in technique. In order to do this we make the following assumptions:

(a) It is not practical at present to measure time intervals with higher precision than 0.01 μsec.

(b) In order to make full use of the time measuring precision, the pulses must be shorter than 1 μsec.

(c) It is not easy to obtain pressures below 10^{-6} mm Hg in the volumes needed for this type of spectrometer (4×10^{10} particles per cc).

(d) It is not practical to produce an ion cloud much smaller than about 0.2 cm.

(e) The total path length between source and detector should not exceed one mean free path in order to avoid pulse distortion due to scattering, and the value of k in Eq. (9) is not less than 10^{-31} ev cm^4.

The parameters at our disposal are the field strength H and the radius R. Using Eq. (10) the mean free path L is

$$L = (4\times 10^{10}\sigma)^{-1} \sim 3RH^{\frac{1}{2}}/M. \tag{14}$$

The slowest speed the ions can have is determined by (b) and (d), namely, 0.2 cm/μsec. The maximum time to traverse L is thus

$$T = 15RH^{\frac{1}{2}}M \text{ μsec.} \tag{15}$$

If this is measured to 0.01 μsec the optimum precision is one part in $1500RH^{\frac{1}{2}}/M$. With $R=12.5$ cm, $H=450$ gauss and $M=100$ this gives almost 2×10^6. The time T would be 2×10^4 μsec and the path 5000 cm.

Since k is most likely several times larger than assumed here, and since our pressure is also five times higher, it is not surprising that the precision obtained so far is from 20 to 40 times less than computed. By increasing H and R it seems possible to improve the precision considerably, provided surface potentials or other factors do not prevent ions from remaining in their prescribed orbit for the long time that is required.

The present apparatus has the disadvantage that the length of the ion paths is essentially limited by geometry to about 15 revolutions or 1200 cm. Various modifications have been suggested to avoid this limitation; the most promising method seems to be one proposed by Smith.[8]

XII. CONCLUSIONS

Though the results obtained should still be considered preliminary, they indicate that the basic principle used in this spectrometer leads to reasonably high precision mass measurements for heavy ions; more work is needed before we understand fully the nature of some of the

[8] L. G. Smith, Rev. Sci. Instr. 22, 115 (1951).

difficulties encountered in the operation of this new instrument. We plan to measure a few more heavy masses and shall also attempt to improve our precision so as to reach in all cases the limit of one milli-mass-unit.

We wish to thank Dr. Joseph Slepian of the Westinghouse Research Laboratories for the loan of the Condon-Hipple magnet, Dr. L. G. Smith for many valuable suggestions during the early stages of this work, and Mr. A. Tuthill for his technical assistance. Thanks are also due to Dr. W. A. Higinbotham of our Electronics Division for the design of the timing equipment and to members of the Chemistry Department for much valuable advice.

PHYSICAL REVIEW VOLUME 84, NUMBER 4 NOVEMBER 15, 1951

Electron-Hole Production in Germanium by Alpha-Particles

KENNETH G. MCKAY
Bell Telephone Laboratories, Murray Hill, New Jersey

(Received August 3, 1951)

The number of electron-hole pairs produced in germanium by alpha-particle bombardment has been determined by collecting the internally produced carriers across a reverse-biased $n-p$ junction. No evidence is found for trapping of carriers in the barrier region. Studies of individual pulses show that the carriers are swept across the barrier in a time of less than 2×10^{-8} sec. The counting efficiency is 100 percent. The energy lost by an alpha-particle per internally produced electron-hole pair is 3.0 ± 0.4 ev. The difference between this and the energy gap is attributed to losses to the lattice by the internal carriers. It is concluded that recombination due to columnar ionization is negligible in germanium.

INTRODUCTION

IN the theories of external secondary emission and of bombardment conductivity, it is desirable to know the actual number of electrons freed in a solid by a bombarding particle. The rate of loss of energy by the bombarding particle has been studied extensively by measurements of stopping power and treated theoretically by Bohr, Bethe, and others[1] for high energy particles. This energy loss is the result of electron excitation and ionization, lattice excitation, and nuclear displacement. Much of the energy may be lost in the production of high energy internal secondary electrons which, in turn, produce tertiaries and so forth. Consequently, only approximate estimates of the number of free electrons produced per bombarding particle can be obtained from theory. No satisfactory method has been devised to obtain this quantity experimentally for metals. For phosphors, the light output per incident particle can be measured but its interpretation in terms of a number of free electrons is complicated by the existence of nonradiative transitions. A better method, which has been used for certain insulators, is bombardment conductivity.[2] It is the purpose of this report to describe an accurate determination by this method of the average energy lost by an alpha-particle in producing one electron-positive hole pair in germanium. The use of germanium is predicated by the fact that it is a valence bonded crystal, with the same structure as diamond for which the average energy lost by an alpha-particle in producing one electron-positive hole pair has been measured.[3] Moreover, large single crystals of germanium of known composition and known electrical properties can now be prepared.

THEORY OF THE METHOD

Consider a rod of germanium of which one half is n-type and the other half p-type. If the n-type end is made positive with respect to the p-type end, the $n-p$ barrier will develop a very high resistance and virtually all of the voltage drop along the rod will be concentrated across the $n-p$ barrier. This can be crudely likened to a thin insulator separating two conductors. If the bombarding particles strike the barrier itself so that the resultant holes and electrons are produced in this high field region, they will be swept across the barrier, thereby registering in the external circuit and will eventually disappear in the main body of the germanium. Although the field is not constant throughout the barrier, that is irrelevant as long as trapping or recombination do not take place within the barrier, i.e., as long as the sum of the voltage drops traversed by a given electron-hole pair is substantially equal to the total voltage drop across the specimen. To date, no evidence has been observed for the existence of trapping or recombination within a well made $n-p$ barrier in germanium. Moreover, the injected current densities normally used are much too small to set up a space charge field which could perturb the barrier field appre-

[1] N. F. Mott and H. Massey, *Theory of Atomic Collisions* (Oxford University Press, London, 1934).

[2] Reviews of this work as applied to crystal counters have been published by R. Hofstadter, Nucleonics 4, No. 4, 2 (1949); 4, No. 5, 29 (1949); Proc. Inst. Radio Engrs. 38, 726 (1950).

[3] A. J. Ahearn, Phys. Rev. 73, 1113 (1948); K. G. McKay, Phys. Rev. 77, 816 (1950).

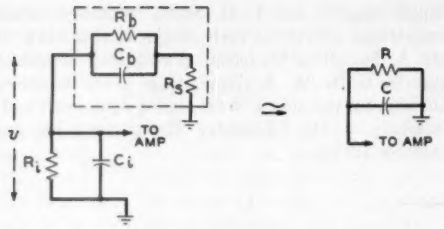

FIG. 1. Equivalent circuit of $n-p$ germanium crystal and amplifier input.

ciably. Thus a germanium $n-p$ barrier has precisely the properties of an ideal insulator for bombardment conductivity. The geometry described has the attractive property that voltage probe measurements can be made along the entire length of the specimen. Thus it can be established that essentially all of the applied voltage is indeed concentrated across the $n-p$ barrier.

It might appear that any rectifying contact to germanium would serve as well as an $n-p$ junction. This is not so because it is known from transistor characteristics that a point contact, acting as a collector, exhibits a current multiplication which depends on its previous history. Thus if we bombard the barrier region around a point contact, the maximum observed charge may be several times the total charge of electrons (or holes) generated in the bulk germanium by the bombarding particle. Unfortunately we usually do not know the amplification factor of the point contact barrier so we cannot thus determine the intrinsic work of ionization in the germanium. No such current multiplication has been observed for a normal $n-p$ barrier. Photoconductivity measurements have demonstrated a quantum yield of unity for such a barrier.[4] Moreover, the theory of the $n-p$ barrier, which has been well-substantiated by experiment, nowhere suggests the possibility of current multiplication.[5]

Figure 1 shows the equivalent circuit of the germanium crystal and the amplifier input as used in these experiments. R_b, C_b represent the constituents of the barrier impedance, R_i, C_i those of the amplifier input, and R_s the series resistance of the body of the germanium. By applying a reverse bias to the barrier, we can ensure that $R_b \gg R_s$ and thus neglect R_s completely. The equivalent circuit then reduces to a simple parallel RC circuit, where $R=R_bR_i(R_b+R_i)^{-1}$ and $C=C_i+C_b$. The time taken to sweep the carriers out of the barrier region is short compared with the RC relaxation time, so that this action is equivalent to the production of an impulse current across the barrier layer, resulting in a peak voltage across the barrier of $v=Q/C$ where Q is the effective charge transported across the barrier. The limitations imposed by the noise spectrum and capacity of the barrier have been discussed previously.[6]

TABLE I. Forbidden energy gap width E_G and average work of ionization ϵ for various solids.

Solid	$-\epsilon$ ev	E_G ev	ϵ/E_G	$\epsilon-E_G$ ev
Diamond[a]	10	~6	~1.7	~4
Germanium	3.0	0.72	4.2	2.3
AgCl[b]	7.6	4.88	1.6	2.7
AgBr[b]	5.8	3.95	1.5	2.4
CdS[c]	5–10	2.37	2–4	2–7

[a] See reference 3.
[b] See reference 2.
[c] Dr. Kallmann in a private communication stated that pulses had been observed with CdS corresponding to $\epsilon=5$ ev in which probably no secondary processes were involved.

EXPERIMENTAL TECHNIQUE

A number of specimens have been used in this work but, since they have all been similar although by no means identical, it will suffice to describe the salient features of one. This is a rod 2 cm long and of square cross section 1 mm wide. It is a single crystal in the middle of which occurs the barrier which is normal to the length of the crystal.[7] The ends of the crystal were sandblasted and then rhodium plated to provide low resistance ohmic electrical contacts. Probe measurements made along the length of the germanium showed that, with several volts reverse bias applied to the crystal, the total voltage drop across the two contacts and across the main body of the germanium was less than 0.3 percent of the voltage drop across the barrier. This justifies the neglect of R_s in the equivalent circuit. The current-voltage characteristic, which was essentially the same as published curves for well behaved $n-p$ junctions,[4] verified the results of the probe measurements.

Figure 2 is a simplified schematic of the circuit used. One end of the crystal is grounded and the other end feeds to the input of a preamplifier. Bias is supplied through a shunt resistor of the same order of magnitude as the barrier resistance. The preamplifier output goes to a slave sweep which is triggered by individual pulses larger than a predetermined magnitude, and also to an attenuator which is calibrated to an accuracy of better than 0.1 db. The attenuator contains a coaxial cable delay line which delays the signal pulse by 0.17 μsec enabling the sweep to start adequately before the arrival of the signal at the main amplifier. The over-all band width of the system is about 35 megacycles/sec and the maximum available gain is 110 db.

The calibrating circuit consists of a pulser which generates a flat-topped pulse with a rise time of 0.01 μsec. The output is fed through an attenuator to a small condenser C_e that is connected to the preamplifier input. The leading edge of the calibrating pulse, when applied to condenser C_e, provides an impulse current

[4] Goucher, Pearson, Sparks, Teal, and Shockley, Phys. Rev. 81, 637 (1951).
[5] W. Shockley, *Electrons and Holes in Semiconductors* (D. Van Nostrand Company, Inc., New York, 1950), p. 309.
[6] K. G. McKay, Phys. Rev. 76, 1537 (1949).
[7] G. K. Teal and J. B. Little, Phys. Rev. 78, 647 (1950).

or quantity of charge to the input circuit of the amplifier. As long as R_i is negligible, this is entirely equivalent to the production of an impulse current across the barrier by one alpha-particle. By comparing the photographed pulses due to alpha-particle bombardment with the calibrating pulse, a direct measurement of the charge collected per individual bombarding alpha-particle is obtained.

The alpha-particle gun provides a collimated beam of alpha-particles from polonium. The maximum beam width striking the sample is 3.5×10^{-3} cm. This is somewhat wider than the barrier width which is expected to be approximately 5×10^{-4} cm at a few volts reverse bias. However, this is compensated for by the effect of diffusion. As long as the total time taken to collect all of the holes or electrons at the barrier by diffusion is much shorter than the RC decay constant or the recombination lifetime, the maximum pulse height will be the same as if all of the carriers were produced in the barrier itself. In these experiments, the RC decay constant was always greater than 5 μsec and the recombination lifetime was greater than 50 μsec as determined from photoconductivity measurements.[4] If the carriers are created at a distance of 10^{-3} cm from the barrier, 90 percent of the carriers will be collected by the barrier in a time of less than 0.5 μsec. This should guarantee fairly uniform pulse heights. All measurements were made in a vacuum of better than 10^{-2} mm Hg to eliminate any effects due to air ionization. At no time during the experiments did the temperature of the germanium exceed room temperature by more than 5°C.

EXPERIMENTAL RESULTS

Figure 3 shows a photograph of 16 alpha-pulses striking around the barrier. The observed spread in pulse heights agrees well with that calculated from the known beam width of the alpha-particle gun. The lower trace is that of the calibrating pulse. The maximum pulse height was taken as that best representing the maximum utilization of the carriers. The experiment has been repeated with seven samples of germanium from different sources and of resistivities ranging from 1 ohm cm to 20 ohm cm. The maximum pulse heights obtained from these different samples agree within 5 percent. Varying the bias across the junction from 0.3 to 15 volts showed no observable trend and the variations observed in maximum pulse height were no greater than the error involved in measuring up the photographs. The intensity calibration of the alpha-particle source was good only to within 25 percent, owing principally to uncertainty in the diameter of the beam defining aperture, but within that accuracy, the counting efficiency was 100 percent, i.e., every alpha-particle that strikes the germanium is registered. The alpha-pulses with the steepest rise time were exact replicas of the calibrating pulses within the accuracy to which the pulses could be superimposed. This indicates that in both cases the rise times are set by the transient response of the amplifier. From this we can set an upper limit to the length of time required to sweep all the holes and electrons across the barrier as 0.02 μsec. For the biases used, the effective barrier width is of the order of 5×10^{-4} cm with applied fields across the barrier of the order of 10^4 volts/cm. In such a strong field, it is probable that the low field value of mobility is no longer valid but it appears safe to assume that the carriers should traverse the barrier with a velocity of at least 10^7 cm/sec. Hence if there are no short time trapping effects in the barrier, the time taken for the carriers to traverse the barrier should be less than 10^{-10} sec. This is certainly not contradicted by the upper limit of 2×10^{-8} sec set by the experiment.

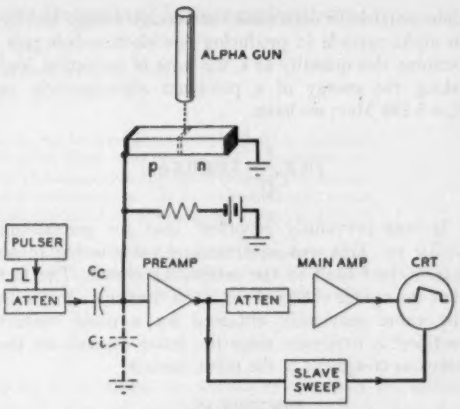

FIG. 2. Schematic of experimental equipment.

The final value for the charge collected per incident alpha-particle is $Q=1.77\times10^6e$, where e is the charge of an electron. According to Seitz,[5] less than 0.1 percent of the energy of an alpha-particle is given up to sources other than the liberation of electrons. Consequently we are justified in dividing Q/e into the initial energy of the

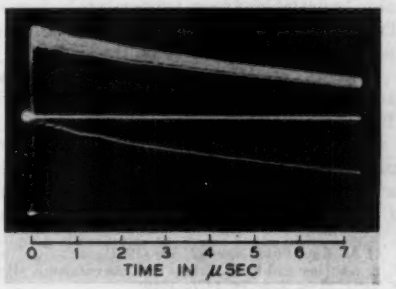

FIG. 3. Photograph of pulses from sixteen alpha-particles striking the $n-p$ barrier.

[5] F. Seitz, Disc. Faraday Soc. (No. 5) 271 (1949).

alpha-particle to determine the average energy lost by an alpha-particle in producing one electron-hole pair. Defining this quantity as ϵ, the work of ionization, and taking the energy of a polonium alpha-particle as $E_\alpha = 5.298$ Mev, we have

$$\epsilon = \frac{E_\alpha}{Q} = 3.0 \pm 0.4 \text{ ev}.$$

It was previously reported[9] that for germanium $\epsilon = 5.6$ ev. This was an erroneous value owing to an intermittent fault in the calibrating circuit. The fact that the charge collected per alpha does not agree with the value previously obtained for a point contact rectifier[6] is irrelevant since the latter depends on the previous treatment of the point contact.

DISCUSSION

Table I summarizes most of the data now available on the work of ionization in various solids. Diamond and germanium are of particular interest as they are both valence bonded crystals with the same crystal structure, yet the forbidden energy gaps differ by almost an order of magnitude. The results show that ϵ is not simply proportional to E_G. Let us consider briefly the energy loss mechanisms. The bombarding particle can lose energy in the following ways: (1) Direct excitation of lattice vibrations or direct nuclear collisions. Seitz[8] has shown that less than 0.1 percent of the energy of an alpha-particle is lost this way. (2) Production of high energy electrons which subsequently leave the crystal carrying their energy with them. Secondary emission data suggests this is a very inefficient process. (3) X-ray production and subsequent emission. This also appears energetically inefficient. (4) Exciton production with subsequent recombination. The agreement between the wavelength dependence of the infrared absorption and the photoconductive yield in germanium argues against any appreciable production of excitons which do not subsequently decompose[10] and Seitz has inferred that an exciton would probably be unstable at room temperature in diamond.[11] (5) Production of electron-hole pairs. These may be produced with sufficient energy on the average to produce tertiaries, etc. Competing with the process of tertiary production will be losses due to lattice excitation by the internally produced carriers.

It appears reasonable to assume that number (5) assimilates essentially all of the energy of the alpha-particle in germanium or diamond. Then $\epsilon - E_G$ represents the excess energy which is transferred to the lattice by the internally produced electrons and holes. In the materials listed in Table I, this quantity shows a certain degree of constancy. To derive values for $\epsilon - E_G$ theoretically requires not only a treatment of the collision process but also a detailed picture of the electron-lattice interaction over a wide range of electron energies. To date, this has not been done. However, the data suggest that energy losses to the lattice do play a considerable role and they appear to be more or less independent of the width of the energy gap E_G.

Although this work has been solely concerned with alpha-particle bombardment, it should be noted that the values of ϵ obtained from alpha-bombardment and electron bombardment for diamond agree within the experimental error. Apparently the same is true for CdS.[12] It is reasonable, therefore, to expect that a value of approximately $\epsilon = 3.0$ ev should be realized for electron bombardment in germanium. Moore and Herman[13] reported a value of $\epsilon = 5$ ev for 10-kv electrons bombarding germanium. Their published data indicates that they had not yet reached saturation, i.e., their published values of ϵ may be too high. Thus the extent of the agreement is quite encouraging. Moreover, this agreement is obtained in spite of the great difference in density of charges produced by electrons as compared with alpha-particles. This suggests that immediate recombination between holes and electrons produced by alpha-particles, does not occur in germanium when a field is present. (This is in contrast with the columnar ionization problem in gaseous ionization chambers.) Actually many of the alpha-particles do not strike the barrier at all but produce holes and electrons in the field free region immediately adjacent to the barrier and the carriers then diffuse to the barrier. In this case the same number of carriers are made available per alpha as when the alpha-particle strikes the barrier. Thus, even in field free germanium, recombination due to density of induced carriers, is negligible within the limits studied.

ACKNOWLEDGMENT

I wish to express my appreciation to G. K. Teal and M. Sparks, both of whom supplied germanium crystals for this work. The equipment used was constructed and maintained by H. C. Meier. I am indebted to A. J. Ahearn for an independent check of the pulse-height calibration.

[9] K. G. McKay, Phys. Rev. **82**, 329 (1951).
[10] F. S. Goucher and H. B. Briggs (private communication).
[11] F. Seitz, Phys. Rev. **76**, 1376 (1949).

[12] This is not true for alkali halides. H. Witt, Z. Physik **128**, 442 (1950) reported a value of $E_\alpha \epsilon / Q = 600$ ev for alpha-bombardment of NaCl at a field strength of 1.5×10^5 volts/cm without reaching a saturation with respect to field strength. This is compared with a value of 60 ev for beta-particles in KCl under similar conditions by H. U. Harten, Z. Physik **126**, 619 (1949). Witt attributes the difference to strong recombination of electrons produced by alpha-particles.
[13] A. R. Moore and F. Herman, Phys. Rev. **81**, 472 (1951).

The $n-p-n$ Junction as a Model for Secondary Photoconductivity

KENNETH G. MCKAY
Bell Telephone Laboratories, Murray Hill, New Jersey
(Received August 3, 1951)

A germanium $n-p-n$ junction with the p region floating, has been subjected to alpha-particle bombardment. The transient currents resulting from individual incident alphas have been studied. This enables one to study the rate of decay of excess holes in the p-region. This decay time appears to increase with applied bias, pass through a maximum, and eventually approach a constant value. The total charge flowing across the unit, as a result of the bombardment by a single alpha-particle, may become large; quantum yields of greater than 60 have been observed.

The unit possesses many of the important characteristics of materials which exhibit "secondary photoconductivity." It is concluded that various forms of $n-p-n$ barriers must therefore play an important role in such materials and that their understanding can be greatly facilitated by studies of $n-p-n$ barriers in germanium.

INTRODUCTION

THE early work by Gudden and Pohl on photoconductivity in insulators separated the observed current into two classifications: the primary current and the secondary current. The former is simply due to the motion of the charges freed by the light and corresponds to the simplest behavior studied more recently in bombardment conductivity. The secondary current does not build up instantaneously on illumination and shows a measurable decay after cessation of illumination. Moreover, it frequently exhibits quantum yields greatly in excess of unity. Interest has been revived in the secondary current, through the development of sensitive infrared detectors, such as thallous sulfide, lead sulfide, lead selenide, and lead telluride and also through the use of cadmium sulfide as a particle or x-ray detector.[1] A number of authors have advanced explanations for the effect. There is now general agreement that in an n-type crystal, the bombardment produces a positive charge in excess of the normal positive charge density, which acts as a control on the electron current flow through the crystal. (In a p-type crystal, the hole conduction is similarly controlled by an excess negative charge.) The earlier explanations were based on a homogeneous model in which trapped positive charges caused an over-all lowering of the conduction band relative to the Fermi level, thus permitting an increased electron flow through the crystal which would continue until the positive charges were neutralized through recombination. As this does not account for all of the observed properties, later explanations proposed $n-p$ barriers interspersed through the crystal or possibly a combination of the two models.[2]

As the actual constants involved in constructing either model are generally unknown and the experimentally measurable quantities do not lend themselves to easy interpretation, the models so far have been primarily of qualitative value. The purpose of this report is to present an actual, rather than theoretical, model of a cell employing a single barrier. This is a narrow barrier of p-type material in an n type body, which exhibits typical secondary currents.* As most of the constants involved are known, such a configuration is capable of being treated quantitatively by theory. Some rather puzzling properties of secondary currents can be explained directly in this case. Moreover, the over-all performance of the unit can be compared with that of a typical photoconductive cell to determine wherein the latter differs from the single barrier model.

$n-p-n$ JUNCTIONS IN GERMANIUM

Structures of this form have been analyzed by Shockley for use as transistors and also to explain high current multiplication ratios at collector points ($p-n$ hook theory).[3] Figure 1 represents the potential distribution when a bias of several volts is applied. As no external contact is made to the p region, it floats at a potential

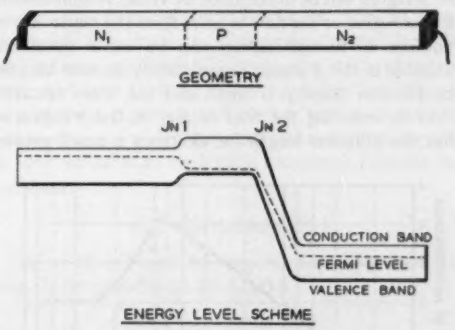

FIG. 1. Relation between geometry and energy level scheme for $n-p-n$ germanium. Length = 1.0 cm, width = height = 0.10 cm. P-type region = 2×10^{-3} cm in length.

[1] See A. W. Ewald, Phys. Rev. **81**, 607 (1951) for references on thallous sulfide type cells. For CdS see R. Frerichs, Phys. Rev. **76**, 1869 (1949).
[2] E. S. Rittner, Science **111**, 685 (1950).

* This use of an n-p-n junction was independently proposed by J. N. Shive.
[3] W. Shockley, *Electrons and Holes in Semiconductors* (D. Van Nostrand Company, Inc., New York, 1950), p. 110. Shockley, Sparks, and Teal, Phys. Rev. **83**, 151 (1951).

determined by the characteristics of the two $n-p$ barriers. If we assume that junction 1 is slightly biased in the forward direction and that saturation current is drawn by junction 2, then the following situation holds: the number of holes which flow across junction 2 into the p region is very small because of the low equilibrium density of holes in the n body N_2. However, there is an appreciable flow of electrons across junction 1 into the p region. If this region is so narrow that recombination here is small, most of these electrons will diffuse across the p region and be collected by junction 2. Thus the resistance of junction 2 will be less than that normally associated with an $n-p$ junction in the saturation region. Now let us inject an impulse charge of holes in the N_2 body near junction 2 by bombardment, such as by an alpha-particle. The holes will diffuse to junction 2 and will be swept across into the p region. In traversing practically the total voltage drop that is applied across the specimen, they will produce a voltage across the capacity of junction 2 which, in a simple $n-p$ junction would then decay with the time constant associated with this junction. If this is all that happened, this would be the usual "primary" current and the voltage pulse so obtained would be identical with that produced by artificially placing an impulse of charge on one end of the specimen. However, the presence of additional holes in the p region lowers the conduction band relative to the Fermi level, thus allowing additional electrons to flow across junction 1 into the p region, diffuse to junction 2, and be collected. In falling through the voltage drop across junction 2 these electrons register externally. Thus as long as an excess of holes remains in the p region, there will be an augmented electron current across junctions 1 and 2. The rate of return to the normal hole concentration in the p region will be determined by either recombination in that region or the flow of holes from the region across junction 1. Recombination can be made quite improbable if the p region is sufficiently narrow because the electron density is small and the holes are free. Thus by reducing the trap density in the p region so that the diffusion length for electrons is much greater than the width of the p region, we can enormously reduce the probability of recombination.

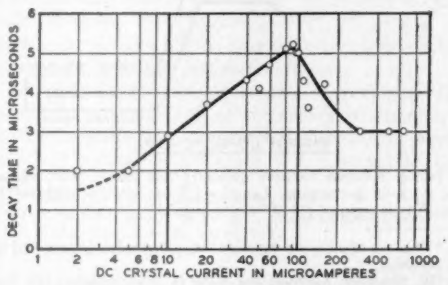

FIG. 2. Dependence of alpha-pulse decay time on dc crystal current.

It should be noted that the voltage pulse observed when a small impulse charge is placed on one end of the specimen is similar to that obtained for a simple $n-p$ junction although the time constant will be reduced because of the extra electron flow over junction 2. However, the pulse resulting from an impulse charge of holes produced near junction 2 will be different. Neglecting diffusion times, the normal "primary" pulse will be produced across the capacity of junction 2 but the voltage will continue to increase due to the augmented electron flow for a time approximately equal to the time constant of junction 2. It will then level off and we shall measure current rather than charge which will die off in a time which is a function of the rate at which the excess holes in the p region disappear.

EXPERIMENT

A germanium $n-p-n$ junction was used with a p region of width approximately 2×10^{-3} cm. The conductivities were to order of magnitude $\sigma_{n1}=1$ ohm^{-1} cm^{-1}, $\sigma_p=10$ ohm^{-1} cm^{-1}, $\sigma_{n2}=1000$ ohm^{-1} cm^{-1}. Photoelectric measurements of diffusion lengths gave lifetimes for holes of $\tau_{n1}=8$ μsec, $\tau_{n2}\leq0.2$ μsec, with evidence in the former case of excessive surface recombination. The narrowness of the p region prevented measurements of electron lifetimes in this region.

The circuit used in observing individual pulses due to alpha-particle bombardment of the unit is identical with that used in previous experiments with simple $n-p$ junctions.[4] The measurements were made with the high conductivity N_2 biased positive with respect to N_1. Photographs were made of pulses resulting from the incidence of individual alpha-particles on or near the p region.

Most of the pulses showed a rise time which was approximately equal to τ_D, the RC decay constant of junction 2 in parallel with the impedance of the amplifier input. The pulses decayed exponentially with a time constant much greater than τ_D. In these respects the pulses differed from those obtained from a simple $n-p$ junction where the rise time is essentially instantaneous and the decay time equals τ_D.[4] Thus we are here observing a time dependent current flow rather than merely an impulse charge. Consequently, the load resistor was chosen to be small compared with the barrier resistance so that the observed pulse actually represented current flow through the crystal and was independent of barrier resistance. If this precaution is not taken, the interpretation of the wave forms is complicated by the fact that for higher values of bias the dynamic resistance of the barrier is time dependent as a result of the voltage change produced by the alpha-pulse. The finite rise time is of course not observed when a very low value of load resistance is used. The in-

[4] K. G. McKay, accompanying paper.

terpretation of the wave forms appears consistent with the mechanism proposed earlier.

Figure 2 shows the observed variation in decay time constant as a function of dc current through the crystal. In general, the observed wave forms followed an exponential decay within the accuracy of measurement. The integral of the wave shape divided by the load resistance yields the total charge flowing through the crystal as a result of bombardment by one alpha-particle. Figure 3 shows the computed charge flow across the unit per alpha-pulse as a function of dc crystal current. The current-voltage characteristic of the unit is also shown. Similar measurements on a second $n-p-n$ crystal showed substantially the same type of behavior. There are several points worth noting. As the bias goes to zero, the charge collected appears to approach the value $Q=1.6\times10^6e$ which is close to the value measured for a simple $n-p$ barrier.[4] With increasing bias the yield increases rapidly and then tends to level off as the collector junction assumes saturation current. The maximum charge collected corresponds to a quantum efficiency[5] of about sixty in this case. The time constant variation is not large but does show a definite trend. At zero bias it is the same as that obtained for an impulse charge applied to the junction through the calibrating circuit, i.e., the time constant of the higher resistance barrier. As the bias increases, the time constant also increases and passes through a maximum at about the same current as that at which the yield begins to level off. At high currents the time constant appears to assume a constant value.

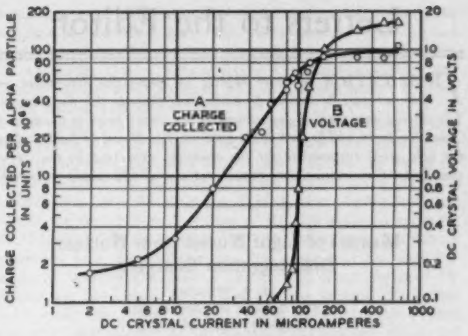

FIG. 3. (a) Charge collected per incident alpha-particle; (b) dc current-voltage characteristic.

DISCUSSION

These experiments are designed to demonstrate an actual physical model for the secondary current mechanism based on $n-p$ barriers. Some of the characteristics of materials exhibiting secondary currents are as follows: (1) The response to an impulse excitation is not immediate but builds up gradually. (2) The quantum efficiency is much greater than unity. (3) Units with a high dark current show the greatest yield. (4) It has been noted that where barriers are postulated, the resistivity of the barriers would have to be much greater than for the bulk material.[6]

These characteristics may not be demonstrated by all materials exhibiting secondary currents but they are generally representative. All of these characteristics are exhibited by the germanium $n-p-n$ junction. The long time constants exhibited by the excess holes in the p region are readily explained by the assumption that they are not locally trapped but are free yet constrained to remain within the p region.

Shockley[3] has shown how to determine theoretically all of the low frequency characteristics of such a unit. With further knowledge of the mechanism of discharge of excess holes in the p region, it should be possible to do the same for the transient case studied here. This is unique among materials exhibiting secondary currents.

It should not be assumed that all of the characteristics of secondary conducting materials can be explained so simply. Many of these materials must be highly complex with many barriers of varying widths and heights. Energy transfer via fluorescent radiation may play a role in maintaining current flow once it is initiated in some materials. However, the mechanism investigated here probably plays an important role in most of these materials and further studies of the response of $n-p-n$ structures in semiconductors should be very valuable in explaining secondary currents in insulators.

ACKNOWLEDGMENT

The $n-p-n$ junctions used in these experiments were kindly supplied by M. Sparks.

[5] What is calculated is the charge traversing the junction divided by the charge produced in the specimen per bombarding alpha-particle. As F. S. Goucher, Phys. Rev. 78, 816 (1950), has shown that for each photon absorbed, one electron-hole pair is produced in germanium, the use of the term "quantum efficiency" is appropriate.

[6] R. P. Chasmar, Nature 161, 281 (1948).

Letters to the Editor

PUBLICATION of brief reports of important discoveries in physics may be secured by addressing them to this department. The closing date for this department is five weeks prior to the date of issue. No proof will be sent to the authors. The Board of Editors does not hold itself responsible for the opinions expressed by the correspondents. Communications should not exceed 600 words in length.

Masses of Light Nuclei from Nuclear Disintegration Energies

H. A. WILSON
Rice Institute, Houston, Texas
(Received August 30, 1951)

IN the paper[1] with the above title, it is stated that now for the first time it is possible to calculate the masses of light nuclei in terms of O^{16} from nuclear reaction energies without using mass spectroscopic results.

In my book[2] in 1937, the masses of light nuclei were calculated from nuclear reaction energies without using mass spectroscopic data. Similar work[3] was done in 1936.

In *Modern Physics* the reaction energies of 17 reactions were used to calculate the energies of formation and the neutron and hydrogen masses. The other masses were obtained by the equation

$$ZH^1+(A-Z)n^1={}_ZA^A+{}_ZE^A,$$

where ${}_ZE^A$ is the energy of formation of the atom out of protons and neutrons.

The neutron mass was found to be 1.00898 and the hydrogen mass to be 1.00815, which are very close to the new values[1] 1.008982 and 1.008142. The other masses differed slightly from the new values.

The reaction energies in 1937 were not known very exactly, and the recent paper[1] is a very thorough and important contribution.

[1] Li, Whaling, Fowler, and Lauritsen, Phys. Rev. **83**, 512 (1951).
[2] H. A. Wilson, *Modern Physics* (Blackie and Son, Glasgow, 1937), second edition, p. 262.
[3] H. A. Wilson, Proc. Roy. Soc. (London) **A154**, 560 (1936).

Application of Collective Treatment of Electron and Ion Vibrations to Theories of Conductivity and Superconductivity

DAVID BOHM,
Princeton, New Jersey
AND
TOR STAVER
Palmer Physical Laboratory, Princeton University, Princeton, New Jersey
(Received September 21, 1951)

THE interaction between electrons and lattice vibrations suggested by Fröhlich[1] and Bardeen[2] as a cause of superconductivity can be treated very advantageously by means of a collective description, originally introduced in connection with the theory of plasma oscillations.[3] It will be shown in a paper to be published in the near future that, if the electrons and ions in a metal are approximated as clouds of charge, then the normal modes for the combined system correspond to two types of collective vibration: (1) the ordinary high frequency ($\sim 10^{16}$ cps) "plasma oscillations" of the electron gas, slightly modified by the small responses of the heavy ions; (2) the comparatively low frequency acoustical oscillations in which the ionic vibrations are almost entirely screened by the rapidly moving electrons. From the frequency of the acoustical vibrations one can calculate the speed of sound in terms of the ionic mass and the interionic spacing. We obtain agreement with the observed values within an error of 20 percent for alkali metals, and within a factor 2 for polyvalent metals.[4] These results are in harmony with the fact that the non-coulombic part of the interionic potential, which we have neglected in our treatment, is small for alkali metals, but appreciable for polyatomic metals.

It will be shown in another paper,[5] however, that a purely collective description of a dense aggregate of charged particles does not adequately treat all the significant properties of this aggregate. To the collectively describable part of the density (which takes the form of organized wave-like oscillations) must be added a randomly fluctuating part associated with the individual particles themselves. In a metal this individual-particles component of the charge density produces two significant effects: (1) each electron is surrounded by a cloud containing a deficiency of electrons (and therefore an excess of positive ions) which screens out most of its field within a distance of the order of 10^{-8} cm;[3,5] (2) each electron is followed by an acoustical disturbance resembling the wake behind a boat in the water. The angular width of this wake is of the order of $v_{\text{sound}}/v_{\text{electron}}$, which for the faster electrons is only about 3×10^{-3} radians in a typical metal. The wake carries away energy from the electron and thus gives rise to an electrical resistance. The latter can be expressed solely in terms of the ionic mass and the interionic spacing, and one obtains agreement with experimentally observed values at low temperatures within a factor of 2 for monovalent metals.

The description of electrical resistance in terms of a "wake" removes certain puzzling difficulties pointed out by Peierls.[6] By taking into account the conservation of the combined momentum of electrons and sound waves, he was led to the conclusion that the only sources of electrical resistance would be "Umklappprozesse" arising from the effects of lattice periodicities, and scattering of sound waves by each other arising from nonlinearities. This theory gives too small a value and a wrong temperature dependence for the resistivity at low temperatures. If one notes, however, that the sound energy is spatially distributed in the form of a wake, it becomes clear that the momentum in the sound waves is extremely unlikely to return to the electron from which it came, and that, as in the case of a boat in water, this momentum is carried far away to be scattered by obstacles, boundaries, etc., so that it is ultimately degraded into random thermal motion. For this reason, the more naive theory, which does not take into account the possibility that the sound momentum can return to the electron, leads to the right values for the resistivity of monovalent metals, while Peierls' theory, which incorrectly describes the possibility of return, does not lead to the correct values.

The acoustical wake of the electrons may also be important in the interaction of electrons. For example, if one electron follows in the wake of another, the energy of the pair is found to be reduced by about 10^{-4} ev. We wish to suggest here that this interaction may provide the basis of a possible model for superconductivity in terms of moving but flexible chains of electrons, each of which is held in the chain by the very narrow wake of the electron ahead of it. The individual electrons could be scattered only by being torn out of the chain. Thus one would obtain metastable chains of current flowing for practically indefinite periods. The entropy of the system would be lowered by the formation of such chains, so that they would be thermodynamically stable only at temperatures for which the binding energy of each electron in the chain is of the order of kT. Such an estimate leads to transition temperatures of the order of magnitude of those observed experimentally. Moreover, the dependence of the interelectronic interaction energy on the mass of the ion (through the sound velocity) has the right functional form to account for the isotope effect. The chief difference between the theory suggested by Fröhlich and Bardeen, and that suggested by us, is that they attribute the cause of superconductivity to the interaction of an electron with itself by way of the phonon field, whereas—in their terminology—

we may be said to attribute it to the interaction of neighboring electrons through the phonon field. This interaction is analogous to the (retarded) Möller interaction resulting from the virtual quanta of the electromagnetic field.

[1] H. Fröhlich, Phys. Rev. **79**, 845 (1950).
[2] J. Bardeen, Phys. Rev. **80**, 567 (1950).
[3] D. Bohm and D. Pines, Phys. Rev. **82**, 625 (1951).
[4] F. Seitz, *Modern Theory of Solids* (McGraw-Hill Book Company, Inc., New York, 1940).
[5] D. Pines and D. Bohm (to be published).
[6] R. E. Peierls, Ann. Physik **12**, 154 (1932).

Alpha-Alpha Scattering*

C. H. Braden, S. M. Carter, and A. G. Ford
Washington University, St. Louis, Missouri
(Received August 27, 1951)

THE differential scattering cross sections for 20.4±1.0-Mev alpha-particles by helium were determined at center-of-mass scattering angles of 60° and 90°. The experimental results are shown in Table I.

The scattered particles were detected by a proportional counter. The amplified pulses from the counter went to a pulse-height discriminator circuit which rejected pulses of amplitude appreciably smaller than those desired. The unscattered particles were collected in a faraday cage which was connected to a one-μf condenser. The voltage across the condenser was measured by a null method using a Compton electrometer as the null device.

There was an appreciable background counting rate resulting from the neutron flux accompanying the operation of the cyclotron. This background was reduced somewhat by shielding the counter with borax and paraffin. The background counting rate was determined before and after each set of scattering runs. Based on the internal consistency of the background data and the number of counts taken, a precision of ±10 percent was assigned to the background correction.

The scattering chamber was filled to a pressure of about 2.2 cm of Hg with helium of 99.5 percent purity furnished in standard cylinders by the Ohio Chemical Company. The pressure was determined by a U-tube manometer filled with Apiezon oil B. Impurity scattering is not believed to be important in this work because the alpha-alpha scattering cross section is at least as great as the alpha-air scattering cross section for the angles studied, hence the possible 0.5 percent impurity in the scattering gas could contribute a maximum error of 0.5 percent. Furthermore, the pulses produced by impurity-scattered particles were smaller than the genuine pulses, and experimental tests showed that impurity-caused pulses were counted with poor efficiency. Outgassing of the metal surfaces of the scattering chamber or leaks in the system would have caused the pressure of the scattering gas to increase during a period of data taking. No increases in pressure greater than one percent were noted.

No direct data on the cyclotron alpha-particle beam energy are available, so it has been estimated from measurements of the proton and deuteron beam energies. The probable errors quoted for the scattering cross section in Table I include the statistical probable error, the probable error in the background counts, and a collection of minor errors that are discussed in a paper on proton-alpha scattering[1] in which the same apparatus was used. A more detailed account of the apparatus and the procedure used in taking data are included there. The paper also describes the procedure by which proton-proton scattering was used to calibrate the apparatus, thus making a precise knowledge of certain geometrical factors and the capacitance of the condenser connected to the faraday cage unnecessary.

The results of the present work are directly comparable with those of Mather[2] who used the same cyclotron, but employed an entirely different apparatus which used photographic plates for the detection of the scattered particles. Mather gives the value 0.123±0.008 barn/sterad for the differential scattering cross section in the center-of-mass system at 60°. He gives no value for 90°, but his cross sections near 90° tend upward in qualitative agreement with the present work. The reasons for the large discrepancy between the present results and those obtained by Mather are not clear.[3] As explained in the account of proton-alpha work,[1] the present method yielded absolute proton-proton scattering cross sections within the estimated probable error, ±5 percent. The alpha-alpha work was made more difficult by the low alpha-particle beam current from the cyclotron (0.14×10^{-9} ampere into the scattering volume) which makes the procurement of data on alpha-alpha scattering require roughly 40 times as long as the procurement of an equivalent amount of data when accelerated protons are used. However, no reasons have been found for suspecting large errors resulting from this increased time required for obtaining the data.

TABLE I. Results of the alpha-alpha scattering work for incident alpha-particles of 20.4±1.0 Mev. θ is the scattering angle in the center-of-mass system, n is the number of counts observed, R is the ratio of the number of genuine counts to the number of background counts, and σ is the differential scattering cross section in the center-of-mass system expressed in barns/sterad.

θ	n	R	σ
60°	900	19	0.086 (±5.5 percent)
90°	900	26	0.14 (±5.5 percent)

* Assisted by the joint program of the ONR and AEC.
[1] C. H. Braden, Phys. Rev. **84**, 762 (1951).
[2] K. B. Mather, Phys. Rev. **82**, 126 (1951).
[3] Our attention has been called to unpublished work on alpha-alpha scattering at 30 Mev by E. Graves at the Massachusetts Institute of Technology. Graves' work indicates that the scattering cross section is quite energy-dependent. A possible explanation of the discrepancy between Mather's results and the present results may be that, because of changes in the cyclotron operating conditions, the present work was performed at an energy slightly different from that used by Mather.

Nuclear Binding Energies for Isotopes with Masses between 50 and 60

A. H. Wapstra
Instituut voor Kernphysisch Onderzoek, Amsterdam, Netherlands
(Received September 24, 1951)

RECENTLY we computed a list of nuclear binding energies and masses[1] for mass numbers <43, using recent reaction energy data[2] and the new mass spectrographical results of Ewald.[3] We tried to extend this list up to about $A=65$. In this mass region several reaction energy data are known, which appear to be reasonably reliable since similar measurements for lower mass numbers, often by the same authors, are in good agreement with one another and with Ewald's results. In the same region several stable isotopes have been measured mass spectrographically.[4–6] Among these measurements, which are not mutually consistent, we consider first those of Duckworth *et al.*[6] Their measurements of the Si- and S-isotopes are in reasonable agreement with the values computed from our aforementioned list (Table I).

It is of great interest to compare the differences in binding energies computed from Duckworth's results for the isotopes with masses $50<A<60$ (collected in Table II, column 3) with the values derived from reaction energy data (Table III). Table II, column 4, shows the binding energies derived from Duckworth's

TABLE I. Packing fraction differences (10^{-4} MU).

Doublet	Duckworth	Computed
$C_3H_4-Si^{28}$	19.45±0.06	19.42 ±0.01
C_2O-Si^{28}	6.45±0.03	6.43 ±0.01
CH_2-Si^{28}	24.53±0.03	24.46 ±0.01
O_2-S^{32}	5.50±0.03	5.54_4±0.00$_5$

results making use of the binding energy values of the C-, O-, and Si-isotopes collected in our list and the conversion factor 1 MU = 931.15 Mev.[7,8] For isotopes measured in more than one way a mean result is given. The differences in these binding energies are shown in Table IV, column 2. The corresponding differences derived from reaction energy data are given in column 3.

TABLE II. Binding energies computed from doublets.

Nuclide	Doublet	$f(10^{-4}$ MU)	Binding energy (Mev)	Assumed value (Mev)
Cr^{52}	$C_3H_3-Cr^{52}$	17.47 ±0.04	456.24 ±0.20	456.24
Fe^{54}	$C_3H_3-Fe^{54}$	19.91 ±0.04	471.77 ±0.20	
	$C_2H_3-Fe^{54}$ [a]	19.99 ±0.04	472.17 ±0.20	
		mean result:	471.97 ±0.16	471.96
Fe^{56}	$Si^{28}-Fe^{56}$	3.32 ±0.02	491.81 ±0.14	
	$CO-Fe^{56}$	9.80 ±0.02	492.05 ±0.14	
	$C_2H_4-Fe^{56}$	22.93 ±0.07	492.79 ±0.38	
		mean result:	491.97 ±0.12	492.43
Ni^{58}	$Si^{29}-Ni^{58}$	3.07 ±0.02	506.45 ±0.14	
	$COH-Ni^{58}$	12.09 ±0.04	506.25 ±0.22	
	$C_2H_3-Ni^{58}$	24.73 ±0.04	506.77 ±0.22	
		mean result:	506.48 ±0.12	506.23
Ni^{60}	$Si^{30}-Ni^{60}$	2.90 ±0.02	527.29 ±0.14	526.83

[a] The second $C_2H_3-Fe^{54}$ result is a combination of the doublets $C_2H_3-Pd^{106}$ and $Pd^{106}-Fe^{54}$.

Comparing these two columns it appears that for $Fe^{56}-Fe^{54}$ and $Ni^{58}-Fe^{56}$ the consistency is outside the errors indicated. Since the reaction data are reliable, as mentioned previously, we arrive at the conclusion that the errors in Duckworth's measurements must be a little underestimated.

We are now able to compute what we think at present are the most reliable values of the binding energies of the isotopes involved. For that purpose we assume rather arbitrarily that the differences in binding energies have the values of Table IV, column 4. Next we adjusted the binding energies to these differences with the least possible deviations from Duckworth's values; the results are shown in Table II, column 5. It is seen that almost all deviations from Duckworth's results are less than 0.5 Mev. Therefore we think that the error in our values will not exceed 0.5 Mev.

TABLE III. Reaction energies (Mev).

No.[a]	Reaction	Q[b]	No.	Reaction	Q
1	$Cr^{52}(\gamma, n)Cr^{51}$	−7.5 ±0.3	10	Co^{57} (K)Fe^{57}	>1.0
2	$Cr^{52}(p, n)Mn^{52}$	−1.37 ±0.05	11	$Ni^{57}(\beta^+)Co^{57}$	4.55 ±0.10
3	$Fe^{54}(\beta^+)Mn^{54}$	4.4 ±0.1	12	$Ni^{58}(\gamma, n)Ni^{57}$	11.7 ±0.2
4	$Fe^{54}(\gamma, n)Fe^{53}$	−13.8 ±0.2	13	$Co^{58}(\beta^-)Ni^{58}$	> −0.8
5	$Fe^{54}(n, \gamma)Fe^{55}$	9.30 ±0.03	14	$Co^{59}(\gamma, n)Co^{58}$	−10.0 ±0.3
6	$Mn^{55}(p, n)Fe^{55}$	−1.01 ±0.01	15	$Co^{59}(n, \gamma)Co^{60}$	7.73 ±0.04
7	$Mn^{55}(n, \gamma)Mn^{56}$	7.25 ±0.03	16	$Co^{60}(\beta^-)Ni^{60}$	2.04 ±0.01
8	$Mn^{56}(\beta^-)Fe^{56}$	2.91 ±0.05	17	$Ni^{58}(n, \gamma)Ni^{59}$	9.01 ±0.03
9	$Fe^{56}(n, \gamma)Fe^{57}$	7.63 ±0.01	18	Ni^{59}(K)Co^{59}	>0.8

[a] Number	Reference
1, 14	Sher, Halpern, and Stephens, Phys. Rev. 81, 154 (1951).
2, 6	P. H. Stelson and W. M. Preston, Phys. Rev. 83, 469 (1951).
3	M. E. Nelson and M. L. Pool, Phys. Rev. 77, 682 (1950); F. I. Boley and L. J. Laslett, Phys. Rev. 83, 215 (1951).
4	McElhinney, Hanson, Becker, Duffield, and Diven, Phys. Rev. 75, 542 (1949).
5, 6, 9, 15, 17	Kinsey, Bartholomew, and Walker, Phys. Rev. 78, 481 (1950).
5, 9, 17	See also J. A. Harvey, Phys. Rev. 81, 353 (1950).
8	K. Siegbahn, Ark. Mat. Astron. Fys. 33A, No. 10 (1946); L. G. Elliott and M. Deutsch, Phys. Rev. 64, 321 (1943).
10	E. H. Plesset, Phys. Rev. 62, 181 (1942).
11	Friedlander, Perlman, Alburger, and Sunyar, Phys. Rev. 80, 30 (1950).
12	Ogle, Brown, and Carson, Phys. Rev. 78, 63 (1950).
16	Waggoner, Moon, and Robert, Phys. Rev. 78, 295 (1950).

[b] For β-processes the table gives the resulting change in binding energy.

The binding energies of the Ni-isotopes computed from the mass spectrographical results of Shaw[4] are about 2 Mev higher than the values computed above; the binding energies of the Cu- and Fe-isotopes computed from Ogata's results[5] scatter around our values by amounts up to 4 Mev, both in violent disagreement with nuclear reaction data.

The author wishes to thank Professor C. J. Bakker for his interest in this work.

TABLE IV. Differences in binding energies (Mev).

Difference	Duckworth	Q-values	Assumed
$Fe^{54}-Cr^{52}$	15.73 ±0.28	15.53 ±0.4	15.72
$Fe^{56}-Fe^{54}$	20.00 ±0.25	20.47 ±0.07	20.47
$Ni^{58}-Fe^{56}$	14.51 ±0.17	<13.78 ±0.23	13.80
$Ni^{60}-Ni^{58}$	20.81 ±0.19	>19.58 ±0.04 <20.57 ±0.3	20.60

Note: After this paper had been submitted for publication a new paper (R. Canada and A. C. G. Mitchell, Phys. Rev. 83, 955 (1951)) changed the β-decay energy of Ni^{57} to 4.01 Mev. This increased the Q-value (Table IV) for the difference $Ni^{58}-Fe^{56}$ to <14.32 Mev, greatly diminishing the largest deviations from Duckworth's results. We would now suggest the following binding energies: Cr^{52}—456.25, Fe^{54}—471.85, Fe^{56}—492.25, Ni^{58}—506.55, and Ni^{60}—527.15 Mev, with an estimated mean error of 0.3 Mev. These changes do not affect the general conclusions in the following paper.

[1] This list may be obtained by writing to the author.
[2] Li, Whaling, Fowler, and Lauritsen, Phys. Rev. 83, 512 (1951).
[3] H. Ewald, Z. Naturforsch. 6a, 293 (1951).
[4] A. E. Shaw, Phys. Rev. 75, 1011 (1949).
[5] K. Ogata, Phys. Rev. 75, 200 (1949).
[6] Duckworth, Johnson, Preston, and Woodcock, Phys. Rev. 78, 386, 479 (1950); H. E. Duckworth and H. A. Johnson, Phys. Rev. 78, 179 (1950); H. E. Duckworth and R. S. Preston, Phys. Rev. 79, 402 (1950).
[7] A. H. Wapstra, Phys. Rev. 82, 756 (1951).
[8] J. M. W. Dumond and E. R. Cohen, Phys. Rev. 82, 555 (1951).

Nuclear Masses and Closed Shells in the Region $A<65$

A. H. WAPSTRA
Instituut voor Kernphysisch Onderzoek, Amsterdam, Netherlands
(Received September 24, 1951)

SOME time ago Low and Townes[1] computed a set of nuclear masses and showed that these masses do not indicate closed nuclear shells for neutron and proton number N or $Z=20$. Recently Duckworth and Preston[2] published a new packing fraction curve which indicates several magic numbers, not, however, including N or $Z=20$. We thought it worthwhile to repeat these investigations using our new list of nuclear masses.[3] For that purpose we made a diagram of the difference between our mass values and the masses computed by Metropolis and Reitwiesner[4] from the Weizsäcker-Bethe formula. We found that the part of this formula describing the even-odd staggering—namely $(0.036/A^{\frac{1}{2}})\lambda$, in which λ is $+1$ for $e-e$ nuclides and 0 and -1 for $e-o$ and $o-o$ isotopes, respectively—exaggerates the real effect. In fact, in the region $15<A<50$ the formula 0.0018λ proves to be a better approximation. Therefore we made this correction in Metropolis and Reitwiesner's values for all masses $A<50$, before subtracting them from the real mass values.

The result is shown in Fig. 1 (in 10^{-4} MU). The errors in the values for $A<43$ are about 1 unit (10^{-4} MU) or less with only a few exceptions. The region $50<A<61$ has been discussed in the preceding letter; the values for $43<A<50$ and $61<A<67$ are computed from Duckworth's[5,6] measurements of Ti[48] and Cu[65] in combination with various nuclear reaction data. The errors in these values are thought to be of the order of 5 units (5×10^{-4} MU). One notices at once that the minimum in the mass differences around the magic numbers is fairly wide. This implies that it is often difficult to choose between two possible values for a magic number. For instance the lower masses in the region around $A=14$ (to be seen most clearly from the values for even-odd isotopes) may be caused by N or $Z=8$, but also by N or $Z=6$. But even allowing for this fact, the magic character of Z or $N=20$ hardly

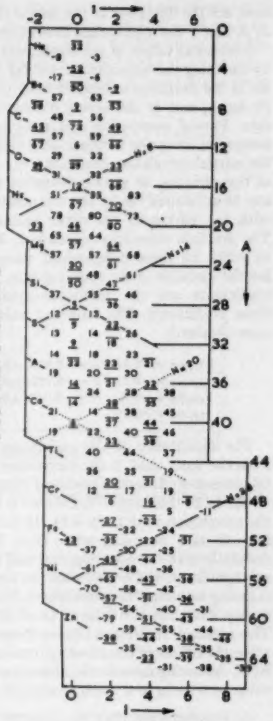

FIG. 1. Differences in 10^{-4} MU between the real atomic masses and the masses computed from a corrected Weizsäcker-Bethe formula, as a function of neutron excess I and mass number A. The values for even-even nuclei are underlined; those for odd-odd nuclei have a line above the values. The position of the magic numbers N or $Z=8$, 14, and 28 is indicated by broken lines, the position of N or $Z=20$ by a dotted line.

can be called convincing, especially as the lower mass of Ca^{40} seems to be a common property of all α-particle nuclei (i.e., even-even nuclei containing the same number of neutrons and protons). On the other hand, a somewhat lower mass in the region around $A=30$ seems to indicate that N or $Z=14$ may be magic (as already remarked by Seidlitz, Bleuler, and Tendham[6]) while the lower part of our plot allows the conclusion that N or $Z=28$ are magic. (The deplorable scarcity of measurements with heavier nuclides prevents this conclusion from being drawn with certainty.) Thus it is questionable whether even the beginning of the magic number series is represented by $\frac{1}{2}m(m^2-1)$ (giving the series 0, 2, 8, 20, 40), changing over to the formula $\frac{1}{2}m(m^2+5)$ for $m=5$;[7] in view of our Fig. 1 it is even tenable that the last formula represents the whole magic number series, which then runs 2, 6, 14, 28, 50, 82, 126. In this picture the exceptional stability of O^{16} and Ca^{40} should be the result of their being α-particle nuclei; while the magic character of $Z=20$ is further suggested by the stability of Ca^{48}, the latter in reality is the result of $N=28$.

We thank Professor C. J. Bakker for his interest in this work, which is part of the research programme of the "Stichting voor Fundamenteel Onderzoek der Materie" and was made possible by financial support from the Nederlandse Organisatie voor Zuiver Wetenschappelijk Onderzoek.

[1] W. Low and C. H. Townes, Phys. Rev. 80, 608 (1950).
[2] H. E. Duckworth and R. S. Preston, Phys. Rev. 82, 468 (1951).
[3] See the preceding letter: A. H. Wapstra, Phys. Rev. 84, 837 (1951).
[4] N. Metropolis and G. Reitwiesner, *Tables of Atomic Masses* (Los Alamos Scientific Laboratory, New Mexico, 1950).
[5] Duckworth, Johnson, Preston, and Woodcock, Phys. Rev. 78, 386, 479 (1950).
[6] Seidlitz, Bleuler, and Tendham, Phys. Rev. 76, 861 (1949).
[7] Haxel, Jensen, and Suess, Z. Physik 128, 295 (1950); L. Rosenfeld, Physica 17, 461 (1951).

The Age of the Elements

RICHARD L. BURLING
Department of Physics, University of Hawaii, Honolulu, Hawaii
(Received September 21, 1951)

THERE are in the literature several computations of an "age of the elements,"[1-9] many of which are shorter than the time required in Urry's hypothesis of the earth's history.[10] Most of these[1-9] are based on the following reasoning: a system containing a measurable quantity of a radioactive nuclide cannot have been isolated for a time greater than that required to produce all of the observed abundance of the daughter nuclide. Since not all of the daughter need be radiogenic, the system may of course have been isolated for a much smaller time. Using data on the average composition of igneous rocks[11] (supposedly representative of the earth's outer crust), and applying it to all known natural radioactivities, the smallest upper limit for this time is about 5×10^9 years, a figure obtained for both U^{238} and U^{235}. This calculation has been performed by Meyer[1] who refers to the result as the "age of the sun," by Koczy[6] as the "age of matter," and by López de Azcona[3] as the "age of the elements." Brewer[4-5] has made the calculations for K^{40} and Rb^{87}, and refers to his result as "an upper limit for the age of matter." Öpik[7] regards his result as a maximum time since the element-forming reactions ceased.

It is the purpose of this note to discuss the interpretation of these figures. Since the calculations were all based on the observed abundances of the elements in the portion of the earth's crust accessible for sampling, the result will be an upper limit to the time since the isolation of the earth's crust. "Isolation" could mean separation from an element-factory or separation from the rest of the earth by a process capable of altering the relative concentrations of the parent and daughter elements. The works cited[1-7] apparently adopt the former interpretation or else regard the interval separating the two isolating events as being negligibly small. If, as is generally supposed, the earth consists of concentric shells of differing composition, then the separation of the crust from the rest of the earth was an element-separating process such as that discussed by Goldschmidt,[12] so that the crust might have contained initially very little lead. Hence the five-billion-year figure should be regarded as an upper limit to the age of the earth's present crust.

Since the concentration of uranium in the crust is much greater than that in meteorites[13] or in the earth as a whole,[14-16] the upper limit for the age of a meteorite or of the whole earth would be much larger; and, if the separation of the planets from their parent was not an element-separating process, as appears reasonable since no gas-phase separations would be expected to produce large differences in the relative concentrations of elements not too widely different in atomic mass, then this longer time may also be taken as an upper limit to the "age of the elements" or the time since heavy-element-forming reactions ceased in the material sampled. The data for its evaluation may be obtainable from meteorites in the way indicated by Brown,[17] and applied by Suess[8] in deriving a figure of 6×10^9 years for this age. The abundances[18] used by Suess are, however, incorrect both for uranium[19] and for lead.[19] Nevertheless, although this "upper limit to the age of the elements" can scarcely be greater than 15×10^9 years, it may easily be large enough to give the circa 7×10^9 years required in Urry's hypothesis of the earth's accretion, radioactive heating, melting with separation into shells, and subsequent cooling. Even the 5×10^9 year figure was of course adequate to cover the 3×10^9 year "short time scale" implied by the apparent recession of the nebulae.

The 3.6×10^9 year "age of the elements" recently published by Katcoff *et al.*[9] can also be shown not to conflict with Urry's hypothesis. Their result is obtained by adding a small interval (0.3×10^9 years, representing the time between the formation of the elements and of the earth) to Holmes' figure[20] of 3.35×10^9 years, which is misinterpreted, as usual, as representing the age of the earth. Holmes' widely quoted figure is the age of the sial

crust,[20] or the time back to the melting and layering in Urry's hypothesis. Katcoff's considerations can be applied equally well to a seven-billion-year-old earth, and give an age of the elements slightly greater than that.

[1] S. Meyer, Naturwiss. **25**, 764 (1937).
[2] F. F. Koczy, Nature **151**, 24 (1943).
[3] J. M. López de Ascona, Rev. real. Acad. cienc. Madrid **42**, 393 (1948).
[4] A. K. Brewer, Science **86**, 198 (1937).
[5] A. K. Brewer, J. Wash. Acad. Sci. **28**, 416 (1938).
[6] A. K. Brewer, Ind. Eng. Chem. **30**, 893 (1938).
[7] E. Öpik, Pop. Astronomy **41**, 78 (1933).
[8] H. E. Suess, Experientia **5**, 278 (1949).
[9] Katcoff, Schaeffer, and Hastings, Phys. Rev. **82**, 688 (1951).
[10] Wm. D. Urry, Trans. Am. Geophys. Union **30**, 171 (1949).
[11] Kalervo Rankama and Th. G. Sahama, *Geochemistry* (University of Chicago Press, Chicago, Illinois, 1950), pp. 38–40.
[12] V. M. Goldschmidt, J. Chem. Soc. 655 (1937).
[13] G. L. Davis, Am. J. Sci. **248**, 107 (1950).
[14] G. L. Davis, Am. J. Sci. **245**, 677 (1947).
[15] G. L. Davis and H. H. Hess, Am. J. Sci. **247**, 856 (1949).
[16] C. Festa and M. Santangelo, Annali Geofisica **2**, 503 (1949).
[17] H. Brown, Revs. Modern Phys. **21**, 625 (1949).
[18] V. M. Goldschmidt, *Geochemische Verteilungsgesetze der Elemente, IX* (Videnskapsakademien, Oslo, 1938).
[19] Harrison Brown (private communication, 1951).
[20] A. Holmes, Nature **163**, 453 (1949).

Effects of the Atmosphere on the Penetrating Component of the Cosmic Radiation

E. S. COTTON AND H. O. CURTIS
Air Force Cambridge Research Center, Geophysics Research Division, Cambridge, Massachusetts
(Received September 28, 1951)

MEASUREMENTS made on the penetrating component of cosmic radiation near sea level for a period of 45 days have been utilized for statistical correlation with data from the daily ascents of two nearby radiosonde stations. The measuring equipment consisted of three trays of G-M tubes mounted as a vertical telescope. The telescope was operated under 12 inches of concrete in floors and roof, and a 10-cm Pb absorber was placed between trays 2 and 3. The pulses from the trays were fed into pulse amplifiers and into a coincidence circuit employing pulse shaping prior to the coincidence measurement. Threefold coincidence pulses were applied to a scaler-pen recorder arrangement which recorded the coincidence through a scale of eight. This allowed continuous monitoring of equipment performance.

To account for the fluctuations of the penetrating intensity at the ground, Duperier[1] introduced the temperature of the μ-meson production layer to be used in addition to the atmospheric pressure and the height of the production layer, the effects of which were already known.[2] According to Duperier's model, the probability that a π-meson will decay into a μ-meson is dependent on the density of the region in which the π-meson finds itself. Therefore, the μ-meson intensity at the ground depends on the temperature of the production region.

The telescope was arranged to have approximately spherical symmetry over the solid angle subtended, so no zenith angle correction was applied. The maximum angular aperture of the arrangement was 17°7′ from the vertical. Hourly counting rates were obtained from the observed data, and the mean rate for each day was computed for the 45 days extending from October 9 to November 22, 1950, which were free from electronic failures.

The mean hourly counting rate, the daily average of the temperture and height of the 100-millibar level, and the daily mean barometric pressure obtained from the filed radiosonde observations of the Portland, Maine, and Nantucket, Massachusetts, Weather Bureau Stations were analyzed for statistical correlation. A linear regression equation

$$\delta I_e = \alpha\delta T + \beta\delta B + \gamma\delta H \qquad (1)$$

was hypothesized, where δI_e is the deviation of the counting rate from its mean, δT the deviation of the temperature of the 100-millibar level from its mean, δB the deviation of atmospheric pressure, δH the deviation of the height of the 100-millibar level, and α, β, and γ the appropriate coefficients.

Numerical values of the coefficients α, β, and γ were computed by imposing the requirement that $(\delta I - \delta I_e)^2$ be a minimum, where δI_e is the deviation computed from (1) of the counting rate from its mean, and δI the actual observed deviation of the counting rate. Partial correlation and total correlation coefficients were computed using the methods described by Ezekiel.[3] The square of the partial correlation coefficient, $r_{IT\cdot BH}$, represents that fraction of the variance, or square deviation of the counting rate, which can be accounted for by the temperature of the 100-millibar level with the effects of the other variables theoretically removed. The multiple correlation coefficient, $R_{I\cdot TBH}$, expresses the extent to which all three independent variables succeed in accounting for the variance of the counting rate. The errors in the regression coefficients are the root-mean-square deviations expected in those coefficients. The following values of the quantities above were obtained:

$R_{I\cdot TBH} = 0.84$ $\quad \alpha = -0.023(\pm 0.027)$ percent/°C
$r_{IT\cdot BH} = -0.13$ $\quad \beta = -0.102(\pm 0.011)$ percent/millibar
$r_{IB\cdot TH} = -0.82$ $\quad \gamma = 0.954(\pm 0.264)$ percent/1000 ft
$r_{IH\cdot TB} = -0.49$

The significance of the correlation coefficients can be judged from the basis that, if the correlation coefficient were truly zero, 68 percent of the values obtained from 45 days' random sampling would lie in the range $-0.158 = r = 0.158$, or from the fact that if the correlation were truly 0.84, 95 percent of the values obtained from 45 days' sampling would lie in the range $0.64 = r = 0.87$. The correlations of the counting rate and the pressure and the height are significant, while that with the temperature is not. The mean counting rate was 918 coincidences/hour. The expected root-mean-square deviation in the average of 24 such measurements is 6.2. The residual root-mean-square deviation in the counting rate when the effects of the three meteorological variables are removed is 5.9. Assuming exponential absorption of the radiation, the above value of β leads to a mean absorption thickness of 1160 g/cm^2.

[1] A. Duperier, Proc. Phys. Soc. (London) **A57**, 464 (1945); Proc. Phys. Soc. (London) **A62**, 684 (1949); Nature **167**, 312 (1951).
[2] L. Janossy, *Cosmic Rays* (Oxford University Press, London, 1950), second edition, pp. 192–196.
[3] M. Ezekiel, *Methods of Correlation Analysis* (John Wiley and Sons, Inc., New York, 1949), second edition, Chapters 12 and 18.

Cross Section for the Reaction $Cu^{65}(\gamma, \alpha)Co^{61}$*

R. N. H. HASLAM, L. A. SMITH, AND J. G. V. TAYLOR
Department of Physics, University of Saskatchewan, Saskatoon, Saskatchewan, Canada
(Received September 20, 1951)

THE successful determination of the $Rb^{87}(\gamma, \alpha)Br^{83}$ cross section[1] by obtaining the residual activity of Br^{82} has led the authors to undertake the measurement of the $Cu^{65}(\gamma, \alpha)Co^{61}$ cross section by the same method.

Twenty-gram samples of reagent grade $CuCl_2 \cdot 2H_2O$ were irradiated in the University of Saskatchewan betatron beam for periods ranging from 5 minutes at high energies to 90 minutes at low energies. Tantalum strips, used as monitors, were irradiated along with the copper chloride. The irradiated copper chloride was dissolved and, after adding a cobalt carrier, the copper was removed as CuSCN. The cobalt was then precipitated and obtained for counting as CoS. By using a Co^{60} tracer and chemical spot tests, this separation was found to be better than 99 percent efficient.

The activation curve, Fig. 1, was obtained after applying the usual counting corrections. The high energy part of the curve is dotted to indicate that the energy was not as accurately controlled as it was for the lower part of the curve. No attempt was made to obtain activation points at energies lower than 15 Mev. The

calculated binding energy is 6.1 Mev; however, in order for α-emission to compete with γ-de-excitation one might expect that an additional energy of 5 or 6 Mev would be necessary, putting the apparent threshold at 11 or 12 Mev. A check on the absolute value of the activation point at 22 Mev was made by monitoring a run

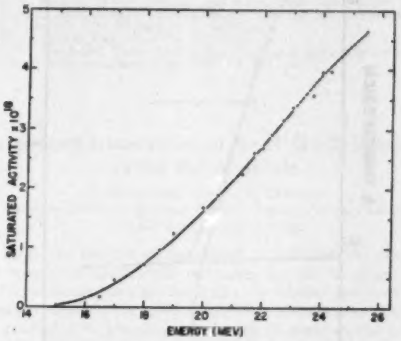

FIG. 1. Activation curve for the reaction $Cu^{63}(\gamma, \alpha)Co^{61}$ showing activations $\times 10^{30}$ per atom of Cu^{63} per 100 roentgens at maximum betatron energy in Mev.

with the $Cu^{63}(\gamma, n)Cu^{62}$ activity arising from the irradiated copper chloride. Agreement within 5 percent was obtained. It was determined that nickel impurity in the irradiated copper chloride could account at most for 0.001 of the Co^{61} activity measured at 23 Mev. Also the possibility of the $Cu^{63}(\gamma, 2p)Co^{61}$ reaction making a substantial contribution to the Co^{61} activity is ruled out by reason of the masses and energies concerned. At 24 Mev the yield

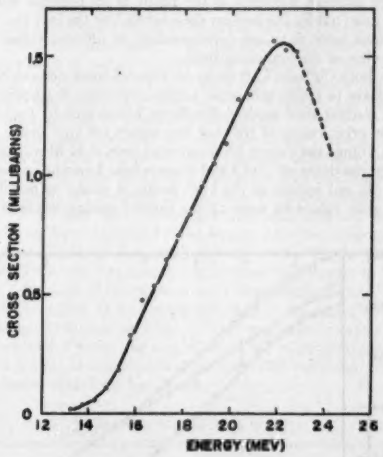

FIG. 2. Cross section for the reaction $Cu^{63}(\gamma, \alpha)Co^{61}$.

is 2.3×10^4 alpha-particles per mole of Cu^{63} per roentgen, which is in satisfactory agreement with the value 4×10^4 alpha-particles per mole of natural copper per roentgen, obtained by Byerly and Stevens.[3] Their experiment did not allow differentiation between alpha-particles produced in (γ, α) reactions and in $(\gamma, \alpha n)$ or

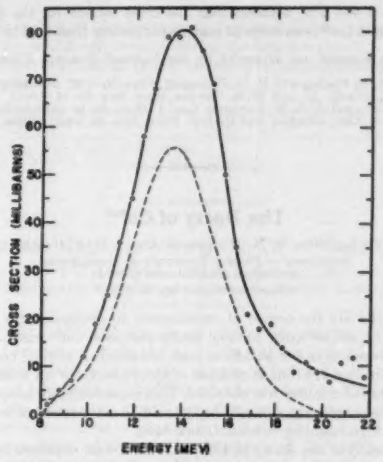

FIG. 3. Minimum cross section for the reaction $Ta^{181}(\gamma, n)Ta^{180}$ (uncorrected for decay scheme). The dotted curve shows the previous determination (see reference 4).

other similar reactions producing α-particles, which, however, would go undetected in our experiment.

The cross section, Fig. 2, was derived from the activation curve using the "photon difference" method.[3] This cross section has a maximum value of 1.5 millibarns at 22 Mev, and the integrated cross section to the peak is 6.2×10^{-3} Mev-barns. The falling off of the cross section above 22 Mev may be the result of the cascade competition of the $(\gamma, \alpha n)$ process.

Before obtaining the above activation curve, the activation curve for $Ta^{181}(\gamma, n)Ta^{180}$ was redetermined since Ta was used to monitor the dosage rate. As this curve was somewhat different from that previously reported,[4] the modified $Ta^{181}(\gamma, n)Ta^{180}$ and $Rb^{87}(\gamma, \alpha)Br^{83}$ cross section curves are reproduced in Fig. 3 and Fig. 4 (the latter reaction was also monitored by Ta). Data concerning these two curves have already been reported.[5] Comparison

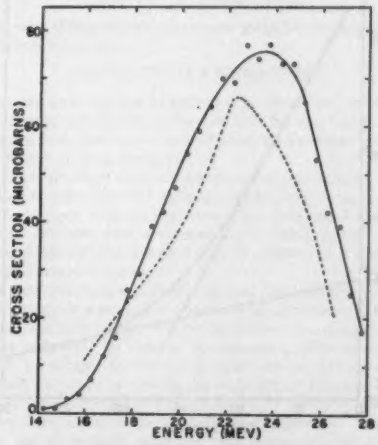

FIG. 4. Cross section for the reaction $Rb^{87}(\gamma, \alpha)Br^{83}$. The dotted line shows the previous determination (see reference 1).

of Fig. 2 and Fig. 4 shows that the cross section for the (γ, α) reaction in Cu^{63} is an order of magnitude greater than that in Rb^{87}.

* This research was supported by the National Research Council of Canada.

[1] R. N. H. Haslam and H. M. Skarsgard, Phys. Rev. 81, 479 (1951).
[2] P. R. Byerly, Jr., and W. E. Stevens, Phys. Rev. 83, 54 (1951).
[3] L. Katz and A. G. W. Cameron, Can. J. Phys. (to be published).
[4] Johns, Katz, Douglas, and Haslam, Phys. Rev. 80, 1062 (1950).

The Decay of Co^{61}*

L. A. Smith, R. N. H. Haslam, and J. G. V. Taylor
Department of Physics, University of Saskatchewan, Saskatoon, Saskatchewan, Canada
(Received September 20, 1951)

DURING the course of experiments to determine the $Cu^{65}(\gamma, \alpha)Co^{61}$ cross section[1] decay curves of Co^{61} which could be followed over ten half-lives were obtained. A typical curve is shown in Fig. 1. From an analysis of eleven such curves a half-life of 99.0 ± 0.3 minutes was obtained. This is considerably lower than previously reported values[2,3] but should be more accurate because of the high counting rates obtained here.

To analyze the decay of Co^{61}, activities were obtained by two reactions, $Cu^{65}(\gamma, \alpha)Co^{61}$ and $Ni^{62}(\gamma, p)Co^{61}$. Both methods gave the same results from the analyses of the absorption curves in aluminum. An aluminum absorption curve is shown in Fig. 2 and the corresponding analysis by the nth power method[4-6] is given in Fig. 3.

It is obvious that two β's are present. The average of two determinations of the maximum beta-energies by the foregoing method showed (55 ± 10) percent of the disintegrations with a maximum energy of 1.42 ± 0.02 Mev and (45 ± 10) percent with a maximum energy of 1.00 ± 0.02 Mev. To search for a possible gamma-ray the Co^{61} was counted with a scintillation counter. Alternately the sample was counted with no filter and with one of two filters, each thick enough to absorb all the betas, (860 and 1340 mg/cm^2). The count through the thick filters decayed with the same half-life as without a filter so a Co^{61} gamma-ray was indicated. A rough lead absorption curve obtained during the same experiment indicated a gamma-energy of about 0.5 Mev. During the chemical separation for absorption experiments, holdback carriers were used to reduce the amount of copper contamination as much as possible.

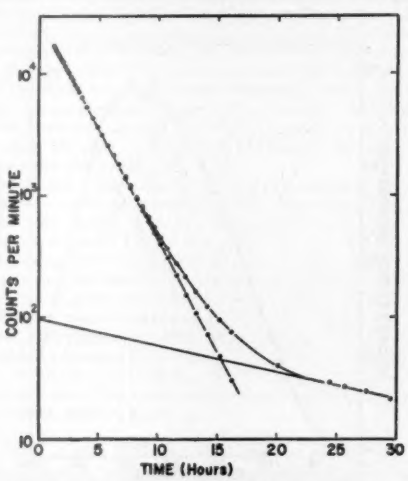

FIG. 1. Decay curve of 99.0-minute Co^{61}. The background activity is 12.9-hour Cu^{64}.

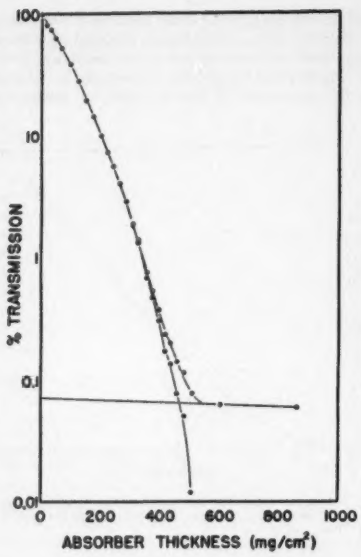

FIG. 2. Aluminum absorption curve for Co^{61}.

The simplest decay scheme on the basis of the above results is that the 1.42-Mev β goes from the ground state of Co^{61} to that of Ni^{61}, and the 1.00-Mev β leads to an excited state of Ni^{61} which decays to ground emitting a 0.42-Mev gamma-ray. The possibility that the complex spectrum is the result of an isomeric state of Co^{61} is ruled out by the nuclear shell model,[7] by the fact that both transitions have ft values corresponding to allowed transitions, and in view of the branching ratio.

Since both Co^{61} and Cu^{61} decay by allowed transitions to Ni^{61}, it is necessary to assign spin orbit values other than those predicted by the nuclear shell model.[7] Nordheim has suggested $j = 5/2$ for the spin orbit values of Ni^{61} but this makes the Cu^{61} decay l forbidden.[8] Since the energy level reported here, 0.42 Mev, does not occur in the decay of Cu^{61},[9] and those which do occur in the Cu^{61} decay did not appear in the Co^{61} decay, it might be possible to assign spin values to some of the excited energy levels of Ni^{61}.

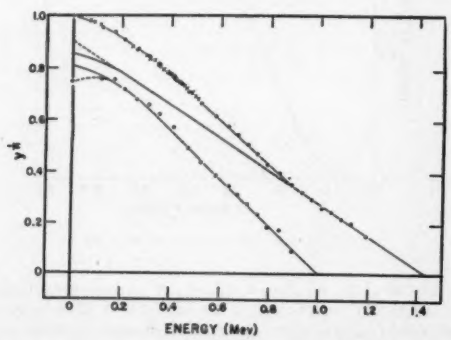

FIG. 3. nth power plot for Co^{61} showing β end point energies of 1.43 Mev ($n = 4.72$) and 1.00 Mev ($n = 3.26$).

However, this must await the clearing up of the values to be assigned the ground states of Co^{61}, Ni^{61}, and Cu^{61}.

* This work was supported in part by the National Research Council of Canada.
[1] Haslam, Smith, and Taylor, Phys. Rev. **84**, 840 (1951).
[2] Parmley, Moyer, and Lilly, Phys. Rev. **75**, 619 (1949).
[3] Miller, Thompson, and Cunningham, Phys. Rev. **74**, 347 (1948).
[4] Katz, Penfold, Moody, Haslam, and Johns, Phys. Rev. **77**, 289 (1950).
[5] Haslam, Katz, Moody, and Skarsgard, Phys. Rev. **80**, 318 (1950).
[6] L. Katz and A. S. Penfold (to be published).
[7] M. G. Mayer, Phys. Rev. **78**, 16 (1950).
[8] L. W. Nordheim, *Tables for β-Decay Systematics* (privately circulated).
[9] Owen, Cook, and Owen, Phys. Rev. **78**, 686 (1950).

Laboratory Observation of the $A^2\Pi - X^2\Sigma$ Bands of the N_2^+ Molecule

F. W. Dalby* and A. E. Douglas
Division of Physics, National Research Council, Ottawa, Canada
(Received September 25, 1951)

BOTH the electron configuration[1] of N_2^+ and the observed spectra of isoelectronic molecules lead one to believe that the N_2^+ molecule has a low-lying $^2\Pi$ state. Meinel[2] has observed a system of bands in the infrared spectrum of the aurora which he has attributed to transitions from this $^2\Pi$ state to the ground state. Up until now, however, no such bands have been observed in laboratory spectra. Recently we have succeeded in exciting these bands in a discharge tube.

A mixture of helium and nitrogen was passed through a hollow cathode discharge tube and the spectrum of the discharge photographed on the first order of a twenty-one foot concave grating. When the pressure of the helium in the discharge tube was high and the quantity of nitrogen very small, the first positive bands of nitrogen appeared only weakly while the ultraviolet bands of N_2^+ were strong. Under these conditions the infrared spectrum of the discharge has been photographed on *N* and *M* plates with exposure times of several hours.

Besides the well-known first positive bands of nitrogen, the infrared spectrum of the discharge tube shows a system of bands degraded to the red. Each of these bands has two prominent heads and others less prominent. The positions of the strong heads, together with a possible vibrational numbering, are shown in Table I. On our plates the (4,2) (3,1) and (2,0) bands are strong and free from overlapping lines, while the (2,1) and (2,0) bands are very weak and the (3,0) band is overlapped.

The agreement between our wavelengths and those of Meinel as shown in Table I leaves no doubt that the bands observed here are the same as those observed in the aurora. The consistent difference of about 3A between the two sets of measurements is the result of the fact that Meinel has measured intensity maxima whereas we have measured band heads. Also the assignment of these bands to the N_2^+ molecule appears certain for the following reasons. First, the structure of the bands is very similar to that of the $^2\Pi - ^2\Sigma$ bands of the isoelectronic CN molecule. Second, within the fine structure of the bands the lines of the series show the alternation of intensities which is to be expected in bands of the N_2^+ molecule. Finally, the magnitude of the vibrational quanta of the lower state of these bands agrees with that calculated from the well-known ultraviolet N_2^+ bands.

Table I. Infrared bands of N_2^+.

Vibrational numbering	Wavelength, A Authors	Meinel	Vibrational numbering	Wavelength, A Authors	Meinel
1,0	9208.00		2,0	7874.63	7879.6
	9147.31(?)			7825.72	7828.2
2,1	9502.27		3,1	8105.31	8107.0
	9428.90(?)			8053.63	8056.8
3,0	6890.49	6892.2	4,2	8345.25	8349.2
				8293.41	8297.6

An analysis of the fine structure of these bands is in progress and the results will be published in the near future.

We are indebted to Dr. G. Herzberg for helpful discussions of this problem.

* Now at the Department of Physics, University of British Columbia, Vancouver, British Columbia.
[1] G. Herzberg, *Spectra of Diatomic Molecules* (D. Van Nostrand and Company, Inc., New York, 1950), p. 345.
[2] A. B. Meinel, Astrophys. J. 113, 583 (1951).

On the Magnetic Moment of $Te^{123,125}$ and Si^{29}*

S. S. Dharmatti and H. E. Weaver, Jr.
Department of Physics, Stanford University, Stanford, California
(Received October 1, 1951)

NUCLEAR induction signals of $Te^{123,125}$ were detected in a solution of TeO_2 (3.1 molar) in HCl and chemically pure tellurium metal in aqua regia. Signals of Te^{125} with a line width of about 1/10 gauss (probably in part determined by the magnetic field inhomogeneity) were observed in both the above solutions without the addition of paramagnetic ions.

A comparison of the resonant frequency of Te^{125} with that of Na^{23} gives the result

$$\nu(Te^{125})/\nu(Na^{23}) = 1.19457 \pm 0.00004. \quad (1)$$

With the known magnetic moment of Na^{23} and the fact that the spin of the tellurium isotopes is $\frac{1}{2}$,[1,2] the sign and value of the magnetic moment of Te^{125} were found to be

$$\mu(Te^{125}) = -0.88235 \pm 0.00004. \quad (2)$$

This value agrees well with the spectroscopic data in the literature.[2]

The abundance of Te^{123} being only 0.85 percent, one would expect the signal amplitude of the isotope to be about $\frac{1}{7}$ that of Te^{125}, whose abundance is 7.0 percent. If was therefore necessary to modify the present spectrometer[4] with the introduction of an amplifier of higher gain and lower noise figure.[5] This apparatus permitted the detection of Te^{123} signals with a signal-to-noise ratio of about seven. Thus a comparison of the resonant frequency with that of Na^{23} yielded the results[1]

$$\nu(Te^{123})/\nu(Na^{23}) = 0.99085 \pm 0.00003 \quad (3)$$

and

$$\mu(Te^{123}) = -0.73188 \pm 0.00004.[3] \quad (4)$$

The ratio of the magnetic moments of the two isotopes is therefore calculated to be

$$\mu(Te^{125})/\mu(Te^{123}) = 1.20560 \pm 0.00007, \quad (5)$$

which is in good agreement with that of Mack and Arroe.[6] The ratio of signal amplitudes of the two isotopes was found to be in agreement with the known ratio of abundances within an experimental error of about 5 percent.

It is known that there exists monatomic tellurium[7] in acid solutions and further, that these atoms are likely to be paramagnetic in analogy with oxygen. It was for this reason that paramagnetic catalysts were not added to the solutions, and the fact that good signals were detected may be ascribed to the action of these paramagnetic atoms.

The first tellurium signals of a natural line width of one gauss were observed in a sample of powdered tellurium metal. The fact that one deals here with nuclear induction in a semiconductor may be of interest in view of the resonance shifts observed by Knight[8] in metals; no observable shift was found between the resonance frequency of Te^{125} in the metal and in solution. In spite of its low conductivity it was necessary to pulverize the metal in order to reduce losses caused by eddy currents.

The use of metallic tellurium was encouraged by previous experiments in which signals of Si^{29} were found in powdered silicon metal. Signals were also found in a solution of 2.5 molar SiO_2 in

NaOH and 0.5 molar $K_3Fe(CN)_6$ and further in different types of glasses: *viz.*, cobalt, lead, uranium, vicor, soft, and Pyrex glasses. This confirms the suggestion by Hatton, Rollin, and Seymour[9] that these latter signals must indeed be attributed to Si^{29}. A comparison of the resonance frequency of Si^{29} signal in cobalt glass with that of deuterium in D_2O gave

$$\nu(Si^{29})/\nu(H^2) = 1.29410 \pm 0.00007. \quad (6)$$

Assuming the spin of Si^{29} to be $\frac{1}{2}$, the sign and value of the magnetic moment were determined to be

$$\mu(Si^{29}) = -0.55492 \pm 0.00004. \quad (7)$$

Experiments are at present under way to determine the spin of Si^{29}. If one accepts the shell model of Mayer,[10] one is led to the conclusion that since the sign of the moment of Si^{29} was found to be negative the spin can only be 1/2 or 5/2 and, inasmuch as the latter value is quite improbable, it is likely that the above assumption about the spin will be justified.

We would like to express our appreciation to Professor Felix Bloch for his continued interest in our work.

* Assisted by the joint programs of the ONR and AEC.

[1] F. Bitter, Phys. Rev. **75**, 1326 (1949).
[2] C. R. Fowler, Phys. Rev. **76**, 571 (1949); Phys. Rev. **78**, 744 (1950); J. E. Mack and O. H. Arroe, Phys. Rev. **76**, 1002 (1949).
[3] J. S. Ross and K. Murakawa, Phys. Rev. **83**, 229 (1951).
[4] W. G. Proctor, Phys. Rev. **75**, 522 (1949).
[5] Details to be published.
[6] J. E. Mack and O. H. Arroe, reference 2. See also reference 3.
[7] *Textbook of Inorganic Chemistry*, edited by J. Newton Friend (Charles Griffin and Company, Ltd., London, 1931), Vol. VII, Part 2, p. 365.
[8] W. D. Knight, Phys. Rev. **76**, 1259 (1949); Phys. Rev. **77**, 852 (1950).
[9] Hatton, Rollin, and Seymour, Phys. Rev. **83**, 672 (1951).
[10] M. G. Mayer, Phys. Rev. **78**, 16 (1950).

Line Breadths in the 5-mm Microwave Absorption of Oxygen*

B. V. Gokhale and M. W. P. Strandberg
Research Laboratory of Electronics, Massachusetts Institute of Technology, Cambridge, Massachusetts
(Received September 27, 1951)

DIRECT measurement of line breadths in the microwave absorption spectrum of oxygen at $\lambda = 5$ mm has been reported by Burkhalter *et al.*[1] and by Anderson *et al.*[2] From these reports it may be seen that the agreement between the two investigations is not entirely satisfactory. Hence it seems desirable to report measurements that we have made.[3]

The measurements were made by means of a Zeeman modulation spectrograph using a modulation frequency of 26.5 cps. The direction of the Zeeman field was chosen to be at right angles to the direction of the magnetic field vector in the radiation. This was accomplished by using two long magnets in the shape of hollow cylinders of rectangular cross section, each having a slot along its length for insertion of the wave-guide absorption cell. The lines of flux were all parallel to a plane at right angles to the length of the cylinder. The direction of the field in the gap was parallel to the electric vector of the radiation in the wave guide, which was propagating in its lowest mode.

The strength of the field was varied between zero and about 50 gauss to produce a square wave time variation. The strength of the field was sufficient to "modulate away" completely the absorption lines at the pressures used (0.75 mm to 6 mm of mercury) during the "field-on" half of the cycle. With the direction of the field as described above, only the transitions $\Delta M = \pm 1$ (σ transitions) are responsible for the absorption. This arrangement may be seen to give a stronger signal than any other field direction.

Five-mm microwave power was generated by a crystal doubler driven by a 1-cm klystron. The latter was locked to the resonant frequency of a K-band wave meter by means of the Pound circuit. The wave meter was slowly tuned to change the frequency. A second 1-cm klystron was made to follow the signal generator at a frequency difference of 12 Mc/sec to provide superheterodyne detection. The shape of the line was ultimately traced on an Esterline-Angus recorder.

TABLE I. Observed line-breadth parameters.

Transition	Frequency, in Mc/sec	Half-breadth at half-intensity, in cm^{-1}/atmos
$K_+ = 1$	56,265.2 ±0.5	0.035 ±0.007
$K_+ = 3$	58,446.3 ±0.4	0.028 ±0.003
$K_+ = 13$	62,412.9 ±0.8	0.025 ±0.003
$K_- = 3$	62,486.2 ±0.4	0.037 ±0.003
$K_- = 7$	59,164.2 ±0.2	0.028 ±0.005
$K_- = 9$	58,324.9 ±0.3	0.021 ±0.003
$K_- = 11$	57,612.3 ±0.4	0.034 ±0.006
$K_- = 15$	56,364.2 ±0.5	0.048 ±0.003

Observations were usually made at four different pressures (about 6, 3, 1.5, 0.75 mm Hg) and the observed widths plotted against the pressure. A straight line was then drawn through these points so as to give the least-square deviation. The slope of this line gave the line-breadth parameter. This straight line shows a nonzero line breadth at zero pressure, presumably caused by residual field in the gap, which could not be balanced out completely. This residual breadth was of little concern since line breadth varied by a factor of about 3 over the range of pressures used in the investigation. Table I gives the results and their probable errors.

These results cannot be immediately compared with those given in references 1 and 2 since they do not contain any limits of error.

* This work has been supported in part by the Signal Corps, the Air Materiel Command, and the ONR.
[1] Burkhalter, Anderson, Smith, and Gordy, Phys. Rev. **79**, 651 (1950).
[2] Anderson, Smith, and Gordy, Phys. Rev. **82**, 264 (1951).
[3] B. V. Gokhale, PhD. Thesis (M.I.T. Physics Department, January, 1951). B. V. Gokhale, and M. W. P. Strandberg, Phys. Rev. **82**, 327 (1951).

The Diffusion of Metastable Neon Atoms in Mixtures of Helium and Neon*

F. A. Grant
Department of Physics, University of Maryland, College Park, Maryland
(Received September 24, 1951)

A SHORT time after the cessation of excitation, the $^3P_2$ metastable level of neon decays exponentially, and the mean life T_m is defined by the equation

$$N = N_0 \exp(-t/T_m),$$

in which N is the number of metastable atoms per cc.

T_m can be expressed as a function of the pressure by the equation:[1]

$$1/T_m = (B/p) + Z,$$

in which

$$B = [(5.81/c^3) + (\pi^2/L^2)]Dp,$$

where p is the pressure in mm of mercury, c is the discharge tube radius in cm, L is the discharge tube length in cm, and D is the diffusion coefficient. The term Z is not proportional to the pressure, but the experimental results are consistent with an equation of the type

$$1/T_m = (B/p) + Cp^n,$$

in which n is 0.7 for pure neon,[2] and approaches 0.5 as the helium-neon ratio increases.

If p/T_m is plotted as a function of Cp^{n+1}, a straight line is obtained; B is the intercept on the p/T_m axis, and C is the slope.

In pure neon the B/p term represents the rate of diffusion to the walls of the energy of excitation of the metastable atoms. This process is complicated by the phenomenon of the imprisonment of resonance radiation. To reduce the relative importance of this effect, helium gas was introduced in the discharge tube. The energy levels of helium are all above the energy of excitation of the $^3P_2$ metastable neon level.

TABLE I. Coefficients B and C for various helium-neon ratios. The helium-neon ratio is that of their partial pressures.

Helium/neon	B	C
0	66±10	135±20
0.75	107±10	250±30
2.0	112±10	350±40
2.5	132±15	430±40
2.6	121±10	390±40
2.6	143±10	390±40
3.6	121±20	440±40
3.65	139±15	440±40
4.5	135±15	410±40
7.15	152±15	400±40
7.15	128±15	470±40

Using previously described techniques,[3] and a discharge tube 6.7 cm in diameter and 150 cm long, the results given in Table I are obtained.

When the helium-neon ratio exceeds 2:1, $B=135$ within the limits of the experimental error. Expressing these results in terms of diffusion coefficients: Diffusion of metastable neon in neon, $Dp=127$. Diffusion of metastable neon in helium, $Dp=260$.

* Supported by the Bureau of Ships.
[1] Mitchell, Allan, and Zemansky, *Resonance Radiation and Excited Atoms* (University Press, Cambridge, 1934).
[2] D. J. Eckl and J. M. Anderson, University of Toronto, Toronto, Canada. (Confirmed by private communication.)
[3] F. A. Grant, Can. J. Research **A28**, 339 (1950).

Theory of Nuclear Photoprocesses*

R. G. SACHS
University of Wisconsin, Madison, Wisconsin
(Received September 27, 1951)

IN a recent paper[1] on deuteron photodisintegration, Avak'yants has predicted that the electrical dipole cross section at 40 or 50 Mev is greatly increased over the usual theoretical value as a result of exchange currents. His work is based on the phenomenological theory[2] of exchange currents which has been shown[3] to lead to no effect at all on electric multipole transitions. Although a complete proof that his result is incorrect is contained in reference 3, the treatment there is so formal that some elucidation of the matter seems desirable.

Avak'yants gives for the interaction with the radiation in dipole approximation:[4]

$$H'=-(ie/2c)\omega_{mn}(\mathbf{r}\cdot\mathbf{u})+(ie/\hbar c)J(\mathbf{r})(\mathbf{r}\cdot\mathbf{u})P, \qquad (1)$$

where $\mathbf{u}$ is the unit polarization vector, $J(\mathbf{r})$ is the shape function for the exchange potential, P is the exchange operator, and $\hbar\omega_{mn}$ is the energy of the transition. The second term represents the exchange effect. The first term presumably is obtained from the usual interaction with the electromagnetic field, $-(e/2\mathrm{Mc})(\mathbf{p}\cdot\mathbf{u})$, where $\mathbf{p}$ is the relative momentum and M the reduced mass, by means of the substitution

$$\mathbf{p}=M\dot{\mathbf{r}} \qquad (2)$$

which implies

$$\mathbf{p}_{mn}/M=i\omega_{mn}\mathbf{r}_{mn}.$$

The error is the assumption that Eq. (2) is valid in the presence of exchange forces. The velocity operator should be calculated by means of the commutator with the hamiltonian,

$$\dot{\mathbf{r}}=(1/\hbar)[H,\mathbf{r}],$$

where H is the sum of kinetic energy T and the exchange potential JP. Now

$$(i/\hbar)[T,\mathbf{r}]=\mathbf{p}/M$$

as usual, but the exchange operator does not commute with $\mathbf{r}$:

$$[P,\mathbf{r}]=-2\mathbf{r}P.$$

Thus

$$\dot{\mathbf{r}}=(\mathbf{p}/M)-(2i/\hbar)\mathbf{r}JP. \qquad (3)$$

The correct form for the interaction is then

$$H'=-(e/2\mathrm{Mc})(\mathbf{p}\cdot\mathbf{u})+(ie/\hbar c)(\mathbf{r}\cdot\mathbf{u})JP=-(e/2c)(\dot{\mathbf{r}}\cdot\mathbf{u}) \qquad (4)$$

in place of Eq. (1). Thus calculation with the ordinary electric dipole moment operator is correct, as originally suggested by Siegert.[5] The cancellation of the exchange term which occurs in Eq. (4) is a direct consequence of the gauge invariance of the theory, as is shown in reference 3.

The article of Avak'yants was translated from the Russian by Miss Fay Ajzenberg.

* Work supported in part by the Wisconsin Alumni Research Foundation and in part by the AEC.
[1] G. M. Avak'yants, J. Exptl. and Theoret. Phys. (U.S.S.R.) **20**, 669, 944 (1950).
[2] R. G. Sachs, Phys. Rev. **74**, 433 (1948).
[3] R. G. Sachs and N. Austern, Phys. Rev. **81**, 705 (1951).
[4] A small error has been corrected by the introduction of the factor i in the second term.
[5] A. J. F. Siegert, Phys. Rev. **52**, 787 (1937).

The Production of Light Nuclei by High Energy Proton Bombardment of Medium Weight Elements*

D. H. GREENBERG AND J. M. MILLER
Chemistry Department, Columbia University, New York, New York
(Received September 11, 1951)

SEVERAL recent papers[1-3] have reported the production of light nuclei such as Be^7, Li^8, Na^{24}, and Cl^{38} by bombardment of medium weight elements with protons of energies up to 340 Mev. On the basis of excitation functions it was concluded that these nuclei may be emitted as a consequence of an inelastic interaction of the incident proton with the target nucleus. Investigations pursued concurrently at Columbia University with 370-Mev protons are in general consistent with these results and have yielded additional information concerning the processes involved in high energy nuclear reactions with medium weight elements. We therefore present the following preliminary report on some of the data obtained in these experiments.

Spectroscopically analyzed copper targets (interfering impurities <0.01 percent) 2.5 to 5.0 Mev thick were bombarded in the circulating beam of the Nevis Cyclotron with 370-Mev protons. After irradiation the target was dissolved, carriers were added, and the elements of interest were chemically isolated. The isolated fractions were counted with a thin mica end-window counter. The usual approximate corrections for the effects attendant upon such measurements were made and absolute cross sections estimated by a comparison of the activities isolated from the copper target with the Na^{24} and/or C^{11} activities produced with known cross section in aluminum[4] and/or polyethylene[5] beam monitors, respectively.[6]

Cross sections, which are estimated to be reliable to about a factor of 2, for the production of the listed isotopes by 370-Mev protons on copper are given in Table I. There are also presented some of the data obtained by other workers with lower energy

TABLE I. Cross section in barns for the production of the listed nuclei in high energy nuclear reactions.

	1 Copper 370-Mev p	2[a,b] Copper 335–340-Mev p	3[b] Copper 200-Mev p	4[c] Cobalt 370-Mev p
Be^7	···	5×10^{-4}	···	···
C^{11}	3×10^{-4}	···	···	2×10^{-3}
F^{18}	3×10^{-5}	···	···	···
Na^{24}	3×10^{-5}	3×10^{-5}	3×10^{-5}	4×10^{-5}
Cl^{38}	···	4×10^{-5}	3×10^{-5}	···
K^{42}	5×10^{-5}	···	···	5×10^{-4}

[a] See reference 1.
[b] See reference 2.
[c] See reference 7.

protons on copper and a few of the results that have been determined with 370-Mev protons on cobalt.[7]

Several interesting aspects of high energy reactions can be seen from the information in Table I.

(1) From columns 1, 2, and 3 it can be seen that the cross section for the production of Na^{24}, which is an increasing function of energy up to 340 Mev,[2] appears to approach the now familiar leveling-off characteristic of high energy reactions.[8]

(2) A comparison of the cross sections for the formation of C^{11} and Na^{24} given in columns 1 and 4 indicates essentially equal probability for forming these light products from the inelastic interaction of 370-Mev protons with nuclei of mass number 59, 63, or 65; whereas the cross section for the production of K^{42} shows a significant decrease in going from mass number 59 to 63 and 65. This latter observation is to be qualitatively expected if K^{42} is formed by a spallation process. On the other hand, the equality of the C^{11} and Na^{24} cross sections from the two different targets suggest that these nuclei do not result from spallation but perhaps are directly emitted from an excited medium weight nucleus. In this connection it should be noted from the data in column 1 that the formation cross sections of K^{42} and C^{11} from copper are essentially the same. Therefore the K^{42} may predominantly be a "fission" product from copper and mainly a spallation product from cobalt.

(3) The information in columns 1 and 2 indicates a rather flat valley extending from mass number 11 to at least 42 on a plot of cross section *versus* mass number. The large increase in information cross section[1] of Be^{7} over that of C^{11} and the difference in K^{42} cross section from Cu and Co suggests that this valley is enclosed by rather steep walls. The wall at the upper end may represent the transition between predominantly "fission products" and predominantly "spallation products"; while that on the lower end is consistent with the theory of particle evaporation[9] and probably will be consistent also with any treatment designed to explain the emission of light nuclei with abnormally high kinetic energy.[10] There is some uncertainty, however, in any argument based on this kind of data since the isotopes examined may not be representative of the mass number yield with protons of these energies. Indeed, other work in this laboratory[7] with protons on cobalt has shown that there may be a variation by a factor of a hundred or more among the yields of products with a given mass number and different atomic numbers; however, the particular species investigated should all be about equally reliable as indicators of the yield of their particular mass number.

A more detailed report on these experiments will be published subsequently.

The authors wish to express their appreciation to the operating staff of the Columbia University Cyclotron at Nevis.

* Work performed under the auspices of the AEC.

[1] L. Marquez and I. Perlman, Phys. Rev. **81**, 952 (1951).
[2] R. Batzel and G. Seaborg, Phys. Rev. **82**, 607 (1951).
[3] S. C. Wright, Phys. Rev. **79**, 838 (1950).
[4] P. Stevenson (personal communication of unpublished work).
[5] Aamodt, Peterson, and Phillips, University California Radiation Laboratory—526 (1949).
[6] The cross sections at 370 Mev were taken to be 10 millibarns for $Al^{27}(p, 3pn)Na^{24}$ and 36 millibarns for $C^{12}(p, pn)C^{11}$.
[7] E. Belmont and J. M. Miller (to be published).
[8] Bartell, Helmholz, Softky, and Stewart, Phys. Rev. **80**, 1006 (1950).
[9] K. J. LeCouteur, Proc. Phys. Soc. (London) **A63**, 259 (1950).
[10] S. O. C. Sörenson, Phil. Mag. (7) **42**, 188 (1950).

Diffusive Separation in the Upper Atmosphere

L. M. Jones, L. T. Loh, H. W. Neill, M. H. Nichols, and E. A. Wenzel
Department of Aeronautical Engineering, University of Michigan, Ann Arbor, Michigan

(Received August 24, 1951)

ANALYSES of new atmospheric samples taken in the altitude range 64 to 72 km show a marked diffusive separation of the component gases. These samples were obtained from Aerobee rocket[1] SC-17 flown at White Sands Proving Grounds, New Mexico, at 11:52 A.M., December 19, 1950, using an improved sampling technique developed at the Engineering Research Institute of the University of Michigan under a contract with the U. S. Army Signal Corps. The gas analyses were made by Professor Paneth and co-workers[2] at Durham University, England, using an improved version of their charcoal adsorption method.[3] This is the first time that diffusive separation has been detected to an extent substantially greater than experimental error.

Several improvements[4] in the sampling technique over that used for previous samples[3,5,6] were incorporated. Straight one-inch diameter copper tubes were used for the intakes to the three evacuated steel sample bottles. The forward cone of the rocket was ejected just before sampling to expose the intake tubes to the air stream at the forwardmost part of the missile. The tubes were opened by motor driven knives and sealed five seconds later by cold-weld sealers.[7] The sampling assembly, separated from the rocket, was lowered with little damage by parachute. After recovery the bottles were shipped directly to Professor Paneth for analysis. The results are given in Table I which also includes the amounts of each sample and the opening and closing altitudes.

It is seen that bottle B-9 shows a much larger sample than the other two bottles which sampled at lower altitudes. It has been found from a number of flights that the amount of sample is roughly a simple exponential of the sampling altitude. On this basis, using the amount of sample in bottles B-6 and B-8, an extrapolation on a semilog plot gives 0.107 cc NTP as the expected sample in B-9. If it is assumed that the increase in sample B-9 was the result of a leak which admitted four parts of surface air to one part of air characteristic of the altitude of sampling, one gets the row in the table "Corrected for 400 percent contamination." Although the measured separations for SC-17 do not agree closely with a simple exponential height distribution, the relative concentrations of the component gases are qualitatively correct for diffusive separation: helium and neon increasing relative to nitrogen and argon decreasing.

TABLE I. Results from charcoal adsorption analysis.[a]

Sample bottle	Glass vial	Rocket number	Altitude km, MSL	Date of sampling	Amt. of sample cc, ntp	Analysis He	Analysis Ne	Analysis A
B-9		SC-17	69.6–71.7	12–19–1950	0.535	1.49	1.07	0.95
B-9		corrected for 400 percent contamination			0.107	3.45	1.35	0.75
B-8		SC-17	67.0–69.6	12–19–1950	0.185	2.02	1.18	0.89
B-6		SC-17	64.3–67.0	12–19–1950	0.388	1.44	1.08	0.93
			Previous samples					
32	1B	V-2#27	61.1–72.0	10– 9–1947		0.93	1.00	1.01
33	1A	V-2#27	61.1–72.0	10– 9–1947		1.00[m*]	1.05[m*]	
45	12A	V-2#44	60.8–69.5	11–18–1948		1.04[m*]	1.07[m*]	
35	2B	V-2#35	55.4–65.5	5–27–1948		1.01	1.00	1.00
35	2A	V-2#35	55.4–65.5	5–27–1948		0.97[m*]	0.99[m*]	
37	3B	V-2#35	55.4–65.5	5–27–1948		0.98	0.99	1.00
37	3A	V-2#35	55.4–65.5	5–27–1948		0.98[m*]	0.98[m*]	
63[b]	19D	SC-4	54.7–58.3	7–21–1949		1.01	1.45[a]	1.01
63[b]	19A	SC-4	54.7–58.3	7–21–1949		1.01[m*]	1.07[m*]	
61[b]	15B	SC-2	53.6–57.7	6– 2–1949		1.00	1.00	1.01
61[b]	15A	SC-2	52.6–57.7	6– 2–1949		1.00[m*]	1.02[m*]	
42[b]	5A	V-2#40	49.0–59.8	7–26–1948		1.05[m*]	1.06[m*]	
77	25D	SC-3	50.4–53.3	12– 6–1949		0.98	1.00	1.00
60	16A	SC-2	49.6–53.6	6– 2–1949		0.96	0.98	1.00
68	21A	SC-5	42.0–45.0	9–20–1949		1.01[m]	1.01[m]	
74	28A	SC-7	41.4–44.9	12– 6–1949		1.00[m]	1.02[m]	

[a] Within the two groups the arrangement is in order of decreasing mean altitude of sampling. The helium, neon, and argon contents are expressed as: (volume of gas, relative to nitrogen, in sample)/(volume of gas, relative to nitrogen, in ground-level air). The ratios marked with the superscript *m* were obtained by the authors and those with *m** were obtained by the authors before the apparatus and techniques were improved to the present state. The results with no superscript were obtained by Paneth *et al.* (see references 2 and 3). The label SC refers to Aerobee rockets. The vial numbers refer to subdivisions of the same sample. All analytical results are quoted to two places of decimals although the errors calculated from several runs on the same vial are often below one-half percent.

[b] The results for these samples are not confirmed by McQueen's measurements on the isotopes of nitrogen (see references 9 and 5). Subsequent measurements on the same isotopes from sample bottles 61 and 42 by both the analytical and Nier isotope ratio instruments at the Consolidated Engineering Corporation of Pasadena, California, are in disagreement with McQueen, and, within the currently estimated experimental error, show no change from surface air.

[c] Unreliable because of contamination by H_2, confirmed by mass spectrometry.

Previous analyses by the charcoal adsorption method are also given in Table I and indicate no diffusive separation even in the case of bottles 32 and 45 which sampled in the vicinity of 65 km. These two and other V-2 samples, because of the location of the bottles in the rocket, were subject to possible contamination by rocket-borne ground air. On the other hand Aerobee instrumentations, particularly that of SC-17, were designed to prevent such contamination. A radioactive tracer technique used on one Aerobee showed contamination by trapped air to be less than 0.002 $\pm$0.002 percent, and it is thought that the other Aerobee samples also were not contaminated.

The diffusive separation found in samples from SC-17 occurred in the 64- to 72-km range. According to recent measurements[6] this is a region of rapidly decreasing temperature. On this basis it would seem that this region would be characterized by considerable turbulence and mixing rather than by the quiescence necessary for the amount of diffusion separation measured in the SC-17 samples. This may indicate that for sufficient lengths of time there is a considerable departure from the temperature pattern reported over White Sands, New Mexico, or that air is moved in without mixing from a different latitude or a higher altitude where the temperature increases with increasing height.

Further measurements at 70 km and an extension of the methods to permit sampling and analysis of 100-km air are planned. A complete description of the apparatus and methods used to obtain the samples will soon be published. We are indebted to Professor Paneth for analyzing the samples and to the Signal Corps Engineering Laboratories for cooperation and financial support.

[1] Van Allen, Fraser, and Floyd, Science **108**, 746 (1948).
[2] Chackett, Paneth, Reasbeck, and Wiborg, "Variations in the chemical composition of stratosphere air" (to be published).
[3] Chackett, Paneth, and Wilson, J. Atmos. Terr. Phys. **1**, 49 (1950).
[4] Progress Report No. 1, Engineering Research Institute, University of Michigan, Signal Corps Contract (January, 1951).
[5] Hagelbarger, Loh, Neill, Nichols, and Wenzel, Phys. Rev. **82**, 107 (1951).
[6] Final Progress Report, Engineering Research Institute, University of Michigan, Signal Corps Contract (October, 1950).
[7] Hagelbarger, Neill, Nichols, and Wenzel, "Remote opening and sealing of metal tubes by soldering and by cold welding" (to be published).
[8] Best, Havens, and LaGow, Phys. Rev. **71**, 915 (1947). Also Havens, Koll, and LaGow, *Pressures and Temperatures in the Earth's Upper Atmosphere* (Naval Research Laboratory Report, Washington, D. C., March, 1950).
[9] J. H. McQueen, Phys. Rev. **80**, 100 (1951).

The Gamma-Ray Spectra of K^{38} and Cl^{34*}

HAROLD K. TICHO
Department of Physics, University of California, Los Angeles, California
(Received September 26, 1951)

BY means of a scintillation γ-ray spectrometer[1] some preliminary results on the energies of the γ-rays of Cl^{34} (33 min)[2] and K^{38} (7.5 min)[3] have been obtained. The activities were produced by (p, pn) reactions on bombardment of NaCl and KI by 18-Mev protons from the U.C.L.A. fm cyclotron.

Three NaI(Th) crystals were mounted in a straight line and 5.6 cm apart, directly on the faces of three 5819 photomultipliers. The output pulses of the center 5819 were clipped, amplified, and applied to the deflecting plates of a specially constructed high stability oscilloscope. The sweep and intensity could be triggered by this same pulse (1-crystal operation)[1] by a twofold coincidence of the center 5819 and either of the outer ones (2-crystal operation)[4] or by a coincidence of pulses from all three counters (3-crystal operation). The pattern on the scope screen was photographed. Calibration by means of artificial pulses demonstrated that the electronic system was linear to $\pm$1 percent.

For γ-ray energy determinations, the apparatus was always calibrated with the 1.28-Mev γ-ray of Na^{22}. The photopeak to pair-peak distance also served as an independent $2m_0c^2$ standard.

Figure 1 shows the 1-crystal spectrum of K^{38} between two Na^{22} spectra. Small pulses were rejected by an integral discriminator.

FIG. 1. γ-ray spectrum of K^{38} between two γ-ray spectra of Na^{22} used for calibration. The gain for K^{38} was reduced by 1.96 relative to the gain for Na^{22}.

On the Na^{22} spectrum the annihilation photoline, and the photoline and Compton distribution of the 1.28-Mev γ-ray are easily identified. For the K^{38} spectrum, the gain of the linear amplifier was reduced by a factor of 1.96. The features of this pattern are interpreted as photoline, pair-line, and Compton distribution of a single γ-ray of 2.16$\pm$0.03 Mev.

The 1-crystal spectrum of Cl^{34} was not well suited for energy determinations. The photoline of a high energy γ-ray is easily located and the corresponding energy is 3.22$\pm$0.03 Mev, in good agreement with previous results.[3] However, the photoline and the

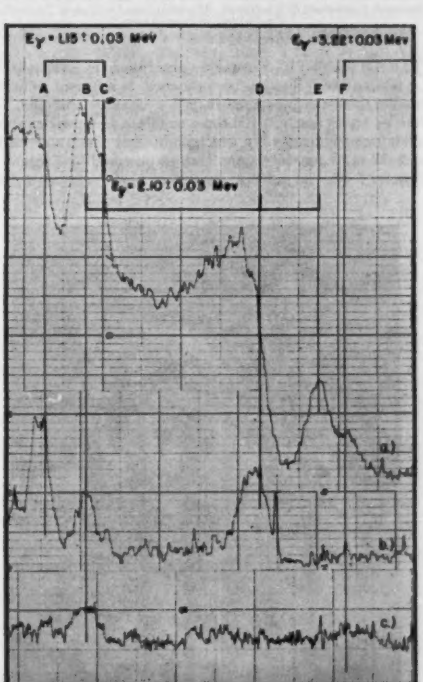

FIG. 2. Microdensitometer trace of Cl^{34} spectrum in the energy region 1–2.5 Mev. (a) 1-crystal operation, (b) 2-crystal operation with second crystal at 135° with respect to incident γ-ray beam. (c) 3-crystal operation.

pair-lines of the second γ-ray overlap the pair-line of the 3.22-Mev γ-ray and the photoline of a third γ-ray, respectively. The microdensitometer trace of the energy region in question is shown in Fig. 2, top. The unresolved doublets are in the region *BC* and *EF*. The next lower trace resulted from 2-crystal operation when the second crystal was oriented such that the line joining the crystals was at 135° with respect to the incident γ-ray beam. Using this trace, the pair-line of the second γ-ray was found at *B*; the γ-ray has an energy of 2.10±0.03 Mev, and its photoline and "135° edge" should be located at *E* and *D*, respectively. It will be noticed that the calculated line *D* does not pass through the center of the 2-crystal Compton line: this is because the recoil electron energy changes very slowly with scattering angle beyond 135°. Using this information, line *A* was drawn for the "135° edge" of the third γ-ray whose energy is then computed to be 1.16±0.03 Mev. The photoline of this γ-ray should lie at *C*. The bottom trace of Fig. 2 results on 3-crystal operation; only the pair-lines of the 3.22- and 2.10-Mev γ-rays remain.

It is a pleasure to thank Professor J. R. Richardson for much helpful advice in the course of this experiment.

* This work was assisted by the joint program of the ONR and AEC.
[1] R. Hofstadter and J. A. McIntyre, Phys. Rev. **80**, 631 (1950). The author is also indebted to Dr. Hofstadter for many helpful suggestions.
[2] L. Ruby and J. R. Richardson, Phys. Rev. **80**, 760 (1950).
[3] Ramsey, Meem, and Mitchell, Phys. Rev. **72**, 639 (1947).
[4] R. Hofstadter and J. A. McIntyre, Phys. Rev. **78**, 619 (1950).

Paramagnetic Resonance in Liquids*

MICHAEL TINKHAM, ROY WEINSTEIN, AND ARTHUR F. KIP†
Research Laboratory of Electronics, Massachusetts Institute of Technology, Cambridge, Massachusetts
(Received October 4, 1951)

PARAMAGNETIC resonance absorption in solutions containing Mn^{++} ions has been observed in solutions sufficiently dilute for the hyperfine structure (hfs) to be easily observed. These solutions are as much as 100 times as dilute as those reported by Halliday and Wheatley,[1] in which no hfs was observable, and are about the same concentrations as those observed by England and Schneider.[2] The microwave apparatus used included a Pound stabilized oscillator, 6 kc/sec crystal modulator, magic Tee, and rectangular cavity (TE_{012} mode). The magnetic field was swept through the resonance region with a period of about 7 seconds. Figure 1 is an example of the observed absorption spectrum.

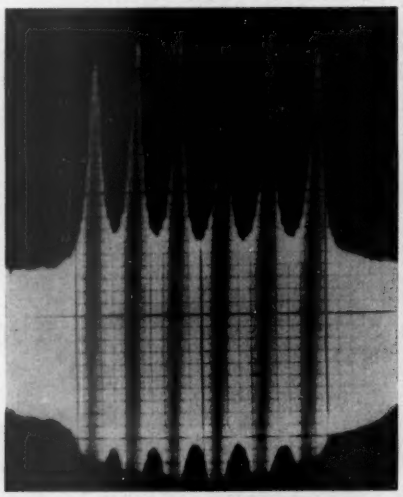

FIG. 1. Absorption spectrum of 0.15*M* $MnCl_2$ solution at 80°C.

All observable structure is explained by the simple Hamiltonian

$$\mathcal{H}=g\beta\mathbf{H}\cdot\mathbf{S}+A\mathbf{I}\cdot\mathbf{S},$$

where g is the g value of a free electron. The Hamiltonian given by Bleaney and Ingram[3] for the Mn^{++} ion in crystals reduces to this form if spherical symmetry is assumed. It predicts absorption lines ($M\leftrightarrow M-1$) when

$$H=\frac{h\nu}{g\beta}-Am-\frac{A^2}{2}\frac{g\beta}{h\nu}\left[\frac{35}{4}-m^2+m(2M-1)\right] \quad \begin{matrix} m=-5/2,\cdots,5/2 \\ M=-3/2,\cdots,5/2. \end{matrix}$$

The term in $(2M-1)$ gives only a broadening, with no shift of the center of each of the hfs lines. The observed lines fit this form with

$$g=2.001\pm0.001 \quad \text{and} \quad A=95 \text{ gauss}.$$

The g value was established by comparison with an organic radical mounted directly on the sample capillary, and the distances of the 6hfs lines from this reference were determined by use of a sychronous flip coil.[4] This observed g value is within experimental error of the free electron value, the values obtained by Bleaney and Ingram in two dilute manganese salts, the value obtained by England and Schneider for Mn^{++} activators in a ZnS phosphor,[2] and their value for Mn^{++} ions in solution. The A value differs markedly from the 68 gauss obtained by England and Schneider for the phosphor, but not so strongly from the approximately 100 gauss obtained by Bleaney and Ingram and the 98 gauss given by England and Schneider for solutions. These differences indicate that the strength of the configurational interaction which produces the hfs depends on the ionic environment more strongly than might have been anticipated.

Line widths have been inferred from the ratio of the depth of the valley between lines to the height of one line, using the assumption of a Lorentz line shape. These widths have been interpreted in terms of electric and magnetic perturbations produced on the absorbing ion by its ionic neighbors and by the sheath of water molecules surrounding it. These perturbations broaden the energy levels in two general ways: by causing small randomly distributed shifts in the positions of the levels and by shortening the lifetimes by inducing transitions. To get a quantitative dependence on temperature, the random Brownian motion is decomposed into a noise spectrum,[5] the intensity of which depends on frequency by the factor $\tau_c/1+\omega^2\tau_c^2$, where τ_c is the "correlation time" of the random motion. The first general mechanism is produced by electric and magnetic fields with frequency components ω small compared to the frequency width of the line; that is, by fields which do not "average out" over the lifetime of a state. Thus the noise factor approximately reduces to τ_c, and this contribution to line width increases with τ_c. The second mechanism acts through components near the Larmor frequency. With X-band frequencies, this makes $\omega\tau_c>1$, causing this contribution to depend approximately on $1/\omega^2\tau_c$. Since τ_c is proportional to η/T, where η is the viscosity, it turns out that the line width W between half-maximum points for a given sample should be approximately expressible in the form

$$W=C_1/(\eta/T)+C_2[W(\eta/T)]^{\frac{1}{2}}.$$

The coefficients C_1 and C_2 depend on the nature and concentration of the ions in solution, and may be approximately fairly well by linear combinations of these concentrations. Figure 2 shows the experimental results for samples containing various concentrations of $MnCl_2$ and $CaCl_2$ solutions. These results fit curves of the above form as well as expected in view of the number of approximations involved. For example, the approximation of $\tan^{-1}2\tau_c/\tau$ by $2\tau_c/\tau$ eliminates the observed leveling off at large τ_c. By holding total ionic strength constant in three of these runs, the effect of the magnetic ions is largely isolated. It should be noted that with dilute solutions and high temperatures the width can be reduced

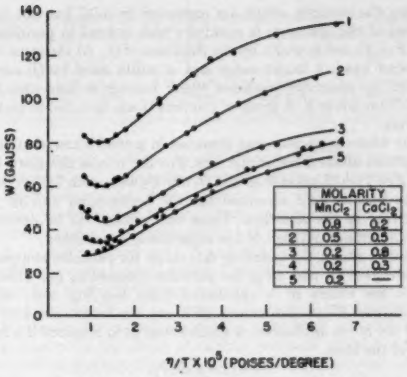

FIG. 2. Line width W as a function at η/T.

below 30 gauss. This corresponds to a relaxation time of about 4×10^{-9} second.

Other measurements have been made at room temperature to test the dependence of the width W on ionic concentrations. It was found that W is very nearly a linear function of Mn^{++} ion concentration when total ionic strength is constant, and also of total ionic concentration when a solution of a nonmagnetic salt was added, holding the Mn^{++} ion concentration constant. To test the effect of the anion, line widths were measured with 0.15-M solutions of $MnCl_2$, $MnBr_2$, $Mn(NO_3)_2$, $Mn(C_2H_3O_2)_2$, and $MnSO_4$. The first three widths were all 43 gauss within experimental error. The width in the acetate was 60 gauss and that in the sulfate was 64 gauss. These results can be interpreted in terms of the effect of ionic size on τ_e and the effect of ionic charge on the magnitude of the perturbation.

Further work on liquids is in progress.

* This work has been supported in part by the Signal Corps, the Air Materiel Command, and the ONR.
† Now at the Department of Physics, University of California, Berkeley, California.
[1] D. Halliday and J. Wheatley, Phys. Rev. **74**, 1724 (1948).
[2] T. S. England and E. E. Schneider, Physica **17**, 221 (1951).
[3] B. Bleaney and D. J. E. Ingram, Proc. Roy. Soc. (London) **A205**, 336 (1951).
[4] R. D. Arnold and A. F. Kip, Phys. Rev. **75**, 1199 (1949).
[5] T. S. England and E. E. Schneider, Nature **166**, 437 (1950).
[6] Bloembergen, Purcell, and Pound, Phys. Rev. **73**, 679 (1948).

Order of Gamma-Ray Emission in the Decay of In^{111} *

M. M. MILLER, C. H. PRUETT, AND R. G. WILKINSON
Department of Physics, Indiana University, Bloomington, Indiana
(Received September 17, 1951)

THE identification of the 247-kev gamma-ray emitted following orbital electron capture in In^{111} with a 0.08-μsec excited state in Cd^{111} at 247 kev seems to have been well established indirectly by several methods. One of these methods[1] depends upon noting that only the 247-kev gamma-ray is common to the activities of In^{111} and Cd^{111m}. Thus the order of emission of the gamma-rays following the decay of In^{111} can be inferred, the 0.08-μsec level found by Deutsch and Stevenson[2] giving rise to the 247-kev gamma-ray. These conclusions have been substantiated in another way by Engelkemeir,[3] who has shown the existence of a beta-ray group in Ag^{111} which feeds a 0.1-μsec level in Cd^{111}. The present work shows the assignment is correct by demonstrating that the 247-kev gamma-ray following the decay of In^{111} is delayed with respect to the 172-kev gamma-ray associated with the same decay.

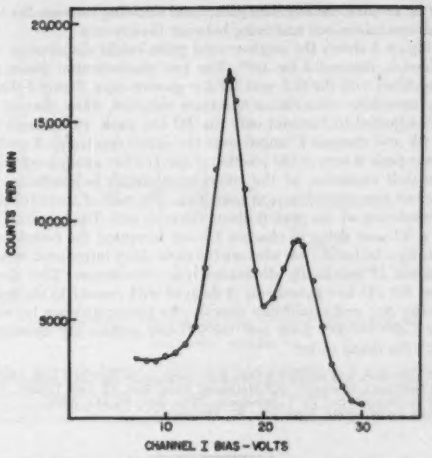

FIG. 1. Single-crystal pulse-height distribution for In^{111} obtained in channel I. The two photoelectron peaks are caused by gamma-rays at 172 and 247 kev.

In this experiment two scintillation spectrometers were used in coincidence. Each channel consisted of a $\frac{1}{2}$-inch NaI(Tl) cube mounted on a RCA 5819 photomultiplier, a cathode follower preamplifier, an Atomic Instruments Model 204-B linear amplifier, and a conventional differential discriminator of variable slit width. The discriminator outputs were mixed in a coincidence circuit of approximately 0.2-μsec resolving time. Delays in the form of RG 65/U cable were introduced in either channel between the linear amplifier and the differential discriminator. Attenuation of pulse height caused by the delay line was completely compensated

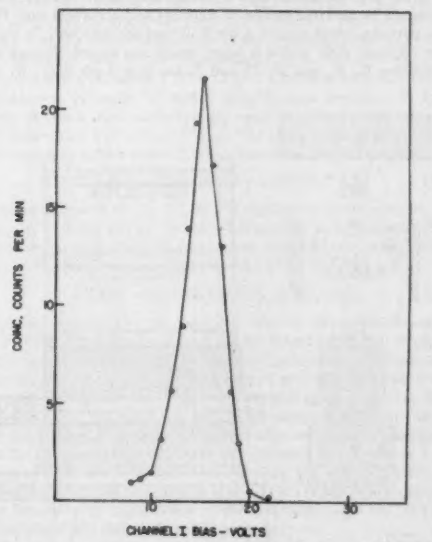

FIG. 2. Coincidence spectrum obtained when channel II transmits only the 247-kev peak while channel I surveys the whole spectrum. No delay has been introduced into either channel.

for by varying the amplifier gain. Lead shielding between the two counters minimized scattering between the crystals.

Figure 1 shows the single-crystal pulse-height distribution obtained in channel I for In^{111}. The two photoelectron peaks are associated with the 172- and 247-kev gamma-rays. Figure 2 shows the zero-delay coincidence spectrum obtained when channel II was adjusted to transmit only the 247-kev peak with a large slit width and channel I ranged over the entire spectrum. A coincidence peak is seen at the position of the 172-kev gamma-ray since the time resolution of the coincidence circuit is insufficient to prevent true coincidences at zero delay. The ratio of true to chance coincidences at the peak is about thirty to one. The introduction of a 0.1-μsec delay in channel I alone increased the coincidence rate by a factor of two, whereas the same delay introduced only in channel II practically eliminated true coincidences. This shows that the 247-kev gamma-ray is delayed with respect to the lower energy one and establishes directly the correspondence between the Cd^{111} 247-kev level and the 247-kev gamma-ray associated with the decay of In^{111}.

* This work was assisted by the joint program of the ONR and AEC.
[1] Helmholz, Hayward, and McGinnis, Phys. Rev. **75**, 1469 (1949).
[2] M. Deutsch and D. T. Stevenson, Phys. Rev. **76**, 184 (1949).
[3] D. Engelkemeir, Phys. Rev. **82**, 552 (1951).

Zenithal Distribution of Low Energy Mesons

ANDRÉ G. VOISIN*
Division of Physics, National Research Council of Canada, Ottawa, Canada
(Received August 8, 1951)

IT is well known that the zenithal distribution of the integral meson spectrum at sea level obeys the empirical law $I_\theta = I_0 \cos^\lambda\theta$, where I_θ is the intensity of cosmic-rays making an angle θ with the zenith. The value of λ is approximately two. It has been shown,[1] however, that this law does not apply for the differential spectrum, in particular, in the momentum range 300–410 Mev/c.

In the present experiments a limited band in the spectrum was obtained by an arrangement of counters and absorbers such that the particles which stop in a block of lead are detected. In Fig. 1 the counters ABC define a beam which has passed through absorbers P_1, P_2, and P_3. P_2 and P_3 are each 5 cm thick. By observing the particles which are registered in ABC but not in D, a band of the spectrum is selected which is fixed in position by $P_1+P_2+P_3$ and in width by the thickness of Q_1. At the same time a second band of longer range and of width fixed by Q_2 can be studied by observing particles which register in coincidence in $ABCD$ but not in E. A group of counters G was included to exclude showers.

The whole apparatus was mounted in a steel frame that could be rotated about a horizontal axis. For the results described here $P_1+P_2+P_3=15$ cm of lead and Q_1 and Q_2 were each 7.5 cm thick.

The results were corrected for the background and for the scattering in the absorber. These corrections will be described when a detailed account of the experiment is published.

Table I shows the counting rate $\Delta I_{\theta D}$ for particles stopped in the absorber Q_1 and $\Delta I_{\theta E}$ for particles stopped in Q_2. Table II shows the values of λ calculated from $\log r/\log\cos\theta$, where $r=\Delta I_\theta/\Delta I_0$. Since the values of λ are far from constant, the $\cos^\lambda\theta$ law is not applicable. A much better fit is obtained if a function of the form

$$r=(1-a\sin^b\theta)$$

is assumed. If $\log(1-r)$ is plotted against $\log\sin\theta$, the points fall on a straight line. The constants a and b have the following values: $a=0.98\pm0.02$, $b=1.47\pm0.12$, for the spectral band 300 to 410 Mev/c; $a=1.03\pm0.03$, $b=1.61\pm0.15$, for the spectral band 410 to 510 Mev/c.

TABLE I. Counting rates at various zenithal angles θ: $\Delta I_\theta D$ represents mesons with momenta between 300 and 410 Mev/c. $\Delta I_\theta E$ represents mesons with momenta between 410 and 510 Mev/c.

θ	0°	30°	60°	75°	80°
$\Delta I_{\theta D}$	3.59 ± 0.10	2.33 ± 0.18	0.75 ± 0.03	0.19 ± 0.02	0.18 ± 0.02
$\Delta I_{\theta E}$	3.62 ± 0.10	2.36 ± 0.11	0.60 ± 0.03	0.13 ± 0.01	0.09 ± 0.01

The measurements were extended to angles greater than 90° in an effort to detect particles coming upward from the earth. Upward moving particles are difficult to distinguish from particles scattered into the ABC telescope from the high flux of downward particles in Q_1 or into $ABCD$ from Q_2. Measurements with one or

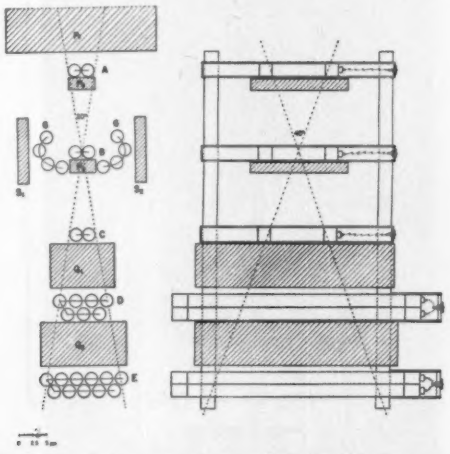

FIG. 1. Arrangements of counters and absorbers to measure the zenithal distribution.

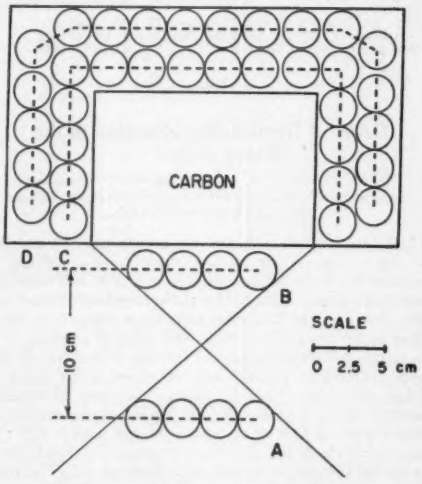

FIG. 2. Arrangement of counters and absorber to detect the upward flux of mesons.

TABLE II. Values of λ calculated from $\log r/\log\cos\theta$, where $r=\Delta I_\theta/\Delta I_0$.

	30°	60°	75°	80°
$\Delta\ \theta D$	3.00±0.53	2.26±0.07	2.17±0.08	1.71±0.06
$\Delta I_{\theta R}$	2.97±0.34	2.59±0.08	2.46±0.06	2.11±0.06

both absorbers Q_1 and Q_2 removed showed that there appeared to be no significant increase in counts for angles greater than 90°.

Another experiment was performed to confirm this. The μ-mesons were detected by their decay electron using a delayed coincidence circuit. The arrangement of apparatus is shown in Fig. 2. Coincidences AB and CD with AB delayed were recorded. The circuit accepted delay periods from 1.2 to 7.2 microseconds but rejected counts where any counter in C or D was tripped at the same time as AB. In this way only μ-mesons coming upward into the block of carbon and stopping there were recorded. The background with the block of carbon removed was 0.42±0.10 count per hour and the count with the block in place was 0.45±0.06 per hour. Therefore, these results show no appreciable upward flux of mesons. Powell *et al.*[2] found an appreciable upward component using photographic plates exposed at high altitude on the Jungfrau, and Ritson[3] using counters observed an upward component of slow mesons from the ground at sea level.

In conclusion, the angular distribution (at angles between 0 and 80°) of cosmic-ray mesons in two momentum bands (300 to 410 Mev/c and 410 to 510 Mev/c) has been found to show a marked decrease in intensity near the zenith and a tendency to more isotropy for the larger angles. The phenomena which could contribute to this isotropic effect are: the scattering of particles through the atmosphere, the decay in flight on heavy mesons giving rise to lighter mesons, and the nuclear disintegration accompanied by a production of mesons. Backward radiation (at angles greater than 90°) measured in the same momentum bands was found to be of very low intensity.

The author wishes to thank Dr. W. Kraushaar for many interesting discussions and particularly Dr. D. C. Rose for his constant interest and help during the experiments.

* Attaché de recherches au Centre National de la Recherche Scientifique, Paris. Holder of a National Research Council postdoctorate fellowship.

[1] A. Rogozinski and A. G. Voisin, Compt. rend. **230**, 2092 (1950).
[2] Camerini, Muirhead, Powell, and Ritson, Nature **162**, 433 (1948).
[3] D. M. Ritson, Proc. Phys. Soc. (London) **A370**, 1098 (1950).

Multiple Scattering and Grain Density Measurements on Electron Tracks in G-5 Emulsions

I. B. McDIARMID
Department of Physics, Queen's University, Kingston, Ontario, Canada
(Received June 21, 1951)

SEVERAL Ilford G-5 plates have been exposed to the x-rays from a 70-Mev synchrotron and a study made of the electron tracks from the pairs produced in the emulsion. The energy of each electron has been determined by the scattering method and in all a total of 13 cm of track has been grain counted.

Multiple scattering theories[1-3] can be put in the form

$$\bar{\theta}(t)=K(t)\sqrt{t}/P\beta, \tag{1}$$

where $\bar{\theta}(t)$ is the mean angle of scattering in degrees measured between tangents a distance t apart, t the cell length in units of 100μ, P the momentum$\times c$ in Mev, and $\beta=v/c$. $K(t)$ is the "scattering constant," and we find from Williams' theory[1,4] for G-5 emulsions and $\beta\to1$

$$K(t)=14.6+(234+148.5\log_{10}t)^{\frac{1}{2}}, \tag{2}$$

and for a large angle cutoff in the measurements $=4\bar{\theta}(t)$

$$K(t)_\infty=(K(t)-25\pi/K(t))/(1-\pi/0.32K(t)^2). \tag{3}$$

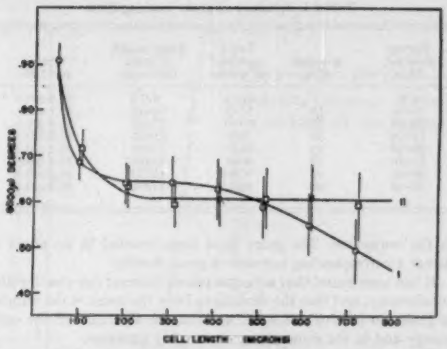

FIG. 1. Curve I: Results of scattering measurements on a long electron track when angles are measured between successive chords. Curve II: Results of measurements on the same track when angles are measured between chords drawn over small intervals "a" of the track and separated by distances $(a+ak)$. The squares are for $a=50\mu$. The triangles are for $a=100\mu$.

The values of $K(t)$ calculated from Eq. (2) agree to within 4 percent with the results of Gottstein *et al.*[5] using Moliere's[3] theory for $\beta=1$, over the entire range of t.

If, instead of measuring angles between tangents, the mean angle of scatttering $\bar{\alpha}(t)$ is measured between successive chords, it has been shown that

$$\bar{\alpha}(t)=(\tfrac{3}{4})^{\frac{1}{2}}\bar{\theta}(t). \tag{4}$$

Therefore, multiplying Eqs. (2) and (3) by $(\frac{3}{4})^{\frac{1}{2}}$ the scattering constant appropriate to the successive chord method is obtained. For a cell length of 100μ ($t=1$) we get from Eqs. (2) and (3) $(\frac{3}{4})^{\frac{1}{2}}K(100\mu)=24.4$ and $(\frac{3}{4})^{\frac{1}{2}}K(100\mu)_\infty=22.6$.

The method used in this work to measure the scattering is a slight modification of Fowler's[6] coordinate method. Instead of measuring angles between successive chords as Fowler describes, angles between chords drawn over small intervals of the track and separated by given distances are measured. This procedure seems to give a better dependence of the measured mean angle on the cell length used in the measurement. As in Fowler's method the positions of the track $Y_1Y_2\cdots Y_k\cdots$ (above an arbitrary line) are taken at intervals "a" apart, then the first deviation D_1 between chords a distance $t=(a+ak)$ apart is given by the second difference $(Y_1-Y_2)-(Y_{k+2}-Y_{k+3})$. The mean angle of scattering $\bar{\psi}(t)$ measured in this way $=\langle|D|\rangle_{\rm av}/a$ and we find the relation

$$\bar{\psi}(t)=[(2+3k)/(3+3k)]\bar{\theta}(t), \tag{5}$$

which corresponds to Eq. (4) for the successive chord method.

Figure 1 shows typical results of scattering measurements obtained using both methods on a 9-mm long electron track. The quantiy $\bar{\theta}(100\mu)$ obtained from the expression

$$\bar{\theta}(100\mu)=[K(100\mu)_\infty/K(t)_\infty][\bar{\theta}(t)/(t)^{\frac{1}{2}}] \tag{6}$$

is plotted against the cell length t used in the measurement. $\bar{\theta}(100\mu)$ should be independent of the cell length except for small t, and here it is large because the "spurious" scattering is of the same order as the true scattering. Readings of position were taken at intervals of 50μ and the mean angle of scattering calculated for different t. For the larger cell lengths overlapping cells were used and the equivalent number of statistically independent readings calculated in each case to obtain the probable errors. Curve 1 is obtained from the measured $\bar{\alpha}(t)$ and Eqs. (4) and (6); curve 2 is obtained from the measured $\bar{\psi}(t)$ and Eqs. (5) and (6). It can be seen that a better dependence of the measured angle on t is obtained when $\bar{\psi}(t)$ rather than $\bar{\alpha}(t)$ is used.

The energies of the electrons available lie in the particular range (E/μ (kinetic/rest energy) $=7$ to 90) in which ionization theories predict an increase of a few percent up to a constant value

TABLE I. Summary of grain-counting data.

Energy interval, Mev	Average E/μ	Total number of grains	Total length of track (microns)	Grains per 100μ
2–5	7	1613	4778	33.8±0.6
5–10	15	5777	16445	35.1±0.4
10–15	25	7818	22149	35.4±0.3
15–20	35	7933	21997	36.0±0.3
20–25	45	6333	17541	36.1±0.3
25–30	55	4947	13834	35.8±0.4
30–35	65	5764	15732	36.6±0.4
35–45	80	5092	13890	36.6±0.4

in the ionization. The gains have been counted in an effort to detect a corresponding increase in grain density.

It has been found that an experienced observer can count grains consistently, and that the deviations from the mean of the number of grains in intervals as small as 180μ, for all tracks of the same energy and in the same plate, are roughly gaussian.

The grain-counting data for all tracks in the same 5-Mev energy interval have been grouped together and the results are shown in Table I. There is an observable increase in grain density of about 7 percent in the region $E/\mu=7$ to 40 or 60 after which the density is constant. This is roughly in agreement with the measurements on cosmic-ray particles of Pickup and Voyvodic[7] who report an increase of 10 percent from a minimum at $E/\mu=3$ to a constant value at $E/\mu=20$. Our results, like theirs, seem to favor the ionization theory of Wick.[8]

I wish to thank Dr. J. A. Gray for his continued interest and help during the course of this work and the National Research Council of Canada for the award of a bursary.

[1] E. J. Williams, Phys. Rev. **58**, 292 (1940).
[2] H. S. Snyder and W. T. Scott, Phys. Rev. **76**, 220 (1949).
[3] G. Molière, Z. Naturforsch. **3a**, 78 (1948).
[4] E. J. Williams, Proc. Roy. Soc. (London) **169**, 531 (1939).
[5] K. Gottstein *et al.*, Phil. Mag. **42**, 708 (1951).
[6] P. H. Fowler, Phil. Mag. **41**, 169 (1950).
[7] E. Pickup and L. Voyvodic, Phys. Rev. **80**, 89 (1950).
[8] C. C. Wick, Nuovo cimento **9**, 1, 3, 303 (1943).

Energy Response of NaI (Tl) Crystals to Alpha-Particles of Less than 10 Mev*

RALPH H. LOVBERG†
University of California, Los Alamos Scientific Laboratory, Los Alamos, New Mexico
(Received September 20, 1951)

RECENT investigation[1] of the response of NaI crystals as scintillation counters of charged particles has shown that, although the light output is essentially linear with energy of incident electrons, protons, and deuterons, there is nonlinearity in the response to alpha-particles of less than 10 Mev. The investigation described here was undertaken to determine in detail the shape of this nonlinearity.

In this experiment, energy control was accomplished by air attenuation and the particles were allowed to strike a freshly cleaved crystal face. To avoid the usual rapid moisture contamination of the crystal surface in the open atmosphere, the entire operation was performed in a dry-box, with signal and high voltage cables brought into the 5819 photomultiplier by means of airtight feed-through connectors. P_2O_5 was used as a drying agent, and no detectable deterioration of crystals cleaved in the box took place in a three-week period.

Two sources of alpha-particles were used, both thin to their own radiations. The first was a "thorium active" deposit yielding alpha-groups at 8.78 Mev and 6.04 Mev from ThC′ and ThC disintegrations, respectively. The second was Pu^{239}, giving 5.16-Mev alphas. Both sources were deposited on the ends of probe rods which passed through a light-tight, sliding seal in the end of the phototube housing. The 1×1×0.1-cm crystal was held to the tube face by a wire clip, with a drop of mineral oil providing additional optical coupling.

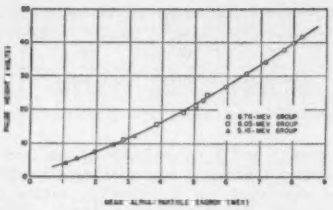

FIG. 1. Mean output pulse height as a function of computed mean energy.

The thorium probe was used in seven positions from 1.00 to 6.00 cm from the crystal, and the Pu source in five positions from 2.00 to 3.62 cm, the near position in each case being the limit at which the source backing reflected a significant amount of light back into the photocathode, producing spurious heightening of output pulses.

Appropriate range corrections for the local atmospheric pressure of 60.2 cm Hg were made, and the mean particle energies were computed from Bethe's range-energy curves.[2]

Output of the 5819 was fed into a low gain preamplifier for polarity inversion, through a Los Alamos model 503 pulse amplifier, and into a continuously variable single-channel pulse-height discriminator. Linearity of the electronic system was checked by applying standard pulses to the phototube anode resistor and observing the corresponding discriminator dial readings. No corrections were found necessary.

In Fig. 1, mean output pulse height for each probe position is plotted against computed mean energy. In every position, the peak of the pulse-height distribution could be determined to within one volt.

I wish to thank Mr. Hugh Stoddart of the Los Alamos cyclotron group for preparation of the sources used in this experiment.

* Work done under the auspices of the AEC.
† Now at the Department of Physics, University of Minnesota, Minneapolis 14, Minnesota.
[1] Taylor, Remley, Jentschke, and Kruger, Phys. Rev. **83**, 169 (1951).
[2] H. Bethe, *The Properties of Atomic Nuclei II.* (Brookhaven National Laboratory, Upton, New York, 1949).

The Hyperfine Structure of $^2P_{\frac{1}{2}}$ State of the Stable Chlorine Isotopes*

JOHN GORDON KING AND VINCENT JACCARINO
Research Laboratory of Electronics, Massachusetts Institute of Technology, Cambridge, Massachusetts
(Received September 27, 1951)

FROM observations of the hyperfine structure (hfs) interaction in an external magnetic field, the nuclear magnetic dipole coupling constants ($a_{1/2}$) for the $^2P_{1/2}$ metastable state of the stable chlorine isotopes have been obtained. As will be shown, the results of these measurements are in excellent agreement with recent work on the ratio of the nuclear magnetic moments of the two isotopes. Use has been made here of the atomic beam magnetic resonance method, as in previous work in the hfs of the $^2P_{3/2}$ state of chlorine.[1,2]

In Fig. 1 the interaction energy of an atom with $I=\frac{3}{2}$ and $J=\frac{1}{2}$ in an external magnetic field is displayed. An estimate of the hfs separation, ΔW, can be had from consideration of the form of the interaction[1,2]

$$\Delta W = h\Delta\nu = 2ha = -\mu_0^2 g_1 \mathfrak{F} \frac{4L(L+1)}{J(J+1)} \langle r^{-3}\rangle_{Av},$$

where $\mathfrak{F}$ is a relativistic correction factor of order 1.0 for both the $P_{1/2}$ and $P_{3/2}$ states of chlorine, and the other symbols have their usual meaning. Since the hfs of the $P_{3/2}$ state is known quite accurately, and one may assume $(\langle r^{-3}\rangle_{Av})_{3/2}$ is equal to $(\langle r^{-3}\rangle_{Av})_{1/2}$ to

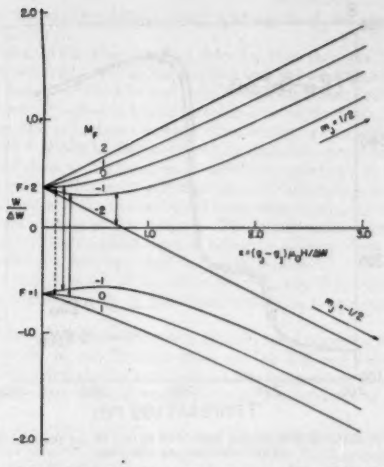

FIG. 1. The energy levels of an atom in an external magnetic field, with electronic angular momentum $J=1/2$ and nuclear angular momentum $I=3/2$.

within a few percent, an approximate value of $\Delta\nu_{1/2}^{35}$ and $\Delta\nu_{1/2}^{37}$ may be estimated. Unfortunately both of these values lie in a region of the radiofrequency spectrum (1700 Mc/sec—2100 Mc/sec) that renders a gross search for the zero field $\Delta F=\pm 1$ transitions most impracticable.

As a consequence, successively more accurate values for $\Delta\nu$ for each isotope had to be obtained from observations of the transition ($F=2$, $m_F=-1\leftrightarrow F=2$, $m_F=-2$) (see Fig. 1) in successively larger magnetic fields[4] since

$$\nu(2,-1\leftrightarrow 2,-2)=g_I(\mu_0 H/h)+(\Delta\nu/2)(1-x+x^2)^{\frac{1}{2}}.$$

The transitions ($F=3$, $m_F=-1\leftrightarrow F=3$, $m_F=-2)_{1/2}^{35}$ and ($F=4$, $m_F=-3\leftrightarrow F=4$, $m_F=-4)_{1/2}^{133}$ of Cl^{35} and Cs^{133}, respectively, were used to calibrate the magnetic field.

A search was then conducted for the $\Delta F=\pm 1$, $\Delta m_F=\pm 1$ transitions, and the Zeeman effect of the following lines was observed in the neighborhood of 2075 Mc/sec for Cl^{35}, and of 1726 Mc/sec for Cl^{37}

(a) $(2, 2\leftrightarrow 1, 1)$

(b) $(2, 1\leftrightarrow 1, 0)$, $(2, 0\leftrightarrow 1, 1)$ } not resolved at small fields;

(c) $(2, -1\leftrightarrow 1, 0)$, $(2, 0\leftrightarrow 1, -1)$ } not resolved at small fields.

The correct dependence on magnetic field was found in all cases, and at a field corresponding to $x^{35}=0.27$ the transitions (c) are easily resolved and are approximately field independent. (These are indicated in Fig. 1.) From this observation a value of $\mu^{35}=0.82\pm 0.08$ nuclear magnetons was obtained.

A precision measurement of $\Delta\nu_{1/2}^{35}$ and $\Delta\nu_{1/2}^{37}$ was made, using a radiofrequency field of special design having components parallel to the external field. For this, the following $\Delta F=\pm 1$, $\Delta m_F=0$ transitions were observed: $(2, 1\leftrightarrow 1, 1)$ field dependent to first order in x; $(2, 0\leftrightarrow 1, 0)$ field independent to first order in x; $(2, -1\leftrightarrow 1, -1)$ field dependent to first order in x. Although the field was kept at a value such that these lines were clearly resolved, the second-order magnetic correction to the transition $(2,0\leftrightarrow 1, 0)$ was less than 0.0005 Mc/sec. In Fig. 2 a resonance curve is shown from which the value of $\Delta\nu_{1/2}^{35}$ was obtained.

Frequencies in the neighborhood of 2075 Mc/sec were obtained from a c.w. Raytheon QK-174A magnetron[5] operated from highly

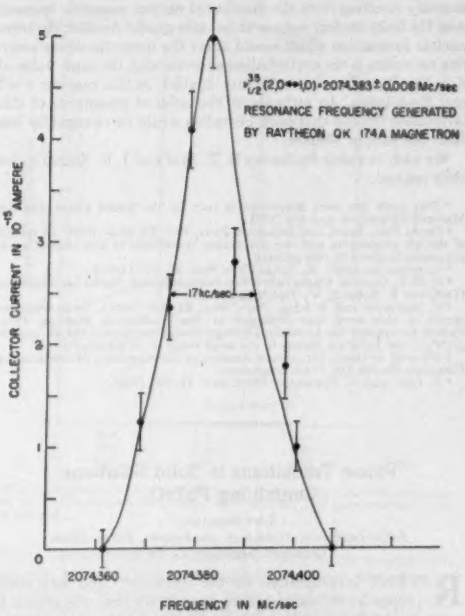

FIG. 2. The transition indicated by the dotted line in Fig. 1, induced by an rf field parallel to the external magnetic field.

filtered power supplies. A suitable modified F-4800 jamming transmitter using a 2C39 lighthouse tube was found to be satisfactory for frequencies in the vicinity of 1726 Mc/sec. Using harmonics from a 5-Mc/sec, crystal-controlled oscillator kept at zero beat with WWV's signal, and a G.R. 620A frequency meter for interpolation purposes, the error in frequency measurement was kept to less than one part in 10^6.

The novel use of a magnetron for atomic beam measurements suggests the feasibility of observing the direct $\Delta F=\pm 1$ transitions for precision measurements of the $\Delta\nu$ of various alkalies as well as of gallium and indium, using existing magnetrons and klystrons.

The following results for the hfs interaction in the $^2P_{1/2}$ state of chlorine 35 and 37 have been established:

$$\Delta\nu_{1/2}^{35}=2074.383\pm 0.008 \text{ Mc/sec};$$
$$\Delta\nu_{1/2}^{37}=1726.700\pm 0.015 \text{ Mc/sec}.$$

In Table I we have listed recent measurements on the ratio of the nuclear magnetic dipole interaction of the two isotopes. It is interesting to consider why one would expect such close agreement between the various ratios. For two isotopes with the same value of I and with similar magnetic moments, combined with the small electron wave function density at the nucleus, both for the $P_{1/2}$ and $P_{3/2}$ configurations for $Z=17$, one would expect any hfs

TABLE I. Data on the nuclear magnetic constants of Cl^{35} and Cl^{37}.

Method	Ratio of magnetic constants
Nuclear induction[a] using HCl	$g_I^{35}/g_I^{37}=1.2014\pm 0.0001$
Nuclear induction[b] using LiCl	$g_I^{35}/g_I^{37}=1.2013\pm 0.0001$
Atomic beam[c] magnetic resonance—$^2P_{3/2}$	$a_{3/2}^{35}/a_{3/2}^{37}=1.20136\pm 0.00005$
Atomic beam magnetic resonance—$^2P_{1/2}$ (this paper)	$a_{1/2}^{35}/a_{1/2}^{37}=1.201357\pm 0.000013$

[a] W. G. Proctor and F. C. Yu, Phys. Rev. **81**, 20 (1951).
[b] G. D. Watkins and R. V. Pound, Phys. Rev. **82**, 343 (1951).
[c] See reference 2.

anomaly resulting from the distributed nuclear magnetic moment over the finite nuclear volume to be quite small.[6] Another electron-nuclear interaction which would affect the magnetic-dipole coupling constants is the perturbation of levels with the same value of F in the $P_{3/2}-P_{1/2}$ fine structure doublet, in this case the $F=2$ and $F=1$ levels. An estimate of the order of magnitude of this interaction reveals that both hfs ratios would be changed by less than one part in 100,000.

We wish to thank Professors B. T. Feld and J. R. Zacharias for their counsel.

[*] This work has been supported in part by the Signal Corps, the Air Materiel Command, and the ONR.

[1] Davis, Feld, Zabel, and Zacharias, Phys. Rev. **76**, 1076 (1949). (A review of the hfs interaction and the observable transitions in this atomic beam apparatus is given in this article.)

[2] V. Jaccarino and J. G. King, Phys. Rev. **83**, 471 (1951).

[3] H. B. G. Casimir, *On the Interaction Between Atomic Nuclei and Electrons*, (DeErven F. Bohn N. V., Haarlem, 1936).

[4] V. Jaccarino and J. King, Phys. Rev. **83**, 209 (1951). (A preliminary report of this work was presented at the Washington meeting, 1951. Failure to consider the anomalous spin gyromagnetic ratio of the electron in $g_J(^2P_{3/2})$ and $g_J(^2P_{1/2})$ results in the large value of $\Delta\nu$ reported.)

[5] We wish to thank Mr. Henry Argento of the Raytheon Manufacturing Company for the QK-174A magnetron.

[6] A. Bohr and V. Weisskopf, Phys. Rev. **77**, 94 (1950).

Phase Transitions in Solid Solutions Containing $PbZrO_3$

GEN SHIRANE
Tokyo Institute of Technology, Oh-okayama, Tokyo, Japan
(Received September 25, 1951)

RECENT investigations on the dielectric[1,2] and structural[3] properties of lead zirconate have shown that this crystal is not a ferroelectric but an antiferroelectric. At the same time, the study[4] of solid solutions of $PbZrO_3$ and $PbTiO_3$ has revealed that when some of the Zr ions in $PbZrO_3$ are replaced by Ti ions, a ferroelectric intermediate phase can be observed between the paraelectric and antiferroelectric phases. The $(Pb-Ba)ZrO_3$[5] and $(Pb-Sr)ZrO_3$ systems have now been investigated to determine whether such an intermediate phase can be observed also in these systems.

Specimens were made from PbO, $BaCO_3$, $SrCO_3$, and high purity ZrO_2 which are the same chemicals as used for the previous study.[3] These ingredients were mixed in the desired compositions and then sintered at temperatures between 1200° and 1300°C after preliminary calcination.

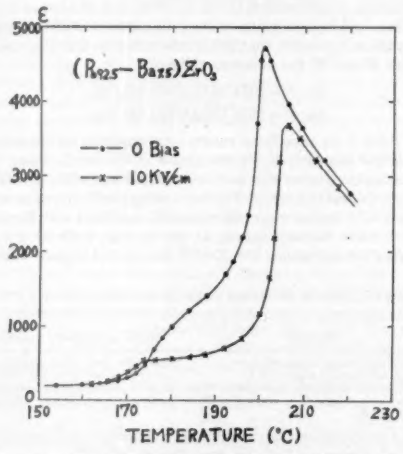

FIG. 1. Effect of a dc biasing field of 10 kv/cm on the permittivity of $(Pb92.5-Ba7.5)ZrO_3$ at 1 Mc/sec.

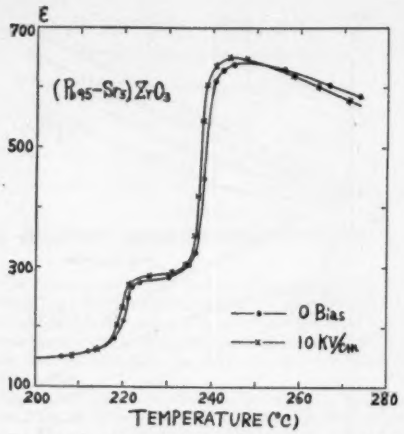

FIG. 2. Effect of a dc biasing field of 10 kv/cm on the permittivity of $(Pb95-Sr5)ZrO_3$ at 1 Mc/sec.

Curves of permittivity *vs* rising temperature for $(Pb92.5-Ba7.5)-ZrO_3$ and $(Pb95-Sr5)ZrO_3$ are shown in Figs. 1 and 2. Besides the remarkable maximum at the ordinary Curie point, another small anomaly can be perceived in these two curves.[6] It is to be noticed here that the anomaly at the lower transition in $(Pb95-Sr5)ZrO_3$ is more pronounced than that of $(Pb92.5-Ba7.5)ZrO_3$, whereas the peak value at the Curie point of the former is smaller than that of the latter.

To confirm whether the properties of these intermediate phases are both ferroelectric, as in the case of $Pb(Zr-Ti)O_3$, we have carried out the study of the $D-E$ characteristics of the present solid solutions under an ac field of 20 kv/cm. The curve for $(Pb92.5-Ba7.5)ZrO_3$ shows typical hysteresis loops in the intermediate phase between 175° and 200°C, insuring the ferroelectricity of this phase. On the other hand, the curve for $(Pb95-Sr5)ZrO_3$ shows no hysteresis loops and is almost linear, not only in the lowest phase but also in the intermediate phase, except at temperatures just below the upper transition point in which a slight upward curvature was observed. This result seems to suggest that the intermediate phase in this specimen is not ferro-

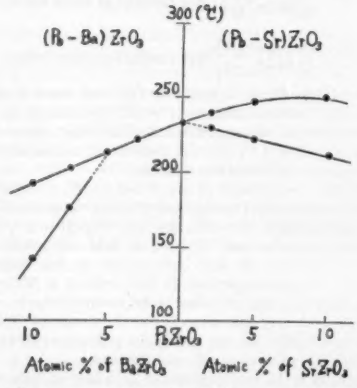

FIG. 3. Phase diagram of the $(Pb-Ba)ZrO_3$ and $(Pb-Sr)ZrO_3$ systems.

electric but antiferroelectric, being different from the phase of pure $PbZrO_3$.

The effect of a dc biasing field of 10 kv/cm upon the permittivity of these two solid solutions was studied, with the results shown in Figs. 1 and 2. In $(Pb92.5-Ba7.5)ZrO_3$, the permittivity value in the ferroelectric phase is lowered considerably by the biasing field as in the case of barium titanate.[7] The situation is very different for $(Pb95-Sr5)ZrO_3$. Below the upper transition temperature, the permittivity of this specimen is slightly increased by a dc field. A comparison of this result with that[2] of pure $PbZrO_3$ gives further support for the above assumption of the antiferroelectricity of the intermediate phase in this specimen. The atomic arrangement of this antiferroelectric phase must of course be different from that of pure $PbZrO_3$. An x-ray study is now in progress.

The phase diagram of the $(Pb-Ba)ZrO_3$ and $(Pb-Sr)ZrO_3$ systems is shown in Fig. 3. The situation is to be summarized as follows:

(1) When some of the Pb ions in $PbZrO_3$ are replaced by other suitable ions, an intermediate phase can be observed between antiferroelectric and paraelectric phases. The temperature range of this intermediate phase increases with the concentration of substituted ions.

(2) In the $(Pb-Ba)ZrO_3$ system, this intermediate phase is clearly ferroelectric, just as in the case of $Pb(Zr-Ti)O_3$ system.

(3) In the $(Pb-Sr)ZrO_3$ system, the intermediate phase seems to be another antiferroelectric phase which is different from the phase of pure $PbZrO_3$.

These facts show that the antiferroelectric phase in pure $PbZrO_3$ is very critical in nature; namely, the free energy of this phase is very closely adjacent to those of a ferroelectric phase and another antiferroelectric phase, especially near the Curie point. This peculiar situation indicates that a ferroelectric state and an antiferroelectric state can be realized by only a small change in the polarizabilities of constituent ions. Detailed results will be reported shortly.

The author wishes to express his sincere thanks to Professor Y. Takagi and Mr. E. Sawaguchi for their helpful discussions and also to Dr. S. Roberts for his helpful communication of unpublished data.

[1] Sawaguchi, Shirane, and Takagi, J. Phys. Soc. Japan (to be published).
[2] Shirane, Sawaguchi, and Takagi, J. Phys. Soc. Japan 6, 208 (1951); Phys. Rev. 84, 476 (1951).
[3] Sawaguchi, Maniwa, and Hoshino, Phys. Rev. 83, 1078 (1951).
[4] G. Shirane and A. Takeda, J. Phys. Soc. Japan (to be published).
[5] S. Roberts, J. Am. Ceram. Soc. 33, 63 (1950).
[6] The permittivity anomaly at the lower transition in $(Pb90-Ba10)ZrO_3$ was also observed by Dr. S. Roberts (private communication to the author, January, 1951).
[7] S. Roberts, Phys. Rev. 71, 890 (1947).

The Change in Electrical Resistance of Magnesium on Melting

F. Hubbard Horn
General Electric Company Research Laboratory, Schenectady, New York
(Received September 27, 1951)

THE change in the electrical resistance of magnesium was determined using Johnson, Matthey and Company, Ltd., spectrographically pure metal (99.95 percent) and two commercially pure magnesium samples (99.52 and 98.67 percent with small amounts of Al, Fe, Mn, Cu, Si, and Cr). The resistivity-temperature data are shown plotted in Fig. 1.

There are three interesting features of the data. First, the ratio of the resistivity of liquid, ρ_l, to that of the solid, ρ_s, is 1.63 for the spectrographic material (1.56 for the commercially pure metal). This value is considerably less than the value 2.1 calculated from the equation of Mott and Wills[1] relating the ratio ρ_l/ρ_s to the latent heat of fusion. The value is also less than that observed for cadmium and zinc with which it may be compared structurally. The low value of ρ_l/ρ_s suggests that there are a larger number of effective free electrons in the liquid than in the solid—a suggestion consistent with the brillouin-zone picture. Second, the temperature coefficient of resistivity for molten magnesium is extremely small (negative in the case of the commercially pure samples). In the case of zinc, in which a marked negative temperature coefficient of resistivity is observed, Mott and Jones[2] have suggested that in the liquid a further distortion of the lattice increases the number of free electrons. Third, for each of the materials studied, the resistivity departs from a linear temperature dependence some 20–30° before the melting point is reached at 651°. This anticipation of melting is evidenced whether the cell is warming or cooling and is therefore not readily explained by a hysteresis effect. The effect may be of an undetermined experimental origin. Such an anticipation of melting has been observed for antimony[3] which, however, has a lower resistance in the liquid than solid phase, thus making direct comparison tenuous. The nonlinear change in resistance at a temperature considerably below that required for melting in the case of magnesium may be real. It would be of interest to clarify this effect through the use of other techniques, such as possibly x-ray diffraction.

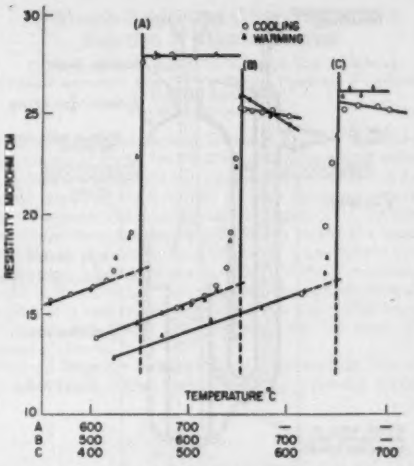

FIG. 1. Magnesium metal resistivity vs temperature. (A) Spectroscopically pure; (B) commercially pure, 98.7 percent; (C) commercially pure, 99.5 percent.

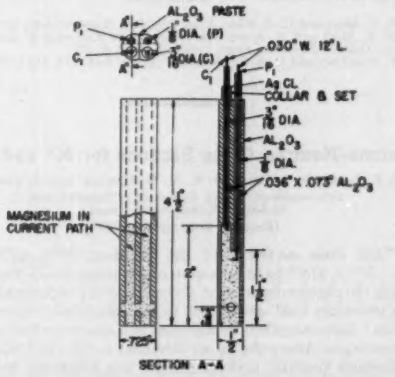

FIG. 2. Ceramic cell for electrical resistance measurement.

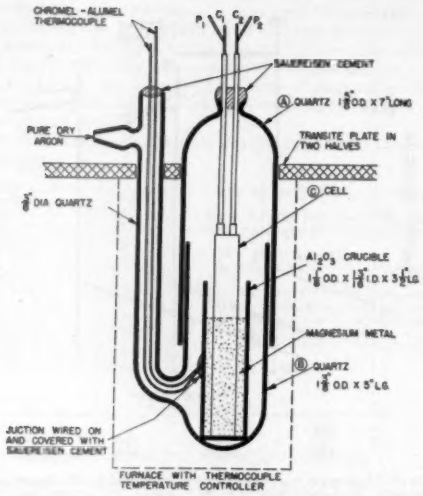

FIG. 3. Assembly for measuring electrical resistance of magnesium.

The cell construction and assembled apparatus for these measurements are shown in Figs. 2 and 3, respectively. The cell and crucible were made of a ceramic containing more than 95 percent Al_2O_3 with added MgO and SiO_2. Tests had shown this a material satisfactory for handling molten magnesium to at least 800°C, if finally fired at 1750°C. The electrodes were tungsten. Spectroscopic analysis of the magnesium metal taken from the electrode region after operation of the cell indicated no tungsten. The magnesium was protected from oxidation by keeping under streaming dry argon. Temperatures were determined using an ice compensated chromel-alumel couple attached to the exterior of the crucible. The resistance of the cell was measured potentiometrically using separate current and potential contacts with the magnesium as indicated in Fig. 2. Measurements were made only when the thermocouple indicated constant temperature. Polarity was reversed during measurement and the average values used to calculate resistance. The resistance of the cell was converted to resistivity from a determination of a cell constant using triple distilled mercury for which the room temperature resistivity was taken at 95.8 microhm cm. No correction was applied for the change in cell constant with temperature.

[1] N. F. Mott and H. H. Wills, Proc. Roy. Soc. (London) **A46**, 465 (1934).
[2] N. F. Mott and H. Jones, *The Theory of the Properties of Metals and Alloys* (Oxford University Press, London, 1934), p. 279.
[3] F. Northrup and V. A. Suydam, J. Franklin Inst. **175**, 153 (1912).

Gamma-Neutron Cross Sections for N^{14} and O^{16} *

H. E. JOHNS, R. J. HORSLEY, R. N. H. HASLAM, AND A. QUINTON
Department of Physics, University of Saskatchewan, Saskatoon, Saskatchewan, Canada
(Received September 4, 1951)

THE cross sections for the reactions $O^{16}(\gamma, n)O^{15}$ and $N^{14}(\gamma, n)N^{13}$ have been determined using the 25-Mev betatron in the physics department of the University of Saskatchewan. The procedure used was similar to that previously reported for carbon.[1] Ammonium nitrate was used as a source for both oxygen and nitrogen. Above the (γ, n) threshold in O^{16} (16.5 Mev) the two-minute positron activity in O^{15} was separated from the 10-minute positron activity in N^{13} by an analysis of the decay

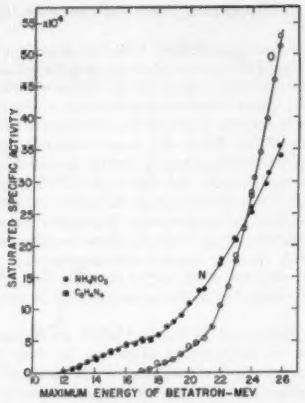

FIG. 1. Saturated specific activity in disintegrations per gram per 100 r as a function of maximum betatron energy, for the reactions $O^{16}(\gamma, n)O^{15}$, and $N^{14}(\gamma, n)N^{13}$. Corrections for geometry etc. have been applied. Points for nitrogen were obtained using NH_4NO_3 and $C_2H_4N_4$.

curve. In this way activities for oxygen and nitrogen were obtained simultaneously. Boric acid was also used as a source for oxygen. Normalization against the $Cu^{63}(\gamma, n)Cu^{62}$ activity[1,2] was carried out at 23 Mev.

The saturated specific activity curve for oxygen obtained in this way is shown in Fig. 1. It has a slowly increasing initial portion with almost constant slope for a range of about 4 Mev. This type of curve is quite different from anything formerly obtained in this laboratory and leads to a rather interesting cross section curve to be discussed below. The neutron yield at 22 Mev is 1.68×10^4 neutrons/mole/r as compared to the value 0.67×10^4 reported by Price and Kerst.[3] Their value is open to some doubt since they report a larger value at 18 than at 22 Mev.

Figure 2 shows the oxygen cross section curve determined by the "photon difference"[4] method. This curve shows an almost constant cross section from 17 to 20 Mev, followed by a rapidly rising portion to a peak value at 24.2 Mev. This anomalous effect can perhaps be explained by a mechanism suggested by Blatt and Weisskopf.[5] These author state that the main contribution to the gamma-ray absorption below 15 Mev comes from electric quadrupole and magnetic dipole interactions. However, at higher energies the absorption is strongly increased by the onset of an electric dipole absorption. The cross section curve in oxygen shows

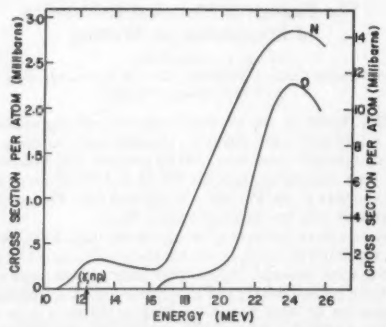

FIG. 2. Cross section *versus* photon energy for the reactions $O^{16}(\gamma, n)O^{15}$ and $N^{14}(\gamma, n)N^{13}$. For nitrogen use left-hand scale and for oxygen, right-hand scale. The (γ, np) threshold in nitrogen is indicated at 12.5 Mev.

TABLE I. Results for (γ, n) reactions in O^{16} and N^{14}.

	O^{16}	N^{14}
Peak (Mev)	24.2	24.2
σ_{max} (millibarns)	11.4	2.84
Integrated cross section to peak position (Mev-barns)	0.0312	0.015

a sharp increase at about 20 Mev, which may be the result of this effect.

In Fig. 1 is shown the saturated specific activity curve for N^{14}. The neutron yield at 22 Mev as determined from this curve is 2.38×10^4 neutrons/mole/r, which is lower than the value 6.5×10^4 obtained by Price and Kerst.[2] A curve drawn through the experimental points shows a small hump in the initial portion of this activity curve. Because of this unexpected behavior, dicyandiamide was irradiated. The nitrogen activity points obtained using it are shown in Fig. 1 as solid squares; they are in agreement with the previous results.

The resulting cross section curve for N^{14} (Fig. 2) shows a small peak at about 13 Mev as well as the larger one at 24.2 Mev. The falling off of the cross section curve immediately above 13 Mev, forming an apparent peak, may be caused by a (γ, np) reaction in N^{14}. The calculated threshold for this reaction, 12.5 Mev, is indicated in Fig. 2. In this process the neutron, presumed to be emitted first, leaves the N^{13} nucleus in a highly excited state from which it decays by proton emission rather than by gamma-emission. The product nucleus is O^{12} which is stable and therefore not detected in our experiment. While this process is not a true competition it has the effect of reducing the apparent (γ, n) yield when this is measured by detecting the radioactivity of the product nucleus (in this case N^{13}). Such processes have been called "cascade processes" by Katz and Cameron.[6] Another mechanism is required to explain why the (γ, n) cross section increases again above 17 Mev. Presumably this could be the result of the strong electric dipole absorption discussed earlier. Even for this portion of the curve it is probable that the cascade (γ, np) competition strongly reduces the measured (γ, n) yield leading to a smaller peak cross section in N^{14} (2.8 mb) than, for instance, in O^{16} (11.4 mb). This explanation requires a much larger (γ, np) cross section in N^{14} than in O^{16}. Evidence for this is amply provided by Gaerttner and Yeater[7] who observed that the (γ, np) reaction in N^{14} is almost 5 times that in O^{16} for 100 Mev-bremsstrahlung. Further, the threshold for the (γ, np) activity in O^{16} occurs much higher (22.9 Mev) and thus a cascade process in oxygen would have a much smaller effect on the (γ, n) cross section.

The information from the oxygen and nitrogen cross section curves is shown in Table I. No attempt has been made to estimate the width at half-maximum. The ratio of the oxygen and nitrogen integrated (γ, n) cross sections up to their peak positions is 2.08. In comparison the ratio of the total integrated cross sections obtained by Perlman and Friedlander[8] is 2.4 for 50-Mev and 2.2 for 100-Mev bremsstrahlung. The value obtained by Gaerttner and Yeater[7] is 1.9 for x-rays of maximum energy 100 Mev. It is seen that our results are in good agreement with those of the aforementioned authors as far as the ratios go.

The authors wish to thank Mr. L. B. Robinson for his assistance with many of the measurements involved. This work is supported by grants from the National Research Council and the National Cancer Institute of Canada.

* This work is supported by grants from the National Research Council and the National Cancer Institute of Canada.

[1] Haslam, Johns, and Horsley, Phys. Rev. **82**, 270 (1951).
[2] Johns, Katz, Douglas, and Haslam, Phys. Rev. **80**, 1062 (1950).
[3] G. A. Price and D. W. Kerst, Phys. Rev. **77**, 806 (1950).
[4] A. G. W. Cameron and L. Katz, Phys. Rev. **83**, 892 (1951), and **84**, 608 (1951).
[5] J. M. Blatt and V. F. Weisskopf (privately circulated notes to appear as a chapter in their forthcoming book, *Theoretical Nuclear Physics*).
[6] L. Katz and A. G. W. Cameron, Phys. Rev. **84** (1951).
[7] E. R. Gaerttner and M. L. Yeater, Phys. Rev. **77**, 714 (1950); **79**, 401 (1950).
[8] M. L. Perlman and G. Friedlander, Phys. Rev. **74**, 442 (1948).

π^+-Meson Production Cross Section as a Function of Atomic Number

D. HAMLIN, M. JAKOBSON, J. MERRITT, AND A. SCHULZ
Radiation Laboratory, Department of Physics, University of California, Berkeley, California

(Received October 2, 1951)

THE relative cross sections for the production of 53±4-Mev mesons at 0°±7° by 340-Mev protons have been measured for C, Al, Fe, Cu, Ag, and Pb. The mesons were produced by the external scattered beam of the 184-inch synchrocyclotron. In order to separate the mesons from the proton beam, the mesons were turned through approximately 90° by means of a magnetic field[1] (Fig. 1). The mesons were detected by trans-stilbene crystals and electronic circuits already reported.[2] Briefly, a coincidence of the pulses caused by a π^+-meson passing through one crystal and stopping in a second generates a delayed gate which is put in coincidence with the μ^+ pulse resulting from the decay of the stopped π^+-meson.

Figure 2 shows the measured relative cross sections. The standard deviations indicated include only the statistical deviations

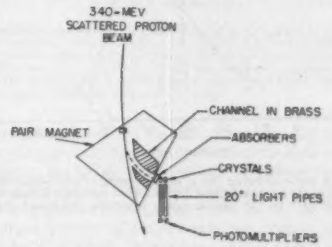

FIG. 1. Schematic diagram of the experimental arrangement.

arising from counting. A curve is given for σ/A as well as σ per nucleus to indicate the effective cross section per nucleon. The cross section divided by A is a decreasing function of A similar to that measured by Mozeley for production of π^+-mesons by photons.[3] The A dependence observed is in agreement with that obtained by Brueckner, Serber, and Watson in an analysis based on the absorption of π-mesons in nuclear matter.[4]

Previously the differential production cross sections for 20-Mev mesons at 150°±15° made by 240-Mev protons have been reported.[5] Results are in qualitative agreement and give the same general functional relation for the production cross section as a function of A.

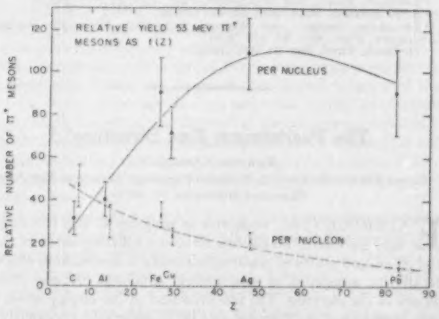

FIG. 2. The relative cross sections in arbitrary units for the production at 0°±7° of 53-Mev π^+-mesons by 340-Mev protons on C, Al, Fe, Cu, Ag, and Pb. The relative cross sections per nucleus are shown in solid lines and the relative cross section σ/A is shown in dotted lines.

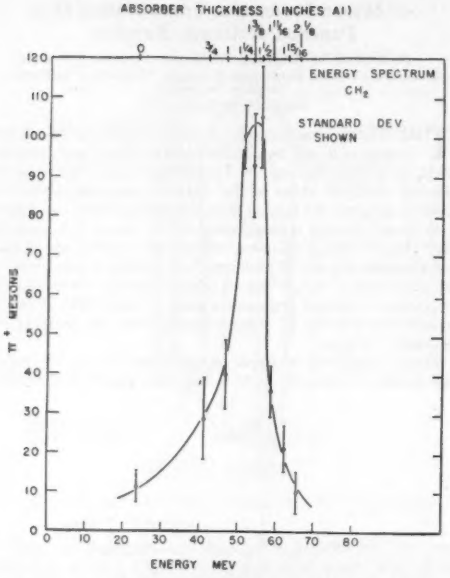

FIG. 3. A curve showing the π^+-meson energy distribution from a 2-inch polyethylene target bombarded by 340-Mev protons. Measurements were made at $0°\pm7°$ to the proton beam direction. Standard deviations are shown.

In order to compare counter detection of π^+-meson with plate techniques, the peak spectrum for the reaction $p+p<d+\pi^+$ was investigated. This spectrum has been investigated previously by plates.[1] Figure 3 shows the spectrum which was obtained with a 2-inch polyethylene target. The peak occurs at the energy expected from the thick production target which was used. The peak obtained by counters is considerably broader than that obtained by plates because of the greater energy width of the crystal detectors.

Thanks are due Professor C. Richman and co-workers for assistance in all parts of the experiment. We also wish to thank Professor O. Chamberlain for helpful discussions concerning the experiment.

[1] The arrangement was similar to that used by Richman, Skinner, Merritt, and Youtz, Phys. Rev. **80**, 900 (1950).
[2] Jakobson, Schulz, and Steinberger, Phys. Rev. **81**, 895 (1951).
[3] R. F. Moseley, Phys. Rev. **80**, 493 (1950).
[4] Brueckner, Serber, and Watson, University California Radiation Laboratory, Phys. Rev. **84**, 258 (1951).
[5] D. Clark, Phys. Rev. **81**, 313 (1951).

The Positronium Fine Structure*,†

RICHARD A. FERRELL
Palmer Physical Laboratory, Princeton University, Princeton, New Jersey
(Received September 27, 1951)

EXPERIMENTAL work now in progress at this laboratory,[1] and elsewhere,[2] on the fine structure splitting between the ^3S and S^1 ground states of positronium make it desirable to study in detail the properties of positronium predicted by the present theory of the electron. The fine structure of the energy levels has been worked out by Pirenne[3] and by Berestetski,[4] apparently independently. With the aim of proceeding to the next higher order (radiative corrections), we have first redone the calculations of these authors, and have found slight errors in both papers. Making the necessary changes in their work is a trivial matter. When this is done, one finds the shifts in energy, ΔE, of the singlet and triplet levels from the nonrelativistic values of $-mc^2\alpha^2/4n^2$ to be

$$\Delta E_{n,l}{}^s=\frac{11mc^2\alpha^4}{64n^4}+\frac{mc^2\alpha^4}{n^3}\epsilon_l{}^s;\quad \Delta E_{n,\,l,\,j}{}^t=\frac{11mc^2\alpha^4}{64n^4}+\frac{mc^2\alpha^4}{n^3}\epsilon_{l,\,j}{}^t,$$

where $\epsilon_l{}^s$, and $\epsilon_{l,\,j}{}^t$ are given by

$$\epsilon_l{}^s=-\frac{1}{2}\frac{1}{2l+1};\quad \epsilon_{l,\,j}{}^t=\epsilon_l{}^s+\delta_{0l}+\frac{(1-\delta_{0l})}{8(l+\frac{1}{2})}\times\begin{cases}\dfrac{3l+4}{(l+1)(2l+3)}, & j=l+1\\ -\dfrac{1}{l(l+1)}, & j=l\\ -\dfrac{3l-1}{l(2l-1)}, & j=l-1\end{cases}$$

(mc^2 is the rest energy of the electron and α the fine structure constant). Since the splittings depend on the principal quantum number, n, only through the factor $mc^2\alpha^4/n^3$, it is possible to study the "intrinsic fine structure" of the quantities $\epsilon_l{}^s$ and $\epsilon_{l,\,j}{}^t$, independent of any particular value of n. $\epsilon_l{}^s$ and $\epsilon_{l,\,j}{}^t$ are given numerically and represented schematically in Table I and Fig. 1. One finds the energy levels by adding the common shift, $0.1719/n^3$ and multiplying by $mc^2\alpha^4/n^3=11.6\ \text{cm}^{-1}/n^3=3.50\times10^5\ \text{Mc}/n^3$, $=1.45\times10^{-3}$ ev$/n^3$ (in terms of inverse centimeters, megacycles, or electron volts, respectively). We find the Lamb shift in positronium to be about one-half the corresponding shift in hydrogen

TABLE I. Numerical values of intrinsic positronium fine structure.

	$-\epsilon_l{}^s$ and $-\epsilon_{l,\,l}{}^t$ for six values of l					
	0	1	2	3	4	5
$-\epsilon_l{}^s$	0.5000	0.1667	0.1000	0.0714	0.0555	0.0454
$-\epsilon_{l,\,l+1}{}^t$	−0.0833	0.1083	0.0762	0.0585	0.0474	0.0399
$-\epsilon_{l,\,l}{}^t$	X	0.2084	0.1083	0.0744	0.0569	0.0462
$-\epsilon_{l,\,l-1}{}^t$	X	0.3334	0.1417	0.0904	0.0664	0.0525

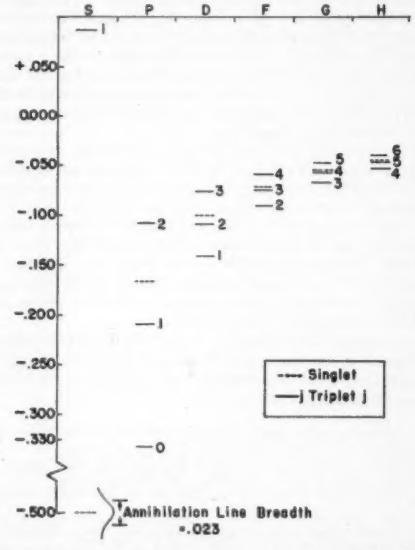

FIG. 1. Intrinsic positronium fine structure. To find energy levels, add $0.1719/n^3$ and multiply by $mc\alpha^4/n^3=11.6\ \text{cm}^{-1}/n^3=3.50\times10^5\ \text{Mc}/n^3$ $=1.45\times10^{-3}$ ev$/n^3$.

and to have no prominent effect on the fine structure. It does not reveal itself by splitting a degeneracy, as in the case of the hydrogen atom. Our calculations of the fine structure and its radiative corrections will be published in detail later.

We wish to thank Professor A. S. Wightman for valuable guidance and help in this problem, and the Atomic Energy Commission for support through a Predoctoral Fellowship.

* The work outlined here is part of a Ph.D. thesis to be submitted to Princeton University.
† This work was supported in part by the AEC.
[1] R. H. Dicke and T. A. Pond (private communication).
[2] M. Deutsch (private communication).
[3] J. Pirenne, Arch. sci. phys. et nat. **28**, 233 (1946); **29**, 121, 207, and 265 (1947). Pirenne omits a term $\pi e^2\hbar^2\delta(r)/m^2c^2$ from the orbital interaction, and his spin-orbit energy should be multiplied by 3/2.
[4] V. B. Berestetski, J. Exptl. Theoret. Phys. (U.S.S.R.) **19**, 1130 (1949). See also V. B. Berestetski and L. D. Landau, J. Exptl. Theoret. Phys. (U.S.S.R.) **19**, 673 (1949). Berestetski's expressions for the interactions are correct. His evaluation of $\overline{V}_4$, however, seems to be in error for $l\neq 0$, for it is too large by a factor of two.

Ionization Potentials and Probabilities Using a Mass Spectrometer

R. E. Fox, W. M. Hickam, T. Kjeldaas, Jr., and D. J. Grove
Westinghouse Research Laboratories, East Pittsburgh, Pennsylvania
(Received October 4, 1951)

A METHOD for determining ionization potentials and ionization probability curves has been devised which eliminates the difficulties arising from uncertainties in the energy of the bombarding electrons.[1]

A sketch of the ion source is shown in Fig. 1(a). Electrons leaving the filament are accelerated into the ionization enclosure by the potential V_1. The intermediate electrode 4 is maintained at a negative potential V_R with respect to the filament so as to prevent the low energy electrons in the distribution from entering the ionization chamber. The increase in the ion current observed when the absolute value of V_R is decreased by ΔV_R, keeping V_1 fixed, represents the ion current produced by a beam of electrons monoenergetic within ΔV_R. If V_{4M} is the larger, and V_{4m} the smaller in absolute value of the two corresponding V_4 readings, this then uniquely determines the maximum and minimum energy of the electrons producing the observed difference in ion current [see Fig. 1(b)]. If now the ion current difference is measured and plotted as a function of V_{4M}, keeping V_R constant, this difference will go to zero at the ionization potential. This curve represents the ionization probability as measured with an electron beam monoenergetic within ΔV_R. In a case where the ionization probability varies linearly with the electron energy, for values of V_{4M} greater than ΔV_R plus the ionization potential, the observed curve should be linear. For values of V_{4M} within ΔV_R above the ionization potential the curve is essentially parabolic, approaching the axis with zero slope at the ionization potential. In the measurements described here, ΔV_R was 0.1 volt and usually no points were taken for V_{4M} within this region. This amounts to extrapolating over the small interval ΔV_R. It may be proved that this will yield a value for the ionization potential too high by $\Delta V_R/2$. To compensate for this, the experimental curves were plotted as a function of the average value of V_4 instead of V_{4M}.

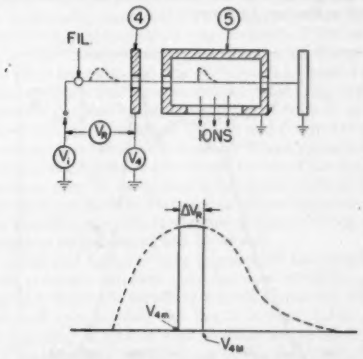

FIG. 1. (a) A sketch of the ion source showing the electrode structure and the voltage references. (b) A distribution in electron energy which is modified by the retarding potential to give the equivalent of a monoenergetic electron beam.

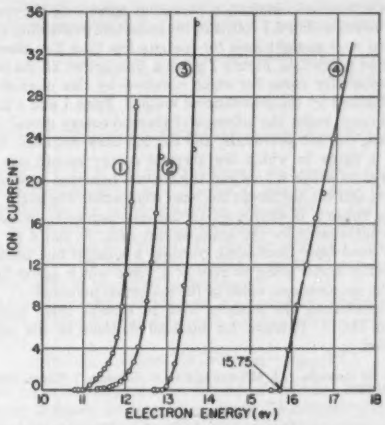

FIG. 2. Ionization probability curves for argon 40^+. Run (1) taken by conventional method. Run (2) taken by conventional method with 0.1 sensitivity at the amplifier. Run (3) the ion difference curve using a retarding potential on the electrons, but with an ion-draw-out voltage of 3 volts. Run (4) the ion difference curve obtained using both a retardation of the electrons and pulsed fields on ions and electrons.

Since the energy scale is determined by the potential between the retarding electrode 4 and the ionization chamber 5 [see Fig. 1(a)] the effect of the contact potentials between the filament and the accelersting electrodes is eliminated. Those contact potentials which can arise between the accelerating electrodes have been reduced or eliminated by gold plating all surfaces.

To obtain ion currents of sufficient magnitude, it is necessary to apply a small electric field across the ionization chamber in a direction normal to the electron beam. In past experiments, this ion-draw-out field created an inhomogeneity and uncertainty in the electron energy. In the present experiments this difficulty has been overcome by giving the electron current and the ion-draw-out voltage a pulsed time dependence such that the electrons reach the ionization chamber only when the draw-out field is zero.

Because magnetic collimation of the electron beam is employed, one might expect that the transverse (spiralling) velocity of the electrons would give rise to a considerable spread in electron energy, which would lead to "tailing" of the ionization probability curve in the region of onset. Experimentally, this "tailing" is not observed, indicating that some mechanism serves to prevent electrons with appreciable transverse energy from reaching the ionization chamber.

Since the electrons are moving very slowly near the retarding plate, space charge effects are quite important in this experiment. By measuring the apparent ionization potential as a function of the electron current, and extrapolating to zero current, a correction term was obtained which was of the order of 0.2 volt for the work reported here. Modifications are underway which should reduce this effect.

Preliminary measurements have been taken on argon (40^+), krypton (84^+), nitrogen (28^+), and carbon monoxide (28^+). In all

cases, the measured ionization potentials agree with the spectroscopic values within 0.1 volt, and the ionization probability curves obtained were straight lines for energies less than 2 ev above the ionization potentials. Figure 2 gives a comparison of the ionization probability curve for argon obtained by this method with that obtained by the conventional method. Runs 1 and 2 show a typical curve under the influence of thermal energy spread in the electrons, contact potentials, and the ion-draw-out field. Run 3 shows a curve in which the thermal energy spread has been narrowed to within 0.1 ev and the contact potential between the filament and the electrodes has been eliminated. The slight "tailing" in curve 3 is attributed to the inhomogeneity in electron energy introduced by the ion-draw-out field. In run 4 all these effects have been eliminated, yielding a straight-line ionization probability curve going to zero at a value which agrees closely with the spectroscopic value of the ionization potential.

In conclusion, the authors wish to express their appreciation to Dr. T. Holstein for his contributions to the method described.

[1] See, for example, J. J. Mitchell and F. F. Coleman, J. Chem. Phys. 17, 44–55 (1949).

Nuclear Structure in Fission

L. E. Glendenin, E. P. Steinberg, M. G. Inghram, and D. C. Hess
Argonne National Laboratory, Chicago, Illinois
(Received September 10, 1951)

MASS spectrometric investigations of the relative abundances of fission product species from uranium fission have been made by Thode and co-workers[1] and Inghram and co-workers.[2] This type of measurement is capable of high precision and, with appropriate normalization, permits the establishment of fission yields to a much higher degree of accuracy than the present radiochemical techniques.

The early results of Thode *et al.* on Kr and Xe abundances in fission indicated abnormally high yields at masses 133 and 134 and, perhaps, in the region 83–86 as well. One would, of course, expect some fine structure in the yield-mass curve as a result of known delayed neutron effects, but these, at most, are of the order of ~0.5 percent in fission yield and cannot account for the magnitude of Thode's results. Recent radiochemical studies on Te and I fission yields have also indicated a high yield at mass 134.[3]

A proposal to account for the observed anomalies which was made by one of us,[4] based on the boiling-off of an extra neutron from the fission fragments containing 51 or 83 neutrons, appeared to be qualitatively successful. This hypothesis, however, predicts a low yield at mass 137 which has been shown not to be the case.[5] The discrepancy between observation and prediction here led Thode to propose a possible preference for an 82-neutron configuration in the fission act in addition to a neutron boil-off effect following fission. It should be noted that an extension of the neutron boil-off hypothesis to fission fragments containing three and five neutrons in excess of a closed shell would account for the observed "normal" yield of mass 137. Fission yield determinations of masses complementary to the mass region 133–137 should establish whether the fine structure observed is the result of a preferential mode of fission or of phenomena following fission. Such studies are now in progress at this laboratory.

In the present work some interesting effects have been noted in the isotopic abundances of Mo and Zr produced in the fission of uranium. These data, together with normalized data on fission Xe and Kr (Thode) and Nd (Inghram), are presented in Fig. 1 where they are compared with the smooth radiochemical fission yield-mass curve.

Since the results obtained from these investigations are relative abundances, the data of one element must be fitted to those of another in some, as yet arbitrary, manner. For the present we have normalized the Xe data to the radiochemical yield-mass curve at mass 131 (=2.8 percent). Since the ratio of total Xe to Kr was

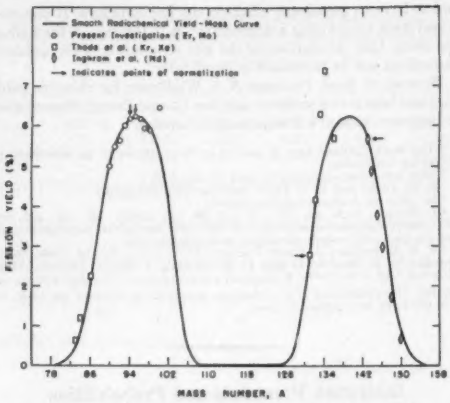
Smooth Radiochemical Yield - Mass Curve
Present Investigation (Zr, Mo)
Thode et al. (Kr, Xe)
Inghram et al. (Nd)
Indicates points of normalization
FISSION YIELD (%)
MASS NUMBER, A

FIG. 1. Comparison of smooth radiochemical U^{235} fission yield data with mass spectrometric data.

obtained in Thode's work, this also fixes the Kr yields. Likewise, the Nd data were normalized to the radiochemical curve at mass 143 (=5.7 percent), Zr was normalized at mass 94=6.20 percent and Mo at 95=6.25 percent. Experiments are in progress to establish absolute abundances of Zr, Mo, and Ru in fission and thus obviate some of the difficulties of normalizing the relative abundance data.

It should be noted, however, that whatever normalization is employed, the present data for Mo indicate an abnormally high yield in the mass region 98–100. The anomalies in the mass 133–136 region are also quite evident on this linear plot. The original Kr^{86} and Xe^{136} data have been corrected for known delayed neutron emission. Thus, the data are corrected for the significant changes known to take place after fission. If a value of 2.5 for the number of neutrons per fission is taken for U^{235}, the data may be plotted as in Fig. 2, with the heavy group reflected over the light group such that the masses of complementary fission products sum to 233.5. In such a "folded" curve the coincidence of the anomalies at masses 98–100 *vs* 133–136 becomes obvious. Although neutron boil-off effects may be operating in the 133–137 mass region (the region in which 82 neutrons are present), there does not appear to be any reasonable basis for this effect in the region of mass 100. The high yield at Mo^{100}, then, suggests a preference for this mass in the fission act, perhaps as the complement of a preferred 82-neutron shell in the heavy fragment.

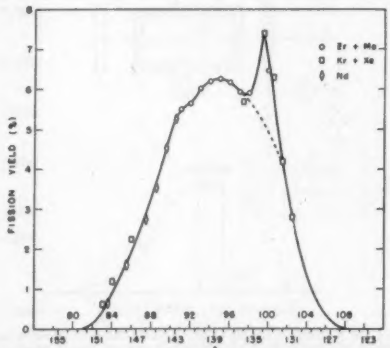

FIG. 2. Mass spectrometric yield-mass curve in U^{235} fission.

In addition to an enhanced yield resulting from some preferential mode of fission, delayed neutron and neutron boil-off effects from the fragments after fission could affect the yields in the 133–136 region further. Evidence supported the latter effects is provided by the abnormally low yield of Xe^{136} (and of I^{136} determined radiochemically[6]). However, the existence of a short-lived isomeric state could account for the observed result in the case of I^{136} and perhaps faulty normalization in the case of Xe^{136}.

A treatment of beta-decay systematics by Suess[7] indicates that the observed energies of Zr^{92} and Zr^{94} are much lower than expected. This may be an indication of a shell at 40 protons. Recent mass measurements by Duckworth and Preston[8] also indicate extra stability for a 40-proton configuration. If this is true, the high yields near mass 100 may also be the result of a preference in fission for a 40-proton configuration. In any event, it appears that the only reasonable explanation for the anomalous yield at Mo^{100} is a nuclear structure preference in the fission act.

The data also indicate a dip in the curve at mass 92 which is unexplained at present. Since low binding of closed shell plus 3 and 5 neutrons seems probable from published data on neutron binding energies,[9] boil-off of the 55th neutron (at Rb^{98}) is perhaps prominent here.

Further investigations are in progress with a view toward establishing as complete a fission yield-mass curve as possible by mass spectrometric measurements of the isotopic abundances of fission produced elements as well as accurate radiochemical determinations. Similar studies on U^{235} and Pu^{239} fission products are planned to observe the effects of change in mass and nuclear charge of the fissile nucleus on the observations reported here.

[1] H. G. Thode and R. L. Graham, Can. J. Research **A25**, 1 (1947); McNamara, Collins, and Thode, Phys. Rev. **73**, 129 (1950).
[2] Inghram, Hayden, and Hess, Phys. Rev. **79**, 271 (1950).
[3] A. C. Pappas and C. D. Coryell (private communication); L. Yaffe (private communication).
[4] L. E. Glendenin, Phys. Rev. **75**, 337 (1949).
[5] H. G. Thode (private communication).
[6] C. W. Stanley and S. Katcoff, J. Chem. Phys. **17**, 653 (1949).
[7] H. E. Suess (private communication).
[8] H. E. Duckworth and R. S. Preston, Phys. Rev. **82**, 468 (1951).
[9] K. Way, Phys. Rev. **75**, 1448 (1949).

Evidence for Production of Hole Traps in Germanium by Fast Neutron Bombardment

J. W. Cleland, J. H. Crawford, Jr., K. Lark-Horovitz,* J. C. Pigg, and F. W. Young, Jr.†
Oak Ridge National Laboratory, Oak Ridge, Tennessee
(Received September 28, 1951)

In Si[1] both acceptors or electron traps and donors or hole traps, presumably associated with lattice vacancies and interstitials, respectively, are introduced near the middle of the forbidden band by nucleon bombardment. Consequently, the Fermi level ζ of N-type Si is depressed and that of P-type Si is elevated by bombardment toward a limiting or saturation value ζ_{limit} causing a corresponding decrease in the conductivity of both N- and P-type Si. Heretofore, experiments on both N- and P-type Ge[2] indicate that bombardment causes an increase in P-type character with an accompanying depression of ζ toward the top of the filled band. This behavior may be interpreted as being the result of the introduction of acceptors only. However, in view of the close similarity of the electronic and crystal structure of Ge and Si, one would expect donors to be introduced into Ge as well.

James and Lehman[3] have investigated the situation in which both acceptors and hole traps (donors) are introduced in equal numbers below the middle of the filled band and find that ζ_{limit} lies half way between the two introduced levels. Thus the ζ of originally N-type or high to moderate resistivity P-type Ge will be depressed toward ζ_{limit} by bombardment while low resistivity P-type Ge with a ζ value below ζ_{limit} will show an elevation of ζ corresponding to a decrease in conductivity.

The conductivity of 5 low resistivity P-type Ge single crystals[4] ($n_A > 7\times10^{17}$ cm^{-3}) was followed during fast neutron bombardment in the Oak Ridge pile. The initial rate of change in carrier concentration per incident neutron $dn_A/d(nvt)_{fast}$, the original hole concentration n_A^0, and the exposure temperature for these samples are listed in Table I. All samples showed a decrease in conductivity with bombardment and a gradual approach to a limiting value as predicted by the model.

TABLE I. Bombardment data for low resistivity P-type Ge.

Sample	n_A^0	$dn_A/d(nvt)_{fast}$	T_e
1	7.0×10^{17} cm^{-3}	−5.0	32°C
2	1.01×10^{18}	−5.0	37
3	1.3×10^{18}	−2.2	48
4	1.5×10^{18}	−2.9	48

The limiting value of the hole concentration, above which a decrease in hole concentration with bombardment is expected, is given by

$$(n_A)_{\text{limit}} = 2(2\pi m_A^* kT/h^2)^{\frac{3}{2}} \exp(-\zeta_{\text{limit}}/kT), \qquad (1)$$

where ζ_{limit} is measured from the top of the filled band. Consequently, it should be possible to choose Ge samples with appropriate hole concentrations which on bombardment would show a decrease in carrier concentration at low temperatures and an increase at high temperatures within a convenient temperature range. Several samples with hole concentrations of $\sim10^{18}$ cm^{-3} were bombarded at −78°C, and the conductivity was followed at that and at ambient temperature (55°C) after the dry ice was sublimed. A typical conductivity *vs* integrated fast neutron flux $(nvt)_{fast}$ curve is shown in Fig. 1. The values of $dn_A/d(nvt)_{fast}$ for both temperatures and the original hole concentrations for these samples are listed in Table II. In every case the slope is negative at

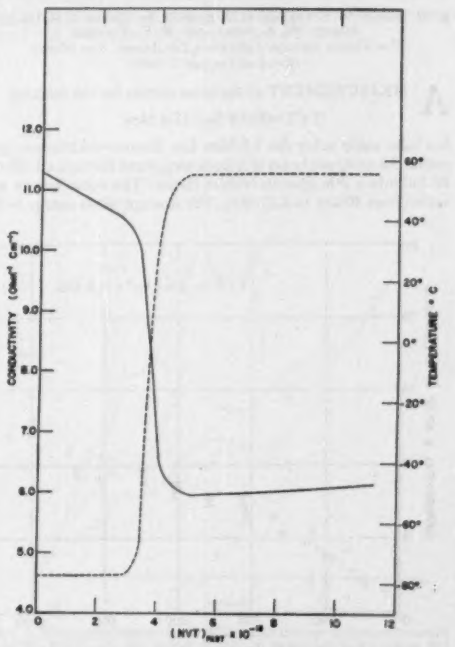

FIG. 1. Conductivity *vs* integrated fast neutron flux for P-type Ge ($n_A^0 \sim 4\times10^{18}$) exposed successively at −78°C and 55°C. The dashed curve is temperature.

TABLE II. Bombardment data for *P*-type samples bombarded successively at −78°C and 55°C.

Sample	n_A^0(−78°C)	$dn_A/d(n_i t)_{fast}$ at −78°C	at 55°C
1	4.01×10^{16}	−0.99	0.20
2	4.69×10^{16}	−1.12	0.396
3	4.86×10^{16}	−1.03	+
4	7.23×10^{16}	−1.10	+

−78°C and positive at 55°C in agreement with theory. Thus the James-Lehman model is qualitatively verified by these experiments.

An idea of the magnitude of ζ_{limit} for Ge may be obtained from Eq. (1) and the experimental data. The values of n_A^0 for sample 1 of Table I and sample 4 of Table II may be used to bracket $(n_A)_{limit}$. At 55°C 7.23×10^{16} cm$^{-3}<(n_A)_{limit}<7.02\times10^{17}$ cm^{-3}, and from Eq. (1) it can be shown that 0.168 ev$>\zeta_{limit}>0.105$ ev. Further experiments designed to determine ζ_{limit} more exactly and to test the model more rigorously are underway.

* Consultant from Purdue University, Lafayette, Indiana.
† Now at the University of Virginia, Charlottesville, Virginia.
[1] V. A. Johnson and K. Lark-Horovitz, Phys. Rev. **76**, 442 (1949).
[2] Cleland, Crawford, Lark-Horovitz, Pigg, and Young, Phys. Rev. **83**, 312 (1951).
[3] K. Lark-Horovitz, Appendix II (Lehman and James) International Conference on Semiconductors, Reading, 1950; see also G. W. Lehman, Phys. Rev. **81**, 321 (1951).
[4] The samples used in these investigations were kindly prepared and furnished by Miss Louise Roth, Purdue University.

Measurement of the Cross Section for the Reaction T+T→He^4+2n+11.4 Mev*

H. M. AGNEW, W. T. LELAND, H. V. ARGO, R. W. CREWS, A. H. HEMMENDINGER, W. E. SCOTT, AND R. F. TASCHEK
Los Alamos Scientific Laboratory, Los Alamos, New Mexico
(Received October 1, 1951)

A MEASUREMENT of the cross section for the reaction

T+T→He^4+2n+11.4 Mev

has been made using the 2.5-Mev Los Alamos electrostatic generator. An analyzed beam of tritons was passed through a 1/20-mil Ni foil into a thin gaseous tritium target.[1] The triton energy was varied from 40 kev to 2.22 Mev. The average triton energy in the center of the target was calculated by taking into account the energy loss in the Ni foil and the target gas. At triton energies below 100 kev the straggling is quite large, and the results at this low energy are presented only to show the general shape of the cross section. The neutrons produced from the reaction were detected with a "long counter."[2]

The neutron spectrum from the reaction has been examined in some detail,[3,4] and except for the presence of two rather broad peaks at 8.1 and 10.4 Mev, there seem to be equal numbers of neutrons per energy interval up to 11 Mev, with few neutrons having an energy greater than 11.5 Mev. The neutron detector had a response which was essentially flat up to 5 Mev and had an efficiency at 14 Mev which was 67 percent of that at 5 Mev. However, since the neutron spectrum from the T+T reaction is similar to that obtained from the Ra−Be source which was used to calibrate the detector, no counter efficiency correction has been applied in computing the cross section.

The main difficulties encountered in this experiment were caused by the presence of background neutrons produced by the interaction of tritons with various materials present on defining slits, etc. It was found that at energies above 1 Mev a large number of neutrons were produced from the action of tritons on aluminum. For this reason 1/20-mil Ni foils instead of aluminum foils were used as windows between the acceleration tube and the target chamber. Backgrounds were taken with He^4 replacing the tritium in the target. Above 1.2 Mev the background neutron yield increased more rapidly than did the (T+T) reaction, and as a consequence the errors of the measurement increased markedly. Since the arc gas contained a high percentage of H_2, the triton beam of highest energy whose composition was known (there was no deuterium in the system) was the HT^+ beam. However, in order to reach higher energies it was necessary to use a mass 3 beam. The mass 3 beam, however, was composed of singly ionized triatomic hydrogen molecules as well as monatomic tritium ions. To correct the beam current measurement for the presence of the triatomic hydrogen molecules the ratio of the yield between singly ionized mass 4 and mass 3 beams was obtained for several energies between 1150 and 1350 kev, and the factor was applied to the data taken with the singly ionized mass 3 beam above 1.35 Mev. The ratio which was obtained was checked at the end of each run, and the beam composition was found to remain quite constant.

Figure 1 gives the differential cross section in millibarns per steradian at 0° for the reaction T+T→He^4+2n+11.4 Mev as determined by detecting the neutrons. If one wishes to obtain the number of neutrons produced, since there are two neutrons pro-

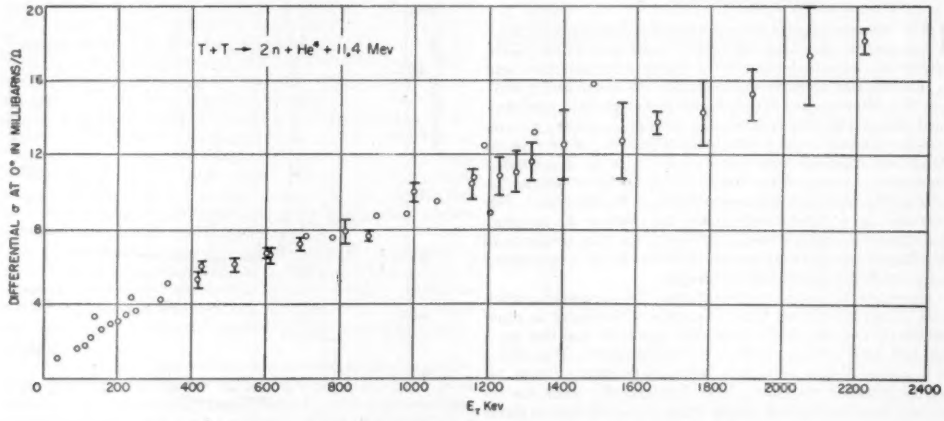

FIG. 1. Differential cross section in millibarns per steradian as determined with the neutron detector at 0° for the reaction T+T→He^4+2n+11.4 Mev.

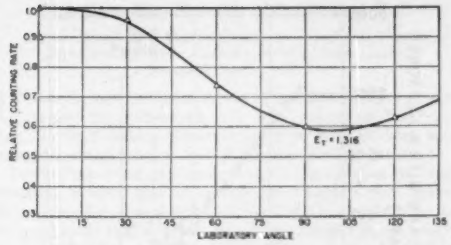

FIG. 2. Neutron angular distribution taken at a triton energy of 1.316 Mev.

duced per reaction, one multiplies the ordinate by two. The deviations indicated in Fig. 1 were obtained from the consistency of at least three sets of data, each of which was obtained under different operating conditions. The statistical error expected at any point should be less than 4 percent, and other errors are believed to be correspondingly small. The larger deviations are caused primarily by the large variable background.

A typical neutron angular distribution, taken at a triton energy of 1.316 Mev, is shown in Fig. 2. A similar shape was found for the entire energy range covered.

If the ordinate of Fig. 1 is multiplied by 10, one obtains a value for the total cross section of the reaction as a function of energy. The purity of the tritium used in the target was determined by means of mass spectrometric analysis, and the arc gas was analyzed for deuterium in the same manner. It was found that deuterium was present in quantities less than 0.02 percent as compared to the other hydrogen isotopes. The authors wish to thank Mr. Robert Potter and Dr. John Mosely for their assistance in the purity determinations.

* Work performed under the auspices of the AEC.
[1] Jarvis, Hemmendinger, Argo, and Taschek, Phys. Rev. **79**, 929 (1950).
[2] A. O. Hanson and J. L. McKibben, Phys. Rev. **72**, 673 (1947).
[3] W. T. Leland and H. M. Agnew, Phys. Rev. **82**, 559 (1951).
[4] Sanders, Allen, Almqvist, Dewan, and Pepper, Phys. Rev. **79**, 238 (1950).

The Anomalous Magnetoresistance of Bismuth at Low Temperatures

P. B. ALERS AND R. T. WEBBER
Naval Research Laboratory, Washington, D. C.
(Received September 26, 1951)

AN investigation of the magnetoresistance of bismuth at liquid helium temperatures was first carried out by de Haas, Blom, and Schubnikow,[1] who used single crystals of very high purity in fields ranging up to 22,000 gauss. These authors showed that for certain orientations of the crystal the resistance was not a simple function of the field, but that rather large anomalies appeared at fields of about 9000 gauss and 18,000 gauss. This anomalous behavior has been associated[2] with the susceptibility oscillations of the de Haas–van Alphen effect.[3]

We have extended the measurements of magnetoresistance of bismuth crystals to fields in excess of 60,000 gauss, supplied by a Bitter-type solenoid.[4] The specimens used in this investigation were monocrystalline cylindrical rods about 2 mm in diameter and 2-to-3 cm long prepared by the methods of Kapitza[5] and Schubnikow[6] from "spectroscopically pure" (Johnson and Matthey) bismuth. To improve the purity of the metal, each crystal was regrown several times using one end as a seed. After each growing the end of the specimen last to solidify was broken off and discarded. The angle between the trigonal axis of a specimen and the geometrical axis is given in Table I.

TABLE I. Characteristics of crystal specimens used. θ is the angle between the trigonal axis of the crystal and the geometrical axis of the specimen. Resistance ratio of the specimen of de Haas *et al.* (No. 4) is given for reference.

Crystal no.	θ	$R_{4.2°K}/R_{0°C}$
1	8°	3.0×10^{-3}
2	19°	5.5×10^{-3}
3	9°	4.8×10^{-3}
...	...	...
4	0.5°	3.0×10^{-3}

The rods were mounted transverse to the magnetic field. By means of a gear mechanism the specimen could be rotated about its own axis, thus allowing measurements to be made of the resistance as a function of the angle between the magnetic field and one of the binary axes. At fields below about 3000 gauss the resistance was a simple function of this angle, giving a maximum for the field perpendicular to a binary axis ($\phi=0°$), and minima for the field parallel to the adjacent binary axes ($\phi=\pm30°$). This is similar to the behavior at higher temperatures. At higher fields, the resistance became a very complex function of the angle ϕ, with several maxima between $\phi=\pm30°$. The most unusual behavior appeared in the vicinity of $\phi=0°$.

A plot of the resistance *vs* magnetic field at 4.2°K and $\phi=0°$ for three specimens is shown in Fig. 1. The de Haas data (with the ordinate drawn half scale) are given by the dashed line. Taking the resistance ratio $R_{4.2°K}/R_{0°C}$ to be a measure of the degree of purity and freedom from strain in the specimens,[7] it is evident from examination of Table I and Fig. 1 that purity has a strong influence on the magnitude of the magnetoresistive effect, but appears to have no great effect on the values of field intensity at which the anomalies appear. If this be the case, the difference between the results of de Haas *et al.*, and those reported here, may reside in the size of the specimens used. The previous work was done using a crystal of square cross section, 7 mm on a side and 22 mm in length, while the crystals used in these experiments were not more than 2 mm in diameter and between 2-and-3 cm long.

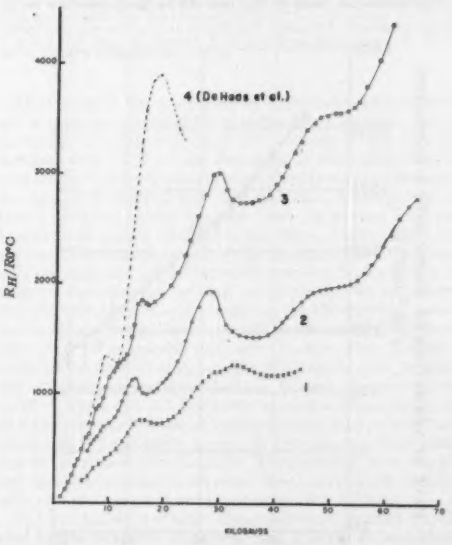

FIG. 1. Magnetoresistance of several bismuth crystals in transverse fields at 4.2°K. $\phi=0°$, i.e., the magnetic field is perpendicular to one of the binary axes. The values of θ (the angle between the trigonal axis and the geometrical axis of the specimen) are given in Table I. Dotted curve represents the data of de Haas, Blom, and Schubnikow (reference 1), with the ordinate drawn half scale.

We plan to extend these measurements to still higher magnetic fields and to publish more complete results in a later issue of this journal.

[1] de Haas, Blom, and Schubnikow, Physica **2**, 907 (1935).
[2] B. Davydov and I. Pomeranchuk, J. Phys. (U.S.S.R.) **2**, 147 (1940).
[3] W. J. de Haas and P. M. van Alphen, Leiden Comm. No. 212a (1930).
[4] F. Bitter, Rev. Sci. Instr. **10**, 373 (1939).
[5] P. Kapitza, Proc. Roy. Soc. (London) **A123**, 292 (1929).
[6] L. W. Schubnikow, Proc. Akad. Sci Amsterdam **33**, 327 (1930).
[7] L. W. Schubnikow and W. J. de Haas, Proc. Acad. Sci. Amsterdam **33**, 350 (1930).

A Search for a Diurnal Variation in the Rate of Star Formation

G. W. Anderson and J. E. Naugle
University of Minnesota, Minneapolis, Minnesota
(Received October 4, 1951)

THE rate of formation of stars with $\geqslant 3$ gray tracks has been measured at night and during the day in Ilford G-5 nuclear research emulsions at balloon altitudes. A gray track is defined as a track whose grain density is $\geqslant 1.5$ times that of a singly charged particle at minimum ionization.

The daytime rate was measured in plates exposed September 27, 1949, at an altitude of 90,000 feet and at a geomagnetic latitude of 55°N. Two identical stacks were flown; one was released when the balloon reached altitude, the other remained at a depth of 18 g/cm² for 7.4 hours. Both stacks were flown near the top of thin-walled aluminum spheres. The drop-load sphere also contained the radio release mechanism and the main load sphere also contained a cloud chamber.

Plates from both stacks were scanned under a magnification of 144 for all stars with $\geqslant 3$ gray prongs. The star density in the drop-load plates was used to correct for stars formed in the other stack during ascent and descent. The integral prong spectrum thus corrected is plotted in Fig. 1. The spectrum shows the characteristic break at $N_T \cong 8$ reported by other workers.[1] Comparison of the star formation rates in the two stacks gave evidence for a transition effect with respect to altitude in the rate of formation of stars with 3, 4, and 5 prongs, as previously reported.[2,3]

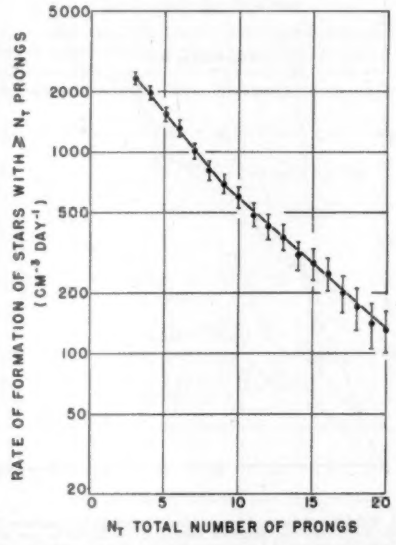

FIG. 1. Integral numbers *vs* prong spectrum of stars formed at 18 g/cm² during a daytime flight on September 27, 1949. Statistical errors ($=100\,N^{-\frac{1}{2}}$ percent for N stars) are shown.

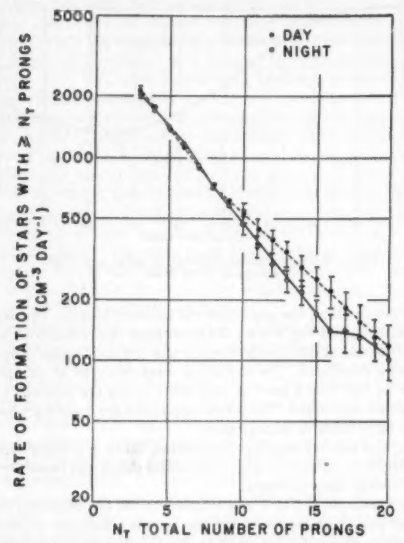

FIG. 2. Comparison of daytime (September 27, 1949, at 18 g/cm² Gross-transformed to 25 g/cm²) and nighttime (October 26, 1949, at 25 g/cm²) integral numbers *vs* prong spectra.

The nighttime rate was measured in plates flown October 26, 1949. This flight reached an altitude of 80,000 feet at 1620 CST and was released 14.9 hours later. The time between sunset and sunrise at the balloon's altitude was 12.2 hours, or 82 percent of the total time at altitude. The mean level altitude was 82,000 feet (25 g/cm² depth). During the flight the balloon traveled approximately along parallel 54.5 geomagnetic latitude. By assuming that the star producing radiation for all sizes of stars is absorbed exponentially in the atmosphere with a mean free path of 120 g/cm², the number of stars formed during the ascent and descent as calculated and subtracted from that observed in the plates. However, because of the long exposure and the rapid rise of the balloon, the actual star formation rates are insensitive to the manner of correction for ascent and descent. The corrected nighttime integral prong spectrum is plotted in Fig. 2.

In order to compare the night with the day rates we make the usual assumption that the star producing radiation is isotropic at the top of the atmosphere, and we transform the daytime rates at 18 g/cm² to rates corresponding to 25 g/cm² by means of the Gross transformation. These rates are plotted in Fig. 2. Within the statistical errors no change appears from day to night in either the magnitude of the rates or the shape of the prong spectrum. These results are in agreement with those of Lord and Schein.[4]

Rates for proton- and neutron-induced stars have also been calculated separately; they also show rough constancy from day to night, but with less statistical and experimental certainty.

The star formation rates found in this and in other surveys at Minnesota are very close to those of Lord[3] at 15 g/cm², but the rate of formation of $\geqslant 3$ prong stars is about 0.7 of that found by Shapiro and co-workers.[5]

[1] E. P. George and A. O. Jason, Proc. Phys. Soc. (London) **A62**, 243 (1949); M. Birnbaum *et al.*, Phys. Rev. **83**, 874 (1951).
[2] Freier, Ney, and Oppenheimer, Phys. Rev. **75**, 1451 (1949).
[3] J. J. Lord, Phys. Rev. **81**, 901 (1951).
[4] J. J. Lord and M. Schein, Phys. Rev. **78**, 484 (1950).
[5] M. Shapiro (private communication).

The Beta-Ray Spectra of Tm^{170} and RaE

SEITARO NAKAMURA, MINORU UMEZAWA, AND HISAO TAKEBE
Department of Physics, University of Tokyo, Tokyo, Japan
(Received August 7, 1951)

IN order to test the Fermi theory of β-decay, we have tried to interpret the well-investigated β-ray spectra of Tm^{170} and RaE. We shall assume these spectra to be first-forbidden, as a reasonable consequence of their ft values and selection rules.

Tm^{170}: Fraser[1] had previously reported the complex spectrum consisting of 0.970-Mev and 0.886-Mev groups. Later, Agnew[2] showed that the allowed Fermi plot of Tm^{170} is straight from the end point down to $W=1.8\ mc^2$, from where the plot shows a slight downward bending, and also that an 85-kev γ-ray is emitted by the decay product. This indicates that the β-ray in question is a single spectrum. As was pointed out by Agnew, the first-forbidden correction factors cannot individually reproduce the observed spectrum, and only the possibility of a mixture of several matrix elements remains. In the tensor and vector interactions the forbidden correction factors will be

$$C_{1T}\Big/\left|\int\beta\boldsymbol{\sigma}\times\mathbf{r}\right|^2=L_0k_{1T}^2+(\tfrac{1}{9}K^2L_0+\tfrac{1}{3}L_1+M_0-\tfrac{2}{3}KN_0)-2k_{1T}(\tfrac{1}{3}KL_0-N_0),\quad(1a)$$

$$C_{1V}\Big/\left|\int\mathbf{r}\right|^2=L_0k_{1V}^2+(\tfrac{1}{9}K^2L_0+2L_1+M_0-\tfrac{2}{3}KN_0)-2k_{1V}(\tfrac{1}{3}KL_0-N_0),\quad(1b)$$

where

$$k_{1T}=\left|\int\beta\boldsymbol{\alpha}\right|\Big/\left|\int\beta\boldsymbol{\sigma}\times\mathbf{r}\right|,\qquad(2a)$$

$$k_{1V}=\left|\int\boldsymbol{\alpha}\right|\Big/\left|\int\mathbf{r}\right|,\qquad(2b)$$

if the selection rule ($\Delta J=\pm1$, parity change yes) holds. L_0, L_1, M_0, N_0 are functions of the momentum of the electron and the nuclear charge Z, which are given by Konopinski and Uhlenbeck,[3] and K is the momentum of the neutrino. If one takes $k_{1T}=10.3$ or $k_{1V}=10.5$, a straight-line Fermi plot is obtained from $W_0=2.95\ mc^2$ down to $W=1.37\ mc^2$ (see Figs. 1 and 2). Since $\alpha Z\ll1$ does not hold for Tm^{170}, the accurate formulas given Osoba[4] and Davidson[5] are used in evaluating Eqs. (1a) and (1b). Although the observed deviation of this spectrum from the allowed form may happen to be slightly modified in the future, it seems likely that the beautiful agreement between the experiment and the theory, obtained under our interpretation by assuming (1a) or (1b), is not illusory. According to the shell model theory, we may expect that the 69th proton is $s_{\frac{1}{2}}$ or d-state and the 101st neutron p-state, and therefore the resultant state will be odd parity. The ground state of $_{70}Yb^{170}$ is probably even with spin zero. Thus, in order to establish the required selection rule, it is inferred that the spin 3 and odd parity ground state of $_{69}Tm^{170}$ decays to the excited state of Yb^{170}, whose spin is 2 and parity is even, accompanied by the 85.4-kev gamma-ray emission leading to the ground state of Yb^{170}, whose spin is 0 and parity is even. In this case, the direct transition to the ground state would be third-forbidden $\Delta J=\pm3$, yes, and therefore could not be observed. The present view is consistent with that of Agnew and at variance with that of Fraser.

The ft value of Tm^{170} under the present interpretation is evaluated by the forbidden f-function,[6] and is found to be 4.2×10^9. Since this f-function is calculated under the approximation $F(\pm Z, W)=1$, the exact f-function obtained with due consideration to the coulomb corrections may, by our crude estimation, change the above value by a factor of about 15.

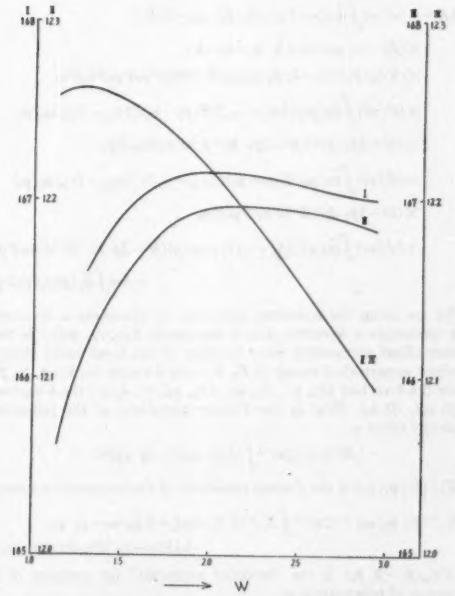

FIG. 1. The first-forbidden correction factors in the tensor interaction C_{1T} and vector interaction C_{1V} for Tm^{170}. I and II represent the correction factors corresponding to $\int\beta\boldsymbol{\sigma}\times\mathbf{r}$ and $\{(\int\beta\boldsymbol{\sigma}\times\mathbf{r})^*\int\beta\boldsymbol{\alpha}+\text{c.c.}\}$, III and IV to $\int\mathbf{r}$ and $\{(\int\mathbf{r})^*\int\boldsymbol{\alpha}+\text{c.c.}\}$, respectively.

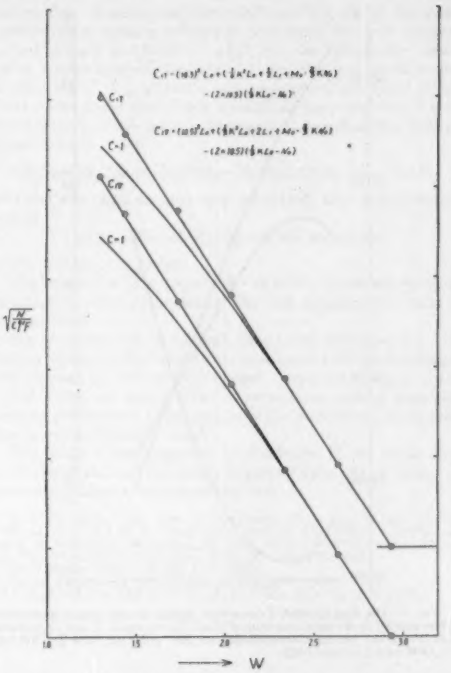

FIG. 2. Tm^{170}. The forbidden Fermi plot in C_{1T} is straight from $W_0=2.95\ mc^2$ down to $W=1.5\ mc^2$, if one takes $k_{1T}=10.3$; and the forbidden Fermi plot in C_{1V} is straight from W_0 down to $W=1.3\ mc^2$, if we take $k_{1V}=10.5$. It is to be noted that the straight-line portion is far greater for the forbidden plot C_{1T} or C_{1V} than the allowed Fermi plot. The choice between C_{1T} and C_{1V} may be obtained from the $\beta-\gamma$ experiments (C. S. Wu, Revs. Modern Phys. 22, 386 (1951)).

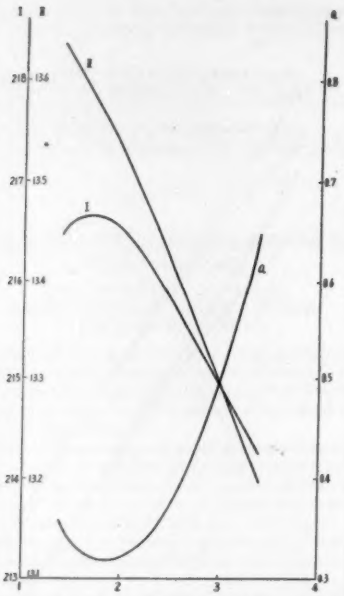

FIG. 3. The first-forbidden correction factors in the tensor interaction, to be applied to the beta-spectrum of RaE. The curves a, I, and II represent the correction factors corresponding to B_{ij}, $\int\beta\boldsymbol{\sigma}\times\mathbf{r}$, and $\{(\int\beta\boldsymbol{\sigma}\times\mathbf{r})^*\times\int\beta\boldsymbol{\alpha}+\text{c.c.}\}$, respectively.

RaE: In 1941, Konopinski and Uhlenbeck[6,7] explained the deviation of the spectrum of RaE from the allowed form by using mixtures of the matrix elements involved in the Fermi theory with vector or tensor interactions. The present analysis, however, leads to a criticism of their viewpoint, for the following two reasons: (1) According to Konopinski and Uhlenbeck, the beta-decay of RaE is classified as a second-forbidden transition. Since the decay of ${}_{83}\mathrm{RaE}^{210}$ to the ground state of ${}_{84}\mathrm{Po}^{210}$ is, on the current version of the shell model ($g_{9/2}$ or $i_{11/2}$, $h_{9/2}$)$\rightarrow$(even, even) and therefore involves a parity change, one would expect that the transition is first-forbidden. (2) The conventional ft value of RaE is, according to the table of Feingold,[8] 1.1×10^8. On the other hand, the recent analysis of the second-forbidden beta-decay of Cl^{36},[9] Tc^{99}, Sb^{124},[10] and Cs^{137},[11] by means of a linear combination of the matrix elements involved in the tensor or vector interactions, indicates that the conventional ft values for these beta-decays are $10^{12}\sim10^{13}$. When the ft values[12] are corrected by the forbidden f-functions, they do not change very drastically. This speaks strongly in favor of the classification of RaE as first-forbidden, not second-forbidden. In fact, for the beta-decays which have an "a" type spectrum and obey the selection rule $\Delta J=\pm2$, parity change yes, Taketani[13] and Davidson[5] found $10^7\approx10^8$ for the ft values, with little Z dependence. Although Konopinski and Uhlenbeck had obtained negative results, we reinvestigated, therefore, the first-forbidden cases for RaE, since the exact expansion of the coulomb correction in the same way as that of Tm^{170} may introduce some alterations.

It is shown that among the transitions involving parity change, (1) $\Delta J=\pm2$ is excluded. As is shown in Fig. 3, the correction factor of "a" type is uniquely determined and the predicted shape is evidently at variance with experiment. (2) $\Delta J=0$ is also rejected. Since the ground state of Po^{210} is presumably spin 0 and even, the nuclear matrix element allowed in the transition is determined to be $\int\beta\boldsymbol{\sigma}\cdot\mathbf{r}$. The correction factor corresponding to $\int\beta\boldsymbol{\sigma}\cdot\mathbf{r}$ is almost energy-independent, which cannot be fitted to experiment. (3) $\Delta J=\pm1$ involves a linear combination of several matrix elements, i.e., $\int\beta\boldsymbol{\sigma}\times\mathbf{r}$ and $\int\beta\boldsymbol{\alpha}$ in the tensor interaction, and $\int\mathbf{r}$ and $\int\boldsymbol{\alpha}$ in the vector interaction. Any real value for the ratio of the nuclear matrix elements, k_{1T} or k_{1V}, cannot yield the required shape of RaE (see Fig. 3).

[1] J. S. Fraser, Phys. Rev. **76**, 1540 (1949).
[2] H. M. Agnew, Phys. Rev. **77**, 655 (1950); see also D. Saxon and J. Richards, Phys. Rev. **76**, 186 (1949).
[3] E. J. Konopinski and E. Uhlenbeck, Phys. Rev. **60**, 308 (1941). See page 315.
[4] J. Davidson, Phys. Rev. **82**, 48 (1951).
[5] J. Davidson, Phys. Rev. **82**, 48 (1951).
[6] Nakamura, Shima, and Kobayashi, J. Phys. Soc. **4**, 166 (1949).
[7] E. J. Konopinski, Revs. Modern Phys. **15**, 209 (1943).
[8] A. M. Feingold, Revs. Modern Phys. **23**, 10 (1951).
[9] C. S. Wu and L. Feldmen, Phys. Rev. **82**, 457 (1951); H. W. Fulbright and J. C. D. Milton, Phys. Rev. **82**, 274 (1951).
[10] Nakamura, Umezawa, and Takebe, Phys. Rev. **83**, 1273 (1951); also Prog. Theoret. Phys. **6**, No. 4 (1951).
[11] L. M. Langer and R. J. D. Moffat, Phys. Rev. **82**, 635 (1951).
[12] Taketani, Nakamura, Umezawa, Ono, and Yamaguchi, Phys. Rev. **82**, 441 (1951).

Relativistic Corrections to the Lamb Shift

MICHEL BARANGER
Cornell University, Ithaca, New York
(Received June 18, 1951)

THE α^5 corrections to the Lamb shift have been partly calculated, using a decomposition of terms due to Feynman. The one-photon part of the Lamb shift corresponds to the diagrams of Fig. 1, and can be written, according to Feynman's standard methods,[1]

$$\Delta E=e^2\int\bar\psi_0(2)\gamma_\mu K_+{}^V(2,1)\gamma_\mu\psi_0(1)\delta_+(s_{21}{}^2)d^3\mathbf{x}_1d^3\mathbf{x}_2d(t_2-t_1)$$
$$-\Delta m\int\bar\psi_0(1)\psi_0(1)d^3\mathbf{x}_1.$$

By going to momentum space, and making an algebraic rearrangement of terms, this can be decomposed in the following way:

$$\Delta E=-(e^2/\pi)\int\bar\phi_0(\mathbf{p}_2)\langle Va\rangle_\mu(p_2,\,p_2+s_2-k)K_+{}^V$$
$$\times(E_0-\omega;\,\mathbf{p}_2+\mathbf{s}_2-\mathbf{k},\,\mathbf{p}_1+\mathbf{s}_1-\mathbf{k})$$
$$\times\langle Ve\rangle_\mu(p_1+s_1-k,\,p_1)\phi_0(\mathbf{p}_1)k^{-2}d^4k_Fd^3\mathbf{p}_1d^3\mathbf{p}_2d^3\mathbf{s}_1d^3\mathbf{s}_2$$
$$+(e^2/\pi i)\int\bar\phi_0(\mathbf{p}_2)(2p_{2\mu}-\gamma_\mu\not{k})\mathfrak{V}(\mathbf{p}_2-\mathbf{p}_1)(2p_{1\mu}-\not{k}\gamma_\mu)\phi_0(\mathbf{p}_1)$$
$$\times(k^2-2p_2\cdot k)^{-1}(k^2-2p_1\cdot k)^{-1}k^{-2}d^4k_Fd^3\mathbf{p}_1d^3\mathbf{p}_2$$
$$-(e^2/\pi i)\int\bar\phi_0(\mathbf{p}_2)\mathfrak{V}(\mathbf{p}_2-\mathbf{p}_1)(2p_{1\mu}-\gamma_\mu\not{k})(2p_{1\mu}-\not{k}\gamma_\mu)\phi_0(\mathbf{p}_1)$$
$$\times(k^2-2p_1\cdot k)^{-2}k^{-2}d^4k_Fd^3\mathbf{p}_1d^3\mathbf{p}_2$$
$$+(e^2/\pi i)\int\bar\phi_0(\mathbf{p})(2p_\mu-\gamma_\mu\not{k})\gamma_\mu\phi_0(\mathbf{p})(k^2-2p\cdot k)^{-1}k^{-2}d^4k_Fd^3\mathbf{p}$$
$$-\Delta m\int\bar\phi_0(\mathbf{p})\phi_0(\mathbf{p})d^3\mathbf{p}.$$

We are using the following notations: $\mathbf{a}$ represents a 3-vector, a represents a 4-vector, and $\not{a}$ represents $\Sigma_\mu a_\mu\gamma_\mu$. $\phi_0(\mathbf{p})$ is the normalized momentum wave function of the level under study, whose unperturbed energy is E_0. k is the 4-vector $(\omega,\,\mathbf{k})$. p, p_1, p_2 are the 4-vectors $(E_0,\,\mathbf{p})$, $(E_0,\,\mathbf{p}_1)$, $(E_0,\,\mathbf{p}_2)$. s_1, s_2 are the 4-vectors $(0,\,\mathbf{s}_1)$, $(0,\,\mathbf{s}_2)$. $\mathfrak{V}(\mathbf{q})$ is the Fourier transform of the potential energy times γ_4,

$$\mathfrak{V}(\mathbf{q})=(2\pi)^{-3}\int\mathfrak{V}(\mathbf{x})\exp(-i\mathbf{q}\cdot\mathbf{x})d^3\mathbf{x}.$$

$K_+{}^V(E;\,\mathbf{p}_1,\,\mathbf{p}_2)$ is the Fourier transform of the propagation kernel

$$K_+{}^V(E;\,\mathbf{p}_1,\,\mathbf{p}_2)=(2\pi)^{-3}\int K_+{}^V(2,1)\exp[-i(\mathbf{p}_2\cdot\mathbf{x}_2-\mathbf{p}_1\cdot\mathbf{x}_1)$$
$$+iE(t_2-t_1)]d^3\mathbf{x}_2d^3\mathbf{x}_1d(t_2-t_1).$$

$\langle Ve\rangle_\mu(p_f-k,\,p_i)$ is the "modified potential" for emission of a photon of polarization μ,

$$\langle Ve\rangle_\mu(p_f-k,\,p_i)=\mathfrak{V}(\mathbf{p}_f-\mathbf{p}_i)(2p_{i\mu}-\not{k}\gamma_\mu)(k^2-2p_i\cdot k)^{-1}$$
$$-(2p_{f\mu}-\not{k}\gamma_\mu)\mathfrak{V}(\mathbf{p}_f-\mathbf{p}_i)(k^2-2p_f\cdot k)^{-1},$$

and makes transitions from momentum $\mathfrak{p}_i$ to momentum $\mathfrak{p}_f-\mathfrak{k}$, $\mathfrak{p}_i$ and $\mathfrak{p}_f$ having the same time component E_0. $\langle Va\rangle_\mu(\mathfrak{p}_f, \mathfrak{p}_i-\mathfrak{k})$ is the modified potential for absorption

$$\langle Va\rangle_\mu(\mathfrak{p}_f, \mathfrak{p}_i-\mathfrak{k}) = -\mathfrak{B}(\mathfrak{p}_f-\mathfrak{p}_i)(2p_{i\mu}-\gamma_\mu\mathfrak{k})(\mathfrak{k}^2-2\mathfrak{p}_i\cdot\mathfrak{k})^{-1} + (2p_{f\mu}-\gamma_\mu\mathfrak{k})\mathfrak{B}(\mathfrak{p}_f-\mathfrak{p}_i)(\mathfrak{k}^2-2\mathfrak{p}_f\cdot\mathfrak{k})^{-1}$$

and makes transitions from $\mathfrak{p}_i-\mathfrak{k}$ to $\mathfrak{p}_f$.

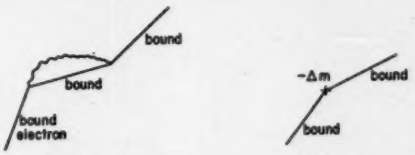

FIG. 1. Feynman diagrams for the one-photon part of the Lamb shift.

The last 4 terms in ΔE are identical with the "first-order Lamb shift," evaluated by several authors,[2] except for the fact that the momenta are not free, $\mathfrak{p}_1^2$, $\mathfrak{p}_2^2$, $\mathfrak{p}^2\neq m^2$, and $\mathfrak{p}\phi_0\neq m\phi_0$. This fact, when taken into account, introduces a term proportional to the square of the potential, and therefore not gauge-invariant. It has been shown by Bethe that this term is compensated by an equal and opposite one coming from the first term in ΔE, or "second-order Lamb shift."

After subtraction of this nongauge-invariant part, the second-order Lamb shift has been calculated by taking a comparison operator

$$R_\mu=(m\omega)^{-1}\nabla_\mu V \quad \text{for} \quad \mu=1, 2, 3$$

and writing: Second-order Lamb shift $=\langle\langle Va\rangle_\mu, \langle Va\rangle_\mu\rangle$, the intermediary state being a relativistic free state, and with electron at rest initially and finally; $-(R_\mu^*, R_\mu)$, the intermediary state being a nonrelativistic free state, electron at rest initially and finally; $+(R_\mu^*, R_\mu)$, all states being nonrelativistic bound states. It has been found that this is a sufficient approximation if only terms of order α^5 are desired. The last part is nothing but Bethe's Lamb shift[3]

$$(2e^2/3\pi m^2)\Sigma_n|(\phi_n|\mathfrak{p}|\phi_0)|^2(E_n-E_0)[\ln(\lambda/2|E_n-E_0|)+5/6].$$

The first two parts we have now calculated; they give a correction of

$$(1+11/128-\ln 2/2)\alpha^4\,\text{Ry}=6.894 \text{ megacycles}$$

to the $2s$ state of hydrogen.

This brings the total Lamb shift[4] to 1058.3 Mc, when vacuum polarization terms are included. The best experimental value is 1061 ± 2 Mc.[5]

The α^5 corrections to the first-order Lamb shift have not yet been investigated. However, in the summer of 1950 Kroll thought that there could be none, the highest corrections being of order $\alpha^2\ln\alpha$. There are several other α^5 corrections, coming from the vacuum polarization term, and from the two-photon term, but they are probably rather small.

This problem was suggested by Professors H. A. Bethe and R. P. Feynman, and the author is greatly indebted to them for continued guidance throughout the work.

[1] R. P. Feynman, Phys. Rev. **76**, 749 (1949); Phys. Rev. **76**, 769 (1949).
[2] N. H. Kroll and W. E. Lamb, Phys. Rev. **75**, 388 (1949); J. B. French and V. F. Weisskopf, Phys. Rev. **75**, 1240 (1949); R. P. Feynman, Phys. Rev. **76**, 777 (1949); J. Schwinger, Phys. Rev. **76**, 790 (1949).
[3] H. A. Bethe, Phys. Rev. **72**, 339 (1947).
[4] Bethe, Brown, and Stehn, Phys. Rev. **77**, 370 (1950).
[5] R. C. Retherford and W. E. Lamb, Jr., Phys. Rev. **75**, 1325 (1949).